# Recognition of DNA Junctions by Metallo-Supramolecular Complexes and their Cellular Delivery by Spherical Nucleic Acids


UNIVERSITY OF BIRMINGHAM

**Hugo David Williams**

A thesis submitted to the University of Birmingham for the degree of

Doctor of Philosophy

School of Chemistry

College of Engineering and Physical Sciences

University of Birmingham

December 2023

# Abstract

The work presented in this thesis investigates the binding of non-canonical DNA structures by a range of metallo-supramolecular structures. The DNA binding properties of a palladium tetra-stranded helicate is investigated and it's platinum analogue (PtCyl) is synthesised for the first time. Both the platinum and palladium complexes bind and stabilise DNA 3WJ and 4WJ structures. The platinum complex displays more effective binding to DNA structures due to its enhanced stability in buffered solution. The B-DNA and junction binding properties of this PtCyl and two other known junction binding agents (NiP and AuPill) are compared through several biophysical studies. These studies reveal insights into the structural properties of the complexes that favour junction binding and also the surprisingly high selectivity of PtCyl for DNA 3WJ structures. The binding affinity of the PtCyl and a three stranded dinuclear nickel supramolecular complex (NiP) for a DNA 3WJ structure are quantified through the use of isothermal titration calorimetry. Mass spectrometry is investigated as a possible method for studying the interactions of these supramolecular metal complexes with DNA structures.

Spherical nucleic acids (SNAs) are studied as a potential vehicle for the delivery of these supramolecular metal complexes. SNAs are successfully synthesised and loaded with the NiP and PtCyl. The gold-SNA nanoparticles are able to release the metal complexes in the presence of their preferred binding target, DNA junctions. Efforts were made to increase the loading of the metal complexes on the nanoparticles, with limited success. Preliminary cell studies indicate very little toxicity of these systems which is likely due to the low loading of the complexes achieved.

# Acknowledgements

I would like to thank my supervisor, Mike Hannon, for his guidance throughout my time at the University of Birmingham. I would also like to thank the Physical Sciences for Health CDT for the opportunity to carry out my research and for the invaluable foundational year of study which it provided. The CDT opened my eyes to the broad range of research which is carried out at the University of Birmingham and connected me with a cohort which spanned the entire breadth of life sciences research. I would like to thank the EPSRC for funding my PhD research.

I would not have progressed through my PhD without the support of all the Hannon group members. I would like to give special thanks to James, Cat, and Sam for keeping me sane throughout this process, and helping with my research whenever possible. The shared coffee, cake, games, and even gigs made my time at the University of Birmingham truly memorable.

All the technical staff at the University of Birmingham have been very helpful over the years, teaching me how to carry out several complex techniques which were new to me before I began this endeavour. I would like to thank Trevor for training on various instruments and always being happy to help solve instrumentation issues. I would also like to thank Chris for all his help teaching me how to use mass spectrometry, and his endless patients for me and the entire Hannon group. The conversations about research, and everyday chats were always appreciated.

Finally, I need to thank my partner Emily for believing in me, and supporting me through some of the best (and most stressful) years of my life. I can't wait to see what comes next.

# Publications

1. James S. Craig, Larry Melidis, Hugo D. Williams, Samuel J. Dettmer, Alexandra A. Heidecker, Philipp J. Altmann, Shengyang Guan, Callum Campbell, Douglas F. Browning, Roland K. O. Sigel, Silke Johannsen, Ross T. Egan, Brech Aikman, Angela Casini, Alexander Pöthig, and Michael J. Hannon, Organometallic Pillarplexes That Bind DNA 4-Way Holliday Junctions and Forks, *Journal of the American Chemical Society,* **2023**, *145* (25), 13570-13580, DOI: 10.1021/jacs.3c00118
2. Hugo D. Williams, Samuel J. Dettmer, Lazaros Melidis, Nikolas J. Hodges, and Michael J. Hannon, DNA junction binding of a platinum tetra-stranded cylinder (Manuscript to be submitted)
3. Samuel J. Dettmer, Hugo D. Williams, and Michael J. Hannon, Supramolecular Recognition of a DNA Four Way Junction by an $M_2L_4$ Metallo-cage, inspired by a simulation guided design approach (Manuscript submitted)

# Abbreviations

| | |
|---|---|
| ACN | Acetonitrile |
| AuPill | Gold pillarplex |
| B-DNA | B for DNA |
| bp | base pair |
| CD | Circular dichroism |
| $CD_3CN$ | Deuterated acetonitrile |
| COSY | $^1H$-$^1H$ correlation spectroscopy |
| CT | Computed tomography |
| CTAC | cetyltrimethylammonium chloride |
| CTAB | cetyltrimethylammonium bromide |
| Ct-DNA | calf thymus DNA |
| Da | Daltons |
| DLS | Dynamic light scattering |
| DMSO | Dimethyl sulphoxide |
| DNA | Deoxyribonucleic acid |
| dsDNA | double stranded DNA |
| ESI-MS | Electrospray ionisation mass spectrometry |
| EtBr | Ethidium bromide |
| Eqv | Equivalents |
| FRET | Föster resonance energy transfer |
| g | Grams |
| G4 | g-quadruplex |
| HSQC | Heteronuclear single quantum coherence |
| ICD | Induced circular dichroism |
| ICP-MS | Inductively coupled plasma mass spectrometry |
| ILD | Induced linear dichroism |
| ITC | Isothermal titration calorimetry |
| K | Kelvin |
| LD | Linear dichroism |
| MeOH | Methanol |
| ml | Millilitre |
| MS | Mass spectrometry |
| MWCO | Molecular weight cut off |
| m/z | mass to charge ratio |

| | |
|---|---|
| NiP | Nickel parent cylinder |
| nM | Nanomolar |
| nm | Nanometre |
| NMR | Nuclear magnetic resonance |
| Oligo | Oligonucleotide |
| PAGE | Polyacrylamide gel electrophoresis |
| PDI | Polydispersity index |
| PET | Positron emission tomography |
| ppb | parts per billion |
| ppm | parts per million |
| PtCyl | $Pt_2(L_1)_4(NO_3)_4$ complex |
| p3WJ | pseudo three-way junction |
| p4WJ | pseudo four-way junction |
| RNA | Ribonucleic acid |
| ssDNA | single stranded DNA |
| TB | Tris-borate buffer |
| TEM | Transmission electron microscopy |
| UA | Uranyl acetate |
| UV-vis | Ultraviolet-visible |
| Y-fork | Forked DNA structure |
| µL | Microlitre |
| µM | Micromolar |
| 3WJ | three-way junction |
| 3WJ18 | three-way junction consisting of 18-mers |
| 3WJT6 | three-way junction on a single DNA strand with two thymine loops |
| 4WJ | four-way junction |

# Contents


Abstract ii
Acknowledgements iii
Publications iv
Abbreviations v
Contents vii
**Chapter 1** - Introduction 1
1.1 DNA 1
1.1.1 Helical DNA 2
1.1.2 DNA structures 3
1.2 Binding to DNA structures 8
1.2.1 Cisplatin (classical DNA crosslinkers) 9
1.2.2 Groove binding 12
1.2.3 Intercalation 17
1.2.4 G-quadruplex binding 22
1.2.5 DNA junctions and bulges 26
1.3 Gold nanoparticles 39
1.3.1 Uptake and Toxicity 40
1.3.2 Spherical nucleic acids 42
1.4 Thesis aims 53
1.5 References 55
**Chapter 2** - Palladium and platinum tetra-stranded complexes 70
2.1 Introduction 70
2.2 Synthesis 80
2.2.1 Synthesis of L1 80
2.2.2 Synthesis of $Pd_2(L_1)_4(BF_4)_4$ 81
2.2.3 Synthesis of $Pt_2(L_1)_4(NO_3)_4$ 83
2.3 Interaction with B-DNA 89
2.3.1 $Pd_2(L_1)_4(BF_4)_4$ interactions with B-DNA 90
2.3.2 $Pt_2(L_1)_4(NO_3)_4$ interactions with B-DNA 97
2.4 Junction binding 103
2.4.1 Junction binding of $Pd_2(L_1)_4(BF_4)_4$ 104
2.4.2 Junction binding of $Pt_2(L_1)_4(NO_3)_4$ 107
2.5 Molecular dynamics (MD) simulations 110
2.5.1 3WJ MD simulations 110
2.5.2 4WJ MD simulations 113
2.5.3. dsDNA MD simulations 115
2.6 Stability of complexes in buffer 116
2.6.1 Stability of $Pd_2(L_1)_4(BF_4)_4$ in buffer 116
2.6.2 Stability of $Pt_2(L_1)_4(NO_3)_4$ in buffer 117
2.7 Interaction of $Pt_2(L_1)_4(NO_3)_4$ with CB10 117
2.8 Conclusions 119
2.9 Future work 120
2.10 References 122
**Chapter 3** – Comparing DNA binding of three metal cylinders 128
3.1 Introduction 128
3.2 Fluorescence displacement assays 130
3.2.1 Ethidium bromide displacement 130
3.2.2 Hoechst 33258 displacement 134
3.3 Melting studies 139
3.3.1 DNA UV melting studies 140
3.3.2 RNA UV melting studies 144

3.3.3 FRET melting studies 147
3.4 PAGE competition experiments 150
3.5 PAGE RNA/DNA structure experiments 155
3.5.1 DNA 3WJ 155
3.5.2 DNA 4WJ 155
3.5.3 RNA 3WJ 161
3.5.4 RNA 4WJ 162
3.6 Mass spectrometry studies 168
3.6.1 PAGE 3WJT6 controls 168
3.6.2 MS of 3WJT6 with metal complexes 175
3.6.3 Competition of metal complexes binding to 3WJT6 181
3.7 PAGE of other DNA structures 185
3.7.1 DNA bulges 185
3.7.2 G-quadruplexes 188
3.8 Isothermal titration calorimetry 190
3.9 Conclusions 192
3.10 Future work 195
3.11 References 196
**Chapter 4** – Spherical nucleic acids for delivery of DNA junction binders 199
4.1 Introduction 199
4.2 Synthesis of gold-SNA 202
4.2.1 Synthesis of AuNP13dsDNA 202
4.2.2 3WJ PAGE release studies 212
4.2.3 LD of AuNP13dsDNANiP 221
4.2.4 4WJ PAGE gel 223
4.2.5 Increasing metal complex loading on AuNP13dsDNA 224
4.2.6 Agarose gel 233
4.2.7 ICP-MS 235
4.2.8 TEM of particles 236
4.2.9 Stability of particles 244
4.3 Biological studies 246
4.3.1 Uptake and cell fractionation 247
4.3.2 Cytotoxicity 248
4.4 Conclusions 249
4.5 Future work 250
4.6 References 251
**Chapter 5** – Conclusions and future work 254
5.1 Conclusions 254
5.2 Future work 256
5.3 References 260
**Chapter 6** – Experimental 261
6.1 Oligomers used thought thesis 261
6.2 Chapter 2 262
6.3 Chapter 3 267
6.4 Chapter 4 272
6.5 References 279
**Appendix** 280
A2 – Chapter 2 280
A3 – Chapter 3 288
A4 – Chapter 4 301
References 308

# Chapter 1 – Introduction

## 1.1 DNA

DNA is the polymeric chemical structure which holds all the information necessary for life in a sequence of nucleobases. Despite the critical role of DNA to cellular function and replication, its most common structure was not discovered until the mid-1950s, and to this day efforts are still being made to understand the importance and role of its more complex structures. DNA exists in cells mainly in a double helix structure, where two antiparallel strands of DNA are held together by intermolecular interactions. This double helix is in turn wrapped around histones to form chromatin in the nucleus which makes up our chromosomes.

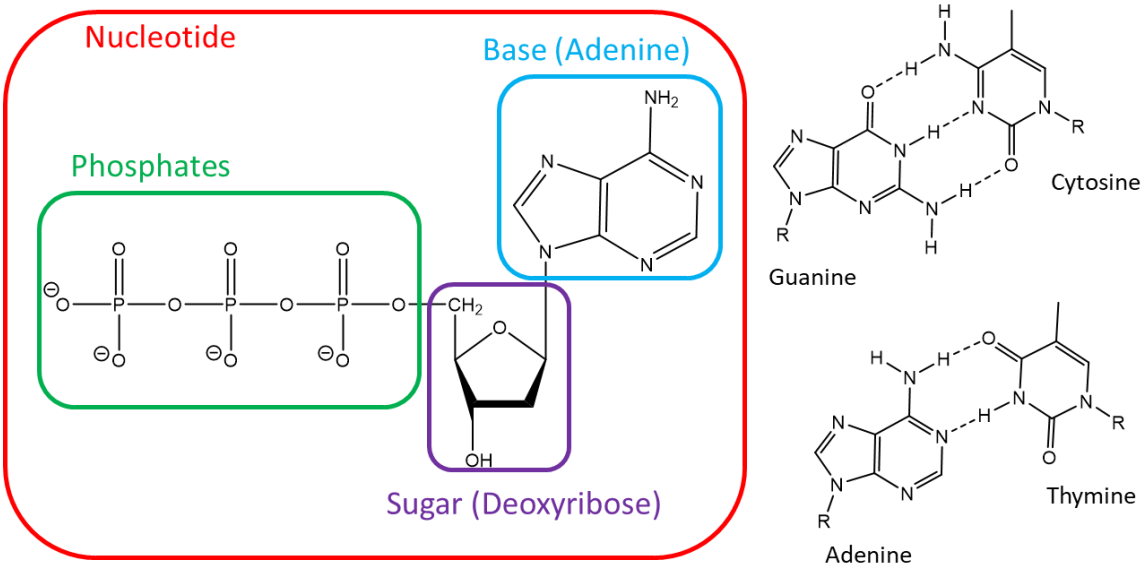


*Figure 1. The structure of a nucleotide (left) and the base pairing and hydrogen bonding in B-DNA of Adenine and Thymine, and Guanine and Cytosine.*

The DNA polymer is composed of three distinct regions, the phosphate, sugar, and nitrogenous base (Figure 1). These three components combined create what is termed a nucleotide. In DNA the sugar is a deoxyribose five membered ring, whereas RNA nucleotides contain a ribose. Individual nucleotides have three phosphate units linked together, but two of these phosphates are lost when nucleotides are joined together to form a polymer. The bases of DNA can be either Adenine, Thymine, Guanine, or Cytosine. The specific sequence of these DNA bases are the code which holds our genetic information. The hydrogen bonding afforded by these nitrogenous bases are what allow DNA do come together and form the classical double helix structure.

### 1.1.1 Helical DNA

There are three helical geometries for DNA which are found in nature, A-, B-, and Z-DNA (Figure 2). B-DNA is the most common structure for DNA to be found as in nature. The structure of B-DNA was discovered in 1953 by Watson and Crick using the X-ray diffraction pattern of DNA obtained by Rosalind Franklin and Raymond Gosling.[1, 2] B-DNA consists of a sugar phosphate backbone in a right-handed double helix structure with interlinked bases between the two strands. The arrangement of the base pairs in a double helix structure creates a major groove and minor groove which are 22 Å and 12 Å wide respectively. The helix completes a full turn around its axis every 10.5 base pairs giving a pitch of 34.3°. The pitch is largely determined by the pi-stacking interactions between bases which greatly stabilises the structure.

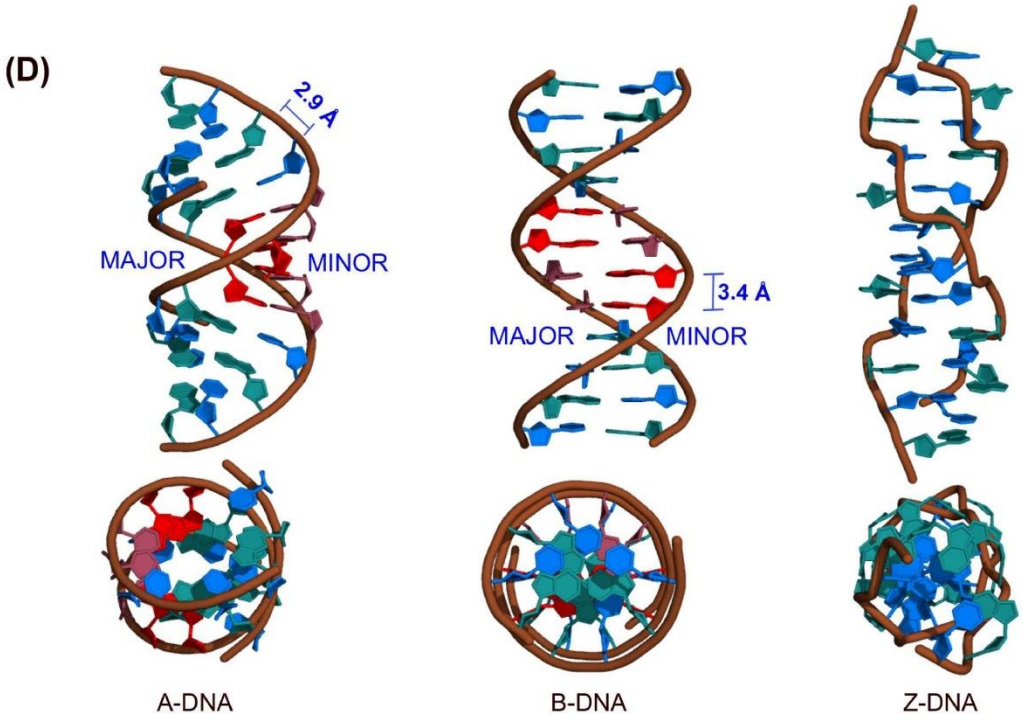


*Figure 2. Tertiary structure of A, B, and Z form DNA viewed from above and perpendicular to the axis. Adapted from publication referenced with permission.[3]*

The other form of right-handed helical DNA is A-DNA which was discovered by Rosalind Franklin and maintains a similar structure to B-DNA.[4] A-DNA has a more compact structure than B-DNA with a significantly deeper but narrower major groove, and a very broad and shallow minor groove.[5] Until relatively recently it was thought that A-DNA was not present in nature and was merely an artificial curiosity. Certain bacteria have been found to utilise this DNA structure to prevent DNA damage under

extreme conditions.[6] The A form may also be induced by the binding of proteins which exclude solvent molecules from the double helix.[7] RNA duplexes are exclusively in the A-form conformation due to the steric constraints placed on it by an extra hydroxyl group. RNA is very similar to DNA with the differences being that it replaces the base thymine with uracil, and the sugar is ribose in place of deoxyribose. RNA is transcribed from DNA and has a multitude of functions in the cell including protein synthesis, gene regulation, catalysis and more.[8, 9]

Z-DNA is made up of a left-handed helical structure with a zigzag backbone, this means that it does not have any distinct major or minor groves. Again, the biological importance of Z-DNA was widely questioned for many years until the identification of the Zα binding domain[10, 11] which was shown to selectively bind Z-DNA in a non-sequence specific way by NMR and X-ray studies.[12, 13] Z-DNA is unstable but is commonly formed when B-DNA is processed by enzymes, such as polymerases and helicases, to provide torsional strain relief. Z-DNA has been linked to several diseases such as alzheimers disease and systemic lupus erythromatosus.[14, 15]

### 1.1.2 DNA structures

The complexity of the DNA molecule allows for the formation of many different complex structures either by changes in external conditions, in the presence of specific proteins, or by careful control of the base sequence. By far the most widely studied non-canonical DNA structure is the G-quadruplex. G-quadruplexes were first identified after the observation that guanylic acid could self-assemble.[16] It was discovered that appropriate nucleic acid sequences would readily form guanine tetrads in solution through the formation of Hoogsteen base pairs to create planar arrays (Figure 3). The arrays can then stack together in the presence of appropriate cations (usually potassium) which stabilize the structure creating a G-quadruplex. The three-dimensional structure of g-quadruplexes was solved first by NMR in 1992,[17, 18] then x-ray crystallography in 1994.[19]

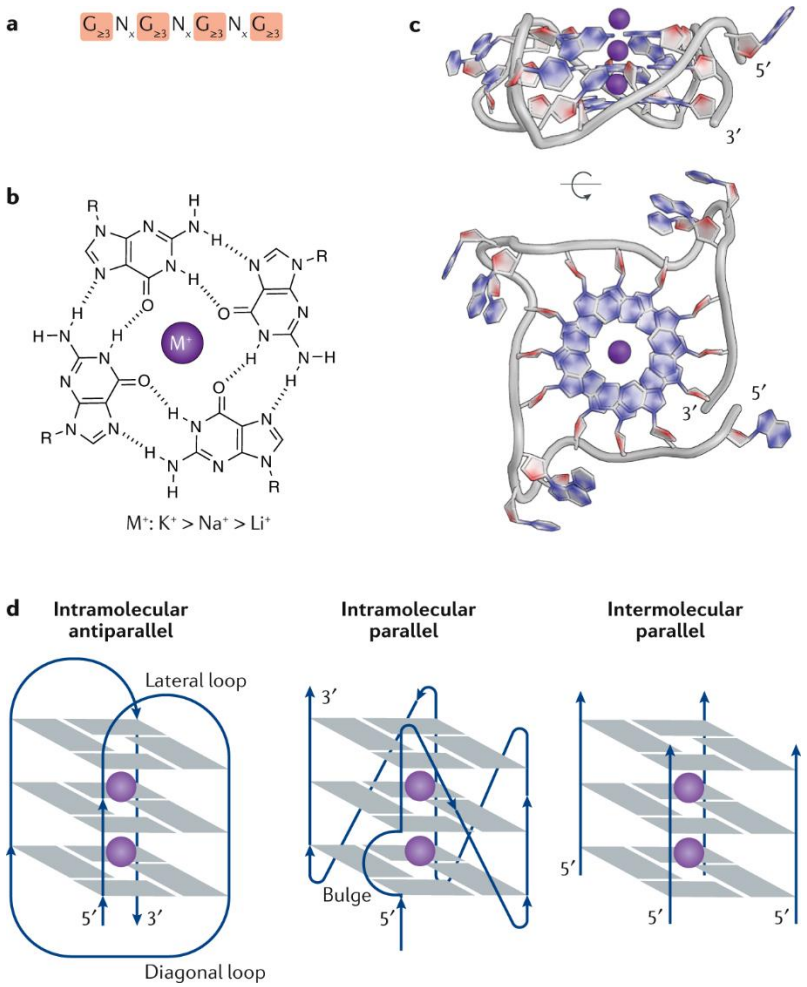


*Figure 3. a) G-quadruplex consensus sequence b) Guanine tetrad resulting from the Hoogsteen base paring and central cation (usually $K^+$), c) X-ray crystal structure of an intramolecular parallel g-quadruplex, and d) Diagrams of some possible g-quadruplex topologies. Adapted from publication referenced with permission.*[20]

Guanine rich regions of DNA with the general sequence $G_{\geq 3}N_{1-7}G_{\geq 3}N_{1-7}G_{\geq 3}N_{1-7}G_{\geq 3}$ are able to form g-quadruplexes.[21] G-quadruplexes can form from a single strand of DNA with the general sequence shown above, but they can also form from multiple DNA strands coming together. G4s have been implicated in a number of biological processes serving many different functions. Quadruplexes have been identified in telomeres possibly to provide stabilization and protection, and several telomere binding proteins have been found to bind to G4s *in vitro*.[22-24] They have also been shown to have a significant role in gene regulation and have been shown to be promoters of several known oncogenes.[25-27]

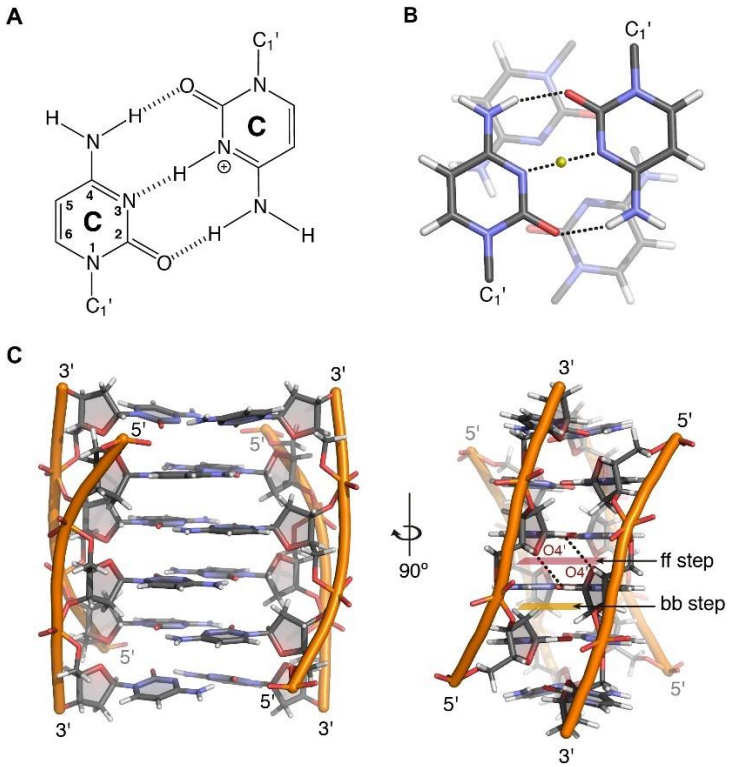


*Figure 4. Intermolecular interaction of hemi-protonated cytosine-cytosine molecules and the general structure of an i-motif. Adapted from referenced publication with permission.*[28]

G4s occur in guanine rich regions of DNA. This implies that there also exists cytosine rich regions on the complementary strand. Indeed, cytosine base-paring has been identified, as has the existence of a tertiary structure termed an i-motif (Figure 4). The i-motif structure was first produced using a short oligomer d(TCCCCC) which, under acidic conditions, formed a pair of antiparallel duplexes with intercalated hemi-protonated cytosine-cytosine base pairs.[29] Soon after the proposal of the i-motif structure a crystal structure was obtained.[30] I-motif structures have been identified in telomeres and in promotor regions of some genes.[31, 32] The presence of i-motifs in the promoter regions of oncogenes has been of particular interest as targets for cancer therapies.

The simplest higher order DNA structure is the junction. Any time that the information contained in our DNA is manipulated or accessed a junction must be formed. The DNA four-way junction (4WJ) was discovered in 1962 by Robin Holliday when he proposed the mechanism for DNA strand exchange.[33] In 1983 the role of 4WJ in homologous recombination repair was elucidated by Stahl and coworkers, but it was not until 2010 that 4WJ were proven to be a key intermediate in recombination.[34] Since their discovery, many proteins have been identified which bind to 4WJ structures.[35-38] Most of these proteins

are involved in homologous recombination such as GEN1 which is responsible for resolving Holliday junctions by forming incisions at the junction site to enable ligation. A significant step towards improving our understanding of the role of 4WJ was the development of a method to map and quantify 4WJ *in cellulo*. This was achieved using an engineered RuvC protein which was tagged with green fluorescent protein.[39] RuvC is an endonuclease which forms part of a larger complex of three proteins RuvA, RuvB, and RuvC. These proteins come together to resolve Holliday junctions in bacteria. RuvC is the component which binds to the face of the junction by forming a dimer. The intimate connection between 4WJs and cell replication and repair make junctions prime targets for cancer therapies.[40-42] An example of recent work which demonstrates the significance Holliday junctions have in cancer progression: Holliday junction-recognizing protein (HJURP) has been shown to be overexpressed in a number of cancers and can even be a prognostic biomarker.[43, 44]

*Figure 5. Schematics of the parallel X-stacked (left), open-planar (middle), and antiparallel X-stacked conformations of the Holliday junction (4WJ). Adapted from reference publication with permission.[45]*

A 4WJ can form spontaneously in DNA anywhere that there is an inverted repeat sequence which have been shown to be present throughout the human genome.[46] There are two possible conformations of the 4WJ, the open-planar structure, or the X-stacked conformation (Figure 5). The X-stacked conformation is observed in the absence of proteins which bind the 4WJ whereas the open-planar structure is observed in all cases where a protein is bound to the junction.[47] Metal ions are also known to have a large influence over the conformation the 4WJ adopts with divalent cations such as magnesium stabilizing the X-stacked structure.[48]

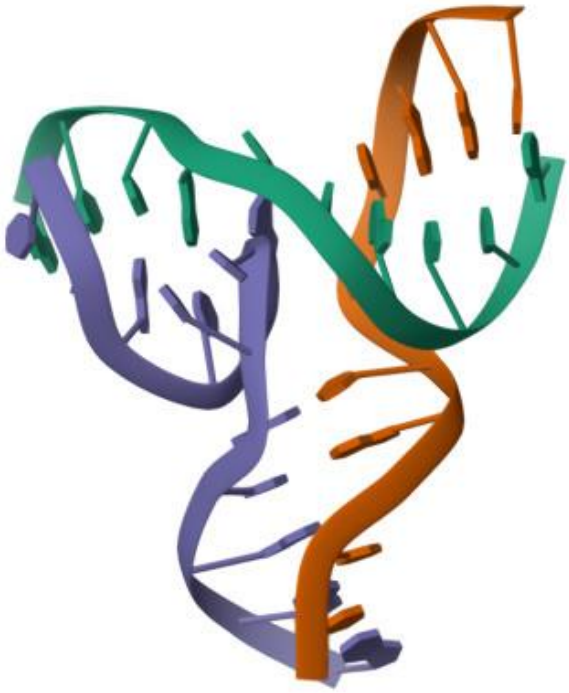

*Figure 6. NMR structure of a DNA three-way junction (1EKW). Image from PDB.*[49]

The other DNA junction structure which will be discussed here is the 3WJ which is the simplest DNA tertiary structure that can be formed (Figure 6). DNA 3WJs can be formed by inverted repeat sequences and are very similar in structure to Y-forks which are present during repair and recombination processes. It is thought that the 3WJ can be considered analogous to a DNA replication fork making a 3WJ an attractive target to inhibit replication.[50] DNA three way junctions may also form dynamically at areas of DNA instability caused by short repeating DNA sequences.[51, 52]

Larger DNA junctions have been produced synthetically for nanotechnology purposes, but no junction with more than 4 arms has been observed in nature.[53-55] These larger junctions also are often less stable than the 3WJ and 4WJ discussed above.

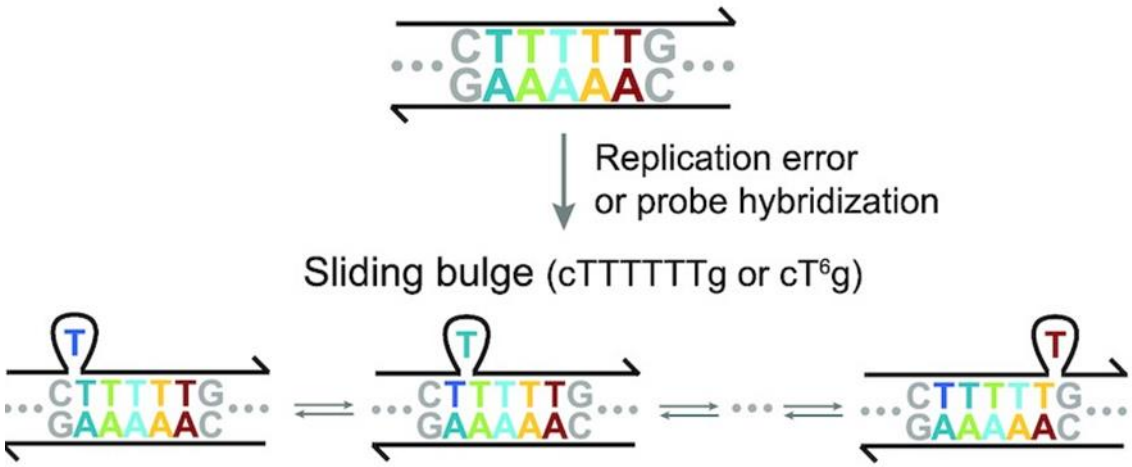


*Figure 7. Formation of a sliding bulge after by a replication error. Adapted from referenced publication with permission.*[56]

Bulges in DNA are another common structure which may represent a potential target. Bulges in DNA are a DNA defect which is formed when one or more bases in a DNA duplex do not have pairing partners. The structure of the bulges can be highly varied and is dependent on the identity of the bases in the bulge as well as the identity of the nucleotides flanking the bulge site.[57] This means that the bulge structure is sequence dependant which is significant as bulges play a role in protein recognition.[58, 59] These extra bases in the duplex may be added as a result of errors during the replication and recombination processes (Figure 7).[56, 60, 61] They are also thought to be intermediates in many DNA and RNA processes.[62] Additionally, bulges have been shown to be formed by unstable expansion of triplet repeats which are linked to a number of neurodegenerative diseases.[63] Bulges may also be formed in RNA sequences and have been shown to be critical components of RNA architecture.[64]

## 1.2 Binding to DNA structures

The sequence as well as the shape of a DNA structure are both very important considerations for DNA binding. There are a number of ways in which molecules may interact with DNA, they may chemically interact with the DNA polymer, they may take advantage of the physical shape and structure of the DNA, or a combination of the two.

It is important to consider that many molecules which can interact with DNA in specific ways will also have non-specific interactions with other features of the DNA structure. Many DNA binding molecules also make use of multiple binding modes simultaneously to achieve their therapeutic effect. An

example of a molecule which exhibits multiple binding modes is Doxorubicin which is widely known to intercalate into DNA but has also been suggested to initially bind in the minor groove of AT rich regions and G-quadruplexes.[65, 66]

There are large libraries of drugs which can bind to DNA so in the following section I will be highlighting primarily drugs which have been influential in their field in the past or are recent developments in their area.

### 1.2.1 Cisplatin (classical DNA crosslinkers)

Platinum drugs are the most common anti-cancer drugs administered across the world, with almost half of all cancer patients receiving a platinum based drug at some point during their treatment.[67] Cisplatin was the first platinum based drug to be approved for use in cancer patients in 1978 in the USA, closely followed by UK and the rest of the world.[68] There are currently three platinum drugs with world-wide approval, cisplatin, carboplatin, and oxaliplatin, and a further five platinum drugs with approval for use in specific countries (Figure 8).

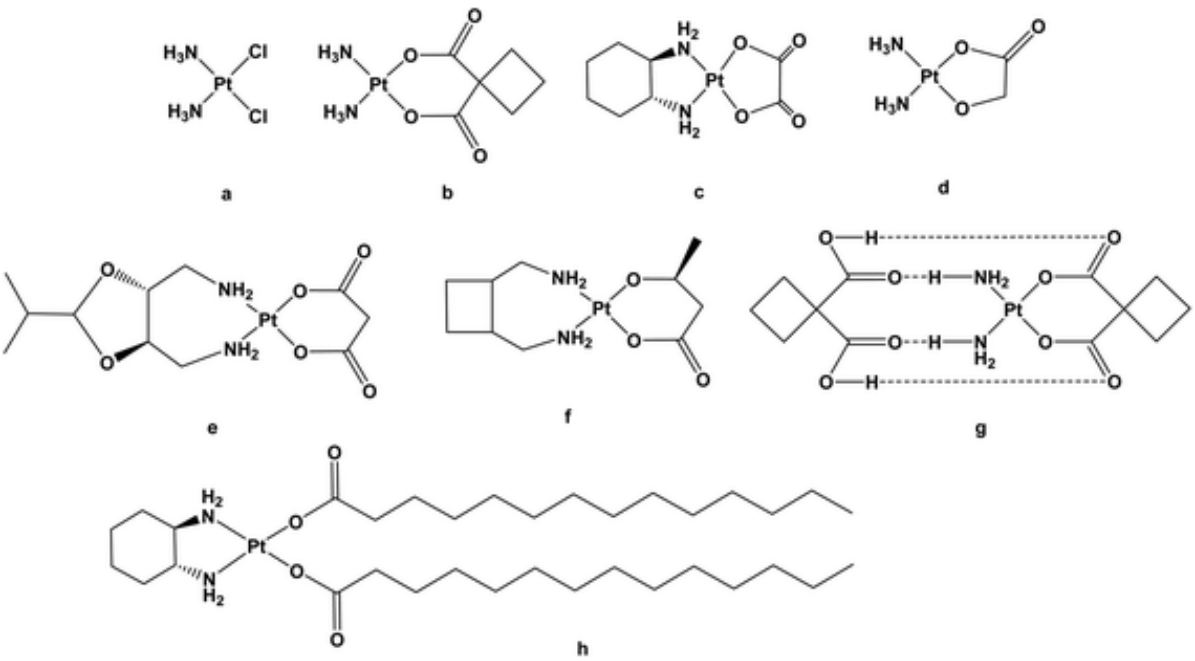


*Figure 8. Chemical structures of all approved platinum based anti-cancer drugs; a) cisplatin, b) carboplatin, C) oxaliplatin, d) nedaplatin, e) heptaplatin, f) lobaplatin, g) dicycloplatin, and h) miriplatin. Adapted from referenced publication with permission.[69]*

All approved platinum drugs have the same general mechanism of action within cells: each requires the removal of the chloride or carboxylate ligands by aquation to produce the active form of the drug.

This aquation is thought to occur predominantly within the cytoplasm, where chloride ion concentration is significantly lower than in the blood.[70] Once activation has occurred, the new platinum complex formed may coordinate to DNA, predominantly through the N7 site on guanine residues (Figure 9).[71] The complex then binds to a second guanine base, which may be on the same DNA duplex or an adjacent one, which induces kinking and unwinding of the DNA and prevents transcription from occurring.[72, 73] This eventually leads to apoptosis of the cells.

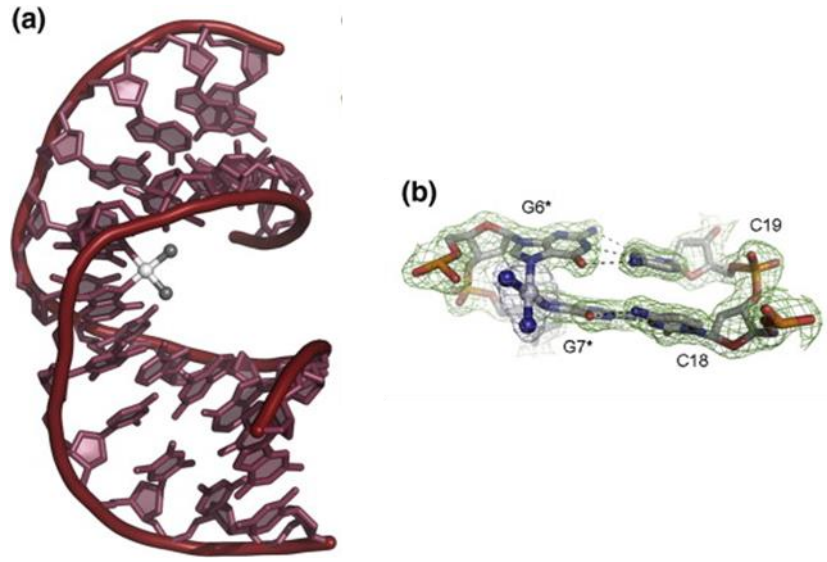


*Figure 9. a) Structure of dodecamer duplex DNA with a centrally bound cisplatin, b) Stereo image of cisplatin crosslinking. Adapted from reference publication with permission.[74]*

There are two major problems faced when using platinum-based drugs: platinum-based drugs lack specificity which causes deleterious side effects, and cisplatin resistance. The major side effects caused by cisplatin include nepherotoxicity, ototoxicity, gastrointestinal toxicity, and hepatotoxicity.[75] These side effects occur because the complex does not specifically target the cancer cells, and also binds to other cellular structures as well as DNA; cisplatin can interact with proteins and RNA which plays a role in its toxicity profile.[76, 77] Significant work has focused on attempting to reduce the off-target effects of platinum-based drugs. Carboplatin is an example where there has been some success in reducing severity of side-effects, and thus improving the quality of life for patients, whilst maintaining an efficacy comparable to cisplatin.[78, 79] Oxaliplatin, on the other hand, has a different spectrum of disease activity (and lack of cross resistance) and is now widely used due to its high efficacy for the treatment of

colorectal cancer; its high efficacy is thought to be due to its ability to act as a substrate for organic cation transporters, which are overexpressed on colon cancers.[80, 81]

Cisplatin resistance can be innate or acquired. Innate resistance is already present in the cell prior to exposure to cisplatin, whereas acquired resistance presents as a result of exposure of the cells to cisplatin. Decrease in cellular uptake and/or increased efflux of the drug from the cell is one mechanism of acquired resistance. Copper transport proteins, particularly CTR1 and CTR2, have been shown to have a significant role in the uptake of platinum-based drugs.[82-84] Levels of APT7, which is responsible for removing excess copper from cells, has been found to be significantly higher in ovarian cancers resistant to platinum drugs.[84, 85] Platinum drugs may also react with species other than DNA in the cells such as glutathione and metallothionein proteins which can lead to reduced toxicity.[86-88] Finally, nuclear repair mechanisms involving a multitude of proteins within the cell may be upregulated to compensate for the DNA damage. An example of one of these proteins is ERCC1, which is key to the rate limiting step of the nucleotide excision repair process. Higher expression of ERCC1 is correlated with reduced efficacy of cisplatin in patients with a variety of cancers.[89-93] Overcoming cisplatin resistance is a challenge which is yet to be resolved; however, a number of solutions are currently under investigation, with the use of nanomedicines and/or combination treatments being two possible avenues.[94-98]

Examples of two alternative platinum based anticancer drugs which are currently only approved for use in a single country, Japan, are Nedaplatin,[99] and more recently Miriplatin.[100] Nedaplatin is used to treat head, neck and oesophageal cancers, as well as small and non-small cell lung cancers. The Drug has significantly higher solubility than cisplatin, and also displays decreased levels of nephrotoxicity and gastrointestinal toxicity.[99] Miriplatin on the other hand is used to treat hepatocellular carcinoma.[100] Miriplatin is a liposoluble drug which means it must be administered in an oil (Lipiodol) as a suspension, due to its extremely poor water solubility.[69, 101] Lipiodol is a combination of four lysophospholipids and calcium silicate which facilitates retention within the tumours and slow release of the platinum agent for reduced side effects.[102, 103]

### 1.2.2 Groove binding

There are two grooves in the classical B-DNA alpha helical structure, the major groove and the minor groove. The major groove is broad and, as a consequence of this, there are few examples of molecules which have been designed to specifically target the major groove of DNA. Conversely, the minor groove is narrow and deep (6 Å wide, 8.2 Å deep) where the functional groups of bases are exposed, creating a very unique environment. There is some variation in minor groove width that is sequence dependant, AT rich regions are narrower and support a single layer of water molecules running along the groove. Small molecules commonly bind to the DNA minor groove through non-covalent interactions, though some do act as alkylating agents. Most minor groove binders are polyaromatic with a generally curved, planar structure and one or more positive charges.

Hoechst dyes are well known minor groove binders, these dyes are a family of molecules with similar structures, which all display strong binding to the minor groove of DNA. Hoechst dyes are commonly used for fluorescent cell staining (Figure 11). The thermodynamics of binding of Hoechst dyes to the minor groove of DNA has been extensively studied.[104, 105] There is a large unfavourable enthalpy cost for this binding interaction and a loss in configurational entropy, this is more than compensated for by the release of water molecules from within the minor groove.[106] Many minor groove binding molecules preferentially bind to AT rich regions of DNA due to the higher negative electrostatic potential and narrower groove dimensions including Hoechst dyes (Figure 10).[107, 108] Recent work has shown in great detail the distortions caused to the DNA structure by the binding interaction of Hoechst 33258.[109] DAPI is another example of a fluorophore which is commonly used to stain the nucleus of cells due to its strong binding to the minor groove of DNA.[110, 111] Minor groove binding agents have been used for a variety of biomedical applications

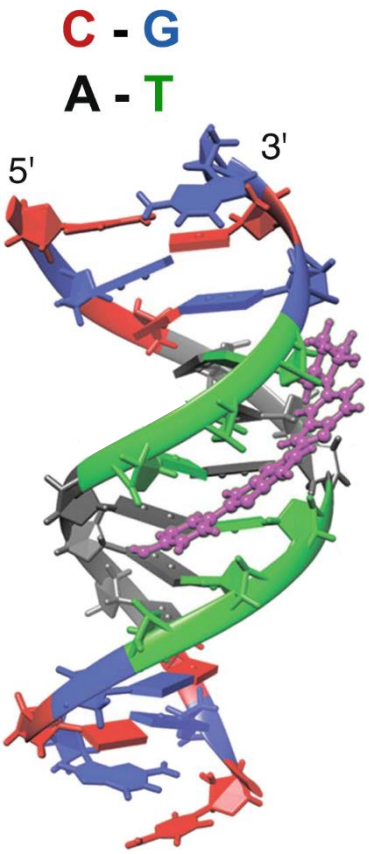


*Figure 10. Minor groove binding of Hoechst 33258. Adapted from referenced publication with permission.[109]*

including chemotherapeutics, antiparasitic, and antibacterial.[112] By binding to the DNA minor groove, they disrupt protein recognition of DNA sequences.

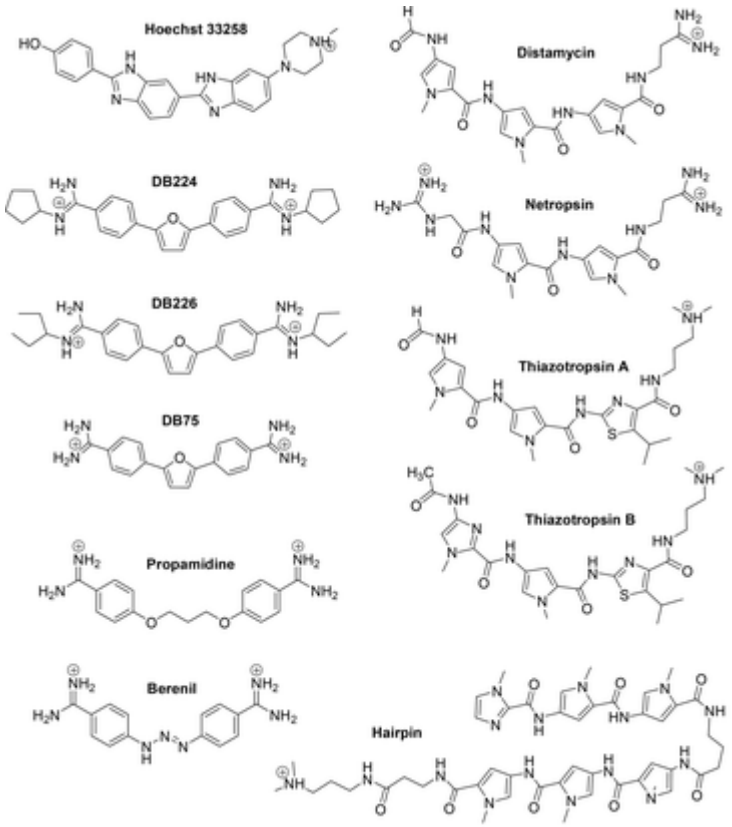


*Figure 11. Examples of widely studied DNA minor groove binding agents. Adapted from referenced publication with permission.[106]*

Distamycin A was isolated in 1964 and has been shown to be a strong minor groove binder but has no anticancer activity alone (Figure 11).[113] Despite this, significant work has focused on developing anti-cancer agents based around the core distamycin A moiety, where the head and tail end of the molecule have been altered. Notable examples include Tallimustine, which replaces the head group with a nitrogen mustard making the new compound highly toxic to cancer cells (Figure 12).[114] The major drawback of this compound was its severe toxicity to bone marrow. Brostallicin is another derivative of distamycin, with a mustard derivative on one end and guanidinium cation on the other end (Figure 12).[115] This compound has significantly fewer severe off-target effects but, interestingly, is only active as an alkylating agent in the presence of glutathione.[116] A different class of minor groove binders which are also alkylating agents are the pyrroleobenzodiazepines, such as anthramycin, tomaymycin, and sibiromycin (Figure 12).[117] These compounds bind to the DNA minor groove and form covalent bonds

to N2 in guanine residues. Each of these compounds has displayed potent anti-cancer properties against a variety of tumours.

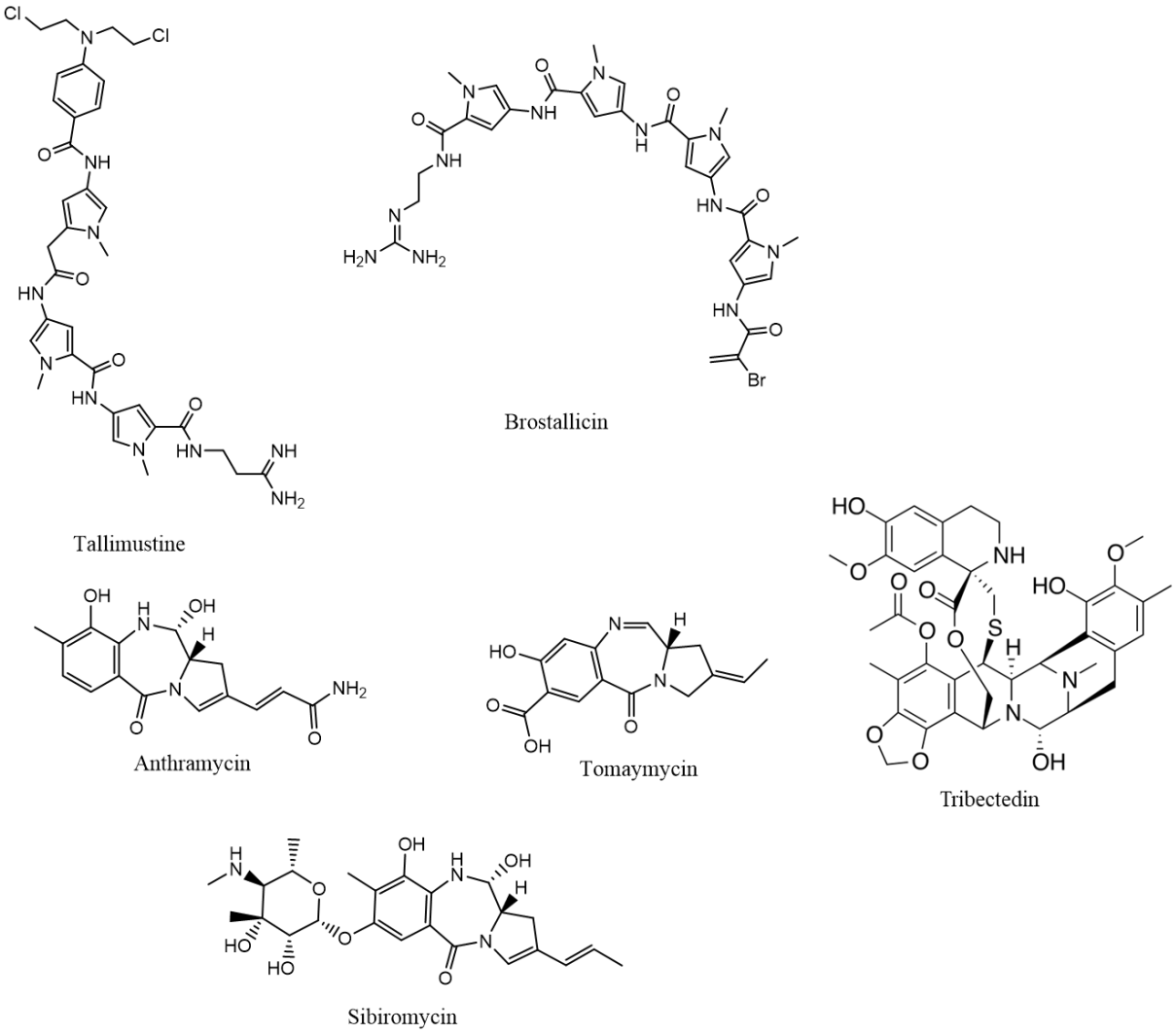


*Figure 12. Chemical structures of minor groove binders Tallimustine, Brostallicin, and Tribectedin, and covalent minor groove binders Anthramycin, Tomaymycin and Sibiromycin.*

The final minor groove binder which has seen application for cancer treatment is Trabectedin (Figure 12).[118] Trabectedin partially inserts its pentacyclic core moiety into the DNA minor groove, whilst the other half of the compound is thought to interact with proteins. This compound has been shown to effectively treat multiple different tumour cell lines *in vitro* and *in vivo*, and is currently used to treat soft tissue sarcoma.[113]

There are fewer examples of synthetic molecules which bind to the major groove of DNA, but many biomolecules are known to interact with the major groove (example crystal structures are shown in Figure 13). The major groove is roughly the same depth as the minor groove but is significantly wider, which allows it to accommodate larger biomolecules. Functional groups from the bases in the centre of the helix are exposed on the floor of the major groove, enabling recognition and binding of specific base sequences. Most proteins which are highly selective for specific base sequences form hydrogen bonds to bases in the major groove.[119, 120] Helix-turn-helix (HTH) and zinc finger motifs, which are commonly found in transcription regulators, bind readily to the major groove of DNA and are able to express a wide variety of functionalities to achieve specific sequence recognition.[121]

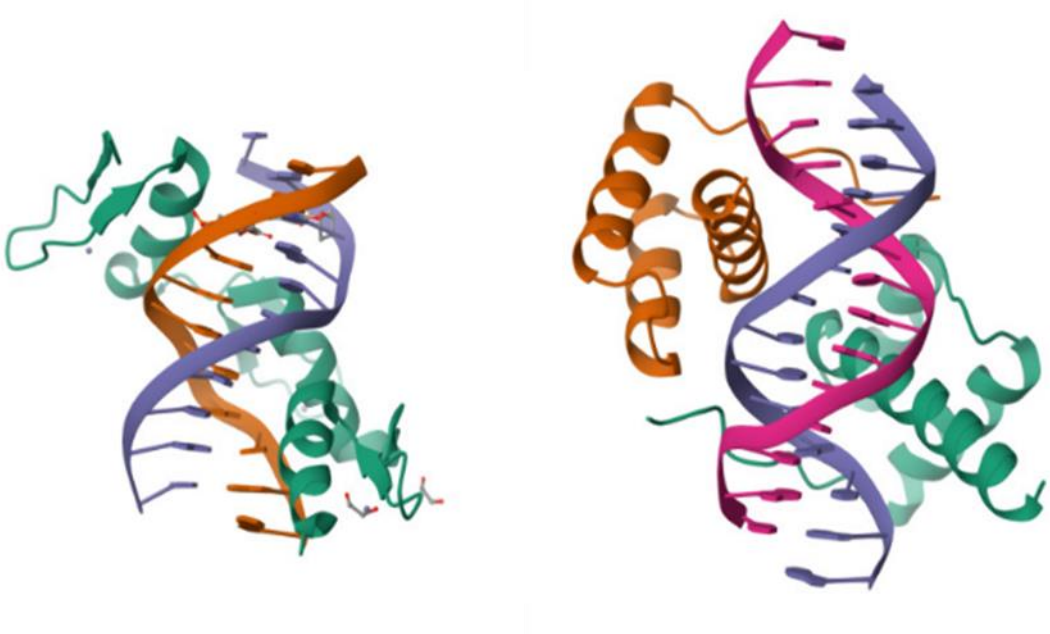

*Figure 13. Examples of the structure of a zinc finger protein bound to duplex DNA (4R2A) (left), and a HTH homeodomain (1FJL) (right). Structures from PDB.[122, 123]*

Pluramycins are a family of natural products; in 1956 it was discovered that they possess biological activity.[124] Two products in this family, hedamycin and altromycin B, have been shown to possess antibiotic and antitumour properties. They have been shown to interact with DNA through binding to the major groove region and subsequent alkylation of the guanine N7 through ring opening of the epoxide. Hedamycin is a good example of a molecule which exhibits multiple simultaneous interactions

with the DNA: intercalation of the aromatic moiety, minor and major groove binding by the carbohydrates, and alkylation in the major groove by the epoxide moiety (Figure 14).[125]

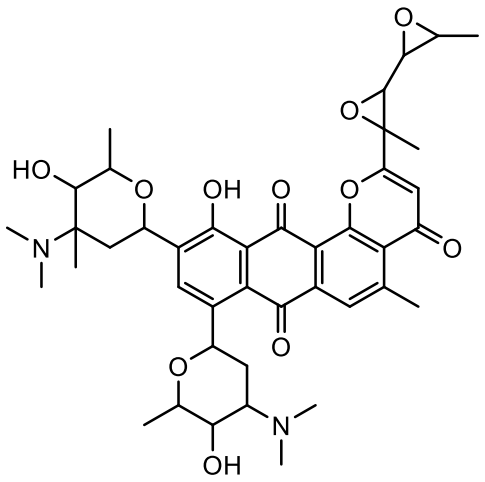


Hedamycin

*Figure 14. Chemical structure of Hedamycin.*

Another classification of structures which bind to the major groove of B-DNA are triplex forming oligonucleotides (Figure 15). Carefully designed sequences may form additional hydrogen bonds to the bases exposed in the major groove, where there is a run of purines, to form a what is termed a triplex.[126] It is predicted than 98% of human genes will have a complementary triplex forming oligomer, and 87% of these target sequences will be unique.[127] Triplex forming oligonucleotides are of interest as they can be designed to bind to specific DNA sequences and supress the specific genes responsible for disease. These triplex forming oligos may be constructed from DNA, RNA or synthetic analogues.[128] The principle behind triplexes as therapeutic agents is very similar to RNAi, with the advantage that triplex formation can permanently silence gene expression.[129]

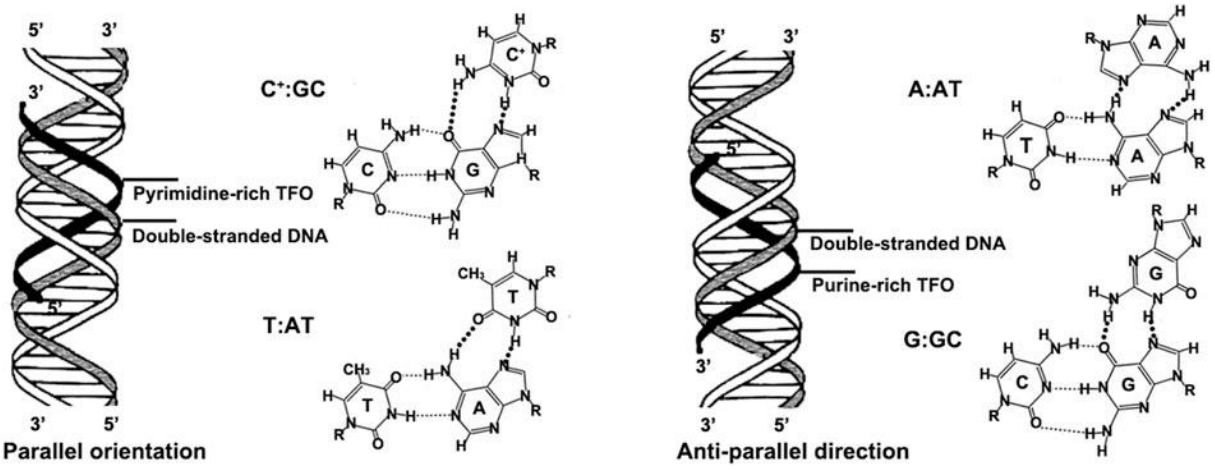


*Figure 15. Triplexes formed in pyrimidine rich and purine rich sections or DNA. Figure adapted from referenced publication with permission.*[127]

Tiwari *et al*. have recently demonstrated the use of triplex forming oligonucleotides to induce DNA damage at HER2 oncogene sites.[130] Through xenografts, they showed that the triplex forming oligonucleotides had comparable effects to that of Trastuzumab which targets the proteins resulting from the HER2 gene. Nanodelivery methods were also investigated and were found to improve delivery of the therapeutic agent. Novel nanosunflowers have also been produced for targeted and controlled delivery of triplex forming oligonucleotides.[131] The triplex strand was used to induce the self-assembly of the gold nanoparticle structures, and could be released upon near infrared irradiation to bind to the P2 promotor of the c-myc oncogene.

The general issues confronting triplex forming oligomers are: uptake into the cells, stability once inside the cell, and target specificity in a cellular environment.[127]

### 1.2.3 Intercalation

DNA intercalators are usually heteroaromatic molecules which are planar and contain one or more positive charges. The cationic nature of many DNA intercalators is preferable to achieve strong binding as it facilitates the close approach of these molecules to the anionic sugar-phosphate backbone of the DNA during the early stages of a binding event. The planar aromatic rings enable the molecule to slide in between a set of base pairs and interact with them through pi-pi interactions and hydrophobic effects. If the molecule is heteroaromatic, hydrogen bonds can also be formed between functional groups on the DNA bases and the molecule. Van der waals forces also play a role in the binding of these molecules to the DNA. Intercalation of drug molecules into the DNA helix can have dramatic effects on

the structure of the DNA. When drugs slot between base pairs, this can cause unwinding and bending of the DNA helix. An example of this is when Ethidium bromide intercalates into DNA which causes a 26° unwinding.[132] This unwinding and bending can lead to larger structural changes in the DNA, such as the formation of toroid or plectonemic structures.[133] On a more local level, the intercalation of small molecules gives rise to the neighbour-exclusion principle.[134] The bases on either side of the intercalated molecule are pushed apart which causes the adjacent potential intercalation sites to become unavailable, giving a maximum ratio of one DNA intercalator for every two base pairs. Due to the distortion of the DNA helix and forcing apart of the base pairs, an increase of up to 50% in the length of the DNA is observed. A "hyperstretched" form of DNA has also been produced when, under high stretching forces, the DNA can be fully intercalated, leading to a 100% increase in duplex length.[135] It is highly unlikely that this could exist in nature though.

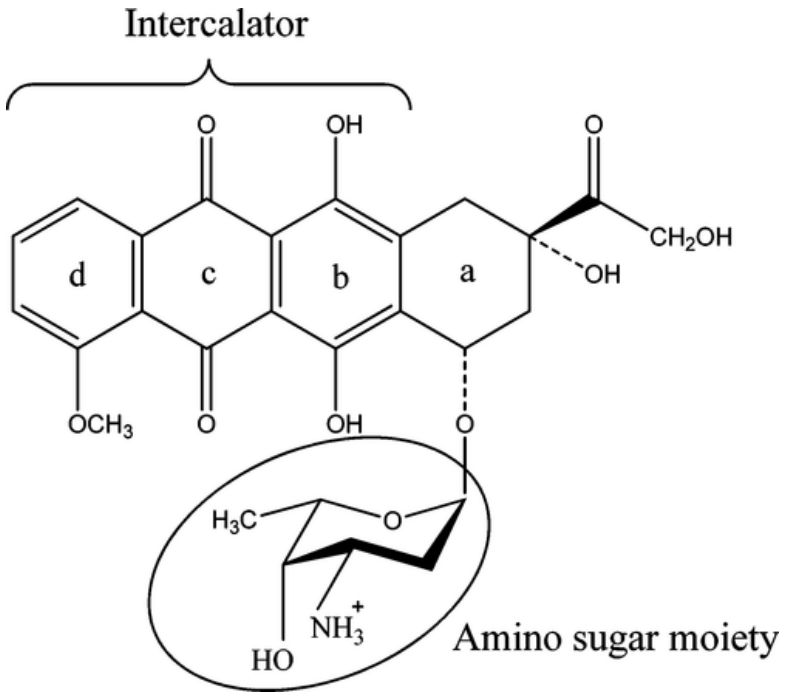


*Figure 16. Structure of Doxorubicin with its functional moieties highlighted. Adapted from referenced publication with permission.[65]*

A highly effective chemotherapeutic drug which intercalates into DNA is Doxorubicin (Figure 16).[136] The mode of action of doxorubicin is not fully understood, but its DNA binding interactions have been widely studied and are thought to play a key role in its mechanism of action.[65] Doxorubicin intercalates at GC rich regions of DNA. The major component of doxorubicin's toxicity is thought to be due to its interaction with the topoisomerase II enzyme, inhibiting its function as well as causing single-strand

DNA breaks.[137] Thermodynamic studies have revealed that minor groove binding of the doxorubicin is also significant in how it forms dox-DNA complexes.[65] Recent work has utilized our understanding of the interactions of doxorubicin with DNA to construct DNA nanostructures loaded with doxorubicin to control its release. The release profile of the drug from the DNA nanostructure could be controlled by varying the architecture of the DNA origami making it more or less susceptible to DNase I digestion (Figure 17).[138]

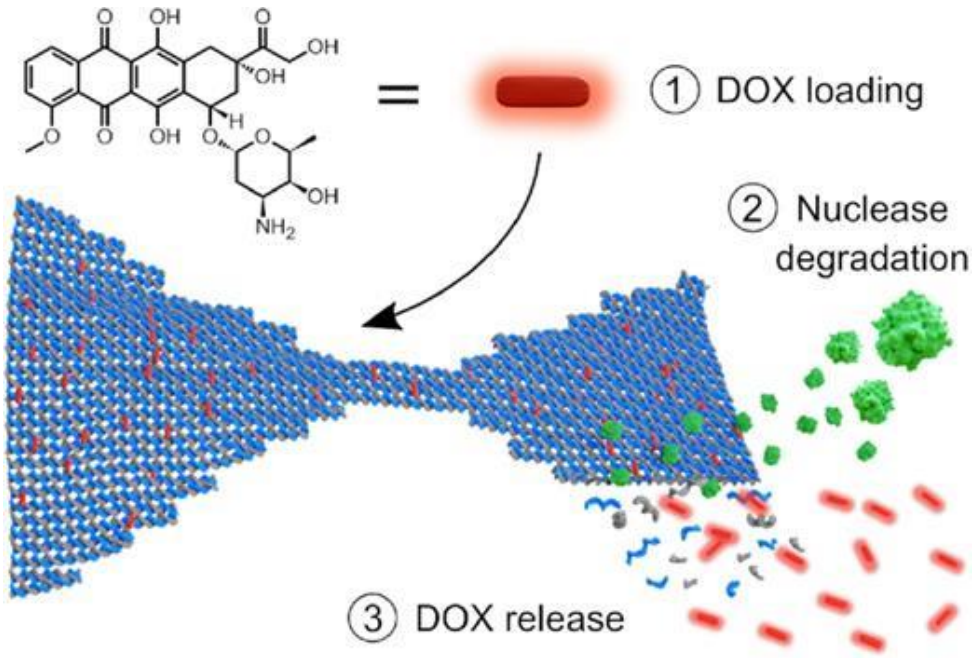


*Figure 17. Schematic of the loading of DNA origami with doxorubicin and its stimulated release by nuclease degradation of the DNA structure. Adapted from referenced publication with permission.[138]*

Mitoxantrone has the same core anthracenedione as doxorubicin with some modifications (Figure 18). The primary drawback of doxorubicin was that its cardiotoxicities severely limited the dose which could be safely prescribed. Additionally, the cardiotoxicity was shown to be cumulative, so patients who have already been treated with doxorubicin cannot be treated with it again if their cancer returns.[139] Mitoxantrone overcomes this cardiotoxicity but maintains a comparable therapeutic effect to doxorubicin.[140] The mechanism of action of mitoxantrone broadly relies on intercalation and inhibition of topoisomerase II but there are numerous other mechanisms which contribute to its overall toxicity profile.[140]

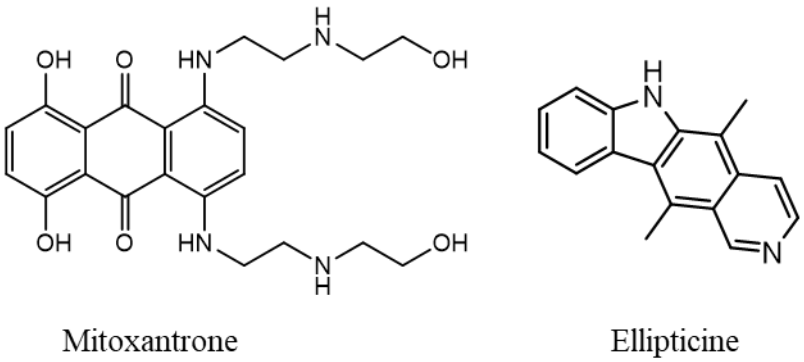


*Figure 18. Chemical structures of DNA intercalators Mitoxantrone and Ellipticine.*

There are many anti-cancer drugs which interact with DNA through intercalation. Ellipticine is a DNA intercalating drug candidate (Figure 18). Ellipticine has shown significant antitumour and anti-HIV activity, leading to cell cycle arrest and apaptosis.[141] A number of different mechanisms contribute to ellipticine's anticancer properties. Ellipticine can intercalate into DNA and inhibit topoisomerase II, and has also been shown to form DNA adducts which contribute significantly to its toxicity.[142] The lack of significant side effects in early studies and total lack of hematological toxicity, coupled with its potent antitumour activity, made ellipticine a promising anticancer drug. It progressed to phase II clinical trials but no further due to side effects and efficacy.[143, 144] With this in mind, further research is ongoing introducing modifications to Ellipticine to improve its antitumour activity further.[145]

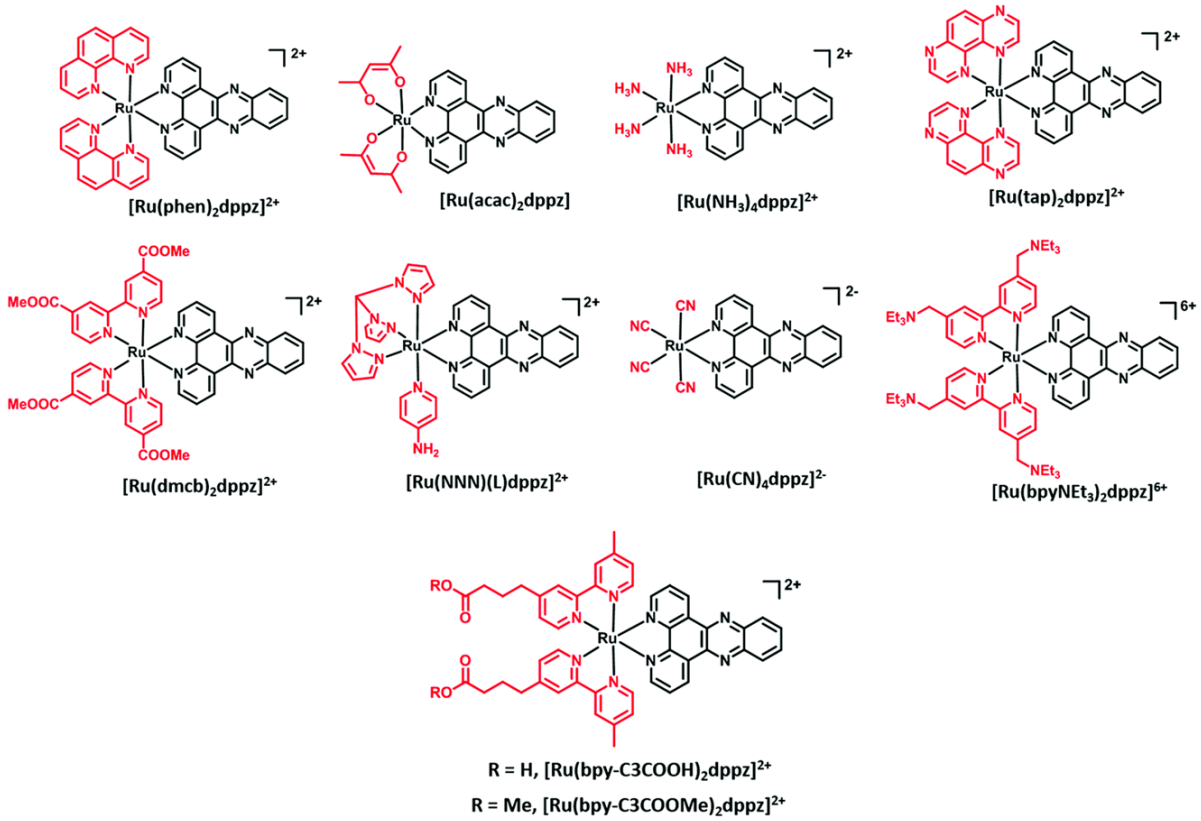


*Figure 19. Some of the Ru-dppz complexes which have been produced with a variety of ancillary ligands. Adapted from referenced publication with permission.*[146]

Metal complexes as well as organic ligands are capable of intercalation. Intercalation of metal complexes into DNA is dependent on the ligands bound to them. The presence of a metal centre can add further possibilities for controlling the geometry of the drug and can convey new and interesting properties onto the molecule as a whole. Many ruthenium based metal complexes have been produced with planar aromatic ligands which can intercalate into DNA primarily due to the interesting photophysical properties of these systems (Figure 19).[147] The light switching of $[Ru(bpy)_2(dppz)]^{2+}$ in the presence of DNA was first reported by Barton *et al.* in 1990. They determined that the ruthenium complex could be used as a highly sensitive reporter of duplex DNA as it would only produce detectable luminescence when intercalated into DNA.[148] Since this discovery, many researchers have sought to understand the exact mechanism of this induced luminescence.[149-152] Modifications to the original complex have been carried out to alter the photophysical properties and its cytotoxicity. The family of $[Ru(bpy)_2(dppz)]^{2+}$ and $[Ru(phen)_2(dppz)]^{2+}$ complexes have been used for probing a variety of DNA

structures (Figure 20)[153-157] and cancer therapies.[146, 158] The high DNA affinity of the Ru-dppz complexes made them interesting targets for development as chemotherapeutics.

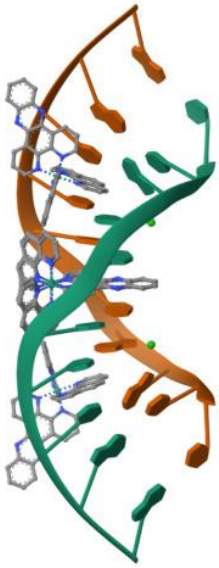

*Figure 20. Duplex DNA with $[Ru(phen)_2dppz]^{2+}$ intercalated via the dppz moiety and semi-intercalated via the phen moiety. Image from PDB.[159]*

The examples discussed above are ruthenium complexes, but many other metals can accommodate ligands which intercalate into DNA. Osmium, Rhodium, and Platinum are some of the other metals which have been used to produce intercalating metal complexes.[160]

### 1.2.4 G-quadruplex binding

Compounds which are designed to bind to G-quadruplexes are generally large planar molecules which are able to interact with the planar pi surfaces of the guanine tetrad which are exposed on the top of the quadruplex. The large size of these aromatic systems causes them to favour binding to G-quadruplexes and reduces the possibility of intercalation into duplex DNA. Cationic moieties are often incorporated into these structures to improve their solubility, the positive charges also enable electrostatic interactions with the negatively charged phosphate backbone of the DNA.[161] A huge quantity of research has focused on developing ligands which are able to effectively bind and stabilize G-quadruplex structures, due to their involvement with gene regulation and specifically oncogene regulation. No drugs which specifically target G4s have successfully progressed through clinical trials thus far.[162, 163]

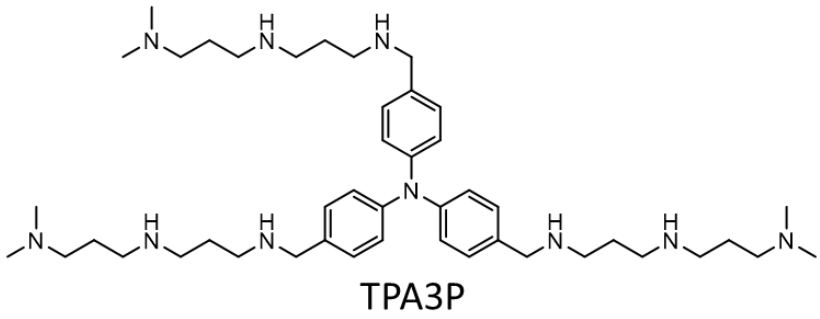

TPA3P

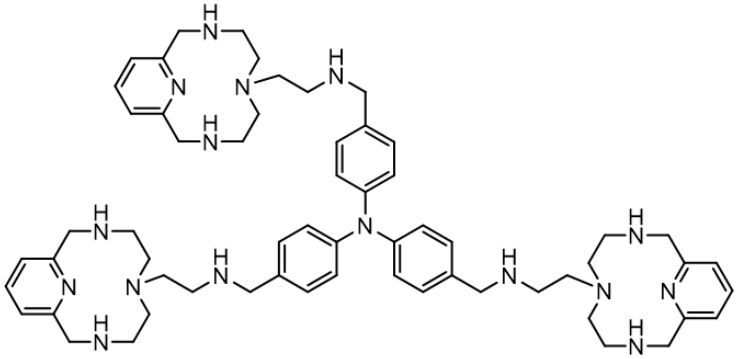

TPA3Py

*Figure 21. Structure of G4 binding ligands TPA3Py and TPA3P.*

A recent example of G4 binding agents are the tripod shaped polyaromatic, planar ligands produced by Pont *et al.* (Figure 21).[164] These ligands utilise all of the characteristics described above to achieve strong stabilisation and selectivity of G-quadruplexes. The affinity of a wide range of these tripodal ligands towards G4s was investigated, along with their cytotoxicity. The TPA3P and TPA3Py were found to have the highest affinity for G4s, with TPA3P being the most selective ligand.[165, 166] Molecular dynamics simulations show similar binding modes for the tripodal compounds; the planar moiety sits on top of the g-tetrad and the three "arms" fold over the sides of the g-quadruplex structure.

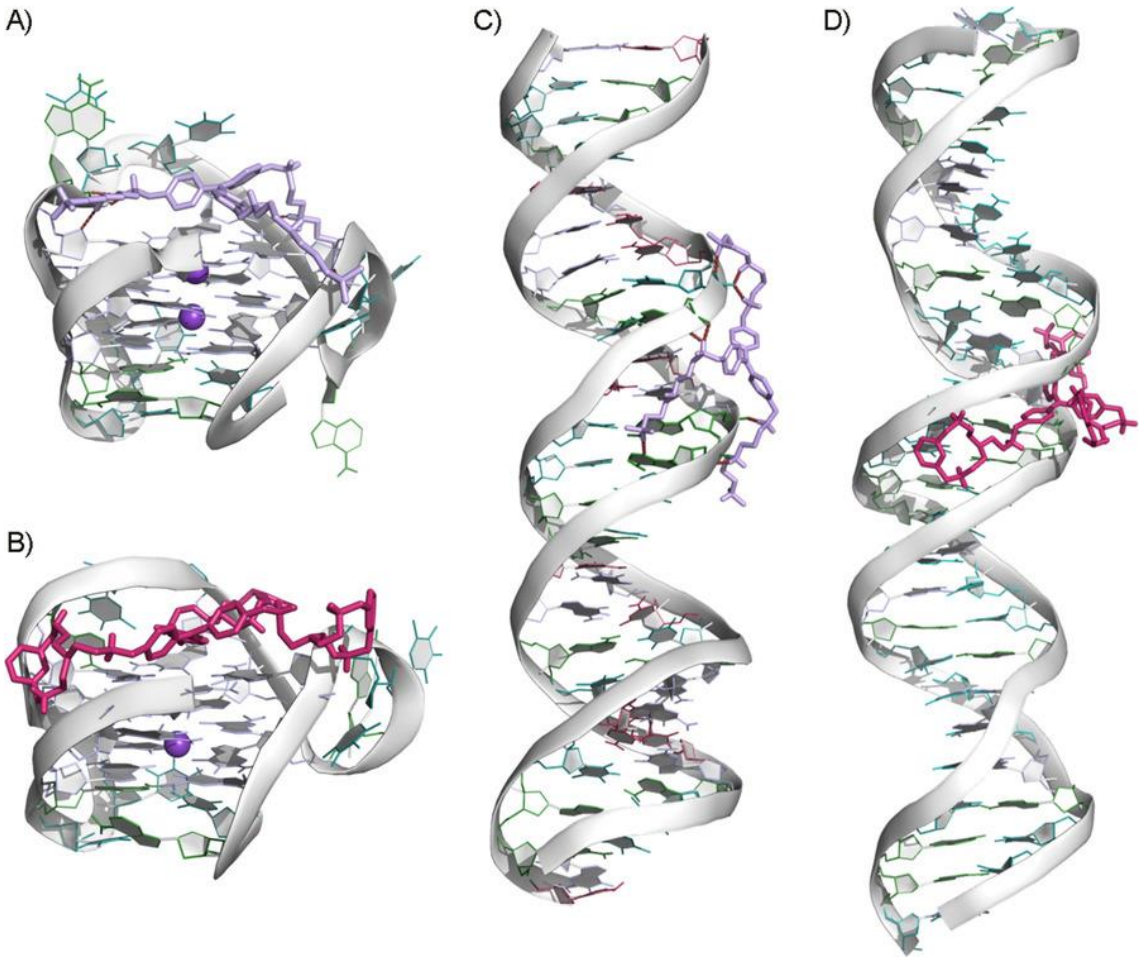


*Figure 22. Molecular dynamics simulations of TPA3P and TPA3Py with G4 DNA (A and B), and TPA3P and TPA3Py with duplex DNA (C and D). Adapted from referenced publication with permission.*[164]

The high selectivity of the TPA3P is thought to be due to its inability to bind in the minor groove of duplex DNA as has been seen in simulations for the TPA3Py compound (Figure 22). Despite the high affinity for G4s, the TPA3P was found to have the lowest cytotoxicity. It was reasoned that the high cationic charge of the trisubstituted ligands decreased their uptake into the cells. Two more ligands were produced with a larger aromatic surface area, which showed similarly high affinity for G4s but a higher cytotoxicity. The increased cytotoxicity was attributed to higher hydrophobicity of the compounds facilitating their uptake into cells. Aptamer (AS1411) functionalised liposomes were used to increase the uptake of these ligands in cells and to enhance their cytotoxic effect. Confocal studies indicated nuclear uptake of the aptamer targeted liposomes.[164]

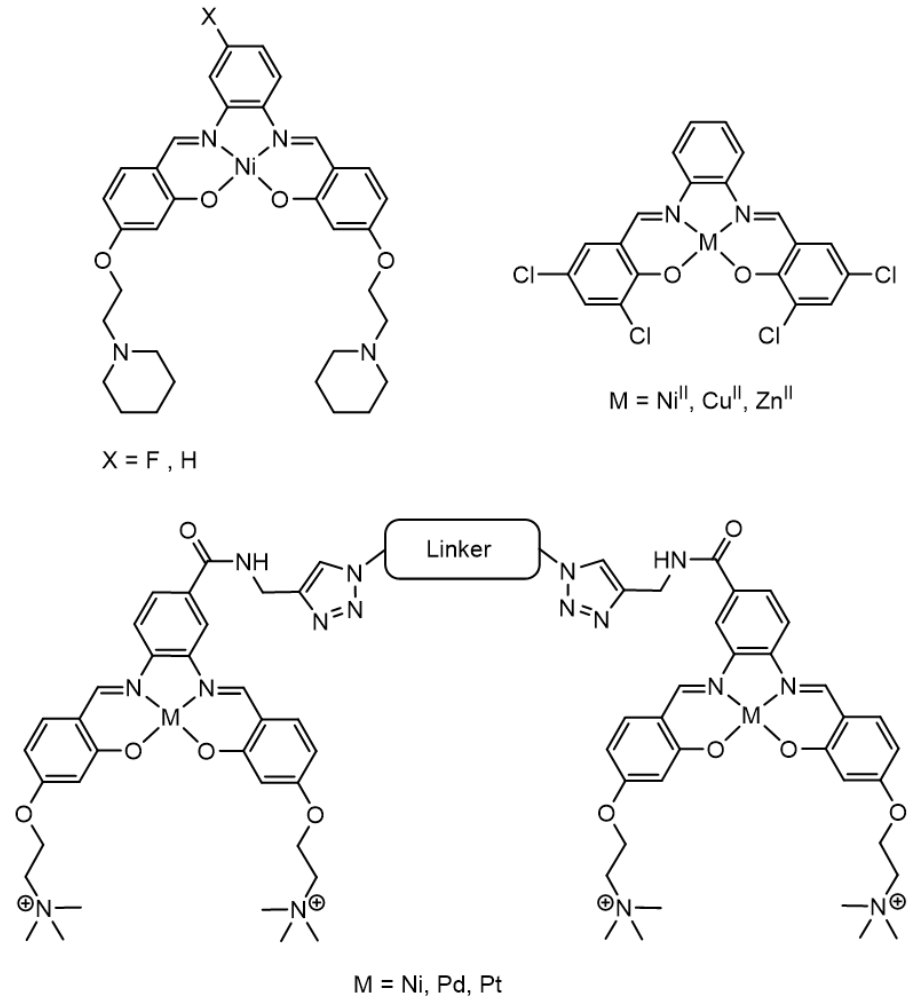


*Figure 23. Chemical structures of metal salphen complexes produced to target G4s. First metal salphen complex to target G4s (top left),[167] recent example of a neutral metal salphen complex (top right),[168] recent example of a dimeric salphen complex (bottom).[169]*

Metal complexes may also be used to target g-quadruplexes. Salen and salphen based metal complexes are the most widely investigated for targeting g-quadruplexes as they have demonstrated remarkably high affinity and selectivity (Figure 23). Metal salen and salphen complexes have a planar aromatic system arranged around a central metal cation, which further enhances the pi-pi interactions with the g-quadruplex. Extended ligands with either positively charged groups which can electrostatically interact with the phosphates of the DNA or groups which can bind in the DNA grooves, are often added to the salphen systems. The first use of these complexes to target G4s was reported by Vilar *and co-workers* in 2006.[167] The strong affinity for g-quadruplexes was largely attributed to the pendant groove binding units of the complex.

Metal salen and salphen complexes are an ongoing area of research; Vilar and co-workers have recently produced dimeric metal salphen complexes which are able to bind two adjacent g-quadruplexes with some selectivity for dimeric g-quadruplexes over monomeric g-quadruplexes.[169] Another metal salphen complex, published in 2023, was designed to target the g-quadruplex units in the KIT promoter specifically.[168] The KIT gene is responsible for the tyrosine kinase KIT receptor, which is involved with cell proliferation, amongst other functions. Mutation of this gene has been linked to numerous cancers.[170] The complexes produced were neutral complexes which dd not have any pendant arms to aid in the binding of G4s. The neutral design was an attempt to improve the selectivity of the complexes for G4s and simultaneously improve their uptake into cells. The complexes displayed modest stabilization of Kit1 and Kit2 G4s with some selectivity and displayed a does dependant toxicity to a range of cancerous cell lines.

Other metal complexes which have shown strong affinities for quadruplexes include terpyridines, phenanthrolines, bipyridines, and some macrocyclic systems.[171]

### 1.2.5 DNA junctions and bulges

Unlike G-quadruplexes, only a very limited number of DNA junction binding agents have been discovered. Many complexes designed to bind to Holliday junctions target the x-stacked conformation and either pi stack at the branch points, where the junction forms, or in the junction itself.[172] This binding mode is enabled by planar compounds with large, polyaromatic groups which can pi stack with the bases. A different class of junction binders has been designed to specifically bind in the open junction cavity as this represents a highly controlled chemical environment, enabling targeting of these sites. To target these cavities, many of the proposed junction binders which will be discussed below take advantage of the three-dimensional geometries afforded by metal centres to appropriately arrange their ligands. Peptides have also been used to target these junction structures.[173-175]

### *1.2.5.1 Small molecules*

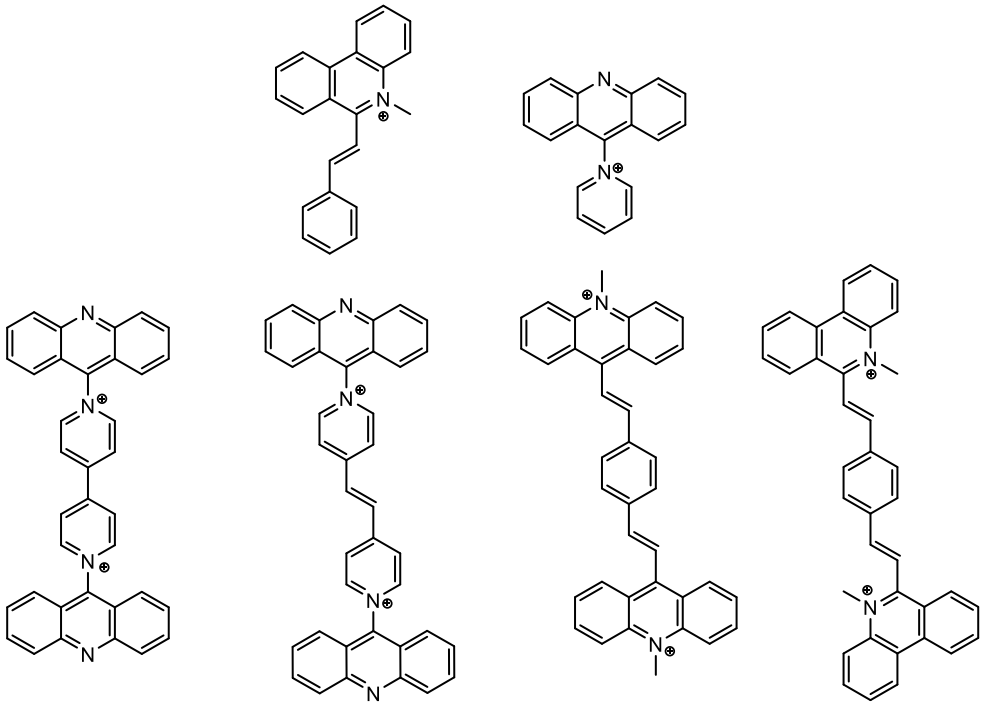

*Figure 24. Dimeric and monomeric acridine and phenanthroline based compounds studied by Carpenter et al. for junction binding.*[176]

The ability of bis-acridine molecules to bind to 3- and 4-way junctions was first investigated by Carpenter *et al. (*Figure 24*)*.[176] They synthesised a range of bis-acridine compounds with rigid linkers intended to prohibit binding to the same duplex DNA strand by forcing the acridine moieties to point in opposite directions. It was shown that these intercalators all inhibited DNase I but not at specific points on parallel duplexes as was expected. However, all the bis-intercalators reduced access to junctions more than the mono-intercalators. Though binding of the junctions in this work was inconclusive it inspired further research into bis-acridine compounds which proved more fruitful.

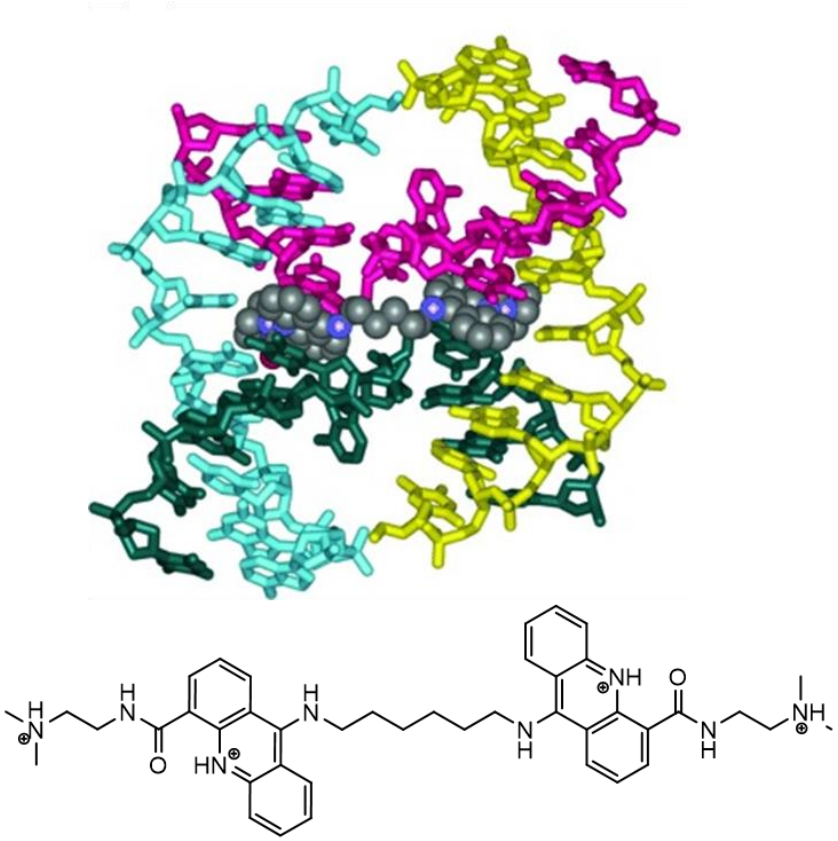

*Figure 25. Crystal structure of a Holliday junction in the x-stacked conformation with a bis-acridine compound bound across the junction (top) and the chemical structure of the bis-acridine $C_6$ compound (bottom). Adapted from referenced publication with permission.*[177]

Similar acridine based compounds were produced by Searcey *et al.* with the key difference of including a flexible linking unit.[178] Positively charged side chains were also included with the structure to provide electrostatic interactions. Binding of Holliday junction structures by a bis-acridine ligand was initially hinted at by its ability to non-covalently cross link DNA duplexes.[178] A crystal structure of this acridine dimeric compound bound across an X-stacked Holliday junction was produced by Searcey, Cardin and co-workers in 2007 (Figure 25).[177] This was shown to be a non-covalent interaction where the $C_6$ carbon chain spanned across the junction site causing the bases at the junction crossover region to fold out, allowing the acridine moieties to replace them and pi stack with adjacent bases. Furthermore, the side chains were found to sit in the minor grooves of the junction structure and provide further stabilisation through hydrogen bonds to the amide groups. Many compounds have been produced since this original bis-acridine $C_6$ compound which also utilise acridine moieties and show strong stabilization of the X-stacked Holliday junction.[179, 180] Of particular note, is the monomeric acridine compound produced by Howell *et al.* which was able to induce the formation of the x-stacked conformation of the Holliday

junction in the absence of $Mg^{2+}$ for the first time.[181] There are some more organic compounds which bind junctions in similar ways which have been nicely summarized by Searcey and co-workers.[172]

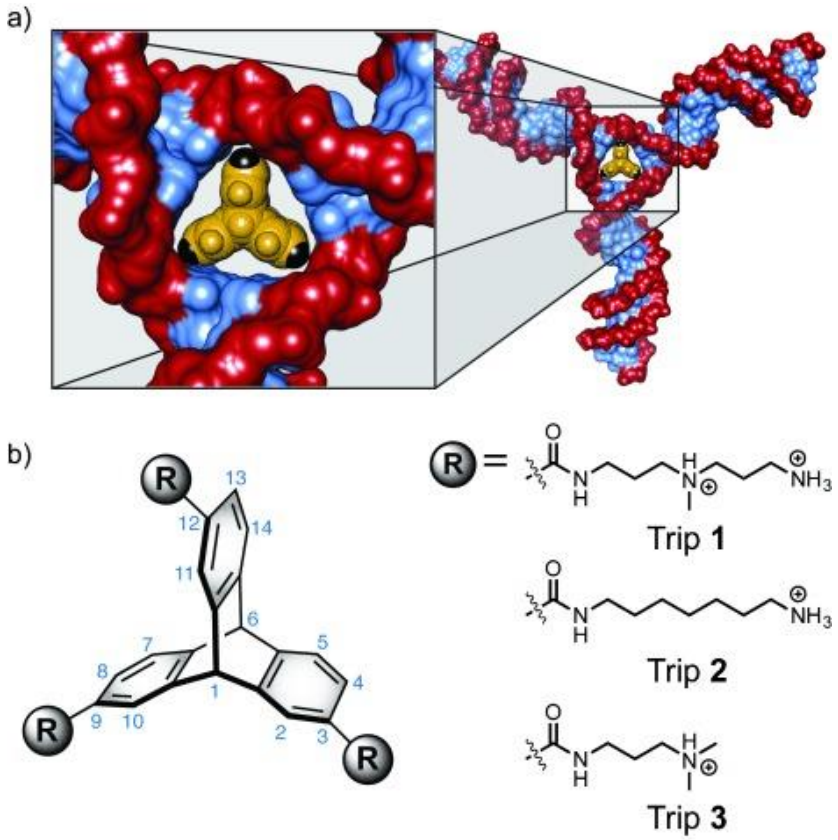


*Figure 26. a) Triptycene in a DNA 3WJ cavity (model junction based on PDB: 1F44) b) Structures of Trip 1, 2, and 3. Adapted from referenced publication with permission.[182]*

Triptycene is a small molecule with a very unusual geometry which has shown to be beneficial for binding to DNA 3WJs.[182] The aromatic system conveys a three dimensional structure to the aromatic molecule which matches that of a 3WJ (Figure 26). Thermal melting studies indicate a strong stabilization of DNA and RNA 3WJ structures by the triptycene molecules. Initial cell studies indicate that the Trip 2 compound is effective against cisplatin resistant cell lines but no $IC_{50}$ value is reported. Interestingly, Trip 1 displays a lower cytotoxicity than Trip 2 despite Trip 1 providing highest stabilisation of 3WJ structures. Triptycene compounds have also been shown to bind to trinucleotide repeats which are associated with degenerative neurological diseases.[183]

### *1.2.5.2 Metallo supramolecular cylinders*

The first three-way junction binding agent was identified by Hannon and co-workers though originally only its ability to distort B-DNA was recognised (Figure 27).[184] The structure of this supramolecular

metal complex consists of three ligands bridging between two metal centres with a helical twist induced by the ligand geometry. The ligands can twist in a clockwise or anti-clockwise directions giving rise to the P or M enantiomers respectively. The dimensions of the metal complex are approximately 2 nm in length by 1 nm in diameter giving it a roughly cylindrical structure which has appropriate dimensions to interact with biological structures such as DNA. A major groove binding mode of this complex was identified with B-DNA however later work revealed a much more significant and unusual binding mode with DNA three-way junctions.

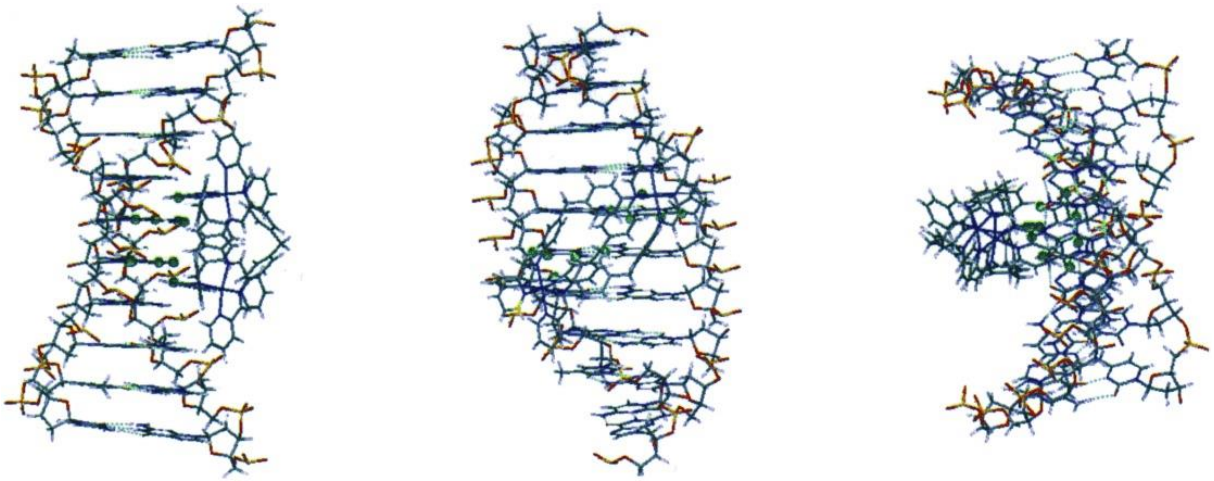

*Figure 27. [Fe2L4]4+ supramolecular cylinder docked with B-DNA major groove informed by NMR experiments. Adapted from the referenced publication with permission.*[184]

Subsequent work by the Hannon group revealed the remarkable three-way junction binding ability of the supramolecular cylinder (Figure 28).[185] This was the first time that molecular recognition of a DNA three-way junction was achieved and has paved the way for further work to target this biologically relevant structure with novel complex designs. A crystal structure of the $[Fe_2L_3]^{4+}$ cylinder with a three-way junction formed around it made up of three identical palindromic hexamers was obtained (Figure 28). The three-fold symmetry of the helicate matches that of the three-way junction which allows for almost perfect alignment of the pi surfaces of the DNA bases at the centre of the cavity, with the pi surfaces of the phenyl rings. Electrostatic interactions between the cationic complex and anionic phosphate backbone of the DNA, as well as some non-standard C-H-X hydrogen bonds also contributed to the junction binding. The binding mode of the cylinder with the 3WJ was further explored through NMR studies.[186] Minimal distortion of the junction structure or of the metal complex was observed

compared to crystal structures of the metal complex alone, and the crystal structure of a similar three-way junction bound to the Cre recombinase protein.[187] A racemic mixture of the helicate was used to obtain the crystal structure but crystals were found with exclusively the M enantiomer in the central junction. This suggests that the M enantiomer stabilizes the junction more efficiently than the P enantiomer. Subsequent work demonstrated that the P enantiomer was also able to bind to the DNA three-way junctions.[188] It has also shown that the helicate could bind to Y-fork structures and that the binding of three-way junctions was not sensitive to the identity of the bases at the junction site.[188]

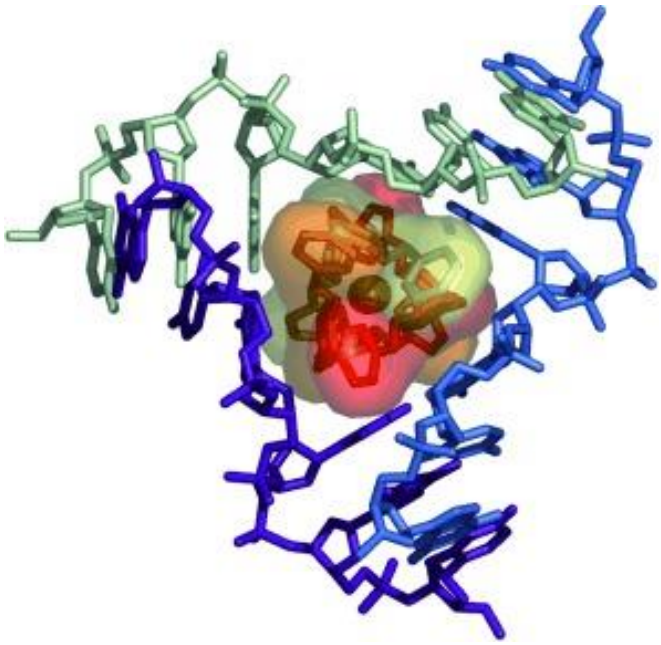

*Figure 28. $[Fe_2L_3]^{4+}$ supramolecular cylinder bound in the central cavity of a DNA 3WJ consisting of three identical palindromic hexamers. Adapted from referenced publication with permission.[185]*

Since identifying the 3WJ binding of the metallo-supramolecular cylinders many synthetic modifications have been made to the structure. The central methyl unit has been modified and even replaced with hetero atoms.[188, 189] Arginine residues have been conjugated to the ends of the cylinder which conveys control over the helicity of the cylinder core and enhances the junction binding of the complex.[190] The enhanced junction binding also results in higher observed cytotoxicity in cancerous cell lines.

The original helicate produced by the Hannon group has also been synthesised with ruthenium as the central metal cations in place of iron which has been shown to dramatically increase the stability of the complex due to the inert nature of the ruthenium. The cytotoxicity of both the iron and ruthenium

helicate was demonstrate both in cancerous and non-cancerous cell lines displaying potency similar to cisplatin despite having completely different mechanisms of toxicity.[191, 192] The difference in mechanism of cell death compared to cross linking agents offers another avenue to target cancers which are resistant to traditional treatments.

DNA bulges maintain a similar hydrophobic cavity as DNA junctions so it is not surprising that these supramolecular cylinders have also been shown to bind to DNA and RNA bulge structures.[193-195] DNA bulge binding was extensively interrogated by Malina *et al.* through the use of radiolabelled PAGE gels. Both enantiomers of the Iron supramolecular cylinders were found to bind well to DNA bulges containing a minimum of two unpaired bases, and showed a particularly high affinity for bulges containing, or flanked, by pyrimidines.[194]

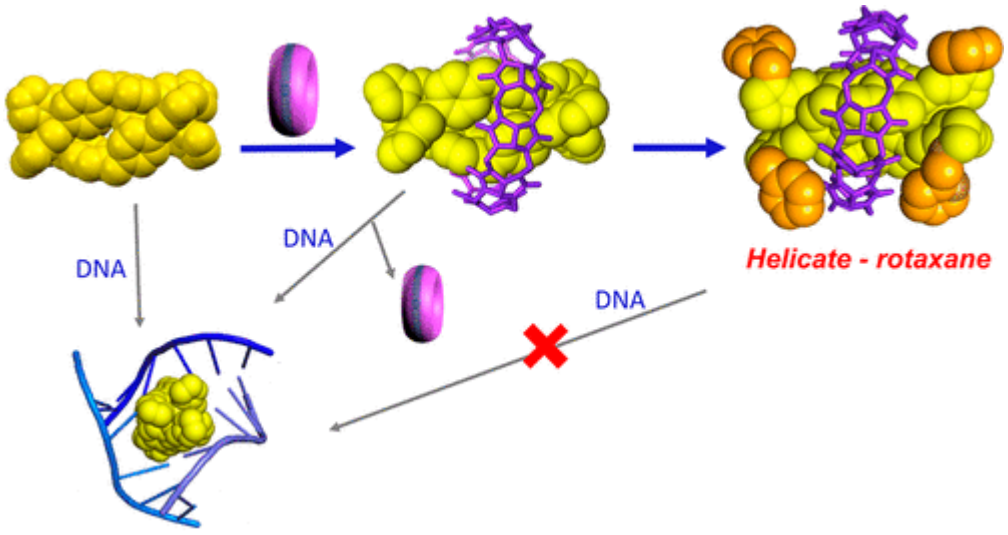


*Figure 29. Schematic to demonstrate the on/off binding of a DNA 3WJ when the cylinder is alone (left), when a pseudo-rotaxane is formed with cu[10]cubituril (middle), and when the cu[10]cubituril is locked onto the cylinder by capping groups (right).*[196]

Recent work by the Hooper *et al.* has used cylinders where the terminal pyridine groups of the ligand have been replaced with imidazole groups enabling the functionalisation through simple alkylation reactions. Using this imidazole based cylinder, a system was developed to control the level of interaction between DNA three-way junctions through the use of a cu[10]cubituril ring which could be "locked" onto the central portion of the ring through the selection of appropriate capping groups (Figure 29).[196] It was envisioned that in the future the capping, and decapping could be controlled *in vivo* to achieve targeted, and specific delivery of helicates.

Holliday junction binding of the supramolecular cylinders has been briefly investigated through gel electrophoresis and molecular dynamics simulations in a recent publication, though the focus of this paper was a gold pillarplex.[197] The cylinder was shown to bind DNA forks and 4WJ but displayed a preference for the 3WJ.

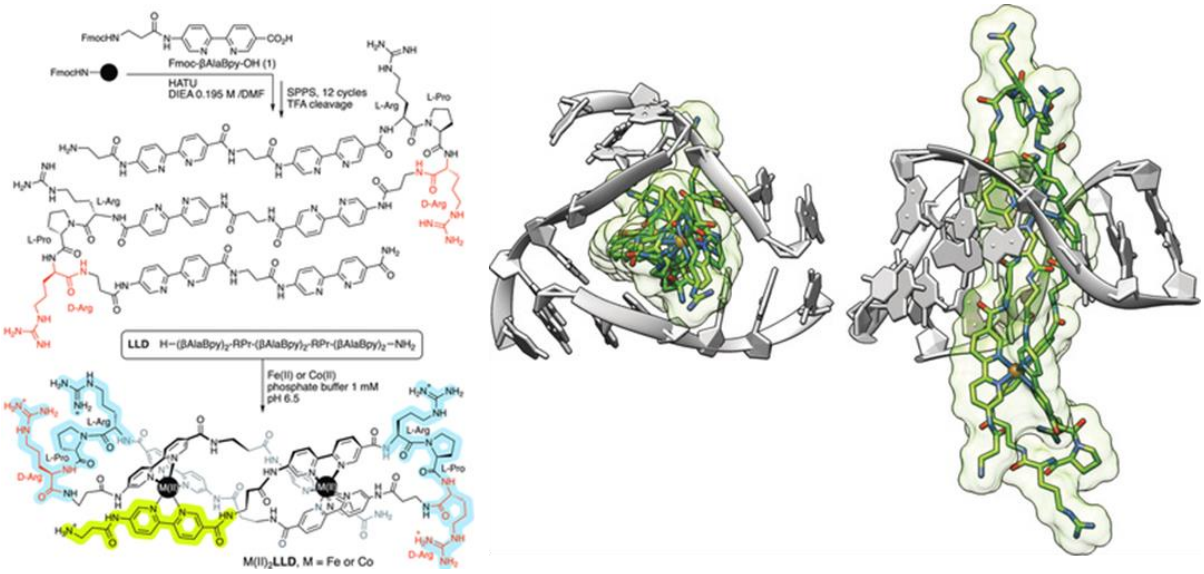


*Figure 30. Shows the synthesis of the triple stranded peptide helicate (left) and its three dimensional structure in a DNA 3WJ (right). Adapted from referenced publication with permission.*[198]

Another class of supramolecular cylinders has been produced by the Vazquez group which are templated using structurally defined peptides (Figure 30).[199] The chirality of the helicate produced was controlled by the orientation of the peptide helices of the T4Ff trimer. The resulting helicate was able to selectively bind DNA three-way junctions *in vitro*. Further work expanded on this principle using peptides to self-assemble and form three stranded helicates in the presence of iron or cobalt cations.[198] The synthesised helicates were shown to bind three-way junctions through molecular dynamics simulations, and gel electrophoresis, and could be fluorescently tagged to selectively label DNA replication foci *in vitro* with Digitonin pretreatment.

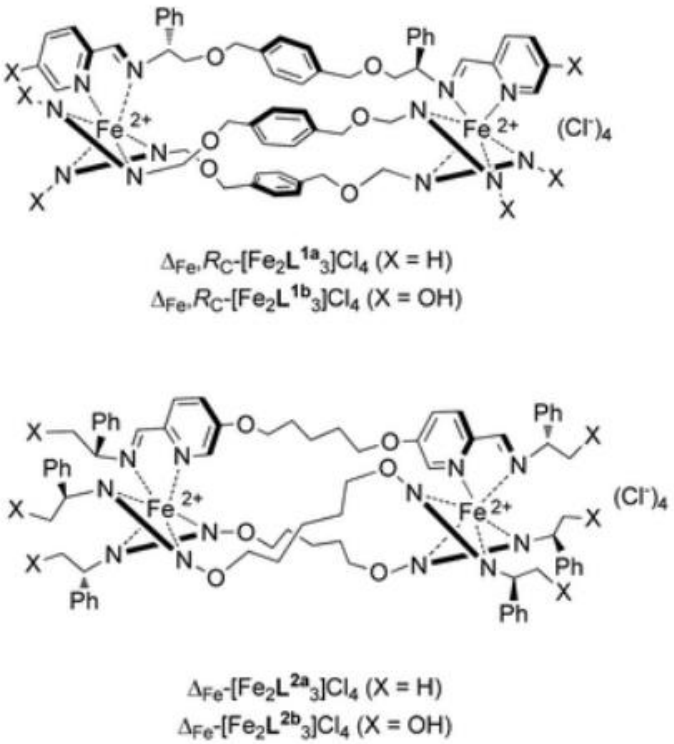


*Figure 31. Diagram of original flexicates designed and synthesised by Peter Scott and co-worders. Adapted from referenced publication with permission.*[200]

Flexicates are a similar class of junction binder with very similar properties to the other supramolecular cylinders discussed above. They were first synthesised in 2012 by Peter Scott and co-workers with the distinct advantage of flexicates being that they can be synthesised as enantiomerically pure complexes (Figure 31).[201] Flexicates consist of three ligands which bridge between two metal centres giving the overall structure a tetracationic charge (Figure 31). The bridging ligands give a helical twist to the complex, with the helicity is determined by the chirality of the ligand. These helicates have demonstrated the ability to bind to many different DNA structures; 4WJ, 3WJ, bulges, and B-DNA.[200] The flexicates distorted B-DNA by binding to the major groove in the order $L^{1a} > L^{2a} > L^{2b}$ which was thought to be controlled by the rigidity of the ligands with 1a being the most rigid. Binding of the flexicates to DNA 3WJ showed the same order of affinity but interestingly only the $L^{1a}$ complex was able to stabilise a DNA 4WJ, with the other structures actually decreasing the stability. Interaction of the complexes with different sized DNA bulges was assessed by thermal melting studies which again showed that only $L^{1a}$ complex was able to significantly improve the stability of the junction. The larger, bulged structures experienced the largest increase in melting temperature.

Significant work has been carried out to synthesise flexicates with functional groups attached to their ends,[202, 203] with a wide array of different central linkers,[204, 205] as well as asymmetric flexicates.[206] Recent work has focused on understanding the DNA damage caused by flexicates in cancer cells.[205]

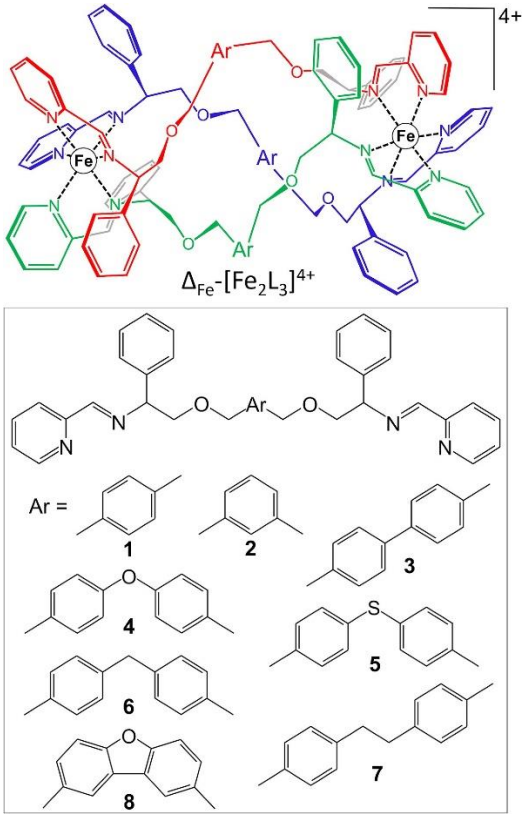


*Figure 32. Structural variations of flexicate used to study DNA binding and damage. Adapted from referenced publication with permission.*[205]

Flexicates 1-8 were able to stabilize all the DNA junction structures which were investigated with the highest selectivity being for Y-3WJ, followed by T-3WJ, and a significantly lower selectivity for 4WJ (Figure 32). Selectivity was determined by monitoring the change in melting temperature of the junctions in the presence of increasing concentrations of dsDNA. Complex 8 stabilized the DNA junctions to the greatest extent and was therefore investigated further in cell studies. Cytotoxicity in colon cancer cells HCT116 gave $IC_{50}$ values of 2.0±0.2 μM and 3.3±0.5 μM for Λ-8 and Δ-8 enantiomers respectively. DNA damage was confirmed and visualized by tagging the phosphorylated histone H2AX with fluorescently labelled anti-γH2AX antibodies, revealing that Λ-8 caused more DNA damage than Δ-8. It is worth noting that these flexicates have also demonstrated binding to G-quadruplexes which could be contributing their mode of action in cancer cells.[207, 208]

### 1.2.5.3 Triazacyclononanes

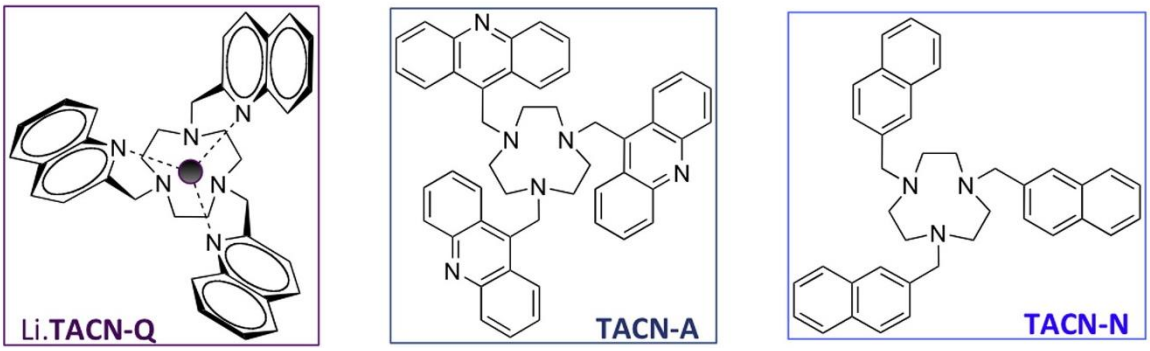


*Figure 33. Structures of some Triazacyclononanes. Adapted from referenced publication with permission.*[209]

Triazacycolnananes are another class of junction binders which strongly resemble the ends of the metallo cylinders described above.[209] They have a C3 symmetry and can accommodate a range of metal centres (Figure 33). The helical geometry of the complexes is enabled by chelation of a metal centre and matches that of DNA 3WJ. Coordination of these complexes has been investigated extensively through melting experiments with TACN-Q providing the greatest stabilization. This was thought to be due to the higher helicity of TACN-Q.

### 1.2.5.4 Pillarplexes

Pillarplexes were first described by Altmann and Pöthig in 2016.[210] They are organometallic complexes with a tetracationic charge, which consist of two organic ligands with ring like structures which with are bound together through eight metal centres (structure shown in Figure 38). The metal centres can be silver or gold but it has been demonstrated that the gold pillarplex is much more stable in biological solutions making it the more promising candidate for studying its biological applications.[211]

Modifications to the rim of the pillarplexes and rotaxanation have been achieved in more recent years.[212, 213]

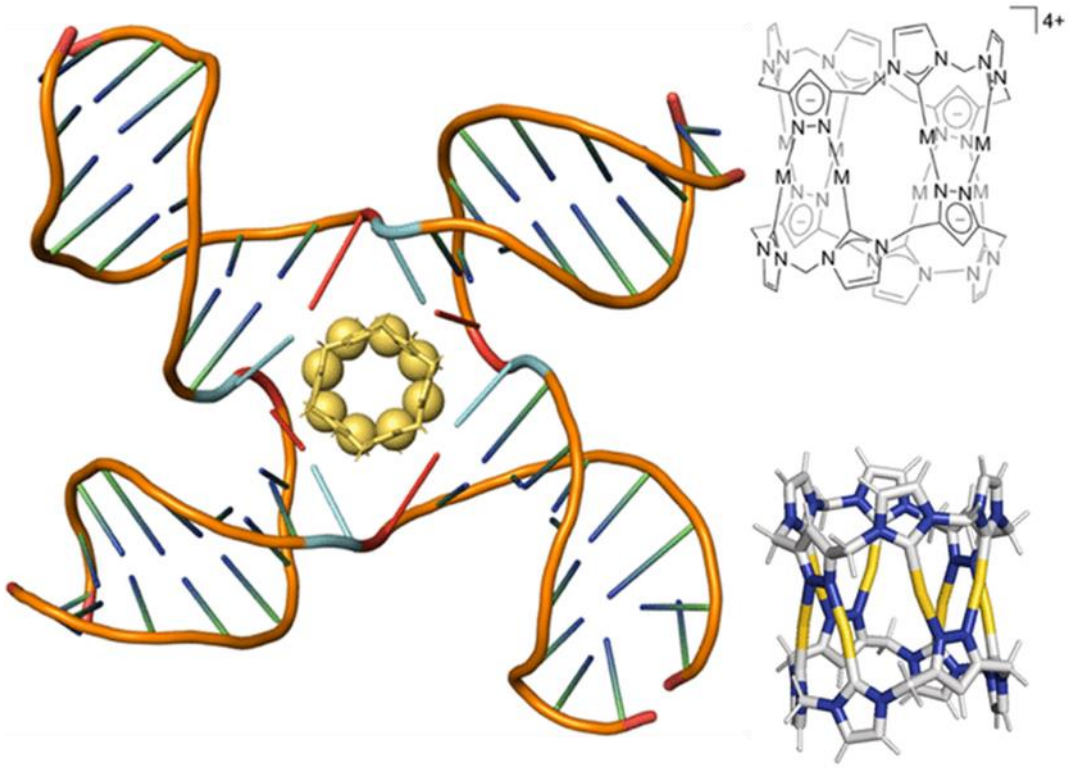


*Figure 34. Molecular dynamics simulation of gold pillarplex in the central cavity of a Holliday junction (left) and chemical structure of pillarplex (right). Adapted from referenced publication with permission.[197]*

Craig *et al.* have recently published on the unusual interactions of pillarplexes with DNA and DNA junction structures.[197] Linear dichroism and circular dichroism indicated that the pillarplex has a strong and specific interaction with B-DNA. Molecular dynamics simulations indicated a minor groove binding mode to B-DNA. Gel electrophoresis revealed that pillarplex could bind to a 3WJ however molecular dynamics simulations suggested that the junction was too small to accommodate the bulk of the pillarplex. The Holliday junction presented a much better fit for the pillarplex and was found to be its preferred binding partner through competition experiments (Figure 34). The pillarplex also exhibited strong binding to DNA Y-forks.[197]

### *1.2.5.5 Azacryptands*

Azacryptands are a class of organic molecules which share many properties with the metallo-supramolecular cylinders discussed above; they are roughly cylindrical in shape, they have similar

dimensions, and they can be multiply charged (Figure 35). In contrast to the metallic helicates, the azacryptands are designed to be flexible to allow them to reorientate their pi surfaces in junction sites to achieve optimal interactions.

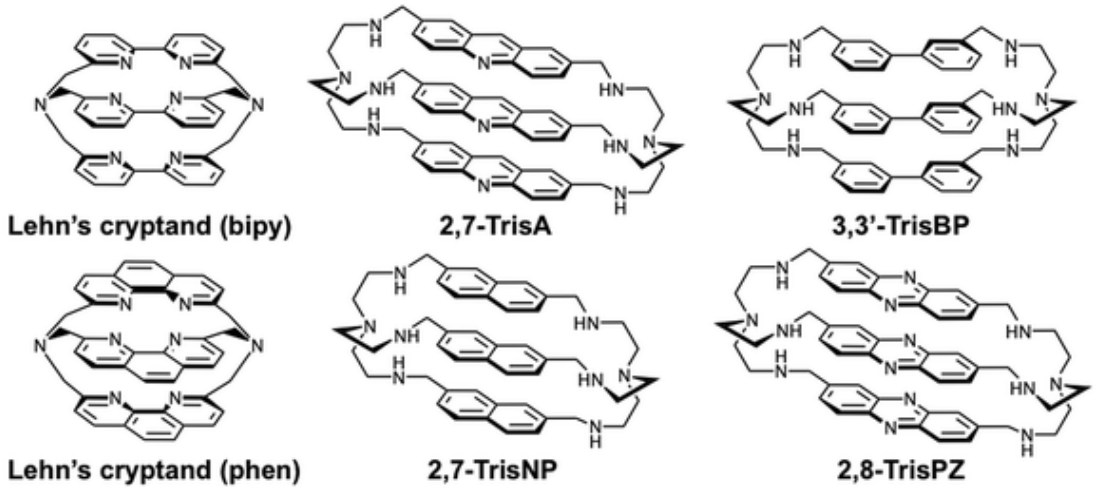


*Figure 35. Structures of Lehn's azacryptands as well as those produced by David Monchaud and co-workers. Adapted from referenced publication with permission.*[214]

These azacryptands were shown to be capable of stabilizing DNA 3WJ, as well as dsDNA, and g-quadruplexes by thermal melting studies.[214] The melting studies carried out utilised DNA structures tagged with FRET pairs at appropriate locations. Increasing equivalents of each azacryptand resulted in increases in the melting temperature of the DNA 3WJ to varying degrees. It was found that 2,7-TrisNP and 3,3'-TrisBP gave the largest increases in melting temperature indicating that they have the highest affinity for the 3WJ structure of the compounds tested. The selectivity of these compounds for junctions was also assessed by adding in competing dsDNA oligomers and measuring the resulting decrease in melting temperature. With up to 50 equivalents of ds26 oligomer there was only a minimal decrease in the melting temperature of the 3WJ indicating that 2,7-TrisNP and 3,3'-TrisBP have a high selectivity for 3WJ.[214] Notably, the compounds which display the highest affinity for DNA 3WJ also display the highest antiproliferative activity *in vitro*.

Further work by Monchaud and co-workers continued with TrisNP and also a new azacryptand, TrisPOB, which are both able to bind to 3WJ as well as G-quadruplexes.[215] Both compounds display high cytotoxicity towards MCF7 and MDA-MB-231 cancerous cell lines with the mechanism of cell death identified as double strand breaks.

### *1.2.5.6 Tetrahedron*

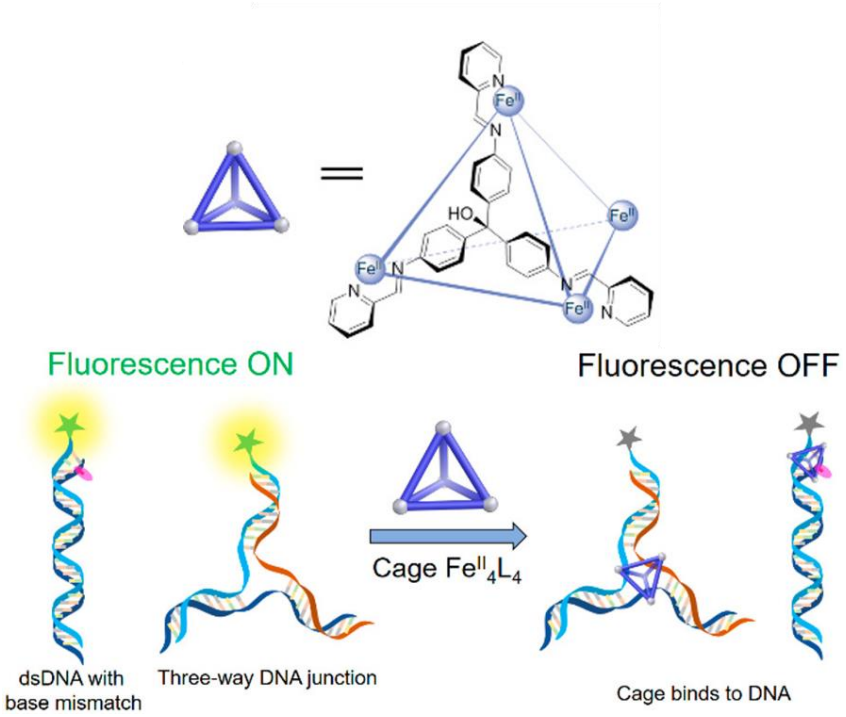


*Figure 36. Structure of $Fe^{II}_4L_4$ tetrahedron (top) and diagram to show binding of the tetrahedron to dsDNA with a mismatched base pair and a DNA 3WJ structure (bottom).*[216]

A three dimensional tetrahedron cage complex which was designed with iron metal centres at the vertices, has been shown to bind DNA 3WJ (Figure 36).[216] The fluorescence quenching properties of this complex were used to assess binding to fluoresceine tagged dsDNA, 3WJ , and 4WJ structures. Using this data, it was determined that the tetrahedral complex showed the highest affinity for ssDNA or DNA 3WJ. The preference for the tetrahedron to bind at sites with DNA base pair mismatches was noted and investigated further. Mismatches containing more unpaired bases resulted in stronger fluorescence quenching and the quenching was determined to be dependent on the distance of the mismatch site to the fluorescein tag. Similar tetrahedron structures have also been shown to bind G4 structures.[217]

## 1.3 Gold Nanoparticles

This thesis will investigate the use of gold spherical nucleic acids (gold-SNAs) for the delivery of DNA binding agents. Particles will be used to improve the uptake of the DNA binding agents into cells. The use of gold nanoparticles in future may also enable theranostic applications, or the addition of targeting moieties to the system. For these reasons, it is prudent to discuss their properties and biomedical applications of gold-SNAs.

Research into the use of gold nanoparticles for biological applications exploded after the development of the Turkevitch synthesis method in 1951.[218] This method produced gold nanoparticles which were extremely monodisperse, water soluble, and the stabilizing agent (citrate) was non-toxic.[219] Development of the Brust synthesis method in 1994 enabled the synthesis of more hydrophobic nanoparticles using a two-phase system.[220] Functionalisation of the surface of gold particles is simple, thiol groups will rapidly form a strong bond to the surface of the gold particles.[221] Other functional groups also interact well with the gold surface such as amines, and alcohols to a lesser extent. The unique optical properties, along with their relative biocompatibility and ease of synthesis/functionalisation are what make gold nanoparticles applicable to many different areas of biomedicine.

### 1.3.1 Uptake and Toxicity

Gold nanoparticles have been widely investigated over the last few decades with many nanoparticle systems being developed to treat a wide range of diseases. An often-overlooked area of nanoparticle research is their uptake into cells and their innate toxicity or biocompatibility. It is essential to understand these properties if gold nanoparticles are to be used *in vivo*. It is important to recognize that all aspects of a nanoparticle, shape, size, and surface coating will all impact their uptake and toxicity profile. For this reason, there are a number of literature articles where the results appear to contradict one another, this is often because each article uses particles with slightly different properties (e.g different surface functionality/size or a different cell line).

Pratim Biswas and co-workers carried out a systematic study where the effect of the size and shape of gold nanoparticles on their uptake and toxicity was evaluated in retinal pigment epithelial cell line.[222] The particles were synthesised via a seeded growth method to produce the various sizes which were all coated with CTAC (cetyltrimethylammonium chloride) as the stabilizing agent giving the particles a high positive surface charge. It was found that larger particles were better tolerated by the cells, though the larger particles also displayed a lower uptake. Interestingly, they found that the biocompatibility of the particles could be correlated with the total surface area of the particles introduced to the cells. Catherine Carnovale *et al.* went a step further and investigated a number of properties of gold

nanoparticles that may affect their uptake and toxicity, including; shape, size, surface coating, and serum proteins.[223] In this study they determined that smaller gold nanoparticles were taken into cells in much higher numbers. However, other literature found that particles with a diameter of ~50 nm showed the highest uptake.[224] The particles in this example were functionalised with RNA oligomers instead of CTAB which was used in the previous study demonstrating how the surface functionality of particles can have a large impact on cellular uptake. The different results may also be influenced by the different cell lines used. Catherine Carnovale *et al.* also determined that spherical particles were taken into cells in higher quantities than similarly sized particles of different shapes.[223] In general, particles with more planar surfaces showed a reduced uptake. It was expected that CTAB (cetyltrimethylammonium bromide) would give rise to a higher uptake into cells compared to citrate coated particles due to the positive surface charge of the CTAB. It was thought this would increase the particles electrostatic interactions with the negatively charged surface membrane of mammalian cells. Higher uptake of cationic particles has been reported in the literature in the past.[225] Despite this, there was little difference observed between the uptake of negatively charged citrate coated particles and the positively charged CTAB coated particles. Tyrosine and tyrptophan coated particles displayed the highest uptake which was thought to be due to the aromatic groups of the amino acids interacting with the cell membrane. These complex interactions with the cell membrane have yet to be fully understood. The role of serum proteins was also investigated, serum proteins are known to bind to gold nanoparticles and form a layer on their surface often termed a biological, or protein, corona.[226] In the presence of serum proteins the uptake of gold particles was shown to be reduced. This was thought to be caused by either the proteins on the particle surface interfering with the particles interactions with the cell membrane, or due to the particles having to compete with the proteins for uptake. The size and shape of the particles have been shown to alter the protein corona thickness and composition.[227]

### 1.3.2 Spherical Nucleic acids

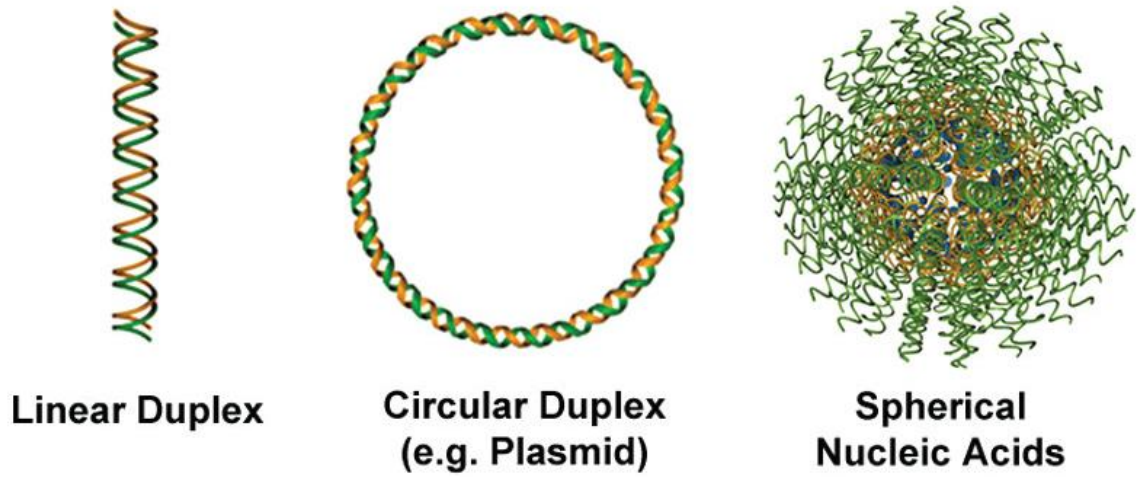


*Figure 37. Illustration of different forms of DNA. Adapted from reference publication with permission.*[228]

Spherical nucleic acids (SNA) consist of two components; they have a core nanoparticle which the structure is based upon, and an outer shell of nucleic acids which are oriented perpendicular to the surface of the nanoparticle (see Figure 37). The core of the SNA's have been composed of a wide range of materials from metallic, liposomes, polymers, proteins and more.[229] The size of the core nanoparticle is important to consider for uptake into cells but also as the curvature of the nanoparticle surface will impact the density of the oligomers exposed to solution.[230] In this work we are using gold nanoparticles so we will only be discussing SNAs based on gold nanoparticle cores in this section. Gold nanoparticle based spherical nucleic acids were selected for this research due to their high stability, biocompatibility and ease of synthesis and functionalisation. Gold nanoparticles also offer many avenues for theranostic applications due to their optical properties further down the line. The first SNAs were produced with gold nanoparticle cores by Mirkin *et al.* in an effort to create programmable nanoparticle architectures.[231] The orientation of the nucleic acids is largely responsible for the properties of these nanoparticle systems which are unique from the DNA oligomers alone, and the core nanoparticle:

- SNAs are much more resistant to enzyme degradation than the DNA sequences alone.[232]

- They have a significantly higher affinity for their complementary sequence than linear nucleic acids.[233]

- They are readily taken into cells without the need for transfection agents.[234]

- They have been shown to be non-toxic to cells and only illicit a minimal immune responses.[235]

These properties have prompted the use of these unique tools for a number of biomedical applications from sensors to gene regulation, to drug delivery and theranostics.

#### *1.3.2.1 Sensors*

Combining the optical properties of gold nanoparticles with the selectivity of oligonucleotide has led to the development of many gold SNA based colorimetric sensors. These sensors come in two broad categories. They either take advantage sensitivity of gold nanoparticles SPR band to aggregation,[236] or the quenching effect of gold nanoparticles on fluorophores in close proximity.[237]

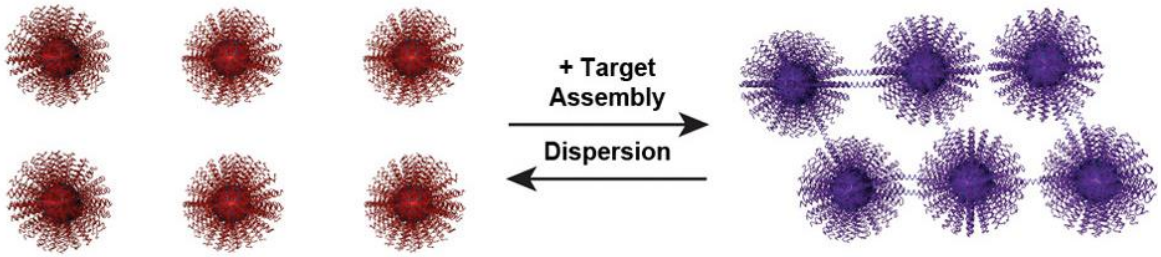


*Figure 38. Diagram to show how gold-SNAs can be cross-linked in the presence of the target strand and change colour from red to purple. Adapted from referenced publication with permission.[228]*

The first sensor applications for SNA were developed by Mirkin *et al.* after they demonstrated the possibility of creating assemblies of gold nanoparticles using programmable oligomers (Figure 38).[231] Two sets of gold nanoparticles were functionalised with DNA oligomers which were partially complementary to a target strand. The target DNA strand could then be added to a solution containing both sets of gold nanoparticles and induce cross-linking between them. Using the same principle, a method for detecting specific DNA sequences in solution was developed which was orders of magnitude more sensitive than comparable fluorescent probes which were used at the time.[238] Similar methods were again used for the detection of proteins at attomolar concentrations and from complex solutions.[239] The system developed was highly sensitive and allowed for the identification of specific proteins from complex solutions, hence the name “bio-barcode assay”. The target protein would first be captured on a magnetic microparticle with appropriate monoclonal antibodies. The gold-SNA particles with a polyclonal antibody could then bind to the captured protein on the magnetic particles, with the whole system isolated using a magnetic field. The complementary DNA strand on the gold-

SNA particles, which is encoded with the identity of the protein, would then be dehybridized and either amplified by PCR or detected on a chip.

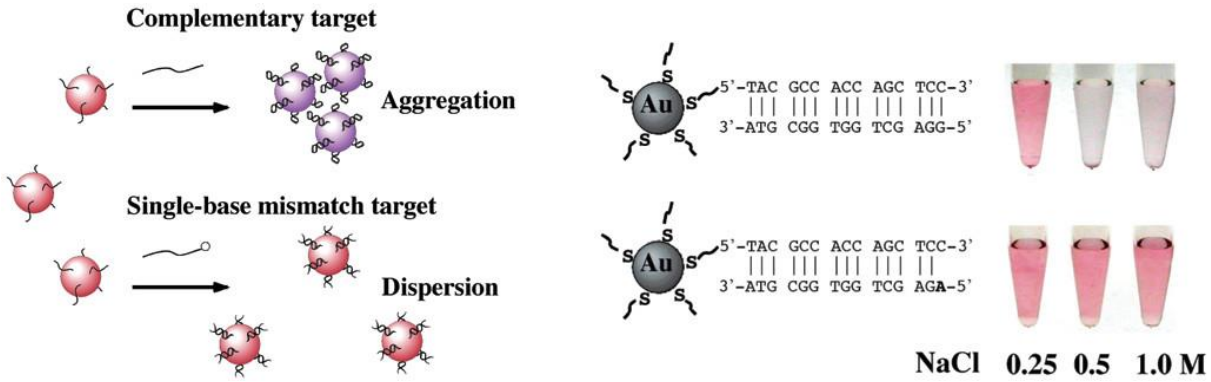


*Figure 39. Non-crosslinking gold-SNA particles for detection of specific oligomers. Adapted from referenced publication with permission.*[240]

The first example of non-crosslinking gold SNAs used for sensing specific DNA oligomers was reported by Sato *et al.* in 2003 (Figure 39).[240] A simple system which functionalised gold nanoparticles with a thiolated DNA oligomer which was complementary to the target DNA sequence was developed. In the presence of the target strand of DNA, and a high salt concentration, duplexes would form on the particle surface. These duplexes would reduce the stability of the system causing almost immediate aggregation of the particles and resulting change in the visible colour of the solution. This nanoparticle assay was shown to be able to differentiate between the target oligomer, and oligomers with single base mismatches. The primary advantages of this system were the simplicity of the design and rapid nature of the assay, but it was not as sensitive as cross-linking gold-SNA systems as many target strands of DNA are required to form enough duplexes on the particles.[238] Cross linking systems in principle only require a single target strand to start aggregating particles.

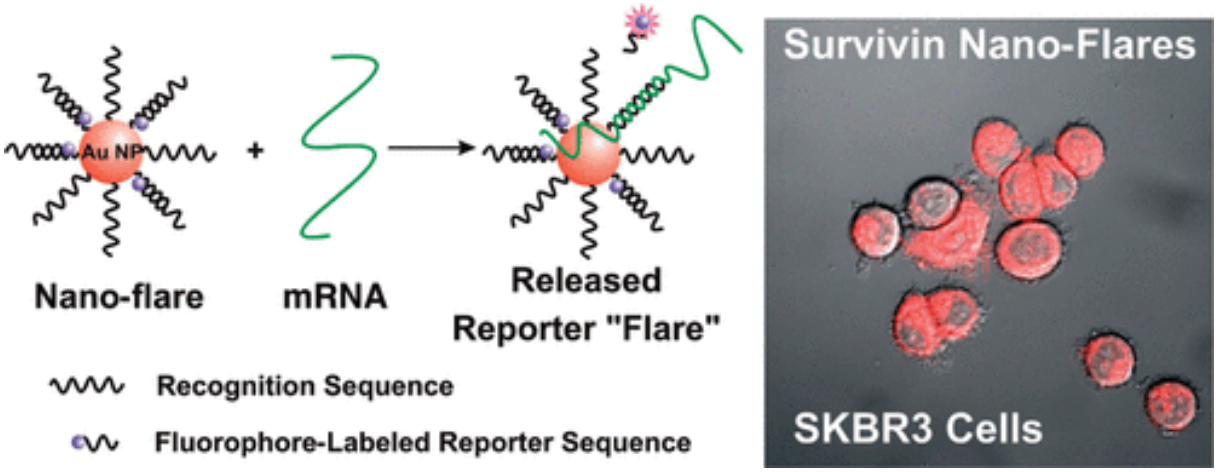


*Figure 40. Gold nanoparticles functionalised with a recognition sequence and reporter sequence which is released in the presence of specific mRNA. Adapted from referenced publication with permission.*[241]

A step forward in the design of SNAs for sensing applications was the development of "Nano-flares"(Figure 40).[241] These gold-SNAs were functionalised with a thiolated oligomer which was then hybridized with a longer oligo specific for an mRNA sequence that also harboured a fluorophore which was located close to the gold nanoparticle core. In the presence of the target mRNA sequence, the fluorescent oligo is then released in the presence of the target mRNA strand allowing it to fluoresce. This technique was used to quantify intracellular mRNA, though they also demonstrate siRNA knock down and the potential of this system for transfection and gene regulation. The same particle system was also synthesised with two different DNA sequences and two distinct fluorophores to simultaneously detect the presence of two different mRNA sequences in live cells.[242] More recently it was demonstrated how nano-flares could be used to detect genetic markers of circulating cancer cells.[243] This technique was able to detect as low as 100 cells per mL of circulating cancer cells from whole blood. Flow cytometry was then used to separate and subsequently culture the cancer cells for further analysis. More complex systems involving nano-flares have also been used. Kyriazi *et al.* produced gold nanoparticle dimers which could simultaneously detect two different mRNA targets as well as deliver one or two different DNA intercalating anti-cancer drugs.[244] Similar particle systems have also recently been used to identify and sort skeletal stem cells.[245]

There are issues faced by these biosensing techniques which utilise SNAs, passive release of fluorophores by nucleases is a potential problem. Recent research has sought to improve nuclease

resistance through the use of modified oligonucleotides,[246] or the addition of PEG tail groups.[247] Some research has taken a different approach, intentionally adding proteins, such as albumin or antibodies, to the surface of the particles during the synthesis.[248] This was shown to increase the particles resistance to nuclease degradation and reduce uptake of the particles by macrophages. The protein corona remained stable over 12 hours with less than 45% loss of protein. The presence of the proteins did not significantly impact the accessibility of the core surface DNA. Gradual displacement of the oligomers on the surface of the particles in the presence of thiol containing biomolecules such as glutathione is another potential issue.[249] Recent work has sought to manage this problem by functionalising the oligomers bound to the surface of the gold particles with fluorophores. [245, 250] The fluorophores are quenched by the presence of the gold nanoparticle. If the oligomers are displaced or degraded and the fluorophore is released then the fluorescence increase can be monitored.

#### *1.3.2.2 Gene regulation*

SNAs may be used to deliver nucleic acids into cells for gene regulation. Linear nucleic acids are degraded rapidly in the body by nucleases. The inherent nuclease resistance of SNAs compared to B-DNA is caused by the high local salt concentration allows them to reach their target before degradation takes place. Transfection has traditionally required the use of transfection agents to aid the uptake of the highly negatively charged nucleic acids into cells. It is not possible to use transfection agents *in vivo* due to their high toxicity, but despite the high negative charge of SNAs they are readily taken up by cells and illicit a minimal immune response.[251] SNAs also have a very high affinity for their complementary oligonucleotide, up to two orders of magnitude higher than the complementary linear ssDNA.[233] Due to these favourable properties, SNAs have been widely used to control gene expression by delivery of siRNA or antisense oligonucleotides. Rosi *et al.* first used antisense SNAs for gene regulation.[234] They were found to produce a higher percentage decrease in green fluorescent protein expression than commercially available alternatives, and were also less toxic.

A notable example of gold-SNAs being used to deliver siRNA was used to treat glioblastoma.[252] Brain tumours are known to be very difficult to treat due to the blood brain barrier which prohibits most drugs from reaching the cancer. These gold-SNAs were able to cross the blood brain barrier in a mouse

model and accumulate in the brain when systemically administered. The oncogene Bcl2L12 was successfully targeted resulting in the reduction of Bcl2L12 protein and mRNA levels, reducing tumour progression. Recently, this gold-SNA system has completed a phase 0 clinical study.[253] These particles were also able to cross the human blood brain barrier and accumulate in the tumour. Perhaps more importantly for the progression of gold nanoparticles into the clinic, the particles were well tolerated and did not cause longer term toxicity. Gold was still detectable in patients tumours which recurred after 174 days, the effects of this very long term exposure to gold particles is yet to be assessed. Many more gold-SNA systems have been developed to deliver siRNA to target specific genes.[254-258]

#### *1.3.2.3 Photothermal therapy*

Photothermal therapy is the use of light to induce an increase in temperature and kill cancer cells. Gold nanoparticles are ideal for this application due to their high absorption cross section and strong photothermal conversion capability. This conversion capability is strongly dependant on the shape and size of the particles.[259] For photothermal therapy to be a viable treatment, small particles are required to maintain a large surface area for functionalisation, high circulation life-time, and to ensure that the particles are fit for renal clearance from the body.[260, 261] However, large particles are necessary for their high SPR absorbance band which is shifted to longer wavelengths which can penetrate tissue. One solution to this problem is to use small gold-SNA particles which can aggregate *in vivo* under specific conditions. The surface plasmons of aggregated gold nanoparticles couple together, shifting their absorbance to longer wavelengths. This phenomenon has been exploited for photothermal therapy.[262] SNAs have been designed for photothermal therapy by making use of their nucleic acid recognition abilities to aggregate under specific conditions.

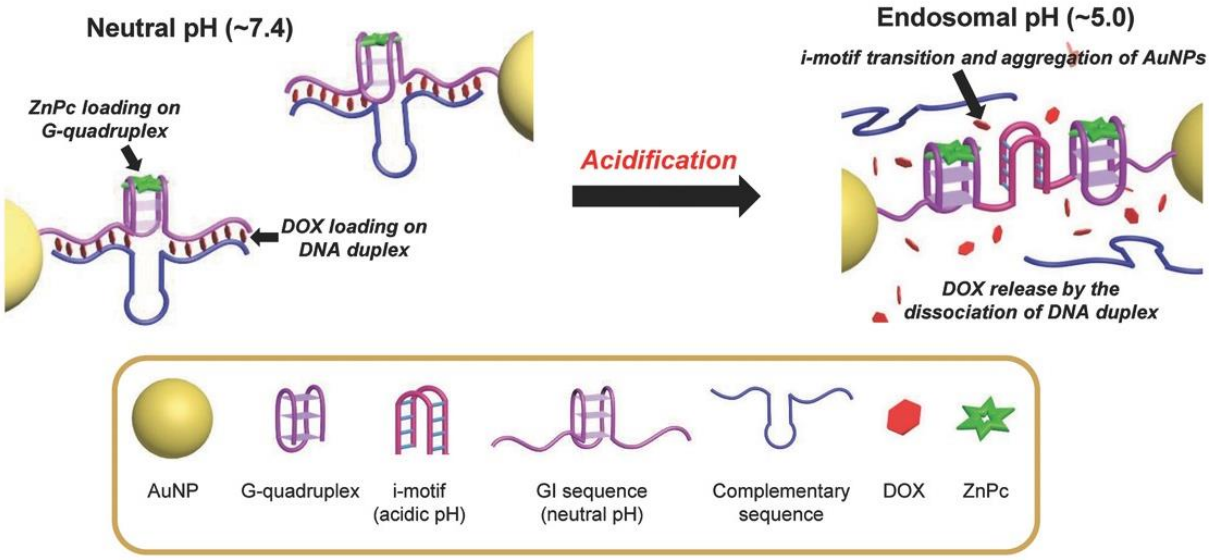


*Figure 41. Gold-SNA particles functionalised with G-quadruplex DNA which can unfold at reduced pH to form an i-motif with adjacent particles. Adapted from reference publication with permission.*[263]

Park *et al*. synthesised gold-SNA particles decorated with G-quadruplexes and a complementary sequence.[263] The G4 was loaded with ZnPc (a photosensitizer) and the duplex portion of the oligo was loaded with doxorubicin. Upon exposure to low pH environment an i-motif structure would form between oligomers on adjacent gold particles causing aggregation (Figure 41). The formation of this new structure would induce the release of the doxorubicin and enable the photothermal and photodynamic therapy to be employed. Tumour regression was observed in mouse models indicating the effectiveness of their strategy. Zhang *et al.* employed a similar strategy using a pH sensitive G-quadruplex which would fold into an i-motif at low pH an release doxorubicin.[264] They also incorporated a fluorescently labelled ATP aptamer as the complementary strand which is displaced at low pH, allowing for ATP imaging (using the Nanoflare principle discussed in section 1.3.2.1). Other researchers have utilised ATP as the stimulus to induce aggregation of gold particles for photothermal therapy.[265] ATP induced structural changes in the DNA triple helix probes on the particles causing aggregation. Enzyme induced aggregation of gold-SNA particles is another avenue which has been recently explored for photothermal therapy.[266] Two sets of SNA particles with complementary DNA strands on were protected by a PEG layer linked to the oligomers by a peptide linker. The peptide linker was a substrate for matrix metalloproteinases which are overexpressed in tumours. In tumour environments the PEG layer is stripped of the particles allowing them to hybridize together which enables the photothermal

therapy. The increase in temperature would also cleave the thermoresponsive linker attaching doxorubicin to the particles.

Each of the gold-SNA systems described here are complex systems making full use of the properties of the gold nanoparticle core and the oligomers on the particle surface. They demonstrate the versatility of the SNA concept in creative ways, using different stimuli to induce aggregation, deliver multiple drugs simultaneously and/or allow for fluorescence imaging.

### *1.3.2.4 Drug delivery*

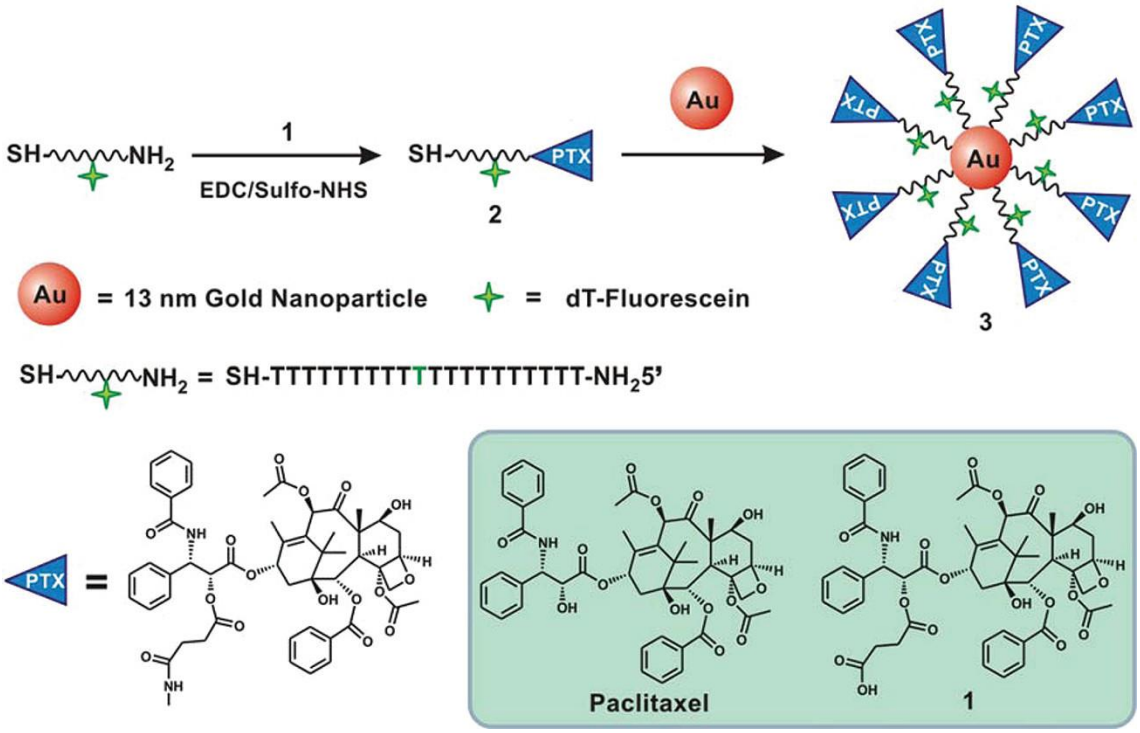


*Figure 42. Synthesis of gold-SNA functionalised with paclitaxel. Adapted from referenced publication with permission.*[267]

An early example of a SNA system for the delivery of a chemotherapeutic drug was published by Zhang *et al.* in 2011 (Figure 42). [267] In this work, the terminal ends of the oligomers on gold-SNA particles were functionalised with paclitaxel, a highly active anticancer drug.[268] A fluorescent tag was also added to the oligomers to enable quantification of drug loading on the particles, and confocal imaging of the particles *in vitro*. Conjugation of the paclitaxel to the gold particles was shown to improve the aqueous solubility of paclitaxel by approximately 50x. It was proposed in the article that this strategy may be used to improve the solubility of other poorly water-soluble drugs. The cytotoxicity of the paclitaxel against a number of cell lines was also found to be enhanced when bound to the particles. It is not

clear whether the drug is released from the surface of the particle in cells or not. No colocalization of the drug and gold nanoparticles was attempted.

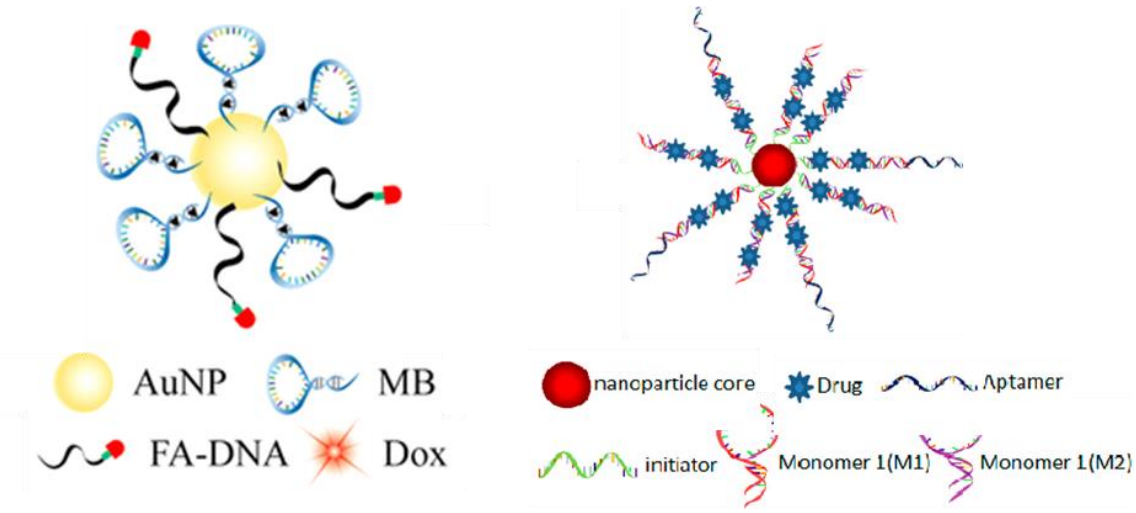


*Figure 43. Gold-SNA loaded with doxorubicin and targeted with folate (left),[269] or with an aptamer (right).[270]*

Targeting moieties have been added to similar SNA systems to enhance targeted delivery. Zheng *et al.* made the addition of an aptamer to gold-SNAs nanoparticles to enhance specificity for cancer cells (Figure 43).[270] The anti-cancer drug doxorubicin was loaded onto the SNA through intercalation into the duplexes on the SNA. The particle size was controlled by changing the length of the oligomer shell, as particle size is known to impact cellular uptake, particle stability, and biocompatibility. Two different aptamers Sgc8, and AS1411 were used in this study to demonstrate the generality of the system for targeted drug delivery. These gold-SNA particles displayed toxicity comparable to free doxorubicin, but significantly improved selectivity for cancerous cell lines. Pan *et al.* used a very similar system to deliver doxorubicin to cancer cells (Figure 43).[269] In this case, auxiliary ssDNA strands were functionalised with folic acid to target the folate receptor on cancer cells in place of an aptamer. The molecular beacon (MB) contained a stem loop which was designed to recognise specific mRNA. On recognition of a complementary mRNA sequence, the MB would unfold, releasing the intercalated doxorubicin. The system was shown to be sensitive to the levels of tumour mRNA expressed in the cells demonstrating controlled release of doxorubicin *in vitro*.

The use of oligomers with recognition sequences on their exposed ends to recognise specific mRNA sequences and induce release of drugs has been built upon to produce more complex drug delivery systems.

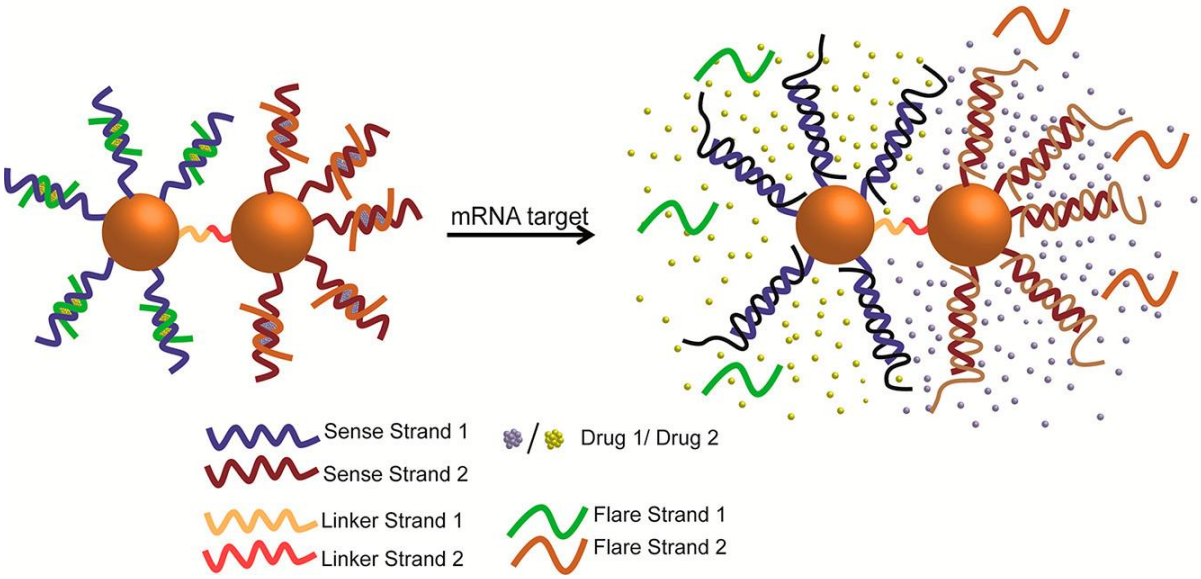


*Figure 44. Illustration to show the SNA dimers and the release of fluorophores and MTX/DOX in the presence of target mRNA.*[244]

An example of a complex SNA design for delivery and sensing applications was developed by Kyriazi *et al.* (Figure 44).[244] Gold nanoparticle dimers were produced by functionalising two batches of gold nanoparticles with an oligomer, and purifying them by agarose gel electrophoresis to ensure a single oligo per particle. The ends of the oligomers were then chemically modified with either an azide or alkyne before the rest of the particle was coated with oligomers designed to bind specific mRNA. Fluorescently tagged short oligomers (flares) were then bound to the oligos on the gold particles' surface. The fluorescence of the flare strands is quenched when in close proximity to the gold nanoparticles surface. The two batches of particles could then be linked together to form dimers which could simultaneously detect two different mRNA oligomers in solution by release of the flare strands in the presence of the complementary mRNA sequences.

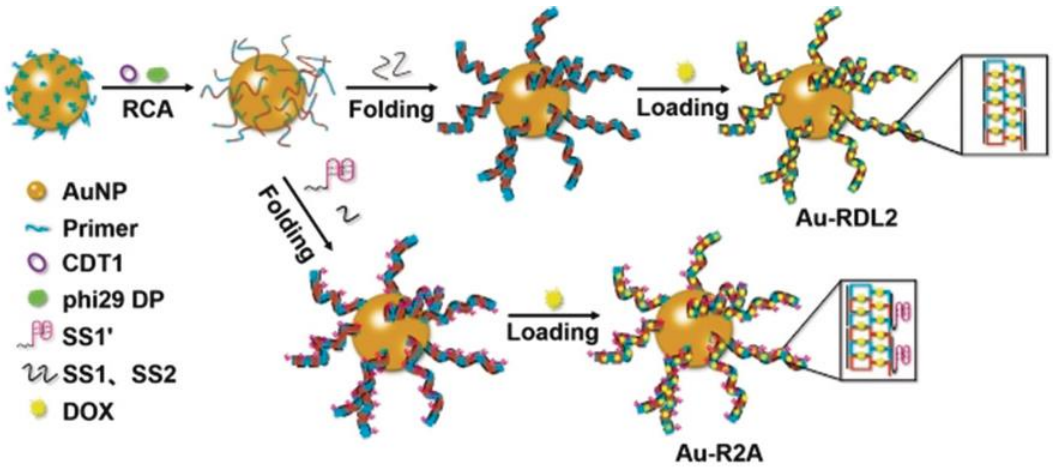


*Figure 45. Synthesis of AuRDL2-DOX and Au-R2A-DOX. SS1 and SS2 are the short oligomers which convert the ssDNA into duplexes, producing a ribbon structure. SS1' is a modified SS1 with the addition of the AS1411 aptamer. Adapted from referenced publication with permission.*[271]

A unique gold nanoparticle DNA system which is closer to DNA origami rather than SNAs due to the DNA "ribbon" design used is described here due to the similarities in drug delivery method. The DNA ribbon was designed from a repeating sequence which could self-assemble to create a wide and dense "ribbon of lattice" structure (Figure 45).[271] Rolling chain amplification was used to produce this repetitive structure which folded to form the ribbon. The AS1411 aptamer was also attached to the DNA ribbon through hybridization. The AS1411 aptamer is a guanine rich oligomer which forms G-quadruplex structures and is an aptamer for the protein nucleolin,[272] which has been shown to be overexpressed on the surface of cancer cells.[273] Once the gold nanoparticles were coated with the DNA ribbon, they were then loaded with doxorubicin which non-covalently binds to the DNA structure. The acidic environment of cancer cells facilitated the continuous release of doxorubicin over a 24 hour period. The gold particles displayed higher uptake into cells than the DNA ribbon alone. It was thought that this was due to the spherical shape of the particles.

Changes in pH have been used to induce changes in the secondary structures of the oligomers on the surface of SNAs. Song *et al.* developed a SNA particle system with a carefully designed oligomer which could form a duplex at the physiological pH of 7.4, but under acidic conditions folds to form an i-motif structure (Figure 46).[274] This duplex was loaded with doxorubicin by intercalation, which could then be released when the duplex is broken to form an i-motif in the acidic tumour environment.

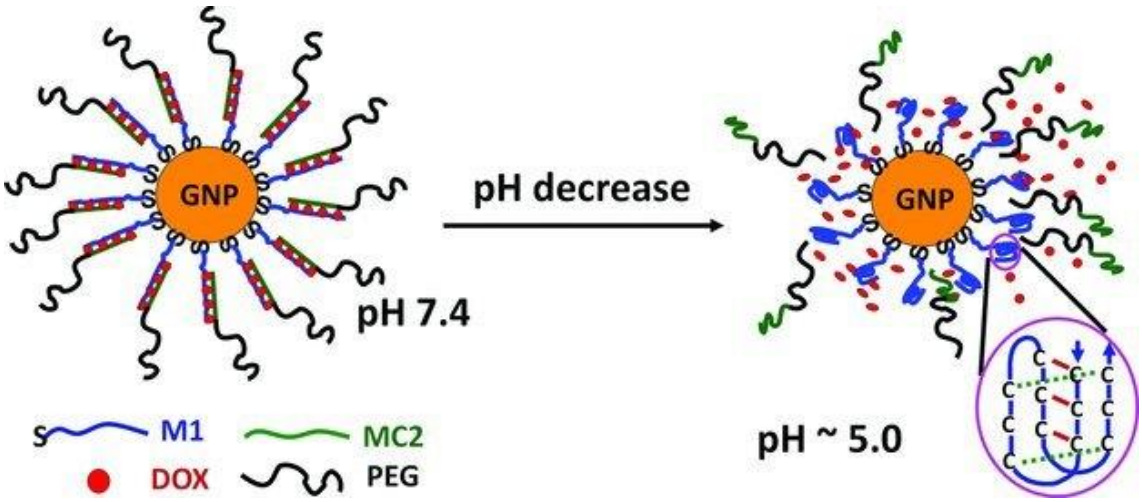


*Figure 46. Reduction in pH induces the formation of an i-motif structure, which breaks the DNA duplex, releasing intercalated doxorubicin. Adapted from referenced publication with permission.*[274]

All of the examples above discuss the delivery of DNA intercalating agents. The only example in the literature of gold-SNA particles used to deliver a DNA groove binding agents was published by Song *et al*.[247] In this system PEG moieties were added to the ends of the complementary DNA oligomers to improve nuclease resistance. This has been shown to significantly reduce serum protein binding and make the particles almost completely resistant to nuclease digestion. The particles are still able to be uptaken by cells and were used as drug delivery vehicles for both intercalating DNA binders and DNA groove binding agents. The groove binding binder used in this work was a dinuclear ruthenium complex which was known to be impermeable to live cells. Fluorescence imaging of cells incubated with this nanoparticle system clearly demonstrated the uptake of the particles and diruthenium complex. Release of the drug was stimulated by a low pH environment using the same method described above (Figure 46). A caveat to this work is that it does not address the accessibility of the core DNA to other nucleotides.

## 1.4 Thesis Aims

DNA is a repository of all our genetic information. The vast majority of our DNA is present in its most stable state, a B-DNA helix structure, however when the information contained within our genome is accessed or manipulated, more complex structures must be formed. DNA junctions are necessary whenever a duplex is split into its constituent strands as it is during replication, transcription, and repair. Non-canonical DNA structures are also known to be crucial for controlling gene expression. For the

reasons stated, targeting of non-canonical DNA structures is highly desirable. The unique structures themselves make it possible for us to design complexes which can target the specific spatial and chemical environment presented.

Chapter two of this thesis investigates the DNA binding potential of a known, but understudied, tetra-stranded palladium supramolecular complex. Synthesis of the platinum analogue of the palladium complex is also carried out. The interaction of both complexes with B-DNA is evaluated by a range of biophysical studies and the binding of these complexes with non-canonical DNA structures is investigated.

Chapter three builds upon recently published work from the Hannon group regarding the interactions of pillarplexes and supramolecular cylinders with 4WJs. The affinity of the pillarplex, supramolecular cylinders, and the new platinum complex to a range of non-canonical DNA structures is evaluated in order to gain insights into the structural characteristics of these similar complexes which favour junction binding.

Spherical nucleic acids are the focus of Chapter four. Spherical nucleic acids are synthesised and investigated for use as a delivery vector for our junction binding metal complexes. The spherical nucleic acids are loaded with supramolecular metal complexes through non-covalent interactions, the release of these complexes from the dsDNA on the surface of the particles to DNA junctions is studied. The use of nanoparticles may improve the uptake of these metal complexes into cells to enhance their therapeutic effect.

## 1.4 References


1. Watson, J. D.; Crick, F. H. C., Molecular Structure of Nucleic Acids: A Structure for Deoxyribose Nucleic Acid. *Nature* **1953,** *171* (4356), 737-738.
2. Wilkins, M.; Stokes, A.; Wilson, H., HR Nature 171 (1953) 738. RE Franklin and RG Gosling. *Nature* **1953,** *171*, 740.
3. Sathyamoorthy, B.; Sannapureddi, R. K. R.; Negi, D.; Singh, P., Conformational characterization of duplex DNA with solution-state NMR spectroscopy. *Journal of Magnetic Resonance Open* **2022,** *10-11*, 100035.
4. Franklin, R. E.; Gosling, R. G., The structure of sodium thymonucleate fibres. I. The influence of water content. *Acta Crystallographica* **1953,** *6* (8-9), 673-677.
5. Trieb, M.; Rauch, C.; Wellenzohn, B.; Wibowo, F.; Loerting, T.; Liedl, K. R., Dynamics of DNA: BI and BII Phosphate Backbone Transitions. *The Journal of Physical Chemistry B* **2004,** *108* (7), 2470-2476.
6. Whelan, D. R.; Hiscox, T. J.; Rood, J. I.; Bambery, K. R.; McNaughton, D.; Wood, B. R., Detection of an en masse and reversible B- to A-DNA conformational transition in prokaryotes in response to desiccation. *Journal of The Royal Society Interface* **2014,** *11* (97), 20140454.
7. DiMaio, F.; Yu, X.; Rensen, E.; Krupovic, M.; Prangishvili, D.; Egelman, E. H., A virus that infects a hyperthermophile encapsidates A-form DNA. *Science* **2015,** *348* (6237), 914-917.
8. Serganov, A.; Patel, D. J., Ribozymes, riboswitches and beyond: regulation of gene expression without proteins. *Nature Reviews Genetics* **2007,** *8* (10), 776-790.
9. Rinn, J. L.; Chang, H. Y., Genome Regulation by Long Noncoding RNAs. *Annual Review of Biochemistry* **2012,** *81* (1), 145-166.
10. Herbert, A.; Alfken, J.; Kim, Y.-G.; Mian, I. S.; Nishikura, K.; Rich, A., A Z-DNA binding domain present in the human editing enzyme, double-stranded RNA adenosine deaminase. *Proceedings of the National Academy of Sciences* **1997,** *94* (16), 8421-8426.
11. Herbert, A. G.; Spitzner, J. R.; Lowenhaupt, K.; Rich, A., Z-DNA binding protein from chicken blood nuclei. *Proceedings of the National Academy of Sciences* **1993,** *90* (8), 3339-3342.
12. Schwartz, T.; Rould, M. A.; Lowenhaupt, K.; Herbert, A.; Rich, A., Crystal Structure of the Zα Domain of the Human Editing Enzyme ADAR1 Bound to Left-Handed Z-DNA. *Science* **1999,** *284* (5421), 1841-1845.
13. Schade, M.; Behlke, J.; Lowenhaupt, K.; Herbert, A.; Rich, A.; Oschkinat, H., A 6 bp Z-DNA hairpin binds two Zα domains from the human RNA editing enzyme ADAR1. *FEBS Letters* **1999,** *458* (1), 27-31.
14. Suram, A.; Rao, J. K. S.; Latha, K. S.; Viswamitra, M. A., First evidence to show the topological change of DNA from B-DNA to Z-DNA conformation in the hippocampus of Alzheimer's brain. *NeuroMolecular Medicine* **2002,** *2* (3), 289-297.
15. Lafer, E. M.; Valle, R. P.; Möller, A.; Nordheim, A.; Schur, P. H.; Rich, A.; Stollar, B. D., Z-DNA-specific antibodies in human systemic lupus erythematosus. *Journal of Clinical Investigation* **1983,** *71* (2), 314-321.
16. Gellert, M.; Lipsett, M. N.; Davies, D. R., HELIX FORMATION BY GUANYLIC ACID. *Proceedings of the National Academy of Sciences* **1962,** *48* (12), 2013-2018.
17. Smith, F. W.; Feigon, J., Quadruplex structure of Oxytricha telomeric DNA oligonucleotides. *Nature* **1992,** *356* (6365), 164-168.
18. Aboul-ela, F.; Murchie, A. I. H.; Lilley, D. M. J., NMR study of parallel-stranded tetraplex formation by the hexadeoxynucleotide d(TG4T). *Nature* **1992,** *360* (6401), 280-282.
19. Laughlan, G.; Murchie, A. I. H.; Norman, D. G.; Moore, M. H.; Moody, P. C. E.; Lilley, D. M. J.; Luisi, B., The High-Resolution Crystal Structure of a Parallel-Stranded Guanine Tetraplex. *Science* **1994,** *265* (5171), 520-524.
20. Varshney, D.; Spiegel, J.; Zyner, K.; Tannahill, D.; Balasubramanian, S., The regulation and functions of DNA and RNA G-quadruplexes. *Nature Reviews Molecular Cell Biology* **2020,** *21* (8), 459-474.
21. Burge, S.; Parkinson, G. N.; Hazel, P.; Todd, A. K.; Neidle, S., Quadruplex DNA: sequence, topology and structure. *Nucleic Acids Research* **2006,** *34* (19).

22. Biffi, G.; Tannahill, D.; Balasubramanian, S., An Intramolecular G-Quadruplex Structure Is Required for Binding of Telomeric Repeat-Containing RNA to the Telomeric Protein TRF2. *Journal of the American Chemical Society* **2012,** *134* (29), 11974-11976.
23. Kanoh, Y.; Matsumoto, S.; Fukatsu, R.; Kakusho, N.; Kono, N.; Renard-Guillet, C.; Masuda, K.; Iida, K.; Nagasawa, K.; Shirahige, K.; Masai, H., Rif1 binds to G quadruplexes and suppresses replication over long distances. *Nature Structural & Molecular Biology* **2015,** *22* (11), 889-897.
24. Giraldo, R.; Rhodes, D., The yeast telomere-binding protein RAP1 binds to and promotes the formation of DNA quadruplexes in telomeric DNA. *The EMBO Journal* **1994,** *13* (10), 2411-2420.
25. Miller, D. M.; Thomas, S. D.; Islam, A.; Muench, D.; Sedoris, K., c-Myc and cancer metabolism. *Clinical cancer research: an official journal of the American Association for Cancer Research* **2012,** *18* (20).
26. Simonsson, T.; Kubista, M.; Pecinka, P., DNA tetraplex formation in the control region of c-myc. *Nucleic Acids Research* **1998,** *26* (5), 1167-1172.
27. Pavlova, A. V.; Kubareva, E. A.; Monakhova, M. V.; Zvereva, M. I.; Dolinnaya, N. G., Impact of G-Quadruplexes on the Regulation of Genome Integrity, DNA Damage and Repair. *Biomolecules* **2021,** *11* (9).
28. Abou Assi, H.; Garavís, M.; González, C.; Damha, M. J., i-Motif DNA: structural features and significance to cell biology. *Nucleic Acids Research* **2018,** *46* (16), 8038-8056.
29. Gehring, K.; Leroy, J.-L.; Guéron, M., A tetrameric DNA structure with protonated cytosine-cytosine base pairs. *Nature* **1993,** *363* (6429), 561-565.
30. Kang, C. H.; Berger, I.; Lockshin, C.; Ratliff, R.; Moyzis, R.; Rich, A., Crystal structure of intercalated four-stranded d(C3T) at 1.4 A resolution. *Proceedings of the National Academy of Sciences* **1994,** *91* (24), 11636-11640.
31. Brown, S. L.; Kendrick, S., The i-Motif as a Molecular Target: More Than a Complementary DNA Secondary Structure. *Pharmaceuticals* **2021,** *14* (96).
32. Dilek, G.; Effrosyni, A.; Kamel El, O.; Zuzana, D.; Rupesh, V. C.; Daniel, P.; Christopher, A. W.; Christopher, J. M.; Shozeb, H.; Gary, N. P.; Zoë, A. E. W., Structural Insights into Regulation of Insulin Expression Involving i-Motif DNA Structures in the Insulin-Linked Polymorphic Region. *bioRxiv* **2023**, 2023.06.01.543149.
33. Holliday, R., A mechanism for gene conversion in fungi. *Genetics Research* **1964,** *5* (2), 282-304.
34. Bzymek, M.; Thayer, N. H.; Oh, S. D.; Kleckner, N.; Hunter, N., Double Holliday junctions are intermediates of DNA break repair. *Nature* **2010,** *464* (7290), 937-941.
35. Young, S. J.; Sebald, M.; Shah Punatar, R.; Larin, M.; Masino, L.; Rodrigo-Brenni, M. C.; Liang, C.-C.; West, S. C., MutSβ Stimulates Holliday Junction Resolution by the SMX Complex. *Cell Reports* **2020,** *33* (3).
36. Zhou, R.; Yang, O.; Déclais, A.-C.; Jin, H.; Gwon, G. H.; Freeman, A. D. J.; Cho, Y.; Lilley, D. M. J.; Ha, T., Junction resolving enzymes use multivalency to keep the Holliday junction dynamic. *Nature Chemical Biology* **2019,** *15* (3), 269-275.
37. Shah Punatar, R.; Martin, M. J.; Wyatt, H. D. M.; Chan, Y. W.; West, S. C., Resolution of single and double Holliday junction recombination intermediates by GEN1. *Proceedings of the National Academy of Sciences* **2017,** *114* (3), 443-450.
38. Elbakry, A.; Juhász, S.; Chan, K. C.; Löbrich, M., ATRX and RECQ5 define distinct homologous recombination subpathways. *Proceedings of the National Academy of Sciences* **2021,** *118* (3), e2010370118.
39. Xia, J.; Chen, L.-T.; Mei, Q.; Ma, C.-H.; Halliday, J. A.; Lin, H.-Y.; Magnan, D.; Pribis, J. P.; Fitzgerald, D. M.; Hamilton, H. M.; Richters, M.; Nehring, R. B.; Shen, X.; Li, L.; Bates, D.; Hastings, P. J.; Herman, C.; Jayaram, M.; Rosenberg, S. M., Holliday junction trap shows how cells use recombination and a junction-guardian role of RecQ helicase. *Science Advances* **2016,** *2* (11), e1601605.
40. Chernikova, S. B.; Game, J. C.; Brown, J. M., Inhibiting homologous recombination for cancer therapy. *Cancer Biology & Therapy* **2012,** *13* (2), 61-68.

41. Puigvert, J. C.; Sanjiv, K.; Helleday, T., Targeting DNA repair, DNA metabolism and replication stress as anti-cancer strategies. *The FEBS Journal* **2016,** *283* (2), 232-245.
42. Song, Q.; Hu, Y.; Yin, A.; Wang, H.; Yin, Q., DNA Holliday Junction: History, Regulation and Bioactivity. *International Journal of Molecular Sciences* **2022,** *23* (17).
43. Su, R.; Huang, H.; Gao, X.; Zhou, Y.; Yin, S.; Xie, H.; Zhou, L.; Zheng, S., A pan-cancer analysis of the oncogenic role of Holliday junction recognition protein in human tumors. *Open Medicine* **2022,** *17* (1), 317-328.
44. Hu, B.; Wang, Q.; Wang, Y.; Chen, J.; Li, P.; Han, M., Holliday junction–recognizing protein promotes cell proliferation and correlates with unfavorable clinical outcome of hepatocellular carcinoma. *OncoTargets and Therapy* **2017,** *10*, 2601-2607.
45. Hays, F. A.; Watson, J.; Ho, P. S., Caution! DNA Crossing: Crystal Structures of Holliday Junctions *. *Journal of Biological Chemistry* **2003,** *278* (50), 49663-49666.
46. Ussery, D. W.; Wassenaar, T. M.; Borini, S., Word Frequencies and Repeats. In *Computing for Comparative Microbial Genomics: Bioinformatics for Microbiologists*, Ussery, D. W.; Wassenaar, T. M.; Borini, S., Eds. Springer London: London, 2009; pp 137-150.
47. Khuu, P. A.; Voth, A. R.; Hays, F. A.; Ho, P. S., The stacked-X DNA Holliday junction and protein recognition. *Journal of Molecular Recognition* **2006,** *19* (3), 234-242.
48. Müller, J., Functional metal ions in nucleic acids. *Metallomics* **2010,** *2* (5), 318-327.
49. Thiviyanathan, V.; Luxon, B. A.; Leontis, N. B.; Illangasekare, N.; Donne, D. G.; Gorenstein, D. G., Hybrid-hybrid matrix structural refinement of a DNA three-way junction from 3D NOESY-NOESY. *Journal of Biomolecular NMR* **1999,** *14* (3), 209-221.
50. Singleton, M. R.; Scaife, S.; Wigley, D. B., Structural Analysis of DNA Replication Fork Reversal by RecG. *Cell* **2001,** *107* (1), 79-89.
51. Khristich, A. N.; Mirkin, S. M., On the wrong DNA track: Molecular mechanisms of repeat-mediated genome instability. *Journal of Biological Chemistry* **2020,** *295* (13), 4134-4170.
52. Zell, J.; Rota Sperti, F.; Britton, S.; Monchaud, D., DNA folds threaten genetic stability and can be leveraged for chemotherapy. *RSC Chemical Biology* **2021,** *2* (1), 47-76.
53. Kadrmas, J. L.; Ravin, A. J.; Leontis, N. B., Relative stabilities of DNA three-way, four-way and five-way junctions (multi-helix junction loops): unpaired nucleotides can be stabilizing or destabilizing. *Nucleic Acids Research* **1995,** *23* (12), 2212-2222.
54. Wang, X.; Seeman, N. C., Assembly and Characterization of 8-Arm and 12-Arm DNA Branched Junctions. *Journal of the American Chemical Society* **2007,** *129* (26), 8169-8176.
55. Wang, Y.; Mueller, J. E.; Kemper, B.; Seeman, N. C., Assembly and characterization of five-arm and six-arm DNA branched junctions. *Biochemistry* **1991,** *30* (23), 5667-5674.
56. Bae, J. H.; Zhang, D. Y., Predicting stability of DNA bulge at mononucleotide microsatellite. *Nucleic Acids Research* **2021,** *49* (14), 7901-7908.
57. Gollmick, F. A.; Lorenz, M.; Dornberger, U.; von Langen, J.; Diekmann, S.; Fritzsche, H., Solution structure of dAATAA and dAAUAA DNA bulges. *Nucleic Acids Research* **2002,** *30* (12), 2669-2677.
58. Malkov, V. A.; Biswas, I.; Camerini-Otero, R. D.; Hsieh, P., Photocross-linking of the NH2-terminal Region of Taq MutS Protein to the Major Groove of a Heteroduplex DNA. *Journal of Biological Chemistry* **1997,** *272* (38), 23811-23817.
59. Payet, D.; Hillisch, A.; Lowe, N.; Diekmann, S.; Travers, A., The recognition of distorted DNA structures by HMG-D: a footprinting and molecular modelling study11Edited by T. Richmond. *Journal of Molecular Biology* **1999,** *294* (1), 79-91.
60. Kunkel, T. A.; Bebenek, K., DNA Replication Fidelity. *Annual Review of Biochemistry* **2000,** *69* (1), 497-529.
61. Baase, W. A.; Jose, D.; Ponedel, B. C.; von Hippel, P. H.; Johnson, N. P., DNA models of trinucleotide frameshift deletions: the formation of loops and bulges at the primer–template junction. *Nucleic Acids Research* **2009,** *37* (5), 1682-1689.
62. Turner, D. H., Bulges in nucleic acids. *Current Opinion in Structural Biology* **1992,** *2* (3), 334-337.
63. Paulson, H., Repeat expansion diseases. *Handbook of clinical neurology* **2018,** *147*, 105-123.

64. Hermann, T.; Patel, D. J., RNA bulges as architectural and recognition motifs. *Structure* **2000,** *8* (3), R47-R54.
65. Pérez-Arnaiz, C.; Busto, N.; Leal, J. M.; García, B., New Insights into the Mechanism of the DNA/Doxorubicin Interaction. *The Journal of Physical Chemistry B* **2014,** *118* (5), 1288-1295.
66. Scaglioni, L.; Mondelli, R.; Artali, R.; Sirtori, F. R.; Mazzini, S., Nemorubicin and doxorubicin bind the G-quadruplex sequences of the human telomeres and of the c-MYC promoter element Pu22. *Biochimica et Biophysica Acta (BBA) - General Subjects* **2016,** *1860* (6), 1129-1138.
67. Armstrong-Gordon, E.; Gnjidic, D.; McLachlan, A. J.; Hosseini, B.; Grant, A.; Beale, P. J.; Wheate, N. J., Patterns of platinum drug use in an acute care setting: a retrospective study. *Journal of Cancer Research and Clinical Oncology* **2018,** *144* (8), 1561-1568.
68. Lebwohl, D.; Canetta, R., Clinical development of platinum complexes in cancer therapy: an historical perspective and an update. *European Journal of Cancer* **1998,** *34* (10), 1522-1534.
69. Alassadi, S.; Pisani, M. J.; Wheate, N. J., A chemical perspective on the clinical use of platinum-based anticancer drugs. *Dalton Transactions* **2022,** *51* (29), 10835-10846.
70. Reishus, J. W.; Martin, D. S., Jr., cis-Dichlorodiammineplatinum(II). Acid Hydrolysis and Isotopic Exchange of the Chloride Ligands1. *Journal of the American Chemical Society* **1961,** *83* (11), 2457-2462.
71. Bancroft, D. P.; Lepre, C. A.; Lippard, S. J., Platinum-195 NMR kinetic and mechanistic studies of cis- and trans-diamminedichloroplatinum(II) binding to DNA. *Journal of the American Chemical Society* **1990,** *112* (19), 6860-6871.
72. Ohndorf, U.-M.; Rould, M. A.; He, Q.; Pabo, C. O.; Lippard, S. J., Basis for recognition of cisplatin-modified DNA by high-mobility-group proteins. *Nature* **1999,** *399* (6737), 708-712.
73. Dutta, S.; Rivetti, C.; Gassman, N. R.; Young, C. G.; Jones, B. T.; Scarpinato, K.; Guthold, M., Analysis of single, cisplatin-induced DNA bends by atomic force microscopy and simulations. *Journal of Molecular Recognition* **2018,** *31* (10), e2731.
74. Todd, R. C.; Lippard, S. J., Structure of duplex DNA containing the cisplatin 1,2-{Pt(NH3)2}2+-d(GpG) cross-link at 1.77Å resolution. *Journal of Inorganic Biochemistry* **2010,** *104* (9), 902-908.
75. Ghosh, S., Cisplatin: The first metal based anticancer drug. *Bioorganic Chemistry* **2019,** *88*, 102925.
76. Casini, A.; Reedijk, J., Interactions of anticancer Pt compounds with proteins: an overlooked topic in medicinal inorganic chemistry? *Chemical Science* **2012,** *3* (11), 3135-3144.
77. Melnikov, S. V.; Söll, D.; Steitz, T. A.; Polikanov, Y. S., Insights into RNA binding by the anticancer drug cisplatin from the crystal structure of cisplatin-modified ribosome. *Nucleic acids research* **2016,** *44* (10), 4978-4987.
78. Santana-Davila, R.; Szabo, A.; Arce-Lara, C.; Williams, C. D.; Kelley, M. J.; Whittle, J., Cisplatin versus carboplatin-based regimens for the treatment of patients with metastatic lung cancer. An analysis of Veterans Health Administration data. *Journal of thoracic oncology: official publication of the International Association for the Study of Lung Cancer* **2014,** *9* (5), 702-709.
79. Vasconcellos, V. F.; Marta, G. N.; da Silva, E. M. K.; Gois, A. F.; de Castria, T. B.; Riera, R., Cisplatin versus carboplatin in combination with third-generation drugs for advanced non-small cell lung cancer. *Cochrane Database of Systematic Reviews* **2020,** *1* (1).
80. Zhang, S.; Lovejoy, K. S.; Shima, J. E.; Lagpacan, L. L.; Shu, Y.; Lapuk, A.; Chen, Y.; Komori, T.; Gray, J. W.; Chen, X.; Lippard, S. J.; Giacomini, K. M., Organic Cation Transporters Are Determinants of Oxaliplatin Cytotoxicity. *Cancer Research* **2006,** *66* (17), 8847-8857.
81. Stein, A.; Arnold, D., Oxaliplatin: a review of approved uses. *Expert Opinion on Pharmacotherapy* **2012,** *13* (1), 125-137.
82. Lai, Y.-H.; Kuo, C.; Kuo, M. T.; Chen, H. H. W., Modulating Chemosensitivity of Tumors to Platinum-Based Antitumor Drugs by Transcriptional Regulation of Copper Homeostasis. *International Journal of Molecular Sciences* **2018,** *19* (5).
83. Schoeberl, A.; Gutmann, M.; Theiner, S.; Corte-Rodríguez, M.; Braun, G.; Vician, P.; Berger, W.; Koellensperger, G., The copper transporter CTR1 and cisplatin accumulation at the single-cell level by LA-ICP-TOFMS. *Frontiers in Molecular Biosciences* **2022,** *9* (1055356).

84. Su, Y.; Zhang, X.; Li, S.; Xie, W.; Guo, J., Emerging Roles of the Copper–CTR1 Axis in Tumorigenesis. *Molecular Cancer Research* **2022,** *20* (9), 1339-1353.
85. Chen, S.-J.; Kuo, C.-C.; Pan, H.-Y.; Tsou, T.-C.; Yeh, S.-C.; Chang, J.-Y., Mechanistic basis of a combination d-penicillamine and platinum drugs synergistically inhibits tumor growth in oxaliplatin-resistant human cervical cancer cells in vitro and in vivo. *Biochemical Pharmacology* **2015,** *95* (1), 28-37.
86. Eastman, A., Cross-linking of glutathione to DNA by cancer chemotherapeutic platinum coordination complexes. *Chemico-Biological Interactions* **1987,** *61* (3), 241-248.
87. Kasahara, K.; Fujiwara, Y.; Nishio, K.; Ohmori, T.; Sugimoto, Y.; Komiya, K.; Matsuda, T.; Saijo, N., Metallothionein Content Correlates with the Sensitivity of Human Small Cell Lung Cancer Cell Lines to Cisplatin1. *Cancer Research* **1991,** *51* (12), 3237-3242.
88. Surowiak, P.; Materna, V.; Kaplenko, I.; Spaczyński, M.; Dietel, M.; Lage, H.; Zabel, M., Augmented expression of metallothionein and glutathione S-transferase pi as unfavourable prognostic factors in cisplatin-treated ovarian cancer patients. *Virchows Archiv* **2005,** *447* (3), 626-633.
89. Huang, J.; Zhou, Y.; Zhang, H.; Qu, T.; Mao, Y.; Zhu, H.; Quan, L.; Xing, P.; Wang, J.; He, J.; Xu, N.; Sun, Y., A phase II study of biweekly paclitaxel and cisplatin chemotherapy for recurrent or metastatic esophageal squamous cell carcinoma: ERCC1 expression predicts response to chemotherapy. *Medical Oncology* **2012,** *30* (1), 343.
90. Simon, G. R.; Sharma, S.; Cantor, A.; Smith, P.; Bepler, G., ERCC1 Expression Is a Predictor of Survival in Resected Patients With Non-small Cell Lung Cancer. *CHEST* **2005,** *127* (3), 978-983.
91. Ryu, H.; Song, I. C.; Choi, Y.-S.; Yun, H.-J.; Jo, D.-Y.; Kim, J. M.; Ko, Y. B.; Lee, H. J., ERCC1 expression status predicts the response and survival of patients with metastatic or recurrent cervical cancer treated via platinum-based chemotherapy. *Medicine* **2017,** *96* (51), e9402.
92. Urun, Y.; Leow, J. J.; Fay, A. P.; Albiges, L.; Choueiri, T. K.; Bellmunt, J., ERCC1 as a prognostic factor for survival in patients with advanced urothelial cancer treated with platinum based chemotherapy: A systematic review and meta-analysis. *Critical Reviews in Oncology/Hematology* **2017,** *120*, 120-126.
93. Villalobos, M.; Czapiewski, P.; Reinmuth, N.; Fischer, J. R.; Andreas, S.; Kortsik, C.; Serke, M.; Wolf, M.; Neuser, P.; Reuss, A.; Schnabel, P. A.; Thomas, M., ERCC1 assessment in upfront treatment with and without cisplatin-based chemotherapy in stage IIIB/IV non-squamous non-small cell lung cancer. *Medical Oncology* **2018,** *35* (7), 106.
94. Bayat Mokhtari, R.; Homayouni, T. S.; Baluch, N.; Morgatskaya, E.; Kumar, S.; Das, B.; Yeger, H., Combination therapy in combating cancer. *OncoTargets and Therapy* **2017,** *8* (23), 38022-38043.
95. Stathopoulos, G. P.; Boulikas, T., Lipoplatin formulation review article. *Journal of Drug Delivery* **2012,** *2012* (581363).
96. Li, M.; Zhao, P.; Fan, T.; Chen, Y.; Zhang, X.; He, C.; Yang, T.; Lee, R. J.; Khan, M. W.; Raza, S. M.; Ma, X.; Lu, Y.; Xiang, G., Biocompatible co-loading vehicles for delivering both nanoplatin cores and siRNA to treat hepatocellular carcinoma. *International Journal of Pharmaceutics* **2019,** *572*, 118769.
97. Liu, X. L.; Dong, X.; Yang, S. C.; Lai, X.; Liu, H. J.; Gao, Y.; Feng, H. Y.; Zhu, M. H.; Yuan, Y.; Lu, Q.; Lovell, J. F.; Chen, H. Z.; Fang, C., Biomimetic Liposomal Nanoplatinum for Targeted Cancer Chemophototherapy. *Advanced Science* **2021,** *8*, 2003679.
98. Chen, S.-H.; Chang, J.-Y., New Insights into Mechanisms of Cisplatin Resistance: From Tumor Cell to Microenvironment. *International Journal of Molecular Sciences* **2019,** *20* (17), 4136.
99. Shimada M; Itamochi H; J, K., Nedaplatin: a cisplatin derivative in cancer chemotherapy. *Cancer Management and Research* **2013,** *8* (5), 67-76.
100. Imai, Y.; Chikayama, T.; Nakazawa, M.; Watanabe, K.; Ando, S.; Mizuno, Y.; Yoshino, K.; Sugawara, K.; Hamaoka, K.; Fujimori, K.; Inao, M.; Nakayama, N.; Oka, M.; Nagoshi, S.; Mochida, S., Usefulness of miriplatin as an anticancer agent for transcatheter arterial chemoembolization in patients with unresectable hepatocellular carcinoma. *Journal of Gastroenterology* **2012,** *47* (2), 179-186.

101. Maeda, M.; Uchida, N. A.; Sasaki, T., LIPOSOLUBLE PLATINUM (II) COMPLEXES WITH ANTITUMOR ACTIVITY. *Japanese Journal of Cancer Research GANN* **1986,** *77* (6), 523-525.
102. Kazutoshi, O.; Toru, B.; Katsuki, H.; Yoshihiro, O.-U.; Sadahiro, Y.; Shinjiro, T.; Tsuyoshi, Y.; Osamu, S.; Toshiro, M.; Akira, C.; Shigetoshi, F.; Hideo, B., Safety and Short-term Therapeutic Effects of Miriplatin–Lipiodol Suspension in Transarterial Chemoembolization (TACE) for Hepatocellular Carcinoma. *Anticancer Research* **2011,** *31* (9), 2983.
103. Yasui, D.; Yamane, A.; Itoh, H.; Kobayashi, M.; Kumita, S.-i., In vivo evaluation of a monodisperse solid-in-oil-in-water miriplatin/ lipiodol emulsion in transcatheter arterial chemoembolization using a rabbit VX2 tumor model. *PLOS ONE* **2020,** *15* (8), e0222553.
104. Fresch, B.; Remacle, F., Atomistic account of structural and dynamical changes induced by small binders in the double helix of a short DNA. *Physical Chemistry Chemical Physics* **2014,** *16* (27), 14070-14082.
105. Ramakers, L. A. I.; Hithell, G.; May, J. J.; Greetham, G. M.; Donaldson, P. M.; Towrie, M.; Parker, A. W.; Burley, G. A.; Hunt, N. T., 2D-IR Spectroscopy Shows that Optimized DNA Minor Groove Binding of Hoechst33258 Follows an Induced Fit Model. *The Journal of Physical Chemistry B* **2017,** *121* (6), 1295-1303.
106. Alniss, H. Y., Thermodynamics of DNA Minor Groove Binders. *Journal of Medicinal Chemistry* **2019,** *62* (2), 385-402.
107. Portugal, J.; Waring, M. J., Assignment of DNA binding sites for 4',6-diamidine-2-phenylindole and bisbenzimide (Hoechst 33258). A comparative footprinting study. *Biochimica et Biophysica Acta (BBA) - Gene Structure and Expression* **1988,** *949* (2), 158-168.
108. Adhikary, A.; Buschmann, V.; Müller, C.; Sauer, M., Ensemble and single-molecule fluorescence spectroscopic study of the binding modes of the bis-benzimidazole derivative Hoechst 33258 with DNA. *Nucleic Acids Research* **2003,** *31* (8), 2178-2186.
109. Zhang, X.-X.; Brantley, S. L.; Corcelli, S. A.; Tokmakoff, A., DNA minor-groove binder Hoechst 33258 destabilizes base-pairing adjacent to its binding site. *Communications Biology* **2020,** *3* (1), 525.
110. Chazotte, B., Labeling nuclear DNA using DAPI. *Cold Spring Harbor Protocols* **2011,** *2011* (1), pdb.prot5556.
111. Banerjee, D.; Pal, S. K., Dynamics in the DNA Recognition by DAPI: Exploration of the Various Binding Modes. *The Journal of Physical Chemistry B* **2008,** *112* (3), 1016-1021.
112. Neidle, S., DNA minor-groove recognition by small molecules. *Natural Product Reports* **2001,** *18* (3), 291-309.
113. Rahman, A.; O'Sullivan, P.; Rozas, I., Recent developments in compounds acting in the DNA minor groove. *MedChemComm* **2019,** *10*, 26-40.
114. Pezzoni, G.; Grandi, M.; Biasoli, G.; Capolongo, L.; Ballinari, D.; Giuliani, F. C.; Barbieri, B.; Pastori, A.; Pesenti, E.; Mongelli, N., Biological profile of FCE 24517, a novel benzoyl mustard analogue of distamycin A. *British Journal of Cancer* **1991,** *64* (6), 1047-1050.
115. Leahy, M.; Ray-Coquard, I.; Verweij, J.; Le Cesne, A.; Duffaud, F.; Hogendoorn, P. C. W.; Fowst, C.; de Balincourt, C.; di Paola, E. D.; van Glabbeke, M.; Judson, I.; Blay, J.-Y., Brostallicin, an agent with potential activity in metastatic soft tissue sarcoma: A phase II study from the European Organisation for Research and Treatment of Cancer Soft Tissue and Bone Sarcoma Group. *European Journal of Cancer* **2007,** *43* (2), 308-315.
116. Cozzi, P., A new class of cytotoxic DNA minor groove binders: α-halogenoacrylic derivatives of pyrrolecarbamoyl oligomers. *Il Farmaco* **2001,** *56* (1), 57-65.
117. Gerratana, B., Biosynthesis, synthesis, and biological activities of pyrrolobenzodiazepines. *Medicinal Research Reviews* **2012,** *32* (2), 254-293.
118. D'Incalci, M.; Badri, N.; Galmarini, C. M.; Allavena, P., Trabectedin, a drug acting on both cancer cells and the tumour microenvironment. *British Journal of Cancer* **2014,** *111* (4), 646-650.
119. Corona, R. I.; Guo, J.-t., Statistical analysis of structural determinants for protein–DNA-binding specificity. *Proteins: Structure, Function, and Bioinformatics* **2016,** *84* (8), 1147-1161.
120. Lin, M.; Guo, J.-t., New insights into protein–DNA binding specificity from hydrogen bond based comparative study. *Nucleic Acids Research* **2019,** *47* (21), 11103-11113.

121. Luscombe, N. M.; Austin, S. E.; Berman, H. M.; Thornton, J. M., An overview of the structures of protein-DNA complexes. *Genome Biology* **2000,** *1* (1), reviews001.1.
122. Hashimoto, H.; Olanrewaju, Y. O.; Zheng, Y.; Wilson, G. G.; Zhang, X.; Cheng, X., Wilms tumor protein recognizes 5-carboxylcytosine within a specific DNA sequence. *Genes Dev* **2014,** *28* (20), 2304-2313.
123. Wilson, D. S.; Guenther, B.; Desplan, C.; Kuriyan, J., High resolution crystal structure of a paired (Pax) class cooperative homeodomain dimer on DNA. *Cell* **1995,** *82* (5), 709-719.
124. Umezawa, H.; Ueda, M.; Maeda, K.; Yagishita, K.; Kondo, S.; Okami, Y.; Utahara, R.; Osato, Y.; Nitta, K.; Takeuchi, T., Production and isolation of a new antibiotic: kanamycin. *Journal of Antibiotics* **1957,** *10* (5), 181-188.
125. Hansen, M.; Yun, S.; Hurley, L., Hedamycin intercalates the DNA helix and, through carbohydrate-mediated recognition in the minor groove, directs N7-alkylation of guanine in the major groove in a sequence-specific manner. *Chemistry & Biology* **1995,** *2* (4), 229-240.
126. Reza, F.; Glazer, P. M., Triplex-Mediated Genome Targeting and Editing. In *Gene Correction: Methods and Protocols*, Storici, F., Ed. Humana Press: Totowa, NJ, 2014; pp 115-142.
127. Li, C.; Zhou, Z.; Ren, C.; Deng, Y.; Peng, F.; Wang, Q.; Zhang, H.; Jiang, Y., Triplex-forming oligonucleotides as an anti-gene technique for cancer therapy. *Frontiers in Pharmacology* **2022,** *13*.
128. Chin, J. Y.; Glazer, P. M., Repair of DNA lesions associated with triplex-forming oligonucleotides. *Molecular Carcinogenesis* **2009,** *48* (4), 389-399.
129. Zuin Fantoni, N.; McGorman, B.; Molphy, Z.; Singleton, D.; Walsh, S.; El-Sagheer, A. H.; McKee, V.; Brown, T.; Kellett, A., Development of Gene-Targeted Polypyridyl Triplex-Forming Oligonucleotide Hybrids. *ChemBioChem* **2020,** *21* (24), 3563-3574.
130. Kaushik Tiwari, M.; Colon-Rios, D. A.; Tumu, H. C. R.; Liu, Y.; Quijano, E.; Krysztofiak, A.; Chan, C.; Song, E.; Braddock, D. T.; Suh, H.-W.; Saltzman, W. M.; Rogers, F. A., Direct targeting of amplified gene loci for proapoptotic anticancer therapy. *Nature Biotechnology* **2022,** *40* (3), 325-334.
131. Huo, S.; Gong, N.; Jiang, Y.; Chen, F.; Guo, H.; Gan, Y.; Wang, Z.; Herrmann, A.; Liang, X.-J., Gold-DNA nanosunflowers for efficient gene silencing with controllable transformation. *Science Advances* **2019,** *5* (10), eaaw6264.
132. Hayashi, M.; Harada, Y., Direct observation of the reversible unwinding of a single DNA molecule caused by the intercalation of ethidium bromide. *Nucleic Acids Research* **2007,** *35* (19), e125-e125.
133. Ahammed, K. S.; Pachal, S.; Majumdar, P.; Dutta, S., DNA Morphology: Global Alteration of DNA Topological States Induced by Chemotherapeutic Agents and Its Implication in Cancer. *ChemBioChem* **2023,** *24* (8), e202200715.
134. Rao, S. N.; Kollman, P. A., Molecular mechanical simulations on double intercalation of 9-amino acridine into d(CGCGCGC) X d(GCGCGCG): analysis of the physical basis for the neighbor-exclusion principle. *Proceedings of the National Academy of Sciences* **1987,** *84* (16), 5735-5739.
135. Schakenraad, K.; Biebricher, A. S.; Sebregts, M.; ten Bensel, B.; Peterman, E. J. G.; Wuite, G. J. L.; Heller, I.; Storm, C.; van der Schoot, P., Hyperstretching DNA. *Nature Communications* **2017,** *8* (1), 2197.
136. Christowitz, C.; Davis, T.; Isaacs, A.; van Niekerk, G.; Hattingh, S.; Engelbrecht, A.-M., Mechanisms of doxorubicin-induced drug resistance and drug resistant tumour growth in a murine breast tumour model. *BMC Cancer* **2019,** *19* (1), 757.
137. Pommier, Y.; Leo, E.; Zhang, H.; Marchand, C., DNA Topoisomerases and Their Poisoning by Anticancer and Antibacterial Drugs. *Chemistry & Biology* **2010,** *17* (5), 421-433.
138. Ijäs, H.; Shen, B.; Heuer-Jungemann, A.; Keller, A.; Kostiainen, Mauri A.; Liedl, T.; Ihalainen, J. A.; Linko, V., Unraveling the interaction between doxorubicin and DNA origami nanostructures for customizable chemotherapeutic drug release. *Nucleic Acids Research* **2021,** *49* (6), 3048-3062.
139. Swain, S. M.; Whaley, F. S.; Ewer, M. S., Congestive heart failure in patients treated with doxorubicin. *Cancer* **2003,** *97* (11), 2869-2879.
140. Evison, B. J.; Sleebs, B. E.; Watson, K. G.; Phillips, D. R.; Cutts, S. M., Mitoxantrone, More than Just Another Topoisomerase II Poison. *Medicinal Research Reviews* **2016,** *36* (2), 248-299.

141. Stiborová, M.; Bieler, C. A.; Wiessler, M.; Frei, E., The anticancer agent ellipticine on activation by cytochrome P450 forms covalent DNA adducts. *Biochemical Pharmacology* **2001,** *62* (12), 1675-1684.
142. Stiborová, M.; Poljaková, J.; Martínková, E.; Bořek-Dohalská, L.; Eckschlager, T.; Kizek, R.; Frei, E., Ellipticine cytotoxicity to cancer cell lines - a comparative study. *Interdisciplinary Toxicology* **2011,** *4* (2), 98-105.
143. Paoletti, C.; Le Pecq, J. B.; Dat-Xuong, N.; Juret, P.; Garnier, H.; Amiel, J. L.; Rouesse, J., Antitumor Activity, Pharmacology, and Toxicity of Ellipticines, Ellipticinium, and 9-Hydroxy Derivatives: Preliminary Clinical Trials of 2-Methyl-9-Hydroxy Ellipticinium (NSC 264-137). In *Cancer Chemo- and Immunopharmacology: 1. Chemopharmacology*, Mathé, G.; Muggia, F. M., Eds. Springer Berlin Heidelberg: Berlin, Heidelberg, 1980; pp 107-123.
144. Rouëssé, J.; Spielmann, M.; Turpin, F.; Le Chevalier, T.; Azab, M.; Mondésir, J. M., Phase II study of elliptinium acetate salvage treatment of advanced breast cancer. *European Journal of Cancer* **1993,** *29* (6), 856-859.
145. Miller, C. M.; O'Sullivan, E. C.; McCarthy, F. O., Novel 11-Substituted Ellipticines as Potent Anticancer Agents with Divergent Activity against Cancer Cells. *Pharmaceuticals (Basel)* **2019,** *12* (2).
146. Li, G.; Sun, L.; Ji, L.; Chao, H., Ruthenium(ii) complexes with dppz: from molecular photoswitch to biological applications. *Dalton Transactions* **2016,** *45* (34), 13261-13276.
147. Jia, F.; Wang, S.; Man, Y.; Kumar, P.; Liu, B., Recent Developments in the Interactions of Classic Intercalated Ruthenium Compounds: [Ru(bpy)2dppz]2+ and [Ru(phen)2dppz]2+ with a DNA Molecule. *Molecules* **2019,** *24* (4), 769.
148. Friedman, A. E.; Chambron, J. C.; Sauvage, J. P.; Turro, N. J.; Barton, J. K., A molecular light switch for DNA: Ru(bpy)2(dppz)2+. *Journal of the American Chemical Society* **1990,** *112* (12), 4960-4962.
149. Brennaman, M. K.; Alstrum-Acevedo, J. H.; Fleming, C. N.; Jang, P.; Meyer, T. J.; Papanikolas, J. M., Turning the [Ru(bpy)2dppz]2+ Light-Switch On and Off with Temperature. *Journal of the American Chemical Society* **2002,** *124* (50), 15094-15098.
150. Brennaman, M. K.; Meyer, T. J.; Papanikolas, J. M., [Ru(bpy)2dppz]2+ Light-Switch Mechanism in Protic Solvents as Studied through Temperature-Dependent Lifetime Measurements. *The Journal of Physical Chemistry A* **2004,** *108* (45), 9938-9944.
151. Olson, E. J. C.; Hu, D.; Hörmann, A.; Jonkman, A. M.; Arkin, M. R.; Stemp, E. D. A.; Barton, J. K.; Barbara, P. F., First Observation of the Key Intermediate in the "Light-Switch" Mechanism of [Ru(phen)2dppz]2+. *Journal of the American Chemical Society* **1997,** *119* (47), 11458-11467.
152. Önfelt, B.; Lincoln, P.; Nordén, B.; Baskin, J. S.; Zewail, A. H., Femtosecond linear dichroism of DNA-intercalating chromophores: Solvation and charge separation dynamics of [Ru(phen)2dppz]2+ systems. *Proceedings of the National Academy of Sciences* **2000,** *97* (11), 5708-5713.
153. Jenkins, Y.; Friedman, A. E.; Turro, N. J.; Barton, J. K., Characterization of dipyridophenazine complexes of ruthenium(II): The light switch effect as a function of nucleic acid sequence and conformation. *Biochemistry* **1992,** *31* (44), 10809-10816.
154. Lim, M. H.; Song, H.; Olmon, E. D.; Dervan, E. E.; Barton, J. K., Sensitivity of Ru(bpy)2dppz2+ Luminescence to DNA Defects. *Inorganic Chemistry* **2009,** *48* (12), 5392-5397.
155. Shi, S.; Geng, X.; Zhao, J.; Yao, T.; Wang, C.; Yang, D.; Zheng, L.; Ji, L., Interaction of [Ru(bpy)2(dppz)]2+ with human telomeric DNA: Preferential binding to G-quadruplexes over i-motif. *Biochimie* **2010,** *92* (4), 370-377.
156. Boynton, A. N.; Marcélis, L.; Barton, J. K., [Ru(Me4phen)2dppz]2+, a Light Switch for DNA Mismatches. *Journal of the American Chemical Society* **2016,** *138* (15), 5020-5023.
157. Spence, P.; Fielden, J.; Waller, Z. A. E., Beyond Solvent Exclusion: i-Motif Detecting Capability and an Alternative DNA Light-Switching Mechanism in a Ruthenium(II) Polypyridyl Complex. *Journal of the American Chemical Society* **2020,** *142* (32), 13856-13866.
158. Lee, S. Y.; Kim, C. Y.; Nam, T.-G., Ruthenium Complexes as Anticancer Agents: A Brief History and Perspectives. *Drug Design, Development and Therapy* **2020,** *2020* (14), 5375-5392.
159. Niyazi H, T. S., Mitchell E, Forsyth T, Cardin C, X-ray crystal structure of ruthenium [Ru(phen)2(dppz)]2+ bound to d(TCGGTACCGA). 30/07/2013 ed.; PDB, 2013.

160. Liu, H.-K.; Sadler, P. J., Metal Complexes as DNA Intercalators. *Accounts of Chemical Research* **2011,** *44* (5), 349-359.
161. Mendes, E.; Aljnadi, I. M.; Bahls, B.; Victor, B. L.; Paulo, A., Major Achievements in the Design of Quadruplex-Interactive Small Molecules. *Pharmaceuticals* **2022,** *15* (3), 300.
162. Monsen, R. C., Higher-order G-quadruplexes in promoters are untapped drug targets. *Frontiers in Chemistry* **2023,** *11* (1211512).
163. Kosiol, N.; Juranek, S.; Brossart, P.; Heine, A.; Paeschke, K., G-quadruplexes: a promising target for cancer therapy. *Molecular Cancer* **2021,** *20* (1), 40.
164. Pont, I.; Galiana-Roselló, C.; Sabater-Arcis, M.; Bargiela, A.; Frías, J. C.; Albelda, M. T.; González-García, J.; García-España, E., Development of potent tripodal G-quadruplex DNA binders and their efficient delivery to cancer cells by aptamer functionalised liposomes. *Organic & Biomolecular Chemistry* **2023,** *21* (5), 1000-1007.
165. Pont, I.; Martínez-Camarena, Á.; Galiana-Roselló, C.; Tejero, R.; Albelda, M. T.; González-García, J.; Vilar, R.; García-España, E., Development of Polyamine-Substituted Triphenylamine Ligands with High Affinity and Selectivity for G-Quadruplex DNA. *ChemBioChem* **2020,** *21* (8), 1167-1177.
166. Pont, I.; González-García, J.; Inclán, M.; Reynolds, M.; Delgado-Pinar, E.; Albelda, M. T.; Vilar, R.; García-España, E., Aza-Macrocyclic Triphenylamine Ligands for G-Quadruplex Recognition. *Chemistry – A European Journal* **2018,** *24* (42), 10850-10858.
167. Reed, J. E.; Arnal, A. A.; Neidle, S.; Vilar, R., Stabilization of G-Quadruplex DNA and Inhibition of Telomerase Activity by Square-Planar Nickel(II) Complexes. *Journal of the American Chemical Society* **2006,** *128* (18), 5992-5993.
168. D'Anna, L.; Rubino, S.; Pipitone, C.; Serio, G.; Gentile, C.; Palumbo Piccionello, A.; Giannici, F.; Barone, G.; Terenzi, A., Salphen metal complexes as potential anticancer agents: interaction profile and selectivity studies toward the three G-quadruplex units in the KIT promoter. *Dalton Transactions* **2023,** *52* (10), 2966-2975.
169. Kench, T.; Rakers, V.; Bouzada, D.; Gomez-González, J.; Robinson, J.; Kuimova, M. K.; Vázquez López, M.; Vázquez, M. E.; Vilar, R., Dimeric Metal-Salphen Complexes Which Target Multimeric G-Quadruplex DNA. *Bioconjugate Chemistry* **2023,** *34* (5), 911-921.
170. Pathania, S.; Pentikäinen, O. T.; Singh, P. K., A holistic view on c-Kit in cancer: Structure, signaling, pathophysiology and its inhibitors. *Biochimica et Biophysica Acta (BBA) - Reviews on Cancer* **2021,** *1876* (2), 188631.
171. Palma, E.; Carvalho, J.; Cruz, C.; Paulo, A., Metal-Based G-Quadruplex Binders for Cancer Theranostics. *Pharmaceuticals (Basel)* **2021,** *14* (7), 605.
172. Ivens, E.; Cominetti, M. M. D.; Searcey, M., Junctions in DNA: underexplored targets for therapeutic intervention. *Bioorganic & Medicinal Chemistry* **2022,** *69*, 116897.
173. Cassell, G.; Klemm, M.; Pinilla, C.; Segall, A., Dissection of bacteriophage λ site-specific recombination using synthetic peptide combinatorial libraries11Edited by M. Gottesman. *Journal of Molecular Biology* **2000,** *299* (5), 1193-1202.
174. Rideout, M. C.; Naili, I.; Boldt, J. L.; Flores-Fujimoto, A.; Patra, S.; Rostron, J. E.; Segall, A. M., wrwyrggrywrw is a single-chain functional analog of the Holliday junction-binding homodimer, (wrwycr)2. *Peptides* **2013,** *40*, 112-122.
175. Bolla, M. L.; Azevedo, E. V.; Smith, J. M.; Taylor, R. E.; Ranjit, D. K.; Segall, A. M.; McAlpine, S. R., Novel Antibiotics: Macrocyclic Peptides Designed to Trap Holliday Junctions. *Organic Letters* **2003,** *5* (2), 109-112.
176. Carpenter, M. L.; Lowe, G.; Cook, P. R., The Structure of 4-way DNA Junctions: Specific Binding of Bis-intercalators With Rigid Linkers. *Nucleic Acids Research* **1996,** *24* (9), 1594-1601.
177. Brogden, A. L.; Hopcroft, N. H.; Searcey, M.; Cardin, C. J., Ligand Bridging of the DNA Holliday Junction: Molecular Recognition of a Stacked-X Four-Way Junction by a Small Molecule. *Angewandte Chemie International Edition* **2007,** *46* (21), 3850-3854.
178. Hopcroft, N. H.; Brogden, A. L.; Searcey, M.; Cardin, C. J., X-ray crystallographic study of DNA duplex cross-linking: simultaneous binding to two d(CGTACG)2 molecules by a bis(9-aminoacridine-4-carboxamide) derivative. *Nucleic Acids Research* **2006,** *34* (22), 6663-6672.

179. Howell, L. A.; Bowater, R. A.; O'Connell, M. A.; Reszka, A. P.; Neidle, S.; Searcey, M., Synthesis of Small Molecules Targeting Multiple DNA Structures using Click Chemistry. *ChemMedChem* **2012,** *7* (5), 792-804.
180. Chien, C.-M.; Wu, P.-C.; Satange, R.; Chang, C.-C.; Lai, Z.-L.; Hagler, L. D.; Zimmerman, S. C.; Hou, M.-H., Structural Basis for Targeting T:T Mismatch with Triaminotriazine-Acridine Conjugate Induces a U-Shaped Head-to-Head Four-Way Junction in CTG Repeat DNA. *Journal of the American Chemical Society* **2020,** *142* (25), 11165-11172.
181. Howell, L. A.; Waller, Z. A. E.; Bowater, R.; O'Connell, M.; Searcey, M., A small molecule that induces assembly of a four way DNA junction at low temperature. *Chemical Communications* **2011,** *47* (29), 8262-8264.
182. Barros, S. A.; Chenoweth, D. M., Recognition of Nucleic Acid Junctions Using Triptycene-Based Molecules. *Angewandte Chemie International Edition* **2014,** *53* (50), 13746-13750.
183. Barros, S. A.; Chenoweth, D. M., Triptycene-based small molecules modulate (CAG)·(CTG) repeat junctions. *Chemical Science* **2015,** *6* (8), 4752-4755.
184. Hannon, M. J.; Moreno, V.; Prieto, M. J.; Moldrheim, E.; Sletten, E.; Meistermann, I.; Isaac, C. J.; Sanders, K. J.; Rodger, A., Intramolecular DNA Coiling Mediated by a Metallo-Supramolecular Cylinder. *Angewandte Chemie International Edition* **2001,** *40* (5), 879-884.
185. Oleksi, A.; Blanco, A. G.; Boer, R.; Usón, I.; Aymamí, J.; Rodger, A.; Hannon, M. J.; Coll, M., Molecular Recognition of a Three-Way DNA Junction by a Metallosupramolecular Helicate. *Angewandte Chemie International Edition* **2006,** *45* (8), 1227-1231.
186. Cerasino, L.; Hannon, M. J.; Sletten, E., DNA Three-Way Junction with a Dinuclear Iron(II) Supramolecular Helicate at the Center: A NMR Structural Study. *Inorganic Chemistry* **2007,** *46* (16), 6245-6251.
187. Woods, K. C.; Martin, S. S.; Chu, V. C.; Baldwin, E. P., Quasi-equivalence in site-specific recombinase structure and function: crystal structure and activity of trimeric cre recombinase bound to a three-way lox DNA junction11Edited by K. Morikawa. *Journal of Molecular Biology* **2001,** *313* (1), 49-69.
188. Malina, J.; Hannon, M. J.; Brabec, V., Recognition of DNA Three-Way Junctions by Metallosupramolecular Cylinders: Gel Electrophoresis Studies. *Chemistry – A European Journal* **2007,** *13* (14), 3871-3877.
189. Parajó, Y.; Malina, J.; Meistermann, I.; Clarkson, G. J.; Pascu, M.; Rodger, A.; Hannon, M. J.; Lincoln, P., Effect of bridging ligand structure on the thermal stability and DNA binding properties of iron(ii) triple helicates. *Dalton Transactions* **2009,** (25), 4868-4874.
190. Cardo, L.; Sadovnikova, V.; Phongtongpasuk, S.; Hodges, N. J.; Hannon, M. J., Arginine conjugates of metallo-supramolecular cylinders prescribe helicity and enhance DNA junction binding and cellular activity. *Chemical Communications* **2011,** *47* (23), 6575-6577.
191. Pascu, G. I.; Hotze, A. C. G.; Sanchez-Cano, C.; Kariuki, B. M.; Hannon, M. J., Dinuclear Ruthenium(II) Triple-Stranded Helicates: Luminescent Supramolecular Cylinders That Bind and Coil DNA and Exhibit Activity against Cancer Cell Lines. *Angewandte Chemie International Edition* **2007,** *46* (23), 4374-4378.
192. Hotze, A. C. G.; Hodges, N. J.; Hayden, R. E.; Sanchez-Cano, C.; Paines, C.; Male, N.; Tse, M.-K.; Bunce, C. M.; Chipman, J. K.; Hannon, M. J., Supramolecular Iron Cylinder with Unprecedented DNA Binding Is a Potent Cytostatic and Apoptotic Agent without Exhibiting Genotoxicity. *Chemistry & Biology* **2008,** *15* (12), 1258-1267.
193. Cardo, L.; Nawroth, I.; Cail, P. J.; McKeating, J. A.; Hannon, M. J., Metallo supramolecular cylinders inhibit HIV-1 TAR-TAT complex formation and viral replication in cellulo. *Scientific Reports* **2018,** *8* (1), 13342.
194. Malina, J.; Hannon, M. J.; Brabec, V., Recognition of DNA bulges by dinuclear iron(II) metallosupramolecular helicates. *The FEBS Journal* **2014,** *281* (4), 987-997.
195. Melidis, L.; Hill, H. J.; Coltman, N. J.; Davies, S. P.; Winczura, K.; Chauhan, T.; Craig, J. S.; Garai, A.; Hooper, C. A. J.; Egan, R. T.; McKeating, J. A.; Hodges, N. J.; Stamataki, Z.; Grzechnik, P.; Hannon, M. J., Supramolecular Cylinders Target Bulge Structures in the 5' UTR of the RNA Genome of

SARS-CoV-2 and Inhibit Viral Replication**. *Angewandte Chemie International Edition* **2021,** *60* (33), 18144-18151.
196. Hooper, C. A. J.; Cardo, L.; Craig, J. S.; Melidis, L.; Garai, A.; Egan, R. T.; Sadovnikova, V.; Burkert, F.; Male, L.; Hodges, N. J.; Browning, D. F.; Rosas, R.; Liu, F.; Rocha, F. V.; Lima, M. A.; Liu, S.; Bardelang, D.; Hannon, M. J., Rotaxanating Metallo-supramolecular Nano-cylinder Helicates to Switch DNA Junction Binding. *Journal of the American Chemical Society* **2020,** *142* (49), 20651-20660.
197. Craig, J. S.; Melidis, L.; Williams, H. D.; Dettmer, S. J.; Heidecker, A. A.; Altmann, P. J.; Guan, S.; Campbell, C.; Browning, D. F.; Sigel, R. K. O.; Johannsen, S.; Egan, R. T.; Aikman, B.; Casini, A.; Pöthig, A.; Hannon, M. J., Organometallic Pillarplexes That Bind DNA 4-Way Holliday Junctions and Forks. *Journal of the American Chemical Society* **2023,** *145* (25), 13570-13580.
198. Gómez-González, J.; Pérez, Y.; Sciortino, G.; Roldan-Martín, L.; Martínez-Costas, J.; Maréchal, J.-D.; Alfonso, I.; Vázquez López, M.; Vázquez, M. E., Dynamic Stereoselection of Peptide Helicates and Their Selective Labeling of DNA Replication Foci in Cells**. *Angewandte Chemie International Edition* **2021,** *60* (16), 8859-8866.
199. Gómez-González, J.; Peña, D. G.; Barka, G.; Sciortino, G.; Maréchal, J.-D.; Vázquez López, M.; Vázquez, M. E., Directed Self-Assembly of Trimeric DNA-Bindingchiral Miniprotein Helicates. *Frontiers in Chemistry* **2018,** *6*, 520.
200. Brabec, V.; Howson, S. E.; Kaner, R. A.; Lord, R. M.; Malina, J.; Phillips, R. M.; Abdallah, Q. M. A.; McGowan, P. C.; Rodger, A.; Scott, P., Metallohelices with activity against cisplatin-resistant cancer cells; does the mechanism involve DNA binding? *Chemical Science* **2013,** *4* (12), 4407-4416.
201. Howson, S. E.; Bolhuis, A.; Brabec, V.; Clarkson, G. J.; Malina, J.; Rodger, A.; Scott, P., Optically pure, water-stable metallo-helical 'flexicate' assemblies with antibiotic activity. *Nature Chemistry* **2012,** *4* (1), 31-36.
202. Song, H.; Allison, S. J.; Brabec, V.; Bridgewater, H. E.; Kasparkova, J.; Kostrhunova, H.; Novohradsky, V.; Phillips, R. M.; Pracharova, J.; Rogers, N. J.; Shepherd, S. L.; Scott, P., Glycoconjugated Metallohelices have Improved Nuclear Delivery and Suppress Tumour Growth In Vivo. *Angewandte Chemie International Edition* **2020,** *59* (34), 14677-14685.
203. Song, H.; Rogers, N. J.; Allison, S. J.; Brabec, V.; Bridgewater, H.; Kostrhunova, H.; Markova, L.; Phillips, R. M.; Pinder, E. C.; Shepherd, S. L.; Young, L. S.; Zajac, J.; Scott, P., Discovery of selective, antimetastatic and anti-cancer stem cell metallohelices via post-assembly modification. *Chemical Science* **2019,** *10* (37), 8547-8557.
204. Kaner, R. A.; Allison, S. J.; Faulkner, A. D.; Phillips, R. M.; Roper, D. I.; Shepherd, S. L.; Simpson, D. H.; Waterfield, N. R.; Scott, P., Anticancer metallohelices: nanomolar potency and high selectivity. *Chemical Science* **2016,** *7* (2), 951-958.
205. Malina, J.; Kostrhunova, H.; Scott, P.; Brabec, V., Metallohelices stabilize DNA three-way junctions and induce DNA damage in cancer cells. *Nucleic Acids Research* **2023,** *51* (14), 7174-7183.
206. Faulkner, A. D.; Kaner, R. A.; Abdallah, Q. M. A.; Clarkson, G.; Fox, D. J.; Gurnani, P.; Howson, S. E.; Phillips, R. M.; Roper, D. I.; Simpson, D. H.; Scott, P., Asymmetric triplex metallohelices with high and selective activity against cancer cells. *Nature Chemistry* **2014,** *6* (9), 797-803.
207. Malina, J.; Kostrhunova, H.; Scott, P.; Brabec, V., FeII Metallohelices Stabilize DNA G-Quadruplexes and Downregulate the Expression of G-Quadruplex-Regulated Oncogenes. *Chemistry – A European Journal* **2021,** *27* (45), 11682-11692.
208. Malina, J.; Scott, P.; Brabec, V., Stabilization of human telomeric RNA G-quadruplex by the water-compatible optically pure and biologically-active metallohelices. *Scientific Reports* **2020,** *10* (1), 14543.
209. Vuong, S.; Stefan, L.; Lejault, P.; Rousselin, Y.; Denat, F.; Monchaud, D., Identifying three-way DNA junction-specific small-molecules. *Biochimie* **2012,** *94* (2), 442-450.
210. Altmann, P. J.; Pöthig, A., Pillarplexes: A Metal–Organic Class of Supramolecular Hosts. *Journal of the American Chemical Society* **2016,** *138* (40), 13171-13174.
211. Craig, J. S. Exploring metallo-supramolecular architectures: towards recognition of functional nucleic acid structures for fighting disease. University of Birmingham, Birmingham, 2022.

212. Altmann, P. J.; Pöthig, A., A pH-Dependent, Mechanically Interlocked Switch: Organometallic [2]Rotaxane vs. Organic [3]Rotaxane. *Angewandte Chemie International Edition* **2017,** *56* (49), 15733-15736.
213. Guan, S.; Pickl, T.; Jandl, C.; Schuchmann, L.; Zhou, X.; Altmann, P. J.; Pöthig, A., Triazolate-based pillarplexes: shape-adaptive metallocavitands via rim modification of macrocyclic ligands. *Organic Chemistry Frontiers* **2021,** *8* (15), 4061-4070.
214. Novotna, J.; Laguerre, A.; Granzhan, A.; Pirrotta, M.; Teulade-Fichou, M.-P.; Monchaud, D., Cationic azacryptands as selective three-way DNA junction binding agents. *Organic & Biomolecular Chemistry* **2015,** *13* (1), 215-222.
215. Zell, J.; Duskova, K.; Chouh, L.; Bossaert, M.; Chéron, N.; Granzhan, A.; Britton, S.; Monchaud, D., Dual targeting of higher-order DNA structures by azacryptands induces DNA junction-mediated DNA damage in cancer cells. *Nucleic Acids Research* **2021,** *49* (18), 10275-10288.
216. Zhu, J.; Haynes, C. J. E.; Kieffer, M.; Greenfield, J. L.; Greenhalgh, R. D.; Nitschke, J. R.; Keyser, U. F., FeII4L4 Tetrahedron Binds to Nonpaired DNA Bases. *Journal of the American Chemical Society* **2019,** *141* (29), 11358-11362.
217. Xi, S.-F.; Bao, L.-Y.; Xu, Z.-L.; Wang, Y.-X.; Ding, Z.-D.; Gu, Z.-G., Enhanced Stabilization of G-Quadruplex DNA by [Ni4L6]8+ Cages with Large Rigid Aromatic Ligands. *European Journal of Inorganic Chemistry* **2017,** *2017* (29), 3533-3541.
218. Turkevich, J.; Stevenson, P. C.; Hillier, J., A study of the nucleation and growth processes in the synthesis of colloidal gold. *Discussions of the Faraday Society* **1951,** *11*, 55-75.
219. Wuithschick, M.; Birnbaum, A.; Witte, S.; Sztucki, M.; Vainio, U.; Pinna, N.; Rademann, K.; Emmerling, F.; Kraehnert, R.; Polte, J., Turkevich in New Robes: Key Questions Answered for the Most Common Gold Nanoparticle Synthesis. *ACS Nano* **2015,** *9* (7), 7052-7071.
220. Brust, M.; Walker, M.; Bethell, D.; Schiffrin, D. J.; Whyman, R., Synthesis of thiol-derivatised gold nanoparticles in a two-phase Liquid–Liquid system. *Journal of the Chemical Society, Chemical Communications* **1994,** (7), 801-802.
221. Yaseen, M.; Humayun, M.; Khan, A.; Usman, M.; Ullah, H.; Tahir, A. A.; Ullah, H., Preparation, Functionalization, Modification, and Applications of Nanostructured Gold: A Critical Review. *Energies* **2021,** *14* (5), 1278.
222. Karakoçak, B. B.; Raliya, R.; Davis, J. T.; Chavalmane, S.; Wang, W.-N.; Ravi, N.; Biswas, P., Biocompatibility of gold nanoparticles in retinal pigment epithelial cell line. *Toxicology in Vitro* **2016,** *37*, 61-69.
223. Carnovale, C.; Bryant, G.; Shukla, R.; Bansal, V., Identifying Trends in Gold Nanoparticle Toxicity and Uptake: Size, Shape, Capping Ligand, and Biological Corona. *ACS Omega* **2019,** *4* (1), 242-256.
224. Yue, J.; Feliciano, T. J.; Li, W.; Lee, A.; Odom, T. W., Gold Nanoparticle Size and Shape Effects on Cellular Uptake and Intracellular Distribution of siRNA Nanoconstructs. *Bioconjugate Chemistry* **2017,** *28* (6), 1791-1800.
225. Fröhlich, E., The role of surface charge in cellular uptake and cytotoxicity of medical nanoparticles. *International Journal of Nanomedicine* **2012,** *2012* (7), 5577-5591.
226. Cedervall, T.; Lynch, I.; Lindman, S.; Berggård, T.; Thulin, E.; Nilsson, H.; Dawson, K. A.; Linse, S., Understanding the nanoparticle–protein corona using methods to quantify exchange rates and affinities of proteins for nanoparticles. *Proceedings of the National Academy of Sciences* **2007,** *104* (7), 2050-2055.
227. García-Álvarez, R.; Hadjidemetriou, M.; Sánchez-Iglesias, A.; Liz-Marzán, L. M.; Kostarelos, K., In vivo formation of protein corona on gold nanoparticles. The effect of their size and shape. *Nanoscale* **2018,** *10* (3), 1256-1264.
228. Cutler, J. I.; Auyeung, E.; Mirkin, C. A., Spherical Nucleic Acids. *Journal of the American Chemical Society* **2012,** *134* (3), 1376-1391.
229. Song, Y.; Song, W.; Lan, X.; Cai, W.; Jiang, D., Spherical nucleic acids: Organized nucleotide aggregates as versatile nanomedicine. *Aggregate* **2021,** *3* (1), e120.
230. Hill, H. D.; Millstone, J. E.; Banholzer, M. J.; Mirkin, C. A., The Role Radius of Curvature Plays in Thiolated Oligonucleotide Loading on Gold Nanoparticles. *ACS Nano* **2009,** *3* (2), 418-424.

231. Mirkin, C. A.; Letsinger, R. L.; Mucic, R. C.; Storhoff, J. J., A DNA-based method for rationally assembling nanoparticles into macroscopic materials. *Nature* **1996,** *382* (6592), 607-609.
232. Seferos, D. S.; Prigodich, A. E.; Giljohann, D. A.; Patel, P. C.; Mirkin, C. A., Polyvalent DNA Nanoparticle Conjugates Stabilize Nucleic Acids. *Nano Letters* **2009,** *9* (1), 308-311.
233. Lytton-Jean, A. K. R.; Mirkin, C. A., A Thermodynamic Investigation into the Binding Properties of DNA Functionalized Gold Nanoparticle Probes and Molecular Fluorophore Probes. *Journal of the American Chemical Society* **2005,** *127* (37), 12754-12755.
234. Rosi, N. L.; Giljohann, D. A.; Thaxton, C. S.; Lytton-Jean, A. K. R.; Han, M. S.; Mirkin, C. A., Oligonucleotide-Modified Gold Nanoparticles for Intracellular Gene Regulation. *Science* **2006,** *312* (5776), 1027-1030.
235. Massich, M. D.; Giljohann, D. A.; Seferos, D. S.; Ludlow, L. E.; Horvath, C. M.; Mirkin, C. A., Regulating Immune Response Using Polyvalent Nucleic Acid−Gold Nanoparticle Conjugates. *Molecular Pharmaceutics* **2009,** *6* (6), 1934-1940.
236. Kreibig, U.; Genzel, L., Optical absorption of small metallic particles. *Surface Science* **1985,** *156*, 678-700.
237. Swierczewska, M.; Lee, S.; Chen, X., The design and application of fluorophore-gold nanoparticle activatable probes. *Physical Chemistry Chemical Physics* **2011,** *13* (21), 9929-9941.
238. Taton, T. A.; Mirkin, C. A.; Letsinger, R. L., Scanometric DNA Array Detection with Nanoparticle Probes. *Science* **2000,** *289* (5485), 1757-1760.
239. Nam, J.-M.; Thaxton, C. S.; Mirkin, C. A., Nanoparticle-Based Bio-Bar Codes for the Ultrasensitive Detection of Proteins. *Science* **2003,** *301* (5641), 1884-1886.
240. Sato, K.; Hosokawa, K.; Maeda, M., Rapid Aggregation of Gold Nanoparticles Induced by Non-Cross-Linking DNA Hybridization. *Journal of the American Chemical Society* **2003,** *125* (27), 8102-8103.
241. Seferos, D. S.; Giljohann, D. A.; Hill, H. D.; Prigodich, A. E.; Mirkin, C. A., Nano-Flares: Probes for Transfection and mRNA Detection in Living Cells. *Journal of the American Chemical Society* **2007,** *129* (50), 15477-15479.
242. Prigodich, A. E.; Randeria, P. S.; Briley, W. E.; Kim, N. J.; Daniel, W. L.; Giljohann, D. A.; Mirkin, C. A., Multiplexed Nanoflares: mRNA Detection in Live Cells. *Analytical Chemistry* **2012,** *84* (4), 2062-2066.
243. Halo, T. L.; McMahon, K. M.; Angeloni, N. L.; Xu, Y.; Wang, W.; Chinen, A. B.; Malin, D.; Strekalova, E.; Cryns, V. L.; Cheng, C.; Mirkin, C. A.; Thaxton, C. S., NanoFlares for the detection, isolation, and culture of live tumor cells from human blood. *Proceedings of the National Academy of Sciences* **2014,** *111* (48), 17104-17109.
244. Kyriazi, M.-E.; Giust, D.; El-Sagheer, A. H.; Lackie, P. M.; Muskens, O. L.; Brown, T.; Kanaras, A. G., Multiplexed mRNA Sensing and Combinatorial-Targeted Drug Delivery Using DNA-Gold Nanoparticle Dimers. *ACS Nano* **2018,** *12* (4), 3333-3340.
245. Xavier, M.; Kyriazi, M.-E.; Lanham, S.; Alexaki, K.; Matthews, E.; El-Sagheer, A. H.; Brown, T.; Kanaras, A. G.; Oreffo, R. O. C., Enrichment of Skeletal Stem Cells from Human Bone Marrow Using Spherical Nucleic Acids. *ACS Nano* **2021,** *15* (4), 6909-6916.
246. Kyriazi, M.-E.; El-Sagheer, A. H.; Medintz, I. L.; Brown, T.; Kanaras, A. G., An Investigation into the Resistance of Spherical Nucleic Acids against DNA Enzymatic Degradation. *Bioconjugate Chemistry* **2022,** *33* (1), 219-225.
247. Song, L.; Guo, Y.; Roebuck, D.; Chen, C.; Yang, M.; Yang, Z.; Sreedharan, S.; Glover, C.; Thomas, J. A.; Liu, D.; Guo, S.; Chen, R.; Zhou, D., Terminal PEGylated DNA–Gold Nanoparticle Conjugates Offering High Resistance to Nuclease Degradation and Efficient Intracellular Delivery of DNA Binding Agents. *ACS Applied Materials & Interfaces* **2015,** *7* (33), 18707-18716.
248. Zhang, W.; Meckes, B.; Mirkin, C. A., Spherical Nucleic Acids with Tailored and Active Protein Coronae. *ACS Central Science* **2019,** *5* (12), 1983-1990.
249. Zhu, Z.-J.; Tang, R.; Yeh, Y.-C.; Miranda, O. R.; Rotello, V. M.; Vachet, R. W., Determination of the Intracellular Stability of Gold Nanoparticle Monolayers Using Mass Spectrometry. *Analytical Chemistry* **2012,** *84* (10), 4321-4326.

250. Moros, M.; Kyriazi, M.-E.; El-Sagheer, A. H.; Brown, T.; Tortiglione, C.; Kanaras, A. G., DNA-Coated Gold Nanoparticles for the Detection of mRNA in Live Hydra Vulgaris Animals. *ACS Applied Materials & Interfaces* **2019,** *11* (15), 13905-13911.
251. Choi, C. H. J.; Hao, L.; Narayan, S. P.; Auyeung, E.; Mirkin, C. A., Mechanism for the endocytosis of spherical nucleic acid nanoparticle conjugates. *Proceedings of the National Academy of Sciences* **2013,** *110* (19), 7625-7630.
252. Jensen, S. A.; Day, E. S.; Ko, C. H.; Hurley, L. A.; Luciano, J. P.; Kouri, F. M.; Merkel, T. J.; Luthi, A. J.; Patel, P. C.; Cutler, J. I.; Daniel, W. L.; Scott, A. W.; Rotz, M. W.; Meade, T. J.; Giljohann, D. A.; Mirkin, C. A.; Stegh, A. H., Spherical Nucleic Acid Nanoparticle Conjugates as an RNAi-Based Therapy for Glioblastoma. *Science Translational Medicine* **2013,** *5* (209), 209ra152-209ra152.
253. Kumthekar, P.; Ko, C. H.; Paunesku, T.; Dixit, K.; Sonabend, A. M.; Bloch, O.; Tate, M.; Schwartz, M.; Zuckerman, L.; Lezon, R.; Lukas, R. V.; Jovanovic, B.; McCortney, K.; Colman, H.; Chen, S.; Lai, B.; Antipova, O.; Deng, J.; Li, L.; Tommasini-Ghelfi, S.; Hurley, L. A.; Unruh, D.; Sharma, N. V.; Kandpal, M.; Kouri, F. M.; Davuluri, R. V.; Brat, D. J.; Muzzio, M.; Glass, M.; Vijayakumar, V.; Heidel, J.; Giles, F. J.; Adams, A. K.; James, C. D.; Woloschak, G. E.; Horbinski, C.; Stegh, A. H., A first-in-human phase 0 clinical study of RNA interference–based spherical nucleic acids in patients with recurrent glioblastoma. *Science Translational Medicine* **2021,** *13* (584), eabb3945.
254. Sita, T. L.; Kouri, F. M.; Hurley, L. A.; Merkel, T. J.; Chalastanis, A.; May, J. L.; Ghelfi, S. T.; Cole, L. E.; Cayton, T. C.; Barnaby, S. N.; Sprangers, A. J.; Savalia, N.; James, C. D.; Lee, A.; Mirkin, C. A.; Stegh, A. H., Dual bioluminescence and near-infrared fluorescence monitoring to evaluate spherical nucleic acid nanoconjugate activity in vivo. *Proceedings of the National Academy of Sciences* **2017,** *114* (16), 4129-4134.
255. Zheng, D.; Giljohann, D. A.; Chen, D. L.; Massich, M. D.; Wang, X.-Q.; Iordanov, H.; Mirkin, C. A.; Paller, A. S., Topical delivery of siRNA-based spherical nucleic acid nanoparticle conjugates for gene regulation. *Proceedings of the National Academy of Sciences* **2012,** *109* (30), 11975-11980.
256. Randeria, P. S.; Seeger, M. A.; Wang, X.-Q.; Wilson, H.; Shipp, D.; Mirkin, C. A.; Paller, A. S., siRNA-based spherical nucleic acids reverse impaired wound healing in diabetic mice by ganglioside GM3 synthase knockdown. *Proceedings of the National Academy of Sciences* **2015,** *112* (18), 5573-5578.
257. Allen, N. C.; Chauhan, R.; Bates, P. J.; O'Toole, M. G., Optimization of Tumor Targeting Gold Nanoparticles for Glioblastoma Applications. *Nanomaterials* **2022,** *12* (21), 3869.
258. Zhang, K.; Hao, L.; Hurst, S. J.; Mirkin, C. A., Antibody-Linked Spherical Nucleic Acids for Cellular Targeting. *Journal of the American Chemical Society* **2012,** *134* (40), 16488-16491.
259. Moustaoui, H.; Saber, J.; Djeddi, I.; Liu, Q.; Diallo, A. T.; Spadavecchia, J.; Lamy de la Chapelle, M.; Djaker, N., Shape and Size Effect on Photothermal Heat Elevation of Gold Nanoparticles: Absorption Coefficient Experimental Measurement of Spherical and Urchin-Shaped Gold Nanoparticles. *The Journal of Physical Chemistry C* **2019,** *123* (28), 17548-17554.
260. Liu, J.; Yu, M.; Zhou, C.; Zheng, J., Renal clearable inorganic nanoparticles: a new frontier of bionanotechnology. *Materials Today* **2013,** *16* (12), 477-486.
261. Alkilany, A. M.; Murphy, C. J., Toxicity and cellular uptake of gold nanoparticles: what we have learned so far? *Journal of Nanoparticle Research* **2010,** *12* (7), 2313-2333.
262. Nam, J.; Won, N.; Jin, H.; Chung, H.; Kim, S., pH-Induced Aggregation of Gold Nanoparticles for Photothermal Cancer Therapy. *Journal of the American Chemical Society* **2009,** *131* (38), 13639-13645.
263. Park, H.; Kim, J.; Jung, S.; Kim, W. J., DNA-Au Nanomachine Equipped with i-Motif and G-Quadruplex for Triple Combinatorial Anti-Tumor Therapy. *Advanced Functional Materials* **2018,** *28* (5), 1705416.
264. Zhang, J.; Cui, Y.-X.; Feng, X.-N.; Cheng, M.; Tang, A.-N.; Kong, D.-M., pH-Controlled Intracellular in Situ Reversible Assembly of a Photothermal Agent for Smart Chemo-Photothermal Synergetic Therapy and ATP Imaging. *ACS Applied Materials & Interfaces* **2019,** *11* (43), 39624-39632.
265. Jiang, Y.; Zhao, W.; Zhou, H.; Zhang, Q.; Zhang, S., ATP-Triggered Intracellular In Situ Aggregation of a Gold-Nanoparticle-Equipped Triple-Helix Molecular Switch for Fluorescence Imaging and Photothermal Tumor Therapy. *Langmuir* **2022,** *38* (12), 3755-3764.

266. Yang, K.; Liu, Y.; Wang, Y.; Ren, Q.; Guo, H.; Matson, J. B.; Chen, X.; Nie, Z., Enzyme-induced in vivo assembly of gold nanoparticles for imaging-guided synergistic chemo-photothermal therapy of tumor. *Biomaterials* **2019,** *223*, 119460.
267. Zhang, X.-Q.; Xu, X.; Lam, R.; Giljohann, D.; Ho, D.; Mirkin, C. A., Strategy for Increasing Drug Solubility and Efficacy through Covalent Attachment to Polyvalent DNA–Nanoparticle Conjugates. *ACS Nano* **2011,** *5* (9), 6962-6970.
268. Gallego-Jara, J.; Lozano-Terol, G.; Sola-Martínez, R. A.; Cánovas-Díaz, M.; de Diego Puente, T., A Compressive Review about Taxol®: History and Future Challenges. *Molecules* **2020,** *25*.
269. Pan, W.; Yang, H.; Zhang, T.; Li, Y.; Li, N.; Tang, B., Dual-Targeted Nanocarrier Based on Cell Surface Receptor and Intracellular mRNA: An Effective Strategy for Cancer Cell Imaging and Therapy. *Analytical Chemistry* **2013,** *85* (14), 6930-6935.
270. Zheng, J.; Zhu, G.; Li, Y.; Li, C.; You, M.; Chen, T.; Song, E.; Yang, R.; Tan, W., A Spherical Nucleic Acid Platform Based on Self-Assembled DNA Biopolymer for High-Performance Cancer Therapy. *ACS Nano* **2013,** *7* (8), 6545-6554.
271. Zhang, S.; Chen, C.; Xue, C.; Chang, D.; Xu, H.; Salena, B. J.; Li, Y.; Wu, Z.-S., Ribbon of DNA Lattice on Gold Nanoparticles for Selective Drug Delivery to Cancer Cells. *Angewandte Chemie International Edition* **2020,** *59* (34), 14584-14592.
272. Carvalho, J.; Paiva, A.; Cabral Campello, M. P.; Paulo, A.; Mergny, J.-L.; Salgado, G. F.; Queiroz, J. A.; Cruz, C., Aptamer-based Targeted Delivery of a G-quadruplex Ligand in Cervical Cancer Cells. *Scientific Reports* **2019,** *9* (1), 7945.
273. Ireson, C. R.; Kelland, L. R., Discovery and development of anticancer aptamers. *Molecular Cancer Therapeutics* **2006,** *5* (12), 2957-2962.
274. Song, L.; Ho, V. H. B.; Chen, C.; Yang, Z.; Liu, D.; Chen, R.; Zhou, D., Efficient, pH-Triggered Drug Delivery Using a pH-Responsive DNA-Conjugated Gold Nanoparticle. *Advanced Healthcare Materials* **2013,** *2* (2), 275-280.

# Chapter 2 – Palladium and platinum tetra-stranded complexes

## 2.1 Introduction

Over the last few decades, a significant volume of research has focused on developing 3D structures with defined cavities for a number of different applications. Metal organic frameworks (MOFs) are typical example of structures with defined cavities; the frameworks consist of metal centres which are bridged by organic ligands to produce three-dimensional structures. The work in this thesis focuses on another type of structure with defined internal cavities; that is supramolecular coordination complexes. Supramolecular coordination complexes are also made up of metal centres and bridging ligands which self-assemble, however, unlike MOFs, they are discreet molecular species. Host-guest chemistry can be precisely controlled by careful design of the ligands and selection of the metal used. Encapsulation of specific molecules is driven by a combination of supramolecular interactions, most prominently hydrogen bonding, electrostatic interactions, and van der Waals forces. The host-guest chemistry characteristic of these supramolecular coordination complexes makes them attractive for many applications, including sensors, catalysis, drug delivery, and molecular sequestration.

Many supramolecular coordination complexes have a $M_2L_4$ motif due to the ease of synthesis and our ability to precisely control the cavity dimensions, however cages with many more metal centres have also been synthesised.[1-5] Such $M_2L_4$ tetra-stranded cages have focused heavily on palladium-based cages due to the palladium's tendency to form square planar complexes and their ease of synthesis but different metal centres have also been used.[6-9] Palladium based supramolecular cages have been developed for a variety of applications: anion recognition,[10-24] neutral molecule recognition,[25-32] drug delivery,[33, 34] anti-cancer activity,[30, 33, 35, 36] and catalysis.[1, 37] Responsive cages have also been an area of focus for many research groups with the aim of controlled release of guest molecules.[34, 38-44]

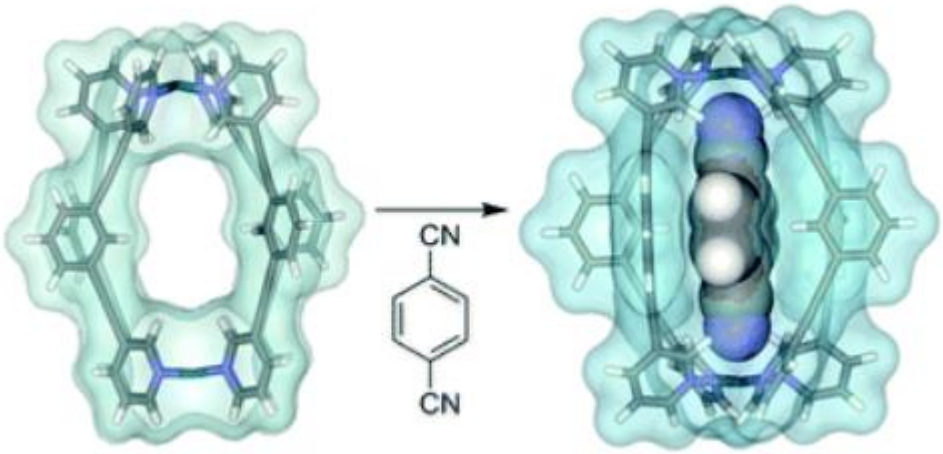


*Figure 1. $M_2L_4$ self-assembled cage structure designed by Hooley et al. encapsulating a neutral guest molecule. Adapted from referenced publication with permission.*[45]

A widely studied palladium cage design was first described by Hooley *et al*. in 2010,[45] the cage was an $M_2L_4$ complex which consisted of four rigid linkers (Figure 1). The cage was shown to have the appropriate cavity size to bind the neutral guest molecule 1,4-benzenedicarbonitrile. The design was then further studied and modified by addition of endothelial amine groups creating strongly fluorescent complexes.[46] Crowley and co-workers were the first to realise the potential biological applications of this kind of palladium tetra-stranded ccomplex.[33] A further iteration of this palladium cage was designed using ligands with a central pyridine, in place of the phenyl previously used, which was able to encapsulate two cisplatin molecules. The cage could then be disassembled in the presence of competing ligands to release the cisplatin guest molecules. A significant volume of work has focused on this type of palladium cage with rigid ligands containing alkyne groups because of its modularity and ease of functionalisation. The work can be separated into a few different categories: functionalisation of the cage for improved solubility and targeting,[46-56] more drastic changes to the ligand design,[12, 35, 57] reduction in the symmetry of the cage,[58-62] and host-guest chemistry.[25, 33, 34, 45, 56] Most recently, work by Woods *et al*. utilised a palladium supramolecular complex to encapsulate a radiolabelled anion for theranostic applications.[56] The palladium host-guest complex produced was able to traverse the blood brain barrier *in vitro* and *in vivo* by functionalisation of the structure with the $C^{PepH3}$ peptide. Work with a modified version of the same palladium cage was continued by Cosialls *et al*..[51] The peptide targeting moiety was replaced with an $F^{18}$ radiolabelled ammonium

tetrafluoroborate group to enable PET imaging. The biodistribution profile of the complex in mice was determined by a combination of *in vivo* PET/CT imaging and *ex vivo* ICP-MS. They found that the ligand design heavily influences where the complex accumulates and that the cage rapidly breaks down *in vivo* releasing the cisplatin. The authors suggest further research to increase the stability of the cage by either changing the palladium metals for platinum, or using more electron donating ligands.

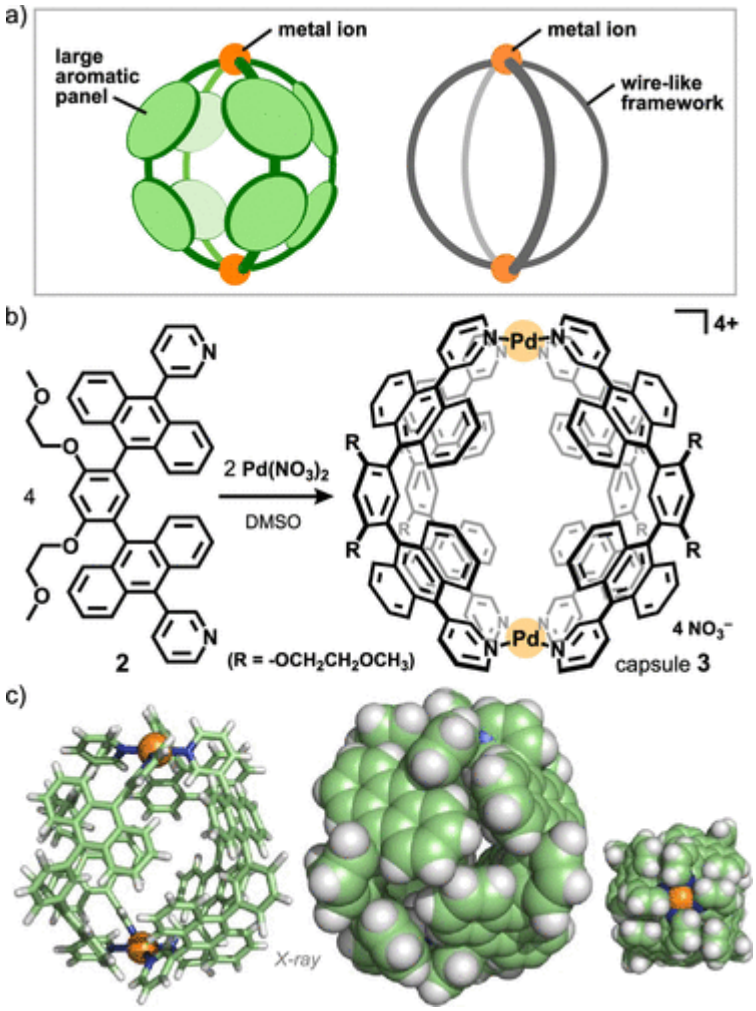


*Figure 2. A) Diagram to show structure of molecular capsule, B) Synthesis of molecular capsule, and C) X-ray structure of molecular capsule. Adapted from referenced publication with permission.*[63]

Michito Yoshizawa and co-workers were inspired by fullerenes to produce an $M_2L_4$ supramolecular palladium complex based around a bent anthracene dimer which they called a "molecular capsule" (Figure 2).[27] This design had large, outward facing aromatic surfaces similar to a fullerene as well as a central cavity approximately 1 nm in diameter which allowed a guest to be segregated from the surrounding chemical environment. The fluorescent properties of this capsule with Pd, Zn, or Ni metal

centres were also investigated.[64] The Zn based complex was found to have the strongest fluorescence which was in the blue region with a quantum yield of 0.81.

A molecular capsule with methyl ether or PEG modifications was assembled with a wide variety of different $M^{II}$ metal centres.[65] The fluorescent properties of these structures were also investigated again showing the Zn species to have the strongest fluorescent properties with weakly emissive Ni and Mn species, and non-emissive Pd, Pt and Co complexes. The Cu complex was found to be emissive with a strong dependence on the solvent used. After investigating the fluorescent properties and syntheses of these molecular capsules the focus of research shifted to the host-guest chemistry and their application as drugs, and drug delivery vehicles. The palladium molecular capsule was able to encapsulate a range of neutral guest compounds in its hydrophobic cavity which were confirmed using NMR, MS and x-ray structure analysis.[26] The hydrophobic cavity of the molecular capsule was shown to be able to selectively bind a number of biologically relevant molecules such as lactic acids, sucrose, and methyl containing aromatics .[66-68] Biological studies of platinum and palladium based molecular capsules revealed a high anti-cancer activity against cisplatin resistant cell lines.[36] The palladium capsule displayed a selectivity towards malignant cells 5.3 times higher than that of cisplatin. This is slightly higher than the platinum capsule with 3.4 fold increase in selectivity over cisplatin. The authors suggest that this difference is due to the difference in stability of the cages with the palladium cage disassembling in the presence of thiol containing biomolecules. Further study Is needed to fully elucidate the reason for this difference in activity. The identity of the guest molecule in the cages was found to modulate the cytotoxicity of the cage complex which is thought to be due to the change in stability of the host-guest complex in the presence of glutathione.[30] Structural changes to the core anthracene ligand have also been investigated to alter the guest binding properties of the capsule, and modulate it's biological activity.[63]

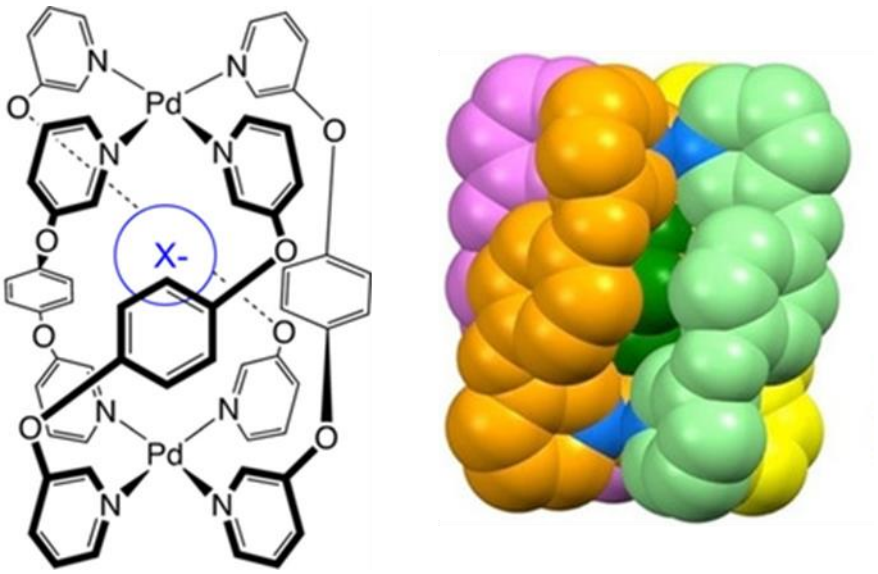


*Figure 3. Structure of helicate produced by Steel and McMorran (left) and the crystal structure of the helicate with $PF_6^-$ counterion encapsulated. Adapted from referenced publication with permission.[10]*

The majority of these $M_2L_4$ palladium complexes are simple cages, but some of them have a twist which introduces chirality to the structure resulting in M and P enantiomers. The helical twist is caused by the design of the ligands used to form the cage. Molecular cages with a helical twist are called helicates. This specific type of supramolecular coordination complex is of interest primarily for biological applications as many biomacromolecules, such as DNA and proteins, use chiral, helical motifs throughout their structures. The prevalence of helices, and chiral structures in general, in nature indicates that they have an important role to play in biological function which we can seek to understand and exploit.

The first coordinatively saturated palladium tetra-stranded helicate was produced by Steel and McMorran in 1998, it consisted of two square planar palladium centres bridged by four ligands, each with terminal pyridine groups (Figure 3).[23] The crystal structure of the complex revealed that three of the $PF_6^-$ counterions remained outside the structure, but one $PF_6^-$ was trapped in the centre and displayed weak Pd-F interactions. More recently, it has been demonstrated that the dimensions of the palladium helicate can be controlled by varying the anion in the central cavity.[10] Crystal structures were obtained for the complex with $PF_6^-$, $ClO_4^-$, $BF_4^-$, and $I^-$, which allowed the length of the helicate to alter by over 1 Å, and the helical pitch of the bridging ligands to vary between 32.8° and 76.7°. The ability of the helicate to accommodate different anions by altering its dimensions demonstrates the flexibility

of the cage. The NMR of the helicate does not show the presence of diastereomers on the ligands, indicating that the complex is rapidly interconverting between the M and P enantiomers. The kinetics of the formation of this particular helicate system has also been investigated in detail by Foianesi-Takeshige *et al*.[69]

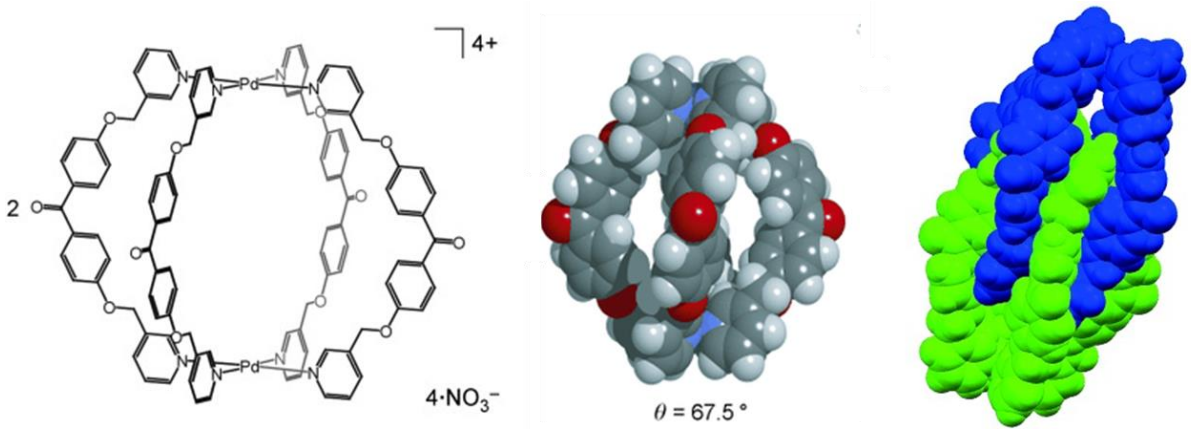


*Figure 4. Skeletal structure of metallohelicate (left), computer simulation of helicate demonstrating helical structure (middle), and the interlocked crystal structure of the metallohelicate. Adapted from referenced publication with permission.*[70]

There are few other examples of palladium tetra-stranded helicates in literature. The next coordinatively saturated palladium helicate to be synthesised was reported by Fukuda *et al*. in 2008.[70] This helicate was larger than that produced by Steel and McMorran and was shown to dimerize in solution creating a chiral interlocked metallohelicate (Figure 4).

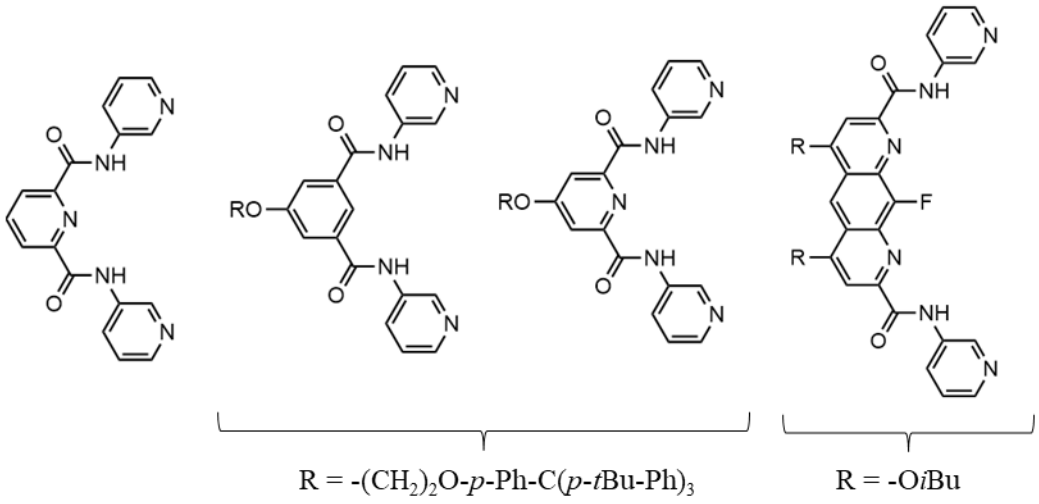


*Figure 5. Structure of the palladium helicate synthesised by Tripathy et al. (left) and subsequent modifications made (middle and right).*

Palladium "lantern complexes" have been around for a couple of decades but have suffered from solubility issues until more recently.[71, 72] In 2012 Tripathy *et al*. synthesised a palladium tetra-stranded

helicate with a ligand design containing hydrogen bond donor and acceptors (Figure 5).[73] In later work the ligands were further modified by changing the central pyridine for a phenyl ring and adding external R group to improve solubility.[74, 75] Exchanging the pyridine ring for a phenyl group introduced a steric clash between the C-H para to the ether group, and the hydrogens of the amide groups. The palladium cage with the phenyl ligand was shown to bind n-octyl glycosides whereas the pyridine analogue did not. This difference in complexation was thought to be due to the reduced rigidity of the phenyl ligand cage. A similar helicate was derived from this structure by introducing a larger aromatic system in the centre of the ligand to make a larger cavity (Figure 5).[76] Crystal structures of this palladium helicate showed how the identity of the guest anion could control the helicity of the cage structure due to the flexible amide moieties of the ligands.

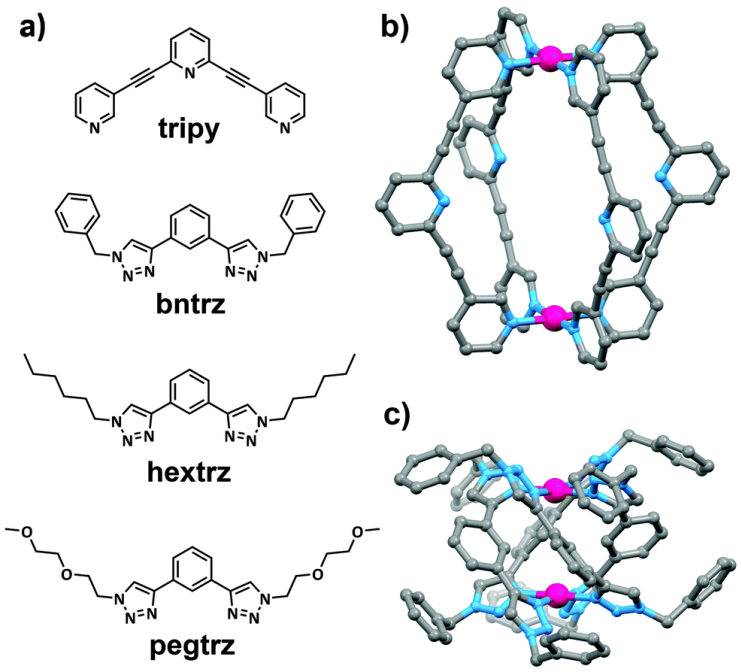


*Figure 6. a) Chemical structures of ligands investigated by McNeill et al., b) structure of $[Pd_2(tripy)_4(BF_4)_4]$ and c) structure of $[Pd_2(bntrz)_4(BF_4)_4]$. All structures exclude counterions for clarity. Adapted from referenced publication with permission.*[35]

Another helicate design much more similar to Crowley's original $Pd_2L_4$ cage has been investigated for its biological applications by McNeill *et al*.[35] The palladium helicates investigated contained an identical core unit of a phenyl ring with two triazole rings meta to eachother. Four of these ligands come together to form the cage (Figure 6). Three variations of this cage were produced with different pendant groups on the end of the triazole rings, toluene, hexane, or an ethylene glycol moiety. The

hexane modified helicate (hextrz) showed by far the highest cytotoxicity across all cell lines tested. The cytotoxicity hextrz was attributed to membrane damage of the cells. The exact mechanism of the toxicity was further investigated by McNeill *et al.* which suggested that pore formation in the membrane induced cell death.[77]

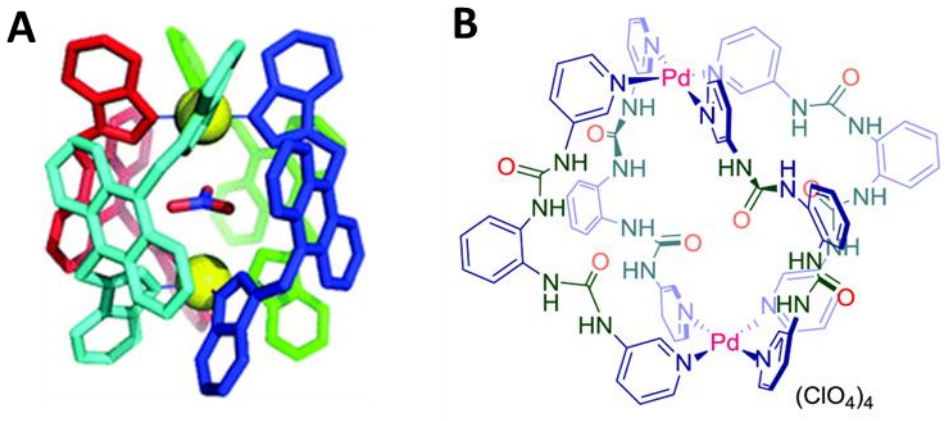


*Figure 7. A) Schematic structure of self-assembled $Pd_2L_4$ cage which selectively binds nitrate and B) Structure of quadruple stranded cage with helicity induced by perchlorate anions. Adapted from referenced publications with permission.[78, 79]*

An unusual helicate was developed by Sarkar *et al.* in 2021 which consisted of a $Pd_2L_4$ cage structure which only developed a helical twist in the presence of specific guest molecules (Figure 7).[79] Encapsulation of a nitrate anion formed a nonhelical structure, whilst the presence of a perchlorate anion induced the formation of a helix with reduced symmetry. Sun *et al*. have also developed a palladium complex which binds nitrate anions (Figure 7).[78] Unlike Sarkar *et al.* this complex is helical when it encapsulates a nitrate anion. The ligands were designed in a way to provide eight hydrogen bond donors all pointing into the central cavity of the cage which shows two orders of magnitude higher affinity for nitrate compared to other anions.

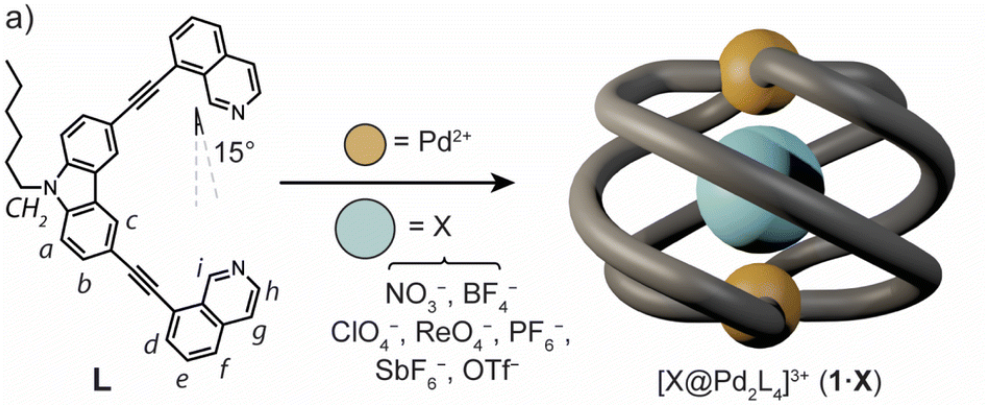


*Figure 8. Scheme showing the structure of a palladium helicate with very high helicity and the ligand used to achieve this. Adapted from reference publication with permission.*[80]

Work by Bloch *et al.* has focused on trying to control the degree of helicity in a $Pd_2L_4$ helicate (Figure 8).[80] They achieved an azimuthal angle of 176° which enabled very tight anion binding. The changes in the structure of the helicate when different anion guests were encapsulated were studied in detail through x-ray crystallography.

Unpublished work from the Hannon group has previously explored the potential of tetra-stranded palladium complexes for DNA junction binding (Figure 9).[81, 82] The ligands used to produce these complexes were based around a diphenyl unit with a methyl or hetero atom linking the two benzene rings together. Functionalised pyridine moieties were attached in the para position on each benzene to create a bent ligand structure which could coordinate to two separate metal centres, allowing the formation of a tetra-stranded cylinder. Many modifications of the core structure were attempted in order to overcome the very poor aqueous solubility of the core structure. Modifications include: replacing the central methyl with hetero atoms, addition of ether groups, alcohols, or fluorine atoms to the pyridine rings, or addition of alkyl groups to the phenyl rings. Solubility in aqueous solutions with small additions of organic solvents was achieved which enabled DNA binding studies. Binding of the complexes to B-DNA was established but junction binding of the complexes was inconclusive.

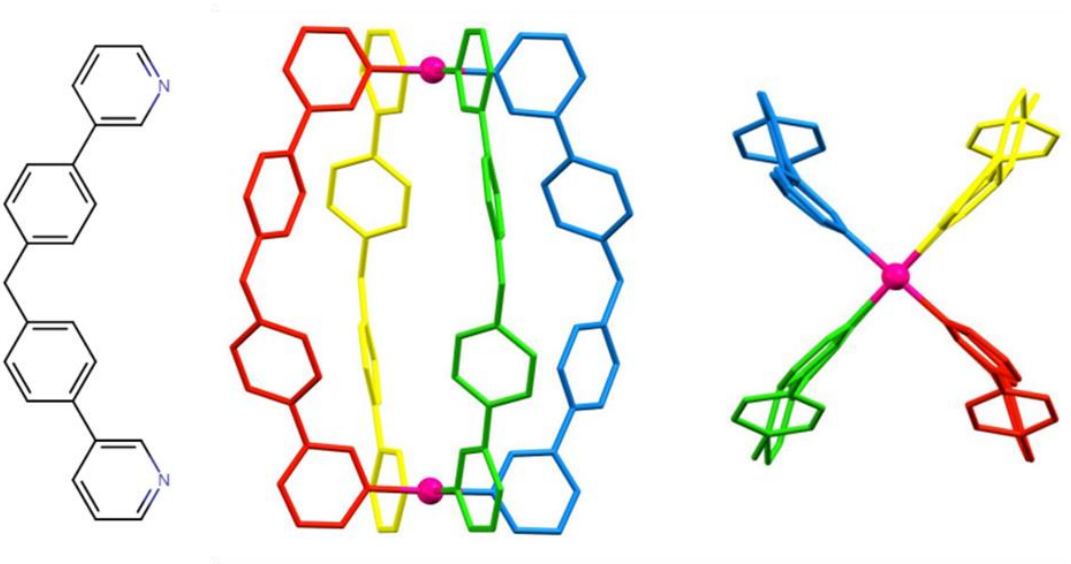

*Figure 9. Structure of the core ligand used (left) and the crystal structure of the resulting palladium tetra-stranded cylinder (middle and right). Adapted from referenced thesis.*[81]

The helical structure of the parent cylinder produced in the Hannon group (discussed in Chapter 1) has been shown to be crucial to the binding to DNA junctions (Figure 10).[83, 84] It was thought that the helical nature of the palladium helicates discussed above may convey interesting properties for DNA binding. The palladium helicate produced by Steel and McMorran was selected for study due to the externally oriented pi surfaces of the central portion of the helicate, the 4+ charge, and the general dimensions of the complex (Figure 10).[23] The dimensions of the Steel palladium helicate are similar to that of the parent cylinder which is known to strongly stabilise DNA 3WJ structures.[83] The 4-fold symmetry of the palladium cylinder may also make it more suited to binding to DNA 4WJ which are significant in many biological processes such as viral RNA insertion, recombination, and regulation of gene expression.[85, 86]

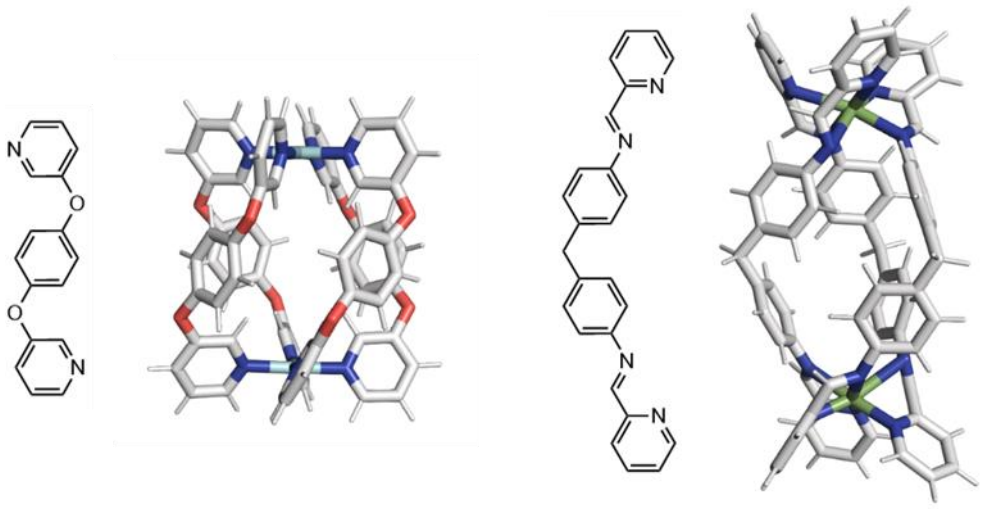

*Figure 10. The three-dimensional structure of the palladium helicate produced by Steel and McMorran and the ligand chemical structure (left).[23] The three-dimensional structure of the three stranded helicate (termed the "parent cylinder") produced by the Hannon group and the ligand chemical structure (right).*

In this chapter the original palladium helicate produced by Steel *et al*. will be synthesised along with the platinum analogue of this complex. The aim of this chapter of work was to determine the extent of the interaction between the palladium and platinum complexes with B-DNA and DNA junctions. It was hypothesised that the palladium helicate would be capable of binding cavities in DNA due to its helical geometry, high positive charge and appropriate dimensions. It was thought that this palladium helicate may show a preference for DNA 4WJ instead of 3WJ due to its four-fold symmetry.

## 2.2 Synthesis

### 2.2.1 Synthesis of $L_1$

The first step in the synthesis of the palladium cylinder was to make the ligand (Scheme 1). The ligand was designed by McMorran and Steel to be flexible allowing the complex to twist and form a helical complex.[23] The ligand has two terminal pyridine groups which are ideal for coordinating to metal centres such as palladium. The reaction proceeded as expected with no issues.

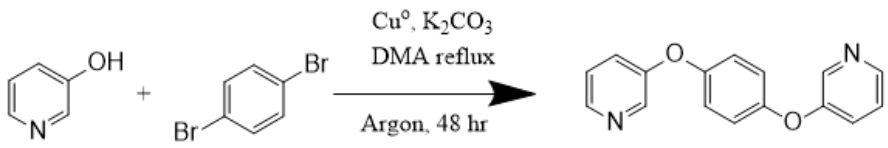


*Scheme 1. Reaction scheme for synthesis of ligand $L_1$.*

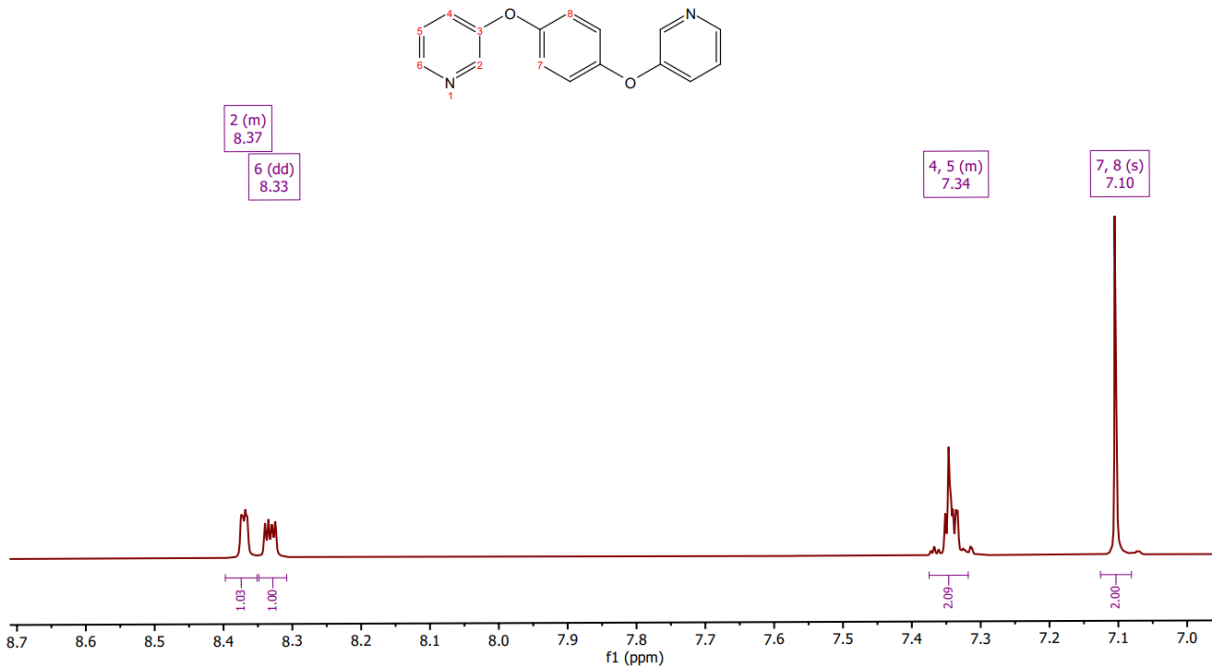


*Figure 11. $^{1}H$ NMR (400 MHz, $CD_3CN$, 298 K) of ligand $L_1$.*

Formation of the desired product was confirmed by NMR and mass spectrometry. The $^{1}H$ NMR is shown in Figure 11, the mass spec, $^{13}C$ NMR, HSQC and COSY are shown in the appendix (A2.1). The characteristic peaks for the ligand can be clearly seen but the coupling cannot be determined due to peak overlap and the limited resolution causing peak broadening.

## 2.2.2 Synthesis of $Pd_2(L_1)_4(BF_4)_4$

A tetra-stranded helicate using ligand $L_1$ was previously synthesised by Steel and MacMorran with palladium metal centres.[23] They have also demonstrated how this complex is able to modulate its size due to the flexibility of the ligands, this allows it to encapsulate different guest anions.[10] The same palladium cage was synthesised here from $L_1$ through a modified one step reaction (Scheme 2). The tetra-stranded helicate self-assembles in solution with heating in acetonitrile and an appropriate source of palladium. No significant side products were produced during the self-assembly, making preparation of the complex a simple process.

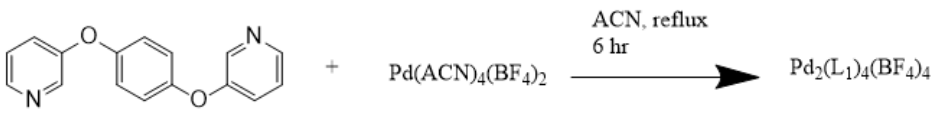


*Scheme 2. Synthesis of $Pd_2(L_1)_4(BF_4)_4$ helicate.*

The product was isolated by removing the solvent under reduced pressure and triturating with diethyl ether. The product was then washed with diethyl ether and dried under vacuum.

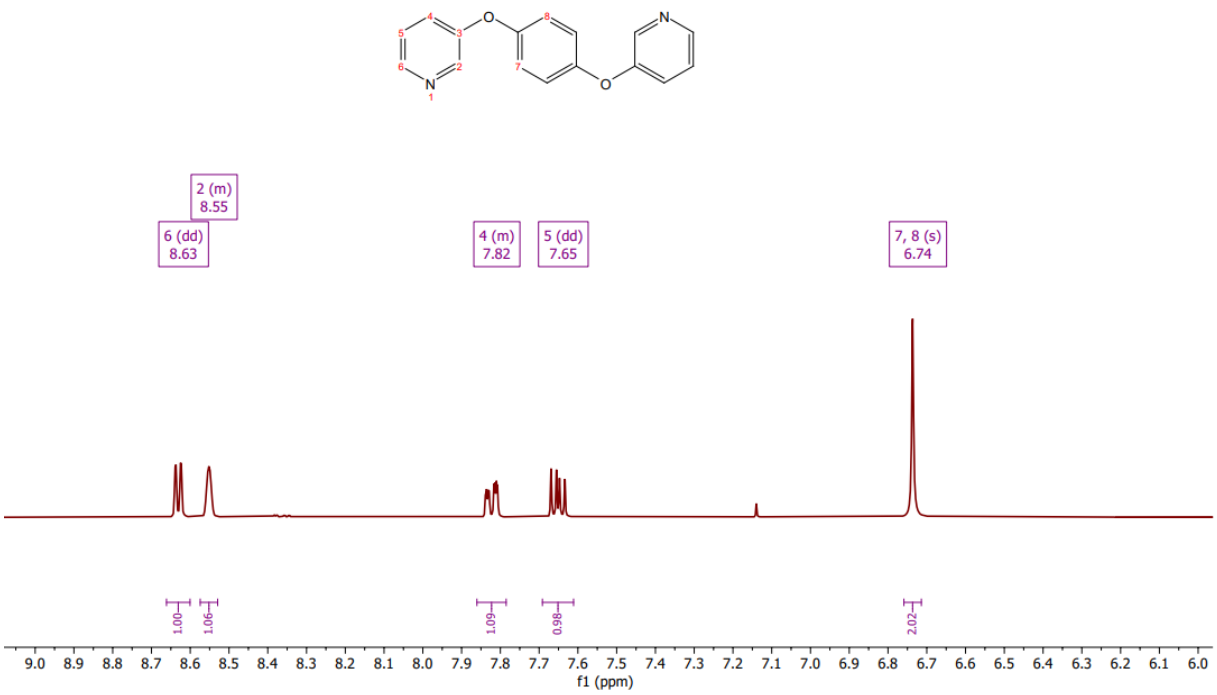


*Figure 12. $^{1}H$ NMR (400 MHz, $CD_3CN$, 298 K) of $Pd_2(L_1)_4(BF_4)_4$.*

Formation of the metal complex is confirmed by mass spectrometry and NMR (Figure 12 and Figure 13). $^{13}C$ NMR, COSY, and HSQC characterisation are shown in appendix (A2.2). Mass spectrometry shows the 452.4 m/z peak as the major species which correspond to the $Pd_2(L_1)_4(BF_4)^{3+}$, as well as peaks at 688.1 m/z and 444.0 m/z. Notably, there is no peak corresponding to $[Pd_2(L_1)_4]^{4+}$, as one of the anions is trapped in the centre of the cage. The trapped anion has been previously shown to have a role in stabilisation of the cage structure through weak interactions with the palladium metal centres.[10]

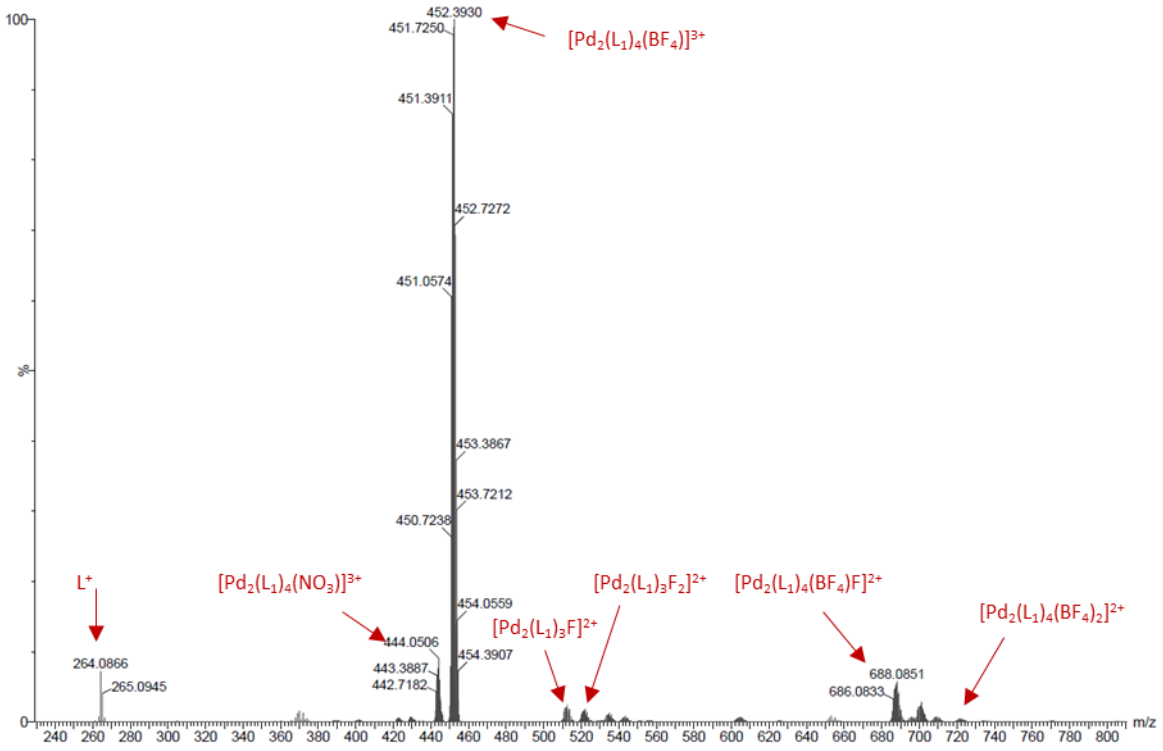


*Figure 13. ESI mass spectrum of $Pd_2(L_1)_4(BF_4)_4$ in ACN. $L_1^+$ = 264 m/z, $[Pd_2(L_1)_4(BF_4)]^{3+}$ = 451 m/z, $[Pd_2(L_1)_4(NO_3)]^{3+}$ = 443 m/z, $[Pd_2(L_1)_4(BF_4)(F)]^{2+}$= 687 m/z.*

## 2.2.3 Synthesis of $Pt_2(L_1)_4(NO_3)_4$

### 2.2.3.1 First attempts at synthesis of $Pt_2(L_1)_4$

A new metal complex utilising, the same ligands as was used to synthesise the palladium helicate (Section 2.2.2) was produced with platinum metal centres instead. Initial attempts to synthesise the platinum complex were adapted from the synthesis of the palladium helicate. A platinum precursor with labile ligands was refluxed with the ligand in a 2:1 ratio in acetonitrile, with the addition of $AgNO_3$ to remove the chloride from solution (Scheme 3).

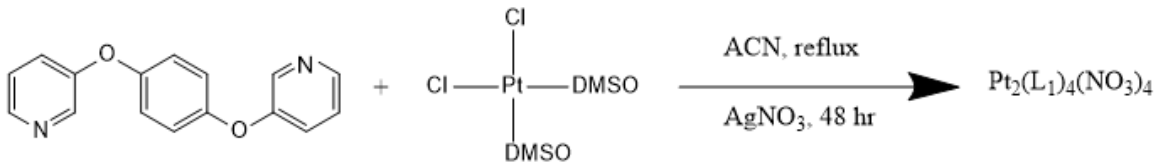


*Scheme 3. First attempted synthesis of $Pt_2(L_1)_4(NO_3)_4$.*

The reaction was monitored by mass spectrometry and halted after 48 hours. After 48 hours the major product observed by MS was 502.9 m/z which was attributed to the desired product $[Pt_2(L_1)_4(NO_3)]^{3+}$ (Figure 14). The $[Pt_2(L_1)_4]^{4+}$ species with no anion is again not observed due to the necessity for a guest anion to stabilise the cage structure. However, an impurity was also visible in the MS at 591.3 m/z,

which was attributed to the $Pt_2(L_1)_5(NO_3)]^{3+}$ complex. It was thought that the longer reaction times up to 48 hours may allow the five ligand complex to rearrange and form the more stable four ligand species but this did not occur. It is worth noting that mass spectrometry is not quantitative, so it is not possible to determine an accurate ratio of the four ligand species to five ligand species with this data. Different species will have different ionisation efficiencies and may also "fly" more/less efficiently in the mass spectrometry instrument which will result in more/less of each species detected than is present in solution.

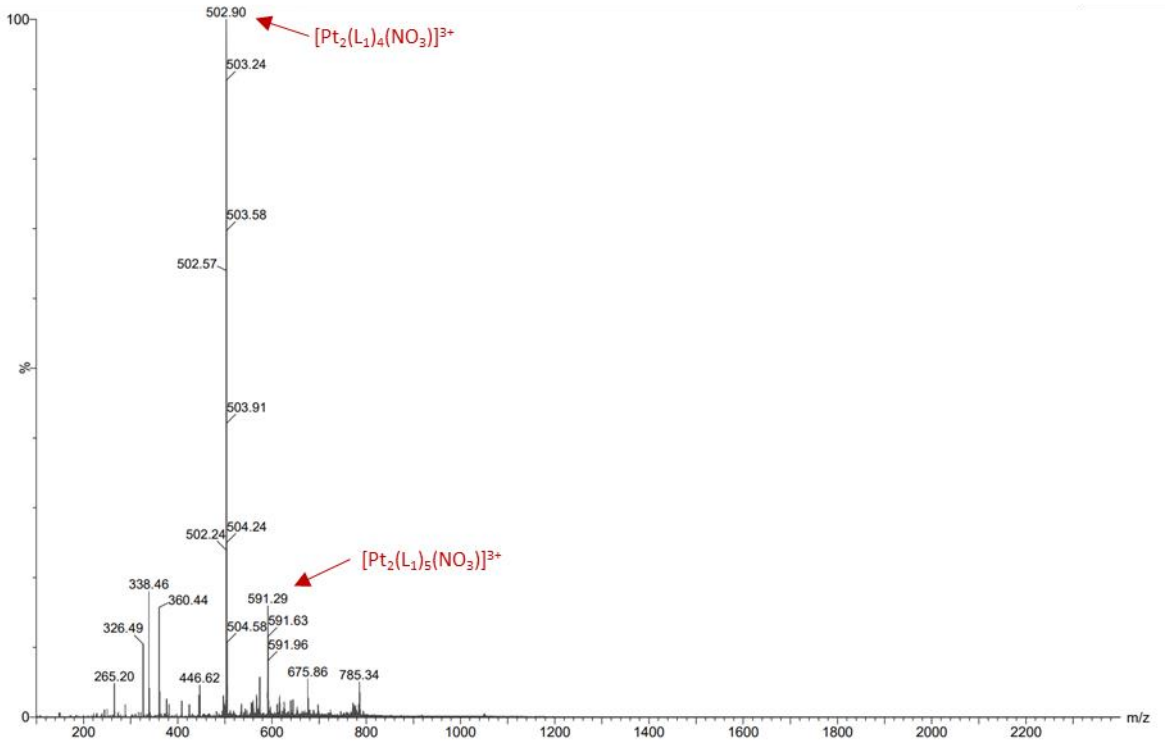


*Figure 14. ESI mass spectrum of attempted synthesis of $Pt_2(L_1)_4(NO_3)_4$. $[Pt_2(L_1)_4(NO_3)]^{3+}$ = 502 m/z, $[Pt_2(L_1)_5(NO_3)]^{3+}$ = 591 m/z.*

Due to the presence of impurities in the crude reaction mixture HPLC was used to try to purify the reaction. Multiple attempts were made to purify the product utilising HPLC with various gradients of water and acetonitrile but achieving adequate separation of the five ligand species and the four ligand species was not possible. The mass spectrum of the purest fraction (determined by analytical HPLC) shows the $[Pt_2(L_1)_4(NO_3)]^{4+}$ species at 502.8 m/z and another major peak at 810.6 m/z which can be attributed to $[Pt_2(L_1)_4(NO_3)(CF_3COO)]^{2+}$(Figure 15). No five ligand species was visible by MS in this solution.

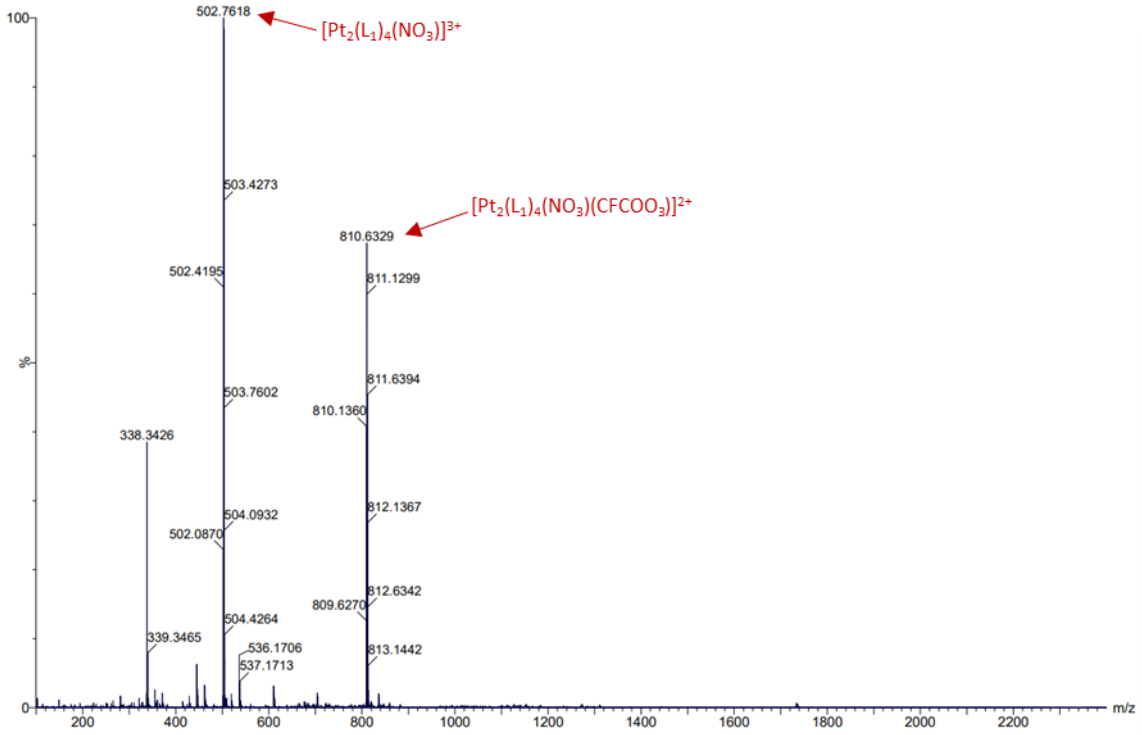


*Figure 15. ESI mass spectrum of $Pt_2(L_1)_4(NO_3)_4$ after purification by HPLC. $[Pt_2(L_1)_4(NO_3)]^{3+}$ = 502 m/z, $[Pt_2(L_1)_4(NO_3)(CF_3COO)]^{2+}$ = 810 m/z*

Despite the mass spectrum of the collected fraction indicating little to no five ligand species present, $^1$H NMR reveals that multiple species are present in the fraction. The $^1$H NMR of the fraction contains peaks which could be assigned to the product $Pt_2(L_1)_4(NO_3)_4$, but also many impurities (Figure 16). The most prominent peaks were tentatively assigned retrospectively, after successful synthesis of the complex (section 2.3.2), but the integrals do not match what is expected of the four ligand species. The impurities do not correspond to free ligand and must therefore be due to other unidentified platinum species.

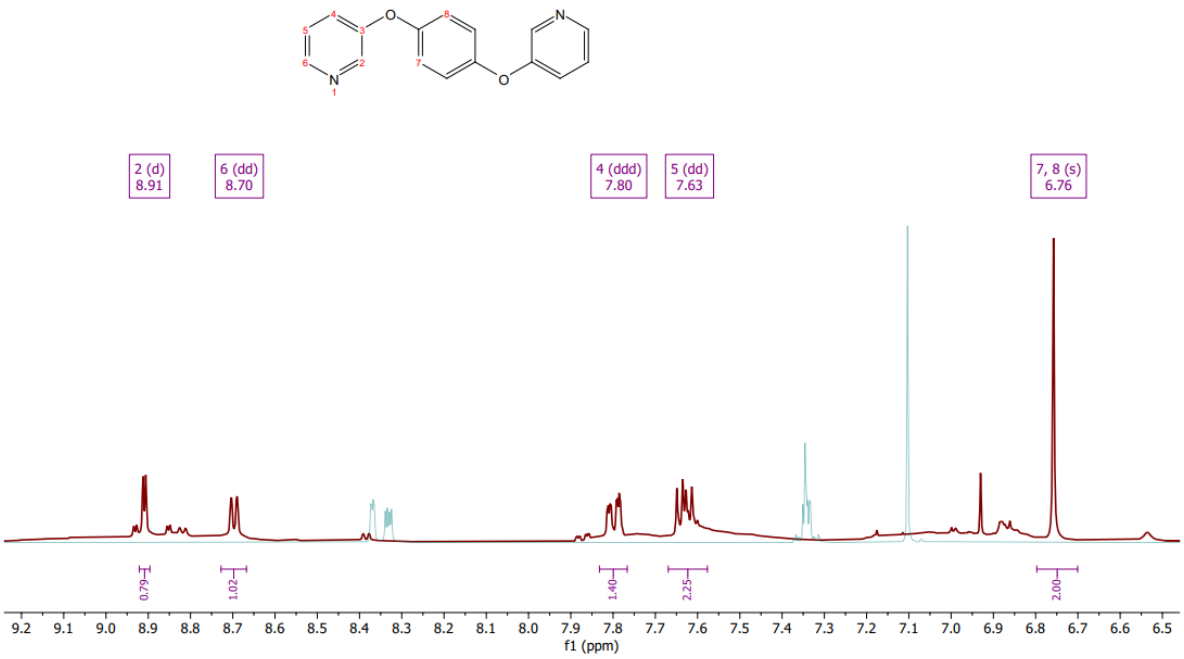


*Figure 16. $^1$HNMR (400 MHz, $CD_3CN$, 298 K) of purest fraction of $Pt_2(L_1)_4(NO_3)_4$ obtained from HPLC. Green spectrum is the $^1$H NMR of $L_1$ (400 MHz, $CD_3CN$, 298 K) for comparison.*

### 2.2.3.2 Final synthesis of $Pt_2(L_1)_4(NO_3)_4$

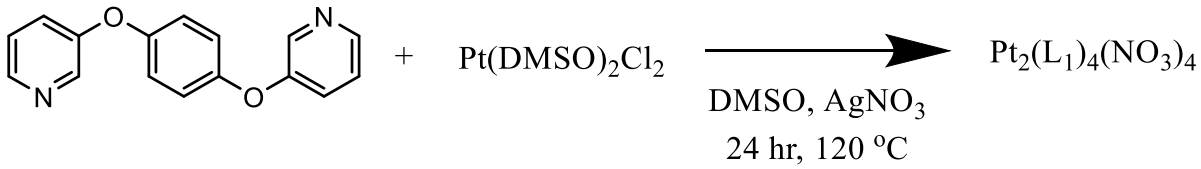


*Scheme 4. Final synthesis of $Pt_2(L_1)_4(NO_3)_4$.*

Purification of the impure $Pt_2(L_1)_4(NO_3)_4$ species was not possible so in order to avoid the use of HPLC purification, the synthesis was modified. Inspiration was taken from other publications which used DMSO as the reaction solvent.[45, 59] The reaction solvent was changed from ACN to DMSO to allow a higher reaction temperature where rearrangement of the complex may be more likely to occur. The progress of the reaction was monitored by MS as shown in Figure 17. The four ligand species is visible as the major species after 30 mins, but a very large five ligand species is also present as well as small peaks for three ligand species. Over the course of the next 22 hours, the proportion of five ligand species gradually decreases and the four ligand species remains as the dominant species. After 22 hours, the product was allowed to cool and was collected by addition of diethyl ether to remove the DMSO and precipitate the product. The only major peak observable in the MS is the product four ligand species (Figure 18).

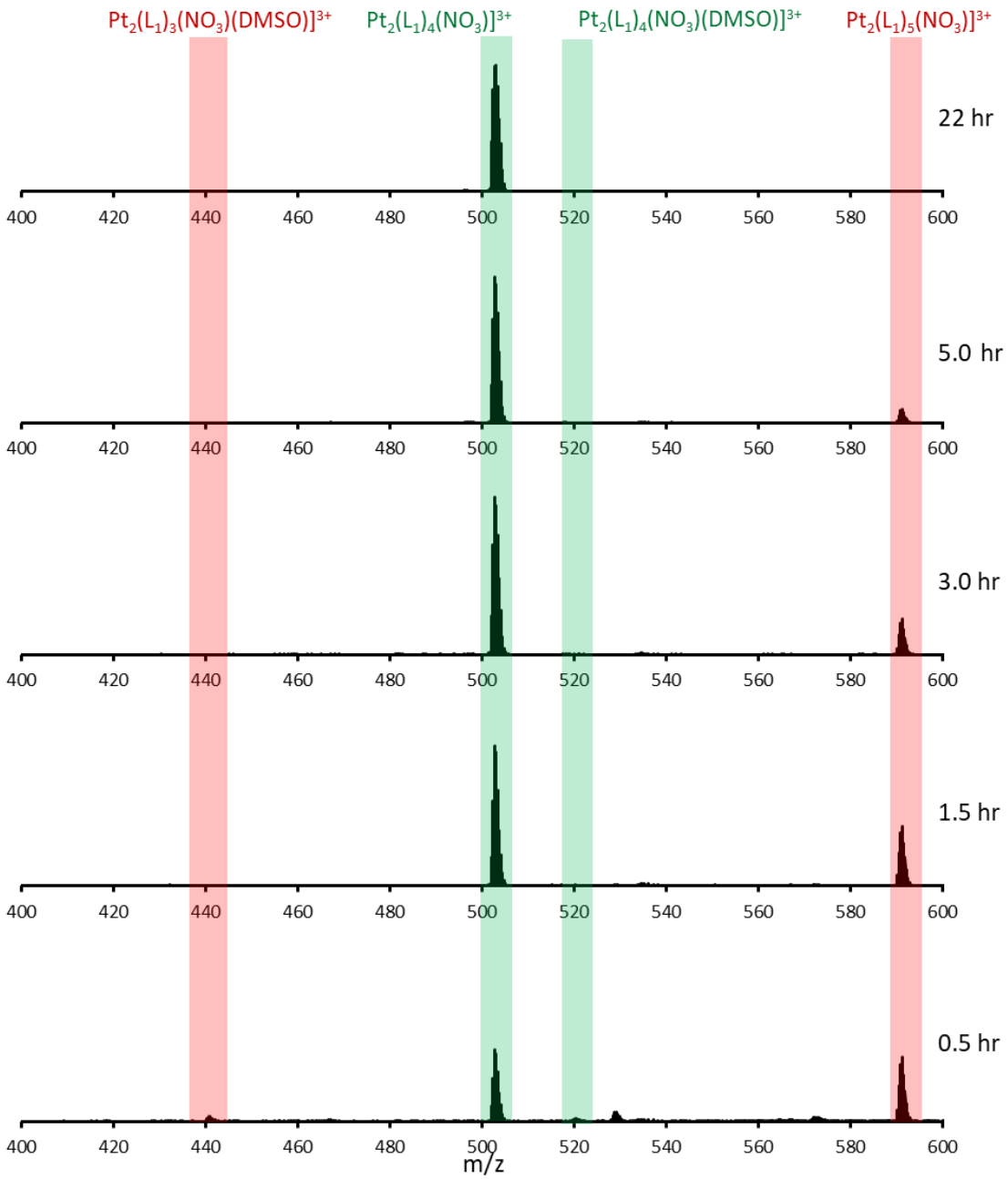


*Figure 17. Monitoring the synthesis of $Pt_2(L_1)_4(NO_3)_4$ by ESI mass spectrometry over 22 hours.*

After isolating the product, characterisation was carried out by MS and NMR (Figure 18 and Figure 19). The mass of $[Pt_2(L_1)_4(NO_3)]^{3+}$ was measured to be 502.77 m/z which closely matches the mass predicted using enviPat for $[Pt_2(L_1)_4(NO_3)]^{3+}$ 502.7584 m/z.[87] Other small signals are observed at 785.13 m/z and 265.1 m/z which correspond to the $[Pt_2(L_1)_4(NO_3)_2]^{2+}$ and $[L+H]^+$ species respectively. The major species is the 3+ cation with a single nitrate counterion accompanying it. It is possible that the nitrate is encapsulated in the cage as crystal structures of the palladium analogue contain counterions

encapsulated within the structures.[10] The isotope pattern for $[Pt_2(L_1)_4(NO_3)]^{3+}$ closely matches the isotope pattern predicted using enviPat software.[87]

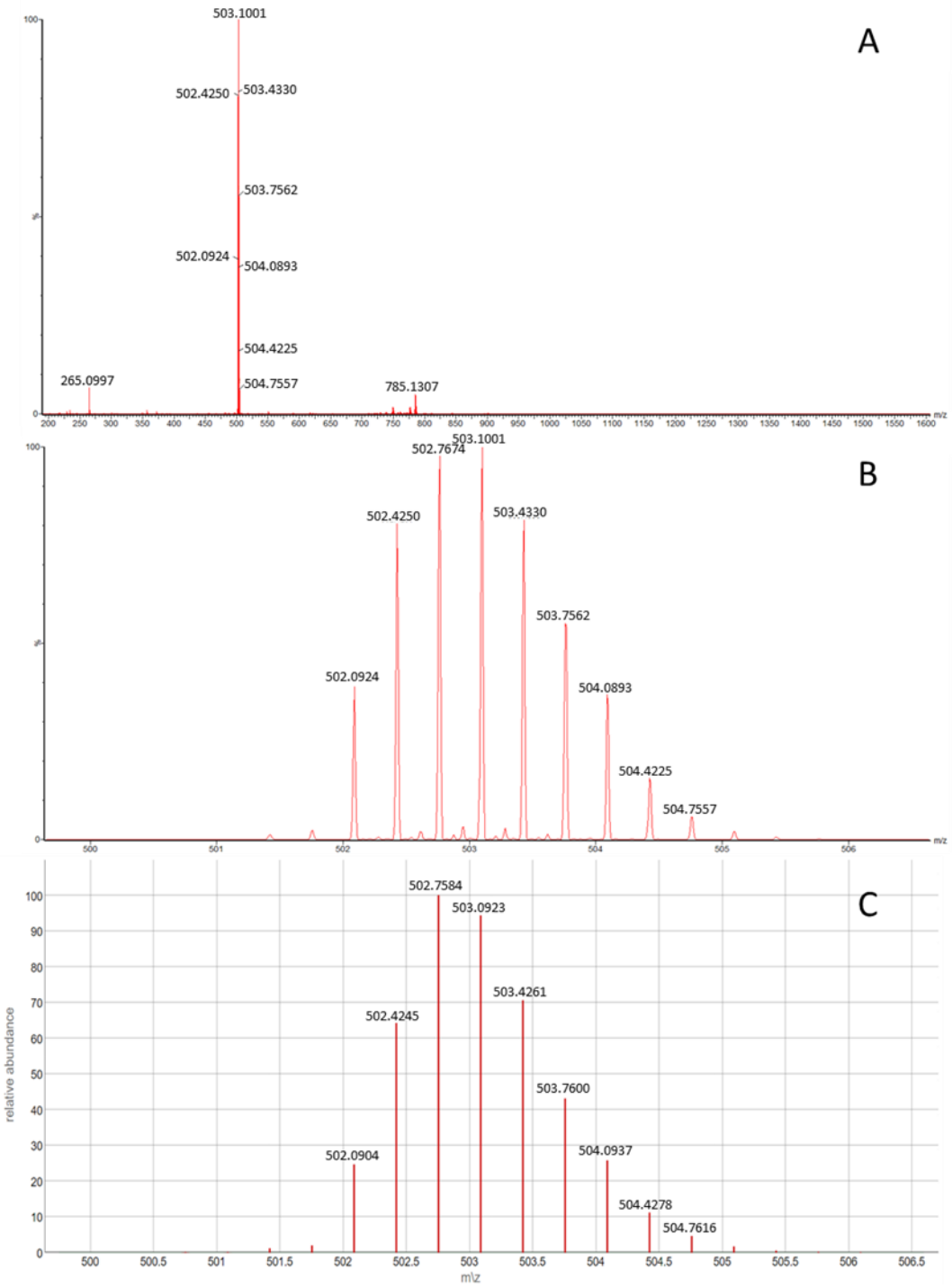


*Figure 18. A) ESI mass spectrum of $Pt_2(L_1)_4(NO_3)_4$, B) Zoom in on isotope pattern of $[Pt_2(L_1)_4(NO_3)]^{3+}$ series, C) Isotope pattern for $[Pt_2(L_1)_4(NO_3)]^{3+}$ predicted using enviPat software.[87]*

The purity of the collected species was confirmed by NMR spectroscopy. The complex was further characterised by HSCQC, COSY and $^{13}C$ NMR, and elemental analysis (A2.2). $^{1}H$ NMR of the complex

reveals sharp peaks which were unambiguously assigned using HSQC and COSY NMR, there is a very small peak at 7.2 ppm which corresponds to free ligand.

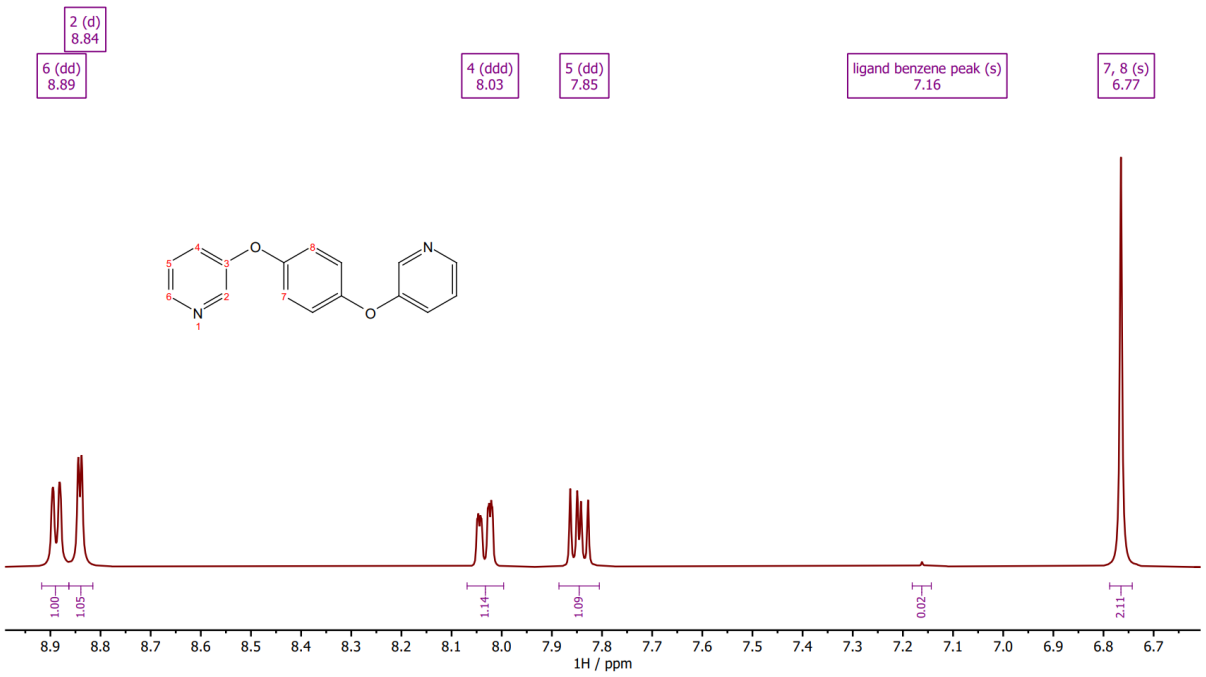


*Figure 19. $^1$HNMR (400 MHz, $d_6$-DMSO, 298 K) of $Pt_2(L_1)_4(NO_3)_4$.*

The characterisation through and NMR and mass spectroscopy presented here confirms that the new platinum species has been synthesised successfully and in good purity. Due to the lack of a crystal structure, the new species cannot be unequivocally said to be a helicate. In this work we will refer to the new platinum species as either the platinum cylinder or PtCyl.

## 2.3 Interaction with B DNA

Linear dichroism is a technique used to assess the interaction of large bio-polymers with other molecules. In order for an LD signal to be observed, the polymers must first be oriented, this can be achieved by stretching them on a polyethylene film or, as is more common now, the molecules can be oriented in flow using a couette cell. A couette cell is a cylindrical quartz cuvette where a transparent rod can be inserted through the centre and rotated rapidly. This leaves a small 1 mm cavity around the circumference of the central rod where the sample is subjected to high shear forces which aligns larger polymeric species in flow. The LD signal is calculated as follows:

$$LD = A_{||} - A_{\perp}$$

*Equation 1. How linear dichroism is calculated.*

DNA has a characteristic LD signal which is caused by the base pairs arranging perpendicular to the flow in the couette cell.[88] Changes to the orientation of the DNA base pairs in solution can be observed in the LD as changes in the magnitude of the signal as well as shifts in the peaks. When small molecules are organised as they are when they interact with DNA they can cause an induced LD signal which can form new peaks. The iron parent cylinder is a good example of a complex which shows an induced LD signal on interaction with DNA.[89]

Circular dichroism uses right handed and left handed circularly polarised light to acquire UV absorption spectra which are compared to give a CD spectra. A CD spectra in the UV region can give information on the secondary structure of proteins and DNA, and can also be used to examine small chiral molecules. DNA with different secondary structures gives rise to different CD signals. By comparing CD spectra of DNA with a DNA binder, and known CD signals for specific DNA conformations, changes to the secondary structure of the DNA caused by the DNA binder can be inferred. Induced CD (ICD) signals can be formed when molecules interact with DNA in a specific manner and become fixed in a chiral environment. ICD signals can be used to confirm that an interaction is occurring between the DNA and the DNA binder.

Calf thymus DNA (ctDNA) was used to study the interaction of the metal complexes with B-form DNA. Calf thymus DNA consists of long duplexes of random lengths which are made up of 41.9% adenine and thymine base pairs, and 58.1% guanine and cytosine base pairs.[90] Due to the random lengths of the DNA strands, the DNA concentration was calculated in base pairs by measuring the absorbance at 260 nm and using the molar extinction coefficient of 13100 $M^{-1}cm^{-1}$.

### 2.3.1 $Pd_2(L_1)_4(BF_4)_4$ interactions with B-DNA

All chiral molecules exhibit a CD signal. A CD spectra of the palladium helicate in solution was carried out to see if the helicate was chiral/enantiomerically pure. The palladium complex alone did not give any ICD signal, the lack of CD signals means that either the species is racemic, so the positive and negative ICD signals cancel out, or that the M and P enantiomers are interconverting faster than the

timescale of the measurement. Given the flexibility allowed in the complex by the ligands used it is probable that the species is rapidly interconverting which is supported by the NMR.

Titration of the palladium tetra-stranded helicate with ctDNA does not appear to have induced any significant changes in the DNA signal, even at very high concentrations of the complex (Figure 20). There also do not appear to be any changes in the UV-vis spectra of the palladium UV-vis spectra in the presence of DNA as shown in Figure 20. The overall spectra appears to be the palladium helicate and ctDNA spectra superimposed on one another.

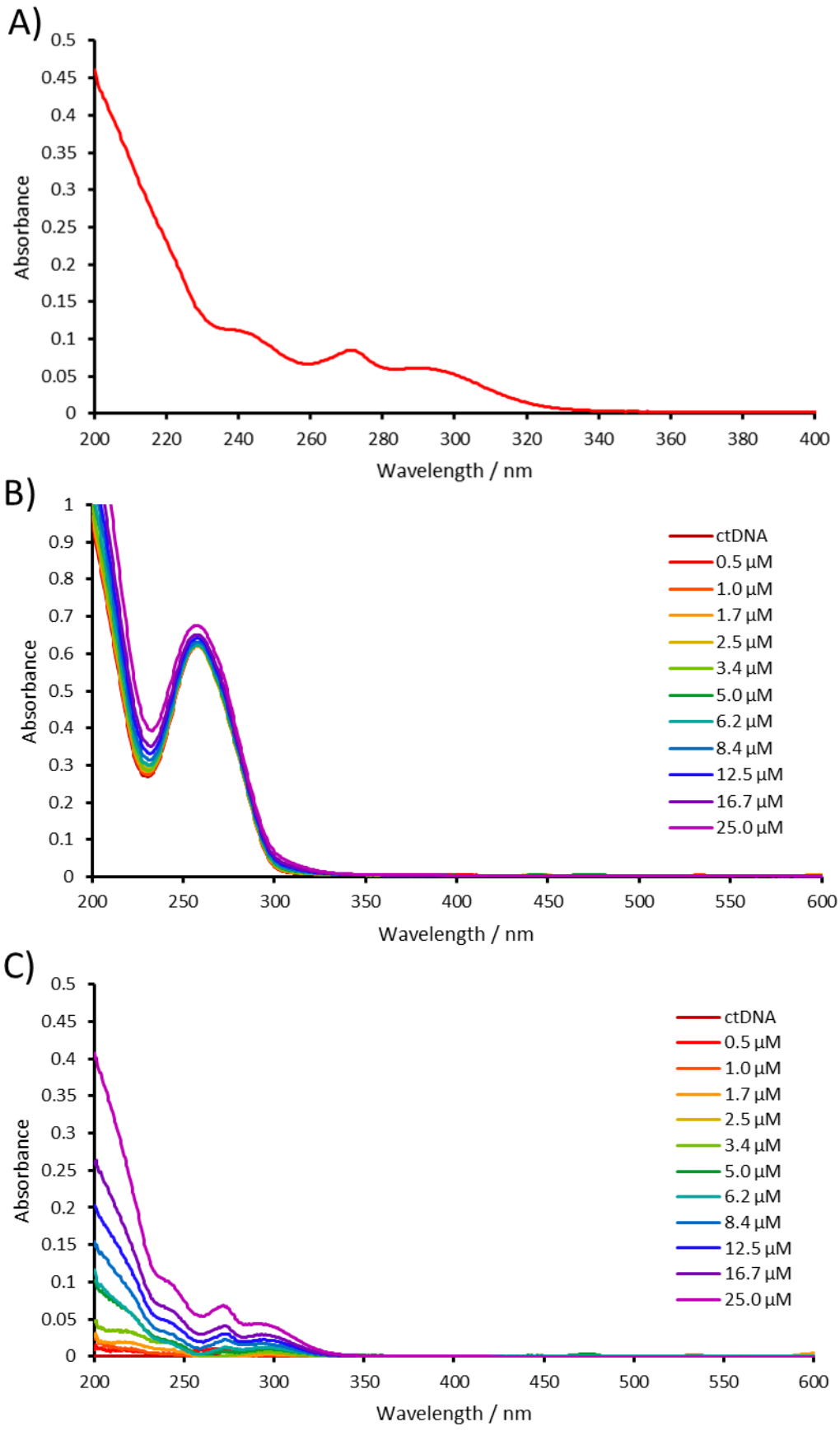


*Figure 20. A) UV-vis spectra of $Pd_2(L_1)_4(BF4)_4$ 2.5µM in water (0.05% ACN), B) UV-vis spectra of $Pd_2(L_1)_4(BF4)_4$ titrated into a solution of ctDNA (50 µM) in buffer (Tris-HCl 1mM, NaCl 20 mM, pH 7.4) where the ctDNA concentration is maintained throughout the titration experiment, and C) the resulting difference in the spectra compared to ctDNA alone. Stock solution of $Pd_2(L_1)_4(BF_4)_4$ was 1mM in water with 10% ACN.*

CD experiments were carried out with the palladium helicate and ctDNA to determine if the complex had a significant interaction with DNA and, if so, to identify its mode of binding. The palladium helicate does not exhibit a CD signal on its own, it is thought that this is because the complex is rapidly interconverting between the M and P enantiomers due to the flexible bridging ligands.[10] A solution of the palladium helicate was titrated into a solution of ctDNA which was made up of: 100 µM ctDNA, 1 mM Tris-HCl buffer pH 7.4, and 20 mM NaCl. After each addition of metal complex solution to the ctDNA, an equal volume of a third solution was added which contained: 200 uM ctDNA, 2 mM Tris-HCl buffer pH 7.4, and 40 mM NaCl. The DNA was kept stable in buffered solution but small amounts of acetonitrile were required to solubilise the complex.

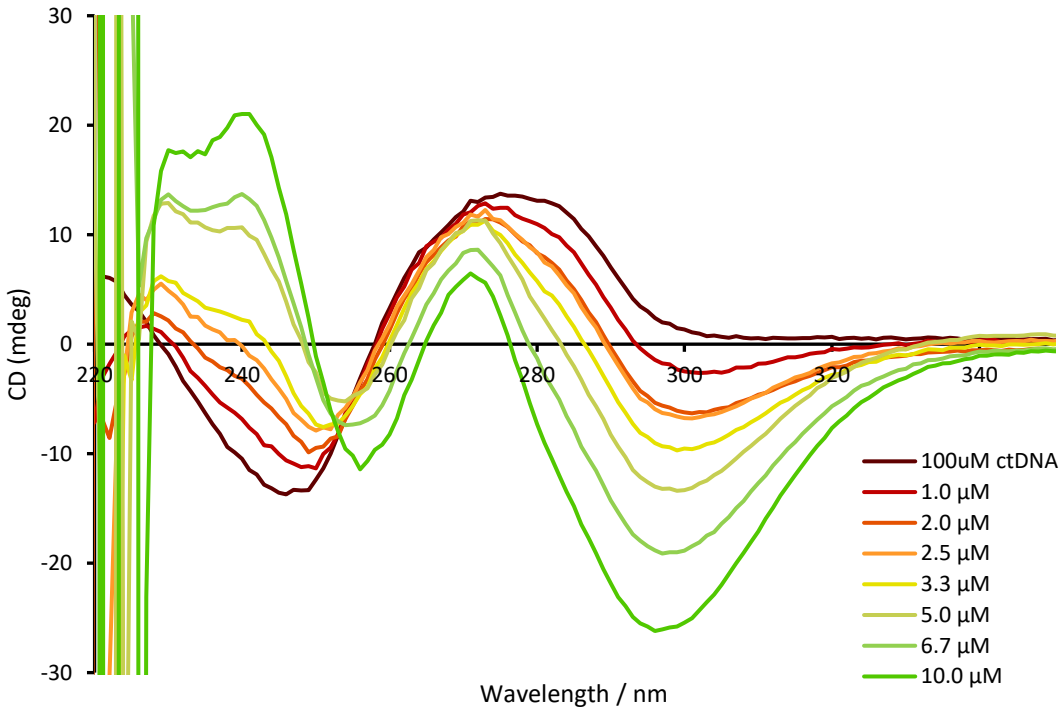


*Figure 21. Circular dichroism of 100 µM ct-DNA in 1 mM Tris-HCl buffer pH 7.4, 20 mM NaCl with increasing concentration of $Pd_2(L_1)_4(BF_4)_4$ where the concentration of ctDNA is maintained throughout the experiment. Stock solution of $Pd_2(L_1)_4(BF_4)_4$ was 1mM in water with 10% ACN.*

Immediately on addition of palladium helicate to the ctDNA there are obvious changes to the CD spectra; a large negative peak appears at 300 nm and a positive peak forms at roughly 240 nm (Figure 21). The peak at approximately 275 nm decreases in intensity with increasing ratios of palladium helicate. These peaks are in a region of the UV-is spectrum where the metal complex absorbs with the peaks at 300 nm and 275 nm aligning well with the absorbance of the palladium helicate (Figure 20,

A). These induced CD peaks can either be formed through metal complex interactions with the DNA, or through changes in the DNA structure. Some G-quadruplex structures have been shown to have CD signals at approximately 300 nm, however these give positive CD signals.[91] The Z-DNA structure has a characteristic negative band at 295 nm, as well as a positive band at 260 nm and a strong negative band at 205 nm.[92] This somewhat matches the CD spectra of the metal helicate with ctDNA meaning that the complex may be inducing the formation of Z-DNA. However, this is unlikely as it is very difficult to form Z-DNA at physiological pH. The LD spectra acquired does not support this theory as we see a decrease in the magnitude of the DNA signal at 260 nm (Figure 22). The formation of Z-DNA would result in an increase in the LD signal due to the lengthening of the DNA structure and the reduction in propellor twist of the base pairs.[93, 94] The UV-vis titration does not reveal any change in the absorbance profile of the palladium complex, and the CD spectrum produced does not match that of other non-canonical DNA structures. The new signals produced could be due to orientation of the metal complex in solution by the DNA strand, this would not result in any changes to UV signal but would be detected by CD spectroscopy.

It is difficult to unambiguously assign the other peaks at 270 nm and 240 nm to the complex rather than to changes in the DNA structure because the UV absorbance of the DNA and the metal complex strongly overlap. The titration was carried out up to a concentration of 33 μM (3 base pairs per metal complex) but at concentrations higher than 10 μM the data became very noisy (full titration shown in A2.4). This was due to a combination of the complex having very high absorption in the 200-220 nm region as well as precipitation of the DNA at high concentrations of the complex. Breakdown of the metal complex in buffered solution could also result in precipitate forming as the ligand is highly insoluble in aqueous solution.

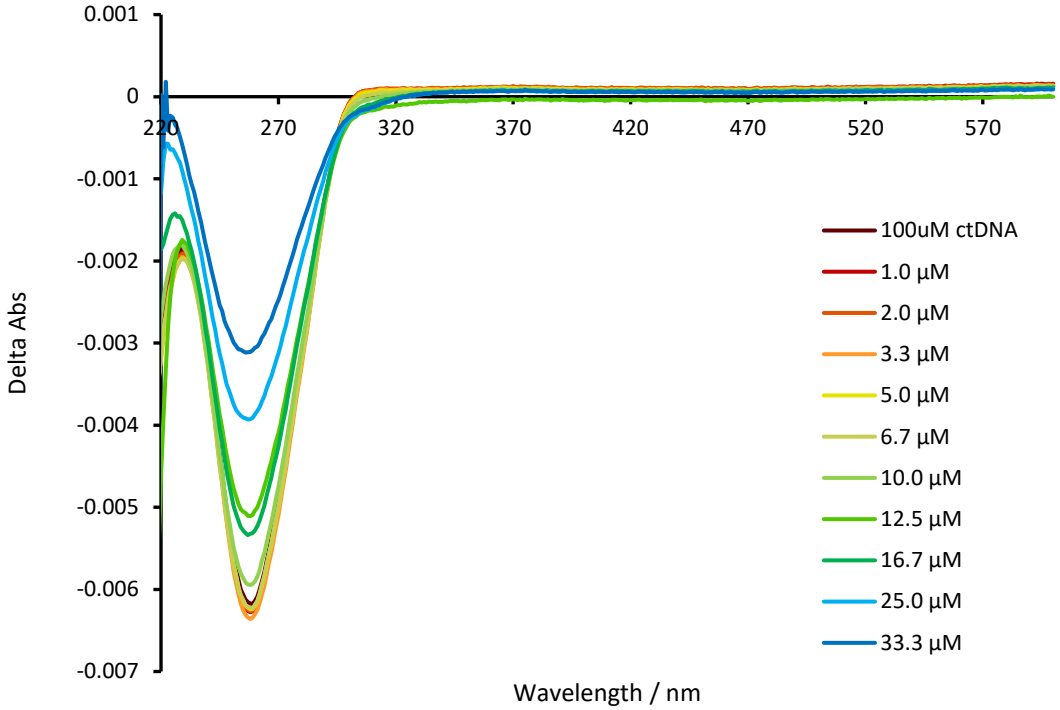


*Figure 22. Linear dichroism of 100 µM ct-DNA in 1 mM Tris-HCl buffer pH 7.4, 20 mM NaCl with increasing concentration of $Pd_2(L_1)_4(BF_4)_4$ where the concentration of ctDNA is maintained throughout the experiment. Stock solution of $Pd_2(L_1)_4(BF_4)_4$ was 1mM in water with 10% ACN.*

Supramolecular cylinders are known to coil ctDNA which is visible as a decrease in the magnitude of the LD peak at 260 nm [89, 95]. The LD titration of the palladium helicate with ctDNA (Figure 22) shows a clear trend where higher concentrations of the palladium complex result in a gradual decrease in the magnitude of the LD signal at 260 nm. This decrease in the magnitude of the signal at 260 nm is common for cationic metal complexes which, at higher concentrations, will cause DNA to coil up and eventually condense. There were no induced LD signals observed.

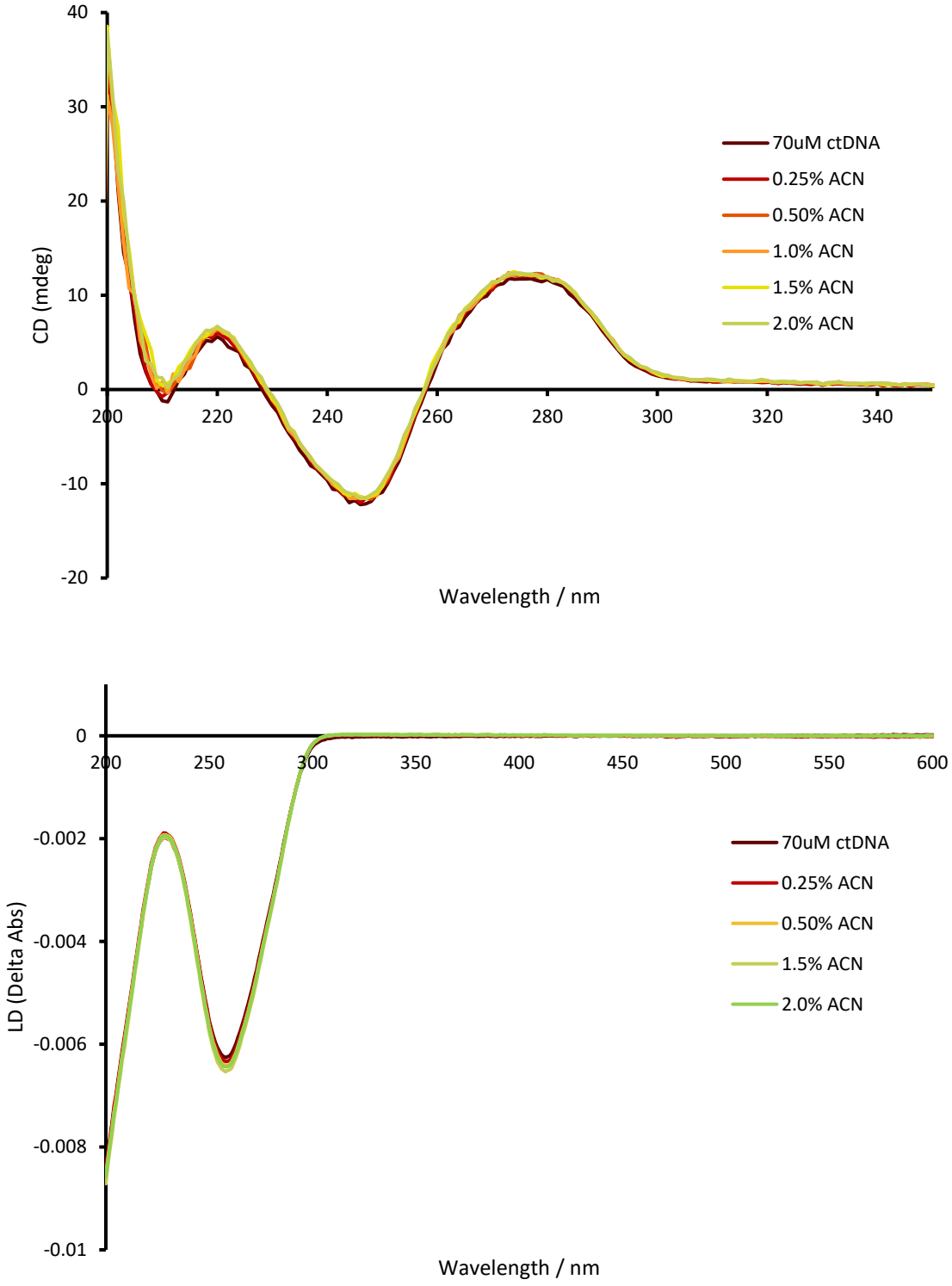


*Figure 23. Circular dichroism (top) and linear dichroism (bottom) of 70 µM ct-DNA in 1 mM Tris-HCl buffer pH 7.4, 20 mM NaCl with increasing concentration of ACN.*

Small quantities of acetonitrile were required for these titration experiments to solubilise the palladium helicate. The maximum concentration of acetonitrile in the working solution was calculated to be 0.6%. Control experiments were carried out to confirm that acetonitrile has no significant effect on the DNA structure at over triple the max ACN concentration used in the titrations. Control

experiments confirm that the low concentrations of acetonitrile used to solubilise the metal complexes does not have any influence on the DNA structure as shown in Figure 22 and Figure 23.

### 2.3.2 $Pt_2(L_1)_4(NO_3)_4$ interactions with B-DNA

The platinum cylinder (PtCyl) produced here shares the same overall structure as the palladium helicate with the metals replaced. It is expected that they show very similar, if not identical, interaction with ctDNA as the only difference is the identity of the metal centres. It is not likely that the DNA is exposed to the metal centres of the complex due to their locations surrounded by ligands. Despite the similarities in the structures of the complexes there are some notable differences in the CD spectra. The palladium helicate displays very noisy data at concentrations higher than 10 µM whereas the PtCyl does not until much higher concentrations. This is likely due to differences in solubility and possibly stability of the complexes used. The Pd helicate was a $BF_4^-$ salt which is poorly water soluble and the Pt helicate was a $NO_3^-$ salt which is generally much more soluble in aqueous solutions.

A UV-vis titration of the PtCyl into a solution of ctDNA was conducted in the same manner as for the palladium helicate (Figure 24). Upon addition of PtCyl there is a small increase in the absorbance of the ct-DNA peak at 258 nm, but if the ct-DNA signal is removed from this spectra then all that is left is a signal which very closely matches that of the PtCyl alone (Figure 24, A). This indicates that there is no change in the PtCyl absorbance spectrum.

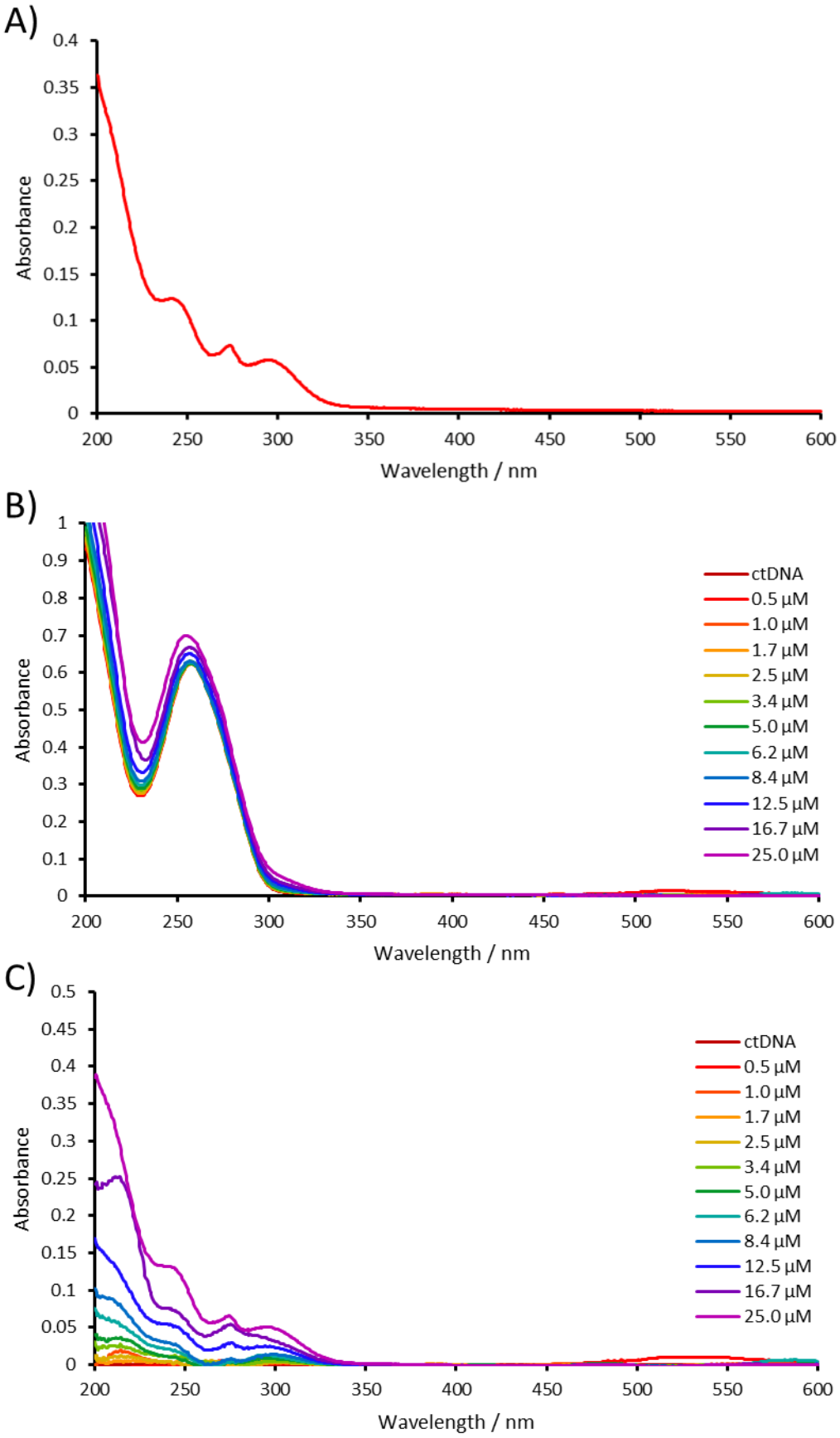


*Figure 24. A) UV-vis spectra of $Pt_2(L_1)_4(NO_3)_4$ 2.5µM in water (0.05% ACN), B) UV-vis spectra of $Pt_2(L_1)_4(NO_3)_4$ titrated into a solution of ctDNA (50 µM) in buffer (Tris-HCl 1mM, NaCl 20 mM, pH 7.4) where the ctDNA concentration is maintained throughout the experiment, and C) the resulting difference in the spectra compared to ctDNA alone. Stock solution of $Pt_2(L_1)_4(NO_3)_4$ was 1mM in water with 10% ACN.*

In the CD titration, upon increasing the concentration of the Pt complex in solution, a negative peak with increasing magnitude forms at 300 nm, as has been seen with the palladium helicate. This can be attributed to the metal complex with some confidence for the same reasons as stated above for the palladium complex. There is also the formation of a sharp peak at 275 nm and the peak at 250 nm changes from negative to positive. Finally, there is a peak at 200 nm which changes from positive to negative. It is possible that the reason for the dramatic changes in the CD spectra of the DNA with metal complex could be due to the DNA inducing the formation of a specific enantiomer of the helicate as the peaks formed with increasing concentration of metal complex match the UV spectra of the PtCyl complex very well (Figure 24, A). At concentrations higher than 16.7 µM the data becomes noisy possibly due to the DNA starting to precipitate in solution (full titration shown in A2.4).

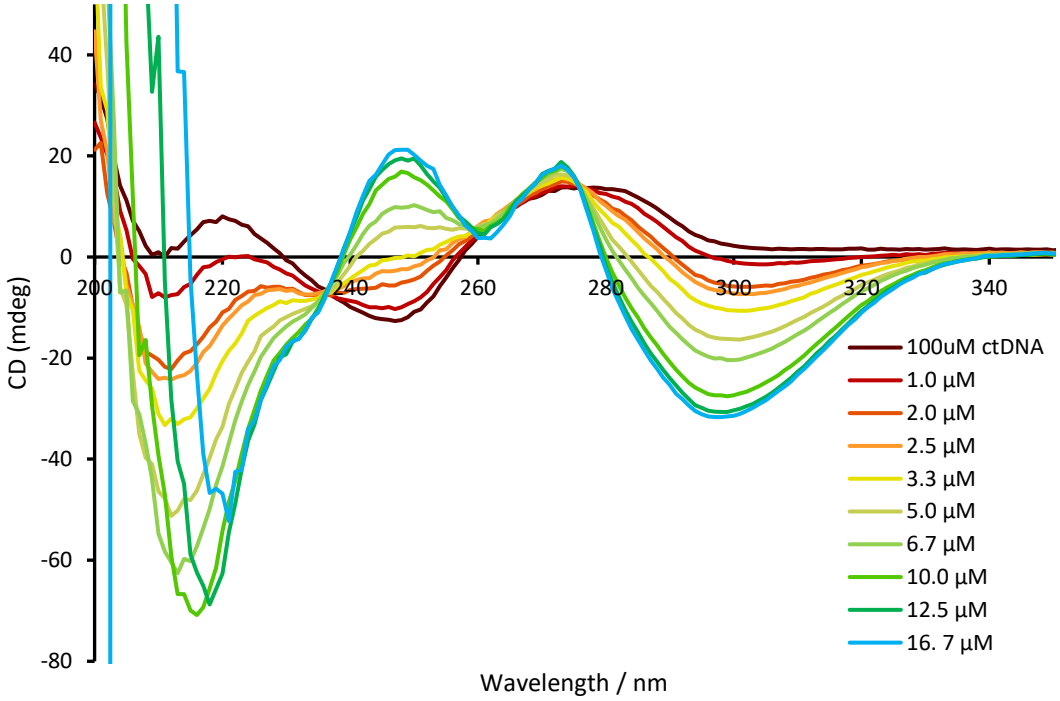


*Figure 25. Circular dichroism of 100 µM ct-DNA in 1 mM Tris-HCl buffer pH 7.4, 20 mM NaCl with increasing concentration of $Pt_2(L_1)_4(NO_3)_4$ where the concentration of ctDNA is maintained throughout the experiment. Stock solution of $Pt_2(L_1)_4(NO_3)_4$ was 1 mM in water with 10% ACN.*

The LD titration of PtCyl (shown in Figure 26) with ctDNA displays the same gradual decrease in magnitude of the peak at 260 nm with increasing concentration of metal complex as the Pd helicate showed. The formation of a very small peak at 500 nm was observed but both the DNA and the metal

complex do not have any measurable absorption in this region. For this reason, it is thought that the small peak is due to the instrumentation.

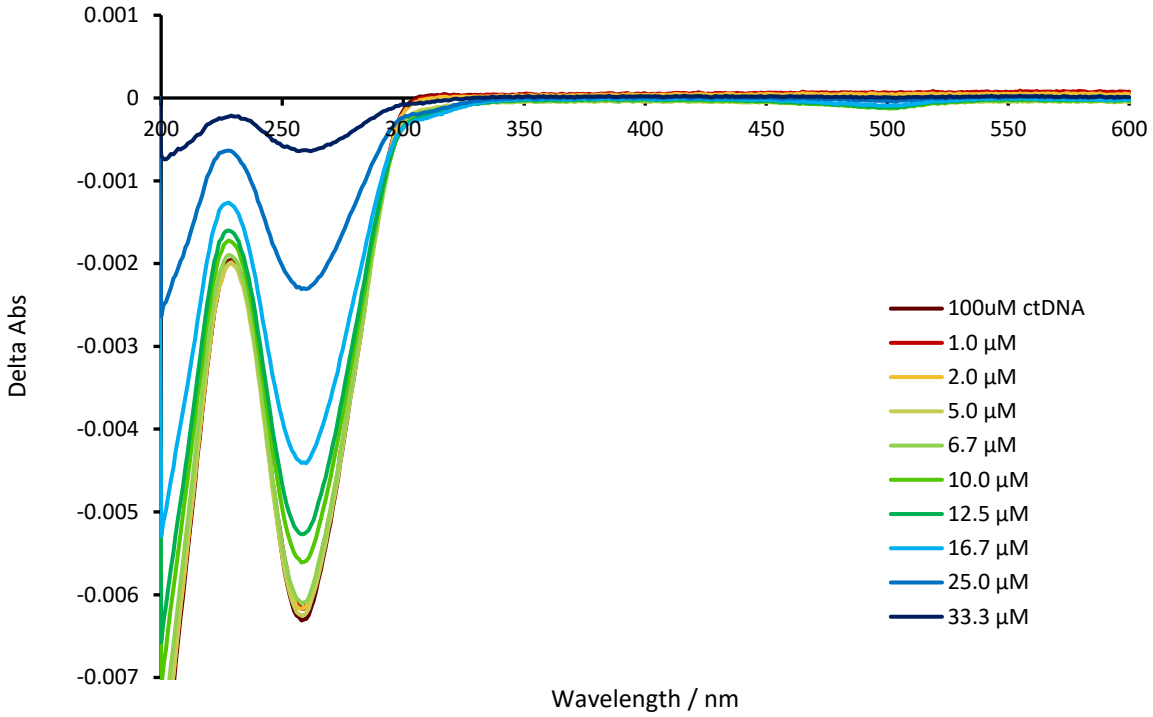


*Figure 26. Linear dichroism of 100 µM ct-DNA in 1 mM Tris-HCl buffer pH 7.4, 20 mM NaCl with increasing concentration of $Pt_2(L_1)_4(NO_3)_4$ where the concentration of ctDNA is maintained throughout the experiment. Stock solution of $Pt_2(L_1)_4(NO_3)_4$ was 1 mM in water with 10% ACN.*

The change in magnitude of the peak at 260 nm is greater with the PtCyl compared to the palladium helicate (Figure 27). At a concentration of 33 µM metal complex the magnitude of the peak at 260 nm with the PtCyl is 10% of the maximum, compared to 49% for the Pd helicate. This difference could again be due to solubility and stability differences between the helicates or it could indicate that the PtCyl has a stronger interaction with the duplex DNA but significant differences in the mode of interaction would be unlikely. The palladium helicate is shown to measurably degrade over the period of 1 hour in buffered solution (data shown later in this chapter, Figure 39).

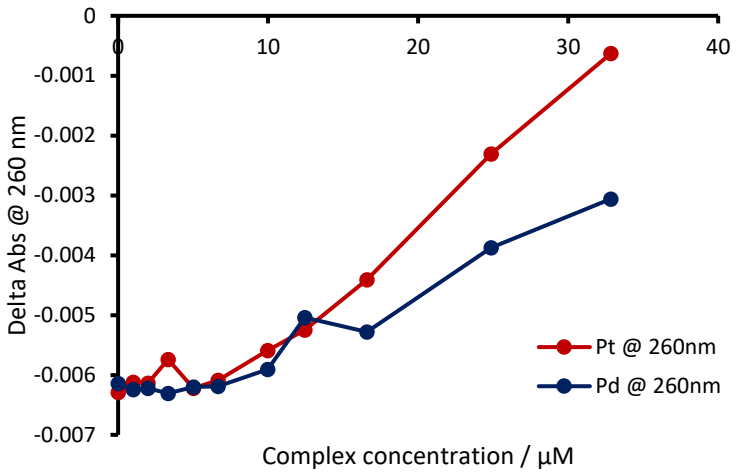


*Figure 27. Plot of the change in LD signal at 260 nm for $Pt_2(L_1)_4(NO_3)_4$ or $Pd_2(L_1)_4(BF_4)_4$ with ctDNA in 1 mM Tris-HCl pH 7.4, NaCl 20 mM.*

Agarose gel electrophoresis was used to further investigate the binding of the PtCyl to bulk B-form DNA. A porous gel matrix is submerged in a buffer solution connecting two reservoirs filled with buffered electrolyte solution. A high voltage is applied between the two reservoirs which results in the charged biomolecules being pulled through the gel matrix. The molecules are separated depending on their size and charge. The degree of separation can be controlled by varying the porosity of the matrix, changing the voltage applied, or changing the time the gel is run for. The buffer used may also be altered but tris-acetate-EDTA or tris-borate-EDTA are used almost exclusively with DNA as they are slightly basic and keep the DNA deprotonated and soluble.

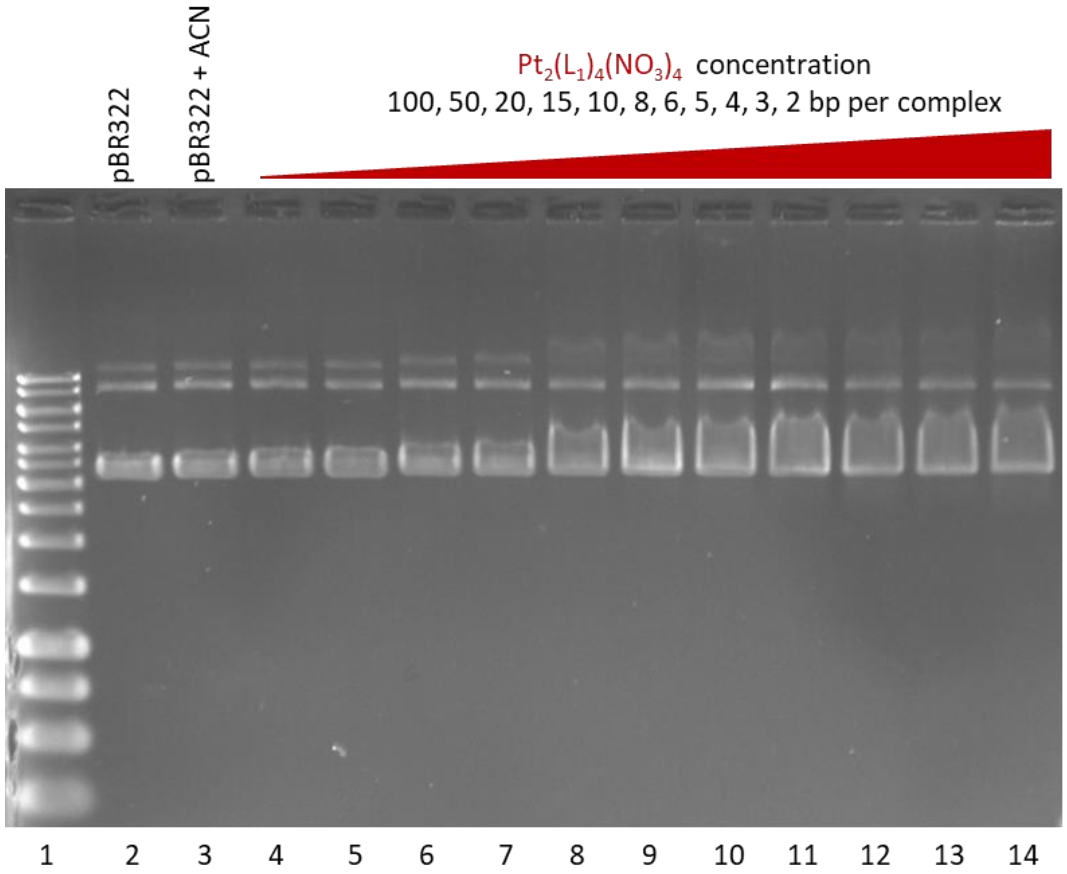


*Figure 28. Agarose gel of pBR322 plasmid DNA with increasing ratio of Pt2(L1)4(NO3)4 in 89 mM Tris-borate buffer pH 8.4. Lane 1 contains a DNA ladder ranging from 250 bp to 10,000 bp.*

The plasmid pBR322 is a well-known and commonly used with a length of 4361 bp. When run in an agarose gel on their own, plasmids often give rise to three distinct bands. The band that has migrated the furthest is the supercoiled DNA, the middle band in the gel is the open circular DNA, and finally the highest band is the nicked open circular DNA. Each well in the agarose gel contained a different condition, either controls or the plasmid with increasing concentration of $Pt_2(L_1)_4(NO_3)_4$ (Figure 28). Lane 3 contains a control of the plasmid with 1% acetonitrile (ACN) as the PtCyl was dissolved in water with a small percentage of acetonitrile. With increasing concentration of the PtCyl the supercoiled DNA band gradually becomes more smeared indicating it is becoming less coiled due to non-specific interactions. The nicked open circular DNA also smears more at higher concentrations. It is unclear why the nicked open circular band shifts significantly with increasing equivalents of PtCyl but the open circular DNA remains unchanged. There is more precipitation visible in the wells of the gel at higher concentrations of PtCyl.

The palladium helicate and PtCyl both interact with ctDNA as shown by LD, CD, and UV titration experiments. The exact binding mode of the complexes to the ctDNA are not known. The lack of formation of new peaks in the UV titration experiments and the formation of ICD signals in the CD titrations suggest organisation of the metal complexes in solution. The PtCyl appears to interact with the DNA to a greater extent than the palladium helicate possibly due to the improved stability of the PtCyl in buffered solution (Section 2.6). This difference is clearly shown by the LD data.

## 2.4 Junction binding

There is a significant volume of literature investigating the interactions of metal complexes with G-quadruplexes with research into other non-canonical DNA structures lagging behind. DNA junctions are an under researched area but, as has been discussed above, they are critical in a number of biological processes such as: DNA replication, DNA repair, and viral RNA insertion.[96] Holliday junctions are also present throughout the genome where inverted repeat sequences occur. It is thought that these structures are associated with transcription inhibition or transcription factor binding.[97]

To investigate the binding of metal complexes to DNA junctions polyacrylamide gel electrophoresis (PAGE) is utilised. PAGE works on the same principles as agarose gel electrophoresis but uses a different matrix which is much denser, allowing for the separation of much smaller DNA fragments.

The interaction of the palladium helicate and PtCyl with DNA cavities was primarily investigated using PAGE gels. The 3WJ binding studies were carried out using a carefully designed 3WJ which consisted of three separate 14-mer DNA strands. These three DNA oligomers are complementary in such a way that they can form a perfect 3WJ however the compensation for the formation of the 3WJ is not enough without some extra external force stabilising the junction. This 3WJ is only able to form with molecules that can occupy the central cavity of the 3WJ. The formation of the 3WJ creates a larger DNA structure with a substantially larger hydrodynamic radius which results in a reduction in the band shift observed compared to the individual oligomers. These PAGE gels were stained with SYBR Gold (an ethidium based fluorescent nucleic acid stain) after running the gel to visualize the DNA.

## 2.4.1 Junction binding of $Pd_2(L_1)_4(BF_4)_4$

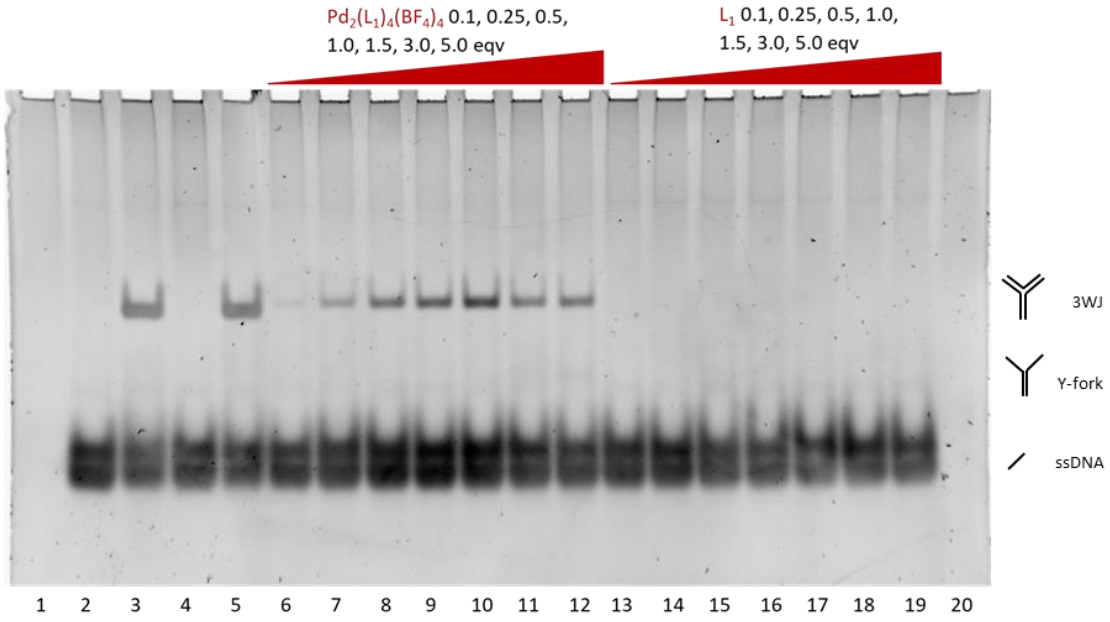


*Figure 29. PAGE gel of 3WJ with increasing concentrations of $Pd_2(L1)_4(BF_4)_4$ or L1 run in 89 mM Tris-borate buffer pH 8.3 (Lane 1-4 contain controls, lane 1 = 3WJ, lane 2 = 3WJ + 1 equivalent of NiP, lane 3 = 3WJ + 10 % ACN, lane 4 = 3WJ + 10 % ACN + NiP).*

The palladium helicate and ligand were incubated with the 3WJ oligomers to determine if they could induce formation of the 3WJ structure (Figure 29). The control lanes utilised the nickel parent cylinder which is known to bind 3WJ very well due to the orientation of its pi surfaces, dimensions, and positive charge.[98] The nickel parent cylinder is used as the positive control for the formation of 3WJ. The palladium cylinder is poorly soluble in water and must have acetonitrile added to completely solubilise the complex. With this in mind, an extra control lane is included for 3WJ with 10% ACN and w/wo nickel cylinder to confirm that the ACN has no effect on the 3WJ formation. With increasing concentrations of the palladium cylinder, more 3WJ is formed up to 1.5 equivalents, above 1.5 equivalents the 3WJ band intensity decreases as shown in Figure 29 and Figure 30. The decrease in 3WJ band intensity at higher concentrations is possibly due to aggregation of the DNA structure with the palladium cylinder or could also be due to the complex binding elsewhere on the structure and inhibiting the SYBR gold from binding. It is notable that the migration of the 3WJ band with palladium cylinder has been retarded in comparison to the 3WJ band with the nickel parent cylinder. This is an effect which has also been observed with the gold pillarplex and was attributed to the larger diameter of the gold pillarplex which, molecular dynamics simulations showed, forces open one of the base pairs

at the centre of the junction.[98] The opening of a base pair at the centre of the junction gives the structure a larger hydrodynamic radius.

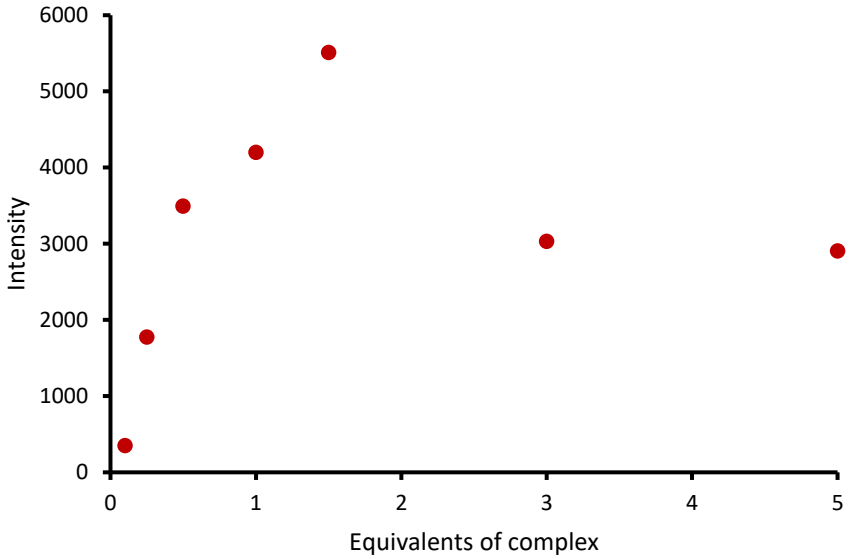


*Figure 30. Quantification of 3WJ band formation with increasing equivalents of $Pd_2(L_1)_4(BF_4)_4$.*

The 3WJ binding of the ligand was investigated to confirm that the active species in the binding events is the metal complex. No 3WJ formation is observed with the ligand, but there is a very faint tertiary structure visible higher in the gel than the 3WJ. It is unclear what the higher order structure with the ligand is.

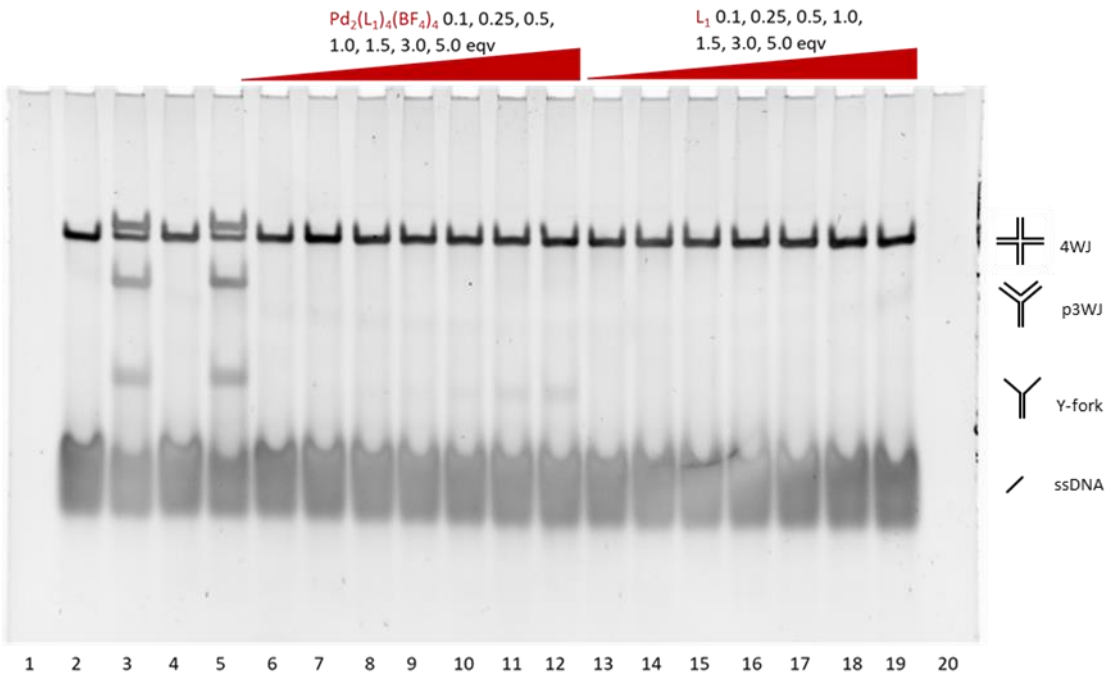


*Figure 31. PAGE gel of 4WJ with increasing concentrations of $Pd_2(L1)_4(BF_4)_4$ or $L_1$ run in 89 mM Tris-borate buffer pH 8.3. (Lane 2-5 contain controls, lane 2 = 4WJ, lane 3 = 4WJ + 1 equivalent of NiP, lane 4 = 4WJ + 10 % ACN, lane 5 = 4WJ + 10 % ACN + NiP).*

To investigate the 4WJ binding potential of the palladium cylinder PAGE gels were again utilised (Figure 31). The 4WJ used in these studies consists of four separate 22-mer oligomers which are complementary and come together spontaneously in solution to form a 4WJ. These 4WJ gels are more challenging to interpret than the 3WJ gels because the 4WJ forms spontaneously and there are also more DNA strands in solution which can form more complex structures than the 3WJ oligos. The 4WJ oligomers with no complexes added are shown in lane 2. The 4WJ oligomers come together to form a 4WJ structure which is visible as a single sharp band high in the gel. A smear further down the lane is also visible and is attributed to single stranded oliogmers which have not formed a junction. In the presence of nickel parent cylinder (the positive control, lane 3), new bands are formed which correspond to a Y-fork, pseudo 3WJ (p3WJ), and a new band above the 4WJ. The highest band in the gel is thought to be the open form of the 4WJ as the cavity at the centre must be forced open to allow the cylinder to enter. Control lanes 4 and 5 confirmed that the low percentage of ACN had no impact on the junction formation.

The palladium cylinder did not show any formation of the open 4WJ structure. There was also no indication of any formation of the pseudo 3WJ structure, however there is a very faint band visible for the Y-fork at high equivalents of palladium cylinder.

There is no indication of any interaction of the ligand ($L_1$) with the 4WJ.

### 2.4.2 Junction binding of $Pt_2(L_1)_4(NO_3)_4$

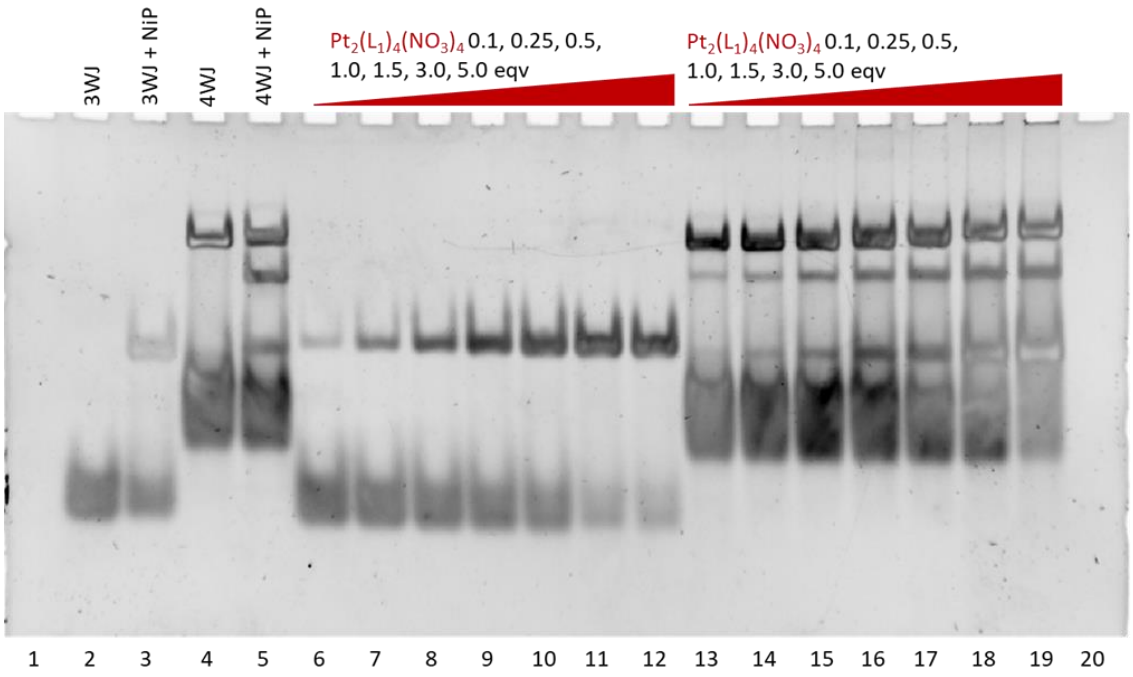


*Figure 32. PAGE gel of 3WJ or 4WJ with increasing concentrations of $Pt_2(L1)_4(NO_3)_4$ run in 89 mM Tris-borate buffer pH 8.3 (Lanes 2-5 contain controls: lane 2 = 3WJ, lane 3 = 3WJ + 1 equivalent NiP, lane 4 = 4WJ, lane 5 = 4WJ + 1 equivalent NiP).*

The junction binding ability of the PtCyl was assessed using the same 3WJ and 4WJ assays as was used for the palladium helicate. Quantification of these fluorescently stained gels was carried out using ImageJ, however there are limitations to the accuracy of the quantification due to the visualization method; the staining itself is not always uniform which can skew the quantification, the stain may not always diffuse to the centre of dense DNA bands, and the fluorophore can be quenched by metal complexes which absorb in the same region that the fluorescence occurs.

In Figure 32 the 3WJ band resulting from the $Pt_2(L_1)_4(NO_3)_4$ did not shift as far through the gel as the 3WJ band resulting from the 3WJ oligomers and NiP cylinder. This retardation of the 3WJ band was also observed for the palladium helicate. This was also observed for the 3WJ band with gold pillarplex

which was thought to be caused by the breaking of a base pair at the centre of the junction as shown in MD simulations.[98] MD simulations of the PtCyl with B-DNA and DNA junctions are discussed below (section 2.5).

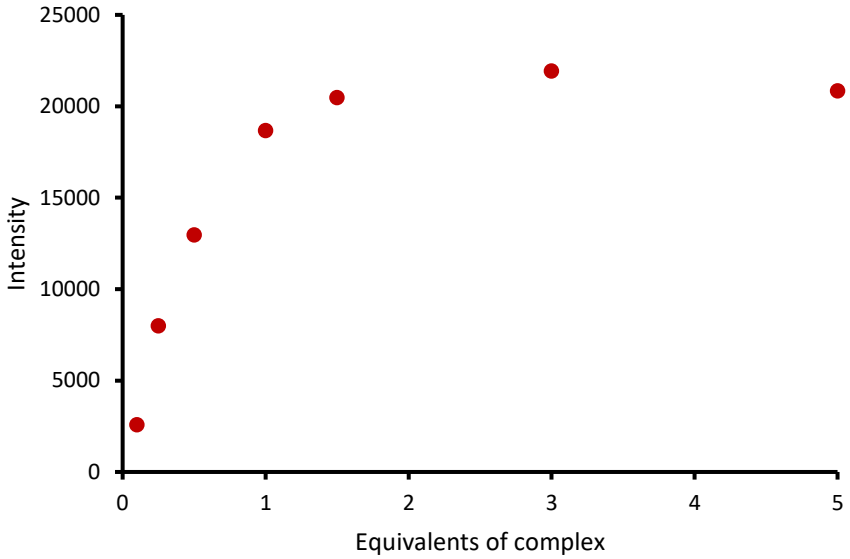


*Figure 33. Quantification of 3WJ band resulting from $Pt_2(L_1)_4(NO_3)_4$ with DNA 3WJ oligomers. Quantification carried out using ImageJ.*

The intensity of the 3WJ band increases with increasing equivalents of PtCyl and begins to plateau at approximately 1 equivalent (Figure 33). Due to the limitations of quantification from PAGE gels this is good evidence of a 1:1 binding mode of the PtCyl with DNA 3WJ. A 1:1 binding mode is what we expected from a junction binding agent which fills the cavity and does not interact strongly with the rest of the DNA structure. Though, the fact that the Intensity of the oligo band continues to decrease up to 5 equivalents of the PtCyl suggests that the staining of the 3WJ band is compromised at higher loading due to the reasons stated above.

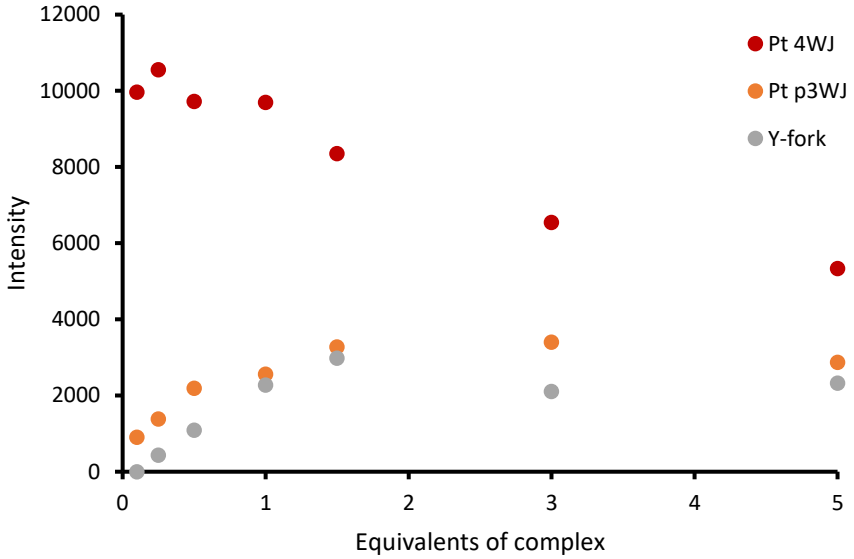


*Figure 34. Quantification of the bands in the 4WJ PAGE gel with ImageJ.*

The intensity of the 4WJ band gradually decreases with increasing equivalents of PtCyl increases (Figure 34), but, as can be seen in the gel (Figure 32), the centre of the band is not staining well with higher equivalents of the complex. There is also a slight retardation of the 4WJ band at higher loadings of the PtCyl which could indicate that new higher order structures are forming. It could also be due to the metal complex non-specifically binding to the 4WJ structure, decreasing the overall charge of the structure and therefore reducing the distance that the structure is pulled through the gel. The intensity of the Y-fork and p3WJ bands also increases in intensity but at the higher concentrations the staining is not efficient as can be seen in the gel image.

These PAGE gel studies of the palladium helicate and PtCyl illustrate the junction binding abilities of each complex. Both complexes displayed strong stabilisation of the 3WJ structure. The same retardation of the 3WJ structure observed for the palladium helicate and PtCyl suggest a similar bindng mode of each complex. The PtCyl was also shown to interact with a DNA 4WJ and form p3WJ structure where possible as has been observed for the nickel pare cylinder.[98] The lack of interaction of the palladium helicate with the DNA 4WJ is thought again to be due to the reduced stability of the palladium complex.

## 2.5 Molecular dynamics (MD) simulations

In order to investigate the exact nature of the junction binding being displayed by the Pt cylinder MD simulations were carried out with different DNA structures (All MD simulations were carried out by Samuel Dettmer, a member of the Hannon group and are summarised here as they add context to the PAGE gel results).

### 2.5.1 3WJ MD simulations

Initial simulations of the PtCyl and palladium helicate were attempted using a hexamer 3WJ which had previously been utilised in other MD simulations with the triple stranded helicates developed by the Hannon group (PDB 2ET0). It was observed during these simulations that the base pair at the centre of the junction would separate. Base pairs at the ends of the duplex arms would also fall apart due to their natural instability because they are only pi-stacking on one side. The breaking of 2/3 of the base pairs in the duplex arms would lead to the whole structure rapidly falling apart making interpretation of the simulations impossible. A more stable 3WJ structure had to be designed for the simulations to provide meaningful results. The 3WJ subsequently used for the simulations was adapted from the x-ray crystal structure of duplex DNA (PDB 1F44). Three separate DNA helices were brought together to form a junction site, the duplex arms were then shortened to 7 base pairs to save computational expense.

It was noted in the PAGE gels presented above that the migration of the 3WJ band with platinum or palladium cylinder was retarded compared to the 3WJ band with the parent cylinder. This effect was also observed with another metal complex in a recent publication by the Hannon group.[99] In MD simulations with 3WJ, the gold pillarplex caused one of the central base pairs at the junction site to break. It is thought that this breaking of a base pair in the central cavity creates a structure with a larger hydrodynamic radius and hence the structure migrates more slowly through the PAGE gel resulting in a small gel shift. The MD simulations of the platinum cylinder with 3WJ also shows a single base pair at the junction site being forced open with one base remaining in the junction and the other being pushed out (Figure 35). The base pair breaking at the junction site has been observed in 5/6

simulations of the 3WJ (20 µS total simulation time). Short simulations for the palladium cylinder were also carried out, the same binding mode was observed.

At the start of the simulation the junction is closed with all base pairs formed and the cylinder is placed in the centre. Initially there is significant rotation and movement of the cylinder in the junction cavity until a single base pair is broken open, when this occurs the rotation of the cylinder in the cavity is halted and there is much less movement of the cylinder. Once the base pair is broken open the structure appears much more stable; there is much less movement of the cylinder once this event has occurred. The breaking of the base pair at the centre of the junction occurs in 5/6 of the simulations and once broken, it remains broken for the rest of the simulation.

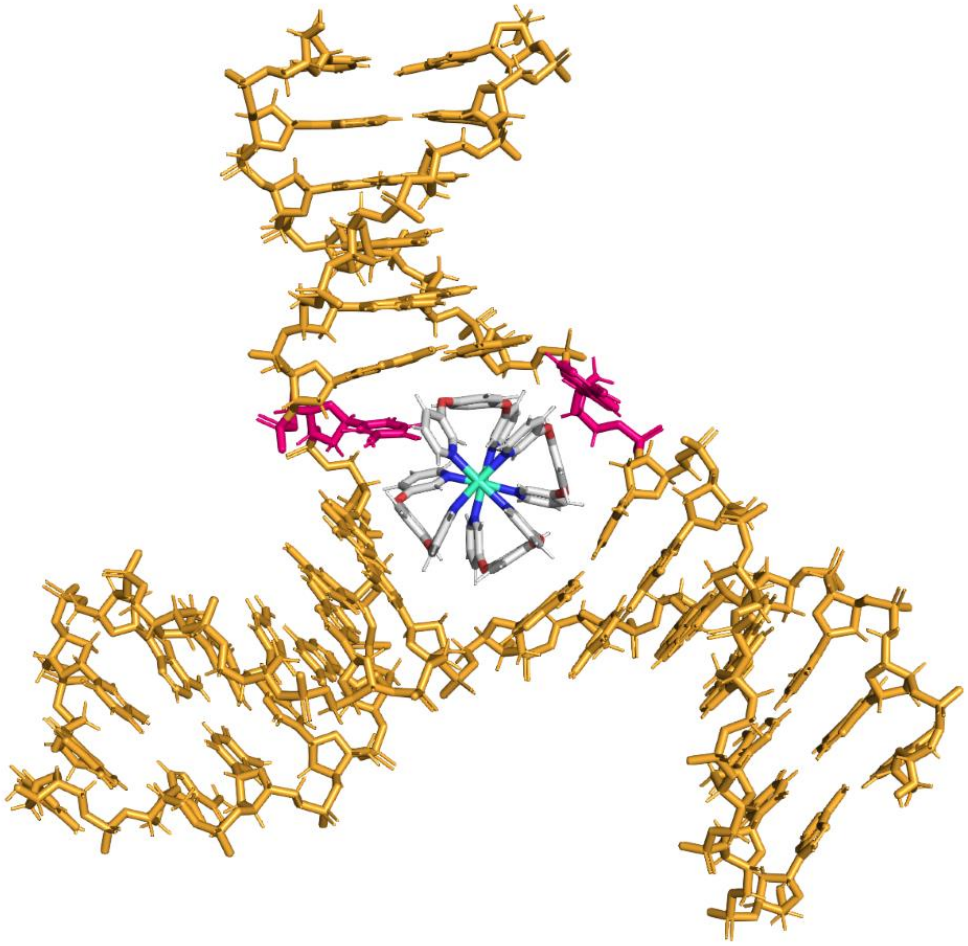

*Figure 35. Molecular dynamics simulation of PtCyl with a DNA 3WJ. The pair of nucleotides highlighted in pink are the broken base pair which allows the formation of a stable structure.*

The M and P enantiomers of the PtCyl may have different modes of interactions with the DNA since the junction itself is a chiral environment. This has been reported previously by the Hannon group

where a three stranded iron helicate showed a much stronger binding as the M enantiomer than the P [95]. To investigate the effect of cylinder enantiomer on 3WJ binding simulations were carried out with M or P enantiomers as the starting point. In all the simulations where the Pt cylinder begins as the P form, it remains as the P enantiomer, however when the Pt cylinder begins the simulation as the M form, in 2/3 of the simulations it converts to the P form after a base pair is broken and a stable DNA conformation is reached.

In this stable state there are a number of pi-pi stacking interactions from the PtCyl to the bases in the junction site (Figure 36). There also appears to be C-H pi interaction between a hydrogen on the pyridine of one of the PtCyl ligands and one of the bases.

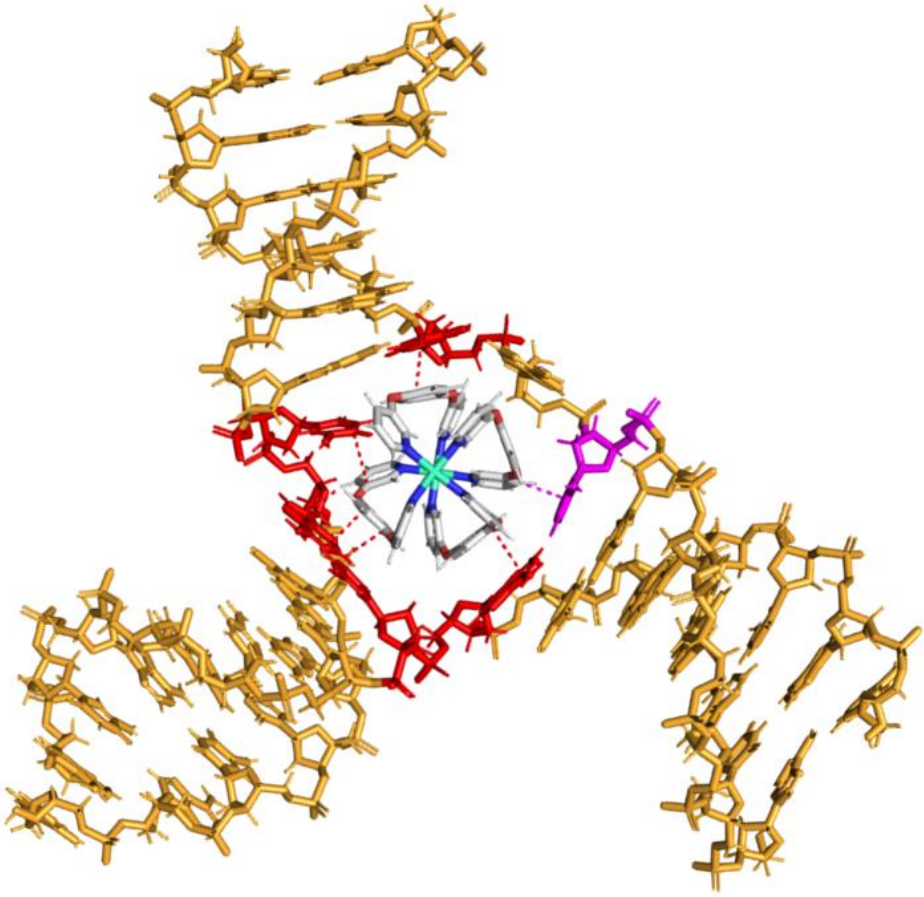

*Figure 36. Molecular dynamics simulation of PtCyl with a DNA 3WJ. Pi-pi interactions are highlighted in red, CH-pi interaction is highlighted in pink.*

All of the simulations discussed so far use a 3WJ structure with three AT base pairs at the junction site. The 3WJ structure used in the PAGE gel experiments has two GC base pairs, and a single AT base pair at the junction. In order to confirm that the observations made with the model system are applicable

to the 3WJ used in PAGE gel experiments, short simulations were conducted with a 3WJ structure containing two GC base pairs and a single AT base pair. Fraying of a single base pair was observed less frequently but was still observed in most simulations. In all cases where fraying occurred, the AT base pair was the one pair that frayed, forming the same general stable structure as seen in previous simulations.

### 2.5.2 4WJ MD simulations

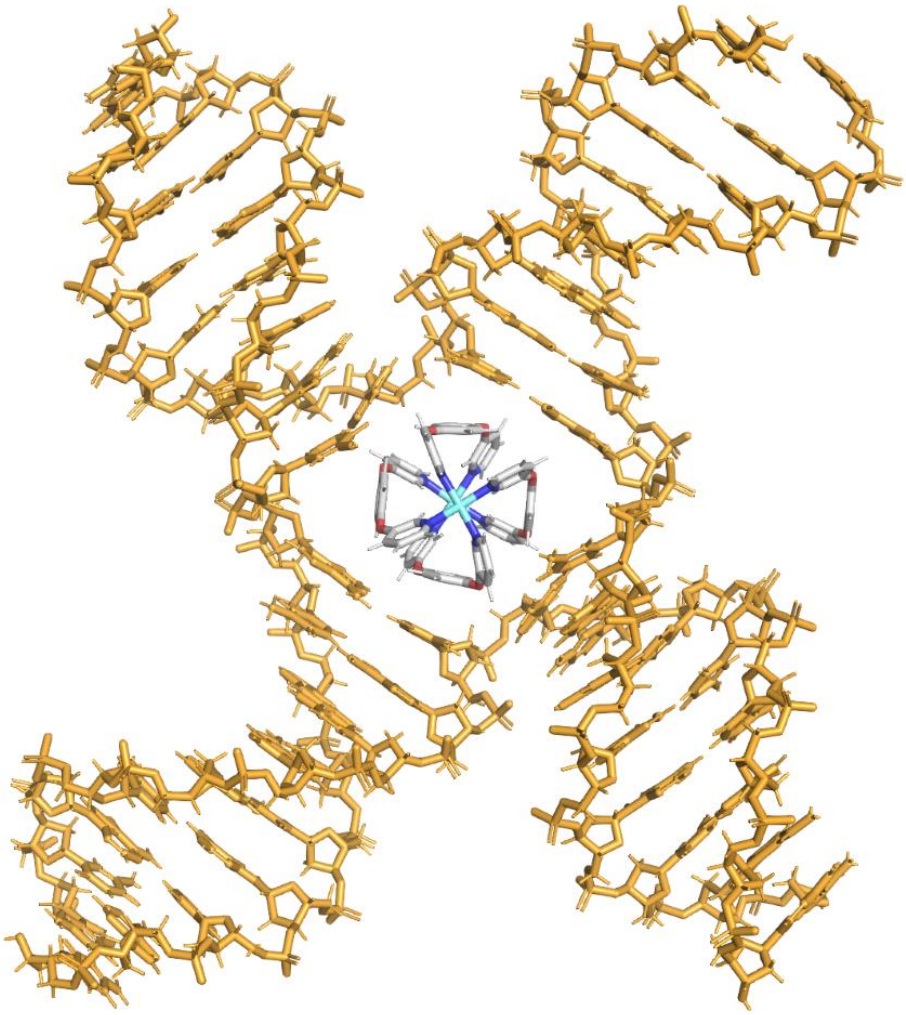

*Figure 37. Molecular dynamics simulation of PtCyl with 4WJ structure.*

MD simulations were also carried out with the Platinum cylinder and 4WJ (Figure 37). The 4WJ structure utilised for these simulations was based on an X-ray crystal structure of an open 4WJ, where the cavity is occupied by a protein, and two of the base pairs at the junction site are formed and two are not. Simulations were attempted with closed 4WJ structures but on no opening of the cavity was observed and hence, no binding of the complex in the cavity was possible on the time scale of the

simulations. When the Pt cylinder is placed in the junction cavity, the junction immediately collapses into a square form, in some simulations all 4 base pairs are reformed, but in others 2 of the base pairs remain apart. When the junction collapses there is a chance that the bases will “fall” in or out of the junction, if the base pairs fall out then the junction will remain with only 2 base pairs at the centre and it is unable to reform the 4 base pair on the time scale of the simulation. In all cases there is a significant amount of rotation of the PtCyl in the junction cavity. The PtCyl appears unable to find a stable energy minimum. Throughout the simulation, the PtCyl appears to have transient interactions with the bases, forming two pi-pi interactions and mildly distorting the junction before rotating and losing contact. This may be due to the PtCyl being slightly too small to form pi-pi interactions to all four base pairs simultaneously. Importantly, the PtCyl remains in the centre of the cavity throughout all the simulations.

### 2.5.3 dsDNA MD simulations

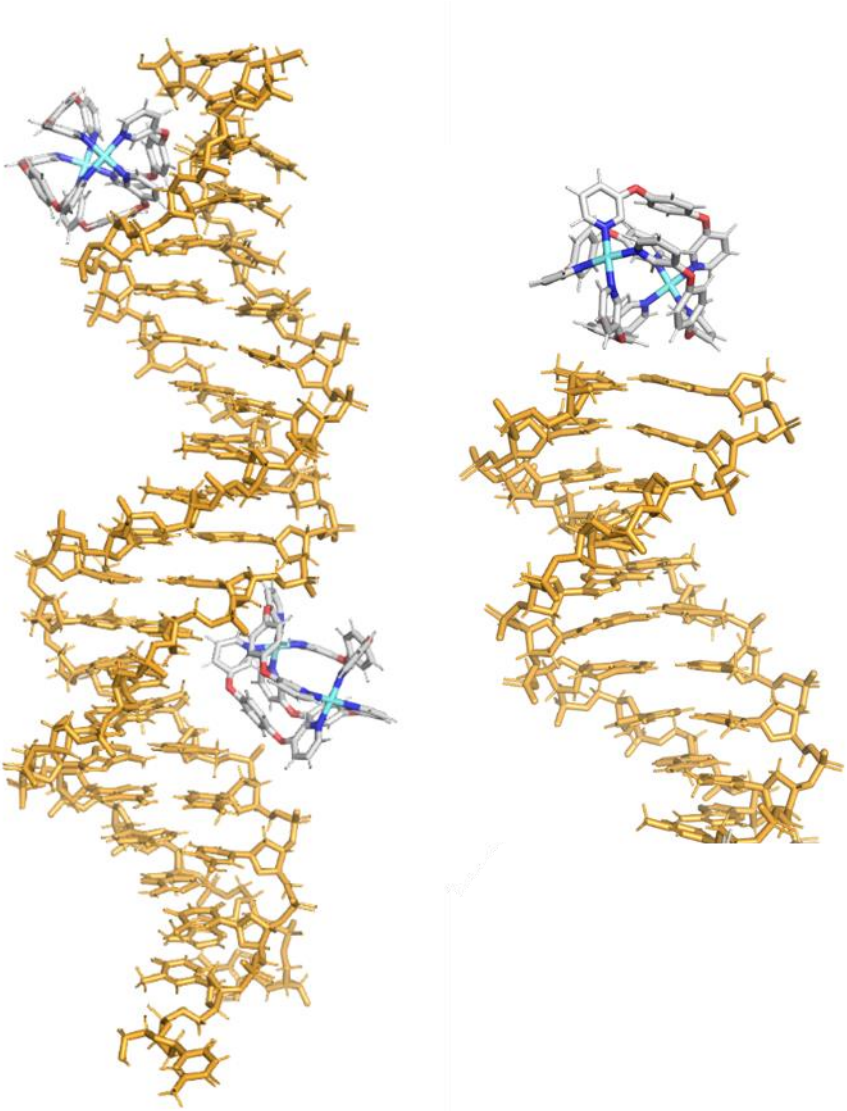

*Figure 38. Frame from molecular dynamics simulation of PtCyl with duplex DNA. Transient groove binding of PtCyl with B-DNA (left), stacking of the PtCyl with exposed bases at end of duplex (right).*

Molecular dynamics simulations of PtCyl with B-DNA were carried out (4.6 µS total simulation time). In all the simulations no stable states are attained, the PtCyl transiently interacts with the major groove of the B-DNA (Figure 38) and has some very weak pi stacking interactions with the exposed ends of the duplex. Binding to the major groove of the duplex distorts the helical structure of the PtCyl, but simulations have indicated that the structure is very flexible so this is not surprising. It is unclear if a specific enantiomer of the PtCyl is favoured for groove binding to the DNA because the binding is transient. Longer simulations will be required to see if specific enantiomers interact more favourably with the duplex, or if specific enantiomers of the PtCyl are induced by the B-DNA interactions. The

weak binding of the PtCyl with duplex DNA is consistent with experimental data which is presented in Chapter 3.

## 2.6 Helicate stability in buffer

### 2.6.1 Stability of $Pd_2(L_1)_4(BF_4)_4$ in buffer

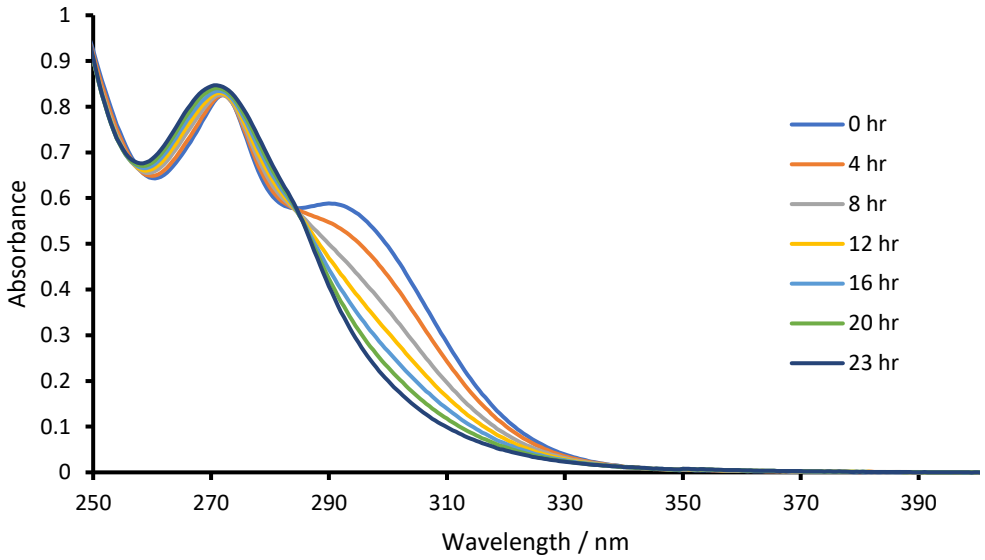


*Figure 39. UV-vis absorbance measurements of $Pd_2(L_1)_4(BF_4)_4$ 25 µM in Tris-borate buffer 89 mM pH 8.3, NaCl 10 mM over time with 1% DMSO.*

The stability of the palladium helicate in buffered solution was monitored by UV-vis measurements over the course of 23 hours (Figure 39). The MLCT peak at 295 nm decreases dramatically over the first 8 hours, until it is no longer visible after 23 hours. The decrease in absorbance of the MLCT peak can be linked to the degradation of the complex as the other peak at 275 nm does not decrease in the same manner indicating that there is a change in the complex structure and that the decrease cannot be attributed to the precipitation of the complex.

Disassembly of palladium cages *in vivo* has been noted in literature. Cosialls *et al*. investigate the biodistribution of a palladium cage based on tripyridyl ligands by PET.[51] Interestingly, they found that the stability of the cage was sensitive to the guest molecule in the cages structure.

### 2.6.2 Stability of $Pt_2(L_1)_4(NO_3)_4$ in buffer

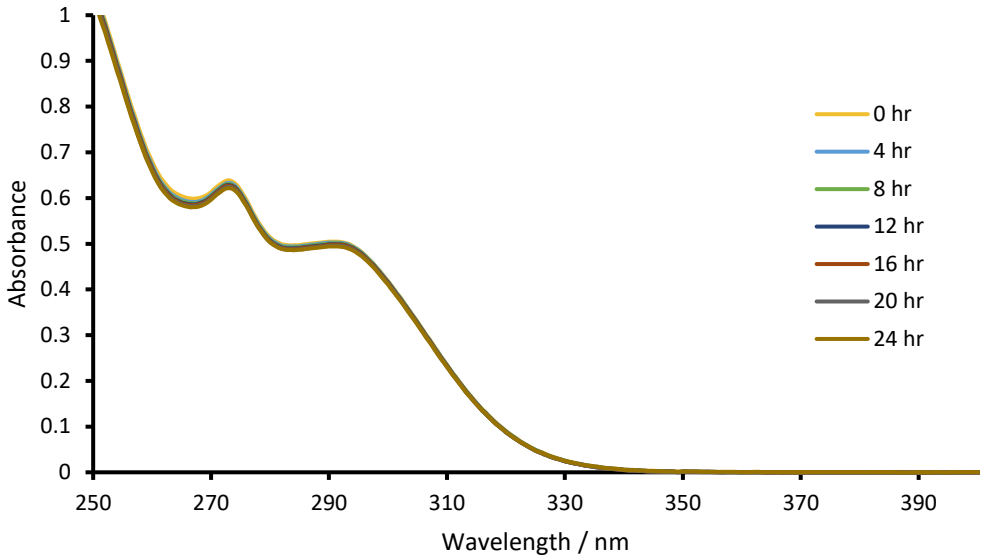


*Figure 40. UV-vis absorbance of Pt2(L1)4(NO3)4 25 µM in Tris-borate buffer 89 mM pH 8.3, NaCl 10 mM over time with 1% DMSO.*

The stability of the PtCyl was also assessed by monitoring the UV-vis absorbance over a period of 24 hours (Figure 40). Neither of the peaks at 270 nm or 300 nm change over a period of 24 hours indicating that the complex is stable in the buffered solution used.

The increase in stability of the platinum complex compared to the palladium complex is not surprising. Platinum possesses kinetics $10^5$ times slower than comparable palladium complexes.[100] Pt also forms stronger bonds that Pd.[101]

## 2.7 Interaction of $Pt_2(L_1)_4(NO_3)_4$ with CB10

It is well known that the parent cylinders produced by the Hannon group bind very well to DNA junctions, both 3WJ and 4WJ.[83, 84, 98] This strong binding is primarily due to the pi-pi stacking of the benzene rings at the centre of the cylinder with the bases at the junction site. It has also been demonstrated by Hooper *et al*. that the cylinder is also capable of binding the synthetic hydrophobic cavity cu[10]cubituril.[99] This was shown to be possible through MS, NMR, and molecular dynamics studies.

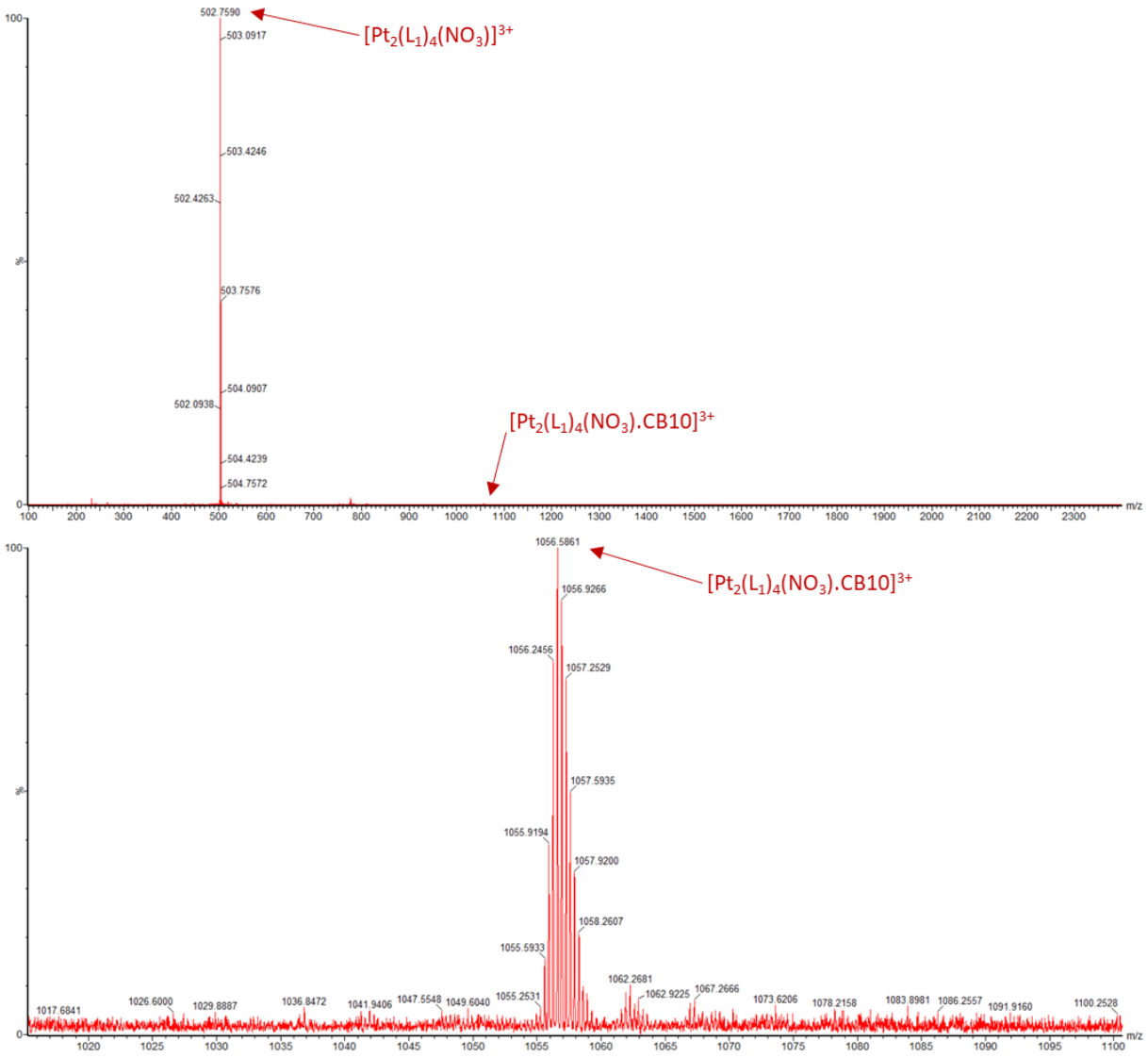


*Figure 41. Mass spectrum of 1:1 mix of $Pt_2(L_1)_4(NO_3)_4$ with CB10 in water with 10% ACN to dissolve PtCyl.*

Given the similarities of the PtCyl complex to the parent cylinder, it was thought that it may also be able to interact with a CB10 ring. In order to test this hypothesis the PtCyl was dissolved in a mix of ACN and water and a stoichiometric ratio of CB10 was added. CB10 is highly insoluble in water but is solubilised by the high charge of the parent cylinder when it binds to the central cavity of the CB10 forming a pseudo-rotaxane system. In contrast to this, the CB10 does not appear to be solubilised by the presence of the PtCyl, but it is worth noting that the PtCyl itself is not as soluble as the nickel parent cylinder in aqueous solutions. Despite this, a mass spectrum of the solution was acquired (Figure 41). The major peak of the spectrum was $[Pt_2(L_1)_4(NO_3)]^{3+}$ species at 502.8 m/z. A very small peak at 1056.6 m/z with a 3+ charge was observed which can be attributed to $[Pt_2(L_1)_4(NO_3).CB10]^{3+}$. The isotope pattern of the peak at 1056.6 m/z closely matches that of the PtCyl with the CB10 host. It is impossible

to tell from this MS spectrum alone if the CB10 is actually bound in the centre of the CB10 host, or whether the species are only loosely associated in solution. It is also possible that there is little affinity between the two species in solution and they only form some kind of association complex under mass spectrometry conditions.

The intensity of the peak corresponding to the PtCyl.CB10 complex indicates that CB10 is not a good fit for the PtCyl. Further investigation into other alternative host complexes may be worthwhile as these could offer new methods for modulating the activity of this PtCyl with DNA species as has been demonstrated with the nickel parent cylidner.[99]

## 2.8 Conclusions

The DNA binding properties of a palladium helicate has been investigated as well as the DNA binding properties of a novel platinum helicate. The PtCyl and palladium helicate share the same overall structure. The platinum in place of the palladium conveys significantly improved stability of the complex in buffered solution which can explain the larger interaction observed by LD and CD with ctDNA. Both the palladium helicate and PtCyl were capable of inducing the formation of a 3WJ in PAGE gels. Furthermore, with the 4WJ oligomers, the PtCyl also induced the formation of Y-forks and p3WJ bands, and shifted the 4WJ band. The improved stability of the PtCyl can explain the apparent stronger interaction observed in the 3WJ and 4WJ PAGE gel assays.

Simulations of the 3WJ with the PtCyl indicate that the 3WJ prefers the P enantiomer instead of the M enantiomer. This is difficult to probe experimentally as we believe that the helicate is rapidly interconverting between M and P in solution. There are palladium cage complexes which have chirality induced by the presence of specific anions which occupy the cavity in the cage.[76, 78] These MD simulations suggest that the chirality of the PtCyl used in these studies is controlled externally by the presence of the DNA 3WJ structure. X-ray crystal or NMR structures of the PtCyl and palladium helicate in the 3WJ cavity will have to be obtained to confirm this. We also speculate that the chirality of the palladium helicate and PtCyl may be controlled by B-DNA which gives rise to the large CD signals

observed experimentally. Simulations with the DNA 4WJ indicate that the PtCyl is too small to pi stack with all four faces of the 4WJ cavity.

The palladium helicate appears less suited to biological applications due to the instability of the complex in buffer. However, the PtCyl appears to be stable in buffered solution over a 24 hr period and warrants further investigation due to the B-DNA and junction binding that have been observed.

## 2.9 Future work

The first steps to continued work in this area would be to obtain a crystal structure of the platinum helicate to obtain accurate measurements of the dimensions of the cylinder and to unambiguously confirm the presence of the nitrate anion in the central cavity. Nitrogen NMR may also be used to confirm that the nitrate counterions are in multiple different environments. Fluorescently labelled DNA structures offer a multitude of possibilities for studying the interactions between metal complexes and the DNA structures in question. Quenching studies utilising a fluorescently labelled DNA junction may be carried out in a similar manner to that demonstrated by Alcalde-Ordónez *et al*.[102] Increasing ratios of the metal complex would be added to the DNA junction and the fluorescence intensity monitored. An apparent dissociation constant and binding ratio could then be calculated from this data. This would be invaluable for comparison to other junction binders and for further supporting the 1:1 cavity binding that is indicated by the data presented herein. FRET labelled DNA junctions may also be used to study the kinetics of formation of the DNA junction, as has been shown by Monchaud and co-workers.[103] The gold standard for confirming the cavity binding of the platinum and palladium complexes with a DNA 3WJ would be to acquire a crystal structure as has been achieved by Michael Hannon with the parent cylinder.[83]

The original hypothesis of this work was that the D4 symmetry of the platinum helicate would enable more effective junction binding to Holliday junctions compared to the parent cylinder. It has been shown that the platinum helicate can effectively interact with the Holliday junction in a similar way to the parent cylinder, but it is also able to strongly interact with the 3WJ. Simulations of the platinum helicate in 4WJ indicate that although the symmetry matches well, the diameter of the helicate is too

small to allow the aryl rings to effectively stack with all the bases of the 4WJ. There are examples of larger palladium helicates which could be synthesised with platinum metal centres for stability before moving on to DNA studies with 4WJ. Computation studies of these helicates could be used to screen for complexes which form stable structures in the centre in order to minimise the amount of synthesis necessary. Using computational chemistry it is possible to obtain a relative value for the biding strength of the interaction between a metal complex and the junction site, this would give a quantifiable metric by which to judge the candidates.

Functionalisation of the platinum helicate may be possible and could be used to improve the drug properties of the complex. The water solubility of the complex could be improved by the addition of glycol units, targeting moieties such as peptides could be added to the complex to improve the uptake. Addition of peptides to palladium complexes has been demonstrated to enable the complexes to pass through the blood brain barrier.[56]

The work presented in this chapter represents the tip of the iceberg in terms of the study of platinum/palladium supramolecular complexes with DNA and RNA structures. There are many platinum and palladium $M_2L_4$ complexes which have been studied in the literature, but have not had their effects on DNA investigated. A prime candidate for investigation of its DNA binding properties is the helicate produced by Qing-Fu Sun and Li-Peng Zhou.[78] This helicate has the appropriate dimensions for junction binding, it is chiral, and it has externally facing pi-surfaces which may interact with DNA bases at the centre of the junction cavity.

## 2.10 References


1. Gramage-Doria, R.; Hessels, J.; Leenders, S. H. A. M.; Tröppner, O.; Dürr, M.; Ivanović-Burmazović, I.; Reek, J. N. H., Gold(I) Catalysis at Extreme Concentrations Inside Self-Assembled Nanospheres. *Angewandte Chemie International Edition* **2014,** *53* (49), 13380-13384.
2. Fujita, D.; Ueda, Y.; Sato, S.; Mizuno, N.; Kumasaka, T.; Fujita, M., Self-assembly of tetravalent Goldberg polyhedra from 144 small components. *Nature* **2016,** *540* (7634), 563-566.
3. Bobylev, E. O.; Poole Iii, D. A.; de Bruin, B.; Reek, J. N. H., Selective formation of Pt12L24 nanospheres by ligand design. *Chemical Science* **2021,** *12* (22), 7696-7705.
4. Zaffaroni, R.; Bobylev, E. O.; Plessius, R.; van der Vlugt, J. I.; Reek, J. N. H., How to Control the Rate of Heterogeneous Electron Transfer across the Rim of M6L12 and M12L24 Nanospheres. *Journal of the American Chemical Society* **2020,** *142* (19), 8837-8847.
5. Bobylev, E. O.; Poole III, D. A.; de Bruin, B.; Reek, J. N. H., How to Prepare Kinetically Stable Self-assembled Pt12L24 Nanocages while Circumventing Kinetic Traps. *Chemistry – A European Journal* **2021,** *27* (49), 12667-12674.
6. Xu, J.; Raymond, K. N., Structurally Characterized Quadruple-Stranded Bisbidentate Helicates. *Angewandte Chemie International Edition* **2006,** *45* (39), 6480-6485.
7. Gao, X.; Li, L.; Sun, W.; Chen, P., Crystallization and single molecule magnetic behavior of quadruple-stranded helicates: tuning the anisotropic axes. *Dalton Transactions* **2020,** *49* (9), 2843-2849.
8. Lisboa, L. S.; Riisom, M.; Dunne, H. J.; Preston, D.; Jamieson, S. M. F.; Wright, L. J.; Hartinger, C. G.; Crowley, J. D., Hydrazone- and imine-containing [PdPtL4]4+ cages: a comparative study of the stability and host–guest chemistry. *Dalton Transactions* **2022,** *51* (48), 18438-18445.
9. Amouri, H.; Mimassi, L.; Rager, M. N.; Mann, B. E.; Guyard-Duhayon, C.; Raehm, L., Host–Guest Interactions: Design Strategy and Structure of an Unusual Cobalt Cage That Encapsulates a Tetrafluoroborate Anion. *Angewandte Chemie International Edition* **2005,** *44* (29), 4543-4546.
10. Steel, P. J.; McMorran, D. A., Selective Anion Recognition by a Dynamic Quadruple Helicate. *Chemistry – An Asian Journal* **2019,** *14* (8), 1098-1101.
11. Löffler, S.; Lübben, J.; Krause, L.; Stalke, D.; Dittrich, B.; Clever, G. H., Triggered Exchange of Anionic for Neutral Guests inside a Cationic Coordination Cage. *Journal of the American Chemical Society* **2015,** *137* (3), 1060-1063.
12. Vasdev, R. A. S.; Findlay, J. A.; Garden, A. L.; Crowley, J. D., Redox active [Pd2L4]4+ cages constructed from rotationally flexible 1,1′-disubstituted ferrocene ligands. *Chemical Communications* **2019,** *55* (52), 7506-7509.
13. Freye, S.; Hey, J.; Torras-Galán, A.; Stalke, D.; Herbst-Irmer, R.; John, M.; Clever, G. H., Allosteric Binding of Halide Anions by a New Dimeric Interpenetrated Coordination Cage. *Angewandte Chemie International Edition* **2012,** *51* (9), 2191-2194.
14. Clever, G. H.; Kawamura, W.; Tashiro, S.; Shiro, M.; Shionoya, M., Stacked Platinum Complexes of the Magnus' Salt Type Inside a Coordination Cage. *Angewandte Chemie International Edition* **2012,** *51* (11), 2606-2609.
15. Clever, G. H.; Tashiro, S.; Shionoya, M., Light-Triggered Crystallization of a Molecular Host−Guest Complex. *Journal of the American Chemical Society* **2010,** *132* (29), 9973-9975.
16. Clever, G. H.; Tashiro, S.; Shionoya, M., Inclusion of Anionic Guests inside a Molecular Cage with Palladium(II) Centers as Electrostatic Anchors. *Angewandte Chemie International Edition* **2009,** *48* (38), 7010-7012.
17. Yazaki, K.; Sei, Y.; Akita, M.; Yoshizawa, M., Polycationic-Shelled Capsular and Tubular Nanostructures and Their Anionic–Guest Binding Properties. *Chemistry – A European Journal* **2016,** *22* (49), 17557-17561.
18. Puig, E.; Desmarets, C.; Gontard, G.; Rager, M. N.; Cooksy, A. L.; Amouri, H., Capturing a Square Planar Gold(III) Complex Inside a Platinum Nanocage: A Combined Experimental and Theoretical Study. *Inorganic Chemistry* **2019,** *58* (5), 3189-3195.
19. Desmarets, C.; Gontard, G.; Cooksy, A. L.; Rager, M. N.; Amouri, H., Encapsulation of a Metal Complex within a Self-Assembled Nanocage: Synergy Effects, Molecular Structures, and Density Functional Theory Calculations. *Inorganic Chemistry* **2014,** *53* (9), 4287-4294.

20. Johnstone, M. D.; Schwarze, E. K.; Ahrens, J.; Schwarzer, D.; Holstein, J. J.; Dittrich, B.; Pfeffer, F. M.; Clever, G. H., Desymmetrization of an Octahedral Coordination Complex Inside a Self-Assembled Exoskeleton. *Chemistry – A European Journal* **2016,** *22* (31), 10791-10795.
21. Sekiya, R.; Kuroda, R., Pd2+···O3SR− interaction encourages anion encapsulation of a quadruply-stranded Pd complex to achieve chirality or high solubility. *Chemical Communications* **2011,** *47* (45), 12346-12348.
22. Ganta, S.; Chand, D. K., Multi-Stimuli-Responsive Metallogel Molded from a Pd2L4-Type Coordination Cage: Selective Removal of Anionic Dyes. *Inorganic Chemistry* **2018,** *57* (7), 3634-3645.
23. McMorran, D. A.; Steel, P. J., The First Coordinatively Saturated, Quadruply Stranded Helicate and Its Encapsulation of a Hexafluorophosphate Anion. *Angewandte Chemie International Edition* **1998,** *37* (23), 3295-3297.
24. Preston, D.; Patil, K. M.; O'Neil, A. T.; Vasdev, R. A. S.; Kitchen, J. A.; Kruger, P. E., Long-cavity [Pd2L4]4+ cages and designer 1,8-naphthalimide sulfonate guests: rich variation in affinity and differentiated binding stoichiometry. *Inorganic Chemistry Frontiers* **2020,** *7* (16), 2990-3001.
25. August, D. P.; Nichol, G. S.; Lusby, P. J., Maximizing Coordination Capsule–Guest Polar Interactions in Apolar Solvents Reveals Significant Binding. *Angewandte Chemie International Edition* **2016,** *55* (48), 15022-15026.
26. Kishi, N.; Li, Z.; Sei, Y.; Akita, M.; Yoza, K.; Siegel, J. S.; Yoshizawa, M., Wide-Ranging Host Capability of a PdII-Linked M2L4 Molecular Capsule with an Anthracene Shell. *Chemistry – A European Journal* **2013,** *19* (20), 6313-6320.
27. Kishi, N.; Li, Z.; Yoza, K.; Akita, M.; Yoshizawa, M., An M2L4 Molecular Capsule with an Anthracene Shell: Encapsulation of Large Guests up to 1 nm. *Journal of the American Chemical Society* **2011,** *133* (30), 11438-11441.
28. Yamashina, M.; Sei, Y.; Akita, M.; Yoshizawa, M., Safe storage of radical initiators within a polyaromatic nanocapsule. *Nature Communications* **2014,** *5* (1), 4662.
29. Li, Y.-H.; Zhang, Y.; Legrand, Y.-M.; van der Lee, A.; Jiang, J.-J.; Chen, C.-X.; Su, C.-Y.; Barboiu, M., Hydrophobic metallo-supramolecular Pd2L4 cages for zwitterionic guest encapsulation in organic solvents. *Dalton Transactions* **2017,** *46* (44), 15204-15207.
30. Ahmedova, A.; Mihaylova, R.; Momekova, D.; Shestakova, P.; Stoykova, S.; Zaharieva, J.; Yamashina, M.; Momekov, G.; Akita, M.; Yoshizawa, M., M2L4 coordination capsules with tunable anticancer activity upon guest encapsulation. *Dalton Transactions* **2016,** *45* (33), 13214-13221.
31. Yamashina, M.; Yuki, T.; Sei, Y.; Akita, M.; Yoshizawa, M., Anisotropic Expansion of an M2L4 Coordination Capsule: Host Capability and Frame Rearrangement. *Chemistry – A European Journal* **2015,** *21* (11), 4200-4204.
32. Chen, B.; Horiuchi, S.; Holstein, J. J.; Tessarolo, J.; Clever, G. H., Tunable Fullerene Affinity of Cages, Bowls and Rings Assembled by PdII Coordination Sphere Engineering. *Chemistry – A European Journal* **2019,** *25* (65), 14921-14927.
33. Lewis, J. E. M.; Gavey, E. L.; Cameron, S. A.; Crowley, J. D., Stimuli-responsive Pd2L4 metallosupramolecular cages: towards targeted cisplatin drug delivery. *Chemical Science* **2012,** *3* (3), 778-784.
34. Preston, D.; Fox-Charles, A.; Lo, W. K. C.; Crowley, J. D., Chloride triggered reversible switching from a metallosupramolecular [Pd2L4]4+ cage to a [Pd2L2Cl4] metallo-macrocycle with release of endo- and exo-hedrally bound guests. *Chemical Communications* **2015,** *51* (43), 9042-9045.
35. McNeill, S. M.; Preston, D.; Lewis, J. E. M.; Robert, A.; Knerr-Rupp, K.; Graham, D. O.; Wright, J. R.; Giles, G. I.; Crowley, J. D., Biologically active [Pd2L4]4+ quadruply-stranded helicates: stability and cytotoxicity. *Dalton Transactions* **2015,** *44* (24), 11129-11136.
36. Ahmedova, A.; Momekova, D.; Yamashina, M.; Shestakova, P.; Momekov, G.; Akita, M.; Yoshizawa, M., Anticancer Potencies of PtII- and PdII-linked M2L4 Coordination Capsules with Improved Selectivity. *Chemistry – An Asian Journal* **2016,** *11* (4), 474-477.
37. Martí-Centelles, V.; Lawrence, A. L.; Lusby, P. J., High Activity and Efficient Turnover by a Simple, Self-Assembled "Artificial Diels–Alderase". *Journal of the American Chemical Society* **2018,** *140* (8), 2862-2868.

38. Stuckhardt, C.; Roke, D.; Danowski, W.; Otten, E.; Wezenberg, S. J.; Feringa, B. L., A chiral self-sorting photoresponsive coordination cage based on overcrowded alkenes. *Beilstein Journal of Organic Chemistry* **2019,** *15*, 2767-2773.
39. Li, R.-J.; Han, M.; Tessarolo, J.; Holstein, J. J.; Lübben, J.; Dittrich, B.; Volkmann, C.; Finze, M.; Jenne, C.; Clever, G. H., Successive Photoswitching and Derivatization Effects in Photochromic Dithienylethene-Based Coordination Cages. *ChemPhotoChem* **2019,** *3* (6), 378-383.
40. Han, M.; Michel, R.; He, B.; Chen, Y.-S.; Stalke, D.; John, M.; Clever, G. H., Light-Triggered Guest Uptake and Release by a Photochromic Coordination Cage. *Angewandte Chemie International Edition* **2013,** *52* (4), 1319-1323.
41. Li, R.-J.; Holstein, J. J.; Hiller, W. G.; Andréasson, J.; Clever, G. H., Mechanistic Interplay between Light Switching and Guest Binding in Photochromic [Pd2Dithienylethene4] Coordination Cages. *Journal of the American Chemical Society* **2019,** *141* (5), 2097-2103.
42. Fu, S.; Luo, Q.; Zang, M.; Tian, J.; Zhang, Z.; Zeng, M.; Ji, Y.; Xu, J.; Liu, J., Light-triggered reversible disassembly of stimuli-responsive coordination metallosupramolecular Pd2L4 cages mediated by azobenzene-containing ligands. *Materials Chemistry Frontiers* **2019,** *3* (6), 1238-1243.
43. DiNardi, R. G.; Douglas, A. O.; Tian, R.; Price, J. R.; Tajik, M.; Donald, W. A.; Beves, J. E., Visible-Light-Responsive Self-Assembled Complexes: Improved Photoswitching Properties by Metal Ion Coordination**. *Angewandte Chemie International Edition* **2022,** *61* (38), e202205701.
44. Li, R.-J.; Tessarolo, J.; Lee, H.; Clever, G. H., Multi-stimuli Control over Assembly and Guest Binding in Metallo-supramolecular Hosts Based on Dithienylethene Photoswitches. *Journal of the American Chemical Society* **2021,** *143* (10), 3865-3873.
45. Liao, P.; Langloss, B. W.; Johnson, A. M.; Knudsen, E. R.; Tham, F. S.; Julian, R. R.; Hooley, R. J., Two-component control of guest binding in a self-assembled cage molecule. *Chemical Communications* **2010,** *46* (27), 4932-4934.
46. Johnson, A. M.; Moshe, O.; Gamboa, A. S.; Langloss, B. W.; Limtiaco, J. F. K.; Larive, C. K.; Hooley, R. J., Synthesis and Properties of Metal–Ligand Complexes with Endohedral Amine Functionality. *Inorganic Chemistry* **2011,** *50* (19), 9430-9442.
47. Schmidt, A.; Molano, V.; Hollering, M.; Pöthig, A.; Casini, A.; Kühn, F. E., Evaluation of New Palladium Cages as Potential Delivery Systems for the Anticancer Drug Cisplatin. *Chemistry – A European Journal* **2016,** *22* (7), 2253-2256.
48. Kaiser, F.; Schmidt, A.; Heydenreuter, W.; Altmann, P. J.; Casini, A.; Sieber, S. A.; Kühn, F. E., Self-Assembled Palladium and Platinum Coordination Cages: Photophysical Studies and Anticancer Activity. *European Journal of Inorganic Chemistry* **2016,** *2016* (33), 5189-5196.
49. Lewis, J. E. M.; Elliott, A. B. S.; McAdam, C. J.; Gordon, K. C.; Crowley, J. D., 'Click' to functionalise: synthesis, characterisation and enhancement of the physical properties of a series of exo- and endo-functionalised Pd2L4 nanocages. *Chemical Science* **2014,** *5* (5), 1833-1843.
50. Schmidt, A.; Hollering, M.; Drees, M.; Casini, A.; Kühn, F. E., Supramolecular exo-functionalized palladium cages: fluorescent properties and biological activity. *Dalton Transactions* **2016,** *45* (20), 8556-8565.
51. Cosialls, R.; Simó, C.; Borrós, S.; Gómez-Vallejo, V.; Schmidt, C.; Llop, J.; Cuenca, A. B.; Casini, A., PET Imaging of Self-Assembled 18F-Labelled Pd2L4 Metallacages for Anticancer Drug Delivery. *Chemistry – A European Journal* **2023,** *29* (3), e202202604.
52. Woods, B.; Döllerer, D.; Aikman, B.; Wenzel, M. N.; Sayers, E. J.; Kühn, F. E.; Jones, A. T.; Casini, A., Highly luminescent metallacages featuring bispyridyl ligands functionalised with BODIPY for imaging in cancer cells. *Journal of Inorganic Biochemistry* **2019,** *199*, 110781.
53. Han, J.; Räder, A. F. B.; Reichart, F.; Aikman, B.; Wenzel, M. N.; Woods, B.; Weinmüller, M.; Ludwig, B. S.; Stürup, S.; Groothuis, G. M. M.; Permentier, H. P.; Bischoff, R.; Kessler, H.; Horvatovich, P.; Casini, A., Bioconjugation of Supramolecular Metallacages to Integrin Ligands for Targeted Delivery of Cisplatin. *Bioconjugate Chemistry* **2018,** *29* (11), 3856-3865.
54. Schmidt, A.; Hollering, M.; Han, J.; Casini, A.; Kühn, F. E., Self-assembly of highly luminescent heteronuclear coordination cages. *Dalton Transactions* **2016,** *45* (31), 12297-12300.

55. Preston, D.; McNeill, S. M.; Lewis, J. E. M.; Giles, G. I.; Crowley, J. D., Enhanced kinetic stability of [Pd2L4]4+ cages through ligand substitution. *Dalton Transactions* **2016,** *45* (19), 8050-8060.
56. Woods, B.; Silva, R. D. M.; Schmidt, C.; Wragg, D.; Cavaco, M.; Neves, V.; Ferreira, V. F. C.; Gano, L.; Morais, T. S.; Mendes, F.; Correia, J. D. G.; Casini, A., Bioconjugate Supramolecular Pd2+ Metallacages Penetrate the Blood Brain Barrier In Vitro and In Vivo. *Bioconjugate Chemistry* **2021,** *32* (7), 1399-1408.
57. Vasdev, R. A. S.; Gaudin, L. F.; Preston, D.; Jogy, J. P.; Giles, G. I.; Crowley, J. D., Anticancer Activity and Cisplatin Binding Ability of Bis-Quinoline and Bis-Isoquinoline Derived [Pd2L4]4+ Metallosupramolecular Cages. *Frontiers in Chemistry* **2018,** *6*.
58. Tarzia, A.; Lewis, J. E. M.; Jelfs, K. E., High-Throughput Computational Evaluation of Low Symmetry Pd2L4 Cages to Aid in System Design**. *Angewandte Chemie International Edition* **2021,** *60* (38), 20879-20887.
59. Lisboa, L. S.; Findlay, J. A.; Wright, L. J.; Hartinger, C. G.; Crowley, J. D., A Reduced-Symmetry Heterobimetallic [PdPtL4]4+ Cage: Assembly, Guest Binding, and Stimulus-Induced Switching. *Angewandte Chemie International Edition* **2020,** *59* (27), 11101-11107.
60. Bloch, W. M.; Holstein, J. J.; Hiller, W.; Clever, G. H., Morphological Control of Heteroleptic cis- and trans-Pd2L2L'2 Cages. *Angewandte Chemie International Edition* **2017,** *56* (28), 8285-8289.
61. Vasdev, R. A. S.; Preston, D.; Casey-Stevens, C. A.; Martí-Centelles, V.; Lusby, P. J.; Garden, A. L.; Crowley, J. D., Exploiting Supramolecular Interactions to Control Isomer Distributions in Reduced-Symmetry [Pd2L4]4+ Cages. *Inorganic Chemistry* **2023,** *62* (5), 1833-1844.
62. Lewis, J. E. M.; Tarzia, A.; White, A. J. P.; Jelfs, K. E., Conformational control of Pd2L4 assemblies with unsymmetrical ligands. *Chemical Science* **2020,** *11* (3), 677-683.
63. Yoshizawa, M.; Catti, L., Bent Anthracene Dimers as Versatile Building Blocks for Supramolecular Capsules. *Accounts of Chemical Research* **2019,** *52* (8), 2392-2404.
64. Li, Z.; Kishi, N.; Hasegawa, K.; Akita, M.; Yoshizawa, M., Highly fluorescent M2L4 molecular capsules with anthracene shells. *Chemical Communications* **2011,** *47* (30), 8605-8607.
65. Li, Z.; Kishi, N.; Yoza, K.; Akita, M.; Yoshizawa, M., Isostructural M2L4 Molecular Capsules with Anthracene Shells: Synthesis, Crystal Structures, and Fluorescent Properties. *Chemistry – A European Journal* **2012,** *18* (27), 8358-8365.
66. Yamashina, M.; Matsuno, S.; Sei, Y.; Akita, M.; Yoshizawa, M., Recognition of Multiple Methyl Groups on Aromatic Rings by a Polyaromatic Cavity. *Chemistry – A European Journal* **2016,** *22* (40), 14147-14150.
67. Yamashina, M.; Akita, M.; Hasegawa, T.; Hayashi, S.; Yoshizawa, M., A polyaromatic nanocapsule as a sucrose receptor in water. *Science Advances* **2017,** *3* (8), e1701126.
68. Kusaba, S.; Yamashina, M.; Akita, M.; Kikuchi, T.; Yoshizawa, M., Hydrophilic Oligo(lactic acid)s Captured by a Hydrophobic Polyaromatic Cavity in Water. *Angewandte Chemie International Edition* **2018,** *57* (14), 3706-3710.
69. Foianesi-Takeshige, L. H.; Takahashi, S.; Tateishi, T.; Sekine, R.; Okazawa, A.; Zhu, W.; Kojima, T.; Harano, K.; Nakamura, E.; Sato, H.; Hiraoka, S., Bifurcation of self-assembly pathways to sheet or cage controlled by kinetic template effect. *Communications Chemistry* **2019,** *2* (1), 128.
70. Fukuda, M.; Sekiya, R.; Kuroda, R., A Quadruply Stranded Metallohelicate and Its Spontaneous Dimerization into an Interlocked Metallohelicate. *Angewandte Chemie International Edition* **2008,** *47* (4), 706-710.
71. Yue, N. L. S.; Eisler, D. J.; Jennings, M. C.; Puddephatt, R. J., Macrocyclic and Lantern Complexes of Palladium(II) with Bis(amidopyridine) Ligands: Synthesis, Structure, and Host−Guest Chemistry. *Inorganic Chemistry* **2004,** *43* (24), 7671-7681.
72. Yue, N.; Qin, Z.; Jennings, M. C.; Eisler, D. J.; Puddephatt, R. J., Host complexes that adapt to their guests: amphitopic receptors. *Inorganic Chemistry Communications* **2003,** *6* (9), 1269-1271.
73. Tripathy, D.; Pal, A. K.; Hanan, G. S.; Chand, D. K., Palladium(ii) driven self-assembly of a saturated quadruple-stranded metallo helicate. *Dalton Transactions* **2012,** *41* (37), 11273-11275.

74. Timmer, B. J. J.; Bobylev, E. O.; Mooibroek, T. J., Comparison of [Pd2L4][BF4]4 cages for binding of n-octyl glycosides and nitrate (L = isophthalamide or dipicolinamide linked dipyridyl ligand). *Organic & Biomolecular Chemistry* **2021,** *19* (30), 6633-6637.
75. Schaapkens, X.; Bobylev, E. O.; Reek, J. N. H.; Mooibroek, T. J., A [Pd2L4]4+ cage complex for n-octyl-β-d-glycoside recognition. *Organic & Biomolecular Chemistry* **2020,** *18* (25), 4734-4738.
76. Lin, Q.; Gao, L.; Kauffmann, B.; Zhang, J.; Ma, C.; Luo, D.; Gan, Q., Helicity adaptation within a quadruply stranded helicate by encapsulation. *Chemical Communications* **2018,** *54* (95), 13447-13450.
77. McNeill, S. M.; Giles, N. M.; Preston, D.; Jones, P. P.; Crowley, J. D.; Giles, G. I., Quadruply Stranded Metallo-Supramolecular Helicate [Pd2(hextrz)4]4+ Acts as a Molecular Mimic of Cytolytic Peptides. *Chemical Research in Toxicology* **2020,** *33* (7), 1822-1834.
78. Zhou, L.-P.; Sun, Q.-F., A self-assembled Pd2L4 cage that selectively encapsulates nitrate. *Chemical Communications* **2015,** *51* (94), 16767-16770.
79. Sarkar, M.; Dasary, H.; Chand, D. K., Helicity induction by innocent anion in a quadruple stranded cage. *Journal of Organometallic Chemistry* **2021,** *950*, 121984.
80. Bloch, W. M.; Horiuchi, S.; Holstein, J. J.; Drechsler, C.; Wuttke, A.; Hiller, W.; Mata, R. A.; Clever, G. H., Maximized axial helicity in a Pd2L4 cage: inverse guest size-dependent compression and mesocate isomerism. *Chemical Science* **2023,** *14* (6), 1524-1531.
81. Alonso, N. C. Tetra-Stranded Metallo-Supramolecular Cylinders. Design, Synthesis and DNA Binding Studies. University of Birmingham, 2012.
82. Banwait, S. K. Metallo-Supramolecular Complexes and their Interactions with Biomolecules and Cells. University of Birmingham, 2009.
83. Oleksi, A.; Blanco, A. G.; Boer, R.; Usón, I.; Aymamí, J.; Rodger, A.; Hannon, M. J.; Coll, M., Molecular Recognition of a Three-Way DNA Junction by a Metallosupramolecular Helicate. *Angewandte Chemie International Edition* **2006,** *45* (8), 1227-1231.
84. Cerasino, L.; Hannon, M. J.; Sletten, E., DNA Three-Way Junction with a Dinuclear Iron(II) Supramolecular Helicate at the Center: A NMR Structural Study. *Inorganic Chemistry* **2007,** *46* (16), 6245-6251.
85. Szostak, J. W.; Orr-Weaver, T. L.; Rothstein, R. J.; Stahl, F. W., The double-strand-break repair model for recombination. *Cell* **1983,** *33* (1), 25-35.
86. Song, Q.; Hu, Y.; Yin, A.; Wang, H.; Yin, Q., DNA Holliday Junction: History, Regulation and Bioactivity. *International Journal of Molecular Sciences* **2022,** *23* (17), 9730.
87. Loos, M.; Gerber, C.; Corona, F.; Hollender, J.; Singer, H., Accelerated Isotope Fine Structure Calculation Using Pruned Transition Trees. *Analytical Chemistry* **2015,** *87* (11), 5738-5744.
88. Rodger, A.; Dorrington, G.; Ang, D. L., Linear dichroism as a probe of molecular structure and interactions. *Analyst* **2016,** *141* (24), 6490-6498.
89. Hannon, M. J.; Moreno, V.; Prieto, M. J.; Moldrheim, E.; Sletten, E.; Meistermann, I.; Isaac, C. J.; Sanders, K. J.; Rodger, A., Intramolecular DNA Coiling Mediated by a Metallo-Supramolecular Cylinder. *Angewandte Chemie International Edition* **2001,** *40* (5), 879-884.
90. Šmidlehner, T.; Piantanida, I.; Pescitelli, G., Polarization spectroscopy methods in the determination of interactions of small molecules with nucleic acids – tutorial. *Beilstein Journal of Organic Chemistry* **2018,** *14*, 84-105.
91. del Villar-Guerra, R.; Trent, J. O.; Chaires, J. B., G-Quadruplex Secondary Structure Obtained from Circular Dichroism Spectroscopy. *Angewandte Chemie International Edition* **2018,** *57* (24), 7171-7175.
92. Kypr, J.; Kejnovská I Fau - Renciuk, D.; Renciuk D Fau - Vorlícková, M.; Vorlícková, M., Circular dichroism and conformational polymorphism of DNA. *Nucleic Acids Res* **2009,** (1362-4962 (Electronic)).
93. Eriksson, M.; Nordén, B.; Lycksell, P.-O.; Gräslund, A.; Jernström, B., Structure of Z-DNA in solution. A flow linear dichroism study. *Journal of the Chemical Society, Chemical Communications* **1985,** (19), 1300-1302.
94. Rodger, A., Nucleic Acid Linear Dichroism. In *Encyclopedia of Biophysics*, Roberts, G. C. K., Ed. Springer Berlin Heidelberg: Berlin, Heidelberg, 2013; pp 1761-1763.

95. Meistermann, I.; Moreno, V.; Prieto, M. J.; Moldrheim, E.; Sletten, E.; Khalid, S.; Rodger, P. M.; Peberdy, J. C.; Isaac, C. J.; Rodger, A.; Hannon, M. J., Intramolecular DNA coiling mediated by metallo-supramolecular cylinders: Differential binding of P and M helical enantiomers. *Proceedings of the National Academy of Sciences* **2002,** *99* (8), 5069-5074.
96. Ivens, E.; Cominetti, M. M. D.; Searcey, M., Junctions in DNA: underexplored targets for therapeutic intervention. *Bioorganic & Medicinal Chemistry* **2022,** *69*, 116897.
97. Brázda, V.; Laister, R. C.; Jagelská, E. B.; Arrowsmith, C., Cruciform structures are a common DNA feature important for regulating biological processes. *BMC Molecular Biology* **2011,** *12* (1), 33.
98. Craig, J. S.; Melidis, L.; Williams, H. D.; Dettmer, S. J.; Heidecker, A. A.; Altmann, P. J.; Guan, S.; Campbell, C.; Browning, D. F.; Sigel, R. K. O.; Johannsen, S.; Egan, R. T.; Aikman, B.; Casini, A.; Pöthig, A.; Hannon, M. J., Organometallic Pillarplexes That Bind DNA 4-Way Holliday Junctions and Forks. *Journal of the American Chemical Society* **2023,** *145* (25), 13570-13580.
99. Hooper, C. A. J.; Cardo, L.; Craig, J. S.; Melidis, L.; Garai, A.; Egan, R. T.; Sadovnikova, V.; Burkert, F.; Male, L.; Hodges, N. J.; Browning, D. F.; Rosas, R.; Liu, F.; Rocha, F. V.; Lima, M. A.; Liu, S.; Bardelang, D.; Hannon, M. J., Rotaxanating Metallo-supramolecular Nano-cylinder Helicates to Switch DNA Junction Binding. *Journal of the American Chemical Society* **2020,** *142* (49), 20651-20660.
100. Prince, S.; Mapolie, S.; Blanckenberg, A., Palladium-Based Anti-Cancer Therapeutics. In *Encyclopedia of Cancer*, Schwab, M., Ed. Springer Berlin Heidelberg: Berlin, Heidelberg, 2014; pp 1-9.
101. Czarnomysy, R.; Radomska, D.; Szewczyk, O. K.; Roszczenko, P.; Bielawski, K., Platinum and Palladium Complexes as Promising Sources for Antitumor Treatments. *International Journal of Molecular Sciences* **2021,** *22* (15).
102. Alcalde-Ordóñez, A.; Barreiro-Piñeiro, N.; McGorman, B.; Gómez-González, J.; Bouzada, D.; Rivadulla, F.; Vázquez, M. E.; Kellett, A.; Martínez-Costas, J.; Vázquez-López, M., A copper(ii) peptide helicate selectively cleaves DNA replication foci in mammalian cells. *Chemical Science* **2023,** *14* (48), 14082-14091.
103. Zell, J.; Duskova, K.; Chouh, L.; Bossaert, M.; Chéron, N.; Granzhan, A.; Britton, S.; Monchaud, D., Dual targeting of higher-order DNA structures by azacryptands induces DNA junction-mediated DNA damage in cancer cells. *Nucleic Acids Research* **2021,** *49* (18), 10275-10288.

# Chapter 3 – Comparing DNA binding of three metal cylinders

## 3.1 Introduction

The aims of this chapter are to further investigate the DNA binding properties of the platinum tetrastranded complex (PtCyl) described in Chapter 2 and compare it against two other similar DNA binding metal complexes (gold pillarplex and nickel parent cylinder). Each of the metal complexes possesses a 4+ charge, has outwards facing, accessible pi surfaces, and are 1-2 nm in each dimension. All three of the complexes have displayed some level of binding interaction with B-DNA, as well as some ability to interact with DNA junctions. It is hypothesised here that the outward facing pi surfaces are key to explaining their junction binding interactions (structures shown in Figure 1).

A major difference between the three metal complexes under investigation (the NiP, AuPill, and PtCyl) is the symmetry; the NiP cylinder has three-fold symmetry which is what enables the perfect pi-pi stacking between the metal complex and the bases at the junction site of a 3WJ, whereas the AuPill has four-fold symmetry which has been shown to allow for a stronger interaction with 4WJ structures.[1] The PtCyl complex has approximately $D_4$ symmetry which should make it a good match for a Holliday junction.[2] The results of the studies carried out in this work will be used to compare the structures of the metal complexes to aid in the design of future DNA junction binding metal complexes.

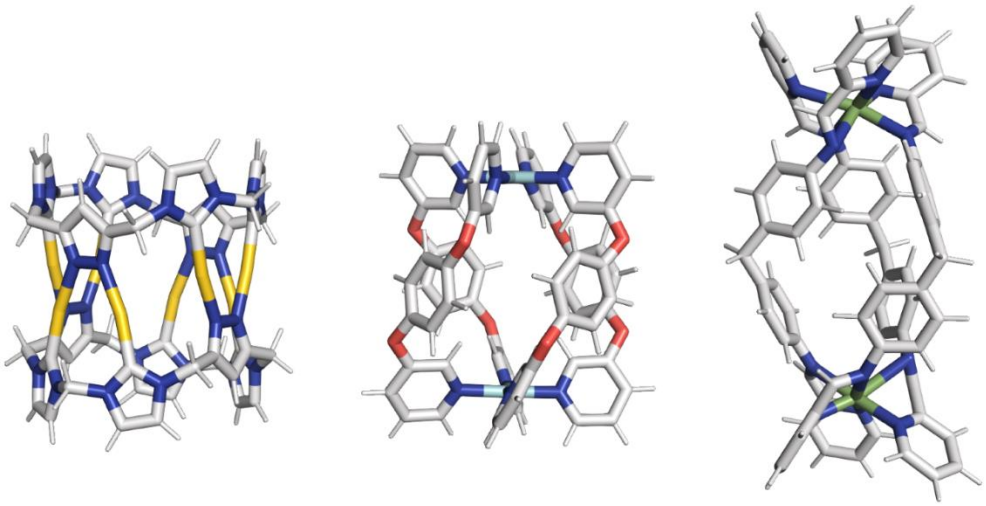

*Figure 1. Three dimensional structures of the AuPill, PtCyl, and NiP metal complexes.*

The basis for the PtCyl complex produced in this work has been thoroughly discussed in the introduction to Chapter 2. In brief, the palladium version of this platinum metal complex was first

produced by McMorran and Steel in 1998.[2] It was found to be approximately 0.9 nm in diameter and 0.9 nm in height, but different anion guests effect the dimensions of the cage structure. Whilst the diameter of the cage does not vary significantly with different guests, the height of the cage can vary from 0.88 nm with a hexafluorophpsophate anion, to 0.74 nm with an iodide anion as the guest.[3] To the best our knowledge no biological studies or biophysical investigations have been published thus far.

The gold pillarplex (AuPill) is a supramolecular organometallic complex which was first synthesised by Alexander Pöthig and co-workers in 2016.[4] The AuPill structure consists of two organic macrocycles which are connected through 8 bridging gold (or silver) metal centres. The overall design of this metal complex gives it a slightly larger girth than the nickel parent cylinder (NiP) and a significantly shorter length (1.2 nm compared to 1.9 nm). Another potentially important difference between the NiP and the AuPill is symmetry: the nickel complex has three-fold symmetry whereas the AuPill $D_{2d}$ has four-fold symmetry. More recently, work from the Pöthig group has demonstrated how the pillarplex may be modified to control the shape of the cavity.[5] A recent publication by the Hannon group has shown that this metal complex has remarkable DNA binding properties; the AuPill shows a binding interaction with DNA 3WJ but competition experiments have revealed that it has a preference for binding to DNA 4WJ and Y-fork structures.[1]

The Hannon group has produced several helical supramolecular cylinders based around three ligands bridging two metal centres. It was demonstrated that iron parent cylinder binds perfectly in DNA 3WJ through crystal structures and NMR analysis.[6] Recent work has shown that a derivative of the parent cylinder is able to thread through a cucurbituril ring, which inhibits its DNA junction binding when locked on by modifications to the cylinder.[7] It has also been shown to bind to stabilize DNA bulges of various sizes and compositions.[8]

## 3.2 Fluorescence displacement assays

Ethidium bromide was first used in the 1960s by Le Pecq and Paoletti to quantify DNA, utilising the 25 fold increase in fluorescence upon intercalation of the ethidium bromide with DNA.[9] This increase in fluorescence upon intercalation is the basis for modern fluorescence intercalation displacement assays, first described by Michael P. Hendrick and co-workers.[10] A fluorescence intercalation displacement assay can be used to determine sequence selectivity but also, more importantly in this case, the DNA binding affinity; the binding affinity is calculated based on the decrease in fluorescence of the solution when ethidium bromide is displaced from the DNA by a competitor. Ethidium bromide is typically used for fluorescence displacement assays as its interaction with DNA is well understood, it rapidly intercalates into DNA, and the intercalation is reversible.

To carry out a fluorescence displacement assay, a DNA solution is loaded with a known concentration of ethidium bromide which fluoresces strongly when intercalated into the DNA duplex. The molecule being investigated can then be titrated into the solution and the fluorescence intensity of the solution is monitored after each addition. If the molecule under investigation binds to the DNA then the fluorescence intensity from the ethidium bromide will decrease as it is displaced by the competing molecule. Hoechst is a well-known DNA minor groove binder, the same process may be carried out with this molecule to investigate another molecules affinity for the DNA minor groove.

Minor groove binders, such as Hoechst dyes, have also been used in fluorescence displacement assays in much the same way as ethidium bromide.[11, 12] Some literature has used this experiment and the resultant decrease, or lack thereof, in fluorescence to add evidence to support the supposed binding mode of the molecule in question to duplex DNA.

In this section fluorescence displacement assays will be used to compare and contrast the affinities of three metal complexes for B-DNA.

### 3.2.1 Ethidium bromide displacement

Researchers have been aware of the existence of ethidium bromide (EtBr) as a molecule for a long time, but its intercalative interaction with DNA was only confirmed in 1975, when the crystal structure

of ethidium bromide with small DNA fragments was produced for the first time.[13] When intercalated into the DNA duplex, the fluorescence of the ethidium bromide increases approximately 20 times.[14] The increase in fluorescence intensity of EtBr upon DNA intercalation is thought to be due to the hydrophobic pocket in which the molecule is binding, excluding water molecules which can quench the fluorescence by proton transfer.[15] The increase in fluorescence upon DNA intercalation enables us to use EtBr in a fluorescence displacement assay. Direct competition for the same binding location on the DNA will result in the largest decrease in fluorescence. The metal complexes are too large to intercalate into the DNA duplex and directly compete with EtBr, but electrostatic interactions can result in the displacement of EtBr.

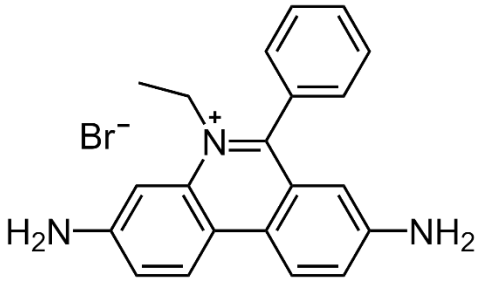

*Figure 2. Chemical structure of ethidium bromide.*

Control experiments indicate that none of the metal complexes (NiP, AuPill or PtCyl) investigated are excited at the 500 nm wavelength used for the EtBr displacement and none of the metal complexes studied show any absorbance at 500 nm (appendix A3.1). The fluorescence spectrum of EtBr with each of the metal complexes in the absence of DNA does not show any significant changes, indicating that they do not interact with the EtBr (appendix A3.2).

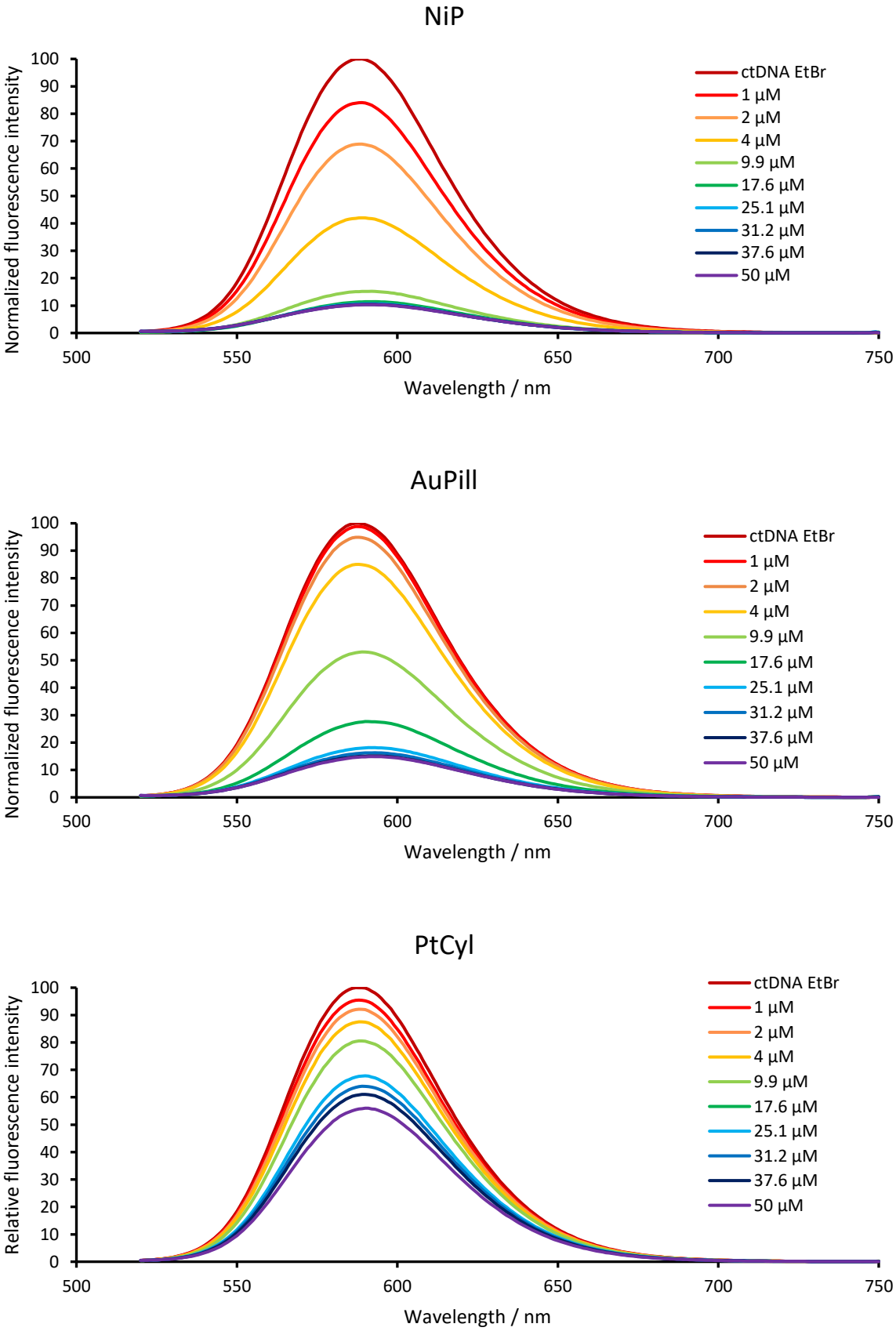


*Figure 3. Fluorescence displacement titration for NiP (top), AuPill (middle) or PtCyl (bottom) with ctDNA 50 µM, Ethidium bromide 25 µM, in Tris-HCl 1 mM pH 7.4, NaCl 20 mM (Excitation wavelength 500 nm, Emission wavelength 520-750 nm).*

The fluorescence intensity of the ethidium bromide intercalated into the DNA decreases with increasing concentrations of each of the metal complexes (Figure 3). A decrease in the fluorescence intensity indicates that the ethidium bromide is being quenched, this is typically caused by the EtBr being displaced from the DNA by the competitor. The quenching may also be caused by an interaction of the ethidium bromide with the metal complex, but control experiments indicate that this is not occurring in this case.

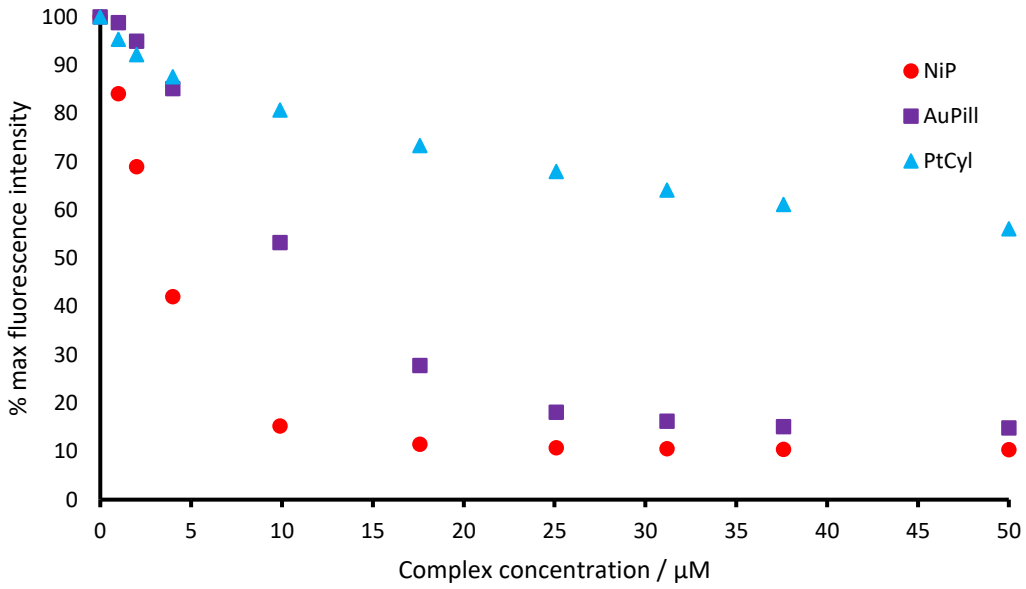


*Figure 4. Percentage fluorescence intensity (measured at 590 nm) for the titration of NiP / AuPill / PtCyl with ctDNA 50 µM, Ethidium bromide 25 µM, in Tris-HCl 1 mM pH 7.4, NaCl 20 mM (Excitation wavelength 500 nm, Emission wavelength 520-750 nm).*

It can be said with confidence that each of the complexes displays some degree of interaction with B-DNA due to the significant decrease in fluorescence in all cases (Figure 4). The NiP induces a sharp decrease in fluorescence when titrated into the DNA solution indicating a strong interaction, as does the AuPill. This is not surprising as it has been suggested in the past that NiP binds in the major groove of B-DNA.[16] Molecular dynamics simulations have indicated that AuPill binds to B-DNA in the minor groove.[1] The gradual decrease in fluorescence intensity of the EtBr DNA solution when the PtCyl was titrated in indicates a weaker interaction between the B-DNA and PtCyl. To compare the affinity each metal complex displays for the B-DNA, the concentration of the complex required to reduce the initial fluorescence intensity to 50% ($C_{50}$) is also calculated from the gradient of the FID plot (Figure 4).

This large difference in binding affinity suggested by the $C_{50}$ values (Table 1) between the PtCyl and the other two metal complexes was not expected as they are all quadruply charged metal complexes, displaying aromatic areas on their surface. One possibility for the large difference in affinity for dsDNA could be due to the PtCyl complex retaining an anion in its central cavity. Previous work has demonstrated that the central anion exhibits weak interactions to the metal centres at each end of the cavity, which traps the anion in the cage-like structure.[3] Mass spectrometry (MS) carried out during this study supports this; the 4+ metal complex is never observed under MS conditions. This is also true for experiments where the PtCyl complex were incubated with a DNA 3WJ (section 3.6) An anion trapped in the centre of the PtCyl complex would give the structure overall a 3+ charge which would result in a significantly weaker interaction with the negatively charged DNA. The significantly more flexible structure of the PtCyl indicated by MD simulations may also contribute to the weaker binding.

### 3.2.2 Hoechst 33258 displacement

Hoechst 33258 is a DNA minor groove binder which strongly fluoresces when bound to DNA and has a strong preference for AT rich regions.[17, 18] The 30-fold increase in fluorescence upon binding and the large Stokes shift make Hoechst dyes ideal candidates for staining the nuclei of cells, both live and dead. These characteristics also make Hoechst 33258 well suited for fluorescence displacement assays.[12] Some researchers use displacement of Hoechst to infer minor groove binding, as this is where Hoechst localises on B-DNA.[12] Since the Hoechst dye binds in the minor groove of the DNA, we might expect the metal complexes to complete against this more effectively than the EtBr.

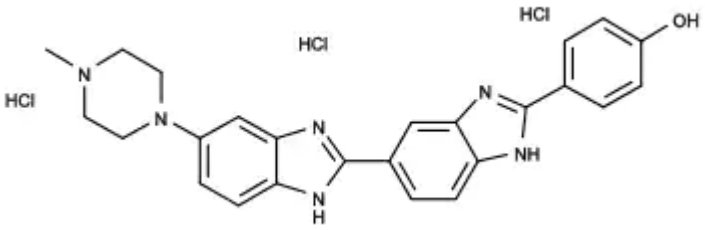

*Figure 5. Chemical structure of Hoechst 33258.*

Control experiments indicate that NiP and PtCyl are not excited at the 350 nm excitation wavelength used to monitor the Hoechst 33258 fluorescence however, the AuPill complex exhibits weak fluorescence when excited at 350 nm (appendix A3.1). The NiP complex was found to strongly quench Hoechst 33258, making interpretation of the fluorescence displacement of NiP difficult (appendix

A3.3). The PtCyl exhibits weak quenching of the Hoechst, and the AuPill does not display a significant interaction.

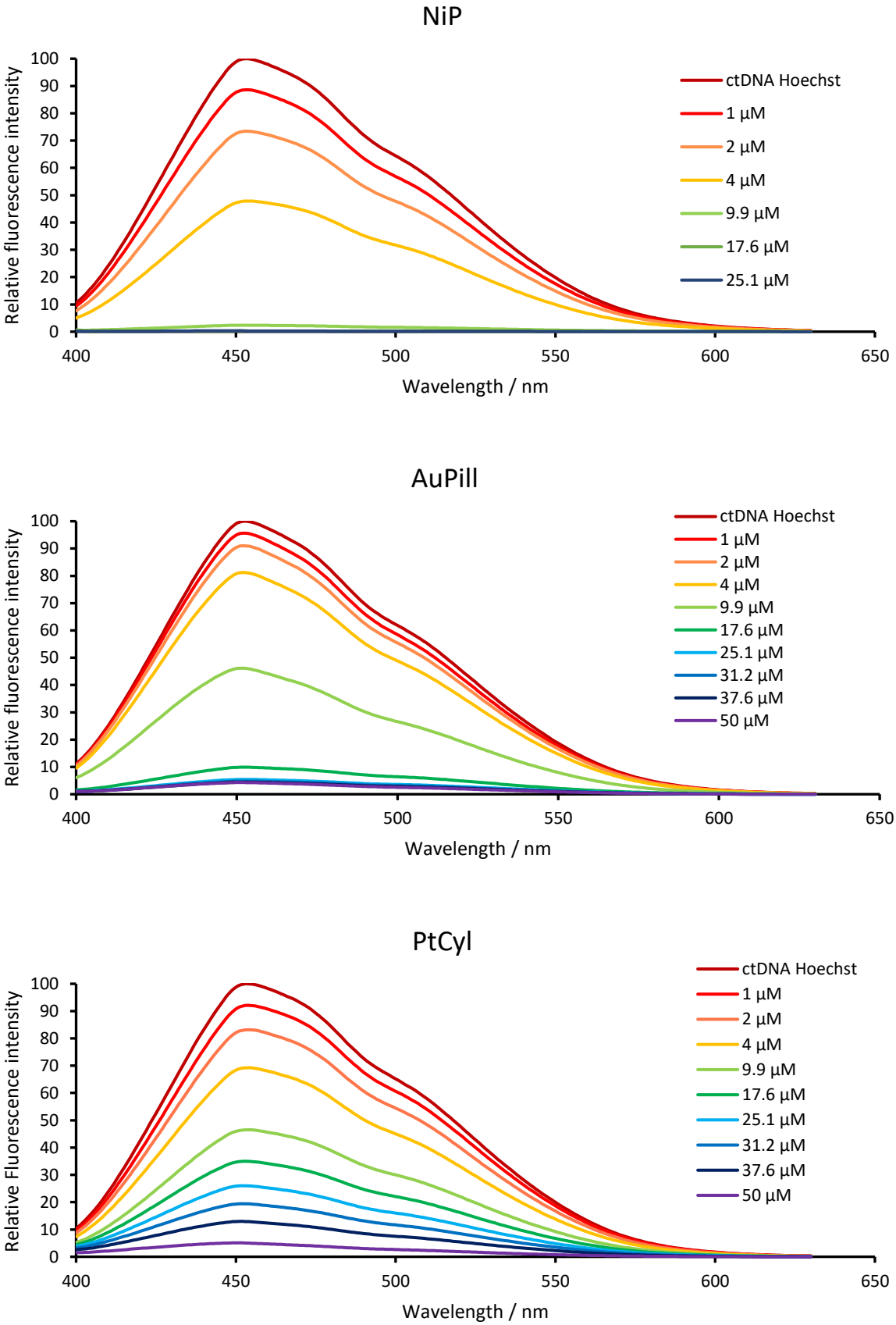


*Figure 6. Fluorescence displacement titration for NiP (top), AuPill (middle), or PtCyl (bottom) complexes with ctDNA 50 µM, Hoechst 33258 5 µM, in Tris-HCl 1 mM pH 7.4, NaCl 20 mM (Excitation wavelength 350 nm, Emission wavelength 400-650 nm).*

Each metal complex was titrated into a solution of ctDNA with Hoechst 33258 (Figure 6 and Figure 7). Immediately on addition of NiP, there is a significant decrease in the Hoechst fluorescence and at higher concentrations of NiP, the Hoechst dye is almost completely quenched. This is likely due to a combination of displacement of Hoechst from the DNA minor groove and the NiP quenching the Hoechst in solution. It is difficult to draw conclusions from this as we do not know to what extent each mechanism is contributing to the quenching of the Hoechst dye. Additions of AuPill produces significant quenching of the Hoechst in the same way as was observed for the NiP. This almost total quenching indicates that nearly all of the dye has been displaced from the DNA. Increasing the concentration of PtCyl leads to the gradual quenching of the fluorescence. A gradual decrease in fluorescence intensity indicates a relatively weak interaction of the platinum complex with DNA and specifically the minor groove of B-DNA. The displacement of the Hoechst by PtCyl also appears to occur at two distinct rates possibly indicating multiple binding modes of the PtCyl to the B-DNA.

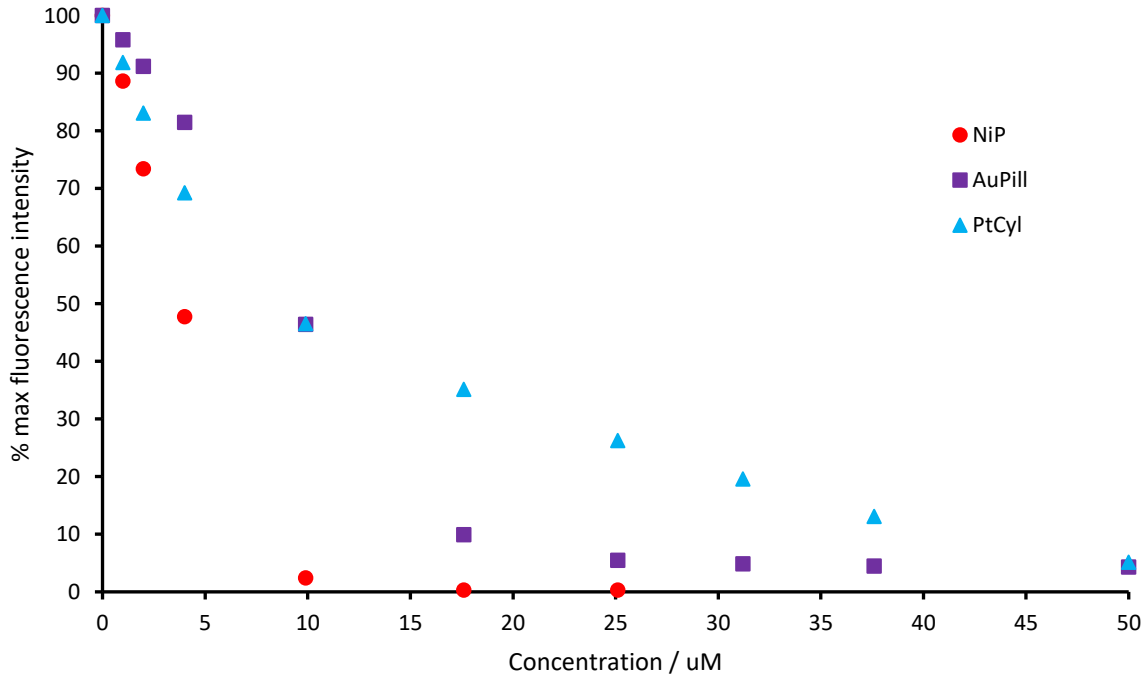


*Figure 7. Percentage fluorescence intensity (measured at 450 nm) for the titration of NiP / AuPill / Pt with ctDNA 50 µM, Ethidium bromide 25 µM, in Tris-HCl 1 mM pH 7.4, NaCl 20 mM (Excitation wavelength 350 nm, Emission wavelength 400-650 nm).*

The concentration required to reduce the fluorescence intensity of the Hoechst-DNA complex to 50% of its initial value was calculated (Table 1). This gives an idea of how strong the interaction is between DNA and each of the three metal complexes, relative to one another. The low concentration of NiP

required to reduce the fluorescence intensity to 50% indicates a strong interaction between the NiP and B-DNA. AuPill and PtCyl have similar values.

*Table 1. C50 = concentration of complex where max fluorescence intensity reaches 50%. Linear relationships for segments of each complex were plotted where $R^2 > 0.98$ in order to calculate the concentrations required to achieve 50% fluorescence intensity. (Appendix A3.4) (* = NiP displayed strong quenching of Hoechst 33258).*

| Metal complex | EtBr $C_{50}$ / µM | Hoechst 33258 $C_{50}$ / µM |
|---|---|---|
| Nickel Parent cylinder (NiP) | 3.4 | 3.8* |
| Gold Pillarplex (AuPill) | 11.9 | 9.7 |
| Platinum cylinder (PtCyl) | 69.2 | 8.7 |

In summary, the Hoechst 33258 and ethidium bromide displacement studies indicate that all three metal cylinders interact with B-DNA to varying degrees. The NiP displays by far the lowest $C_{50}$ value, indicating the strongest displacement of EtBr. The concentration of AuPill required to reduce the fluorescence intensity of EtBr to 50% of the initial value is almost four times higher than NiP. The $C_{50}$ value of PtCyl for EtBr is over twenty times higher than NiP. This very large difference was unexpected and indicates that the PtCyl has the weakest interaction with B-DNA. If displacement of the EtBr is occurring primarily through electrostatic interactions, then this will be strongly affected by the potentially lower charge of the PtCyl. The B-DNA may be able to accommodate more PtCyl before an EtBr molecule is displaced, which would inflate the $C_{50}$ value of PtCyl even though it is binding to the DNA.

The $C_{50}$ values for Hoechst displacement by NiP and AuPill are very similar to their $C_{50}$ values measured for EtBr displacement. Despite the absorption displayed by NiP at 350 nm, the similarity of the values displayed by AuPill for the displacement of EtBr and Hoechst suggest that the value for NiP displacement of Hoechst may not be unreasonable. Surprisingly, PtCyl reduces the fluorescence intensity of Hoechst to 50% at a concentration almost 8 times lower than that required for the EtBr displacement. This perhaps indicates that PtCyl exhibits minor groove binding, but the PtCyl does appear to have some interaction with the Hoechst dye, as it displays some fluorescence quenching. The results from the Hoechst displacement must be carefully considered due to the slight quenching of shown by PtCyl, and strong absorbance at 350 nm (excitation wavelength of Hoechst 33258) by NiP.

## 3.3 DNA melting studies

DNA is a polymer made up of bases which are linked by a sugar phosphate backbone, two strands of DNA come together by hydrogen bonding between the bases on opposing strands to form a duplex structure. The Watson-Crick model for base pairing tells us that two hydrogen bonds can from between Adenine and Thymine bases and three can form between Guanine and Cytosine residues.[19] DNA melting is the process of breaking the DNA duplex by causing the hydrogen bonding holding the two single strands of DNA to fall apart, to do this energy must be put in. Melting of DNA can be achieved by heating the system but can also be achieved by the use of organic solvents,[20] altering the pH, or lowering the salt concentration.[21] The melting temperature of a DNA sequence refers to the temperature at which half of the DNA is present as the dsDNA (double stranded DNA) form, and half as the ssDNA (single stranded DNA) form.[22] The melting temperature is specific to each DNA sequence and varies based on three main factors:

1. Nucleotide makeup – GC rich sequences will have higher melting temperature than AT rich sequences due to the three hydrogen bonds in a GC base pair compared to two hydrogen bonds in an AT base pair.
2. Number of base pairs – DNA duplexes that are longer and contain more base pairs will require more energy to break into singles strands.
3. Secondary structure – Some DNA sequences can form more complex DNA structures such as G-quadruplexes, which will have very different melting temperatures compared to a typical duplex. Mismatched base pairs and insertions will also have a large effect on the melting temperature.

The experimental conditions must be considered for a DNA melting experiment as they will heavily influence the observed melting temperatures. The primary condition which can drastically change the melting temperature of a DNA sequence is the salt concentration.[21, 23, 24] Phosphate anions are present on the sugar backbone of a DNA duplex, these anions repel one another and encourage the formation of ssDNA. The electrostatic repulsion between phosphate anions can be overcome by the hydrogen bonding between bases, which allows DNA hybridization. Higher salt concentrations provide greater

screening of the negative charges of the phosphate anions on the DNA backbone, which leads to higher melting temperatures. The concentration of DNA in the solution measured also has a large effect on the DNA melting temperature due to the probability of complementary base pairing occurring.[24]

Once the melting data has been acquired, the mathematical method used to determine the melting temperature of a DNA sequence will also have an effect on the melting temperature number acquired. In the work presented below, we utilise the first derivative method as this is a robust method which is preferred for complex solutions which may have multiple melting temperatures.[25] The melting temperature ($T_m$) is determined by in-built software which plots the derivative of the melting data to find the point at which the rate of change is greatest. Errors in melting experiments reported are the standard deviation between three separate measurements of the melting temperature of three separately prepared samples. These errors may arise (for example) due to the accuracy of pipetting required to prepare the solutions, sample evaporation, and how evenly the samples are heated.

In this section, DNA melting studies will be undertaken with a variety of DNA structures (DNA, and RNA, 3WJ and 4WJ) and metal complexes (NiP, AuPill, PtCyl) in order to understand the impact the metal complexes have on the stability of each DNA structure.

### 3.3.1 DNA UV melting studies

DNA bases have a strong absorption peak at 260 nm due to the π to $\pi^*$ transition in the p-orbitals of the purine and pyrimidine rings.[26] Hydrogen bonding in hybridized DNA disrupts the π to $\pi^*$ transitions, resulting in a lower extinction coefficient than the single stranded equivalent. The difference in the absorption coefficients of dsDNA and ssDNA allows us to measure the melting temperature of DNA structures. To determine the melting temperature of a DNA structure, the DNA must first be annealed. Annealing the DNA sample before carrying out the melting experiment is very important as this ensures that the most stable form of the DNA structure is formed before the experiment begins. The DNA solution is then slowly heated from 15°C to 95°C in a buffered solution, where the absorbance at 260 nm is measured at defined temperature intervals. The melting temperature can then be determined

by plotting the first derivative of the absorbance vs temperature and finding where the rate of absorbance change is greatest (derivative plots are shown in appendix A3.5).

#### *3.3.1.1 3WJ*

The first DNA structure investigated was the DNA 3WJ which has been widely used by the Hannon group. It consists of three oligomers, 14 bases in length, which do not form a 3WJ alone but will come together to form a junction in the presence of a junction binding agent. This is also the same 3WJ structure used in PAGE gels with the PtCyl in Chapter 2. The disadvantage of the standard 14-mer 3WJ is that it does not form spontaneously in buffered solution, even at reduced temperature. This means that we cannot compare the melting temperature difference between the native structure and the structure formed with the metal complexes (NiP, AuPill, PtCyl). The $T_m$ of the complexes with the 3WJ may be compared against each other (Figure 8).

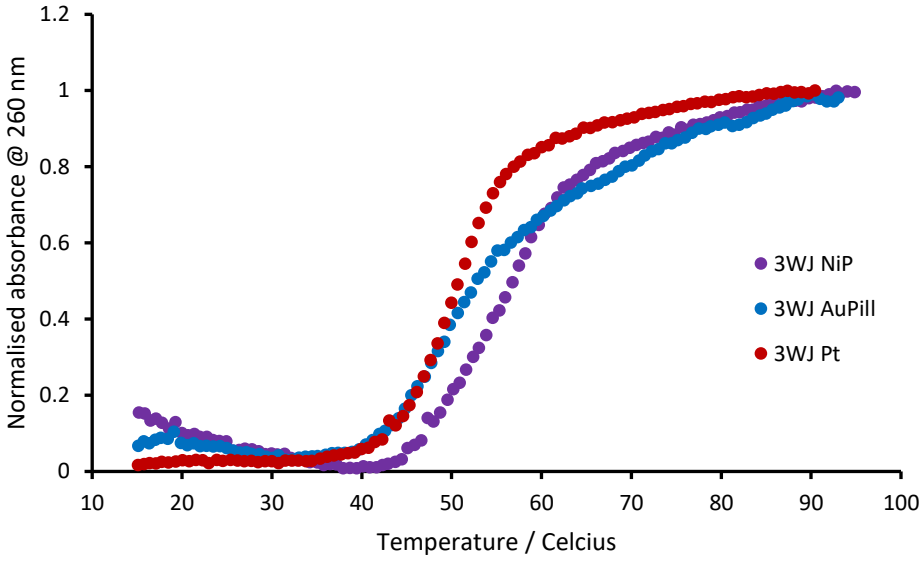


*Figure 8. UV melting of DNA 14-mer 3WJ (2 µM) with metal complex (2 µM) from 15 °C – 95 °C at 1 °Cmin$^{-1}$ (sodium cacodylate 10 mM, NaCl 100 mM, pH 7.4).*

Each melting experiment was repeated three separate times with three freshly prepared individual samples to ensure reproducibility. The structure with the highest melting temperature is the 3WJ.NiP $T_m$ = 56.2 ± 0.08 °C. The melting temperature of the AuPill and PtCyl with 3WJ are both measurably lower than the NiP with the same 3WJ structure (3WJ.AuPill $T_m$ = 48.8 ± 0.5 °C, 3WJ.PtCyl $T_m$ = 49.4 ± 0.6 °C). This indicates that both complexes have a weaker interaction with the junction and provide

less stabilisation to the structure than the NiP. This is not surprising as crystal structures of the NiP reveals that it has a perfect fit for the cavity dimensions, the pi surfaces of the cylinder are also perfectly oriented to interact with the pi surfaces of the bases in the junction.[27] Crystal structure of a DNA junction with AuPill or PtCyl have not yet been obtained.

#### *3.3.1.2 3WJ18*

The 3WJ18 DNA structure consists of the same oligomers used in the 14-mer 3WJ which have been extended by 4 bases to give 18-mers. The increased number of complementary base pairs allows the 3WJ18 structure to form spontaneously as shown by PAGE gels (appendix A3.6).

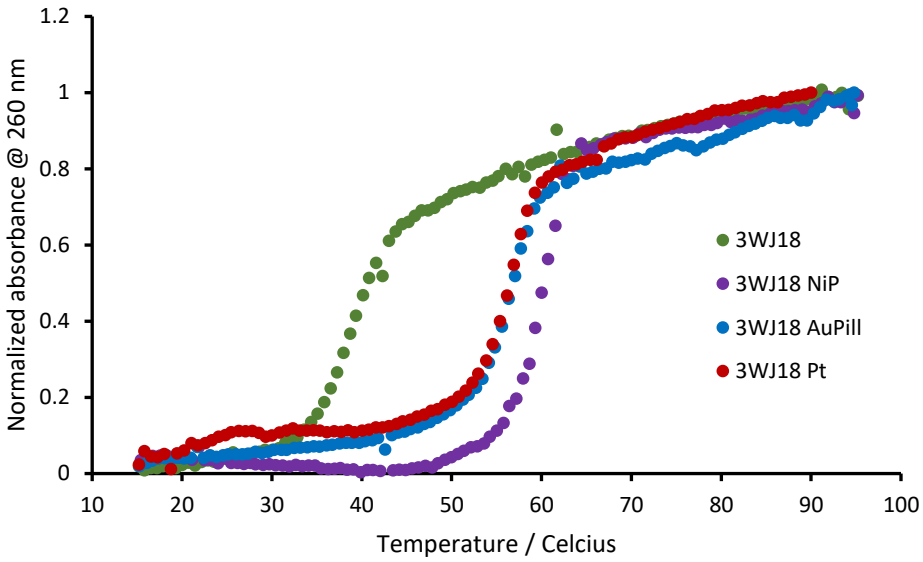


*Figure 9. UV melting of DNA 18-mer 3WJ (1 µM) alone and with metal complex (1 µM) from 15 °C – 95 °C at 1 °Cmin$^{-1}$ (sodium cacodylate 10 mM, NaCl 100 mM, pH 7.4).*

The 3WJ18 melting temperatures display the same trends as were observed for the 14-mer 3WJ. The increased stability of 3WJ18 enables us to record a baseline melting temperature for the structure with no metal complexes in the junction cavity ($T_m$ = 39.2 ± 0.9 °C) (Figure 9). This allows us to measure the change in melting temperature when metal complexes are added. With one equivalent of the NiP, the melting temperature of the structure increases by 19.8 ± 1.6 °C. Monchaud *et al.* have measured a comparable increase in the melting temperature of a similar 3WJ (19.2 °C), however 5 equivalents of the junction binder were required to achieve this increase.[28] The AuPill and PtCyl also show large increases in melting temperature of the 3WJ18 but not as substantial as the NiP (3WJ18.AuPill $\Delta T_m$ = 17.1 ± 1 °C, 3WJ18.PtCyl $\Delta T_m$ = 17.3 ± 0.7 °C), again corresponding to the trends seen for the 14-mer

3WJ. Both the AuPill and NiP cylinder have also been shown to interact strongly with B-DNA (section 3.2) on its own which will also increase the melting temperature of the structure.

#### *3.3.1.3 4WJ*

Binding of the three metal complexes to DNA 4WJ structures was carried out using a 4WJ, which is formed from 4 separate oligomers, 22 bases in length. PAGE gels show that a 4WJ structure is spontaneously formed in solution when these four oligomers are combined (section 3.5.1), however, the exact conformation of the 4WJ is not clear. When the metal complexes are incubated with this 4WJ structure, multiple structures are formed which is shown in PAGE gels (Figure 18). The formation of multiple species in solution can make interpreting meting data complicated.

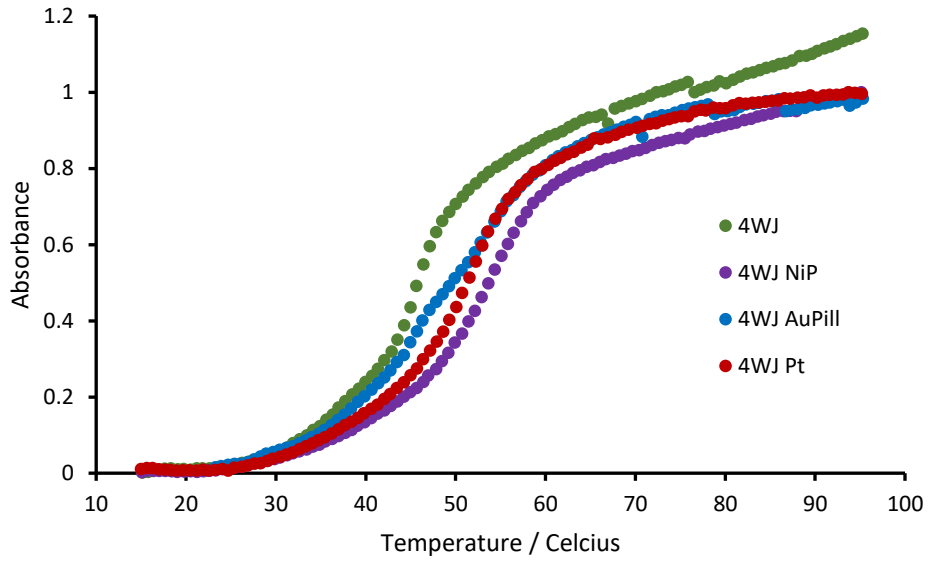


*Figure 10. UV melting of DNA 4WJ (1 µM) alone and with metal complex (1 µM) from 15 °C – 95 °C at 1 °Cmin$^{-1}$ (sodium cacodylate 10 mM, NaCl 100 mM, pH 7.4).*

The melting temperature of the 4WJ with no metal complexes in sodium cacodylate buffer was $T_m$ = 45.8 ± 0.6 °C (Figure 10). With the addition of NiP, the melting temperature increased by 8.1 °C degrees (4WJ.NiP $\Delta T_m$ = 8.1 ± 0.9 °C). This increase is substantial, but it is less than half of the increase in melting temperature observed for the 3WJ18 structure with NiP. The $\Delta T_m$ with the NiP is again higher than the increase observed for the PtCyl, which only saw an increase of 6.0 °C (4WJ.PtCyl $\Delta T_m$ = 6.0 ± 0.5 °C). The AuPill with the 4WJ saw very similar increases in the melting temperature to the PtCyl that were within error but, interestingly, two melting temperatures were observed (4WJ.AuPill $\Delta T_m1$ = 0.7 ± 1.3 °C, 4WJ.AuPill $\Delta T_m2$ = 6.7 ± 0.6 °C). The first aligns roughly with the baseline 4WJ melting

temperature and the other is similar the melting temperature observed for 4WJ.PtCyl. This was consistently observed for multiple repeats of the experiment with fresh solutions each time. The presence of two melting temperatures indicates the presence of two species in solution. In PAGE gels, multiple bands are observed when the AuPill is incubated with the 4WJ oligomers, which also indicates the presence of multiple structures in solution. Multiple bands are also observed in PAGE gels when NiP or PtCyl are incubated with the 4WJ oligomers, yet these metal complexes do not display multiple melting temperatures. The bands formed by the AuPill with 4WJ are distinct from those formed by PtCyl or NiP and are thought to be due to a Y-forked structure which has been discussed in a recent publication by the Hannon group.[1]

For each DNA junction investigated the NiP complex displays the strongest stabilization of the structure. The significant increase in melting temperatre of the 3WJ structures with NiP is not surprising as the almost "lock and key" fit of the NiP in a 3WJ has been demonstrated in the past.[27] The PtCyl and AuPill also stabilize the structures but to a lesser extent. This suggests that the PtCyl is a much better fit in the 3WJ cavities than AuPill as we suspect it is a 3+ complex when bound in the junction, compared to the 4+ charge of the AuPill.

### 3.3.2 RNA UV melting

RNA is also composed of nucleotides connected through a sugar phosphate back bone. Ribose is the sugar which forms the biopolymer RNA, whereas deoxyribose is the sugar found in DNA. The other significant difference between DNA and RNA is the replacement of thymine base with uracil. The structural flexibility of RNA allows it to form a wide range of conformations which is essential for its many functions. It is commonly found as a single strand which can fold to form an A-RNA duplex, but can also form hairpin loops, bulges, pseudoknots and branched loops.[29] RNA is not only the template for protein structures, but the existence of non-coding RNAs has led to the discovery a wide array of other functions which RNA is involved in.[30] RNA is used to regulate epigenetic modifications, transcription, translation, metabolism and more. Many diseases have been linked to aberrant RNA expression, particularly neurodegenerative diseases. [31]

The melting temperature of RNA can be measured in much the same way as DNA. The main difference is the increased stability of the RNA duplex, compared to the same DNA duplex, as a result of the extra hydroxyl group on the RNA sugars, which allows more hydrogen bonds to form.[32] Melting of RNA junctions with the three metal complexes was carried out to observe any differences compared to the melting temperatures of the DNA junctions with the metal complexes. The melting temperature of the RNA structures was also determined by the derivative method (derivative plots sown in appendix A3.14).

#### *3.3.2.1 RNA 3WJ*

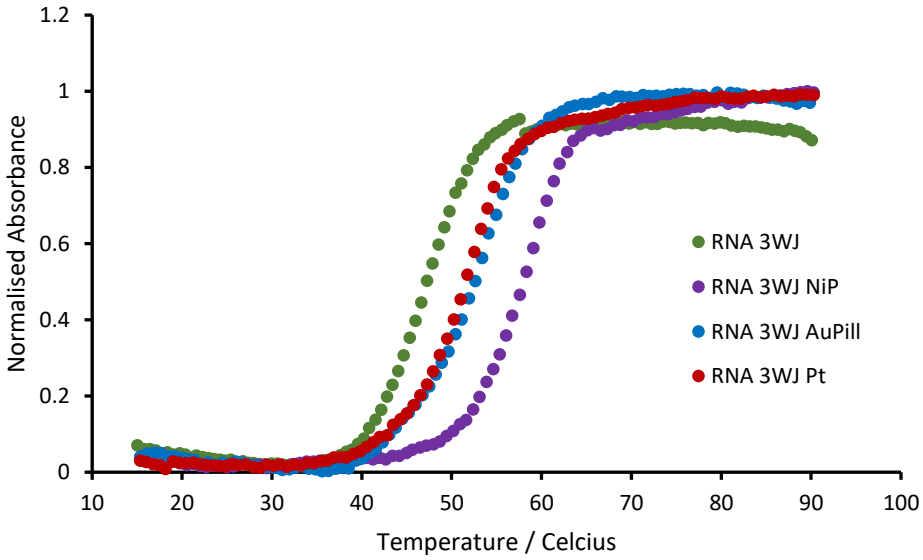


*Figure 11. UV melting of RNA 14-mer 3WJ (2 μM) alone and with metal complex (2 μM) from 15 °C – 95 °C at 1 °Cmin$^{-1}$ (sodium cacodylate 10 mM, NaCl 100 mM, pH 7.4).*

Due to the increased stability of the RNA, the $T_m$ of the RNA 14-mer 3WJ with no junction binder present can be measured: RNA 3WJ $T_m$ = 47.4 ± 0.6 °C (Figure 11). The melting temperatures of the RNA 3WJ with metal complexes follow the same trends observed with the DNA 3WJ with the NiP produces the most stable structure RNA 3WJ.NiP $\Delta T_m$ = 11.3 ± 0.6 °C, followed by RNA 3WJ.AuPill $\Delta T_m$ = 6.0 ± 0.3 °C, and RNA 3WJ.PtCyl $\Delta T_m$ = 5.0 ± 0.1 °C. Compared to the DNA 3WJ, the increases in melting temperature with addition of metal complexes is modest. The RNA 3WJ is inherently more stable than the DNA 3WJ and 3WJ18 structures, giving it a higher melting temperature. The smaller increases in melting temperature may also be due to the A-form of RNA duplex, which has a significantly narrower major groove.

### 3.3.2.2 RNA 4WJ

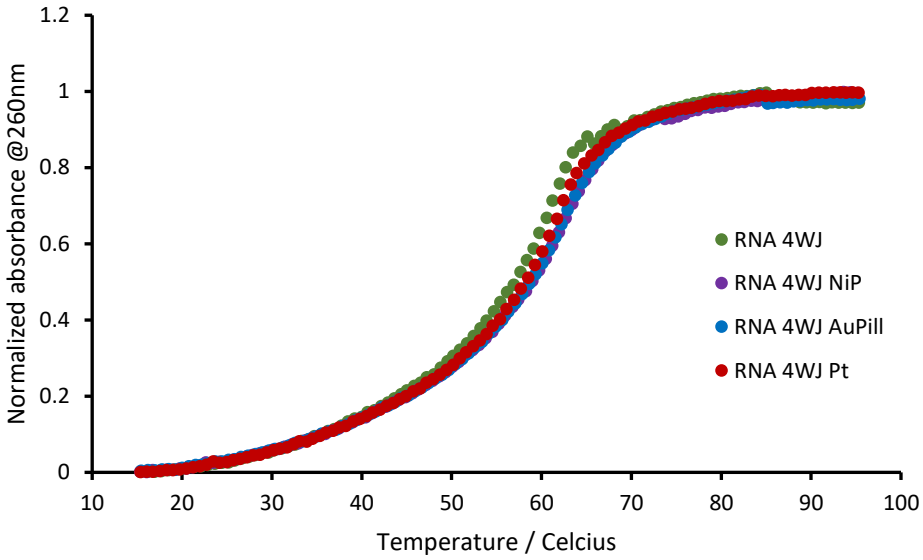


*Figure 12. UV melting of DNA 4WJ (1 μM) alone and with metal complex (1 μM) from 15 °C – 95 °C at 1 °Cmin$^{-1}$ (sodium cacodylate 10 mM, NaCl 100 mM, pH 7.4).*

The RNA 4WJ used in this melting study has the same sequence as the DNA 4WJ used above. PAGE gels have shown that this RNA 4WJ forms spontaneously in solution and also forms a number of structures in the presence of the metal complexes (Figure 24). The melting temperatures of the RNA 4WJ with and without metal complexes are all very similar (Figure 12). The RNA 4WJ has a melting temperature of 60.4 ± 0.1 °C, and the addition of metal complexes has very little effect (RNA 4WJ.NiP $\Delta T_m$ = 2.0 ± 0.1 °C, RNA 4WJ.AuPill $\Delta T_m$ = 1.7 ± 0.5 °C, and RNA 4WJ.Pt $\Delta T_m$ = 1.0 ± 0.1 °C). Interestingly, with the RNA 4WJ, the AuPill does not display two melting temperatures as it did with the DNA, this could be due to increased stability of the 4WJ itself.

The same trends for stabilization of the RNA 3WJ are observed as were seen for the DNA 3WJ. None of the metal complexes studied here offer any significant stabilisation to the RNA 4WJ structure formed here.

### 3.3.3 FRET melting studies

FRET (foster resonance energy transfer) is a phenomenon where energy can be absorbed by a donor molecule and transferred a short distance to an acceptor molecule which releases the energy either radiatively or non-radiatively via other quenching states (Figure 13).

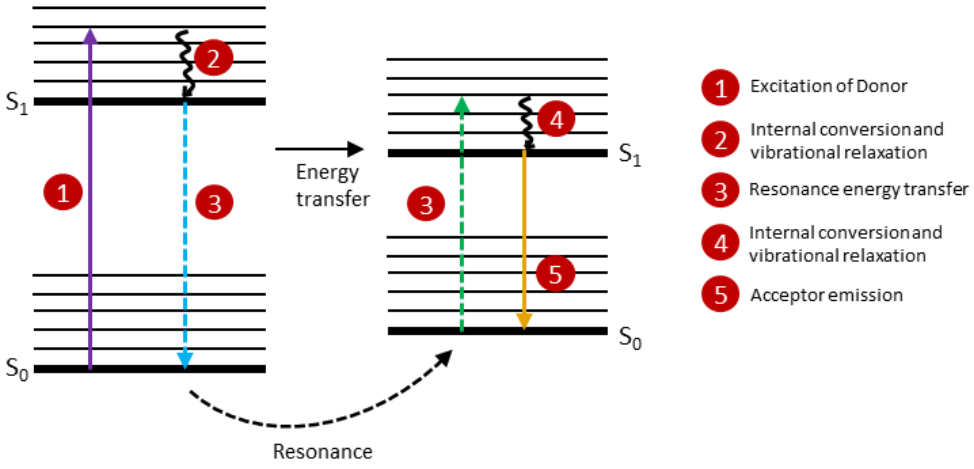


*Figure 13. Jablonski diagram of foster energy resonance transfer (FRET) process.*

The energy transfer observed during FRET is extremely sensitive to the distance between the donor and acceptor molecules. For this reason, FRET is a commonly used to measure distances between bio-macromolecules and is sometimes called the spectroscopic ruler.[33] FRET has been applied to DNA in a multitude of different ways.[34-36] The simplest way in which FRET probes have been used to study DNA is to detect the formation of DNA secondary structures. A DNA strand or multiple strands can be tagged at the appropriate ends, or even partway through a sequence, such that the fluorescence of the donor molecule is quenched when a structure is formed. Alternatively, the fluorescence increase can be measured when the structure is disrupted.

Monchaud and co-workers have regularly utilised FRET to investigate the interactions of ligands with G-quadruplex structures and, more recently, three-way junction structures.[28, 37] A single stranded DNA oligomer was designed with a fluorescein molecule tagged on one end and TAMRA (tetramethylrhodamine) on the other, the structure folds up to form a three-way junction under physiological pH and ambient temperature, bringing the donor and acceptor molecules in close

proximity to one another. This three-way junction structure can then be probed by carrying out fluorescence melting studies, the fluorescence intensity of the fluorescein will increase when the structure melts and the fluorescein is no longer quenched by the TAMRA. The 3WJ structure consists of five base pairs in each duplex, and a hairpin loop made up of six thymine bases at two of the three arms of the structure (called 3WJT6 from here onwards). Both the 14-mer 3WJ and 3WJT6 have the same number of bases in their overall structure (42 bases), but the 3WJ has 21 base pairs compared to 15 in the 3WJT6. Complexes which have a higher affinity for duplex DNA may stabilise the 14-mer 3WJ structure to a greater extent compared to the 3WJT6. A disadvantage of FRET for this experiment was that the metal complexes may have interactions with the fluorophores on the DNA. Any interaction with the fluorophores may affect the fluorescence measurements but may also stabilise or destabilise the DNA structure.

FRET melting studies were used to investigate how higher equivalents of metal complex would affect the melting temperature of a 3WJ structure, a fluorescently tagged 3WJT6 in this case (Figure 14). FRET melting was used instead of UV melting as the high concentration of metal complex would give very high absorbance. The DNA concentration could not be reduced to resolve this issue as this as the change in UV absorbance would then be too small, leading to unreliable readings.

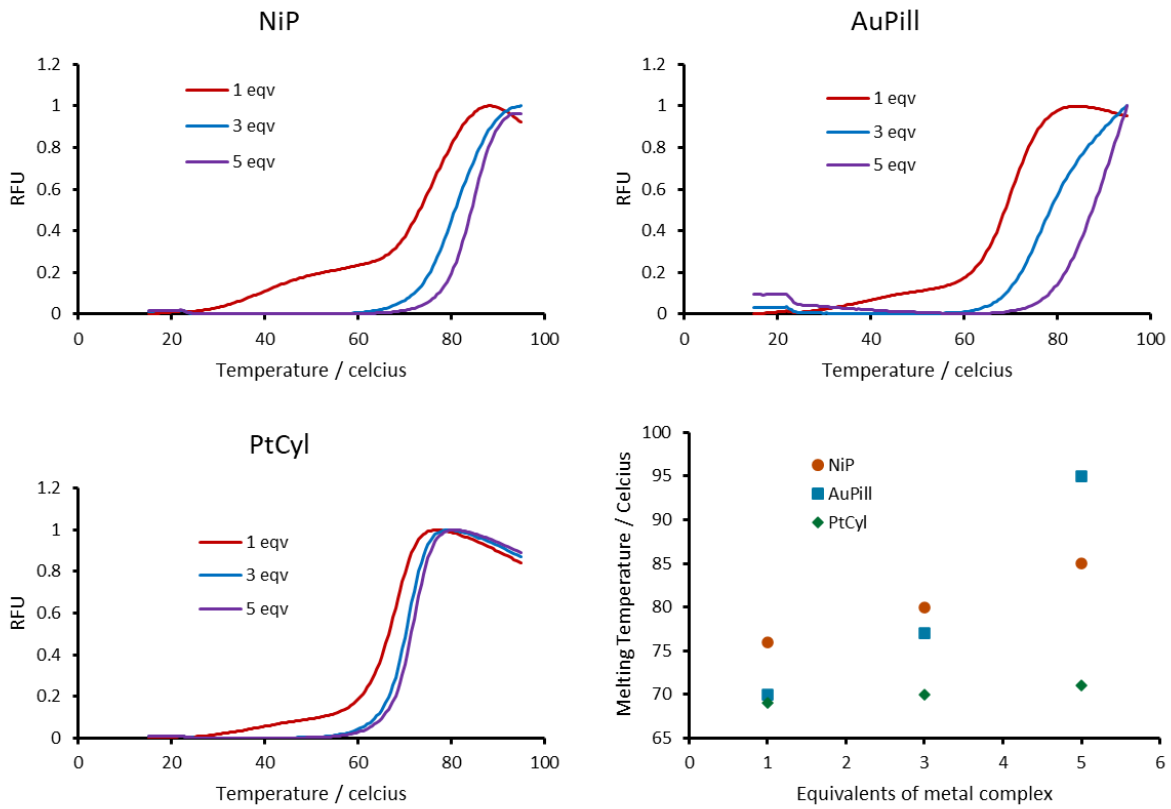


*Figure 14. Fluorescent melting data for TAMRA-3WJT6-FAM oligo (0.2 µM, 20 µL) in sodium cacodylate buffer (10 mM Sodium Cacodylate, 100 mM NaCl pH 7.4) with 1, 3, or 5 equivalents of NiP, AuPill, or PtCyl (derivative plots are shown in appendix A3.7).*

The FRET melting of the TAMRA-3WJT6-FAM structure gives rise to two melting temperatures 3WJT6 $T_m1$ = 39.5 ± 0.9 °C, and $T_m2$ = 58.8 ± 0.3 °C (appendix A3.8). This indicates there are two different species in the solution, or two stages to the melting process. The 3WJT6 structure in PAGE gels only reveal a single structure. However, these PAGE gels are run under different buffer conditions and with an unlabelled 3WJT6 which may impact the structures formed. The FRET melting temperature of TAMRA-3WJT6-FAM oligo structure with increasing equivalents of NiP increased significantly from 58.8 °C, to 76 °C, to 80 °C and finally to 85 °C with 0, 1, 3 or 5 equivalents of NiP respectively. The increase in melting temperature of the 3WJT6 structure with even a single equivalent of metal complex is significantly higher than the 3WJ or 3WJ18. It was initially thought this could be due to the complexes binding in the hairpin loops of the structure as well as the junction cavity, but ITC data (section 3.8) suggests this is not the case. The initial large increase in melting temperature is expected and can be explained by the NiP binding to the 3WJ cavity. Increasing the equivalents of cylinder above 1 equivalent gives significantly smaller, but still very noticeable, increases in the melting temperature.

The AuPill follows a similar trend to the NiP, with an initial significant increase in melting temperature from 58.8 °C to 70 °C. This is a smaller increase in the melting temperature than what was observed for the NiP, likely due to the slightly less optimal binding mode revealed by MD studies which was discussed further in Chapter 2. With higher equivalents of AuPill, the melting temperature again increases less than the initial increase, as observed for the NiP; however the increases are still higher than the NiP. This could suggest that AuPill interacts more strongly than NiP with the rest of the 3WJT6 structure. It is not clear if this interaction would be with the double stranded DNA in the structure, or the thymine hairpin loops. MD simulations have also indicated that the AuPill can interact with the ends of DNA duplexes through pi stacking.[1] PAGE gels have revealed that with high equivalents of AuPill, larger more complex structures are formed with the 3WJT6 (Figure 32 and Figure 33).

The PtCyl shows an increase in melting temperature from 58.8 °C to 69 °C which is very similar to the AuPill and can be explained by the similar junction binding of AUPill and PtCyl seen in MD simulations (Chapter 2). Increases in the equivalents of PtCyl result in only very marginal increases in the melting temperature from 69 °C, to 70 °C, and 71 °C for 1, 3, and 5 equivalents of the PtCyl. The minimal increase in melting temperature suggests that the PtCyl has little interaction with the rest of the 3WJT6 structure which is supported by PAGE gels (Figure 32). These results hint that the PtCyl is more selective for DNA 3WJs than either the AuPill or NiP. It is important to note that higher specificity does not mean that the PtCyl binds the 3WJ more strongly than either the AuPill or NiP.

## 3.4 PAGE competition experiments

The experiments presented in this section were completed by myself with some of the data published in JACS 2023.[1] Competition experiments were conducted where a fluorescently tagged 3WJ was competed against various other DNA structures and metal complexes in PAGE gels. These competition experiments aimed to assess the relative affinity each of the metal complexes had for the DNA 3WJ vs other DNA structures. Fluorescently tagged DNA was required for these competition experiments for a number of reasons:

1. Many of the DNA structures that we wanted to compete have similar hydrodynamic sizes and often overlap with one another in PAGE gels making determination of relative concentrations impossible when stained with SYBR gold;
2. Staining with SYBR gold works well for qualitative analysis but the staining is not always uniform across the gel, some areas may be stained more or less than other areas, which would lead to significant errors when quantifying;
3. This enabled us to use shorter gel run times as we only needed to separate the 3WJ and ss3WJ oligos for quantification.

The competition experiments were carried out utilising PAGE gels. The standard 14mer 3WJ was used with the 5' end of the S1 strand tagged with fluorescein. The benefit of using a fluorescent tag is that it allows us to observe the 3WJ structures in isolation, making band overlaps due to the competing structures a non-issue. Attaching fluorescent tags to the DNA structure does present a few issues which must be considered:

1. The aromatic rings of the ligands which make up the metal complexes being studied may interact with the aromatic system of the fluorophore effecting the fluorescence signal.
2. The presence of a large aromatic fluorophore on the end of a duplex may be able to interact with the duplex, this can influence the stability of the structure.
3. It is possible that the junction binders may bind to the fluorophore instead of the junction which would again affect the structure stability.
4. Only S1 is labelled, meaning that any bands observed can only be attributed to S1 with certainty.

The competition assay was carried out by first mixing one equivalent of the fluorescently tagged 3WJ with a known number of equivalents of a competitor in buffer. The junction binder was added, and the solution was left at room temperature for 1 hour to equilibrate. Glycerol was then added to the samples, which were subsequently loaded into the gel and run for 1 hour. The gel was initially imaged with no staining in order to visualise the fluorescently labelled bands with no interference. After initial

imaging, the gel was stained with SYBR Gold and imaged again to reveal the other DNA structures and confirm that all of the expected structures were present. Quantification was carried out using ImageJ to measure the intensity of the 3WJ-FAM band in each lane (example of the quantification shown in appendix A3.9). The intensity of the bands in the lanes with competitors were normalised to the intensity of the 3WJ-FAM band with no competitor. Each competition experiment was run in triplicate.

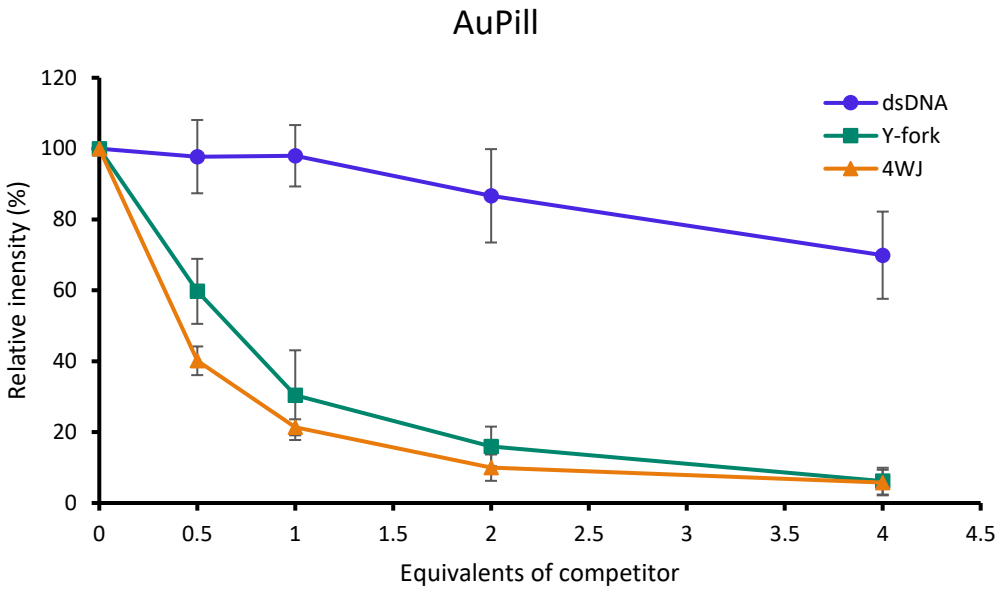


*Figure 15. PAGE competition of 3WJ-FAM vs dsDNA, Y-fork, and 4WJ with AuPill (1xTris Borate buffer pH 8.4, 120 V, 2.5 hours, average of 3 gels). Quantification of 3WJ-FAM band intensity carried out using ImageJ.*

The AuPill does not show a strong interaction with dsDNA, the intensity of the 3WJ-FAM band decreased to approximately 70% with 4 equivalents (Figure 15). This is, however, much lower than for the NiP (101%) or the PtCyl (86%) (Figure 16 and Figure 17). This evidence for a stronger interaction of the AuPill with dsDNA compared to the platinum and nickel cylinders is corroborated by the fluorescence displacement experiments discussed above (Section 3.2). It is interesting that the AuPill shows a strong interaction with both the Y-fork and 4WJ structures introduced to it. In both cases, the fluorescence intensity of the 3WJ-FAM band decreases to almost zero when four equivalents of the competitor are present.

It has been suggested that the 4WJ could potentially be considered as two Y-forks in solution.[1] PAGE gels indicate the spontaneous formation of 4WJ under electrophoresis conditions, but with the AuPill there is also the formation of the new band attributed to the Y-fork. If the number of equivalents of

the 4WJ is doubled to represent the presence of two Y-forks, the new adjusted points for the 4WJ roughly match that of the Y-fork and are within error (shown in appendix A3.10). It is likely that in the gel there is a mixture of Y-forks and 4WJ present as indicated in previous PAGE gels; this explains why the 4WJ intensities closely match the fork but not perfectly.

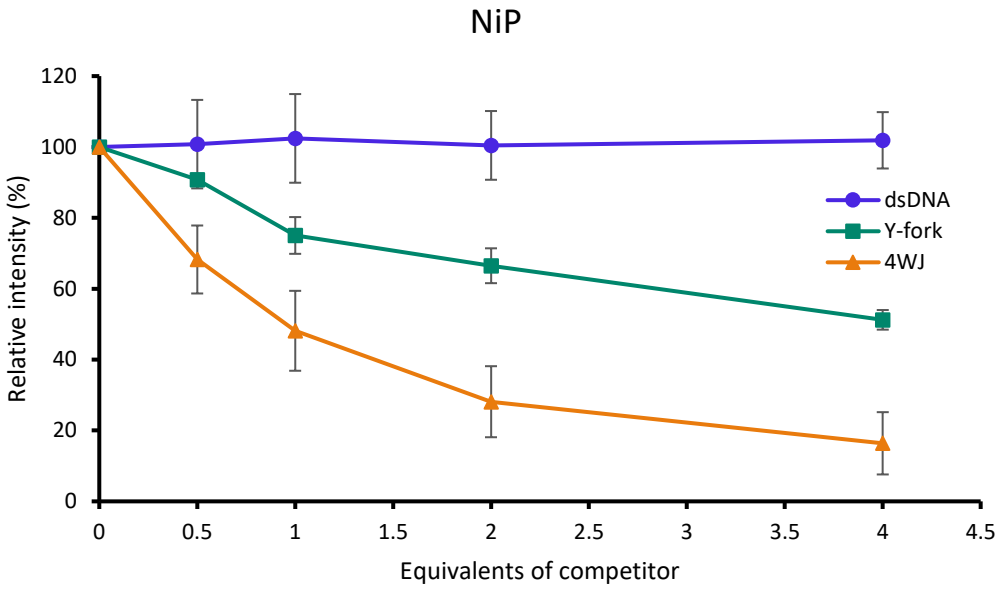


*Figure 16. PAGE competition of 3WJ-FAM vs dsDNA, Y-fork, and 4WJ with NiP (1xTris Borate buffer pH 8.4, 120 V, 2.5 hours, average of 3 gels). Quantification of 3WJ-FAM band intensity carried out using ImageJ.*

In the competition assay with NiP and Y-fork, the 3WJ-FAM band intensity decreases to 51% with four equivalents of the Y-fork competitor (Figure 16). The 3WJ-FAM band intensity with the 4WJ competitor decreased to 16% at four equivalents of 4WJ which indicates that the parent cylinder has a relatively high binding affinity for 4WJ. Competition of the 3WJ-FAM against dsDNA resulted in no decrease in fluorescent intensity even at four equivalents of the dsDNA structure. This shows that the NiP has a very high preference for 3WJ binding compared to dsDNA alone.

The 3WJ-FAM band intensity with PtCyl decreases to 78% with 4 equivalents of Y-fork, and to 67% with 4 equivalents of 4WJ. This decrease in fluorescence is much less than that observed for the NiP or AuPill suggesting that the PtCyl has a higher selectivity for the 3WJ-FAM structure.

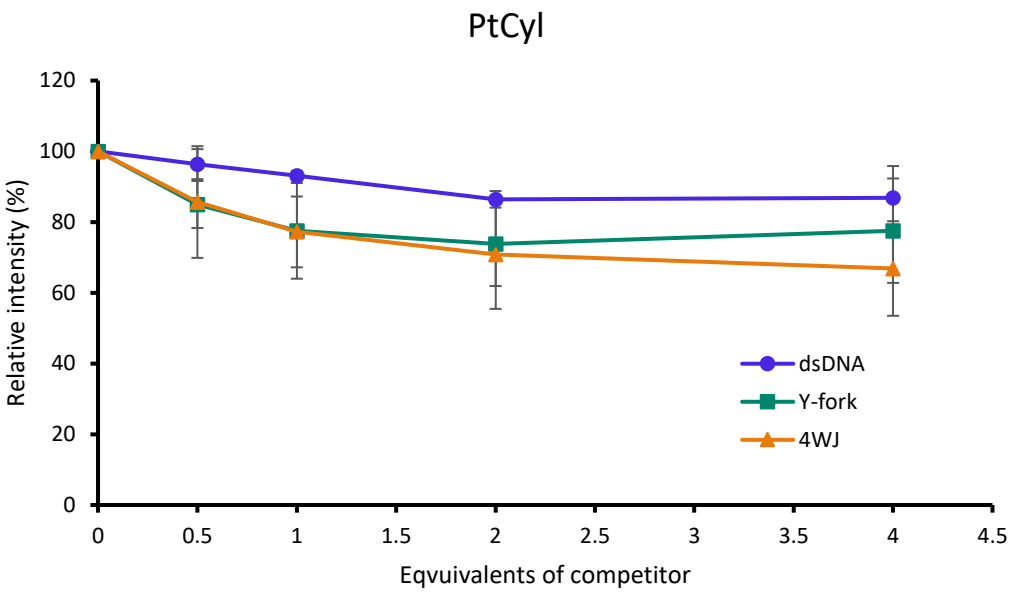


*Figure 17. PAGE competition of 3WJ-FAM vs dsDNA, Y-fork, and 4WJ with PtCyl (1xTris Borate buffer pH 8.4, 120 V, 2.5 hours, average of 3 gels). Quantification of 3WJ-FAM band intensity carried out using ImageJ.*

An argument could be made that the metal complexes will show a preference for whichever structure has the most bases in the structure, simply due to probability and electrostatic interactions. The 3WJ consists of three 14mer oligomers which means the overall structure has 21 base pairs overall. The dsDNA strand used for this experiment was a 21-mer duplex in order to match the number of bases of the 3WJ-FAM. The 4WJ used four 22mer oligomers to make up the overall structure. This means that the structure consisted of 44 base pairs overall. Finally, the Y-fork was created from the S2+S3 of the 4WJ 22mer strands, giving 11 base pairs total. With the number of base pairs in each structure considered, we might expect the order of preference to be 4WJ > dsDNA = 3WJ > Y-fork. With the number of bases alone considered, we might expect the order of preference to be 4WJ > Y-fork > dsDNA = 3WJ. However, the PtCyl does not follow this trend as the 3WJ is heavily preferred in all cases, despite the significantly higher number of bases and base pairs in the 4WJ structure. This again reflects the preference of PtCyl for the 3WJ structure.

## 3.5 PAGE RNA/DNA structure experiments

In these PAGE experiments, we attempt to identify the oligos and potential DNA structures involved in the many bands formed when the metal complexes are added to solutions of complementary oligos designed to form a 4WJ. In this work we are using the same 4WJ oligos utilised by both Mark Searcey and the Hannon group to study 4WJ binding.[1]

### 3.5.1 DNA 3WJ

PAGE gels have been used extensively in the Hannon group to investigate how our metal complexes interact with DNA structures. The 3WJ structure consists of three 14 base oligomers. Recent published work has already compared how the NiP metal complex and AuPill interact with the 14-mer DNA 3WJ structure.[1] The interactions of the PtCyl with the 14-mer 3WJ has also been investigated in Chapter 2. In brief, each metal complex readily forms the DNA 3WJ structure, inducing the formation of a new band in the PAGE gel. The PtCyl and AuPill complexes both form the new DNA 3WJ band which is shifted slightly higher in the gel than the band formed by NiP with the 3WJ oligomers. This indicates the formation of a structure with a larger hydrodynamic diameter. Molecular dynamics simulations of either AuPill or PtCyl with the 3WJ cavity suggest that each both complexes force one of the base pairs at the junction site to break in a very similar manner. This could be responsible for the increased hydrodynamic diameter of the 3WJ formed with these complexes.

### 3.5.2 DNA 4WJ

PAGE gels were used to assess the interaction of our metal complexes with 4WJ. The 4WJ used has been widely studied in the Hannon group and other groups.[1, 38] It is known to readily form a 4WJ structure when all four of the 22 base oligos are mixed in buffered solution. The sharp band at the top of the gel is thought to be the 4WJ in the x-stacked conformation, with the large smear further down the gel being attributed to free 4WJ single stranded oligomers which have not come together to form a junction (Figure 18).

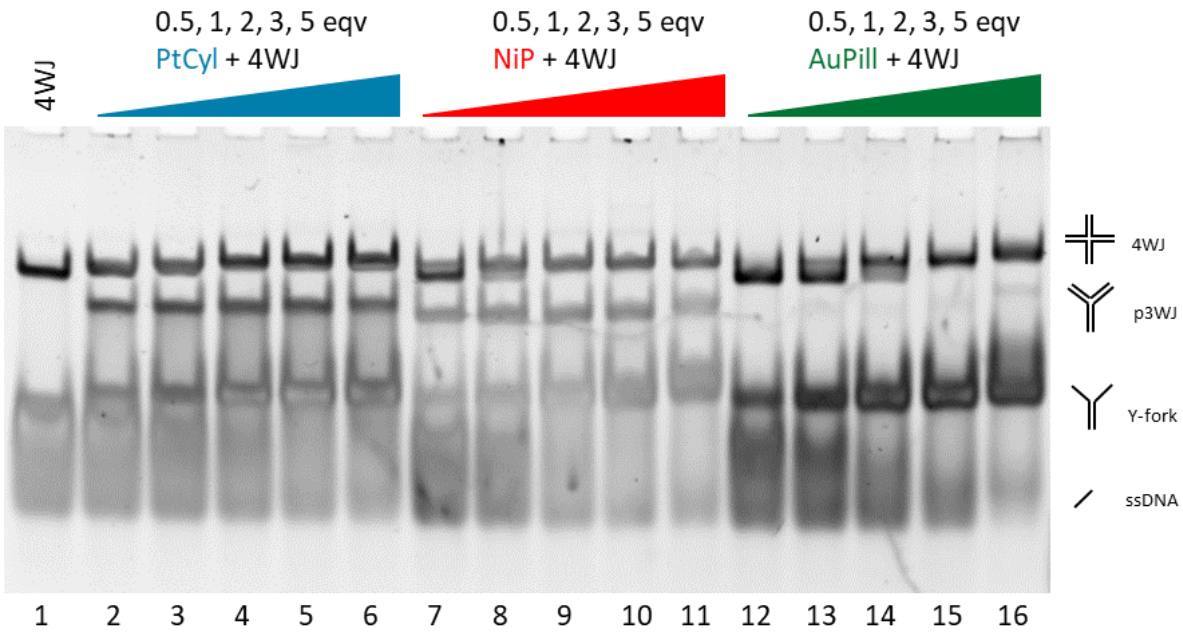


*Figure 18. PAGE gel (1xTris Borate buffer pH 8.4, 120 V, 2.5 hours) of all possible combinations of S1, S2, S3, and S4 that make up the 22mer DNA 4WJ structure with 1 eqv PtCyl in each lane.*

The 4WJ in the presence of NiP produces a number of new bands visible in the gel. The 4WJ band itself begins to split into two separate bands with low equivalents of cylinder, with excess cylinder, the new band slightly higher in the gel takes over completely. It is thought that the new band slightly higher in the gel is due to the 4WJ transforming from an x-stacked from to the open cruciform structure in order to accommodate the metal complex. The new band formed below the 4WJ band is likely the pseudo 3WJ, which is formed due to the partial complementarity of S4 of the 4WJ shown in appendix A3.11. Finally, there is a new band which is formed just above the smear caused by the single stranded oligomers, which is probably due to the Y-fork structures which can form. This Y-fork band appears to broaden and begin to smear with high equivalents of the NiP.

The PtCyl displays the same interactions with the 4WJ as was observed with the NiP (Figure 18). This is surprising given that competition gels indicated that the PtCyl has a lower preference for the 4WJ. In the absence of a 3WJ competitor, it appears that the PtCyl can interact with the 4WJ, Y-fork and p3WJ structures seen in this gel. The PtCyl complex does not induce as much broadening of the Y-fork band as the NiP complex with high equivalents.

The AuPill with 4WJ forms a 4WJ band higher in the gel, much like the PtCyl and NiP complexes did. However, the shift of this band with AuPill was more significant than what was induced by either the PtCyl or NiP. There was a notable absence of the p3WJ when the AuPill was run through the gel with the 4WJ, with only a very faint band appearing with high equivalents of AuPill. This demonstrates the preference that the AuPill has for 4WJ and Y-forks. The Y-fork band increases in intensity across the series with increasing equivalents of pillarplex. The dramatic decrease in intensity of the smear caused by the single stranded oligomers, and the corresponding increase in the Y-fork band, indicates the high affinity the AuPill has for Y-forks.

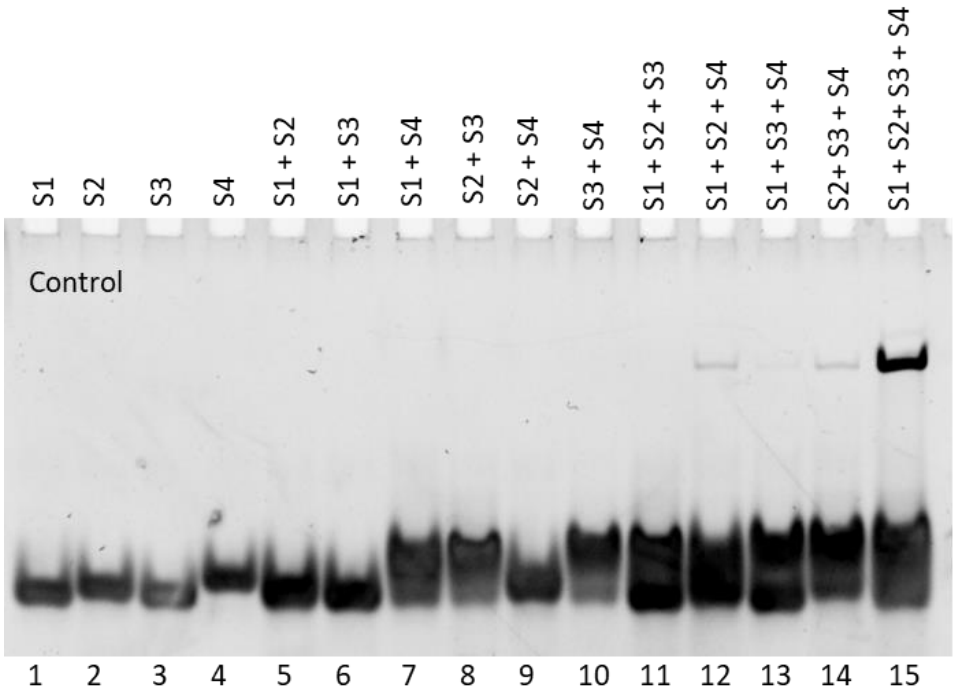


*Figure 19. PAGE gel (1xTris Borate buffer pH 8.4, 120 V, 2.5 hours) of all possible combinations of S1, S2, S3, and S4 that make up the 22mer DNA 4WJ structure used in these studies.*

All combinations of the DNA 4WJ oligomers were run on a PAGE gel to further understand the multitude of bands formed on addition of junction binders to the 4WJ oligomers (Figure 19). The individual single strands of the 4WJ shown in lanes 1-4 do not display any secondary structures and only small differences in the migration of the individual oligos. Lanes 5-10 contain all possible combinations of two of the oligomers which make up the 4WJ structure. No larger structures are observed in lanes 5, 6, and 9. However, lanes 7, 8, and 10 form new bands. These new bands are smeared and not well defined, indicating that they are most likely caused by a multitude of different

species. All possible combinations of three of the oligomers which constitute the 4WJ are presented in lanes 11-14. Each of the lanes containing three oligomers shows some smearing near the location of the single stranded oligomers, as was seen with the combinations of two strands, as well as a new faint band much higher in the gel in all lanes containing S4. The band present much higher in the gel is possibly a pseudo-4WJ (p4WJ) which is made possible by the partial self-complementary nature of S4. Lane 15 contains the combination of all four oligomers which make up the 4WJ structure. A very faint band above the 4WJ band is also visible, this may be due to the open cruciform DNA structure.

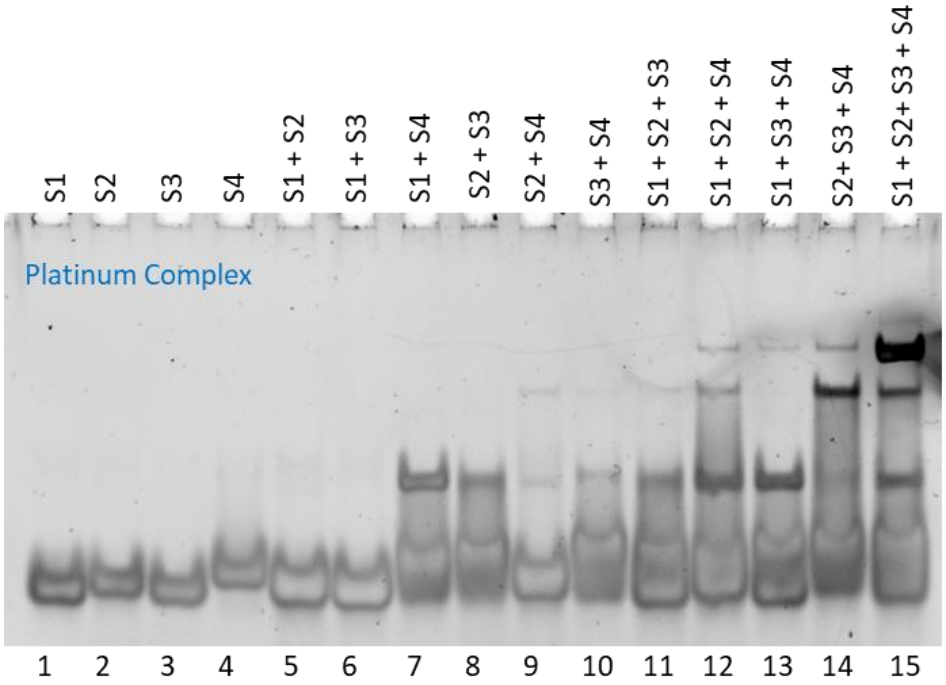


*Figure 20. PAGE gel (1xTris Borate buffer pH 8.4, 120 V, 2.5 hours) of all possible combinations of S1, S2, S3, and S4 that make up the 22mer DNA 4WJ structure with 1 eqv PtCyl in each lane.*

A further PAGE gel was carried out, again with all combinations of the 4WJ oligomers but with 1 equivalent of PtCyl in each lane. On addition of the PtCyl, there is no change to lanes 1-4 containing S1, S2, S3, or S4 (Figure 20). Lanes 7-10 show formation of a new secondary structure which does not migrate as far through the gel as the single stranded oligomers, indicating that it is a larger and/or less highly charged structure. When the PtCyl binds an oligomer, there will be a decrease in the net charge of the structure, however, it is doubtful that this decrease in magnitude of the net charge would cause such a significant retardation in migration rate of the band through the gel. Therefore, the new band is attributed to the formation of a new, larger DNA structure. The new band formed is attributed to a

Y-fork structure as only two oligomers are present, and online software (RNAstructure) shows how the base pairing allows this to occur. We theorize that the metal complex is able to bind at the Y-fork junction in much the same way as it does in a 3WJ, lowering the energy barrier to formation of this new structure. Lane 9 containing S2 + S4 displays a small amount of the Y-fork structure (which is surprising as S2 and S4 are not complementary, and so may represent an S4-S4 structure) as well as a third, faint band, higher up in the gel. This third band is attributed to the formation of a p3WJ which is made possible by the partial self-complementarity of S4.

The four lanes (lanes 11-14) containing combinations of three of the oligomers which make up the 4WJ containing S4 all have a new, faint peak which is attributed to the p4WJ. Notably, the lane containing S1 + S2 + S3, but no S4, does not contain the p4WJ structure. This supports the theory that the p4WJ is thought to be due to the partial self-complementarity of the S4 strand. Finally, lane 15 contains all four of the oligomers and the PtCyl. The 4WJ band is still present and is broadened compared to the 4WJ without the metal complex, there is also the formation of Y-fork structures and p3WJ.

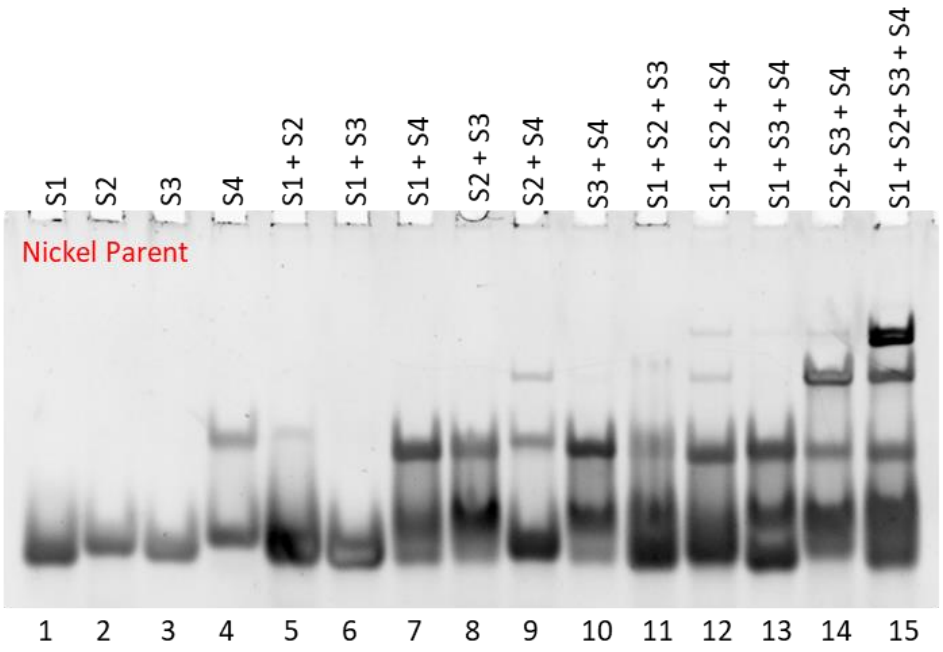


*Figure 21. PAGE gel (1xTris Borate buffer pH 8.4, 120 V, 2.5 hours) of all possible combinations of S1, S2, S3, and S4 that make up the 22mer DNA 4WJ structure with 1 eqv NiP in each lane.*

Another PAGE was carried out with all possible oligo combinations but this time with NiP in all lanes. The NiP with the 4WJ oligo combinations forms the same structures as has been observed with the

PtCyl complex, with some subtle differences (Figure 21). The Y-fork structures observed in many of the lanes are generally more intense than what has been observed with the PtCyl complex. In particular, the Y-fork in lane 14 is much more intense with the NiP. The 4WJ band in lane 15 has formed broadened and appears to be separating into two distinct bands.

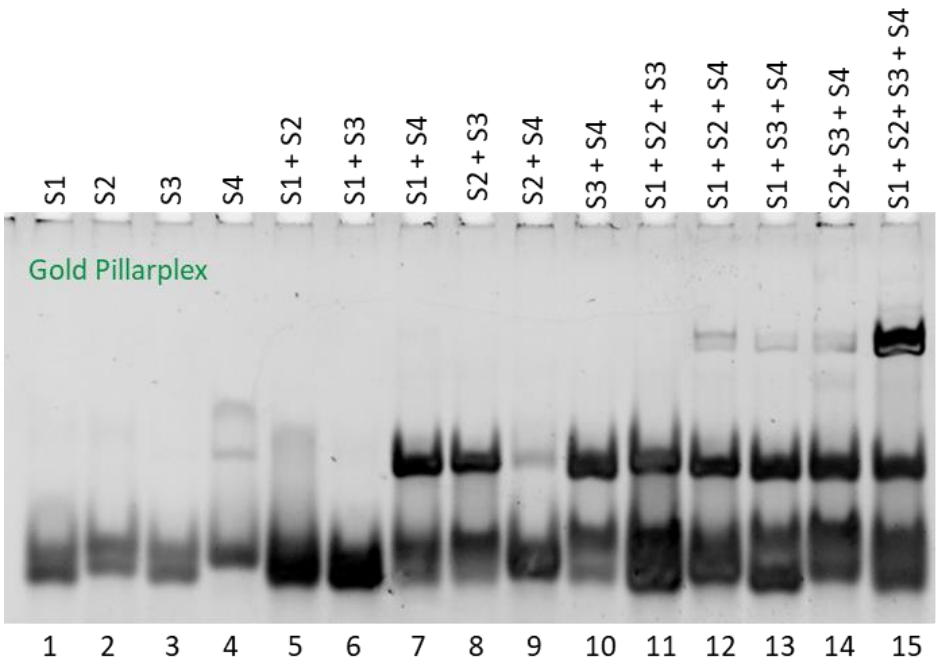


*Figure 22. PAGE gel (1xTris Borate buffer pH 8.4, 120 V, 2.5 hours) of all possible combinations of S1, S2, S3, and S4 that make up the 22mer DNA 4WJ structure with 1 eqv AuPill in each lane.*

In another PAGE with AuPill, addition of the AuPill to S1, S2, and S3 causes some splitting of the band attributed to the single stranded oligomers (Figure 22). Two new bands are formed on addition of AuPill to S4, one of which is again probably due to the self-complementarity of the S4 strand. Where possible, a band which is attributed to a Y-fork structure is formed, demonstrating the preference of AuPill for a forked DNA structure. There is a noticeable absence of the pseudo-3WJ which is observed with the PtCyl and NiP complexes. The p4WJ band appears to be separated into two distinct bands in lanes 12, 13 and 14. The reason for this is not currently known.

The PAGE gels presented here emphasise the preference of the NiP and PtCyl for 3WJ and p3WJ structures where possible. The clear preference of the AuPill complex for Y-forks is also seen. The AuPill forms Y-forks with combinations of the 4WJ oligomers whenever it is possible. The formation of p4WJ

structures by all of the complexes was not anticipated but can be explained by the partial complementarity of the S4 oligomer.

### 3.5.3 RNA 3WJ

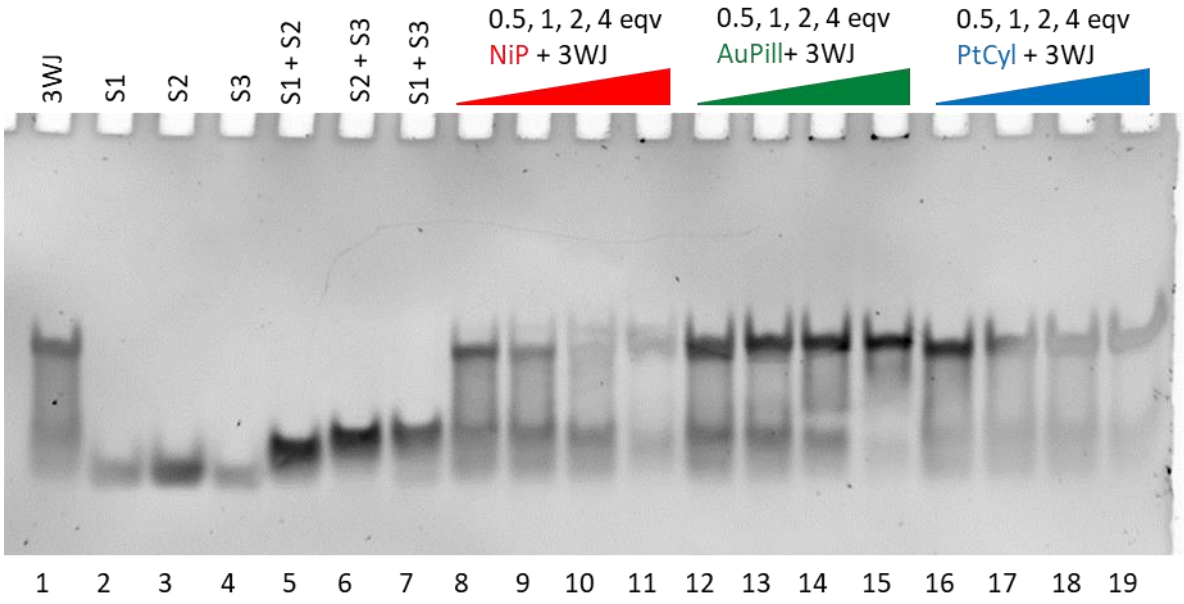


*Figure 23. PAGE gel (1xTris-Borate pH 8.4, 120 V, 2.5 hours) of RNA 3WJ with increasing equivalents of NiP, AuPill, or PtCyl.*

A major difference between the DNA 3WJ and RNA 3WJ is the increased stability of the RNA junction, which allows the RNA 3WJ to form spontaneously with no junction binder present in solution. This is shown in Figure 23, where the 3WJ band is clearly visible with a significant smear beneath it, representing undefined structures which are also forming in solution. Unlike the DNA 3WJ, combinations of two of the oligomers cause the formation of new bands, which indicate Y-fork formation. With increasing equivalents of NiP, the RNA 3WJ formed another structure which is visible as a separate band which moves more slowly through the gel than the 3WJ alone. This is similar to what was observed by Phongtongpasuk *et al.* with the analogous iron helicate, though the fork structure was more prominent in their studies.[39] It is unclear at this point what the identity of this new structure is, but one possibility is that the different enantiomers of the NiP interact differently with the RNA 3WJ structure, causing the formation of the two separate bands. This is unique compared to the PtCyl or AuPill, which both display a single band in the region of the 3WJ structure. Increasing equivalents of PtCyl or AuPill with the RNA 3WJ did not induce the formation of any new bands but

there was a visible decrease in the intensity of the smear attributed to the single stranded oligomers indicating that they promote the formation of the 3WJ. It was somewhat surprising that the AuPill promotes the formation of RNA 3WJ, as the cavity of the RNA 3WJ is smaller than that of the DNA 3WJ which is already a tight fit for the AuPill.[39]

### 3.5.4 RNA 4WJ

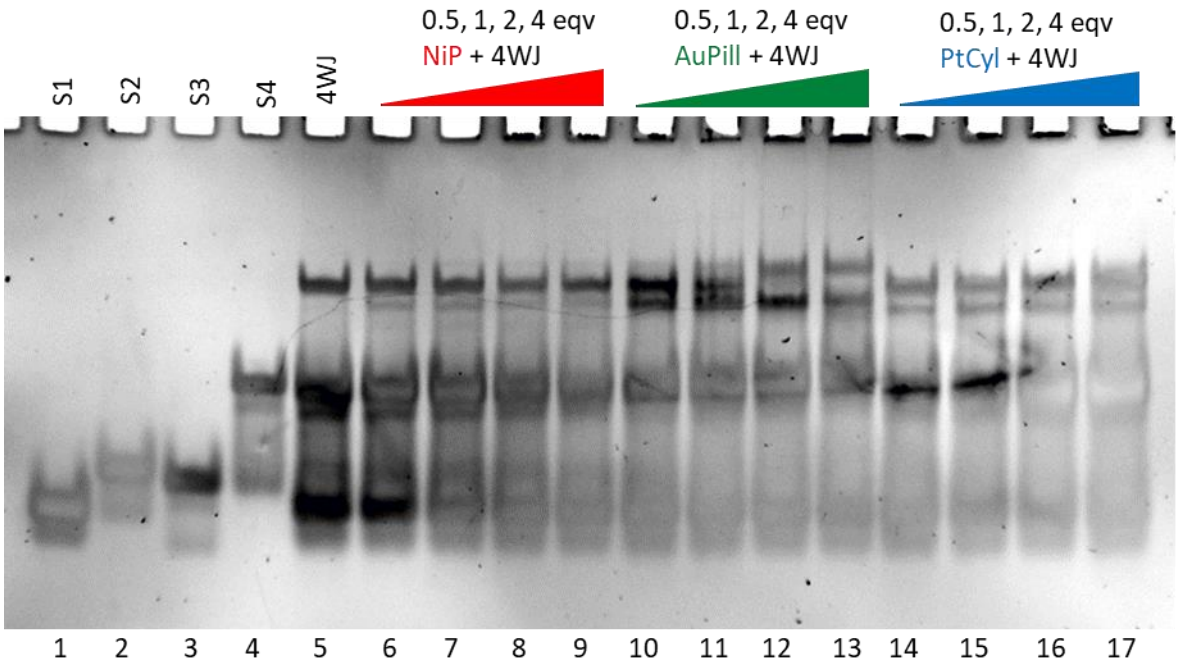


*Figure 24. PAGE gel (1xTris-Borate pH 8.4, 120 V, 2.5 hours) of RNA 4WJ with increasing equivalents of NiP, AuPill, or PtCyl Lanes 1-4 contain S1-S4 with no metal complex. Lane 5 contains a combination of S1+S2+S3+S4 and no metal complex.*

The interaction of the metal complexes with the RNA 4WJ was first investigated by using PAGE gels (Figure 24). The 4WJ was incubated with increasing equivalents of metal complex to see if any new DNA structures form, by observing the bands migration through the PAGE gel. Each of the single strands (S1-S4) contained the same number of bases but shifted differently through the gel as they can all form different secondary structures. The S4 strand interacts strongly with itself as it has a large component which is self-complementary, this new band is most likely a dimer of S4. Lane 5 containing all four oligomers produces a new band which did not shift as far through the gel, this is attributed to the 4WJ structure. The second, intense band in the gel is attributed to a Y-fork structure. This structure is not observed with the DNA 4WJ alone suggesting that the RNA forked structure is more stable than the DNA forked structure.

In the presence of the NiP, a new band forms below the RNA 4WJ band, at higher equivalents, a faint band higher up in the gel also forms. The band below the 4WJ could be due to the cylinder binding to the 4WJ, creating a more compact structure. This would be the opposite of what is observed with the DNA 4WJ, which opens to form a cruciform structure which is larger. Alternatively, it could be due to the formation of a p3WJ as is seen with the DNA 4WJ. The band is significantly less intense than is observed with the DNA, though. The PtCyl causes the formation of what appears to be the same band below the 4WJ band (lanes 14-17). With higher equivalents of the PtCyl, the 4WJ band with the platinum complex begins to smear and move slightly higher in the gel. The AuPill with the RNA 4WJ also induces the formation of a new band below the 4WJ. This potential p3WJ band is more intense than what is observed for either PtCyl or NiP. This questions the identity of this band, as we have shown in previous gels that the AuPill has a strong preference for Y-fork and 4WJ structures. Higher equivalents of the AuPill with the RNA 4WJ causes the 4WJ band to shift higher in the gel, indicating that the AuPill is binding to the junction, possibly with more than one pillarplex per junction. This suggests a different binding mode other than the typical binding in the central cavity of the junction. This may also simply be the AuPill interacting with the ends of the duplexes. Simulations described in recent publications also show that the AuPill interacts strongly with the ends of duplexes.[1]

The PtCyl behaves in a similar way to the NiP with the RNA 4WJ. The Y-fork structure band does not change across the series, and two bands are visible high in the gel around where we expect to observe the 4WJ band. However, with increasing equivalents of the PtCyl, the RNA 4WJ band begins to broaden.

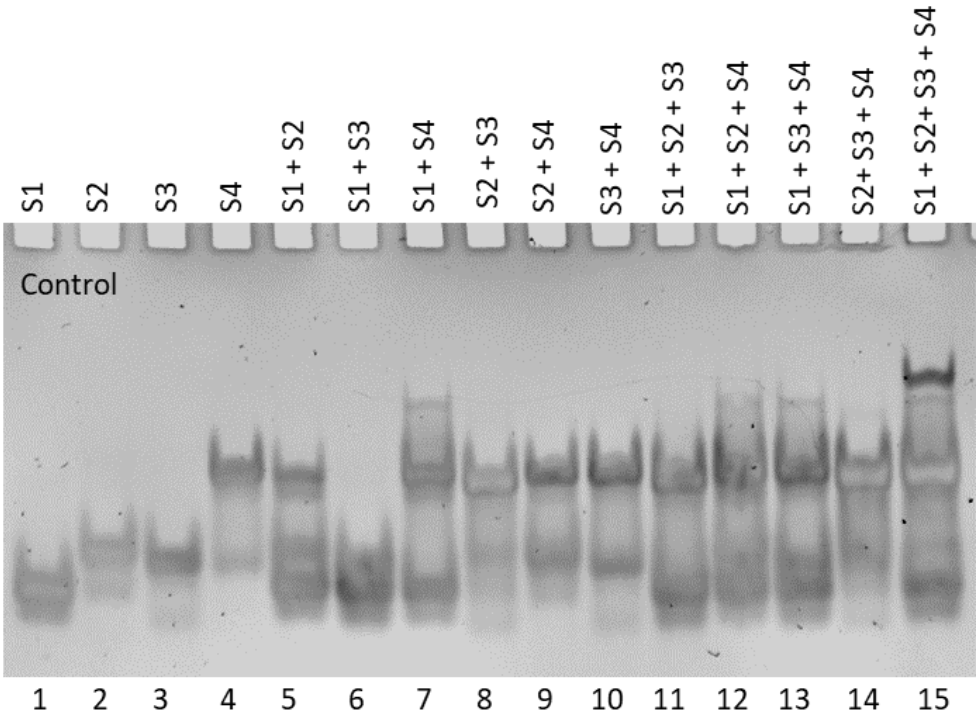


*Figure 25. PAGE gel (1xTris Borate buffer pH 8.4, 120 V, 2.5 hours) of all possible combinations of S1, S2, S3, and S4 that make up the 22mer RNA 4WJ structure utilised in these studies.*

To further investigate the interaction of the metal complexes with the RNA 4WJ and other RNA structures which can form, one equivalent of a metal complex is incubated with all of the possible combinations of the oligomers constituting the RNA 4WJ structure. The control gel where all possible combinations of the RNA strands S1, S2, S3, and S4 were combined is shown in Figure 25. The individual strands all migrate differently through the gel due to the strong secondary structures formed by the RNA. S4 is partially self-complementary causing the formation of a much larger structure and hence a much smaller band shift. All combinations of two RNA oligomers (lanes 5 to 10), apart from S1 + S3, form new bands which are attributed to the Y-fork as expected. S1 + S3 displays no new secondary structure indicating no significant interaction between the two oligomers. The combination of S1 + S4 forms a Y-fork band but also another band, which is likely due to a p3WJ structure. The fact that S3 + S4 does not form a p3WJ implies that there is some additional partial hybridization between S1 and S4 (shown in appendix A3.12). Only lanes containing S1 and S4 appear capable of forming a p3WJ structure, as seen in lanes 7, 12, 13, and 15. Finally, all of the RNA 4WJ oligomers combined together (lane 15) lead to the formation of a new band which does not migrate very far through the gel, which we attribute to the RNA 4WJ.

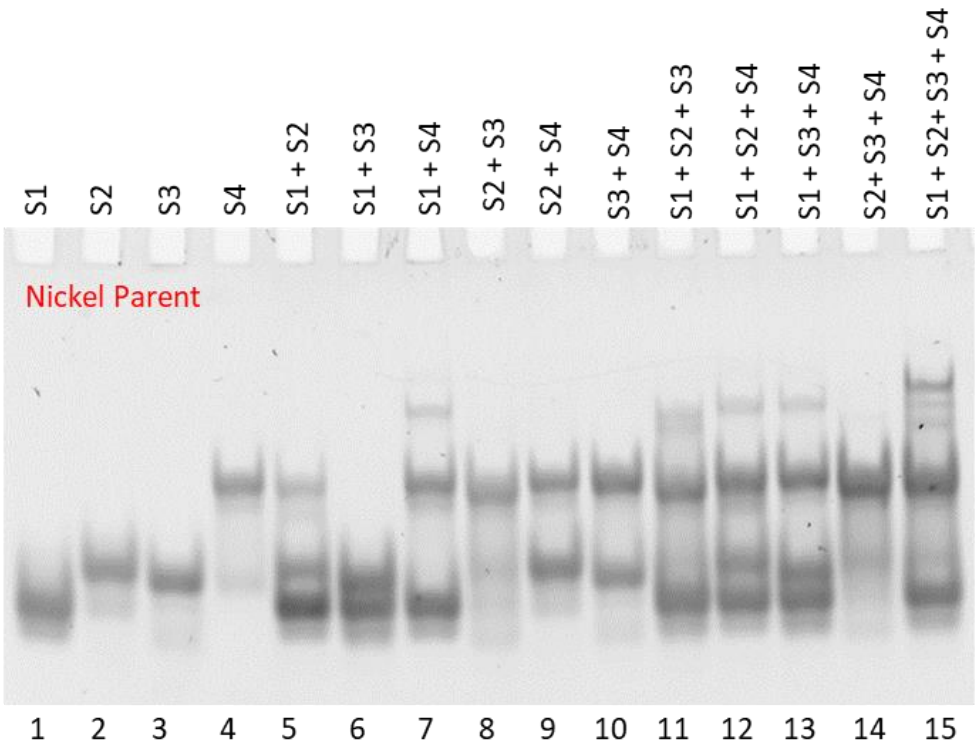


*Figure 26. PAGE gel (1xTris Borate buffer pH 8.4, 120 V, 2.5 hours) of all possible combinations of S1, S2, S3, and S4 that make up the 22mer RNA 4WJ structure with one equivalent of NiP in all lanes.*

The addition of 1 equivalent of NiP to each of the individual RNA 4WJ oligomers does not induce any change in the band shifts (Figure 26). There are also no changes to the combinations of two oligomers when NiP is added. All the lanes with three RNA oligomers, apart from that containing S2 + S3 + S4, form a p3WJ band. The p3WJ formed with S1 + S2 + S3 appears to have migrated further through the gel, further than the p3WJ formed in lanes 12 and 13. There are no further structures formed in lane 14 containing S2 + S3 + S4. Lane 15, containing all four of the RNA 4WJ oligomers, displays the expected 4WJ and Y-fork bands with two fainter bands present roughly where p3WJ bands align. This again demonstrates the strong preference of NiP for 3WJ structures.

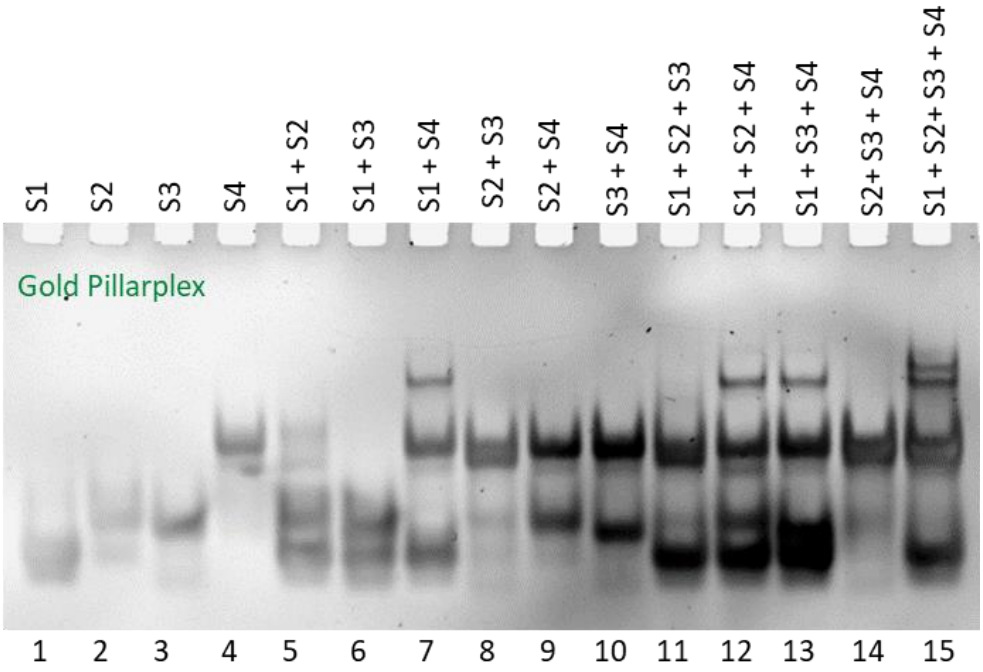


*Figure 27. PAGE gel (1xTris Borate buffer pH 8.4, 120 V, 2.5 hours) of all possible combinations of S1, S2, S3, and S4 that make up the 22mer RNA 4WJ structure with one equivalent of AuPill in all lanes.*

Addition of AuPill to combinations of RNA 4WJ oligomers displays similar effects to those observed when NiP is added, with differences only observed in lanes 11 and 15 (Figure 27). In lane 11, the AuPill does not induce the formation of a p3WJ structure. With all the RNA 4WJ oligomers combined in lane 15, the AuPill forms a clear and defined single p3WJ band compared to the two faint bands included by the NiP.

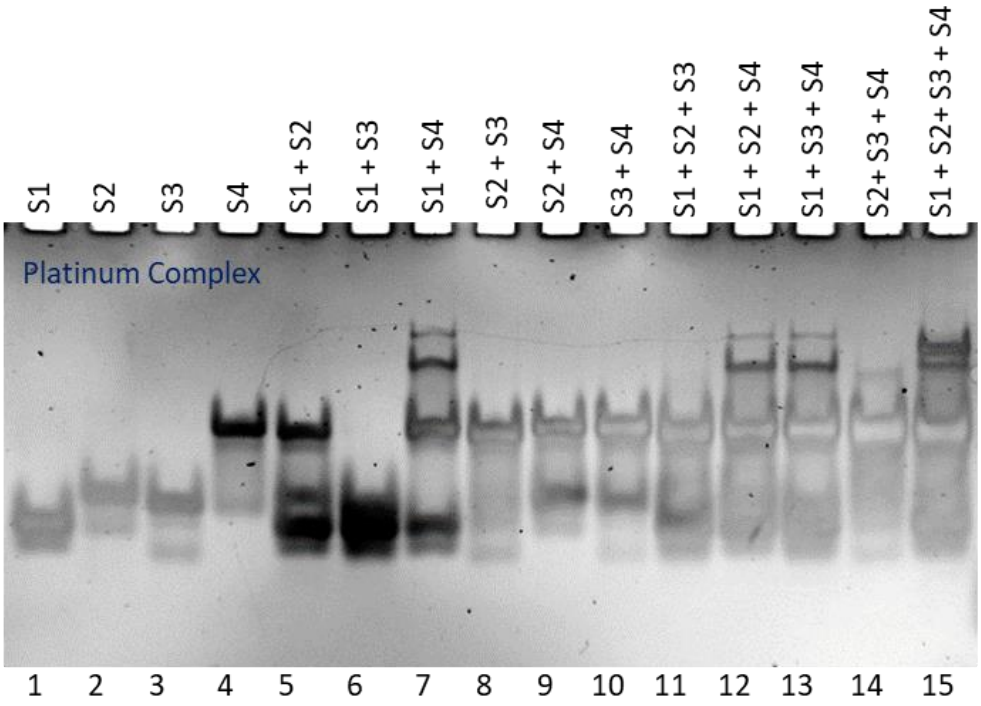


*Figure 28. PAGE gel (1xTris Borate buffer pH 8.4, 120 V, 2.5 hours) of all possible combinations of S1, S2, S3, and S4 that make up the 22mer RNA 4WJ structure with one equivalent of PtCyl in all lanes.*

The PtCyl complex with RNA 4WJ oligomers leads to the formation of some new structures (Figure 28). Most surprisingly, lane 7, containing S1 + S4, forms a very distinct p3WJ as well as a band which aligns with the RNA 4WJ but has not shifted quite as far through the gel. The 4WJ band formed in lanes 12 and 13 also form a 4WJ band which does not shift as far through the gel as the 4WJ alone indicating that a larger structure is formed. This is unusual and hints that the PtCyl may have some unique interactions with the RNA 4WJ in comparison to the other two metal complexes investigated. This gel was repeated with fresh RNA solutions to confirm the results.

The metal complexes display interesting interactions with the RNA 4WJ which are distinct from the interactions observed with the DNA 4WJ. The NiP forms new and, as yet unidentified structures with the 3WJ which are not formed with the other metal complexes. The NiP and AuPill both show little interaction with the RNA 4WJ oligomers, perhaps due to the inherent stability of the RNA structures already formed. However, they both induce the formation of more p3WJ bands. The AuPill does appear to have a unique effect on the RNA 4WJ structure with high equivalents of the complex, inducing the formation of a much larger structure. The PtCyl complex displays some interesting interactions with

the RNA 4WJ with a surprising affinity for a p4WJ structure which appears larger than the RNA 4WJ alone. The unique interactions of the PtCyl with the RNA 4WJ warrants further investigation.

## 3.6 Mass spectrometry studies

Mass spectrometry has proven to be a versatile tool to investigate biomolecules, from proteins to DNA. Indeed, mass spectrometry has been extensively used for proteomics for many years. It has been used for identification, characterisation of protein interactions with small molecules and DNA, as well as kinetic studies.[40] Mass spectrometry can be used in much the same way for nucleic acid structures. In more recent years, mass spectrometry of native DNA structures has become more wide-spread, particularly of G-quadruplexes.[41] Valerie Gabelica and co-workers have been prolific in their use of native mass spectrometry to study the thermodynamic and kinetic properties of G-quadruplexes alone, and their interactions with binding agents.[42-48] Gabelica states in a Accounts of Chemical Research article that:

> "the next objective will be to generalize these methodologies to a wider range of nucleic acid structures"[49]

Thus far, the only published work which has used native mass spectrometry to study DNA 3WJ is that carried out by Monchaud and co-workers.[28, 50] They were able to observe the binding of an azacryptand to a 3WJ using mass spectrometry. In this section, mass spectrometry was investigated as a potential tool to further our understanding of metal complex binding to DNA and RNA junctions.

### 3.6.1 PAGE 3WJT6 controls

In order to study the binding of these metal complexes to 3WJ by mass spectrometry, a suitable 3WJ structure had to be found. Initial attempts to utilise the 14mer 3WJ or 18mer 3WJ were unsuccessful as the complex falls apart under the mass spectrometry conditions, revealing only the individual oligomers when analysed. Work by David Monchaud and co-workers has previously studied binding of an organic compound to 3WJ by using a 3WJ structure which self-assembled from a single oligomer

with hairpin loops inserted to allow the folding.[28] We decided to use the same DNA structure (3WJT6, Figure 29) to study the binding of our metal complexes to a 3WJ by mass spectrometry.

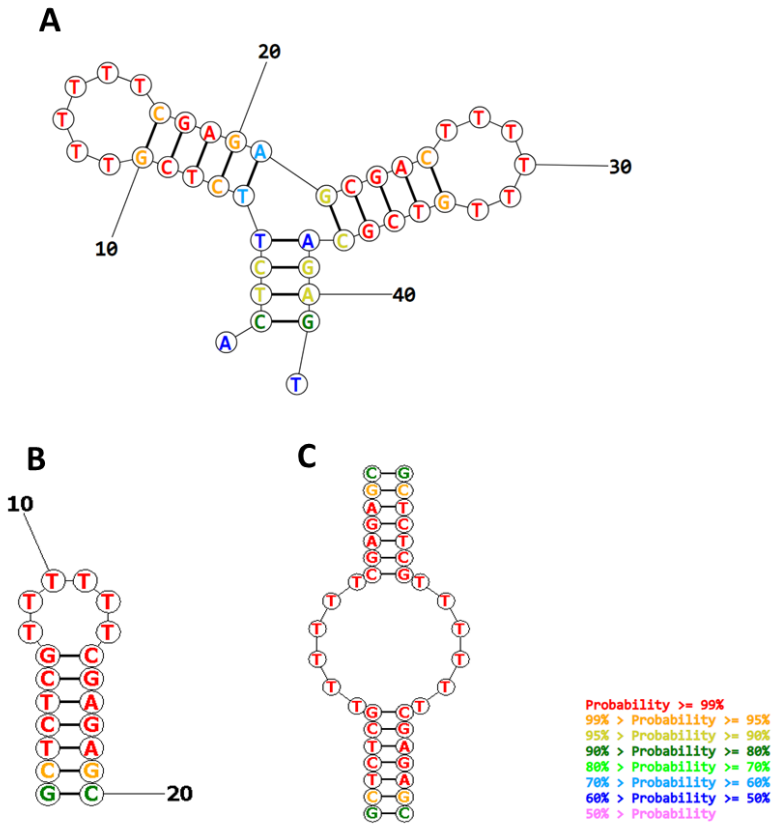


*Figure 29. Structures as predicted by RNAstructure software: A) 3WJT6, B) 3WJT6 loop, and C) 3WJT6 loop dimer.*[51]

Some concerns arose around using the 3WJT6 with our metal complexes. First and foremost, we needed to determine if the 3WJ structure we sought was forming. We then needed to determine if our metal complexes were binding to the junction created.

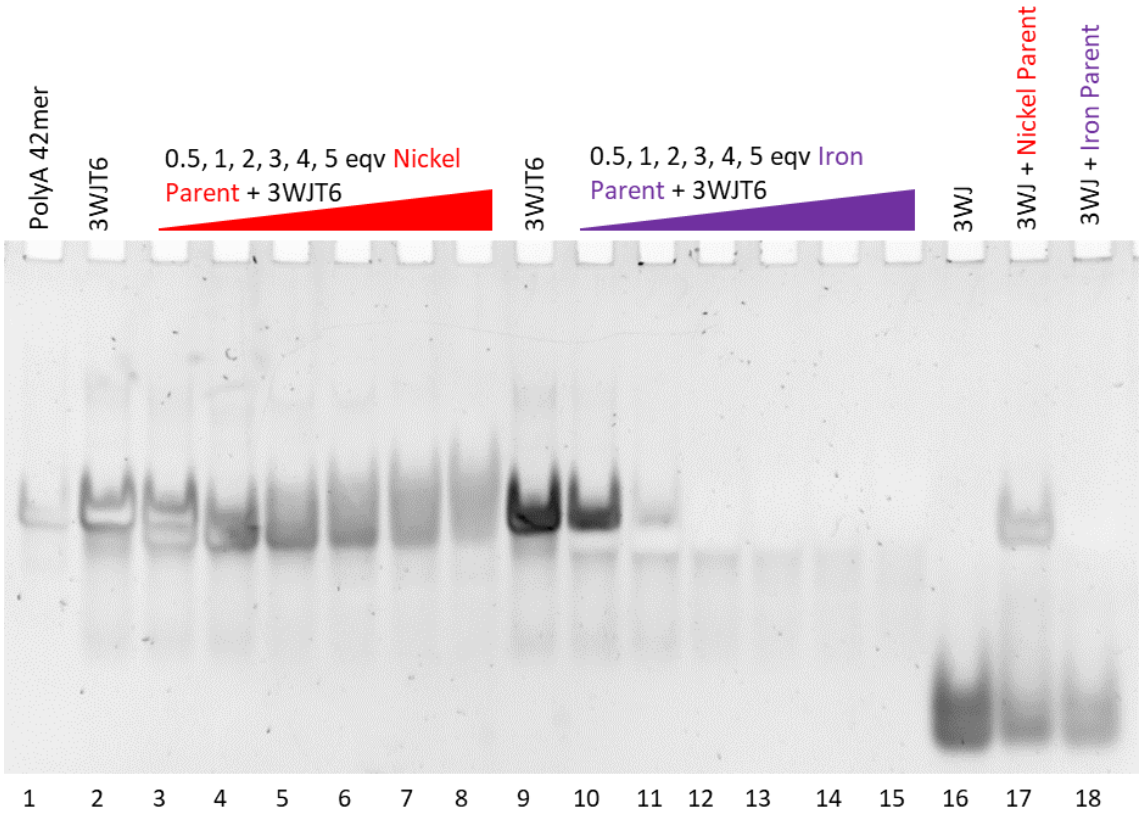


*Figure 30. PAGE gel (1xTris Borate buffer pH 8.4, 120 V, 2.5 hours) of 3WJT6 with increasing equivalents of NiP or FeP.*

The gel presented in Figure 30 contains the 3WJT6 with varying equivalents of either NiP or equivalent complex with iron metal centres (FeP – iron parent). Lane 1 of the gel contains a polyadenine (PolyA) oligo, of the same length as the 3WJT6 structure, as a control to determine if the 3WJT6 structure is folding and forming a secondary structure or is linear under electrophoresis conditions. Comparing the 3WJT6 (lane 1) to the PolyA (lane 2) reveals little difference in the band shifts, indicating that the 3WJT6 oligo is not folded. In the presence of the NiP, a second band forms which moves further through the gel, indicating the formation of a smaller, more compact structure, we take this to be the folded junction structure. DNA folding software was used to confirm that the DNA oligo was able to form the junction structure (Figure 29).[51] At 1 equivalents of the NiP, there is almost none of the original 3WJT6 structure band left, indicating a 1:1 binding mode which is what we expect for the junction structure. With increasing equivalents of the cylinder, the bands become smeared, indicating the formation of undefined, random structures in solution. Non-specific binding of the NiP to the DNA could cause the formation of these random structures. To confirm that the complex is present in the new 3WJ band formed, identical solutions were prepared with the FeP (lanes 10-15).

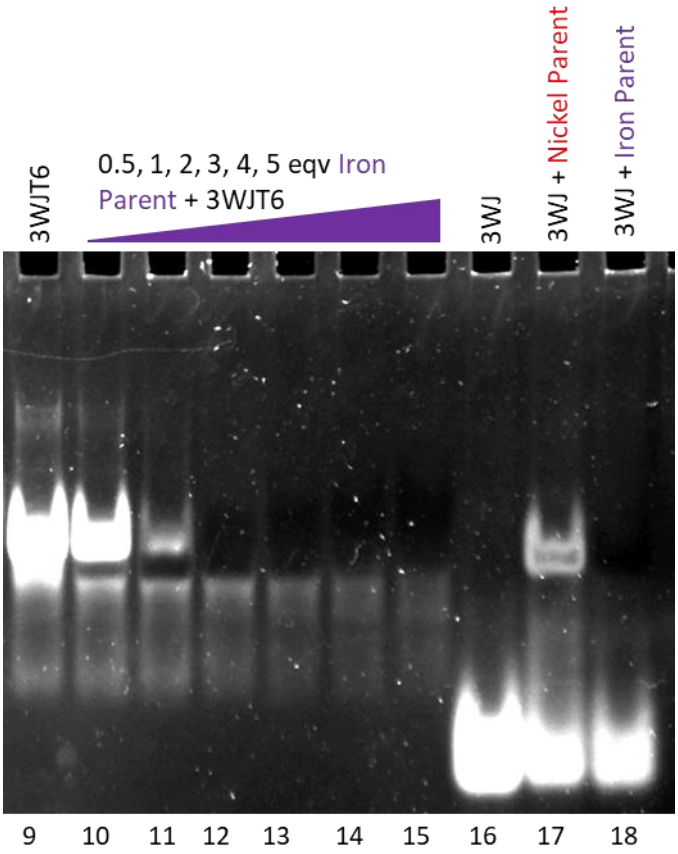


*Figure 31. Stretched image of PAGE gel showing 3WJT6 oligo with increasing concentrations of iron parent cylinder and controls (89 mM Tris-borate pH 8.4, 120 V, 2.5 hours).*

The FeP helicate strongly absorbs at ~580 nm and quenches the SYBR gold which we used to visualise the DNA bands in the gel. At 1 equivalent of the iron parent cylinder, almost no band is visible due to the quenching by the FeP helicate (lane 11, Figure 30). The new 3WJT6 band can be visualised as "negative contrast" if the image is inverted and the contrast is aggressively enhanced using ImageJ (Figure 31). With the contrast of the gel image enhanced, the 3WJT6 band is visible along with the smearing with increasing concentrations of the iron parent cylinder. This is the same as was observed for the NiP. This confirms that the metal complex (iron parent cylinder in this case) is present with this new DNA structure in solution.

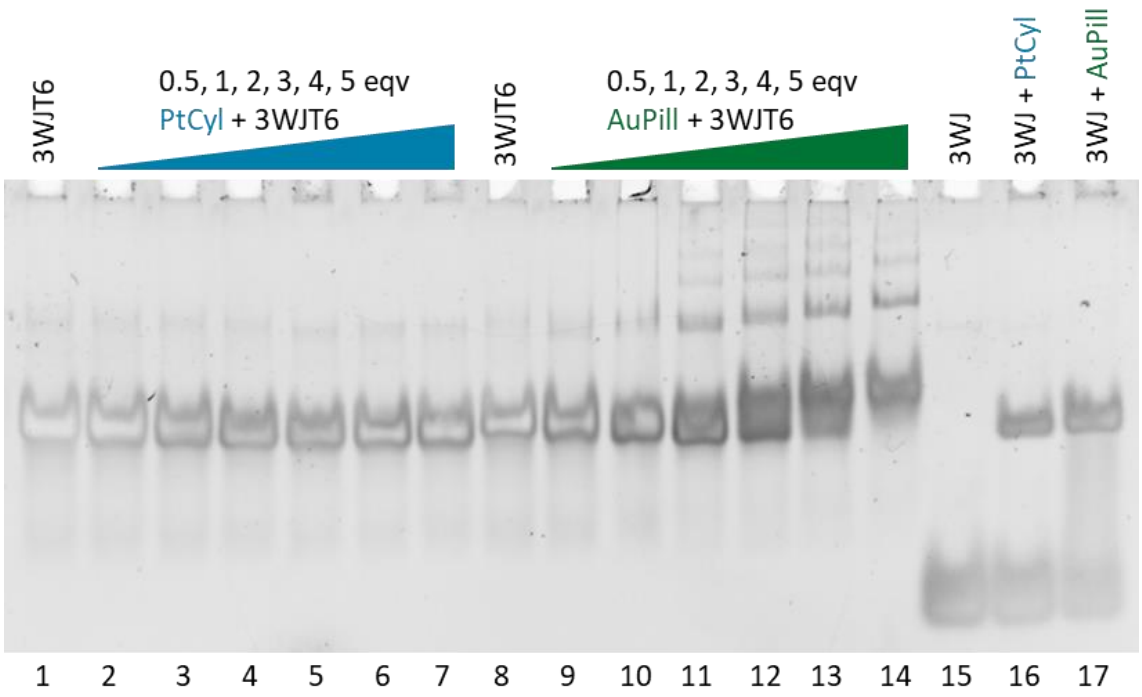


*Figure 32. PAGE gel (1xTris Borate buffer pH 8.4, 120 V, 2.0 hours) of 3WJT6 with increasing equivalents of PtCyl or AuPill.*

The interaction of PtCyl and AuPill with 3WJT6 was also investigated by PAGE (Figure 32). The PtCyl appears to have little interaction with the 3WJT6, with only a slight increase in the migration of the DNA structure through the gel. This increased migration is most obvious when comparing lanes 7 and 8. A slight shift in the 3WJT6 band is also observed when incubated with AuPill. With higher equivalents of the complex, smearing begins to occur and new bands begin to form higher in the gel, indicating significantly larger structures. These larger structures appear to be unique to the AuPill but what they are is unclear. An alternative binding mode for the metal complexes to the 3WJT6 was to bind in the hairpin loop sections of the DNA. It has been demonstrated in the past, by Victor-Brabec and co-workers, how FeP readily binds to DNA bulges which are similar to hairpin loops.[8] To address this possibility, another PAGE gel was carried out where the metal complexes were incubated with a hairpin loop structure derived from the 3WJT6 (Figure 33).

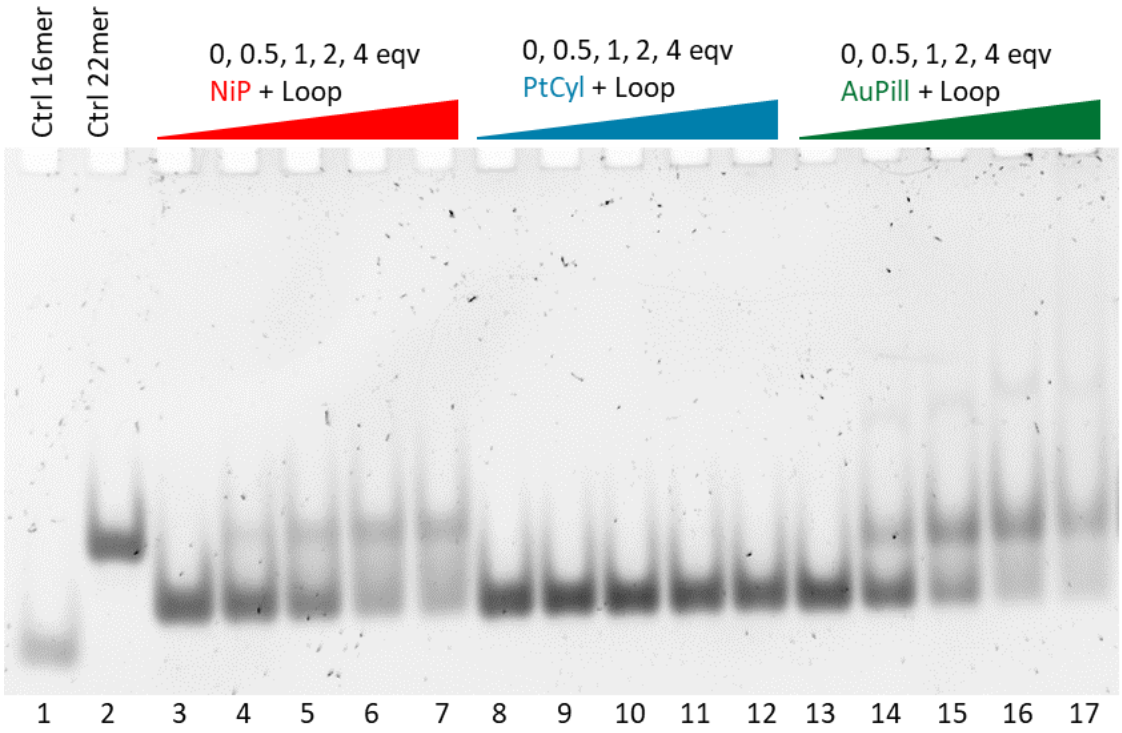


*Figure 33. PAGE gel (1xTris Borate buffer pH 8.4, 120 V, 2.5 hours) of 3WJT6 loop with increasing concentrations of NiP, AuPill, and PtCyl.( Lane 1 = Control oligomer 16 bases in length, Lane 2 = Control oligomer 22 bases in length)*

One of the hairpin loop sections of the 3WJT6 was obtained (Figure 29) (called "Loop" from here on) and a PAGE gel was carried out with the Loop and increasing concentrations of each metal complex (Figure 33). The Loop oligo is 20 bases in length; the location of the band between the 16mer and 22mer controls indicate that the Loop is likely in its compact, looped structure without any of the metal complexes present. With increasing concentration of NiP, a new band forms higher in the gel which increases in intensity across the series. This new structure is larger than the original oligo and could be due to a dimer forming (Figure 29). This dimer would have a very large 12 base bulge making quite unstable, binding of NiP to this bulge suggests that it has a low affinity for the Loop structure. The PtCyl does not appear to show any interaction with the Loop oligomer. The AuPill displays a similar interaction to the NiP, with the formation of a new band which increases in intensity with higher equivalents of AuPill. This new band appears to shift slightly further than that produced by the NiP complex. Due to how close the bands are, it is likely that the general structure is the same but the AuPill structure with the DNA is more compact. The AuPill also produces a faint band much higher in the gel, indicating the formation of much larger, more complex structures which have not been identified.

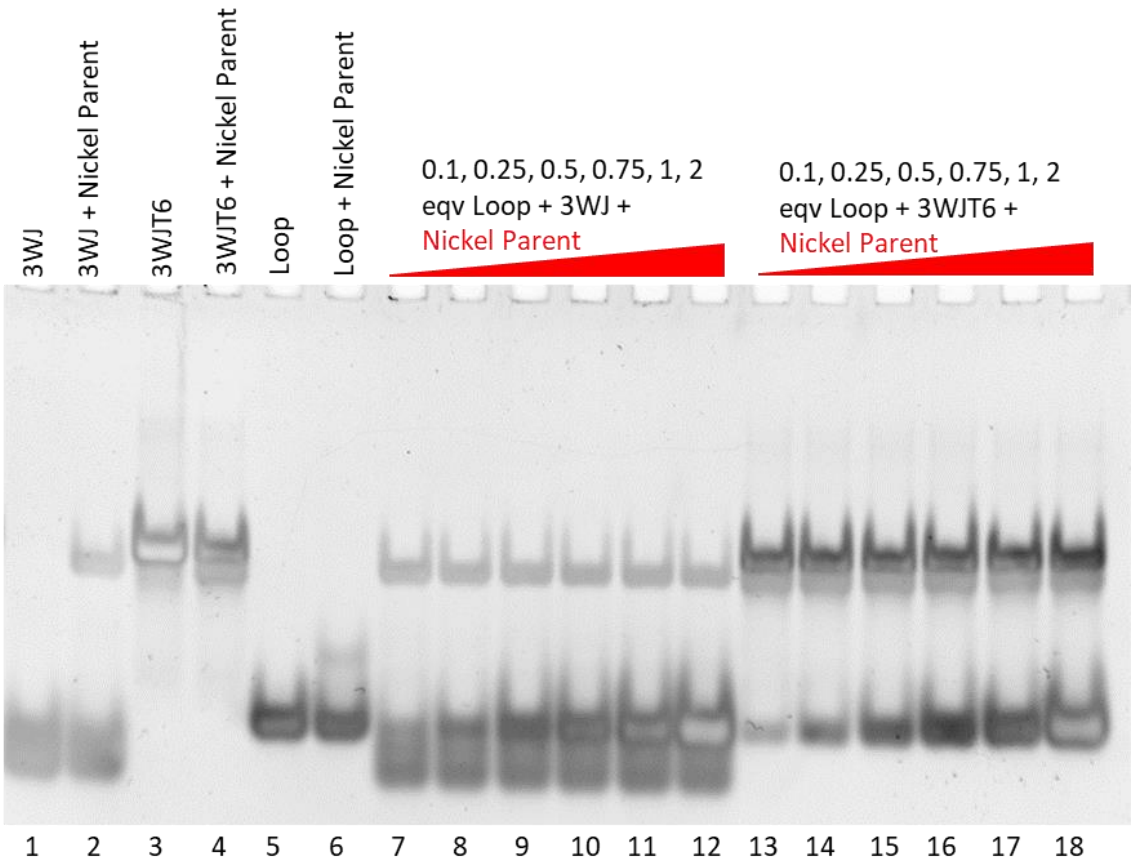


*Figure 34. PAGE gel (1xTris Borate buffer pH 8.4, 120 V, 2.5 hours) of Nickel Parent with either 3WJ or 3WJT6 and increasing equivalents of a competing 3WJT6-loop structure.*

A PAGE gel was used to compete the Loop structure with three-way junction structures, with the aim to determine which structures the metal complexes would have a higher affinity for (Figure 34). The experiment was carried out by keeping the ratio of NiP to junction constant and increasing the concentration of the Loop structure. Even with 2 equivalents of the loop structure, none of the dimer structure observed for the loop with the metal complex alone (Figure 33) form, indicating that the metal complex has a strong preference for the junction structure. Due to the suspected formation of the dimer structure, future work would benefit from using an oligomer with a longer duplex section to encourage formation of the hairpin loop.

### 3.6.2 Mass Spectrometry of 3WJT6 with metal complexes

Appropriate conditions for running nucleic acids on the mass spectrometer setup had to be established before any data could be acquired. The parameters used by Zell *et al.* were used as a starting point for our optimization; the concentration of ammonium acetate had to be reduced from 100 mM to 10 mM in order to obtain clear MS signals (appendix A3.13), but the methanol concentration in these studies could be reduced from 20 % to 10 % and still reliably give a good MS signal.[28] Addition of methanol improves the ionisation efficiency due to its effect on the surface tension and solvent viscosity.[52] However, adding organic solvents can also effect the equilibria in solution. A concentration of 150 mM ammonium acetate mimics physiological ionic strength making this the ideal concentration if the purpose is to mimic physiological conditions.[41]

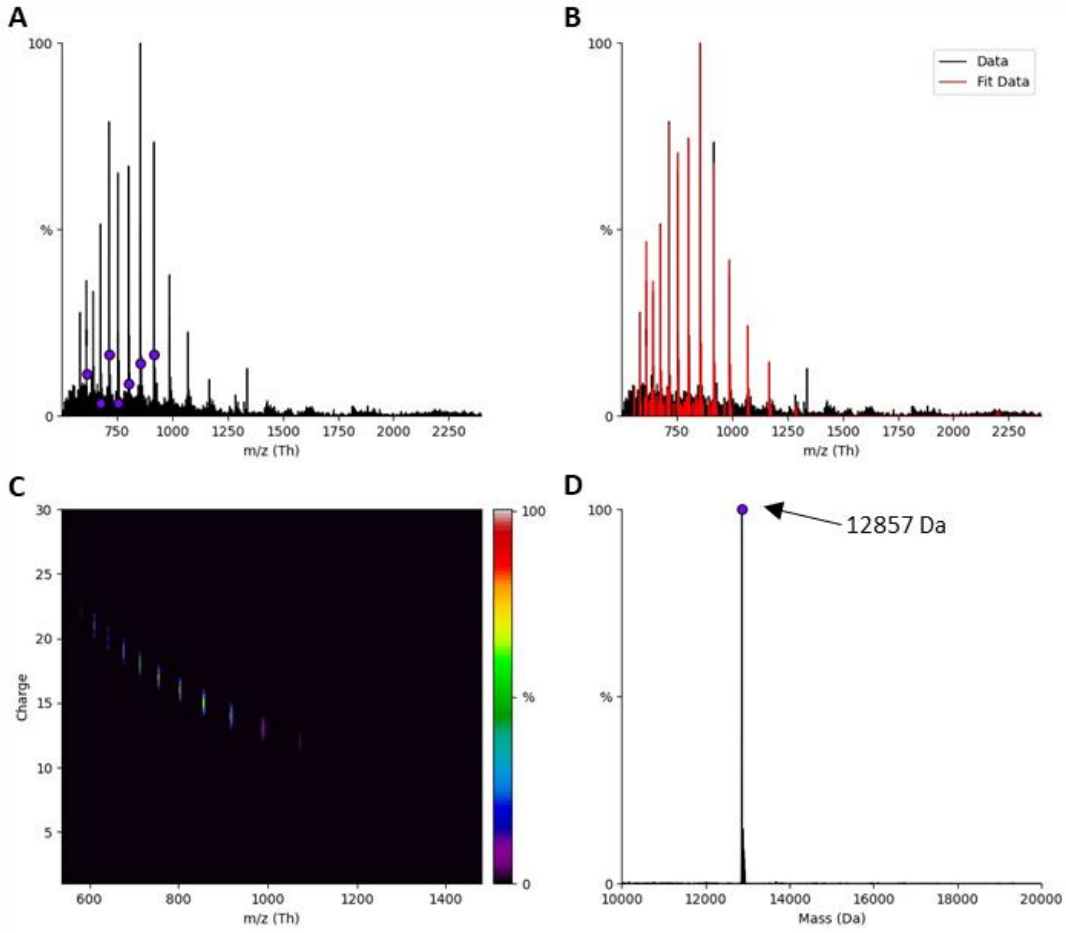


*Figure 35. A) Mass spectra of 3WJT6 10μM in Ammonium Acetate buffer (10 mM, pH 7.2) with 10% methanol added, B) Fitted data overlapped with ray mass data of 3WJT6, C) m/z vs the charge to display charge distribution of 3WJT6 species, and D) Deconvoluted mass spectrum of 3WJT6 oligomer.*

The mass spectrum of the DNA 3WJT6 structure alone produces a complex spectrum due to the many possible charge states of the DNA. UniDec free software was used to simplify and process the raw data

by deconvoluting it to produce a spectrum where the charge of each species is removed (Figure 35).[53] As can be seen in Figure 35 D, the 3WJT6 deconvoluted spectra produces a single peak with a measured mass of 12857 Da which corresponds very closely to the expected mass of the 3WJT6 oligomer, 12858 Da. The slight discrepancy in mass can be explained by the use of the deconvolution algorithm and is within 5 ppm error standard for publication of MS data. The fitted data is overlapped with the raw data to demonstrate how well the deconvoluted data matches the raw data.

Significant effort has been made throughout this work to determine whether the metal complexes in question are bound in the junction cavity or if they are interacting with the DNA structures in other ways. Determining whether the metal complexes are indeed binding in the junction cavity is a problem also encountered when using mass spectrometry (MS); it is possible that the metal complexes are only being brought together with the DNA under the experimental conditions in the mass spectrometer. PAGE gels shown above have demonstrated the strong preference of the metal complexes for 3WJ structures as opposed to loops. ITC data presented later in this chapter also gives a binding stoichiometry of 1:1, which supports junction binding to the 3WJT6 structure (section 3.8). To try to determine whether the metal complexes were binding to the junction under MS conditions a number of control experiments were carried out.

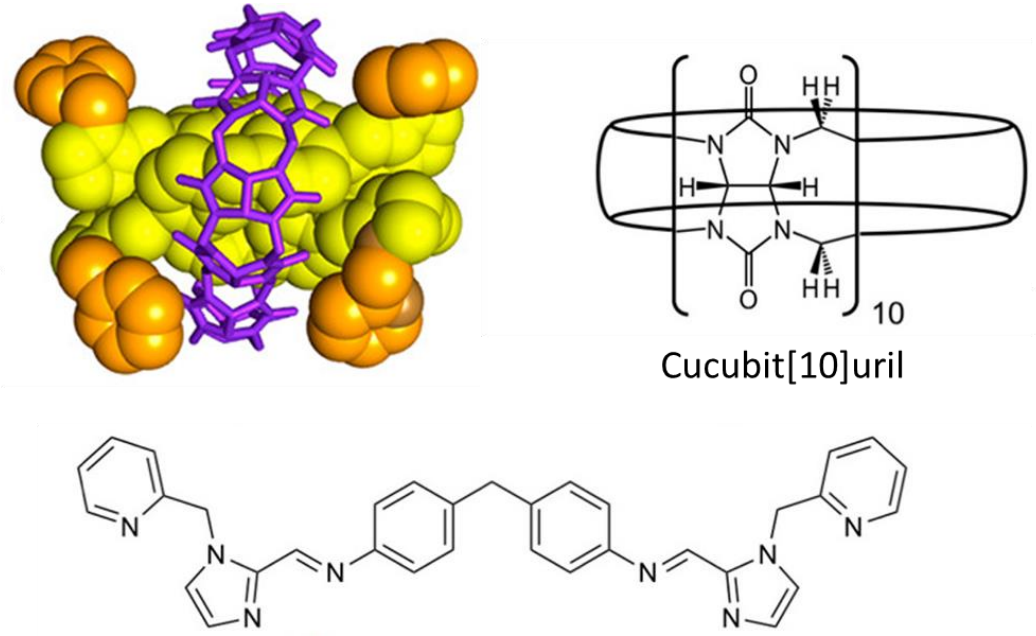


*Figure 36. Structure of the nickel pyridine rotaxane cylinder (top left), the cucubituril ring (top right) and chemical structure of the pyridine capped ligand (bottom).*[7]

The main control experiment involved incubating the 3WJT6 structure with one and two equivalents of each metal complex to observe if multiple cylinders could bind to the junction at a time. If multiple cylinders are observed with the DNA structure, this could indicate that they are binding to the DNA via non-specific interactions under the mass spectrometry conditions. A further control experiment involved incubating the nickel pyridine rotaxane cylinder (PyRot) with the 3WJT6. The PyRot has a similar structure to the NiP  but is unable to bind in a 3WJ due to a CB10 ring shrouding the central portion of the cylinder (Figure 36).[7] If a signal was observed in the mass spectrum of the 3WJ structure and PyRot, then this would indicate that the metal complexes could interact with the junction in a way other than junction binding.

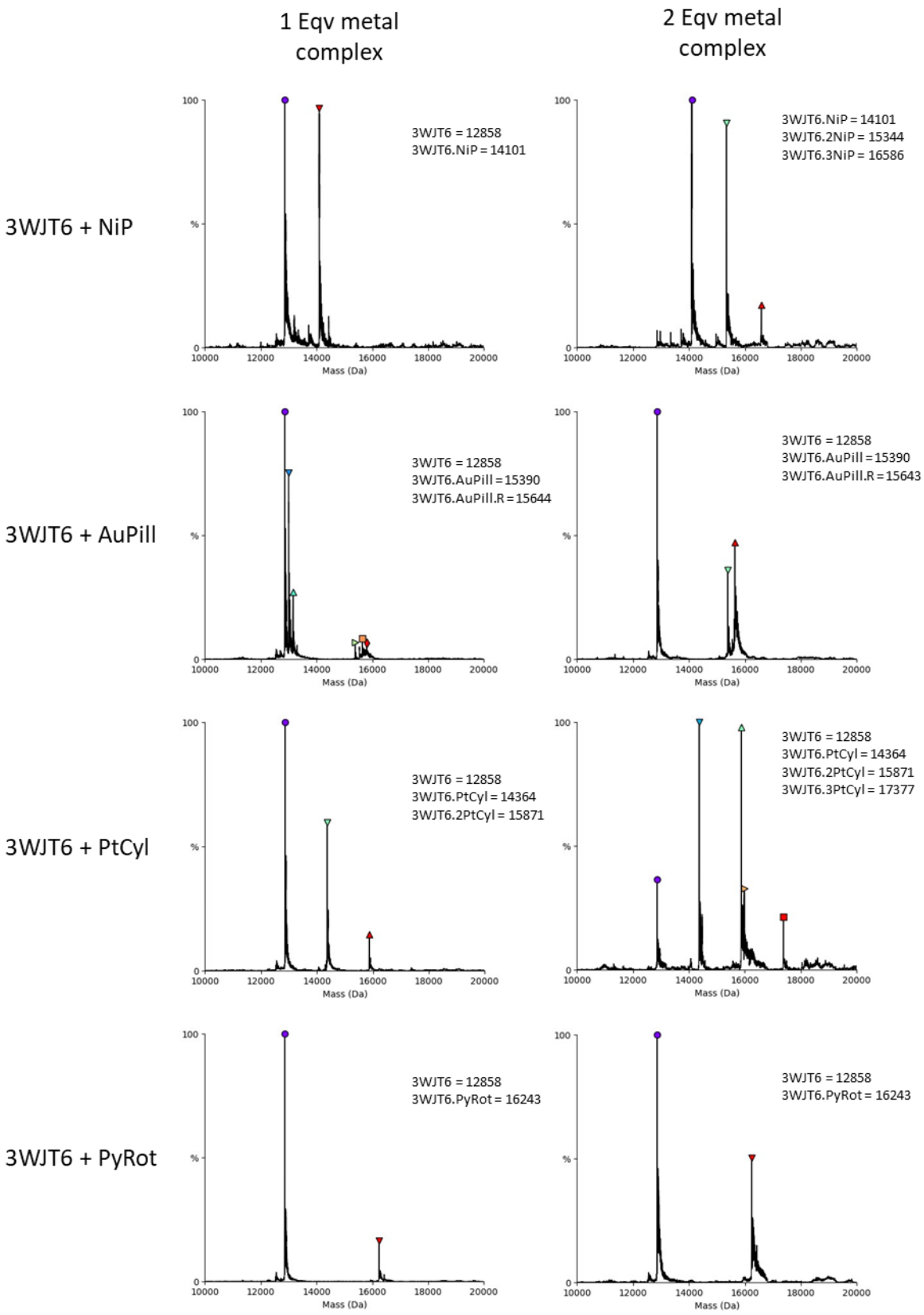


*Figure 37. Deconvoluted mass spectra - using UniDec software - of 3WJT6 with 1 or 2 equivalents of NiP, AuPill, PtCyl, or PyRot (Ammonium acetate 10 mM, 10 % MeOH, pH 7.2).*

The 3WJT6 structure incubated with one equivalent of each metal complex was analysed by mass spectrometry to ensure that we can observe the 3WJT6 + metal complex under the mass spectrometry

conditions (Figure 37). The 3WJT6 with one equivalent of NiP displays two prominent peaks of roughly equal intensity; the peak at 12858 Da corresponds to the DNA alone, and the second peak at 14100 Da corresponds to the DNA structure with one NiP cylinder bound to it. The 3WJT6 incubated with two equivalents of NiP results in the increase in the peak corresponding to 3WJT6.NiP and the formation of a new species which matches the mass of 3WJT6.2NiP. There is also a very small peak which matches the mass of 3WJT6.3NiP.

The 3WJT6 structure with one equivalent of the AuPill produces a much less clear spectra which contains a small peak for the 3WJT6.AuPill and a much larger peak for the DNA structure alone. There are also multiple other small peaks which have not been identified but do not correspond to the DNA structure with multiple equivalents of the AuPill. Two equivalents of AuPill results in the increase in the intensity of the 3WJT6.AuPill peak and the formation of a new unidentified peak. This peak at 15643 Da is denoted 3WJT6.AuPill.R as it was identified in all MS of AuPill with 3WJT6 indicating that it is most likely the AuPill with some impurity or counterion (R).

When one equivalent of the PtCyl complex was incubated with the 3WJT6 structure, a series of peaks arose which corresponded to the 3WT6 alone, 3WJT6.PtCyl and a small peak for 3WJT6.2PtCyl. With two equivalents of PtCyl, large signals are observed for 3WJT6.2PtCyl, a smaller peak for 3WJT6.3PtCyl was also observed. This is in contrast to what Monchaud and co-workers observed with their azacryptand ligands, where only peaks corresponding to the 3WJT6 alone and 3WJT6 with one equivalent of ligand were observed.[28] This could be explained by our metal complexes interacting with duplex DNA more strongly than the azacryptand ligands developed by Monchaud. The MS instrumentation used will also have a large effect on the spectra obtained (this work used a Waters G2 synapt, whereas Monchaud used a Thermofisher LTQ Orbitrap XL).

The PyRot was incubated with the 3WJT6 and run on the mass spectrometer as a control to see whether or not the cylinders are binding in the junction cavity, as the PyRot is known to be unable to bind in the junction site (Figure 37).[7] Only a small peak corresponding to the DNA structure with PyRot cylinder is observed. This is more than has been seen in the PAGE gels reported by Hooper *et al.* but

the peak is substantially smaller than the other cylinders display with the 3WJT6.[7] This indicates that there is likely a component of non-specific binding of the metal complexes to the 3WJT6.

The 3WJT6 DNA was observed by mass spectrometry alone and with each of the metal complexes. The NiP and PtCyl each produce strong signals for the 3WJT6 with up to three metal complexes. This indicates that there must be some amount of binding that is not taking place via the DNA junction. Signal for the 3WJT6.AuPill structure is very weak indicating perhaps less favourable binding to the 3WJ as has been seen in the competition PAGE gels. The PyRot control does show some interaction with the 3WJT6, but the signal is much weaker than that observed for the NiP or PtCyl. This interaction of PyRot with the 3WJT6 must be due to either binding outside of the junction cavity or electrostatic interactions.

### 3.6.3 Competition of metal complexes binding to 3WJT6

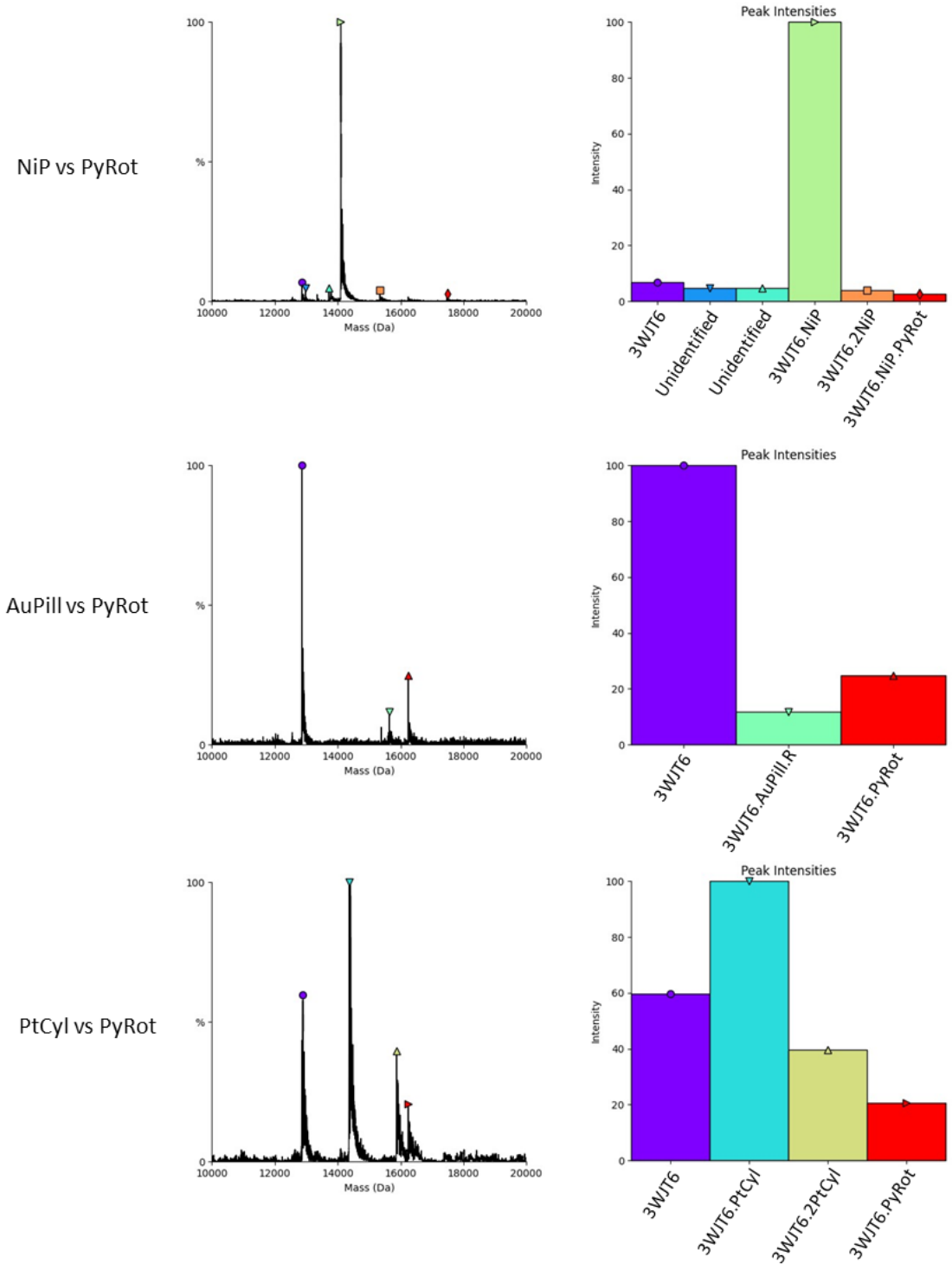


*Figure 38. Mass spectra of 3WJT6 and the junction binder NiP / AuPill / PtCyl competed against a PyRot – a similar complex which is known to not bind DNA 3WJ (10 mM Ammonium acetate, 10% MeOH, pH 7.2).*

With the aim of determining an order of affinity of each metal complex for the 3WJ cavity relative to eachother; each individual metal complex was competed against the others. To do this, one equivalent of 3WJT6 was incubated with one equivalent of two metal complexes for one hour before running the sample on the mass spectrometry instrument. To begin with, each metal complex was first competed

against the PyRot which should not bind the junction cavity (Figure 38). One equivalent of the 3WJT6 was incubated with one equivalent PyRot and one equivalent of another metal complex (Figure 38). When one equivalent of NiP and the PyRot are incubated with the DNA 3WJT6, the only prominent peak is for the 3WJT6.NiP. On the other hand, the AuPill and PyRot with 3WJT6 only shows a small peak for 3WJT6.PyRot and no peak for the 3WJT6.AuPill. The PtCyl complex and PyRot with DNA 3WJT6 produces a more complex spectra were the 3WJT6, 3WJT6.PtCyl and 3WJT6.2PtCyl are each prominent, with a small peak for the 3WJT6.PyRot. This data demonstrates that the PtCyl and NiP bind to the 3WJT6 structure much more strongly than the PyRot, suggesting that they are binding in the junction cavity.

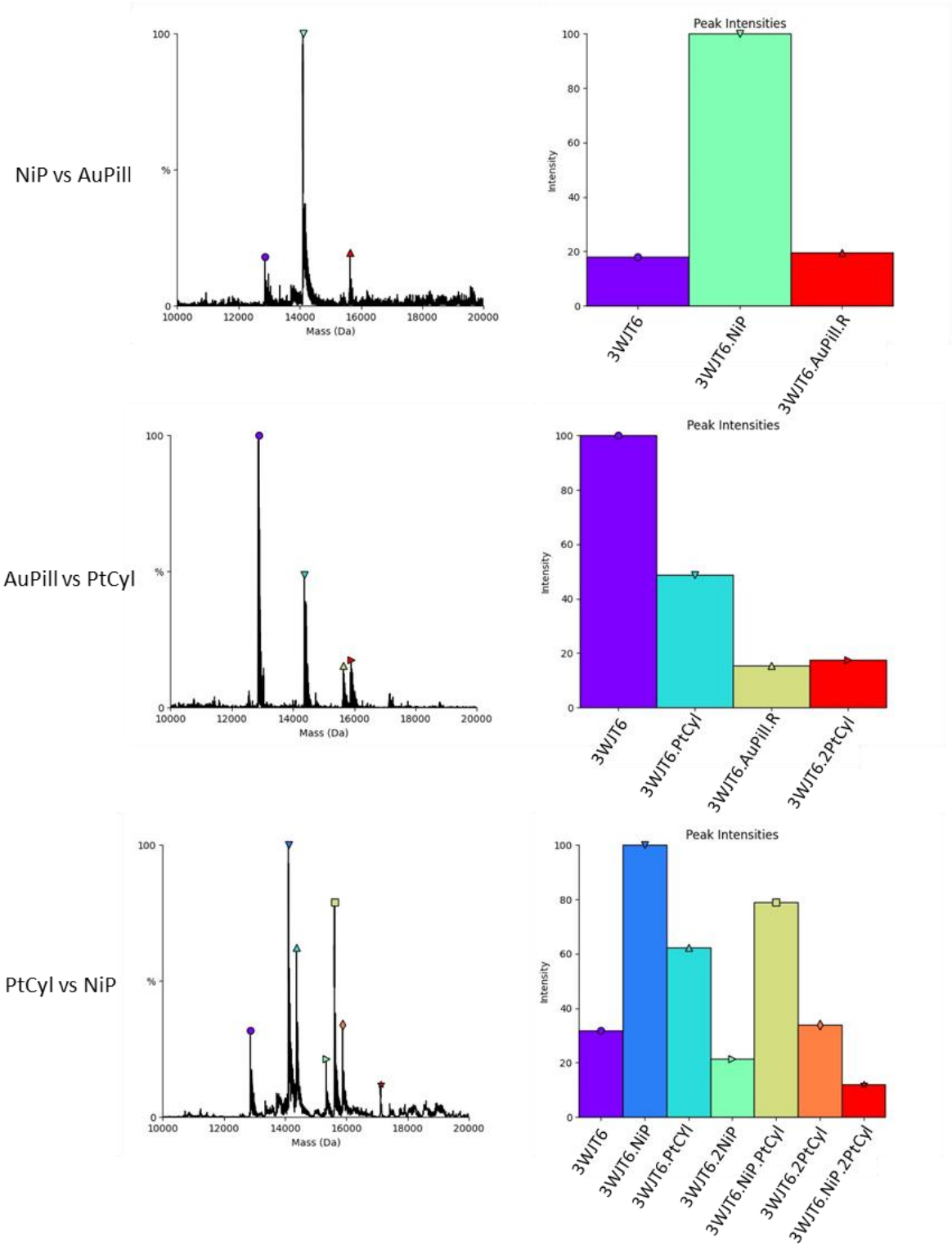


*Figure 39. Mass spectra of 3WJT6 with multiple metal complexes in competition (10 mM Ammonium acetate, 10% MeOH, pH 7.2).*

Further to the competition studies with PyRot, each junction binding metal complex was then competed against each other to observe if there was a preference for which metal complex can bind in the DNA cavity (Figure 39). Competition of the AuPill and NiP produces a peak for the 3WJT6, and a large peak for 3WJT6.NiP. There is a final, smaller peak which is due to the 3WJT6.AuPill. Competing

the PtCyl with the AuPill yields a similar result: a large peak corresponding to the 3WJT6.PtCyl is observed, a small peak corresponds to the 3WJT6.AuPill, and a final peak is seen, corresponding to 3WJT6.2Pt.

Competition of the PtCyl and NiP metal complexes to determine which binds preferentially to the DNA 3WJT6 produced many different species (Figure 39). A peak is observed for the DNA 3WJT6 alone, and the most intense peak corresponds to 3WJT6.NiP; 3WJT6.2NiP is also visible as a small peak. The second most intense peak is due to the 3WJT6.Pt complex, indicating that the nickel and platinum complexes both bind well to the 3WJT6. It is interesting that the intensity of the 3WJT6.NiP is greater than the 3WJT6.PtCyl but inverse is true for two metal complex species, where the intensity of the 3WJT6.2PtCyl is greater than 3WJT6.2NiP. This could suggest that the PtCyl interacts more strongly with the rest of the junction structure than NiP, but the opposite has been observed in PAGE gels. Alternatively, this could be simply due to more of the NiP forming 3WJT6.NiP leaving less NiP to form 3WJT6.2NiP.

The work produced by Monchaud and co-workers has demonstrated how mass spectrometry could be used to observe the binding of junction binders to a DNA 3WJ.[28] We attempted to take this concept further by competing different junction binders with each other to see what complexes are formed by mass spectrometry. This assumes that each DNA structure with a metal complex bound to it flies the same, or at least very similarly, in the mass spectrometer. This is likely a reasonable assumption as the metal complexes all have the same charge and, through PAGE gel experiments, it has been shown that each metal complex is able to bind to the DNA 3WJ in a similar manner. Isothermal titration calorimetry presented later in this chapter again exemplifies the similarities of binding to the 3WJT6 by the NiP cylinder and PtCyl. Under the conditions utilised in this set of experiments, prominent peaks were observable for multiple metal complexes binding to a single DNA oligomer. This brings into question whether the metal complexes are binding in the junction cavity of the DNA or whether they are simply binding to the DNA duplex under the MS conditions. PAGE gels and the ITC data presented in this chapter indicate that the metal complexes are binding to the DNA junction, but it is entirely possible

that under the harsh mass spectrometry conditions, multiple metal complexes are being brought into contact with the 3WJT6 as the electrospray droplets shrink.

Future work may involve the use of ion mobility mass spectrometry to try to separate structures with different cross-sectional areas, to further confirm that the metal complexes are bound in the junction cavity. PAGE gels have indicated that the DNA structure becomes slightly smaller and more compact when a metal complex is bound in the 3WJ cavity. This apparent change in size of the 3WJT6 with metal complexes may be observable through ion mobility mass spectrometry. It would also be more informative to collect a titration series where the equivalents of metal complex are increased from 0 to 2. Another improvement which could be made would be to add a control oligomer (e.g a PolyT) which would allow for better quantification.

More long term, if these experiments prove reliable, then other DNA structures such as G-quadruplexes and DNA 4WJ could be investigated. Competition experiments could then be used to try to determine the preference of metal complexes for different non-canonical DNA structures.

## 3.7 PAGE of other DNA structures

As has been discussed in the literature review (Chapter 1), the majority of DNA present in our body is in the form of B-DNA. When the information contained within our genome is accessed, DNA junctions are formed. DNA bulges may form due to slippage, and G-quadruplexes have been implicated in regulating gene expression and a number of diseases. Binding of our metal complexes to these DNA structures are briefly investigated here, using PAGE gels, due to the biological significance of G-quadruplexes and the strong similarity of DNA bulges to the hydrophobic junction cavities which have been studied so far.

### 3.7.1 DNA bulges

It has been demonstrated that these helicates are able to bind in the cavity of 3WJ primarily through pi-pi and electrostatic interactions. Other publications have also shown how the parent cylinder and pillarplexes have strong interactions with hydrophobic cavities such as DNA bulges and cucubiturils.[7, 8]

With this in mind, the interactions of the PtCyl complex, NiP, and AuPill with various sized DNA bulges were investigated. The bulges were designed based on the publication by Victor Brabec *et al.*, GC base pairs flank each of the bulges to increase the stability of the structure.[8] Thymine bases were selected to inhabit the bulge itself, due to the higher affinity shown for pyrimidine bulges by the iron parent cylinder.

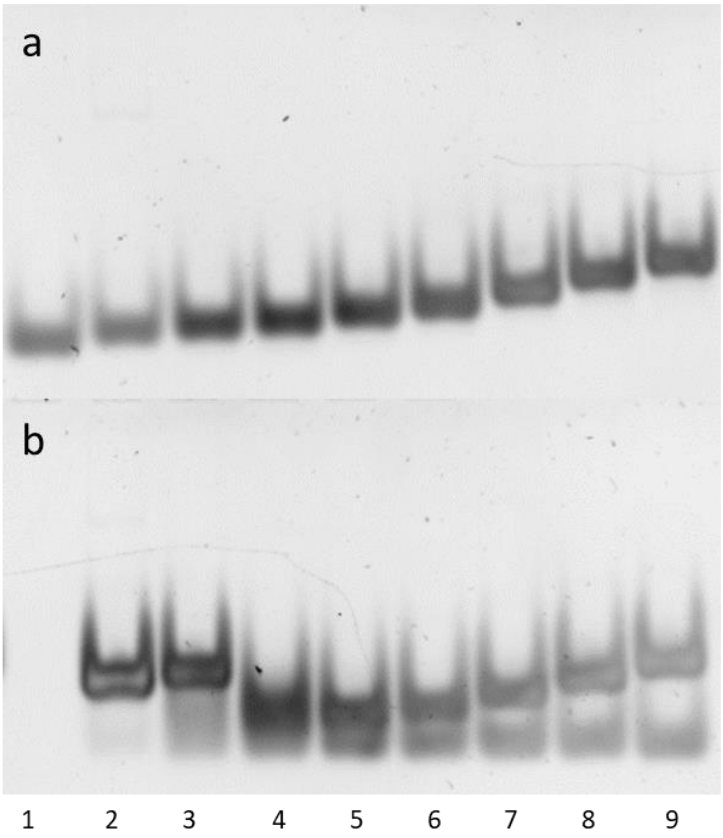


*Figure 40. PAGE gel (1xTris Borate buffer pH 8.4, 120 V, 2.5 hours, 5 °C) of controls for bulge DNA, a) S1 in lane 1 then S2(0)-(7) in lanes 2-9 respectively, b) lanes 2-9 contain S1 + S2(0)-(7).*

The control PAGE gel shown in Figure 40 shows that the single strands lack any secondary structure. The duplexes with either 0 or 1 bases inserted form a duplex, but the duplexes with larger bulges do not show the presence of any duplex structure. This is contrary to what was observed by Victor Brabec *et al.*, these sequences differ in that they contain thymines in the bulge instead of adenine. [8] It is not clear why there is a discrepancy between these observations and those made by Victor Brabec and co-coworkers.

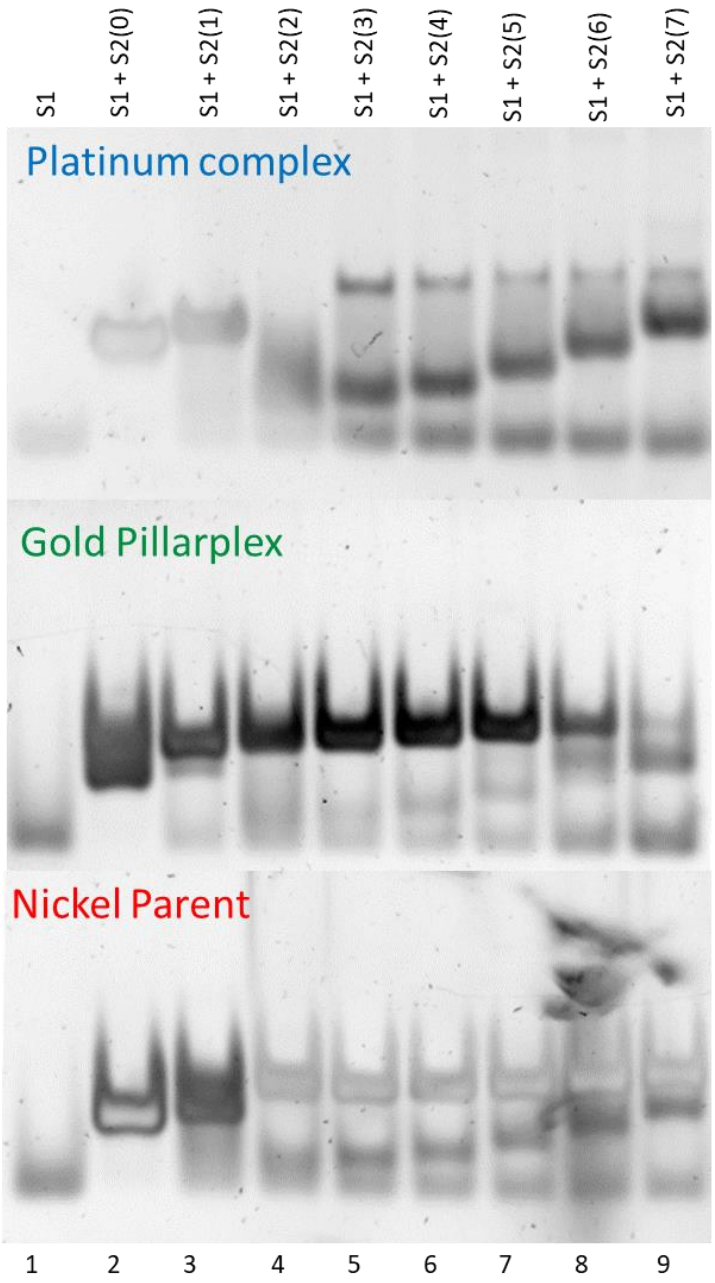


*Figure 41. PAGE gels (1xTris Borate buffer pH 8.4, 120 V, 2.5 hours, 5 °C) of different sized DNA thymine bulges with different metal complexes.*

For this PAGE gel experiment, the DNA bulges consisted of two strands of DNA, S1, and S2, where S2 contained 0-7 inserted thymine residues in the middle of the sequence. S1 and S2 combined, with no DNA binder present, did not hybridize (other than S1 + S2(0) and S1+S2(1)). In the presence of the PtCyl complex, all lanes showed smearing which is indicative of non-specific interactions with the DNA but there were also new structures formed with S2(3), S2(4), S2(5), S2(6), and S2(7) (Figure 41). The new structures formed are thought to be due to the formation of the DNA bulge structures, however, the

new bands are faint. The PtCyl displayed almost identical interactions with the bulge structures as the palladium helicate (palladium PAGE gel shown in appendix A3.14). The NiP cylinder displayed strong interactions with all the DNA bulges, with new bands forming in all cases. AuPill also showed strong interactions with the bulge structures but, interestingly, a weaker interaction with S2(7) despite the greater girth of the AuPill compared to the NiP cylinder.

The work with DNA bulges presented in this thesis is far from comprehensive. If this work were to be continued, other residues in the bulge should be considered. Consideration should also be given to the bases at the fork locations where the bulge is located, as these could play an important role in the binding of helicates to the bulges through pi-pi stacking. Simulations and PAGE gels in a recent publication have shown how cylinders can interact strongly with Y-forks.[1]

### 3.7.2 G-quadruplexes

G-quadruplexes are a non-canonical DNA structure which consist of tetrads of guanine residues which fold around specific cations (usually potassium) and stack to form their characteristic structure. The general G-quadruplex structure may form as an intramolecular structure on a single strand of DNA, or it may form from multiple strands of DNA which come together. There are three forms of the intramolecular G-quadruplex: parallel, anti-parallel, or hybrid (Figure 42). G-quadruplexes are discussed in more detail in Chapter 1.

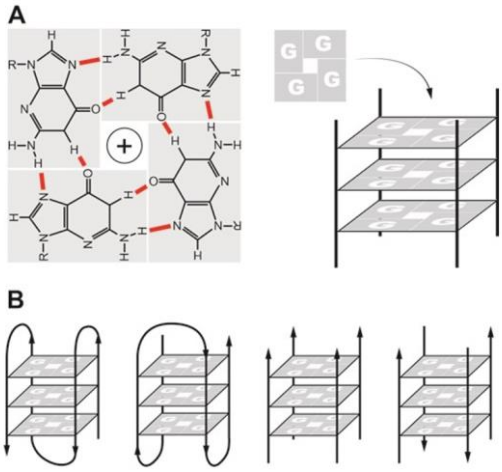


*Figure 42. Diagram to show Hoogesteen hydrogen bonding between guanine residues and the many different conformations of G-quadruplexes which may arise.*

The NiP and FeP cylinder were shown to interact G4s in one publication.[54] The P enantiomer specifically was shown to stabilize G4 structures through DNA melting studies ($\Delta T_m$ = 10 °C at 1:1 ligand:G4) and PAGE experiments. Remarkably, the M enantiomer conferred no increase in melting temperature to the G4 structure. Selectivity for G4 structures over dsDNA was also demonstrated through melting studies. It was thought that the similar structures of the PtCyl and AuPill may enable them to also interact with G4s in a similar way to that observed for NiP.

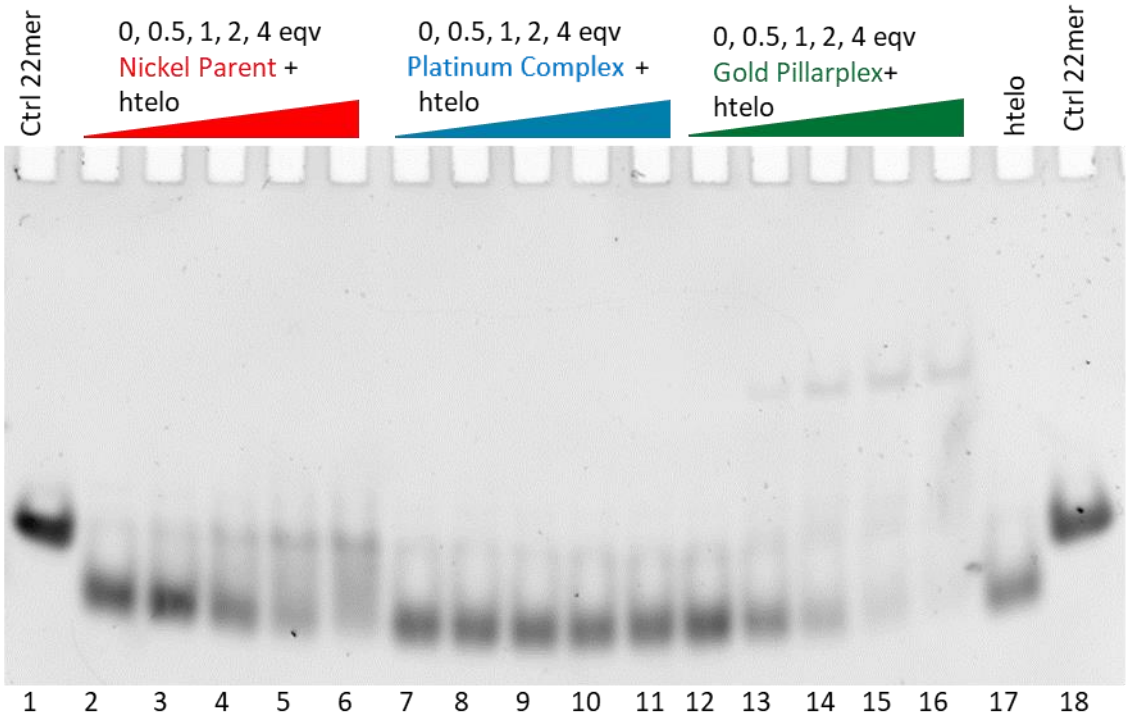


*Figure 43. PAGE gel (1xTris Borate buffer with 100 mM KCl, pH 8.4, 120 V, 2.5 hours, 5 °C) of htelo G-quadruplex with 0, 0.5, 1, 2, and 4 equivalents of NiP / PtCyl / AuPill.*

A G-quadruplex structure (htelo) was incubated with NiP, AuPill, and PtCyl at various concentrations to observe if any changes in the G-quadruplex structure were induced (Figure 43). The first obvious characteristic in this PAGE gel is the curve, which is visible across the whole gel. This curve is due to uneven heating of the gel caused by the very high concentration of KCl salt required for the formation of the G-quadruplex. To confirm the formation of the G-quadruplex, a single stranded oligomer with the same number of bases was included for comparison.

Increasing equivalents of NiP cylinder induces the formation of a new band which is retarded compared to the folded G-quadruplex structure. This new band aligns well with the expected position of the 22-

mer single stranded control oligo; however, it is not possible to determine if this is a new structure forming or if the G-quadruplex is simply unfolding to a single stranded structure. The bands associated with the G-quadruplex and PtCyl did not display any changes with increasing equivalents of PtCyl complex. The lack of shifts of the bands or formation of new bands indicates there is little to no interaction of the PtCyl with the G-quadruplex. AuPill with the G-quadruplex structure forms new bands much higher in the gel, even with low equivalents of the pillarplex structure. The location of the new band formed indicates that the respective structure is significantly larger that the htelo G-quadruplex.

## 3.8 ITC experiments

Isothermal calorimetry (ITC) is often used to study the binding interaction of biomolecules by monitoring the heat of reaction when the substrate is titrated into a solution of the binding agent or *vice versa*. ITC allows us to determine the binding affinity ($K_D$) and the binding enthalpy $\Delta H^o$ through the equation shown in Equation 1.

$$\Delta G^o = -RTlnK_{eq} = \Delta H - T\Delta S^o$$

*Equation 1. Gibbs free energy and binding affinity equation.*

A 3WJ was designed to carry out the ITC experiment and to determine the thermodynamic parameters of the binding event of different cylinders to a 3WJ. The 14mer 3WJ used in the PAGE gel experiments consisting of 3 separate 14-mer oligos were not suitable for ITC, as it was necessary to isolate the binding of the cylinder into the junction cavity from the hybridization of the 14-mer strands. Two other 3WJ structures were tried in an effort to determine the best system to use: an 18-mer 3WJ consisting of 3 separate oligos 18 bases in length was designed. The 18-mer 3WJ forms spontaneously in solution with no junction binder present (shown in appendix A3.6). This experiment showed some promise, but the results were not reliably reproducible. It was thought that this could be due to incomplete formation of the 18mer 3WJ in solution. In an effort to simplify the system and acquire reliable results, it was decided to try the same experiment with a 3WJ on a single strand of DNA. The 3WJ settled on was the same used for the mass spectrometry experiments described above, which consists of a single oligomer with two (6 thymine) hairpin loops (Figure 29).[28]

*Table 2. Thermodynamic parameters for the binding interaction of two metal complexes with a DNA three-way junction structure (3WJT6, 10 µM) as measured by isothermal titration calorimetry (ITC) (10 mM Sodium Cacodylate, 100 mM NaCl, pH 7.4, 25 °C).*

| | **NiP / $Ni_2(L_2)_3Cl_4$** | **PtCyl / $Pt_2(L_1)_4(NO_3)_4$** |
|---|---|---|
| $K_D$ / M | $7.17x10^{-9} \pm 0.51x10^{-9}$ | $9.94x10^{-9} \pm 4.36x10^{-9}$ |
| N / sites | $1.023 \pm 0.05$ | $1.044 \pm 0.11$ |
| ΔH / $kcalmol^{-1}$ | $-31.4 \pm 0.87$ | $-25.3 \pm 2.98$ |
| TΔS / $kcalmol^{-1}$ | $-20.3 \pm 0.87$ | $-14.3 \pm 3.14$ |
| ΔG / $kcalmol^{-1}$ | $-11.1 \pm 0.06$ | $-11.0 \pm 0.25$ |

Each experiment was carried out in triplicate to show the reproducibility and confirm the results (Figure 44 and Figure 45). A concern with using the 3WJT6 structure was that gels have shown the supramolecular cylinders to be capable of binding to DNA bulges containing thymine residues. Binding to these hairpin loops may be possible, but the number of binding sites calculated from the experimental data was close to 1 (Table 2). If binding to the hairpin loops was occurring, then we would have expected 2 or 3 binding sites to be calculated.

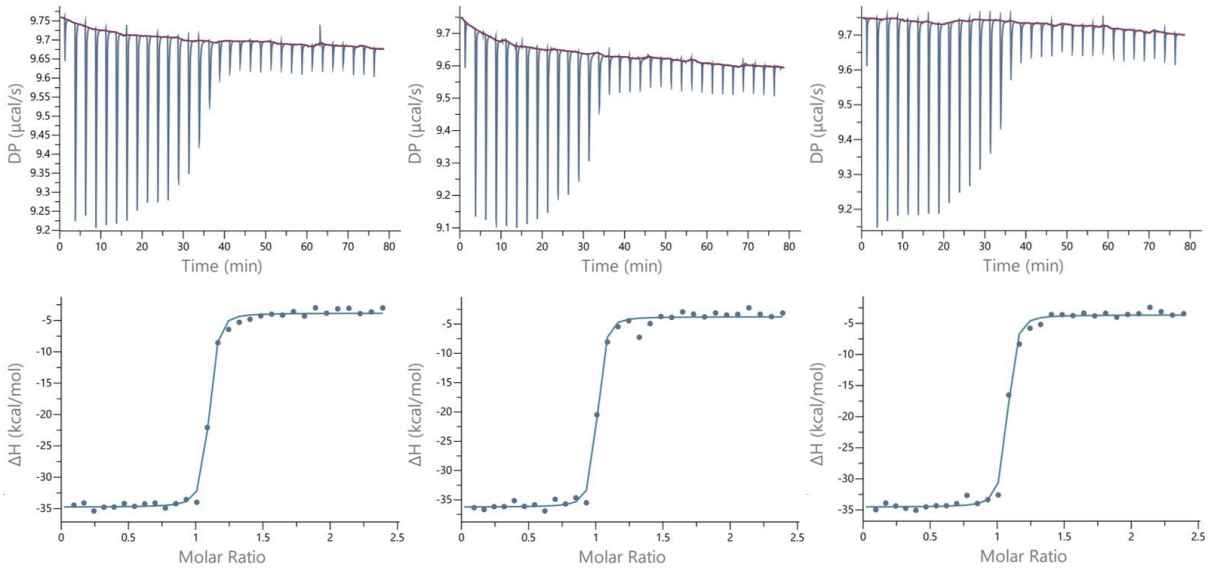


*Figure 44. ITC of NiP with 3WJT6 10 µM in 10 mM sodium cacodylate buffer pH 7.4, 100mM NaCl.*

The platinum complex appears to have a higher dissociation constant than the NiP cylinder but the error on this measurement is significantly larger and well within error of the value measured for the NiP (Table 2). This indicates that the PtCyl has a similar affinity for DNA 3WJ as the NiP which binds 3WJ exceedingly well, due to the well-matched symmetry and alignment of pi surfaces with the DNA bases at the junction site. Each metal complex has one binding site on the 3WJT6. The Gibbs free energy of each binding event is almost identical with the NiP having a larger enthalpy of binding, as well as a larger entropy of binding. An important consideration when comparing these two

experiments was that the PtCyl required the addition of a small proportion of acetonitrile in order to solubilise the complex (0.5 %). To control for this, the titration for the NiP was repeated once with the same volume of acetonitrile which did not induce any significant changes to the thermodynamic parameters measured (shown in appendix A3.15).

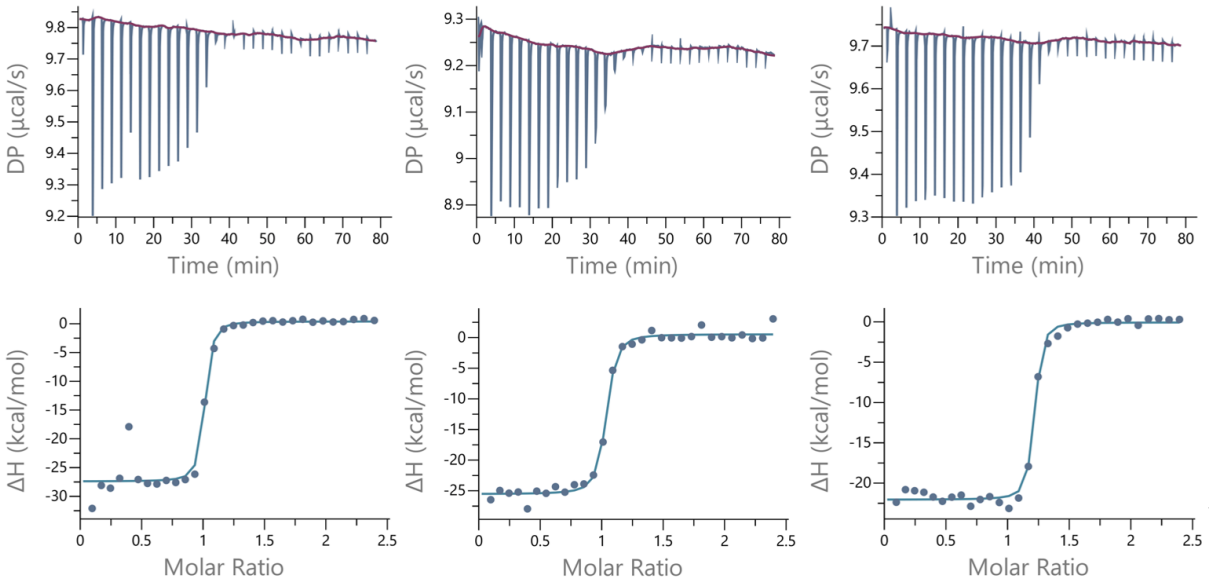


*Figure 45. ITC of $Pt_2(L_1)_4(NO_3)_4$ with 3WJT6 10 µM in 10 mM sodium cacodylate buffer pH 7.4. 100mM NaCl.*

Finally, we also attempted to measure the binding properties of the AuPill with the 3WJT6 but this was unsuccessful. It is not certain why it was not possible to obtain a curve for the AuPill, but the poor solubility of the pillarplex in buffered solution could be a contributing factor. Any precipitation in the ITC instrument would heavily affect the readings. Other experiments, such as the fluorescence displacement assays, indicate that the AuPill has a high affinity for duplex DNA which could create competing binding modes which would make obtaining clear data from an ITC titration more challenging.

## 3.9 Conclusions

The work presented in this chapter has attempted to compare the DNA binding properties of three different metal complexes (NiP, AuPill and PtCyl) which share structural similarities: they all have comparable dimensions, each complex has a 4+ charge and, importantly, they all have external pi surfaces.

Fluorescent displacement assays have indicated that the PtCyl has a significantly weaker interaction with duplex B-DNA when compared to the AuPill and NiP cylinder. This weaker interaction is thought to be due to the PtCyl cage trapping an anion in the centre giving the structure an overall charge of 3+ instead of 4+. Despite the apparent weak interaction of PtCyl with B-DNA, it induces a large CD signal (shown in Chapter 2). This large CD signal could be explained by the formation of a specific PtCyl enantiomer when the cylinder interacts with the chiral DNA environment. The comparatively weak binding of PtCyl to the DNA duplex can help to explain the PAGE competition experiment results. The PtCyl shows a higher preference for the DNA 3WJ than the AuPill or NiP cylinder when competed against other DNA structures 4WJ, dsDNA, and Y-fork. The NiP cylinder shows a strong interaction with 4WJ and Y-fork, but the AuPill shows the highest preference for the 4WJ and also a strong affinity for the Y-fork. The increased girth of the AuPill likely contributes to its preference for binding DNA 4WJ.

FRET melting studies with higher equivalents of metal complexes reveal an interesting result: with higher equivalents of PtCyl, there is practically no change in melting temperature, whereas with higher equivalents of AuPill or NiP cylinder, the melting temperature of the structure increases dramatically. The increase in melting temperature for the AuPill and NiP cylinder is thought to be caused by the complexes strongly interacting with the DNA major grooves and further stabilising the structure. The PtCyl only weakly interacts with the DNA duplex and so does not offer any significant stabilisation to the structure and the melting temperature does not change.

Analysis of PAGE gels of RNA 3WJ and 4WJ structures with each metal complex was carried out. There are clear differences in the structures formed with the RNA junctions compared to the DNA junctions. The most surprising result was the formation of a unique structure with the PtCyl complex which appears to be larger than the RNA 4WJ alone. This hints that the PtCyl may have a higher affinity for RNA 4WJ than expected. Other experiments in Chapter 3 found that the PtCyl displayed a higher affinity for DNA 3WJ vs DNA 4WJ, but did not compete RNA structures.

MD simulations (Chapter 2) support the experimental data presented in this chapter which suggests that the PtCyl has a very weak and transient interaction with duplex B-DNA. Simulations with 3WJ and

the NiP cylinder showed a perfect match with pi-pi stacking between the aryl surfaces on the metal complex and the bases at the centre of the junction.[6] The AuPill and PtCyl both bind in the central cavity of the 3WJ but they also cause the breaking of one of the base pairs at the junction site.[1] From the MD simulations, we would expect the NiP cylinder to have the strongest binding and hence strongest stabilization of the 3WJ, followed by the PtCyl and AuPill at similar values. This is what is observed in the UV and FRET melting experiments carried out. The ITC data, however, shows that the PtCyl and NiP have binding affinities for 3WJT6 that are the same order of magnitude (NiP $K_D = 7.17x10^{-9} \pm 0.51x10^{-9}$ M, PtCyl $K_D = 9.94x10^{-9} \pm 4.36x10^{-9}$ M). Taking the maximum errors on the ITC measurements of $K_D$, the PtCyl may have a binding affinity 2/3 that of the NiP.

Mass spectrometry was investigated as a technique to study the interactions of metal complexes with DNA junctions. Preliminary results show potential but there are issues which must be overcome. The PyRot complex, which is known to be unable to bind to DNA 3WJs, did appear to bind to the DNA 3WJT6 structure in the MS instrument. This is likely simple electrostatic interactions causing the DNA and PyRot to fly together. Encouragingly, the PyRot complex was out competed by the NiP and PtCyl indicating that the junction binding of these other complexes did confer an advantage to binding to the 3WJT6 structure. Competing the junction binding complexes against one another indicated that the NiP had the highest affinity for the 3WJT6, followed by the PtCyl, and the AuPill. This is the order of affinity for 3WJ structures expected based on the other studies carried out in this chapter. MS has successfully been used to detect a DNA 3WJ structure with metal complexes bound. Further optimisation of the technique and improvements can be made, such as the use of ion mobility.

Overall, these studies demonstrate the significance of outward facing pi surfaces for enabling the DNA cavity binding interaction. They also show how a lower overall charge, like that on the PtCyl, may allow for higher structural selectivity of DNA. The diameter of the metal complexes is an important parameter to consider for junction binding, this is shown by the high preference of the AuPill for the 4WJ cavity compared to the 3WJ. It is unclear if the symmetry of the PtCyl conveys any advantages to structural selectivity as the PtCyl is highly flexible. The fact that the PtCyl appears to bind to 3WJ as a

specific enantiomer in MD simulations suggests that there are advantages to designing binding agents with chirality appropriate for their target.

## 3.10 Future work

There is work that could be done to further expand and improve upon the work carried out with mass spectrometry of the 3WJT6. Competition experiments involving different DNA structures such as hairpin loops, G-quadruplexes, or Holliday junctions would be interesting. The use of ion mobility would be invaluable for identification of conformational changes in the DNA under different conditions or upon addition of metal complexes to solution. Baker *et al.* has demonstrated the potential of ion mobility to differentiate between two different conformations of DNA cruciform structure.[55]

ITC is a convenient method that can be used to quantify the strength of the interaction between a host and its guest molecule without any modification to either. ITC also provides information on other thermodynamic parameters including dissociation constant ($K_D$), enthalpy ($\Delta H$), entropy ($\Delta S$), and stoichiometry (n). In this case, the DNA junction and the metallic complex are the host and guest respectively. Titrations were carried out successfully with the 3WJT6 oligomer and both the PtCyl complex and NiP cylinder, demonstrating that this technique is applicable to DNA junctions and junction binders. Future work could look at measuring the binding of these metal complexes to other DNA structures such as the DNA 4WJ. In order to avoid the formation of multiple species, it may be advantageous to design a 4WJ analogous to the 3WJT6, where it is contained on a single oligo which folds to form the desired structure. It may be possible to also investigate binding of these metal complexes to other DNA structures such as G-quadruplexes. RNA junctions would also present another avenue of research.

Building on the work here, attempts should be made to obtain crystal structures of the DNA junctions with the PtCyl and AuPill if possible. Crystal structures are the gold standard for determining the exact binding interactions and location of the metal complexes in the DNA structures. Another alternative method to investigate the exact binding mode would be to carry out NMR studies; this has been done in the past, with the iron parent cylinder.[6]

## 3.11 References


1. Craig, J. S.; Melidis, L.; Williams, H. D.; Dettmer, S. J.; Heidecker, A. A.; Altmann, P. J.; Guan, S.; Campbell, C.; Browning, D. F.; Sigel, R. K. O.; Johannsen, S.; Egan, R. T.; Aikman, B.; Casini, A.; Pöthig, A.; Hannon, M. J., Organometallic Pillarplexes That Bind DNA 4-Way Holliday Junctions and Forks. *Journal of the American Chemical Society* **2023,** *145* (25), 13570-13580.
2. McMorran, D. A.; Steel, P. J., The First Coordinatively Saturated, Quadruply Stranded Helicate and Its Encapsulation of a Hexafluorophosphate Anion. *Angewandte Chemie International Edition* **1998,** *37* (23), 3295-3297.
3. Steel, P. J.; McMorran, D. A., Selective Anion Recognition by a Dynamic Quadruple Helicate. *Chemistry – An Asian Journal* **2019,** *14* (8), 1098-1101.
4. Altmann, P. J.; Pöthig, A., Pillarplexes: A Metal–Organic Class of Supramolecular Hosts. *Journal of the American Chemical Society* **2016,** *138* (40), 13171-13174.
5. Guan, S.; Pickl, T.; Jandl, C.; Schuchmann, L.; Zhou, X.; Altmann, P. J.; Pöthig, A., Triazolate-based pillarplexes: shape-adaptive metallocavitands via rim modification of macrocyclic ligands. *Organic Chemistry Frontiers* **2021,** *8* (15), 4061-4070.
6. Cerasino, L.; Hannon, M. J.; Sletten, E., DNA Three-Way Junction with a Dinuclear Iron(II) Supramolecular Helicate at the Center: A NMR Structural Study. *Inorganic Chemistry* **2007,** *46* (16), 6245-6251.
7. Hooper, C. A. J.; Cardo, L.; Craig, J. S.; Melidis, L.; Garai, A.; Egan, R. T.; Sadovnikova, V.; Burkert, F.; Male, L.; Hodges, N. J.; Browning, D. F.; Rosas, R.; Liu, F.; Rocha, F. V.; Lima, M. A.; Liu, S.; Bardelang, D.; Hannon, M. J., Rotaxanating Metallo-supramolecular Nano-cylinder Helicates to Switch DNA Junction Binding. *Journal of the American Chemical Society* **2020,** *142* (49), 20651-20660.
8. Malina, J.; Hannon, M. J.; Brabec, V., Recognition of DNA bulges by dinuclear iron(II) metallosupramolecular helicates. *The FEBS Journal* **2014,** *281* (4), 987-997.
9. Le Pecq, J.-B.; Paoletti, C., A new fluorometric method for RNA and DNA determination. *Analytical Biochemistry* **1966,** *17* (1), 100-107.
10. Boger, D. L.; Fink, B. E.; Brunette, S. R.; Tse, W. C.; Hedrick, M. P., A Simple, High-Resolution Method for Establishing DNA Binding Affinity and Sequence Selectivity. *Journal of the American Chemical Society* **2001,** *123* (25), 5878-5891.
11. Shahabadi, N.; Hadidi, S.; Taherpour, A., Synthesis, Characterization, and DNA Binding Studies of a New Pt(II) Complex Containing the Drug Levetiracetam: Combining Experimental and Computational Methods. *Applied Biochemistry and Biotechnology* **2014,** *172* (5), 2436-2454.
12. Li, C.; Xu, F.; Zhao, Y.; Zheng, W.; Zeng, W.; Luo, Q.; Wang, Z.; Wu, K.; Du, J.; Wang, F., Platinum(II) Terpyridine Anticancer Complexes Possessing Multiple Mode of DNA Interaction and EGFR Inhibiting Activity. *Frontiers in Chemistry* **2020,** *8* (210).
13. Tsai, C. C.; Jain, S. C.; Sobell, H. M., X-ray crystallographic visualization of drug-nucleic acid intercalative binding: structure of an ethidium-dinucleoside monophosphate crystalline complex, Ethidium: 5-iodouridylyl (3'-5') adenosine. *Proceedings of the National Academy of Sciences* **1975,** *72* (2), 628-632.
14. Lepecq, J. B.; Paoletti, C., A fluorescent complex between ethidium bromide and nucleic acids: Physical—Chemical characterization. *Journal of Molecular Biology* **1967,** *27* (1), 87-106.
15. Olmsted, J., III; Kearns, D. R., Mechanism of ethidium bromide fluorescence enhancement on binding to nucleic acids. *Biochemistry* **1977,** *16* (16), 3647-3654.
16. Hannon, M. J.; Moreno, V.; Prieto, M. J.; Moldrheim, E.; Sletten, E.; Meistermann, I.; Isaac, C. J.; Sanders, K. J.; Rodger, A., Intramolecular DNA Coiling Mediated by a Metallo-Supramolecular Cylinder. *Angewandte Chemie International Edition* **2001,** *40* (5), 879-884.
17. Portugal, J.; Waring, M. J., Assignment of DNA binding sites for 4',6-diamidine-2-phenylindole and bisbenzimide (Hoechst 33258). A comparative footprinting study. *Biochimica et Biophysica Acta (BBA) - Gene Structure and Expression* **1988,** *949* (2), 158-168.
18. Bucevičius, J.; Lukinavičius, G.; Gerasimaitė, R., The Use of Hoechst Dyes for DNA Staining and Beyond. *Chemosensors* **2018,** *6* (2).
19. Watson, J. D.; Crick, F. H. C., Molecular Structure of Nucleic Acids: A Structure for Deoxyribose Nucleic Acid. *Nature* **1953,** *171* (4356), 737-738.
20. Blake, R. D.; Delcourt, S. G., Thermodynamic Effects of Formamide on DNA Stability. *Nucleic Acids Research* **1996,** *24* (11), 2095-2103.
21. Schildkraut, C.; Lifson, S., Dependence of the melting temperature of DNA on salt concentration. *Biopolymers* **1965,** *3* (2), 195-208.
22. Wartell, R. M.; Benight, A. S., Thermal denaturation of DNA molecules: A comparison of theory with experiment. *Physics Reports* **1985,** *126* (2), 67-107.

23. Manning, G. S., On the application of polyelectrolyte “limiting laws” to the helix-coil transition of DNA. I. Excess univalent cations. *Biopolymers* **1972,** *11* (5), 937-949.
24. Khandelwal, G.; Bhyravabhotla, J., A phenomenological model for predicting melting temperatures of DNA sequences. *PLoS One* **2010,** *5* (8).
25. De Cian, A.; Guittat, L.; Kaiser, M.; Saccà, B.; Amrane, S.; Bourdoncle, A.; Alberti, P.; Teulade-Fichou, M.-P.; Lacroix, L.; Mergny, J.-L., Fluorescence-based melting assays for studying quadruplex ligands. *Methods* **2007,** *42* (2), 183-195.
26. Tataurov, A. V.; You, Y.; Owczarzy, R., Predicting ultraviolet spectrum of single stranded and double stranded deoxyribonucleic acids. *Biophysical Chemistry* **2008,** *133* (1), 66-70.
27. Oleksi, A.; Blanco, A. G.; Boer, R.; Usón, I.; Aymamí, J.; Rodger, A.; Hannon, M. J.; Coll, M., Molecular Recognition of a Three-Way DNA Junction by a Metallosupramolecular Helicate. *Angewandte Chemie International Edition* **2006,** *45* (8), 1227-1231.
28. Zell, J.; Duskova, K.; Chouh, L.; Bossaert, M.; Chéron, N.; Granzhan, A.; Britton, S.; Monchaud, D., Dual targeting of higher-order DNA structures by azacryptands induces DNA junction-mediated DNA damage in cancer cells. *Nucleic Acids Research* **2021,** *49* (18), 10275-10288.
29. Vicens, Q.; Kieft, J. S., Thoughts on how to think (and talk) about RNA structure. *Proceedings of the National Academy of Sciences* **2022,** *119* (17), e2112677119.
30. Fu, X.-D., Non-coding RNA: a new frontier in regulatory biology. *National Science Review* **2014,** *1* (2), 190-204.
31. Nussbacher, J. K.; Tabet, R.; Yeo, G. W.; Lagier-Tourenne, C., Disruption of RNA Metabolism in Neurological Diseases and Emerging Therapeutic Interventions. *Neuron* **2019,** *102* (2), 294-320.
32. Swadling, J. B.; Ishii, K.; Tahara, T.; Kitao, A., Origins of biological function in DNA and RNA hairpin loop motifs from replica exchange molecular dynamics simulation. *Physical Chemistry Chemical Physics* **2018,** *20* (5), 2990-3001.
33. Sobakinskaya, E.; Schmidt am Busch, M.; Renger, T., Theory of FRET “Spectroscopic Ruler” for Short Distances: Application to Polyproline. *The Journal of Physical Chemistry B* **2018,** *122* (1), 54-67.
34. Fang, C.; Huang, Y.; Zhao, Y., Review of FRET biosensing and its application in biomolecular detection. *American Journal of Translational Research* **2023,** *15* (2), 694-709.
35. Didenko, V. V., DNA probes using fluorescence resonance energy transfer (FRET): designs and applications. (0736-6205 (Print)).
36. Bandyopadhyay, D.; Mishra, P. P., Decoding the Structural Dynamics and Conformational Alternations of DNA Secondary Structures by Single-Molecule FRET Microspectroscopy. *Frontiers in Molecular Biosciences* **2021,** *8*.
37. Guyon, L.; Pirrotta, M.; Duskova, K.; Granzhan, A.; Teulade-Fichou, M.-P.; Monchaud, D., TWJ-Screen: an isothermal screening assay to assess ligand/DNA junction interactions in vitro. *Nucleic Acids Research* **2018,** *46* (3), e16-e16.
38. Howell, L. A.; Waller, Z. A. E.; Bowater, R.; O'Connell, M.; Searcey, M., A small molecule that induces assembly of a four way DNA junction at low temperature. *Chemical Communications* **2011,** *47* (29), 8262-8264.
39. Phongtongpasuk, S.; Paulus, S.; Schnabl, J.; Sigel, R. K. O.; Spingler, B.; Hannon, M. J.; Freisinger, E., Binding of a Designed Anti-Cancer Drug to the Central Cavity of an RNA Three-Way Junction. *Angewandte Chemie International Edition* **2013,** *52* (44), 11513-11516.
40. Gingras, A.-C.; Aebersold, R.; Raught, B., Advances in protein complex analysis using mass spectrometry. *The Journal of Physiology* **2005,** *563* (1), 11-21.
41. Largy, E.; König, A.; Ghosh, A.; Ghosh, D.; Benabou, S.; Rosu, F.; Gabelica, V., Mass Spectrometry of Nucleic Acid Noncovalent Complexes. *Chemical Reviews* **2022,** *122* (8), 7720-7839.
42. Rosu, F.; Gabelica, V.; Houssier, C.; Colson, P.; Pauw, E. D., Triplex and quadruplex DNA structures studied by electrospray mass spectrometry. *Rapid Communications in Mass Spectrometry* **2002,** *16* (18), 1729-1736.
43. Marchand, A.; Gabelica, V., Folding and misfolding pathways of G-quadruplex DNA. *Nucleic Acids Research* **2016,** *44* (22), 10999-11012.
44. Smargiasso, N.; Rosu, F.; Hsia, W.; Colson, P.; Baker, E. S.; Bowers, M. T.; De Pauw, E.; Gabelica, V., G-Quadruplex DNA Assemblies: Loop Length, Cation Identity, and Multimer Formation. *Journal of the American Chemical Society* **2008,** *130* (31), 10208-10216.
45. Monchaud, D.; Allain, C.; Bertrand, H.; Smargiasso, N.; Rosu, F.; Gabelica, V.; De Cian, A.; Mergny, J. L.; Teulade-Fichou, M. P., Ligands playing musical chairs with G-quadruplex DNA: A rapid and simple displacement assay for identifying selective G-quadruplex binders. *Biochimie* **2008,** *90* (8), 1207-1223.
46. Reznichenko, O.; Leclercq, D.; Franco Pinto, J.; Mouawad, L.; Gabelica, V.; Granzhan, A., Optimization of G-Quadruplex Ligands through a SAR Study Combining Parallel Synthesis and Screening of Cationic Bis(acylhydrazones). *Chemistry – A European Journal* **2023,** *29* (4), e202202427.

47. Gros, J.; Rosu, F.; Amrane, S.; De Cian, A.; Gabelica, V.; Lacroix, L.; Mergny, J.-L., Guanines are a quartet's best friend: impact of base substitutions on the kinetics and stability of tetramolecular quadruplexes. *Nucleic Acids Research* **2007,** *35* (9), 3064-3075.
48. Gabelica, V.; Shammel Baker, E.; Teulade-Fichou, M.-P.; De Pauw, E.; Bowers, M. T., Stabilization and Structure of Telomeric and c-myc Region Intramolecular G-Quadruplexes: The Role of Central Cations and Small Planar Ligands. *Journal of the American Chemical Society* **2007,** *129* (4), 895-904.
49. Gabelica, V., Native Mass Spectrometry and Nucleic Acid G-Quadruplex Biophysics: Advancing Hand in Hand. *Accounts of Chemical Research* **2021,** *54* (19), 3691-3699.
50. Duskova, K.; Lamarche, J.; Amor, S.; Caron, C.; Queyriaux, N.; Gaschard, M.; Penouilh, M.-J.; de Robillard, G.; Delmas, D.; Devillers, C. H.; Granzhan, A.; Teulade-Fichou, M.-P.; Chavarot-Kerlidou, M.; Therrien, B.; Britton, S.; Monchaud, D., Identification of Three-Way DNA Junction Ligands through Screening of Chemical Libraries and Validation by Complementary in Vitro Assays. *Journal of Medicinal Chemistry* **2019,** *62* (9), 4456-4466.
51. Reuter, J. S., Watson, Richard, M. https://rna.urmc.rochester.edu/index.html. (accessed 22/09/2023).
52. Chen, B.; Mason, S. F.; Bartlett, M. G., The Effect of Organic Modifiers on Electrospray Ionization Charge-State Distribution and Desorption Efficiency for Oligonucleotides. *Journal of the American Society for Mass Spectrometry* **2013,** *24* (2), 257-264.
53. Marty, M. T.; Baldwin, A. J.; Marklund, E. G.; Hochberg, G. K. A.; Benesch, J. L. P.; Robinson, C. V., Bayesian Deconvolution of Mass and Ion Mobility Spectra: From Binary Interactions to Polydisperse Ensembles. *Analytical Chemistry* **2015,** *87* (8), 4370-4376.
54. Yu, H.; Wang, X.; Fu, M.; Ren, J.; Qu, X., Chiral metallo-supramolecular complexes selectively recognize human telomeric G-quadruplex DNA. *Nucleic Acids Research* **2008,** *36* (17), 5695-5703.
55. Baker, E. S.; Dupuis, N. F.; Bowers, M. T., DNA Hairpin, Pseudoknot, and Cruciform Stability in a Solvent-Free Environment. *The Journal of Physical Chemistry B* **2009,** *113* (6), 1722-1727.

# Chapter 4 – Spherical Nucleic acids for delivery of DNA junction binders

## 4.1 Introduction

Spherical nucleic acids (SNAs) were first introduced by Mirkin *et al.* in 1996, with densely packed oligomers around a gold nanoparticle core.[1] The term "spherical nucleic acid" refers to any particle which is coated with DNA oligomers which are oriented perpendicular to the surface of the particle core. It is the orientation of the DNA oligomers in relation to the particle surface, and their dense packing, which conveys the unusual properties onto the particles themselves.[1] The core of the particle can be made of any nanoparticle material; gold and polymeric materials are the most common core materials.[2] Work has also been carried out to create hollow spherical nucleic acids by creating micelle structures[3] or by coating a solid core and then removing the core material.[4]

DNA itself consists of four bases, guanine (G), cytosine (C), thymine (T) and adenine (A) which all contain nitrogen heterocycles capable of interacting and adsorbing onto gold surfaces. Much work has been carried out to understand the interaction of DNA bases with the surface of gold nanoparticles, as well as to determine the relative affinities of the bases for gold particles. Publications agree unanimously that thymine has the weakest interaction with gold surfaces, likely due to a lack of an exocyclic amine group.[5, 6] There is some disagreement about the order of affinity of the remaining three bases which can be explained by the difference in gold substrates used, as well as by differences in the exact base moiety used and measurement technique. The general consensus shows that A > G > C > T.[6-11] As it is the bases in the DNA structure which strongly interact with the surface of the gold, the availability of the bases has a large influence on the affinity of a given oligo for the gold surface. For this reason, single stranded (ss) oligomers interact with the surface of the gold much more readily than double stranded (ds) oligomers.[12] This high affinity of nucleobases for gold surfaces has been used to create systems for sensing, and the high affinity of adenine has even been used to functionalise particles with oligomers containing adenine tails and no thiol group.[13] Yao *et al.* recently demonstrated how gold particles can be functionalised with one long single stranded adenine oligomer which can have a recognition sequence on it to create monovalent particles.[14]

The work in this chapter investigates the use of gold-SNA particles for the delivery of DNA binding agents. There are a number of different methods which can be used to coat gold nanoparticles with thiolated oligomers. Functionalisation of the particle surface with oligomers is itself quite straightforward, as DNA oligomers with thiols on the 5' or 3' end can be easily synthesised or purchased. Thiols are known to bind to gold surfaces very strongly and are commonly used to decorate the surface of gold particles with stabilizing groups and functional moieties. As discussed above, the bases of the DNA oligomers may also interact with the particle surface, this can lead to many different binding modes of the oligomers to the particle surface.

Methods have been developed to improve the density and uniformity of the oligomer coating on the gold particle surfaces. The earliest approaches introduced the process of "salt aging" which entailed gradually increasing the salt concentration of the particle solution in the presence of the oligomers to increase the ionic strength of solution. As the ionic strength of solution increases, the electrostatic repulsion experienced between neighbouring oligomers decreases, enabling them to pack more densely onto the surface of the particles. Other processes utilise surfactants or small amounts of thiolated polymers to provide extra stabilization to the particles through the salt aging process, particularly with larger gold nanoparticles.[15-17] More recently, a low pH method has been demonstrated which allows for coating of gold particles with high concentrations of DNA oligomers.[18] The distinct advantage of this low pH method is that the salt aging step takes less than an hour, rather than multiple days. At a pH lower than 3, both adenine and cytosine are protonated which significantly reduces the repulsion between DNA oligos on the particles and incoming oligomers.[18]

A PhD student, who graduated from the Hannon group, investigated the prospect of delivering supramolecular cylinders by using DNA tetrahedra.[19] The vertices of the tetrahedra have a three-way junction-like structure which could house a supramolecular cylinder as a guest. This DNA tetrahedra structure was shown to be absorbed into cells along with its cargo, increasing the uptake of the supramolecular cylinder. This increased uptake only resulted in modest cytotoxicity. The DNA tetrahdra were also functionalised with a ruthenium based cylinder which was able to act as a

photosensitizer, breaking down the DNA tetrahedron under irradiation with a weak light source and releasing the supramolecular complex. It was envisioned that this could be used *in vivo* to release the supramolecular cylinder in the desired areas. A limitation of the work carried out by Peter Cail with DNA tetrahedra was the relatively low loading of metal complexes that could be achieved on these DNA structures.[19] The use of gold-SNA may enable a much higher loading of metal complexes, and also opens the door for more elaborate particle systems in the future by making use of the unique properties of gold nanoparticles. The work presented in this chapter utilised gold-SNAs which were loaded with metal cylinders (NiP, AuPill, and PtCyl, discussed in Chapter 3). These metal cylinders have been shown to interact with B-DNA but, in competition studies, their preferred target is a junction structure. It was hypothesised that gold-SNAs could be loaded with metal cylinders which would weakly bind to the B-DNA on the surface of the particles but would be released in the presence of their preferred binding targets, DNA junctions.

The concept for this work has been demonstrated in a number of literature articles utilising DNA intercalators.[20-23] In all four examples referenced, doxorubicin or mitoxantrone (both DNA intercalating anti-cancer drugs) were loaded onto the gold-SNA particles. The drug was then released passively, by pH sensitivity, or through triggered release, by the complementary strand of the SNA recognising specific mRNA sequences. This causes the release of the intercalating drug as there is no longer a duplex to intercalate into. Most recently, "DNA ribbons" were prepared on the surface of gold particles through a rolling circle amplification reaction, (though this system is not strictly a SNA, the loading and release of drugs is similar) after which the particles could be loaded with the DNA intercalator, doxorubicin, by incubating the particles with the drug.[23] The drug was found to be released from the particles under low pH conditions, such as that often found in cancerous cells. The metal complexes studied in this work, NiP, AuPill, and PtCyl, are not DNA intercalators, but are thought to bind the grooves of DNA (PtCyl studied in Chapter 2).[24, 25] To the best of our knowledge, there is only one example in the literature of gold-SNA particles being used for the delivery of DNA groove binding agents.[26] Delivery of a ruthenium groove binding agent was shown to be successful by fluorescence

imaging. Successful delivery of this groove binder was notable as it was known to be impermeable to live cell membranes.[27]

## 4.2 Synthesis of Gold nanoparticles

Gold nanoparticles have been investigated for use in a variety of biological applications from diagnostics, therapy, drug delivery, and theranostics.[28, 29] Gold nanoparticles are quick and simple to synthesize, and are also very simple to functionalise. Furthermore, they display unique optical and electronic properties which can be controlled by varying the particle's shape and size. They have been shown by many papers to be biocompatible and have favourable uptake in cancers, which has been a large area of research.[30, 31]

### 4.2.1 Synthesis of AuNP13dsDNA

There are many methods of synthesising gold nanoparticles but, for this work, the Turkevitch method was selected. Particles produced by the Turkevitch method are stabilized by citrate which has no known adverse biological effects, they are also relatively small particles which are very monodisperse.[32] Monodispersity is very important for biological applications as we need to fully characterise and understand a particle system before *in vivo* studies can be considered.

#### *4.2.1.1 First method for synthesis of AuNP13dsDNA[M]*

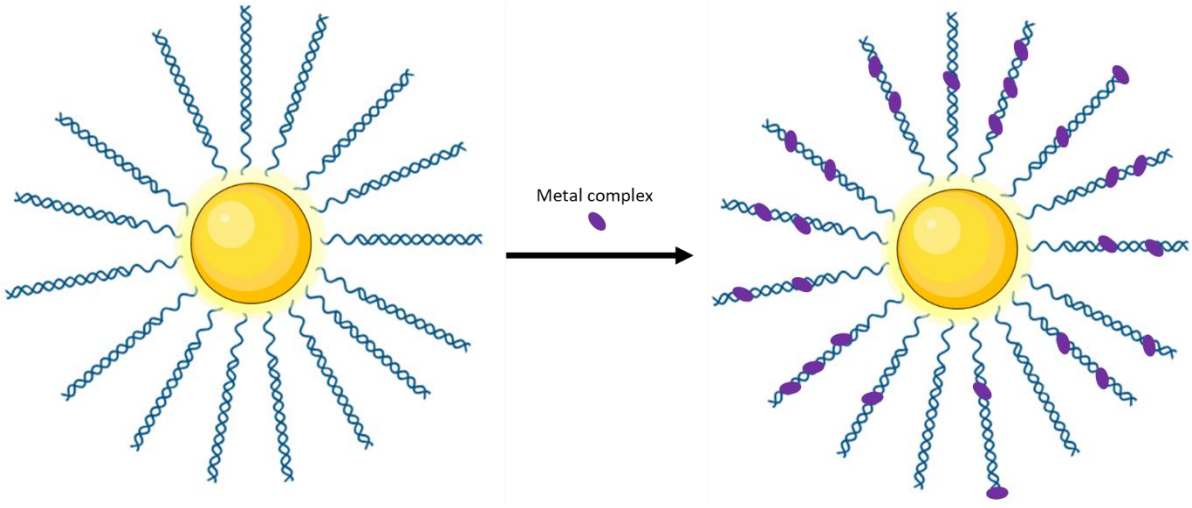


*Figure 1. Illustration of the first method attempted for loading of metal complexes onto gold-SNA particles (not to scale).*

The DNA sequence chosen to functionalise the surface of the particles has been previously utilised to produce spherical nucleic acids.[18] The sequence was specifically designed to not have any secondary structures or self-complementarity which could cause the particles to aggregate. Initial attempts in this

work to produce spherical nucleic acids utilised a low pH method, first employed by Zhang *et al.*[18] This method was shown to give a high loading and coverage of the particles with short thiolated oligomers. The first step in this process was to activate the thiol by reducing it with a mild reducing agent, TCEP (tris(2-carboxyethyl)phosphine). TCEP was not removed after activating the thiol groups on the DNA oligomers as it has a very low affinity for the gold surface.[33, 34] The activated DNA was then added to the gold nanoparticle solution, followed by a low pH citrate buffer. After stirring this solution for 30 minutes in the dark, the salt concentration of the solution was increased by the dropwise addition of concentrated salt solution over 30 minutes. This increase in ionic strength of the solution reduces the repulsion between oligomers, allowing for the oligomers to rearrange themselves and increase the coverage of the particle surface with the oligomer. The particles are then purified by centrifugation and removing the supernatant, followed using 30kda MWCO filters to further remove the excess DNA oligomers and TCEP. The complementary strand of DNA was then incubated with the gold particles, creating dsDNA helices on the surface of the particles which bind well to the metal complexes we are interested in. Small volumes of the NiP were then titrated onto the particles to try to load the dsDNA with metal complex, this immediately led to aggregation of the particles, even at low concentrations. This aggregation is thought to be caused by the cationic nature of the metal complexes which leads to the neutralization of the negative charge on the SNAs. The NiP is also known to interact with the ends of dsDNA through pi stacking interactions.[35] This may also contribute to aggregation of the particles as the complex may pi-stack onto the ends of the DNA oligomers of adjacent particles.

*Table 1. Data from the UV-vis absorption spectra of gold nanoparticles and their functionalised with NiP. FWQM is measured as the width of the SPR peak at 0.75 absorbance units after normalisation.*

| Sample | SPR / nm | FWQM / nm |
|---|---|---|
| AuNP13 | 519 | 56.5 |
| AuNP13dsDNA | 524 | 56.5 |
| AuNP13dsDNA + NiP | 556 | 97.5 |

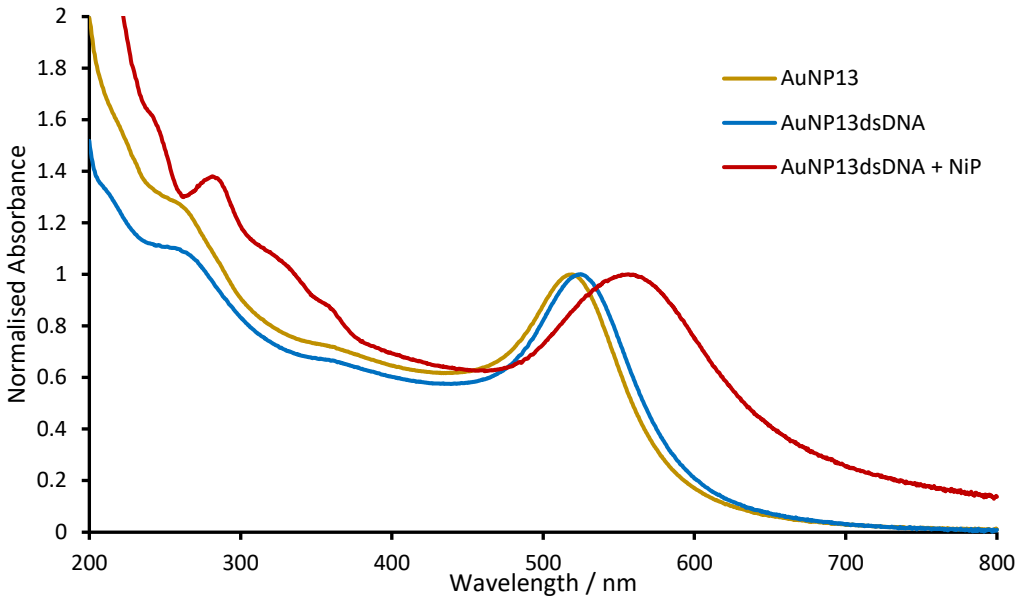


*Figure 2. UV-vis spectra of gold nanoparticles and their functionalisation with thiolated DNA oligomers and NiP normalised to the SPR peak of each sample for comparison.*

UV-vis spectra demonstrates that functionalisation of the particles with dsDNA appears to have been successful, as indicated by the slight shift in SPR (surface plasmon resonance) band of the particles (Figure 2 and Table 1) as well as the noticeable increase in the particle size as measured by DLS (dynamic light scattering) (Figure 3 and Table 2). The particle's hydrodynamic diameter, measured by DLS, increased from 20.0 nm to 36.7 nm when stabilized with the short thiolated oligomer. The length of the thiolated oligomer was 12 bases; assuming equal coverage all over the particle, a size increase of approximately 9.5 nm would be expected (accounting for 12 bases each side of the particle and the addition of the C6 spacer between the oligomer and the thiol). The larger than expected increase in particle size is likely due to very mild aggregation. The PDI (polydispersity index) of the particles increases from 0.1 to 0.2, suggesting some aggregation, but the particles are still relatively monosdisperse. Aggregation may be caused by non-specific interactions between oligomers on adjacent particles. The quality of the particles produced was also monitored by the FWQM (full width quarter maximum) measurement, which is the width of the SPR peak of the particles at three quarters of the normalised peak. The FWQM is simply a measurement to quantify any broadening of the SPR peak. The SPR of gold nanoparticles is known to broaden when the particles begin to aggregate, there is also generally a large redshift as the particles aggregate more significantly.[36]

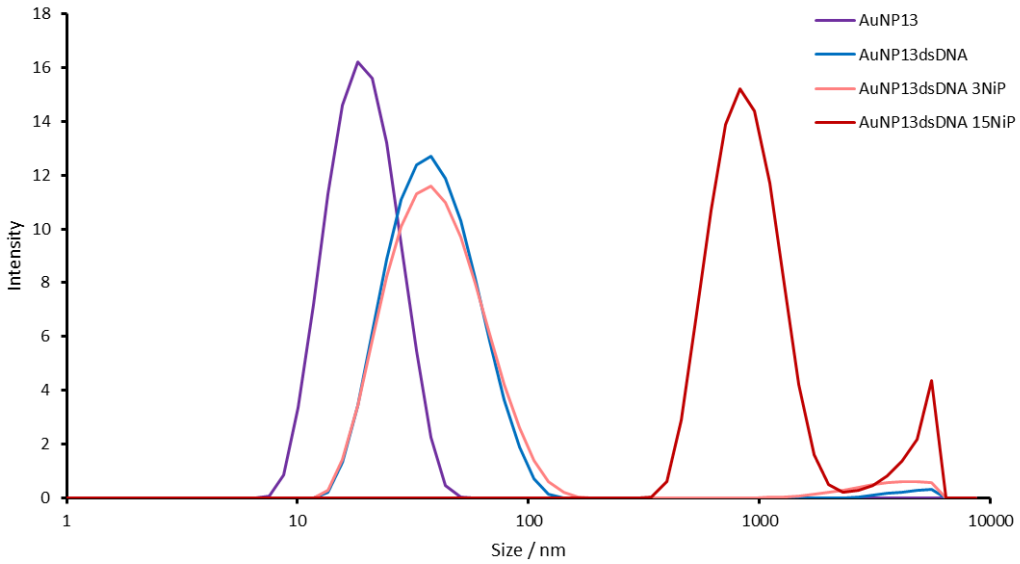


*Figure 3. DLS measurements of gold nanoparticles and their functionalisation with DNA oligomers and varying concentrations of NiP (AuNP13dsDNA 3NiP = 2.5 µM NiP, AuNP13dsDNA 15NiP = 12.5 µM NiP).*

When the NiP metal complex is titrated onto the gold particles, there is an immediate increase in particle size and a subsequent increase in the PDI of the particles. The particles which were titrated with a lower concentration of the NiP complex resulted in a modest PDI of 0.248, which is considered fairly monodisperse. However, there is the formation of a peak at approximately 4500 nm which indicates some aggregation of the particles. The formation of aggregated particles would make these particles unsuitable for use in biological studies. It was therefore decided that an alternative method would have to be used to functionalise the particles with the metal complexes.

*Table 2. DLS data of gold nanoparticles and their functionalisation with DNA and carrying concentrations of NiP measured by Intensity (AuNP13dsDNA 3NiP = 2.5 µM NiP, AuNP13dsDNA 15NiP = 12.5 µM NiP).*

| Sample | Hydrodynamic diameter / nm | PDI (polydispersity index) |
|---|---|---|
| AuNP13 | 20.0 | 0.1 |
| AuNP13dsDNA | 41.56 (99 %) | 0.203 |
| | 4449 (1 %) | |
| AuNP13dsDNA 3NiP | 43.6 (96 %) | 0.248 |
| | 4449 (4 %) | |
| AuNP13dsDNA 15NiP | 899.7 (90 %) | 0.42 |
| | 4752 (10 %) | |

#### 4.2.1.2 Final method for producing AuNP13dsDNA[M]

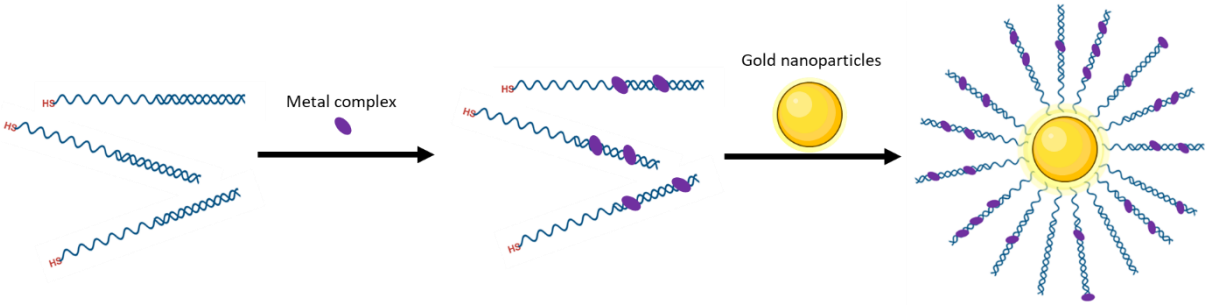


*Figure 4. Illustration of the final method used to thiolated dsDNA with metal complex followed by functionalisation of gold nanoparticles with the dsDNA (not to scale).*

Loading the negatively charged DNA coated gold nanoparticles with positively charged metal complexes was not possible in a sequential manner, as this led to irreversible aggregation of the particles. The next method investigated involved loading the dsDNA oligomers with the metal complex prior to functionalising the surface of the gold particles with the duplex DNA. The low pH method for functionalising the surface of gold particles with thiolated oligomers has only been carried out with ssDNA so the standard salt ageing method was used instead.

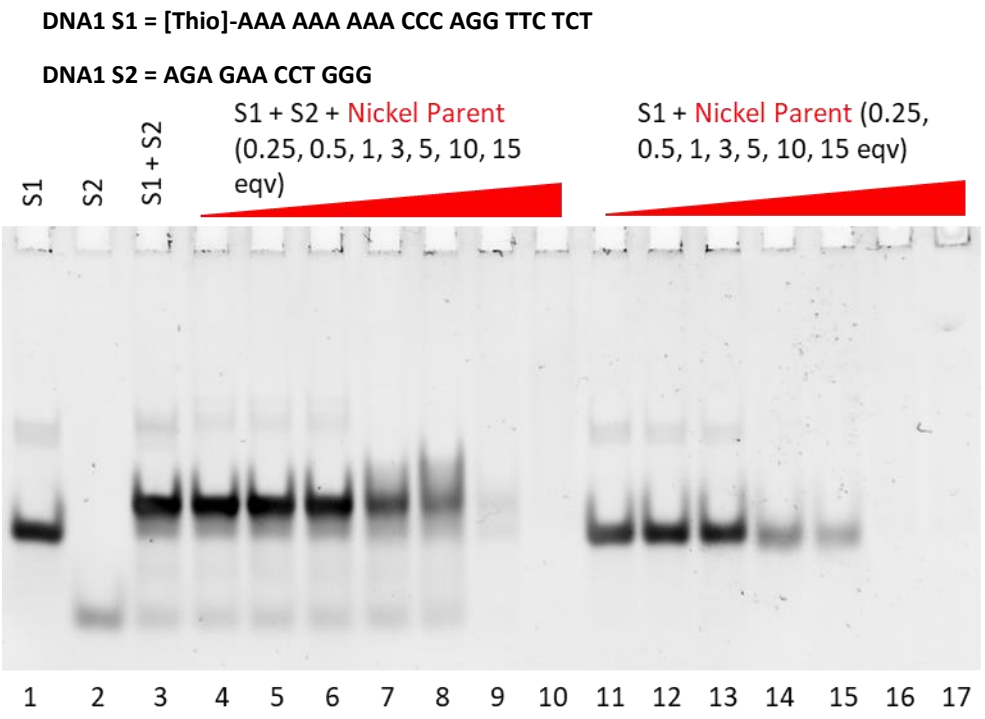


*Figure 5. PAGE gel (89 mM Tris base, 89 mM Boric acid, pH 8.3, 15% acrylamide gel) for the loading of thiolated DNA oligomer and its complementary strand with NiP (lanes 4-10) and thiolated oligomer with NiP (lanes 11-17).*

PAGE gels were carried out to determine the appropriate loading of metal complex onto the dsDNA (Figure 5, Figure 6, and Figure 7); the thiolated dsDNA used to coat the particles was incubated with

varying concentrations of metal complex. The individual oligomers are shown in lanes 1 and 2 of each PAGE gel as controls. S1 is significantly longer than S2 as it contains an adenine spacer unit which is intended to remain as a single strand when bound to the particles. The spacer unit allows for a denser covering of dsDNA and ensures that the recognition sequence is accessible. The nature of the base which makes up the spacer is also significant; adenine was selected as this base interacts strongly with the gold particle's surface and aids in the initial attachment of the oligomers to the gold surface.[14] The complementary strand S2 is much shorter than the thiolated oligomer and therefore migrates further through the PAGE gel. S2 produces a single band in the gel as expected, whereas S1 shows some secondary structure formation with a faint band higher in the gel indicating the formation of a larger structure in Figure 5 (possible structure shown in appendix A4.1). It is not clear why this extra secondary structure is not present in Figure 6 or Figure 7. Lane 3 in each of the three PAGE gels contains a 1:1 mixture of S1 and S2 which is designed to form a duplex with a 9 base spacer. As expected, S1 + S2 creates a new band in the gel which does not migrate as far as either S1 or S2, indicating that the duplex structure has been formed. There are also some faint bands in lane 3 which can be attributed to small amounts of S1 and S2 left in solution.

With increasing equivalents of the NiP, the structure of the dsDNA is not altered until a ratio of 5:1 is reached (Figure 5). At a 5:1 ratio of metal complex to the dsDNA structure, the band in the PAGE gel begins to smear significantly, indicating a mixed and undefined species in the gel. For this reason, it was decided to load the dsDNA with a ratio of three NiP per oligomer duplex. Loading of just the S1 strand was also investigated (Figure 5). Smearing of the S1 band alone also began at a ratio of 5:1 NiP per oligomer, at 15 complexes per oligo, the band is no longer visible in the gel. The high concentration of the cationic metal complex is sufficient to saturate the negative charge of the oligomer, causing it to precipitate out of solution.

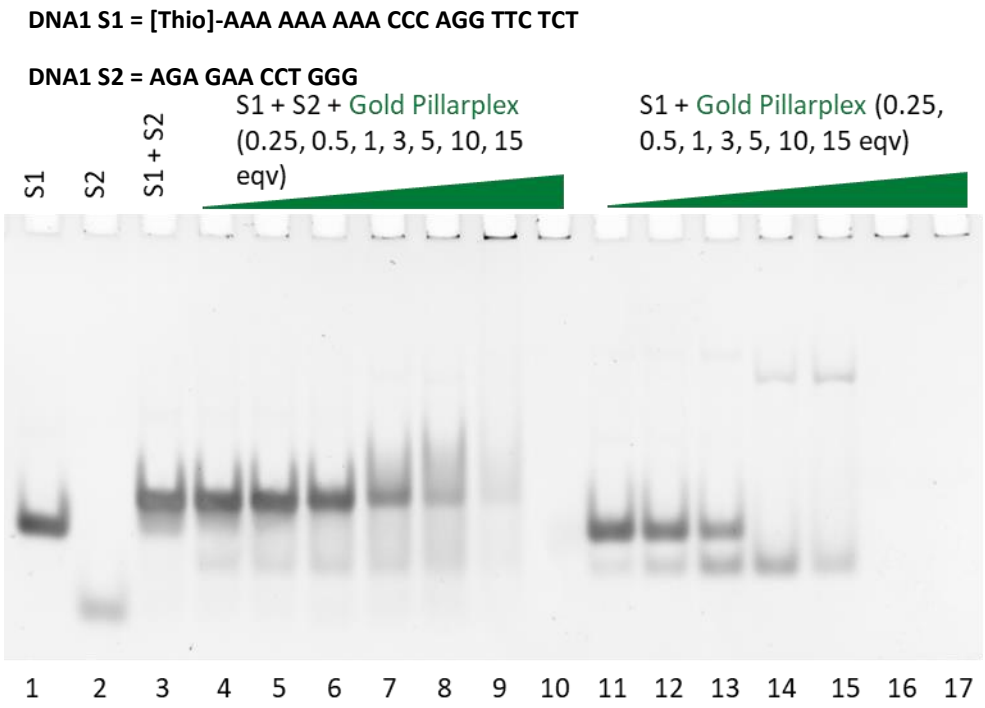


*Figure 6. PAGE gel (89 mM Tris base, 89 mM Boric acid, pH 8.3, 15% acrylamide gel) for the loading of thiolated DNA oligomer and its complementary strand with AuPill (lanes 4-10) and thiolated oligomer with AuPill (lanes 11-17).*

Increasing equivalents of AuPill with the duplex DNA1 does not have a significant effect on the structure until 5 equivalents of metal complex are added (Figure 6). This is much the same as has been observed with the NiP. In lane 3, containing S1+S2, there is a small faint band which aligns with the shift of S1 alone. With increasing equivalents of AuPill up to 3 equivalents, the S1 band appears to decrease in intensity, suggesting that the AuPill encourages the formation of the duplex. Additions of AuPill to S1 (lanes 11-17) initially results in the formation of a new band which migrates further through the gel than the S1 oligomer alone. This is unexpected and appears to be unique to the AuPill metal complex. With high equivalents of AuPill, the S1 band completely disappears leaving just the new band, which shifts further through the gel. Another new structure which has had its migration significantly retarded in relation to the S1 band. This new band appears to be unique to the AuPill. It was speculated that this may be due to the adenine spacer unit on the DNA1 S1 oligomer interacting with the pi surfaces of the AuPill, but this was not investigated further.

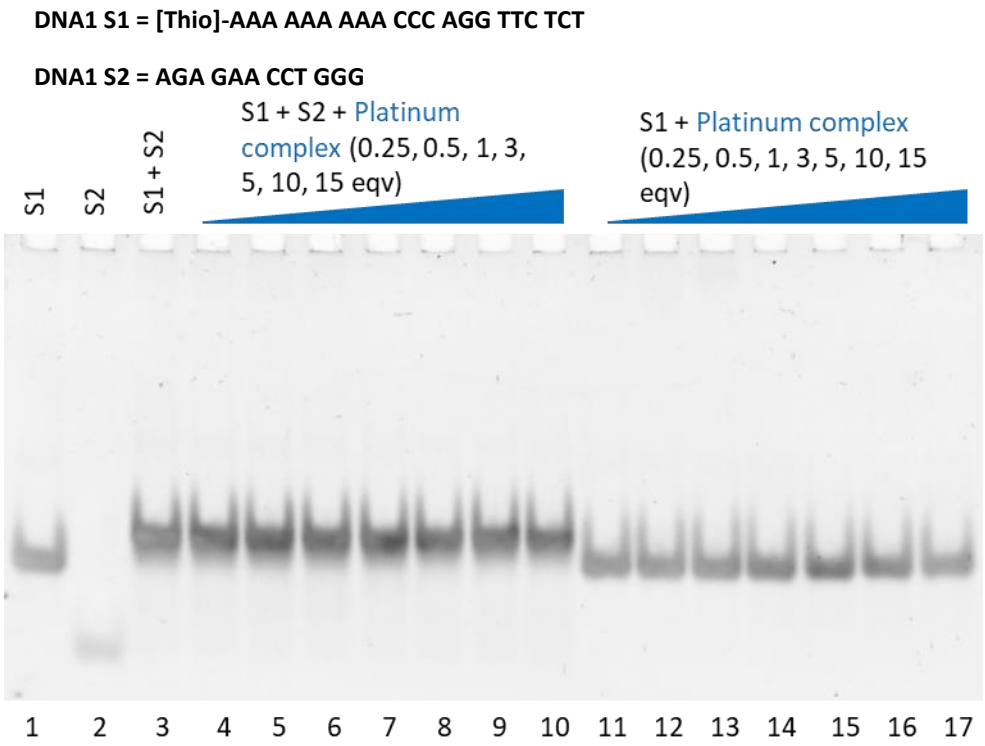


*Figure 7. PAGE gel (89 mM Tris base, 89 mM Boric acid, pH 8.3, 15% acrylamide gel) for the loading of thiolated DNA oligomer and its complementary strand with PtCyl complex (lanes 4-10) and thiolated oligomer with PtCyl (lanes 11-17).*

With higher equivalents of the PtCyl, the duplex structure of S1 + S2 does not show any change (Figure 7). There is also no change in the S1 oligomer alone with increasing equivalents of the PtCyl complex. This lack of change in the DNA structure is not entirely unexpected, as fluorescence displacement studies presented in Chapter 3 indicate a significantly weaker interaction of PtCyl with B-DNA compared to the AuPill or NiP.

With these PAGE gels in mind, it was decided to move forward with a ratio of 3 metal complexes per oligomer, as this ratio does not appear to have a significant effect on the duplex (or S1) structure of the DNA. The gold nanoparticles were functionalised by incubating them with excess duplex DNA, pre-loaded with a metal complex. Aliquots of saline solution were then added gradually to the particle solution over a period of 8 hours. The particles were then collected by centrifugation and removal of the supernatant, followed by further purification using 30 kDa MWCO filters.

*Table 3. UV-vis SPR and FWQM data for gold nanoparticles and gold nanoparticles functionalised with thiolated DNA and either NiP, AuPill, or PtCyl complex in water.*

| Sample | SPR / nm | FWQM / nm |
|---|---|---|
| AuNP13 | 518.5 | 56 |
| AuNP13dsDNA | 523.5 | 65 |
| AuNP13dsDNA NiP | 526 | 60.5 |
| AuNP13dsDNA Pt | 524 | 60.5 |
| AuNP13dsDNA AuPill | 524 | 64.5 |

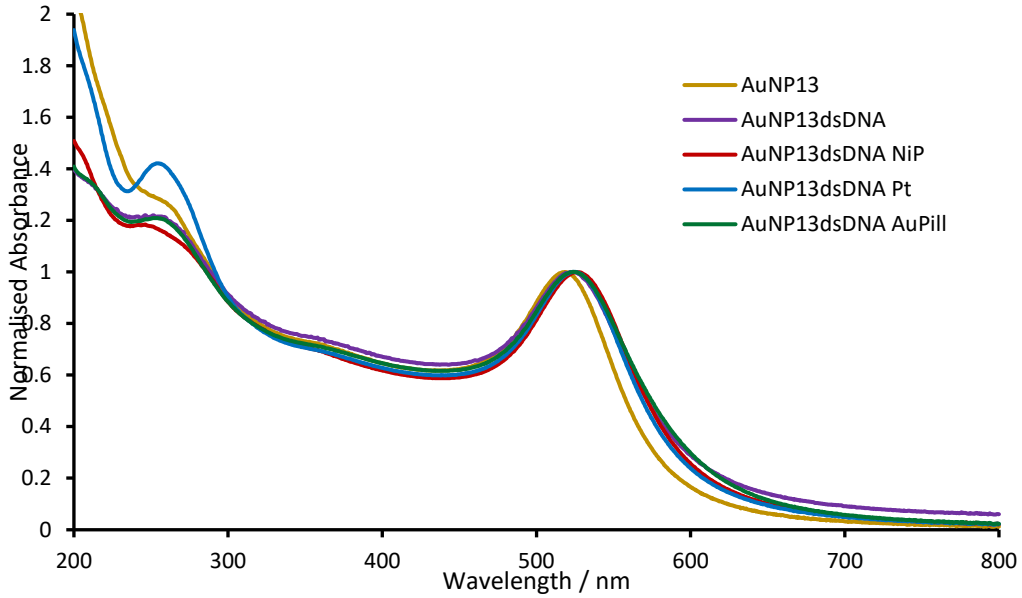


*Figure 8. UV-vis spectra of gold particles and gold nanoparticles functionalised with thiolated DNA and either NiP, AuPill, or PtCyl complex in water.*

UV-vis measurements of the particles after functionalisation with the duplex DNA, which has already been loaded with the metal complexes, is shown in Figure 8. The oligomers were functionalised with the metal complex by incubating at room temperature for 1 hour, before adding the solution to the gold nanoparticles, followed by a salt aging process and purification to remove excess oligomer and metal complex in solution. The lack of aggregation visually observed when adding the concentrated salt solution to the particles was a quick indication that the particle surface was modified with the oligomers. Gold nanoparticles coated in citrate will aggregate almost instantaneously, even with the addition of low concentrations of salt. The redshift observed also indicates that the particles have been successfully functionalised with the oligomers. The FWQM of the nanoparticle SPR peak is measured to quantify any broadening of the SPR peak. Broadening of gold nanoparticles' SPR peak is indicative of aggregation of the particles. Only mild broadening of the SPR peak of the gold particles is observed when they are functionalised with the DNA oligomers. This suggests that the particles remain monodisperse in solution.

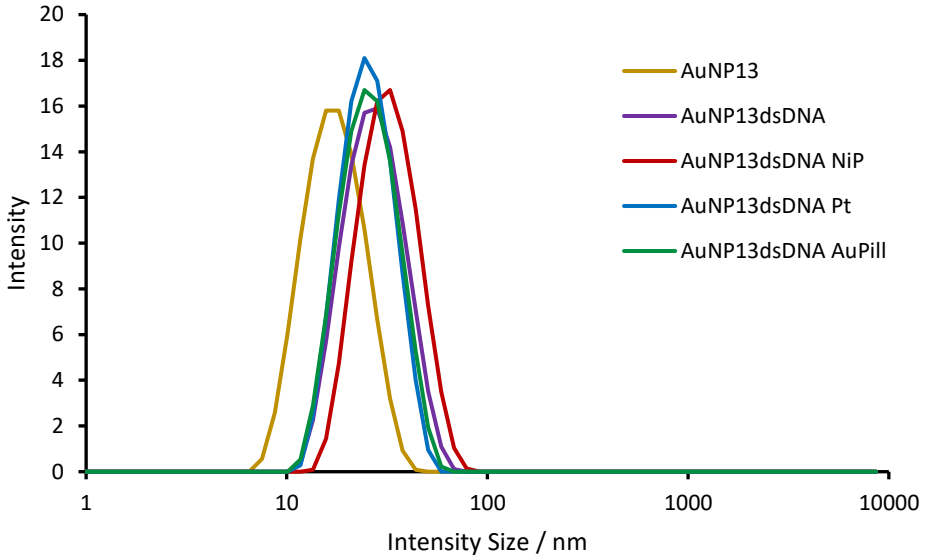


*Figure 9. DLS intensity data of AuNP13 and AuNP13 functionalised with thiolated DNA and NiP, PtCyl or AuPill.*

Dynamic light scattering (DLS) was used to check the quality of the particles as well as to confirm whether the functionalisation of the particles' surface with the DNA oligomers had been successful or not. Figure 9 shows that each particle solution is composed of a single distribution of particles. The hydrodynamic diameter of the citrate coated gold particles (AuNP13) is measured to be 18.1 nm, there is a drastic increase in particle size to 28.5 nm when functionalised with the dsDNA (Table 4). The PDI of each particle solution functionalised with dsDNA was below 0.2 indicating highly monodisperse particles. The particles functionalised with the dsDNA, which had been pre-loaded with NiP, shows an even greater increase in size of the particles to 33.5 nm in diameter. The particles functionalised with the oligomer loaded with PtCyl or AuPill had a hydrodynamic diameter of 26.2 nm and 26.9 nm, respectively. A decrease in hydrodynamic diameter of the particles compared to the AuNP13dsDNA could be explained by a contraction in the dsDNA layer, caused by the reduction in repulsion between adjacent oligomer due to the presence of a positively charged metal complexes. The increase in size of the AuNP13dsDNA NiP compared to the AuNP13dsDNA is unexpected but could be caused by mild aggregation of some of the particles, which would skew the DLS measurement. The zeta potential of the AuNP13dsDNA alone, and loaded with AuPill and PtCyl are very similar (AuNP13dsDNA = -29.5$\pm$6.48, AuNP13dsDNAAuPill = -30.7$\pm$6.95, and AuNP13dsDNAPtCyl = -27.4$\pm$7.46). This suggests that the loading of AuPill or PtCyl onto the AuNP13dsDNA has not been very successful. A high loading

of the cationic metal complex on to the particles would be expected to result in a decrease in the magnitude of the zeta potential. A decrease in the magnitude of the zeta potential for AuNP13dsDNANiP (AuNP13dsDNANiP = -18.2±13.24) is observed suggesting a higher loading of NiP on the particles compared to the AuPill and PtCyl (appendix A4.2).

*Table 4. DLS intensity data of AuNP13 and AuNP13 functionalised with thiolated DNA and NiP / AuPill / PtCyl.*

| Sample | Hydrodynamic diameter / nm | PDI |
|---|---|---|
| AuNP13 | 18.08 | 0.125 |
| AuNP13dsDNA | 28.52 | 0.173 |
| AuNP13dsDNA NiP | 33.53 | 0.168 |
| AuNP13dsDNA Pt | 26.18 | 0.111 |
| AuNP13dsDNA AuPill | 26.85 | 0.192 |

Of primary concern when functionalising gold particles was the removal of any left-over oligomers and free metal complexes in solution. Purification of the particles was achieved by successive washes by centrifugation and removal of the supernatant. This was followed using 30KDa MWCO filters to concentrate the particles and allow excess oligomers and metal complexes to pass through. The purification was verified by incubating the final wash solution with 3WJ oligomers. This solution was then run on a PAGE gel where any formation of 3WJ could be observed (lane 18 in Figure 10, Figure 13, and Figure 16). The lack of a 3WJ band formed indicates that the concentration of metal complex in solution is lower than 0.01 µM. The limit of detection of a DNA 3WJ band on a PAGE gel stained with SYBR gold was found to be 0.01 µM (shown in appendix A4.3).

### 4.2.2 3WJ PAGE release studies

The gold nanoparticles were successfully synthesised with a coating of double stranded DNA which was loaded with metal complexes. The experiments carried out in this section were used to determine if the metal complexes could be released from the surface of the gold-SNA particles to DNA junctions. To achieve this, a 3WJ PAGE gel assay was. The particles were incubated with the 14-mer 3WJ which consists of three separate oligomers; the three oligomers only come together to form a 3WJ structure when a junction binding agent is present. The gold-SNA particles should become stuck in the wells of the gel, as they are too large to pass through the poly acrylamide matrix. Any free DNA oligomers in solution would be able to migrate through the gel which will reveal if any of the oligomers coating the

particles are free in solution, as well as allowing the 3WJ oligos and 3WJ structure to move freely through the gel. There are a few drawbacks when quantifying the metal complex released in this way:

1. Staining of the DNA structures may be inhibited by the metal complexes binding to the DNA.
2. There may be some degree of fluorescence quenching of the SYBR gold by the metal complexes.
3. Staining of the PAGE gel with SYBR gold is not always uniform.
4. Dense bands of DNA are sometimes not stained through to the centre due to complex binding mentioned in point 1, or perhaps due to the high concentration of DNA.

Future work could use the fluorescently tagged 3WJ used in Chapter 3 for competition PAGE gels (the fluorescently tagged 3WJ was unfortunately not available at the time this work was carried out). Fluorophore or radiolabelled 3WJ would overcome some of the problems related to staining the gel.

Figure 10 contains the PAGE gel of AuNP13dsDNANiP with 3WJ. Lane 10 was a control lane to show that there were no free oligomers coming off the AuNP13dsDNA particles. Lane 11 was a further control to confirm that the oligomers on the surface of the gold particles were not interacting with the 3WJ oligomers. There was no indication of any 3WJ formation with AuNP13dsDNA. AuNP13dsDNANiP was loaded in lane 12 with no 3WJ to confirm that there were no free oligomers coming off the particles because of the presence of the metal complex. Lanes 13-17 contain samples where 1 μM of 3WJ was incubated with varying concentrations of the AuNP13dsDNANiP to quantify the concentration of metal complex per particle. To confirm there was minimal free metal complex in solution, the final wash of the particles was incubated with 3WJ oligomers in lane 18. No 3WJ structure was formed indicating that there was a less than 0.01 μM metal complex in solution (PAGE testing the limit of detection of each metal complex with DNA 3WJ shown in appendix A4.3).

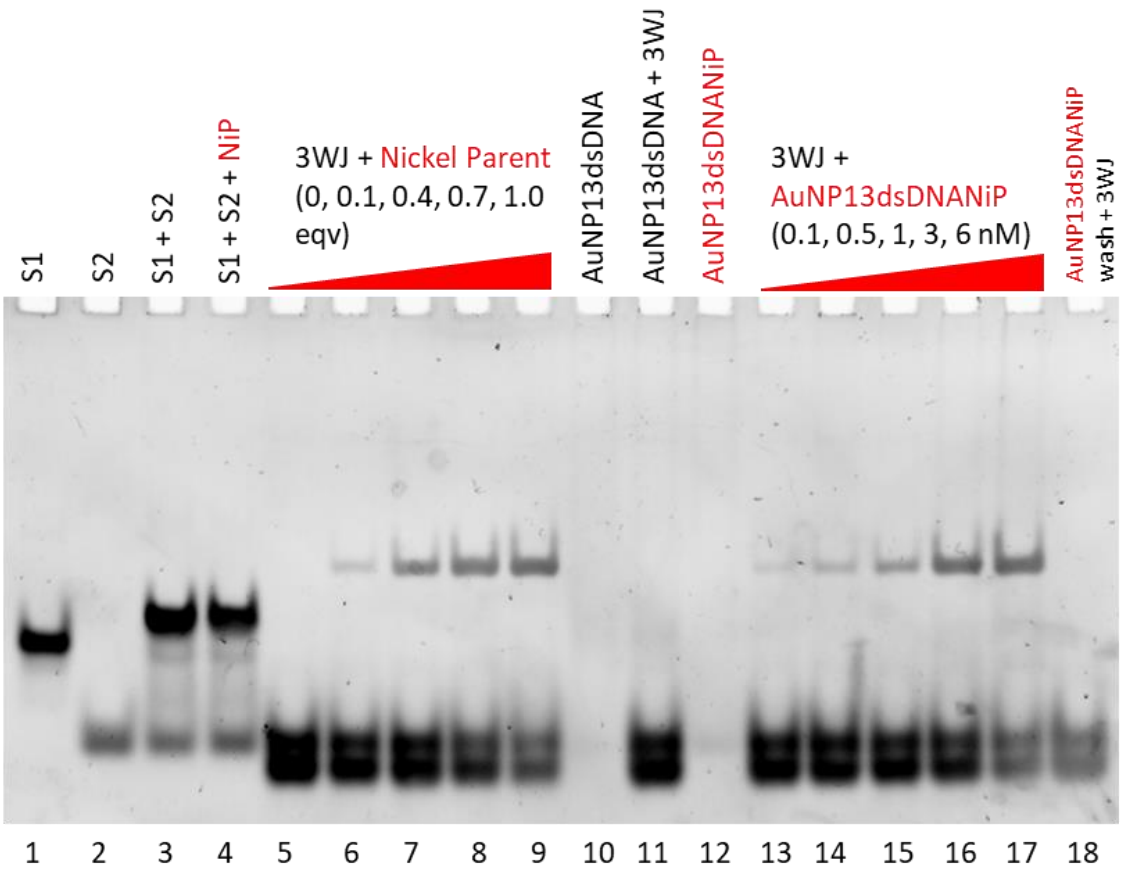


*Figure 10. PAGE gel (89 mM Tris base, 89 mM Boric acid, pH 8.3, 15% acrylamide gel) of AuNP13dsDNA3NiP with 3WJ oligomers.*

Quantification of the amount of metal complex that was released from the surface of the gold particles was possible by measuring the intensity of the 3WJ band formed. SYBR Gold was used to stain the gel and visualise the DNA structures present. The intensity of the 3WJ band should be proportional to the amount of DNA present.[37] All intensity measurements were carried out using ImageJ and its inbuilt gel analysis feature. A series of controls were carried out by varying the concentration of NiP with 3WJ (Figure 10, lanes 5-9), in order to determine the expected 3WJ band intensity with different concentrations of the NiP (Figure 11). A linear fit was expected but the measured intensity deviates at higher concentrations. The lower-than-expected 3WJ band intensity is likely caused by staining of more concentrated bands in the gel being less efficient, and by NiP binding to the 3WJ making it more difficult for the SYBR Gold to intercalate into the DNA duplex. Using the equation derived from Figure 11, the intensity of the 3WJ band induced by the varying concentrations of AuNP13dsDNANiP can be plotted to reveal the concentration of metal complex released from the surface of the particles (Figure 12).

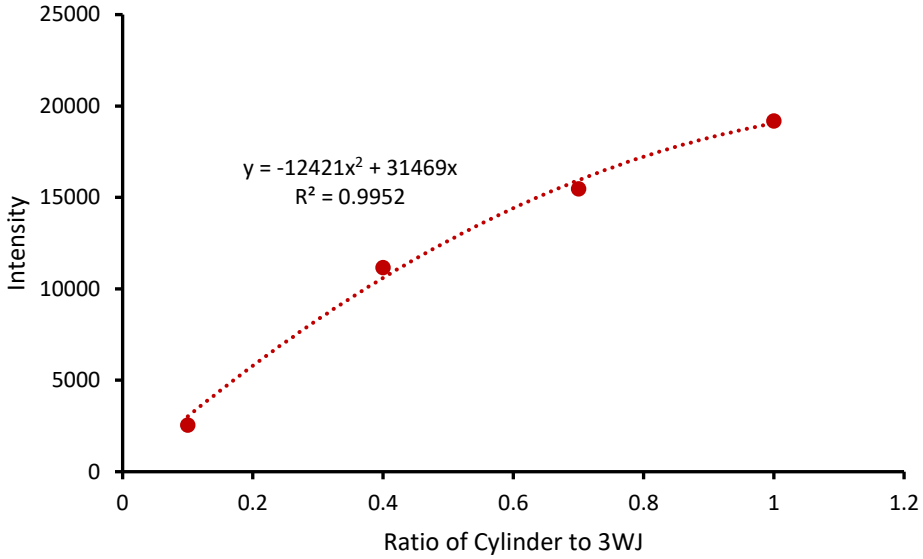


*Figure 11. Calibration for 3WJ intensity with known concentrations of NiP (3WJ band intensity measured using ImageJ).*

The concentration of NiP on AuNP13dsDNA3NiP is calculated to be 330 complexes per particle (Figure 12). This is close to the expected loading capacity on the particle which was approximated based on literature which shows that the number of oligomers per 13.5 nm gold nanoparticles should be approximately 100 oligomers per particle.[15, 18, 38, 39] The intensity of the 3WJ band increases in a linear manner, with increasing concentration of the AuNPdsDNANiP particles up to 3 nM of AuNP13dsDNANiP. This indicates that there is a steady release of the metal complex from the surface of the particles.

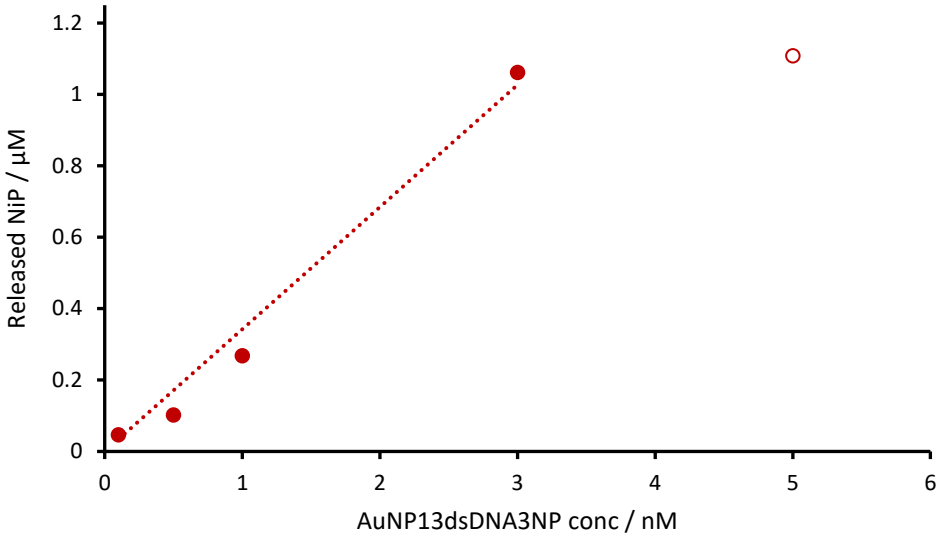


*Figure 12. Concentration of particles vs the derived concentration of NiP which is released from the particles (calculated from the 3WJ intensity). Hollow data point is excluded from the trendline.*

The same PAGE gel assay which was carried out with AuNP13dsDNANiP was also used to study AuNP13dsDNAPt (Figure 13). Unlike AuNP13dsDNANiP, AuNP13dsDNAPt did display some free oligomers in solution, despite the purification carried out. The excess oligomers can be seen in lane 12 and at higher concentrations of the particles with 3WJ shown in lanes 16 and 17. The presence of free oligomers in solution, which correspond to the double stranded DNA1, complicate the attempts at quantification as any PtCyl released could be from the free oligomers, or from the particles. Since there are no free oligomers visible for AuNP13dsDNANiP, some possibilities, such as the electrophoresis pulling the oligomers off the surface of the particles, can be discounted. There are no free oligos in the wash solution in lane 18 which indicates that the oligomers are coming off the surface of the particles or that the washing step is somehow retaining the free oligomers in solution.

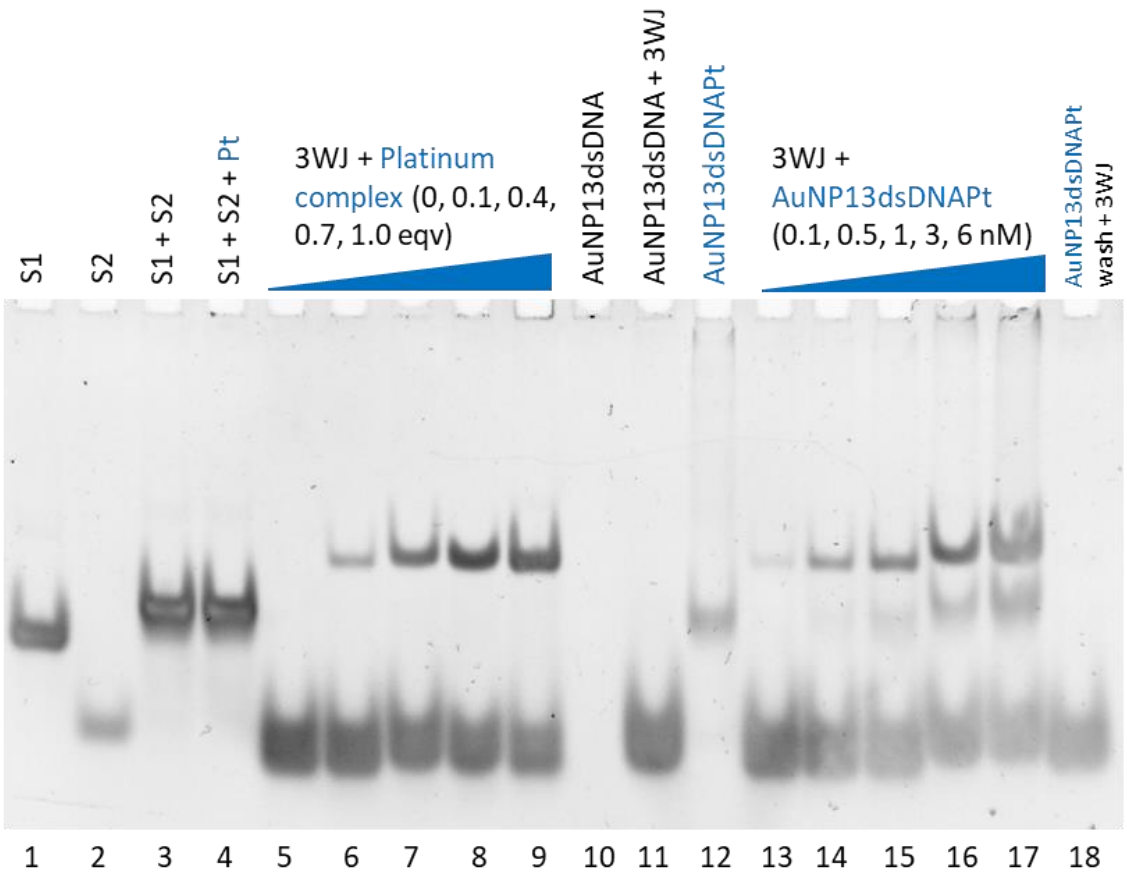


*Figure 13. PAGE gel (89 mM Tris base, 89 mM Boric acid, pH 8.3, 15% acrylamide gel) of AuNP13dsDNA3Pt with 3WJ oligomers.*

Despite the difficulties described above, quantification of the 3WJ band was attempted, to get an estimate of the amount of PtCyl loaded onto the particles' surface (Figure 14). The control lanes containing known concentrations of PtCyl and the 3WJ again show a linear relationship at low concentrations which plateaus with higher concentrations of metal complex.

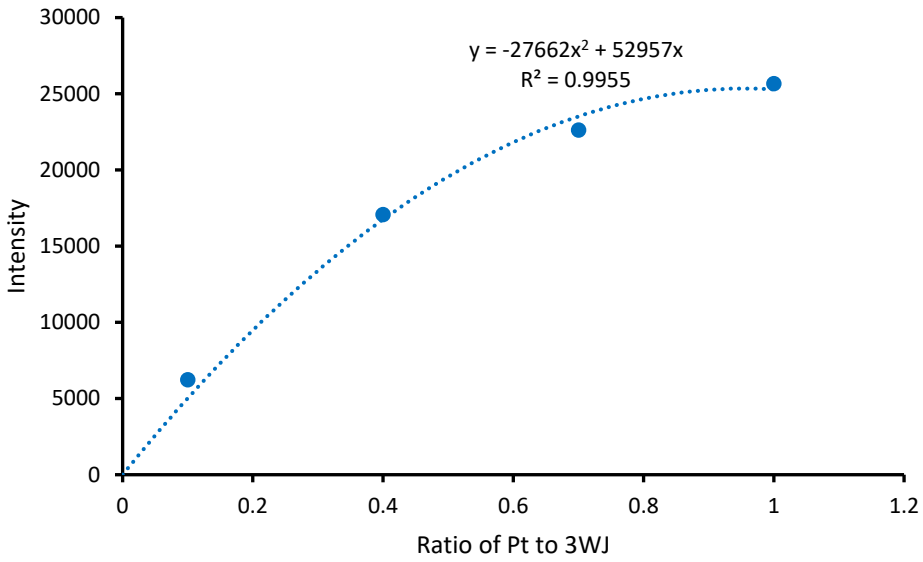


*Figure 14. Calibration for 3WJ intensity with known concentrations of PtCyl.*

Quantification of the amount of PtCyl per particle is shown in Figure 15. There is a clear plateauing of the series at high concentrations of AuNP13dsDNAPt. This is thought to be due to the issues related to staining using SYBR gold which were discussed earlier in this section. If the data points for the higher concentrations of particles are ignored, then we can plot a trendline to estimate the loading of PtCyl on the particles. This method estimates a loading of 225 PtCyl per particle.

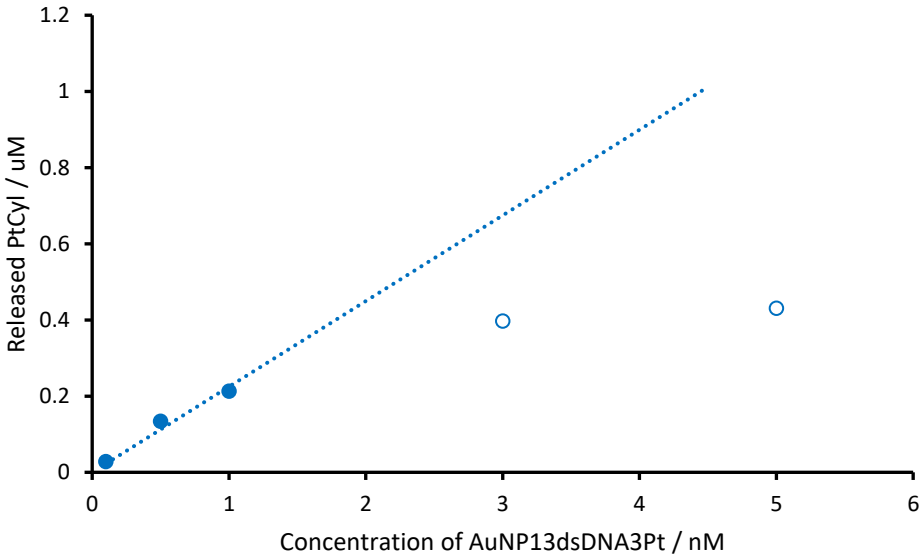


*Figure 15. Quantification of the concentration of PtCyl on a given concentration of AuNP13dsDNAPt. Hollow data points are excluded from the trendline.*

The interaction of AuNP13dsDNAAuPill with DNA 3WJ was investigated by the same PAGE experiment described for AuNP13dsDNANiP and AuNP13dsDNAPt (Figure 16). AuNP13dsDNAAuPill alone reveals

a small quantity of free dsDNA which is visible in the PAGE gel (lane 12). The 3WJ with increasing concentrations of AuNP13dsDNAAuPill only induced the formation of the 3WJ structure at very high concentrations of the particles. This could indicate that the loading of AuPill onto the particles is very low, or that the AuPill is not being released from the particles' surface. The second possibility seems unlikely, given the competition experiments described in Chapter 3 where the AuPill shows a clear preference for 3WJ over double stranded DNA. However, the DNA environment created by a spherical nucleic acid could be considered to be quite different from simple double stranded DNA, due to the close packing of many parallel strands of DNA.[40]

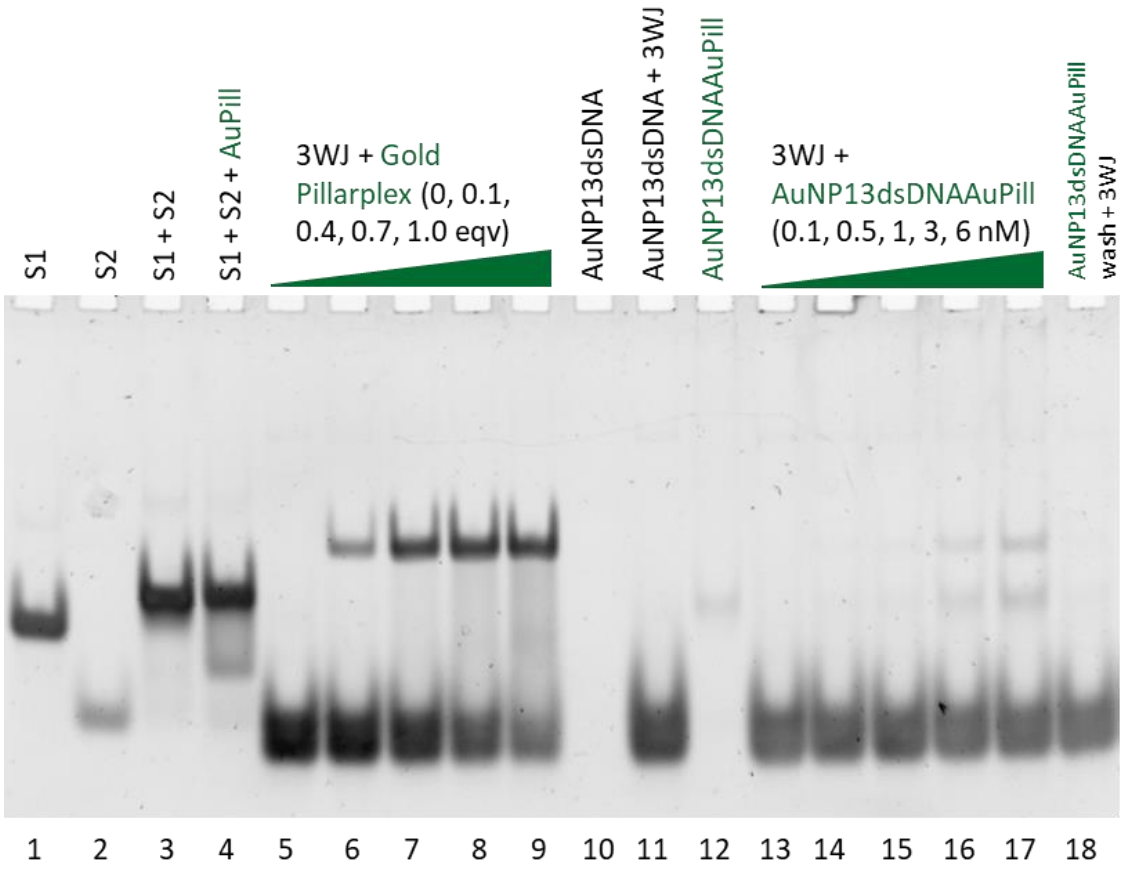


*Figure 16. PAGE gel (89 mM Tris base, 89 mM Boric acid, pH 8.3, 15% acrylamide gel) of AuNP13dsDNA3AuPill with 3WJ oligomers.*

Quantification of the release of AuPill from the AuPill loaded gold nanoparticles was carried out using ImageJ but there were some difficulties due to the control lanes of the AuPill complex with the 3WJ (lanes 5-9). As can be seen in Figure 16, in lanes 5-9, with increasing ratio of AuPill to 3WJ, there is a noticeable increase in the smearing of the 3WJ band in the gel, but no significant increase in the intensity of the 3WJ band itself. For this reason, we simply measured the maximum intensity of the

3WJ band with one equivalent of AuPill to determine when the 3WJ was saturated with AuPill. Increasing equivalents of AuNP13dsDNAAuPill with one equivalent of 3WJ (Figure 16, lanes 13-17) gives a very small increase in the 3WJ band intensity, as shown in Figure 17.

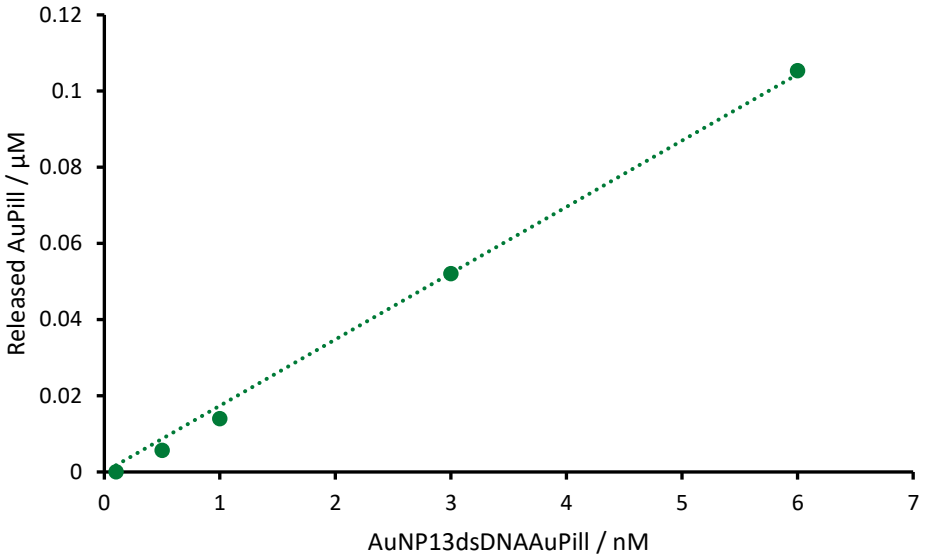


*Figure 17. Quantification of the concentration of AuPill on a given concentration of AuNP13dsDNAAuPill.*

Overall, these PAGE gel experiments confirm that the particles were successfully loaded with PtCyl, NiP, and AuPill. The gold-SNA particles loaded with NiP show good release of the NiP to a 3WJ structure, with a relatively high loading of NiP achieved. Loading of gold-SNA with PtCyl appears to be somewhat successful but these particles also released oligomers into solution, it is currently not clear what caused this. The AuPill was loaded onto gold-SNA particles, but very little release was observed by PAGE gel. This indicates that either very little AuPill was loaded, or that the AuPill is retained on the particles' surface. The NiP loaded particles were the most promising due to their high loading and release of NiP, and the lack of free oligomers detected by PAGE gel. For this reason, the AuNP13dsDNANiP particles are further studied below (Sections 4.2.3 and 4.2.4).

### 4.2.3 LD of AuNP13dsDNANiP

Linear dichroism (LD) was used to investigate whether the NiP could be released from the surface of the AuNP13dsDNANiP in the presence of B-DNA. The NiP cylinder is known to have a strong interaction with B-DNA, causing a decrease in the B-DNA signal due to coiling of the duplex and eventual condensation at high concentrations.[41]

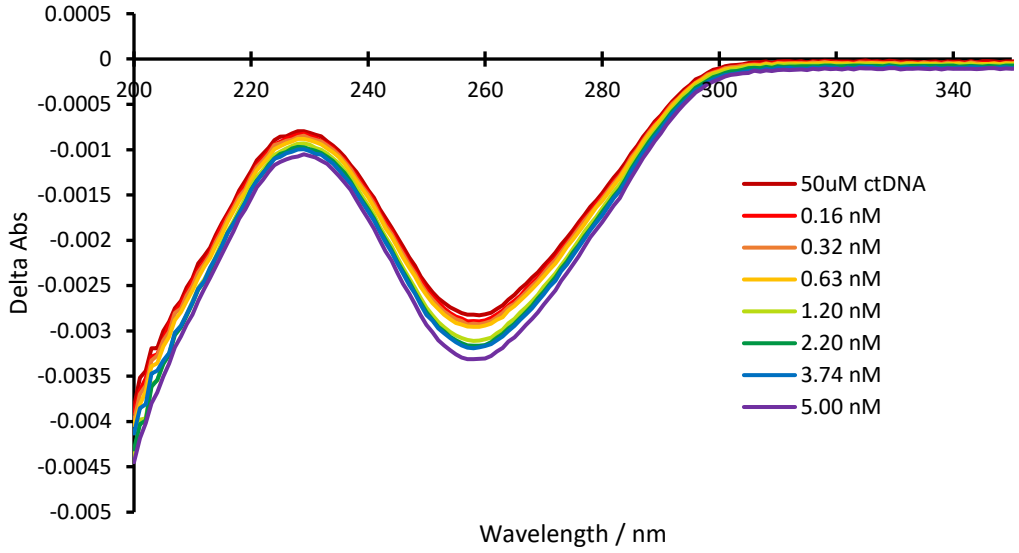


*Figure 18. LD of ctDNA 50 µM with AuNP13dsDNA in Tris-HCl buffer (Tris 10 mM, NaCl 20 mM pH 7.2).*

First, the AuNP13dsDNA with no metal complex loaded onto the particles was titrated into a solution of ct-DNA (Figure 18). Linear dichroism measurements of ctDNA with increasing concentrations of AuNP13dsDNA displays a gradual increase in the magnitude of the peak at 260 nm. This slight increase is possibly due to an increase in DNA concentration of the solution, which would be caused by the addition of the spherical nucleic acids.

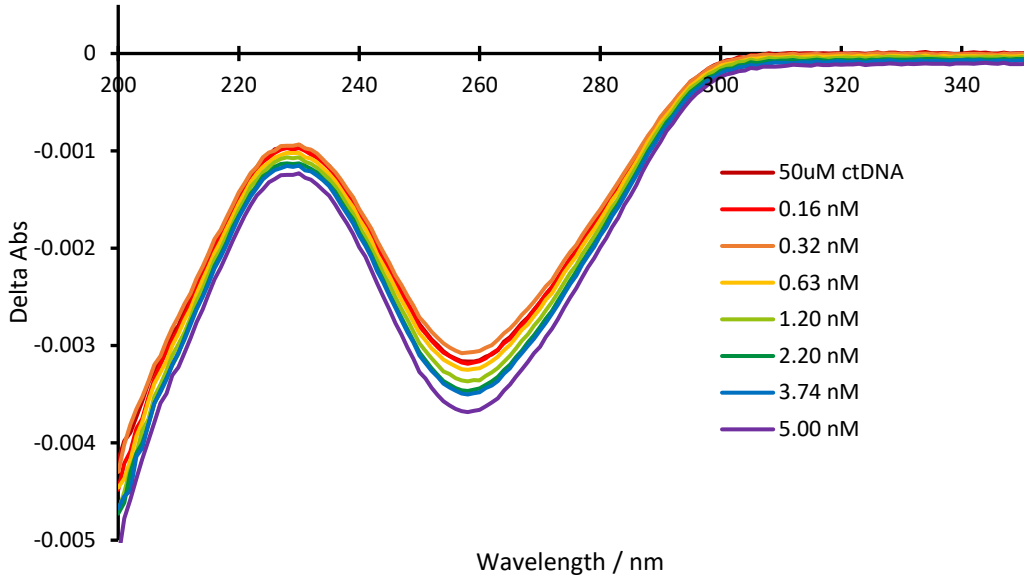


*Figure 19. LD of ctDNA 50 µM with AuNP13dsDNANiP in Tris-HCl buffer (Tris 10 mM, NaCl 20 mM pH 7.2).*

A titration of AuNP13dsDNA loaded with NiP at the same ratios as AuNP13dsDNA also results in a gradual increase in the magnitude of the signal at 260 nm (Figure 19). These results suggest that little to no NiP is released from the surface of the spherical nucleic acids to the ctDNA in solution. Comparing the change in signal at 260 nm, induced by the AuNP13dsDNA and AuNP13dsDNANiP, shows very little difference (Figure 20). To confirm these results, the LD titration was repeated with even higher concentration of AuNP13dsDNANiP and produced the same results (appendix A4.4).

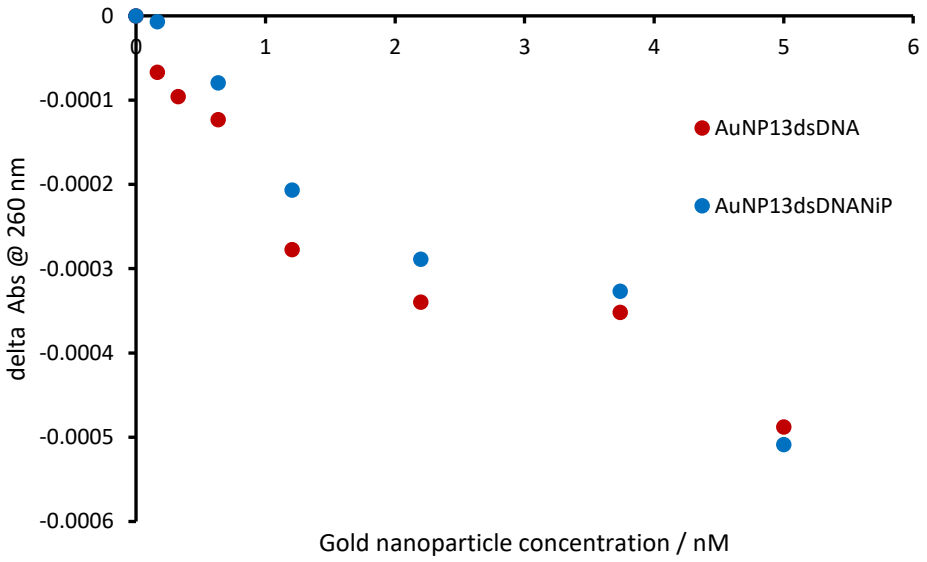


*Figure 20. Change in absorbance at 260 nm for LD of AuNP13dsDNA and AuNP13dsDNANiP with ctDNA.*

The similarity in the changes observed for the DNA signal at 260 nm when AuNP13dsDNA or AuNP13dsDNANiP are titrated suggests that the SNA may present a more attractive binding substrate for the NiP than ctDNA. This could be due to the arrangement of the DNA oligomers parallel to one another on the nanoparticle surface, which creates an environment unique from regular duplex DNA. Further study is needed to understand the binding of NiP to an SNA environment.

### 4.2.4 4WJ PAGE gels

The particle system which displayed the most success with release of metal complex, and also a lack of contaminating DNA, was AuNP13dsDNANiP. The ability of the metal complex to be released from the particles to a 4WJ was investigated by PAGE shown in Figure 21.

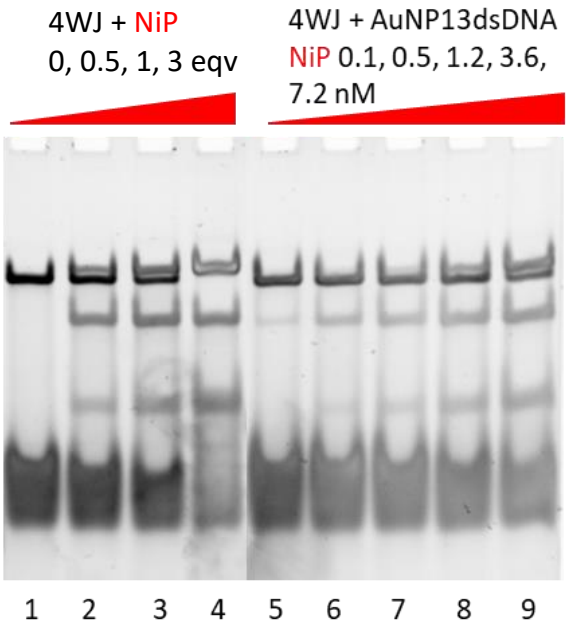


*Figure 21. PAGE gel (89 mM Tris base, 89 mM Boric acid, pH 8.3, 15% acrylamide gel) of 4WJ oligomers with NiP, and gold nanoparticles loaded with dsDNA1 and NiP.*

The clear formation of the new Y-fork, p3WJ, and second band higher than the 4WJ band indicates that the NiP has been successfully released from the particles. This suggests that the release of the NiP from the particles is not specific for 3WJ structures; Y-forks and 4WJ are also capable of inducing release of the NiP from the particles.

### 4.2.5 Increasing metal complex loading on AuNP13dsDNA

The aim of this work was to increase the uptake of these metal complexes into cells. Therefore, it was imperative to achieve the highest loading of the complexes on the particles as was possible. There were three obvious methods for increasing the concentration of metal complex on the particles:

- The size of the particles could be increased in order to allow for a larger number of oligomers to bind to the surface of the particles and hence give a larger number of metal complexes per particle. This has been demonstrated in the literature but it has been commented that larger particles are generally less amenable to the salt aging method for functionalisation of the particles with DNA.[39]
- The number of complexes per oligomer could be increased. PAGE gels have been carried out to determine the optimum number of metal complexes per oligomer: higher loadings would lead to changes in the oligomer structure and therefore likely have large implications on the subsequent functionalisation of the particles.
- The length of the oligomer used to functionalise the DNA surface could be increased. A longer oligomer could accommodate a higher number of metal complexes before the overall structure of the oligo is altered.

With these three possibilities considered, longer thiolated oligomers were investigated to try to increase the loading of metal complexes onto the gold nanoparticles.

#### *4.2.4.1 AuNP13dsDNA2*

A longer oligomer (DNA2) was designed to be able to accommodate higher loadings of metal complexes per nanoparticle. The adenine spacer at the base of the oligomer, where it is designed to attach to the gold nanoparticle through a thiol unit, is retained. The structure of the duplex DNA was confirmed using RNAStructure, with the predicted structure shown in the appendix (A4.1).[42] In the previous section, only the particles loaded with NiP achieved a high loading and released well to DNA 3WJ. For this reason, only loading with NiP was attempted for this oligomer.

**DNA2 S1 = [Thio]-AAA AAA AAA CCA CGC CGT TCA ATG TCG CAG AGG GGA AGG AGG TG**

**DNA2 S2 = CAC CTC CTT CCC CTC TGC GAC ATT GAA CGG CGT GG**

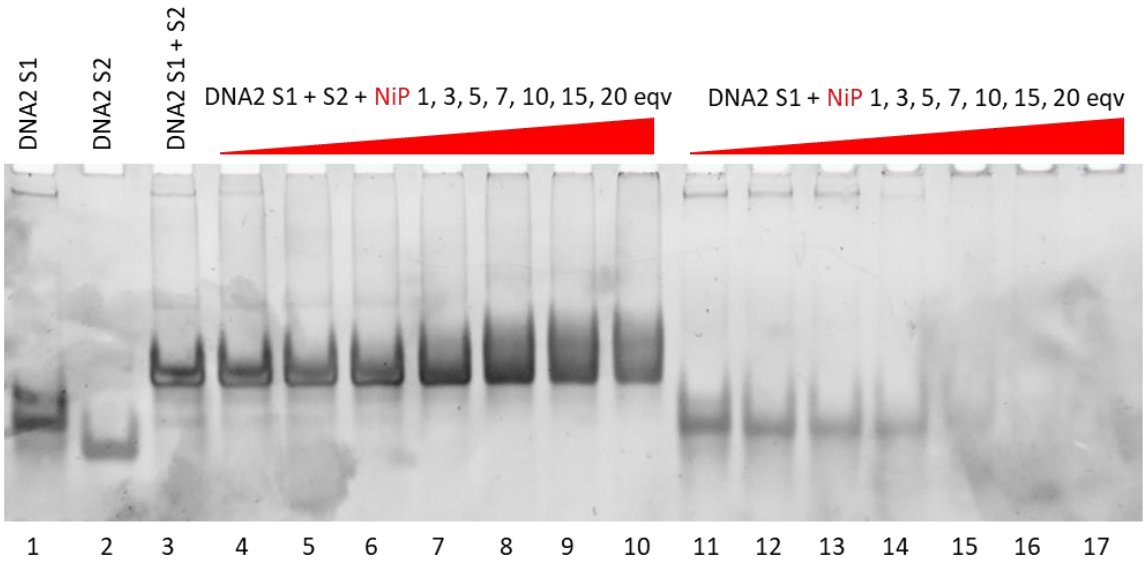


*Figure 22. PAGE gel (89 mM Tris base, 89 mM Boric acid, pH 8.3, 15% acrylamide gel) of DNA2 oligomers with varying concentrations of NiP.*

DNA2 S1, shown in lane 1 of Figure 22, indicates that there is some secondary structure being formed, as there is a faint band high in the gel indicating a very large structure. DNA2 S2 in lane 2 is a shorter oligomer than S1 and migrates further through the acrylamide gel, as expected, with no secondary structures visible. S1 + S2, shown in lane 3, induces the formation of a new band which does not migrate as far through the gel as S1 or S2 indicating a larger secondary structure is likely formed. There is no S2 band visible in lane 3, and only a faint band visible for S1, suggesting it is likely that the new band is the dsDNA structure formed from the hybridization of S1 + S2. Two faint bands higher in the gel are also observed: one can be attributed to the S1 strand but the other only appears when both S1 and S2 are present. With increasing concentrations of NiP, the faint bands decrease in intensity, and the intense band attributed to the dsDNA structure begins to smear and become less defined. S1 with increasing concentrations of NiP (lanes 11-17) gradually decreases in intensity until the S1 band is no longer visible with 15 equivalents of NiP. The band high in the gel also decreases in intensity with increasing equivalents of NiP.

*Table 5. SPR and FWQM measured for AuNP13 functionalised with DNA2 oligomers and NiP.*

| Sample | SPR / nm | FWQM / nm |
|---|---|---|
| AuNP13 | 518.5 | 60.5 |
| AuNP13ssDNA2 | 528.5 | 67.5 |
| AuNP13dsDNA2 | 525.5 | 65.0 |
| AuNP13ssDNA2 NiP | 528.5 | 66.5 |
| AuNP13dsDNA2 NiP | 527.5 | 62.0 |

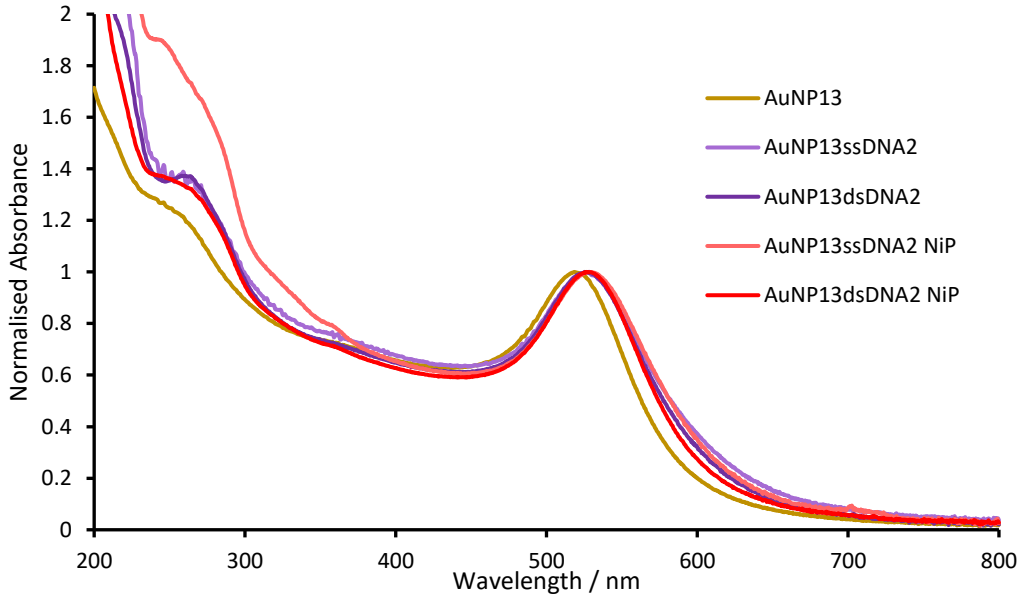


*Figure 23. UV-vis of AuNP13 and subsequent functionalisation with thiolated DNA2 oligomers and NiP.*

Based on the gel displayed in Figure 22, it was decided to attempt to load the dsDNA2 and ssDNA2 with 10 NiP per oligo structure. UV-vis analysis of the gold nanoparticles functionalised with DNA2 and NiP is shown in Figure 23. This clearly shows the shift in SPR band when the particles are functionalised, with broadening of the peaks also visible. The broadening and shift of the SPR peak of the particles are tabulated in Table 5. The dsDNA particles with and without NiP, compared to the ssDNA counterparts, display smaller redshifts and less broad peaks.

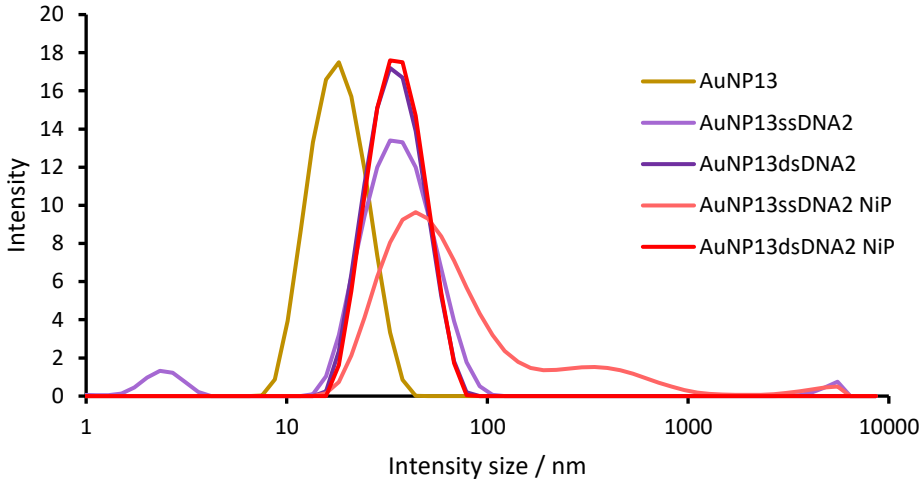


*Figure 24. DLS Intensity data plotted for AuNP13 with thiolated DNA2 oligomers and NiP.*

DLS data of gold nanoparticles functionalised with ssDNA2 or dsDNA2 shows that the nanoparticles are fairly monodisperse, with PDIs of 0.288 and 0.237 respectively. With the addition of NiP, the ssDNA2 particles show significant aggregation with a PDI of 0.405 and multiple peaks visible on the Intensity graph shown in Figure 24. The gold nanoparticles functionalised with dsDNA2 and loaded with NiP show a monodisperse distribution, with a narrow PDI of 0.176.

*Table 6. DLS intensity data for AuNP13 with thiolated DNA2 oligomers and NiP.*

| Sample | Hydrodynamic diameter / nm | PDI |
|---|---|---|
| AuNP13 | 18.77 | 0.113 |
| AuNP13ssDNA2 | 38.4 (93.2%) | 0.288 |
| | 2.428 (5.2%) | |
| | 5063 (1.4%) | |
| AuNP13dsDNA2 | 36.21 | 0.237 |
| AuNP13ssDNA2 NiP | 59.18 (84.1%) | 0.405 |
| | 439.3 (14%) | |
| | 4288 (1.9%) | |
| AuNP13dsDNA2 NiP | 36.68 | 0.176 |

Polyacrylamide gel electrophoresis was used to determine if the NiP is able to be released from the gold nanoparticles to a DNA three-way junction (Figure 25). Upon staining, it is noticeable that the 3WJ structure observed in lanes 5-8 overlaps perfectly with the DNA2 S2 band. The overlap of the 3WJ and dsDNA2 band makes quantification of the release of the metal complex from the particles impossible. Control lanes 9-11 clearly show the presence of DNA bands, indicating that either the purification of

the particles was not successful, the DNA is not firmly attached to the particles, or the particles have excess DNA loosely associated with them.

The lack of DNA bands present in the wash (lane 18, Figure 25) indicates that there is no cylinder present in the wash. This points to the possibility that there is excess DNA loosely associated with the gold particles. The other possibility is that the DNA oligomers were not successfully separated from the particles, but there is no evidence of DNA oligomers by DLS (Figure 24). The longer the oligomer is on the particles, the less selectivity the particles will have for a specific complementary strand due to partial matches.[43] This may be why there was excess DNA coming off the particles. If the DNA has only partially hybridized with its complementary strand, it may be held relatively weakly onto the particle's surface.

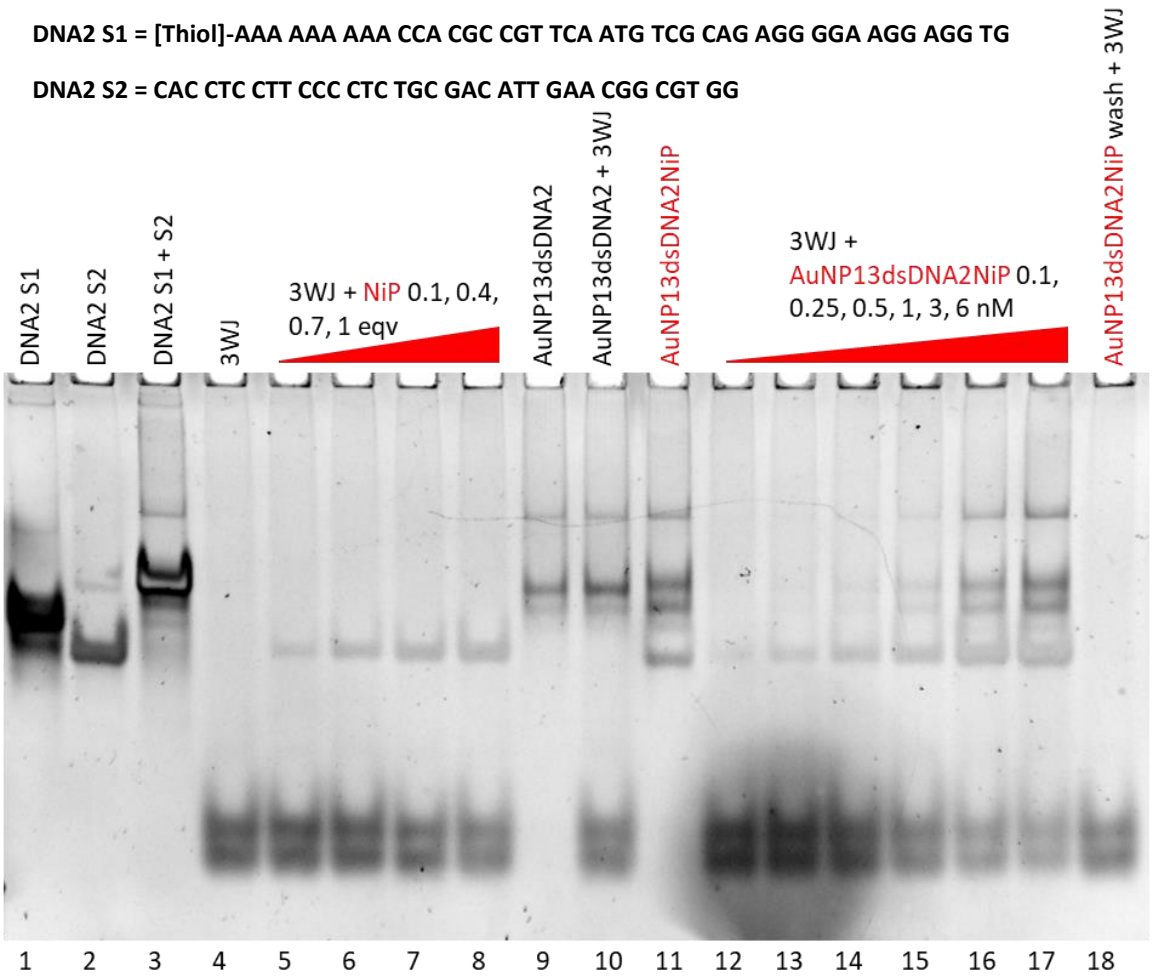


*Figure 25. PAGE gel (89 mM Tris base, 89 mM Boric acid, pH 8.3, 15% acrylamide gel) of 3WJ with NiP, and gold nanoparticles loaded with dsDNA2 and NiP with 3WJ.*

There is a decrease in the intensity of the individual 3WJ oligomer's band in lanes 12-17, which is evidence of 3WJ formation and indicates release of the NiP (Figure 25). It is not possible to determine if the metal complex released is from the particles or free DNA in solution. This PAGE gel indicates that the DNA2 oligomers may not be suitable for this application, so an alternative DNA oligomer was investigated (section 4.2.4.2). In future, radio labelled PAGE gels or fluorescently tagged 3WJ oligomers may be used to enable quantification of the binding.

### *4.2.4.2 AuNP31dsDNA3*

A new oligomer (DNA3), which was longer than DNA1 but shorter than DNA2, was designed to increase the loading of metal complex onto the DNA but hopefully avoiding the issues shown with the use of DNA2. DNA3 is 30 bases in length, slightly shorter than the 44 bases of DNA2 in order to improve the specificity of the oligomer and reduce the partial hybridization observed with DNA2. The structure of the DNA3 duplex predicted by RNAStructure software is shown in the appendix (A4.1).[42]

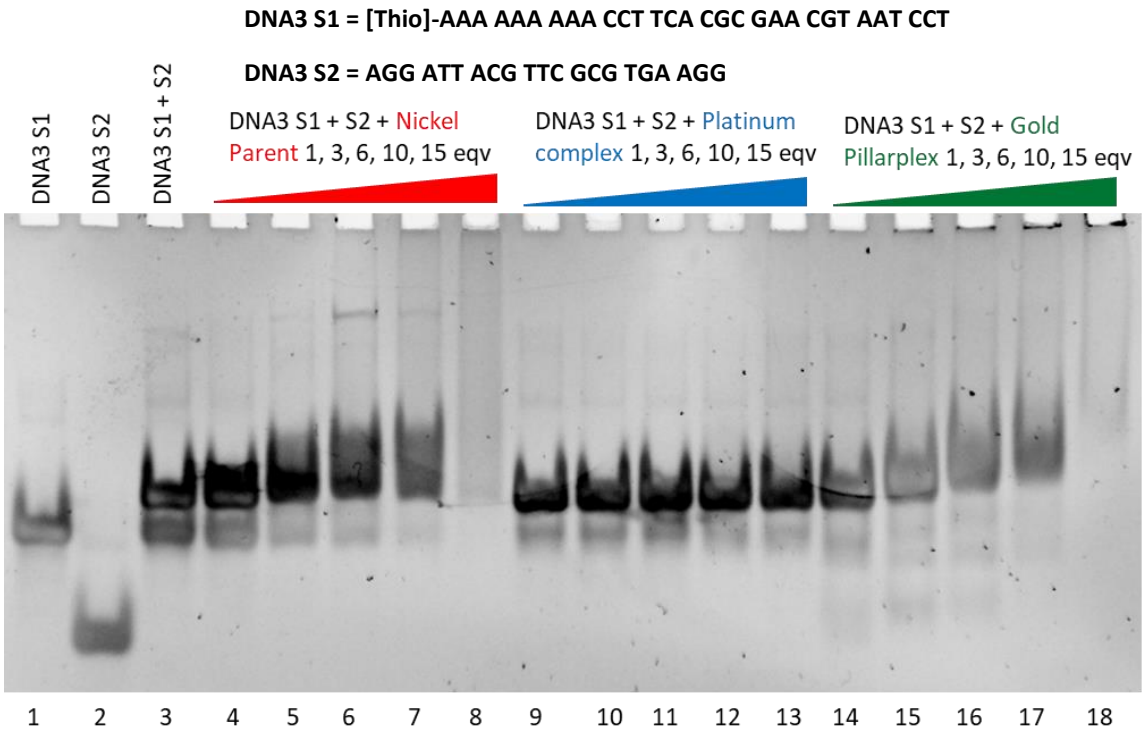


*Figure 26. PAGE gel (89 mM Tris base, 89 mM Boric acid, pH 8.3, 15% acrylamide gel) of DNA3 oligomers with varying concentrations of NiP, PtCyl, and AuPill.*

PAGE was used to determine how much of each metal complex could be loaded onto dsDNA3 (Figure 26). There was significant smearing of the DNA3 band when increased ratios of NiP or AuPill were added to the dsDNA3. The NiP also induces the formation of a new band, at ratios of 6:1 and 10:1. The PtCyl does not display any effect on the dsDNA3, even with high ratios of the metal complex. Based on these results, it was decided to attempt loading the dsDNA with 6 equivalents of metal complex as this does not induce significant changes in the structure of the dsDNA3 indicated by the lack of smearing.

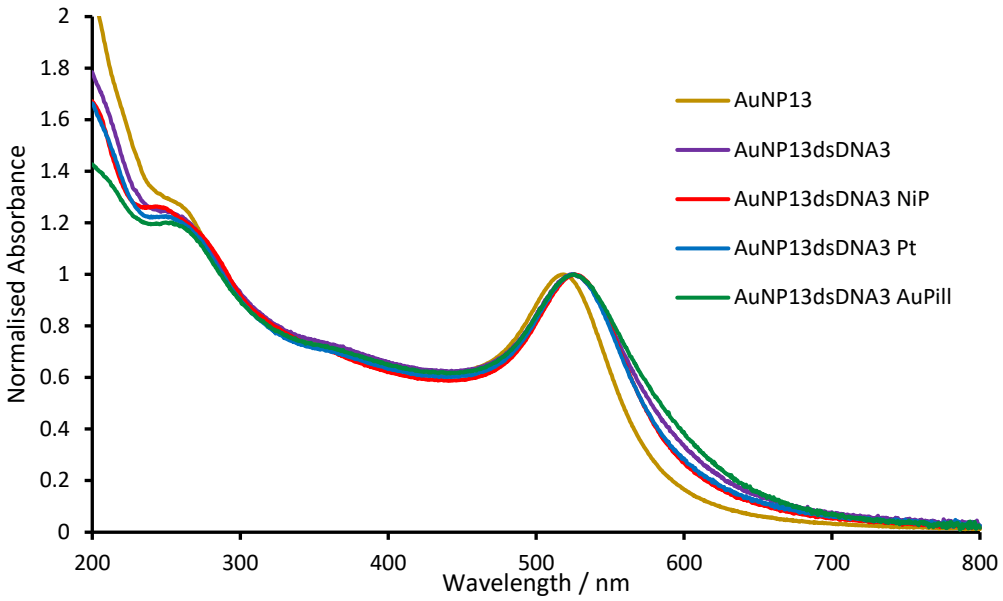


*Figure 27. UV-vis of AuNP13 and subsequent functionalisation with thiolated DNA3 oligomers and NiP.*

The shift in the SPR band of the particles, as well as the broadening of the SPR peak for the gold nanoparticles when loaded with dsDNA3 or dsDNA3 loaded with 6 equivalents of each metal complex, is clearly visible (Figure 27). The SPR of the gold nanoparticles shifts by 6 – 8 nm when the particles are loaded with dsDNA3 and a metal complex. The FWQM also increases by 4.5 – 11.5 nm, with the most significant broadening observed for AuNP13dsDNA3AuPill. This is expected, as the loading of the AuPill onto the oligomers likely resulted in some coiling and loss of structural integrity as indicated by the PAGE gel shown in Figure 26. This coiling may lead to interactions between particles.

*Table 7. SPR and FWQM measured for AuNP13 functionalised with DNA3 oligomers and NiP.*

| Sample | SPR / nm | FWQM / nm |
|---|---|---|
| AuNP13 | 518.5 | 56.0 |
| AuNP13dsDNA3 | 525.5 | 65.5 |
| AuNP13dsDNA3 NiP | 526.5 | 60.5 |
| AuNP13dsDNA3 Pt | 524.5 | 61.0 |
| AuNP13dsDNA3 AuPill | 525.5 | 67.5 |

DLS measurements of the particles loaded with dsDNA3 and dsDNA3 with metal complexes are displayed in Figure 28 and Table 8. There are small peaks at roughly 1 nm for all of the particles which could be due to small amounts of DNA in solution. There are no aggregates visible by DLS for any of the particles coated with AuNP13dsDNA3. The PDI of all of particles ranges from 0.247 – 0.317, with the AuNP13dsDNA3AuPill displaying the largest PDI which aligns with the SPR data showing it is the

most polydisperse species. DLS measurements of the AuNP13dsDNA3 particles indicates that they are significantly smaller than the AuNP13dsDNA2 particles which is expected due to the use of a shorter oligomer. There is a noticeable peak at approximately 1 nm on DLS measurements of each of the particles which could be due to free oligomers in solution. This indicates that DNA3 may suffer from the same partial hybridization issues seen with DNA2.

*Table 8. DLS intensity data for AuNP13 with thiolated DNA2 oligomers and NiP.*

| Sample | Hydrodynamic diameter / nm | PDI |
|---|---|---|
| AuNP13dsDNA3 | 32.83 (95.3%)<br>2.12 (3.5%)<br>0.92 (1.2%) | 0.290 |
| AuNP13dsDNA3 NiP | 34.28 (99%)<br>1.83 (1%) | 0.247 |
| AuNP13dsDNA3 Pt | 28.81 (96.5%)<br>1.00 (3.5%) | 0.273 |
| AuNP13dsDNA3 AuPill | 30.62 (91.8%)<br>1.78 (7.3%)<br>0.70 (0.9%) | 0.317 |

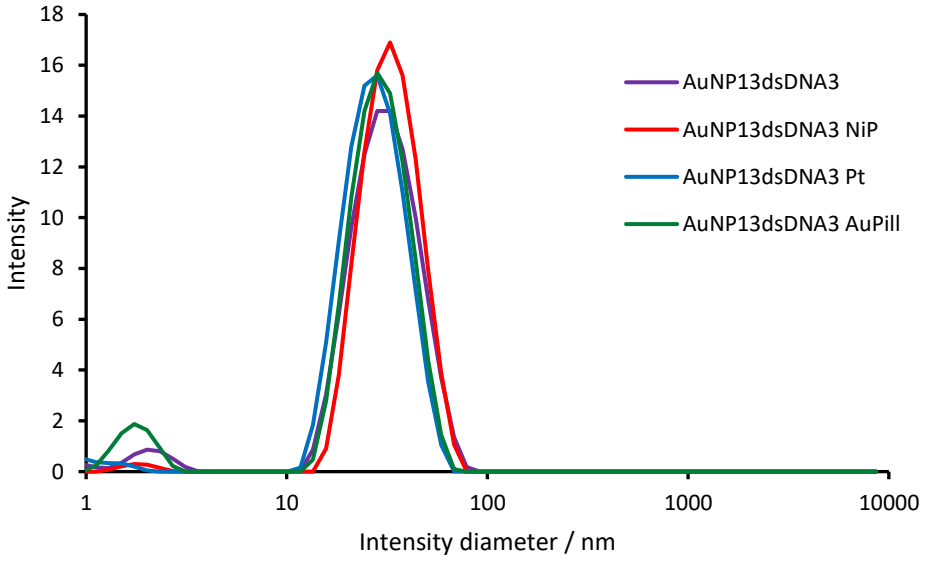


*Figure 28. DLS Intensity data of AuNP13 and subsequent functionalisation with thiolated DNA3 oligomers and NiP.*

The 3WJ PAGE assay to determine the amount of metal complex released from the particles and check the particle quality was applied to AuNP13dsDNA3NiP (Figure 29). Control lanes 10 – 12 display faint bands, indicating some free DNA in solution, DNA coming off the surface of the particles. There is no indication of 3WJ being formed with the control particles indicating that the DNA3 on the particles does not interact with the DNA 3WJ.

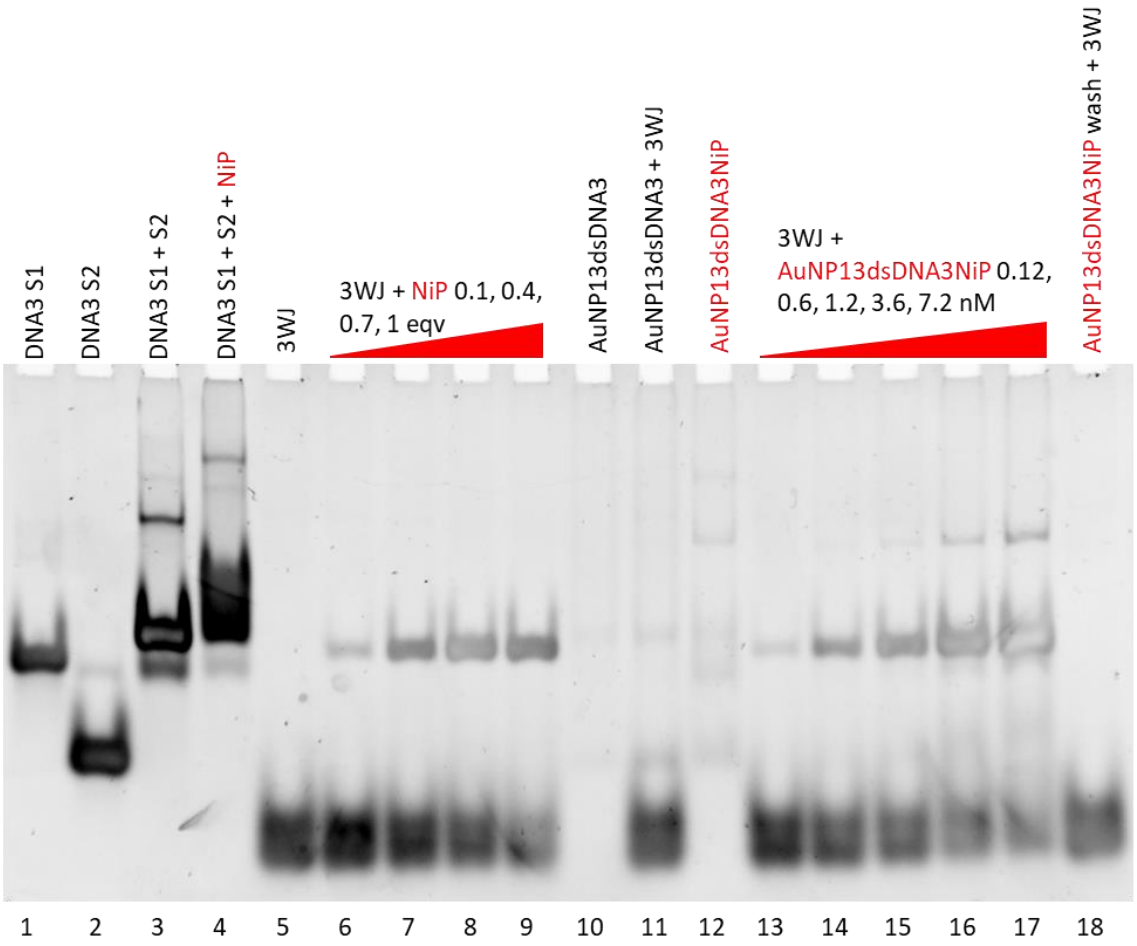


*Figure 29. PAGE gel (89 mM Tris base, 89 mM Boric acid, pH 8.3, 15% acrylamide gel) of 3WJ with NiP, and gold nanoparticles loaded with dsDNA2 and NiP with 3WJ.*

Increasing concentration of AuNP13dsDNA with 3WJ in lanes 13-17 results in a band of increasing intensity which aligns with the expected location of the 3WJ band. Unfortunately, the staining of the 3WJ band in lanes 13-17 was not uniform enough to allow for quantification of the loading of NiP on the particles. The decrease in the intensity of the single stranded 3WJ oligomers is a clear indication that NiP is being released from the particles and inducing the formation of the 3WJ. The increasing intensity of the faint band higher in the gel in lanes 13-17 indicates there is some free DNA coming off the particles.

### 4.2.6 Agarose gel

Agarose gel electrophoresis is commonly used to separate large oligomers consisting of hundreds to thousands of base pairs. The oligomers are separated by their size and charge by pulling them through an agarose gel matrix with a high voltage. Spherical nucleic acids are also highly negatively charged; it has been shown that particles of different shape and size can be separated using agarose gel

electrophoresis.[14, 44, 45] Agarose gel electrophoresis was used here to observe any changes in size or charge of the particles after incubation with a DNA 3WJ.

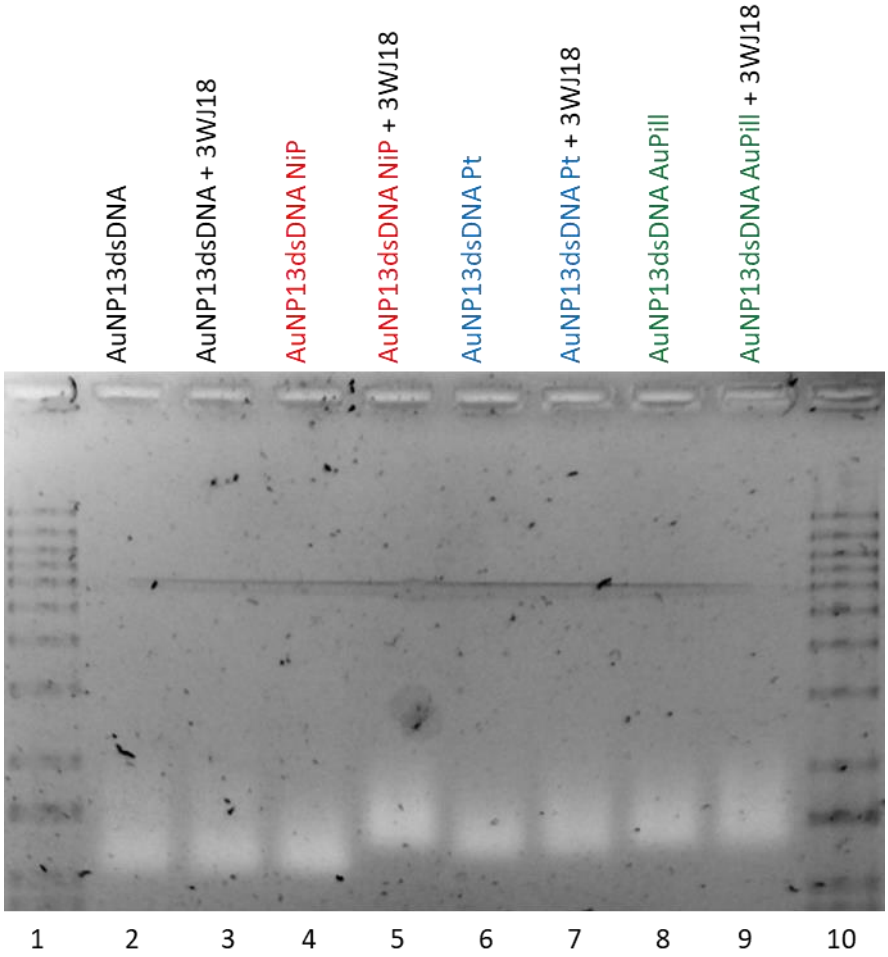


*Figure 30. Agarose gel of AuNP13 with thiolated DNA1 oligomers and loaded with no metal complex, NiP, PtCyl, or AuPill, with and without the presence of 3WJ18 (89 mM Tris base, 89 mM Boric acid, pH 8.3, 1.6 % agarose, 50 V, 6 hours, SYBR Gold stained).*

Gold nanoparticles functionalised with dsDNA1 alone, or dsDNA1 and NiP, PtCyl, or AuPill were incubated alone, or in the presence of 3WJ18 (Figure 30). The 3WJ18 structure was selected for this experiment as the junction is formed spontaneously in solution. The bands in the gel are the gold nanoparticles, the 3WJ18 is very small and migrates almost all the way through the gel (full gel shown in appendix A4.5). The particles with metal complexes all migrated through the gel slower than the particles with no metal complexes. This could indicate a slight difference in charge of the particles, however zeta potential measurements do not show a substantial change (appendix A4.2). Each set of particles functionalised with a metal complex in the presence of the 3WJ18 does not shift quite as far through the gel. This difference in migration is most obvious for AuNP13dsDNANiP which could be due

to the significantly higher loading of NiP onto the particles compared to AuPill or PtCyl. It was expected that the particles would migrate further through the gel matrix if they released metal complexes to the junction due to the resulting increase in magnitude of the negative charge of the particles. The observed retardation of the particle bands with 3WJ18 could be caused by the 3WJ18 oligomers interacting with the metal complexes on the particles and effectively sticking to the particles. The crystal structure of the iron parent cylinder (analogous to NiP but with iron metal centres) with an RNA 3WJ revealed stacking of the cylinder to the terminal ends of the junction duplexes as well as junction binding.[35]

### 4.2.7 ICP-MS of particles

ICP-MS (Inductively coupled plasma mass spectrometry) was used to confirm the concentration of the particles. ICP-MS is an extremely sensitive technique which can be used to quantify the exact concentration of heavy elements in a given solution (with a couple of exceptions). TEM of the gold nanoparticles can be used to accurately determine the size of the particles. TEM measurements, combined with the ICP-MS data for the gold concentration in solution, allows us to calculate the exact particle concentration of a solution. The ratio of metal complexes per particle can also be calculated from this data (method shown in appendix A4.6).

*Table 9. Quantification of loading of AuNP13dsDNA with NiP/PtCyl/AuPill by ICP-MS and 3WJ PAGE gel assay.*

| Sample | Metal complexes per particle calculated by ICP-MS | Metal complexes per particle calculated by PAGE gel |
|---|---|---|
| AuNP13dsDNA NiP | 320 | 330 |
| AuNP13dsDNA PtCyl | 65 | 225 |
| AuNP13dsDNA AuPill | NA | 17 |

The measurements for the NiP functionalised particles agree well between the PAGE gel approximation and the ICP-MS measurements (Table 9). The measurement of the PtCyl loading on the particles differs significantly between the ICP-MS measurement and the quantification by 3WJ PAGE gel assay. The reason for this discrepancy could be due to the excess oligomers detected in the PAGE gel also being loaded with PtCyl. Quantification of the loading of AuPill onto the AuNP13dsDNA was not possible by ICP-MS and very little of the AuPill appeared to be released from the particles on the PAGE assay. This

low concentration of AuPill could either indicate that the AuPill is not bound to the particles, or that it is bound very strongly and will not be released to the DNA 3WJ target.

### 4.2.8 TEM of particles

Transmission electron microscopy (TEM) was used to accurately determine the size of the gold core of the nanoparticles as well as confirm their monodispersity (Figure 31 and Figure 32). TEM, unlike DLS, allows the direct measurement of the core particle diameter excluding the electrical double layer. TEM images of citrate gold nanoparticles with no DNA coating reveals spherical particles which are grouped together in close proximity; the particles are in contact with neighbouring particles (Figure 32). Though the close packing of the particles could indicate aggregation, the DLS data acquired for these particles shows a low PDI; therefore, it is likely that any aggregation observed is a result of the drying process of the particles on the TEM grids. A notable difference between the bare citrate gold nanoparticles (AuNP13) and the particles coated with DNA is that, even when packed close together, the particles coated with DNA do not contact one another. The spacing of the gold particles from each other is a good indication that the coating of the particles with the DNA has been successful. The spacing of the particles is most obvious on the AuNP13dsDNAPt particles due to the high density of particles on the TEM grid.

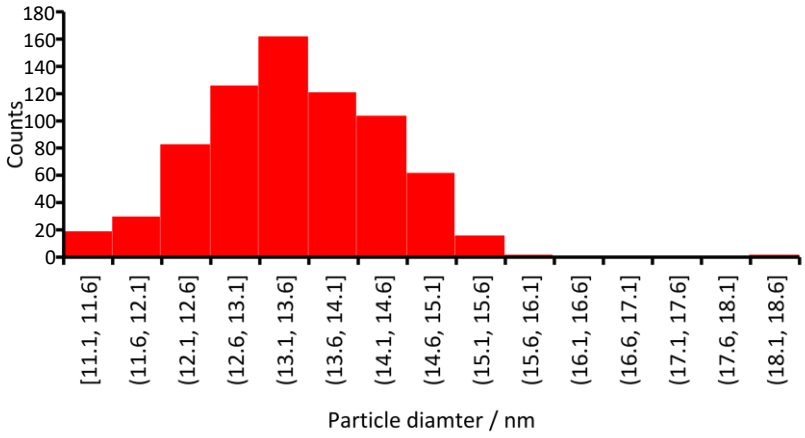


*Figure 31. Size of AuNP13 measured by TEM, average particle size = 13.5±0.9 nm (particles counted displayed in appendix A4.7).*

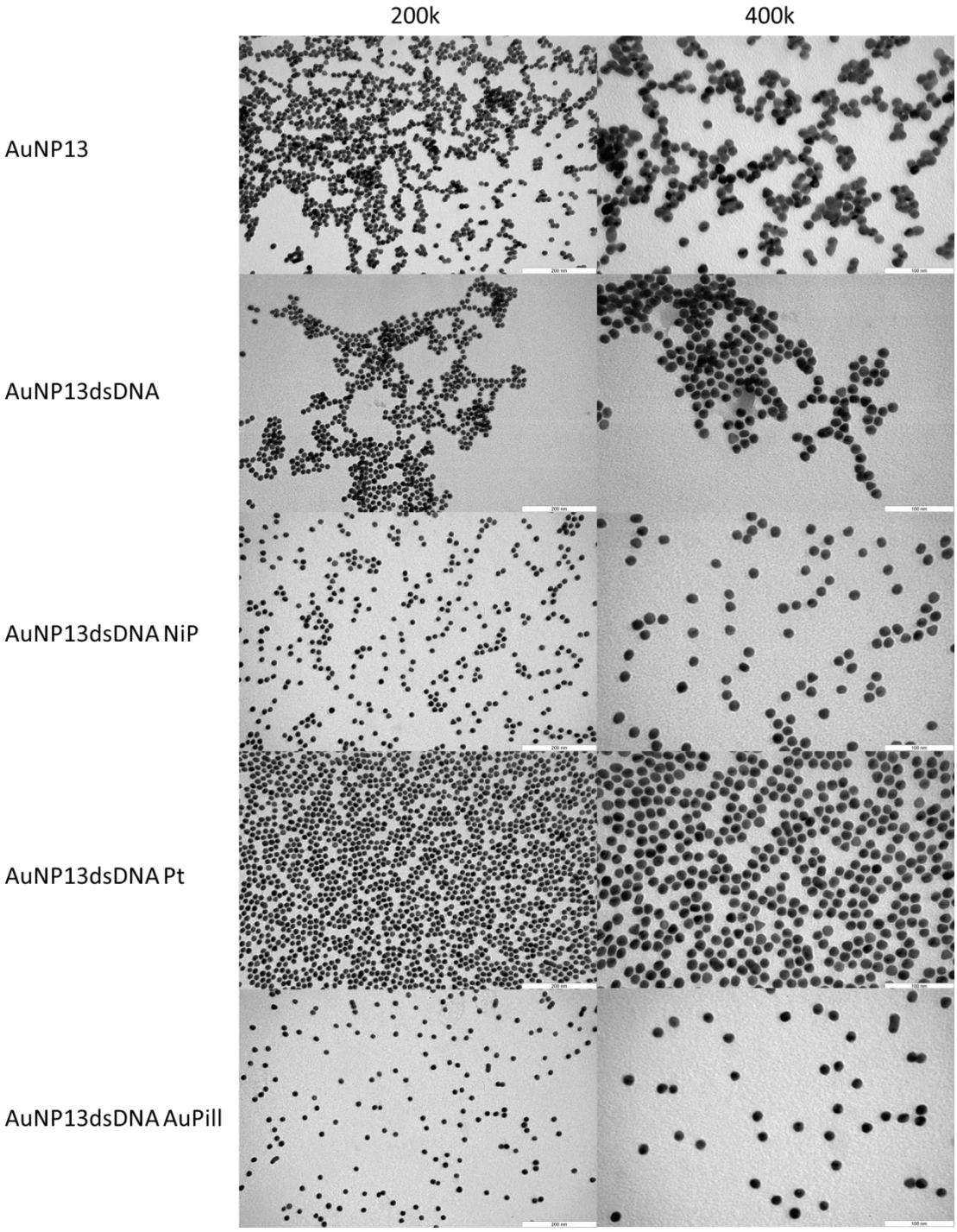


*Figure 32. TEM images of gold nanoparticles before and after functionalisation with dsDNA and metal complexes at 200,000 and 400,000 x magnification (200k and 400k).*

Uranyl acetate is a quick and easy negative stain which is commonly used on biological substrates and has been used to stain DNA structures.[46] Staining of the TEM grids loaded with the gold particles was attempted by the Materials and Metallurgy department at the University of Birmingham. Comparing the images obtained of our stained particles to those found in literature (Figure 33), it does not appear that the staining procedure was successful. (Moving forward it is assumed that the uranyl acetate

staining was unsuccessful. Images of particles which were supposedly stained with uranyl acetate are marked UA). However, the uranyl acetate staining does not appear to have been essential to visualise the DNA. High magnification TEM images of the particles with DNA clearly reveals halos around the gold particles (Figure 34, Figure 35, Figure 36, and Figure 37). Halos such as those seen here are commonly ascribed to organic coronas around the particles.[47-49] Gold-SNA particles have also been shown to display a halo in the same manner.[50] This is good evidence that the gold nanoparticles have been passivated with the thiolated DNA oligomers.

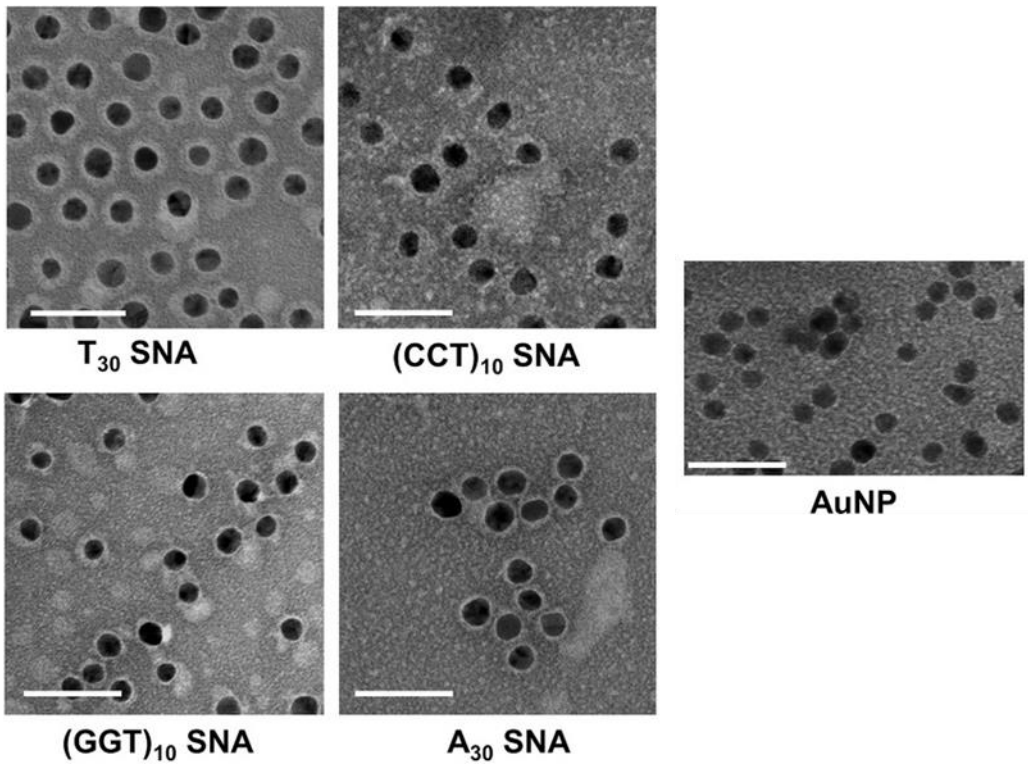


*Figure 33. Literature example of uranyl acetate stained gold-SNA particles imaged by TEM (white scale bar = 50 nm). Adapted from referenced publication with permission.[51]*

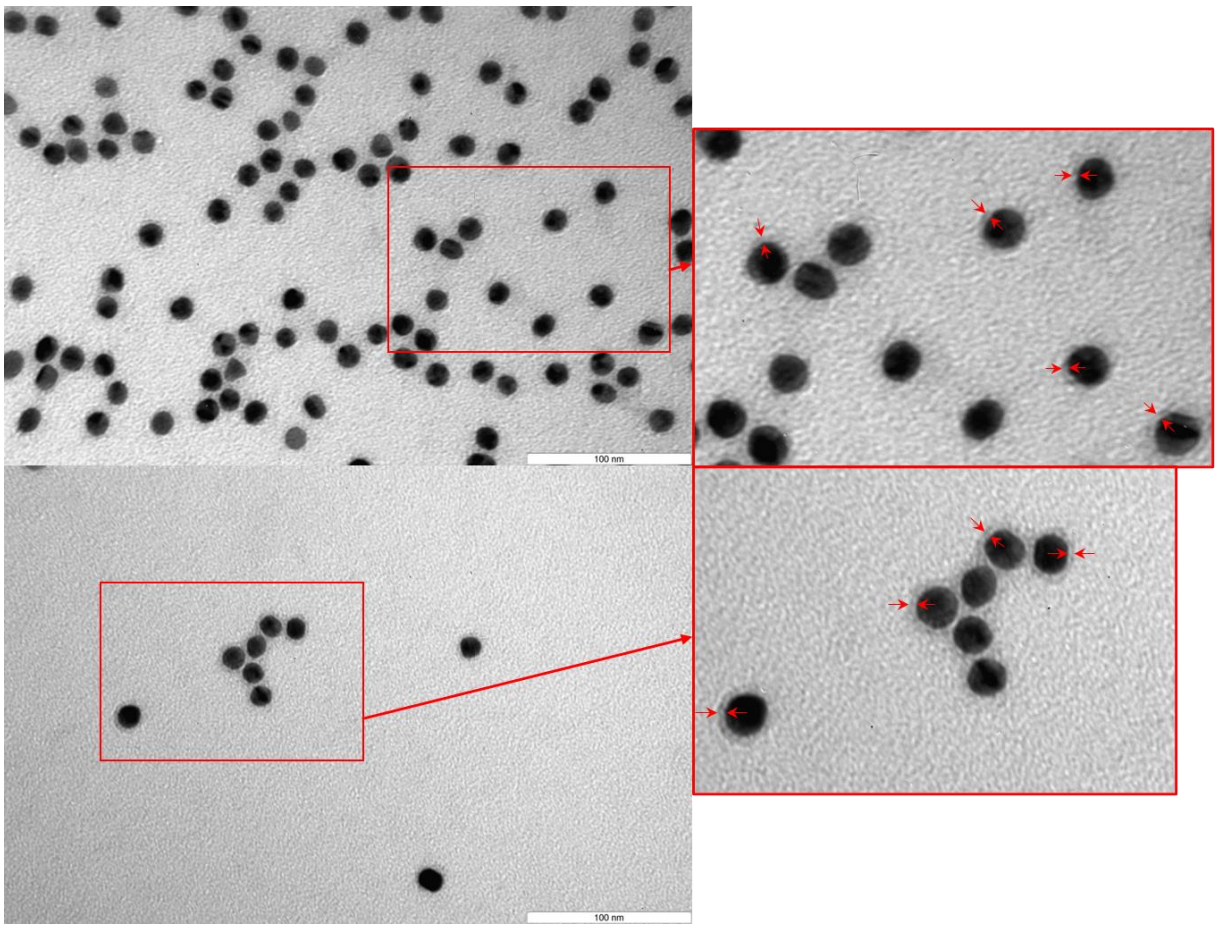


*Figure 34. TEM images of AuNP13dsDNAPt (UA). Red arrows indicate where the corona diameter was measured.*

Under high magnification, there is a corona which is visible around most of the nanoparticles (Figure 34). The halo around the AuNP13dsDNAPt measures 2.2 $\pm$ 0.4 nm. The double stranded portion of the DNA1 would measure roughly 4 nm in length if the oligomer was in a linear conformation. It is possible that the drying of the particles on the TEM grid caused the contraction of the DNA coating. It should also be noted that the halo is not visible on all of the particles. This could again be caused by the drying process disrupting the surface layer on the particles.

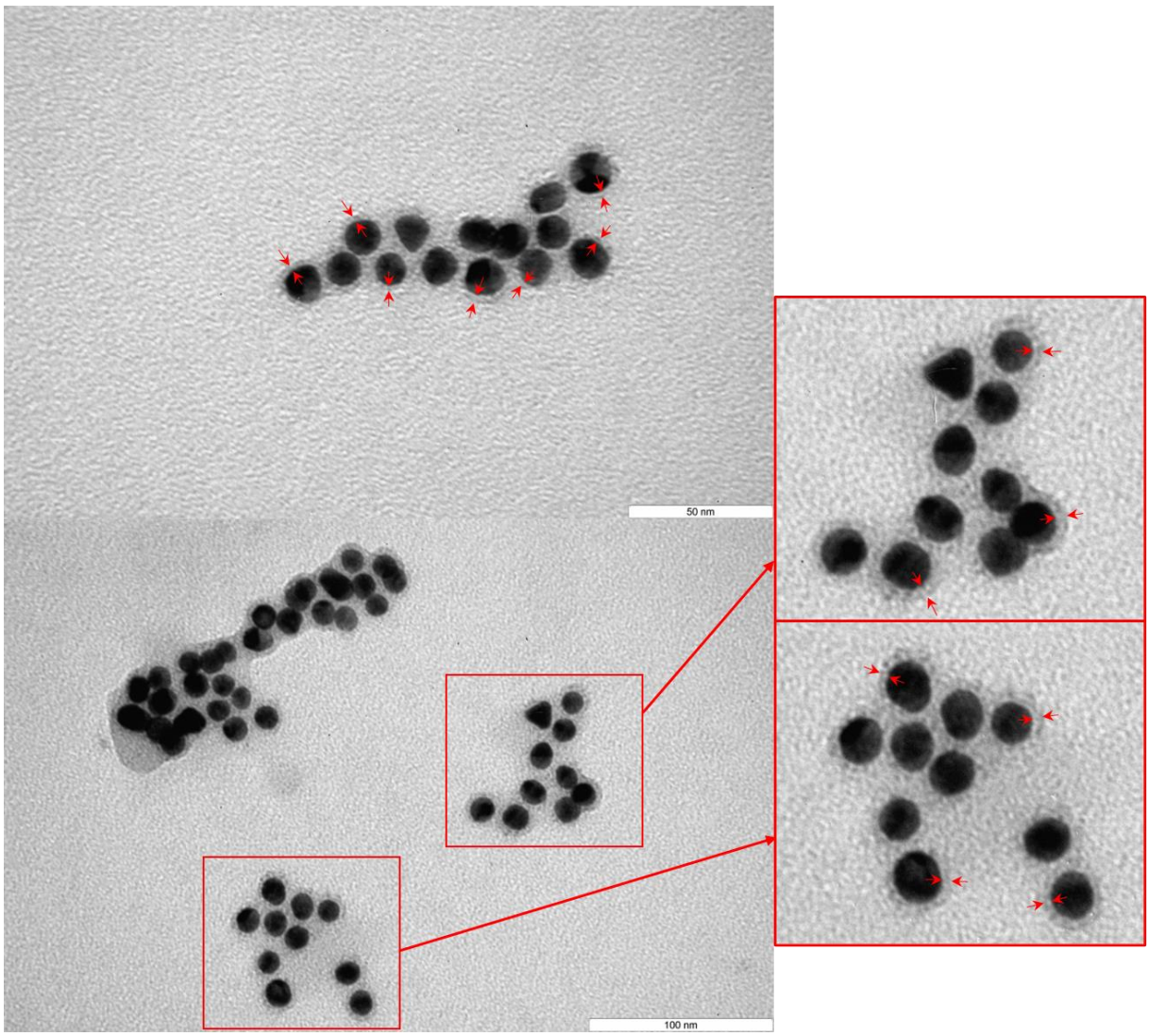


*Figure 35. TEM images of AuNP13dsDNANiP (UA). Red arrows indicate where the corona diameter was measured.*

High magnification TEM images of AuNP13dsDNANiP showed a visible halo on the particles which indicates the presence of the DNA oligomers on the particles (Figure 35). The halo measures $2.3 \pm 0.5$ nm which is very similar to that observed for the AuNP13dsDNAPt. The TEM images also show how some of the particles appear grouped together which is observed as mild aggregation by DLS. Drying of the particles on the TEM grids may contribute to the formation of the aggregates. In the image above (Figure 35), a triangular nanoparticle is visible. The formation of a small proportion of triangular gold nanoparticles when using the Turkevitch synthesis method is not uncommon and has been investigated in the literature.[52, 53]

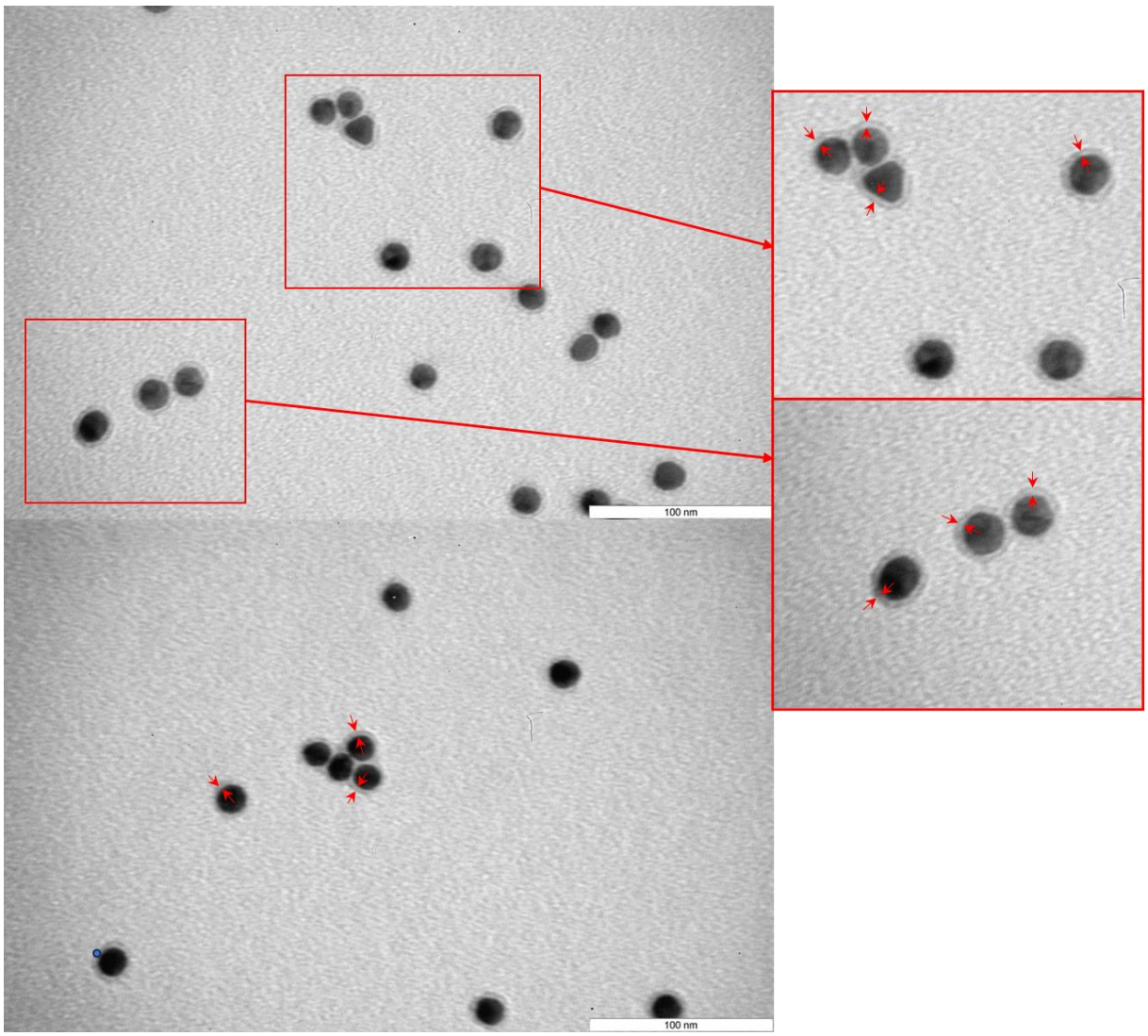


*Figure 36. TEM images of AuNP13dsDNAAuPill. Red arrows indicate where the corona diameter was measured.*

The AuNP13dsDNAAuPill particles display the same halo observed on the other particles functionalised with dsDNA (Figure 36). The halo around the AuNP13dsDNAAuPill measures 2.6 $\pm$ 0.3 nm. The halo around these particles is notably clear and uniform when compared to some of the other particles.

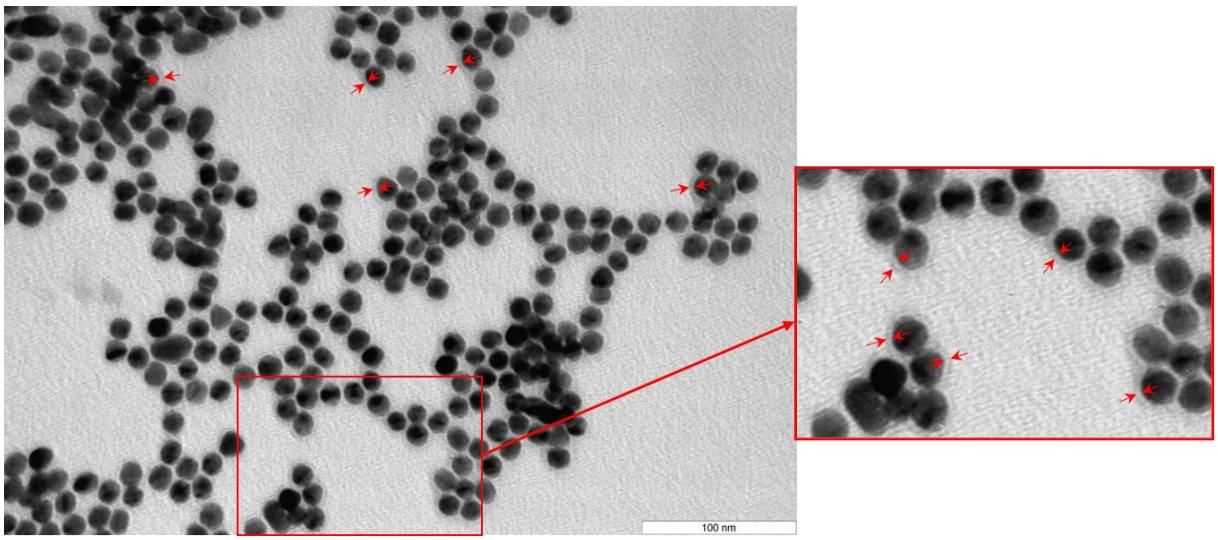


*Figure 37. TEM images of AuNP13dsDNA. Red arrows indicate where the corona diameter was measured.*

Halos around the AuNP13dsDNA (Figure 37) with no metal complex are harder to see but are still present. Though the halos are more difficult to see, the particle distribution with spaces between most particles also indicates the presence of a passivating layer on the surface when compared to bare AuNP13 (Figure 38). The halo measures 2.4 $\pm$ 0.2 nm, which is comparable to those measured on the particles loaded with metal complexes.

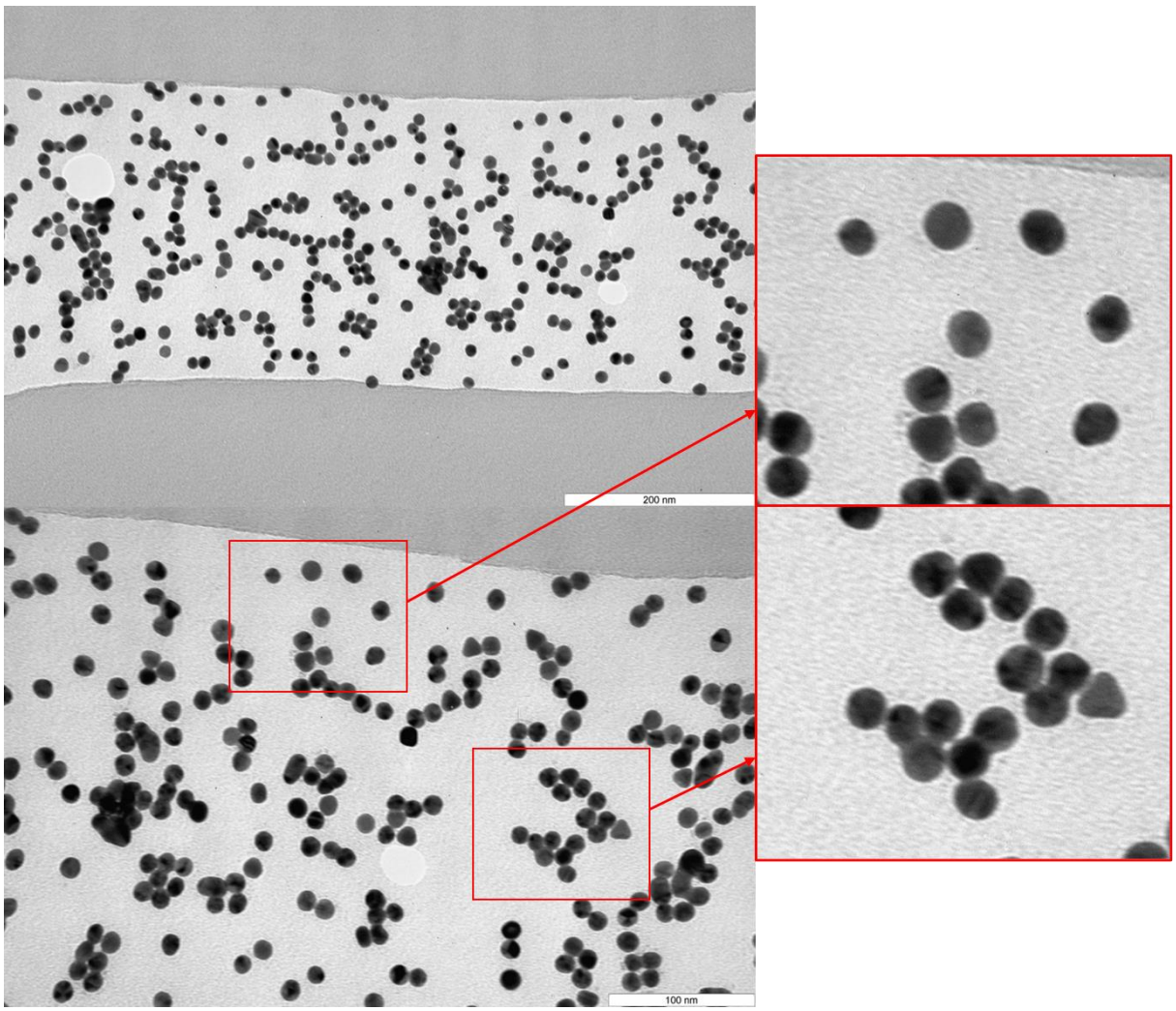


*Figure 38. TEM images of AuNP13 (UA).*

High magnification images of the AuNP13 show that the particles are in close proximity to one another and appear to be in contact in many instances (Figure 38). This indicates that there is no substantial stabilising ligand on the surface of the particles.

TEM images have been essential for quantifying the exact size of the nanoparticle cores. This imaging has also provided further evidence of the successful functionalisation of AuNP13 with DNA, through visualization of the halo around the particles. In future work, acquiring EDS imaging data would be very useful to co-localise the platinum and nickel with the gold from the particles. This would be a method to indisputably prove that the metal complexes are on the gold-SNA particles and not free in solution.

### 4.2.9 Stability of particles

Stability of the nanoparticle system developed in this work is very important as, in a biological system, particle aggregation can have a large impact on the uptake of the particles and how they are treated by the body in general. Stability of the particles in water was monitored over time by DLS and UV-vis as the particles cannot be dried and are therefore stored as concentrated solutions in water. The intensity measurements for DLS are reported as this is the measurement value which is most sensitive to large particles and aggregates as larger particles scatter more light.

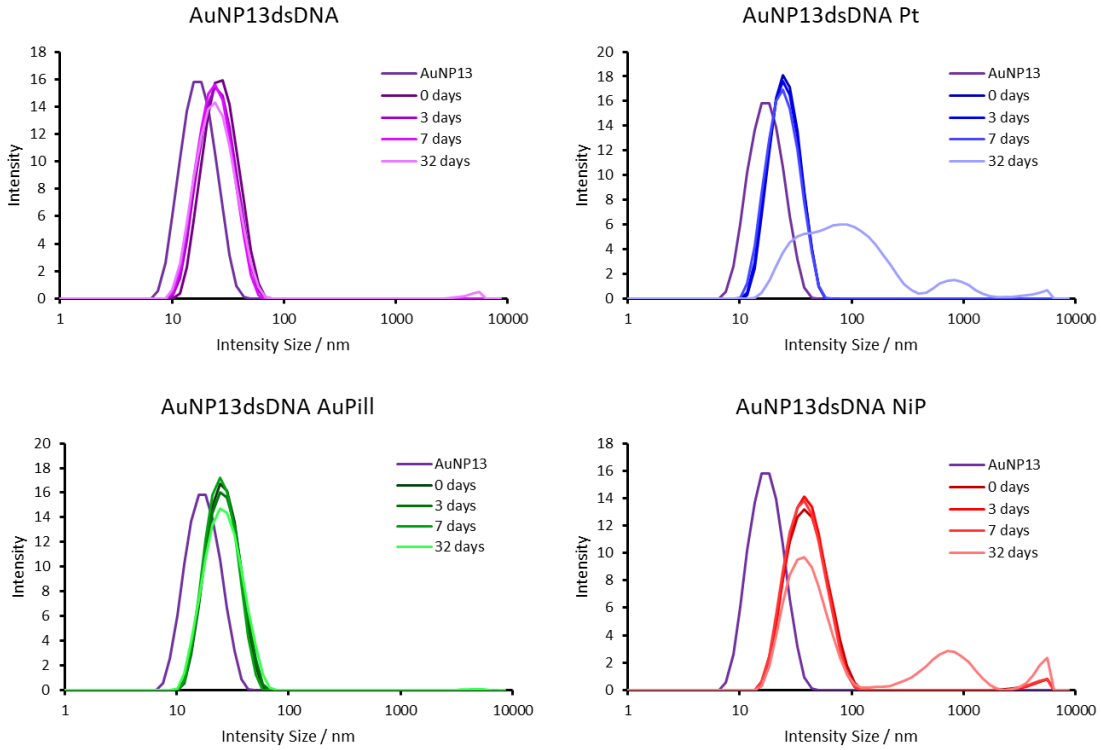


*Figure 39. DLS measurements of AuNP13dsDNA unloaded and loaded with either NiP, AuPill, or PtCyl at a concentration of 1 nM in water over time. Particles were stored in at 4 °C.*

Gold nanoparticles functionalised with dsDNA1 and either no complex, NiP, PtCyl, or AuPill were monitored over a period of 32 days by both DLS and UV-vis absorbance. DLS data graphed in Figure 39 (data tabulated in appendix A4.8) shows that, in all cases, the particles show minimal aggregation over a period of 7 days. The AuNP13dsDNANiP does show a small peak at 4590 nm, indicating the presence of some major aggregates. The AuNP13dsDNA which were loaded with the PtCyl or NiP complexes show the formation of larger particles with broader distributions of sizes after 32 days.

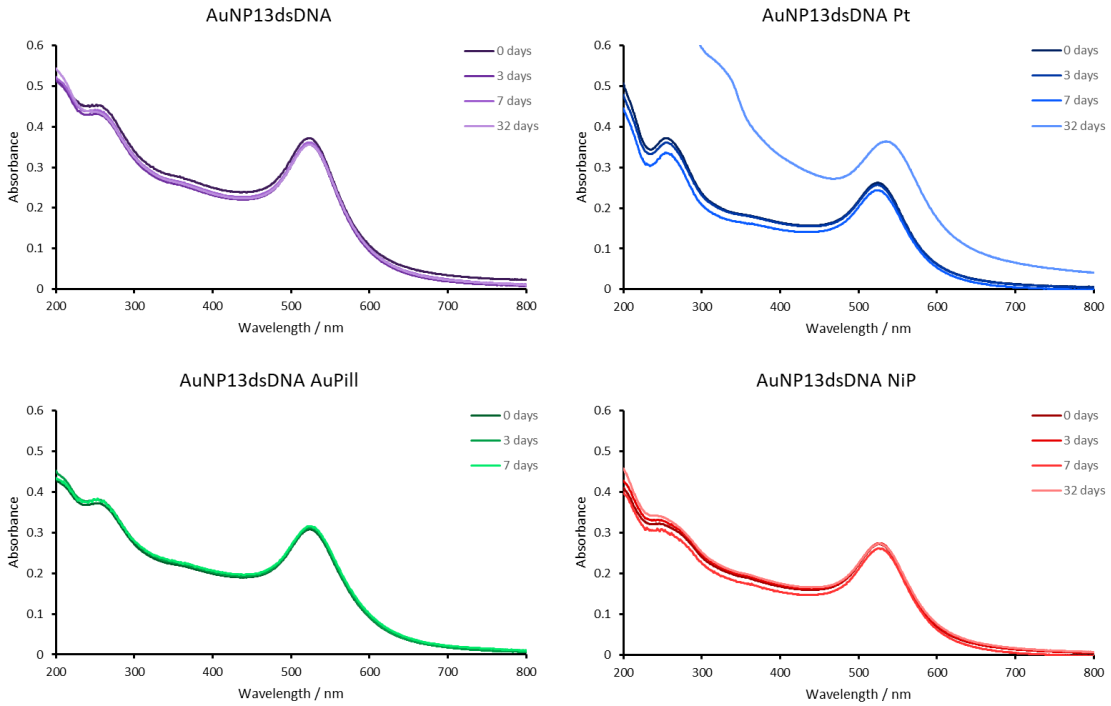


*Figure 40. Stability of particles in water over a 32 day period monitored by Uv-vis (the 32 day measurement for AuPill was not incleded as the particles had completely aggregated).*

The SPR peak of gold nanoparticles was used to assess particle aggregation (Figure 40). After 7 days, the UV-vis absorbance spectra of each of the particles does not display any notable decrease in intensity of the SPR band which would indicate aggregation and sedimentation, or any significant broadening. After 32 days, the AuNP13dsDNAPt shows significant broadening and increase in intensity indicating aggregation and AuNP13dsDNANiP shows a small decrease in intensity which is likely due to precipitation of some particles. The small change in SPR peak for AuNP13dsDNANiP indicating little change is in contrast to the DLS measurements which indicated the presence of large aggregates. This is due to the high sensitivity of DLS intensity data to larger particles. The SPR data and DLS number data is likely more representative of the bulk solution. Particles with a diameter > 1000 nm are also likely to sediment rapidly in solution and will therefore not be detected by UV-vis measurements. The measurement for AuNP13dsDNAAuPill after 32 days is excluded as the particles had completely aggregated.

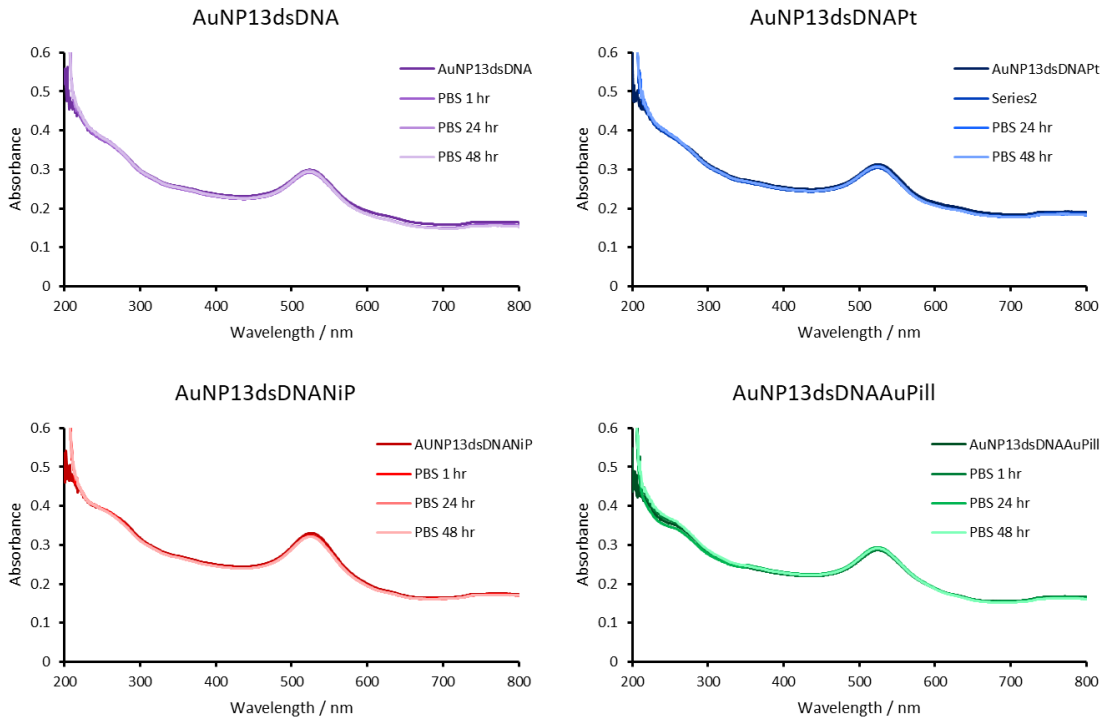


*Figure 41. Stability of particle systems over 48 hours in (1xPBS, pH 7.4) monitored by UV-vis absorbance.*

The stability of the gold nanoparticles functionalised with dsDNA1 and metal complexes in buffered solutions was also monitored by UV-vis absorbance (Figure 41). The UV vis of each particle system was monitored at 1, 24 and 48 hours. In all cases, there was minimal change in the SPR peak broadness or peak shift. The particles all appeared to be stable in buffer over the time period of the experiment.

Finally, the stability of the particles in DMEM media was also examined by UV-vis absorbance (appendix A4.9). Over a period of 18 hours, no discernible broadening or redshift of the SPR peak of the particles was observed. In all cases, the intensity of the SPR band of the particles decreased slowly, indicating that some aggregation and sedimentation of particles from solution was occurring.

## 4.3 Biological studies

After synthesising the gold-SNA particles and successfully loading them with metal complexes, as shown by PAGE gels, ICP-MS, and TEM, the next step was to investigate their uptake into cells and their toxicity. Due to time constraints, the cell work presented here is preliminary with no repeats carried out.

### 4.3.1 Uptake and cell fractionation

Cell fractionation was carried out in order to gain insight into where the nanoparticles were localising in the cells and where the metal complexes they were carrying end up. If the metal complexes and particles are localised in the same part of the cell, this may be an indication that the complexes are failing to be released.

The cell membranes were lysed by using a homogenisation buffer and vigorous pipetting. The nuclear fraction was then collected with mild centrifugation. The supernatant was extracted and kept as the cytosolic fraction. There is a risk that this centrifugation to collect the nuclear fraction may also cause aggregated nanoparticles to pellet with the nucleus, which would artificially inflate the amount of gold detected in the nucleus. Some aggregation of gold nanoparticles is observed when they were monitored in DMEM media.

*Table 10. Data for concentration of Ni, Au, and Pt measured in whole cell, nuclear, and cytosolic fractions by ICP-MS. (* Measurement is thought to be anomalous and requires repeats.)*

| Sample | AuNP13dsDNA | AuNP13dsDNANiP | AuNP13dsDNAAuPill | AuNP13dsDNAPtCyl |
|---|---|---|---|---|
| Whole cell / AuNP (nM) | 0.6 | 3.7 | 1.5 | 0.3 |
| Whole cell / metal complex (nM) | - | 818 | - | 20.3* |
| Nucleus / AuNP (nM) | 0.2 | 1.0 | 0.6 | 0.1 |
| Nucleus / metal complex (nM) | - | 290 | - | 232 |
| Cytosol / AuNP (nM) | 0.1 | 0.5 | 0.1 | <0.1 |
| Cytosol / metal complex (nM) | - | 360 | - | 2.7 |

The AuNP13dsDNANiP is uptaken into cells at high concentrations and nickel is detected at high concentrations in the nucleus and cytoplasm of the cells (Table 10). The concentration of gold is significantly higher in the nucleus than in the cytoplasm; this could be explained by the gold

nanoparticle aggregates also being collected in this fraction as mentioned above. AuNP13dsDNAAuPill also appears to be uptaken into cells at relatively high concentrations, but still at half the concentration of the AuNP13dsDNANiP particles. They also display a high concentration of gold in the nucleus, possibly due to the same aggregation issue. The quantity of platinum measured in the whole cell is very low and likely anomalous. The concentration of platinum measured in the nucleus is much higher than that of the cytoplasm. Interestingly, the gold concentration in the nucleus is low, possibly indicating that the PtCyl is coming off the particles.

### 4.3.2 Cytotoxicity

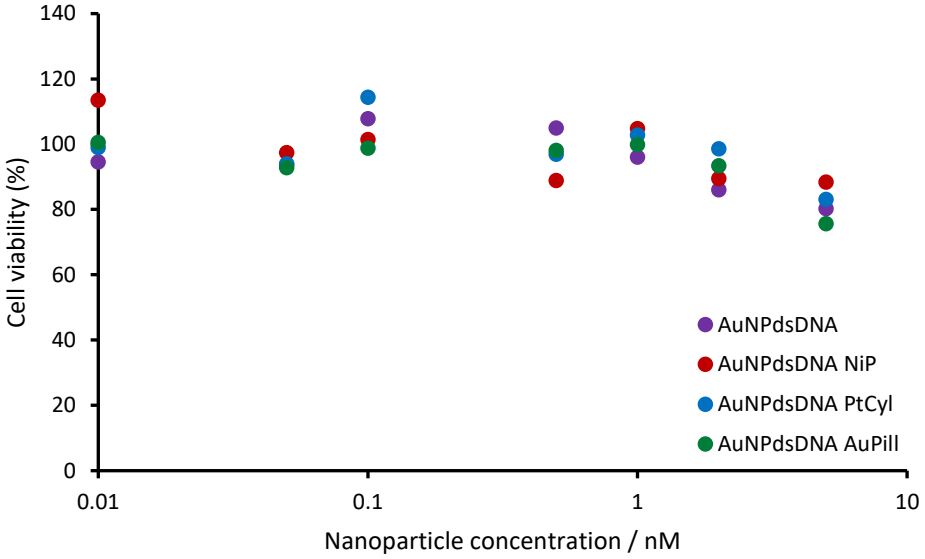


*Figure 42. MTT assay for AuNP13dsDNA alone and loaded with NiP/PtCyl/AuPill against MDA MB 231 cell line.*

A preliminary MTT assay was conducted with the AuNP13dsDNA1 particles alone, and loaded with either NiP, PtCyl, or AuPill against the MDA MB 231 cell line (Figure 42). MDA MB 231 is a commonly studied model of triple negative breast cancer. Repeats of the MTT assay were not obtained due to time constraints. The MTT results indicate that the SNAs are mildly toxic at high concentrations (5 nM) and, when loaded with a metal complex, this toxicity is not enhanced. This was disappointing but not surprising, as 5 nM of AuNP13dsDNANiP should correspond to approximately 1.5 µM of NiP. This result emphasises the necessity of increasing the loading of metal complexes onto the particles to make them a viable option for delivery of supramolecular metal complexes.

## 4.4 Conclusions

Gold nanoparticles were functionalised with DNA oligomers and the DNA junction binders NiP, PtCyl, and AuPill with the aim of improving the uptake of these metal complexes in cells and offering new avenues for targeted delivery of these metal complexes. Release of the metal complexes from the gold-SNA nanoparticles was demonstrated through the use of PAGE gels with 3WJ oligomers, which form the 3WJ structure only in the presence of the metal complexes. The NiP was successfully released from the gold nanoparticles and was able to form 3WJ in the gels. The loading of NiP onto the particles was quantified by the 3WJ PAGE gel assay as well as ICP-MS. Loading of PtCyl onto the particles was partially successful but was not as high as the NiP, possibly due to the lower affinity of the PtCyl for B-DNA (Chapter 3). It is not certain if loading of AuPill onto the particles was successful, as ICP-MS is not able to distinguish the metal complex from the gold particles, and release of AuPill to 3WJ was very low in PAGE gels. The AuNP13dsDNA particles were shown to be non-toxic by MTT assay, and loading of the particles with metal complexes did not increase the toxicity. The lack of increase in toxicity is thought to be due to the relatively low loading of particles achieved onto the particles.

Attempts were made to increase the loading of the metal complexes on the gold nanoparticles by using longer DNA sequences. The gold nanoparticles were functionalised with longer DNA oligomers shown by DLS and UV-vis measurements, however PAGE gels revealed that purification of the particles was not entirely successful. Bands corresponding to the individual DNA oligomers were visible, indicating that some oligomers were only weakly bound to the particles. This made quantification of the loading of metal complexes on the particles by 3WJ PAGE gel assay impossible.

In conclusion, spherical nucleic acids based on gold nanoparticle cores were successfully synthesized and loaded with NiP metal complex. The release of the supramolecular cylinder to its preferred binding target, DNA junctions, was shown to be possible through PAGE gels. This work demonstrated the proof of concept for delivery of DNA junction binding metal complexes by gold-SNA particles.

## 4.5 Future work

TEM EDS (energy dispersive x-ray spectroscopy) data could be used to unequivocally confirm the presence of the metal complexes on the surface of the gold nanoparticles. This characterisation technique would only be suitable for the NiP or PtCyl functionalised particles as it cannot distinguish between the gold in AuPill, and the gold from the particle cores. More accurate quantification of the loading of the metal complexes could be achieved through the use of fluorescent or radio labelled 3WJ to avoid issues with staining PAGE gels. Further efforts should also be made to determine if the metal complexes are being passively released from the particles over time. This could be carried out using the same PAGE gel assay used to determine the loading of the metal complexes on the particles with freshly made particles, compared to particles aged and washed. DNA melting studies of the particles with and without metal complexes would also be useful for characterisation.[40]

Larger gold nanoparticles could be investigated for use as drug delivery vectors for the junction binding metal complexes as larger particles can accommodate significantly larger numbers of oligomers on their surface. However, larger particles may exhibit different affinities for the metal complexes as it has been shown how larger particles support less dense oligomer monolayers.[38] Particles with a diameter over 200 nm present an SNA surface very similar to planar gold functionalised with DNA oligomers. Functionalisation of a series of particles with increasing size may help reveal how the metal complexes interact with the organised arrays of nucleic acids presented by SNAs.

Finally, more significant improvements could be made to the nanoparticle system. The ruthenium version of the NiP cylinder could be used and then irradiated to induce oxidative damage to the duplex DNA and subsequent release of the cylinder from the particles. Peter Cail utilised this strategy to induce release of the ruthenium cylinder from DNA tetrahdera.[19] In the future, more complex DNA strands could also be used to decorate the particles; such as aptamers for targeting specific proteins,[20] or DNA toehold switches for controlled drug release.[54]

## 4.6 References


1. Mirkin, C. A.; Letsinger, R. L.; Mucic, R. C.; Storhoff, J. J., A DNA-based method for rationally assembling nanoparticles into macroscopic materials. *Nature* **1996,** *382* (6592), 607-609.
2. Song, Y.; Song, W.; Lan, X.; Cai, W.; Jiang, D., Spherical nucleic acids: Organized nucleotide aggregates as versatile nanomedicine. *Aggregate* **2021,** *3*, e120.
3. Garcia-Guerra, A.; Ellerington, R.; Gaitzsch, J.; Bath, J.; Kye, M.; Varela, M. A.; Battaglia, G.; Wood, M. J. A.; Manzano, R.; Rinaldi, C.; Turberfield, A. J., A modular RNA delivery system comprising spherical nucleic acids built on endosome-escaping polymeric nanoparticles. *Nanoscale Advances* **2023,** *5* (11), 2941-2949.
4. Young, K. L.; Scott, A. W.; Hao, L.; Mirkin, S. E.; Liu, G.; Mirkin, C. A., Hollow Spherical Nucleic Acids for Intracellular Gene Regulation Based upon Biocompatible Silica Shells. *Nano Letters* **2012,** *12* (7), 3867-3871.
5. Gourishankar, A.; Shukla, S.; Ganesh, K. N.; Sastry, M., Isothermal Titration Calorimetry Studies on the Binding of DNA Bases and PNA Base Monomers to Gold Nanoparticles. *Journal of the American Chemical Society* **2004,** *126* (41), 13186-13187.
6. Jang, N. H., The Coordination Chemistry of DNA Nucleosides on Gold Nanoparticles as a Probe by SERS. *Bulletin of The Korean Chemical Society* **2002,** *23*, 1790-1800.
7. Storhoff, J. J.; Elghanian, R.; Mirkin, C. A.; Letsinger, R. L., Sequence-Dependent Stability of DNA-Modified Gold Nanoparticles. *Langmuir* **2002,** *18* (17), 6666-6670.
8. Yang, J.; Pong, B.-K.; Lee, J. Y.; Too, H.-P., Dissociation of double-stranded DNA by small metal nanoparticles. *Journal of Inorganic Biochemistry* **2007,** *101* (5), 824-830.
9. Östblom, M.; Liedberg, B.; Demers, L. M.; Mirkin, C. A., On the Structure and Desorption Dynamics of DNA Bases Adsorbed on Gold: A Temperature-Programmed Study. *The Journal of Physical Chemistry B* **2005,** *109* (31), 15150-15160.
10. Bano, F.; Sluysmans, D.; Wislez, A.; Duwez, A.-S., Unraveling the complexity of the interactions of DNA nucleotides with gold by single molecule force spectroscopy. *Nanoscale* **2015,** *7* (46), 19528-19533.
11. Zhou, T.; Zhang, C.; Wang, H.; Kang, X.; Zhang, Z.; Wang, F.; Wang, X.; Zhang, G., Comparison Investigation on the Adsorption Affinity of DNA Molecules to the Gold Surface Based on the Kinetic and Thermodynamic Analysis of 4-Nitrophenol Reduction. *The Journal of Physical Chemistry C* **2020,** *124* (8), 4595-4604.
12. Carnerero, J. M.; Jimenez-Ruiz, A.; Grueso, E. M.; Prado-Gotor, R., Understanding and improving aggregated gold nanoparticle/dsDNA interactions by molecular spectroscopy and deconvolution methods. *Physical Chemistry Chemical Physics* **2017,** *19* (24), 16113-16123.
13. Pei, H.; Li, F.; Wan, Y.; Wei, M.; Liu, H.; Su, Y.; Chen, N.; Huang, Q.; Fan, C., Designed Diblock Oligonucleotide for the Synthesis of Spatially Isolated and Highly Hybridizable Functionalization of DNA–Gold Nanoparticle Nanoconjugates. *Journal of the American Chemical Society* **2012,** *134* (29), 11876-11879.
14. Yao, G.; Pei, H.; Li, J.; Zhao, Y.; Zhu, D.; Zhang, Y.; Lin, Y.; Huang, Q.; Fan, C., Clicking DNA to gold nanoparticles: poly-adenine-mediated formation of monovalent DNA-gold nanoparticle conjugates with nearly quantitative yield. *NPG Asia Materials* **2015,** *7* (1), e159-e159.
15. Hurst, S. J.; Lytton-Jean, A. K. R.; Mirkin, C. A., Maximizing DNA Loading on a Range of Gold Nanoparticle Sizes. *Analytical Chemistry* **2006,** *78* (24), 8313-8318.
16. Xu, S.; Yuan, H.; Xu, A.; Wang, J.; Wu, L., Rapid Synthesis of Stable and Functional Conjugates of DNA/Gold Nanoparticles Mediated by Tween 80. *Langmuir* **2011,** *27* (22), 13629-13634.
17. Li, J.; Zhu, B.; Yao, X.; Zhang, Y.; Zhu, Z.; Tu, S.; Jia, S.; Liu, R.; Kang, H.; Yang, C. J., Synergetic Approach for Simple and Rapid Conjugation of Gold Nanoparticles with Oligonucleotides. *ACS Applied Materials & Interfaces* **2014,** *6* (19), 16800-16807.
18. Zhang, X.; Servos, M. R.; Liu, J., Instantaneous and Quantitative Functionalization of Gold Nanoparticles with Thiolated DNA Using a pH-Assisted and Surfactant-Free Route. *Journal of the American Chemical Society* **2012,** *134* (17), 7266-7269.

19. Cail, P. J. DNA Nanotechnology and Supramolecular Chemistry in Biomedical Therapy Applications. University of Birmingham, Birmingham, 2017.
20. Zheng, J.; Zhu, G.; Li, Y.; Li, C.; You, M.; Chen, T.; Song, E.; Yang, R.; Tan, W., A Spherical Nucleic Acid Platform Based on Self-Assembled DNA Biopolymer for High-Performance Cancer Therapy. *ACS Nano* **2013,** *7* (8), 6545-6554.
21. Li, W.; Yang, X.; He, L.; Wang, K.; Wang, Q.; Huang, J.; Liu, J.; Wu, B.; Xu, C., Self-Assembled DNA Nanocentipede as Multivalent Drug Carrier for Targeted Delivery. *ACS Applied Materials & Interfaces* **2016,** *8* (39), 25733-25740.
22. Kyriazi, M.-E.; Giust, D.; El-Sagheer, A. H.; Lackie, P. M.; Muskens, O. L.; Brown, T.; Kanaras, A. G., Multiplexed mRNA Sensing and Combinatorial-Targeted Drug Delivery Using DNA-Gold Nanoparticle Dimers. *ACS Nano* **2018,** *12* (4), 3333-3340.
23. Zhang, S.; Chen, C.; Xue, C.; Chang, D.; Xu, H.; Salena, B. J.; Li, Y.; Wu, Z.-S., Ribbon of DNA Lattice on Gold Nanoparticles for Selective Drug Delivery to Cancer Cells. *Angewandte Chemie International Edition* **2020,** *59* (34), 14584-14592.
24. Craig, J. S.; Melidis, L.; Williams, H. D.; Dettmer, S. J.; Heidecker, A. A.; Altmann, P. J.; Guan, S.; Campbell, C.; Browning, D. F.; Sigel, R. K. O.; Johannsen, S.; Egan, R. T.; Aikman, B.; Casini, A.; Pöthig, A.; Hannon, M. J., Organometallic Pillarplexes That Bind DNA 4-Way Holliday Junctions and Forks. *Journal of the American Chemical Society* **2023,** *145* (25), 13570-13580.
25. Hannon, M. J.; Moreno, V.; Prieto, M. J.; Moldrheim, E.; Sletten, E.; Meistermann, I.; Isaac, C. J.; Sanders, K. J.; Rodger, A., Intramolecular DNA Coiling Mediated by a Metallo-Supramolecular Cylinder. *Angewandte Chemie International Edition* **2001,** *40* (5), 879-884.
26. Song, L.; Guo, Y.; Roebuck, D.; Chen, C.; Yang, M.; Yang, Z.; Sreedharan, S.; Glover, C.; Thomas, J. A.; Liu, D.; Guo, S.; Chen, R.; Zhou, D., Terminal PEGylated DNA–Gold Nanoparticle Conjugates Offering High Resistance to Nuclease Degradation and Efficient Intracellular Delivery of DNA Binding Agents. *ACS Applied Materials & Interfaces* **2015,** *7* (33), 18707-18716.
27. Gill, M. R.; Garcia-Lara, J.; Foster, S. J.; Smythe, C.; Battaglia, G.; Thomas, J. A., A ruthenium(II) polypyridyl complex for direct imaging of DNA structure in living cells. *Nature Chemistry* **2009,** *1* (8), 662-667.
28. Milan, J.; Niemczyk, K.; Kus-Liśkiewicz, M., Treasure on the Earth - Gold Nanoparticles and Their Biomedical Applications. *Materials* **2022,** *15* (9), 3355.
29. Hu, X.; Zhang, Y.; Ding, T.; Liu, J.; Zhao, H., Multifunctional Gold Nanoparticles: A Novel Nanomaterial for Various Medical Applications and Biological Activities. *Frontiers in Bioengineering and Biotechnology* **2020,** *8*.
30. Kesharwani, P.; Ma, R.; Sang, L.; Fatima, M.; Sheikh, A.; Abourehab, M. A. S.; Gupta, N.; Chen, Z.-S.; Zhou, Y., Gold nanoparticles and gold nanorods in the landscape of cancer therapy. *Molecular Cancer* **2023,** *22* (1), 98.
31. Jain, S.; Hirst, D. G.; O'Sullivan, J. M., Gold nanoparticles as novel agents for cancer therapy. *The British Journal of Radiology* **2012,** *85* (1010), 101-113.
32. Wuithschick, M.; Birnbaum, A.; Witte, S.; Sztucki, M.; Vainio, U.; Pinna, N.; Rademann, K.; Emmerling, F.; Kraehnert, R.; Polte, J., Turkevich in New Robes: Key Questions Answered for the Most Common Gold Nanoparticle Synthesis. *ACS Nano* **2015,** *9* (7), 7052-7071.
33. Georgiadis, R.; Peterlinz, K. P.; Peterson, A. W., Quantitative Measurements and Modeling of Kinetics in Nucleic Acid Monolayer Films Using SPR Spectroscopy. *Journal of the American Chemical Society* **2000,** *122* (13), 3166-3173.
34. Zhang, X.; Gouriye, T.; Göeken, K.; Servos, M. R.; Gill, R.; Liu, J., Toward Fast and Quantitative Modification of Large Gold Nanoparticles by Thiolated DNA: Scaling of Nanoscale Forces, Kinetics, and the Need for Thiol Reduction. *The Journal of Physical Chemistry C* **2013,** *117* (30), 15677-15684.
35. Phongtongpasuk, S.; Paulus, S.; Schnabl, J.; Sigel, R. K. O.; Spingler, B.; Hannon, M. J.; Freisinger, E., Binding of a Designed Anti-Cancer Drug to the Central Cavity of an RNA Three-Way Junction. *Angewandte Chemie International Edition* **2013,** *52* (44), 11513-11516.

36. Montaño-Priede, J. L.; Sanromán-Iglesias, M.; Zabala, N.; Grzelczak, M.; Aizpurua, J., Robust Rules for Optimal Colorimetric Sensing Based on Gold Nanoparticle Aggregation. *ACS Sensors* **2023,** *8* (4), 1827-1834.
37. Kolbeck, P. J.; Vanderlinden, W.; Gemmecker, G.; Gebhardt, C.; Lehmann, M.; Lak, A.; Nicolaus, T.; Cordes, T.; Lipfert, J., Molecular structure, DNA binding mode, photophysical properties and recommendations for use of SYBR Gold. *Nucleic Acids Research* **2021,** *49* (9), 5143-5158.
38. Hill, H. D.; Millstone, J. E.; Banholzer, M. J.; Mirkin, C. A., The Role Radius of Curvature Plays in Thiolated Oligonucleotide Loading on Gold Nanoparticles. *ACS Nano* **2009,** *3* (2), 418-424.
39. Liu, B.; Liu, J., Methods for preparing DNA-functionalized gold nanoparticles, a key reagent of bioanalytical chemistry. *Analytical Methods* **2017,** *9* (18), 2633-2643.
40. Cutler, J. I.; Auyeung, E.; Mirkin, C. A., Spherical Nucleic Acids. *Journal of the American Chemical Society* **2012,** *134* (3), 1376-1391.
41. Hooper, C. A. J.; Cardo, L.; Craig, J. S.; Melidis, L.; Garai, A.; Egan, R. T.; Sadovnikova, V.; Burkert, F.; Male, L.; Hodges, N. J.; Browning, D. F.; Rosas, R.; Liu, F.; Rocha, F. V.; Lima, M. A.; Liu, S.; Bardelang, D.; Hannon, M. J., Rotaxanating Metallo-supramolecular Nano-cylinder Helicates to Switch DNA Junction Binding. *Journal of the American Chemical Society* **2020,** *142* (49), 20651-20660.
42. Reuter, J. S.; Mathews, D. H., RNAstructure: software for RNA secondary structure prediction and analysis. *BMC Bioinformatics* **2010,** *11* (1), 129.
43. Lytton-Jean, A. K. R.; Mirkin, C. A., A Thermodynamic Investigation into the Binding Properties of DNA Functionalized Gold Nanoparticle Probes and Molecular Fluorophore Probes. *Journal of the American Chemical Society* **2005,** *127* (37), 12754-12755.
44. Zheng, Y.; Hong, Y.; Wu, W.; Sun, D.; Wang, Y.; Huang, J.; Li, Q., Separation of different shape biosynthesized gold nanoparticles via agarose gel electrophoresis. *Separation and Purification Technology* **2015,** *151*, 332-337.
45. Hanauer, M.; Pierrat, S.; Zins, I.; Lotz, A.; Sönnichsen, C., Separation of Nanoparticles by Gel Electrophoresis According to Size and Shape. *Nano Letters* **2007,** *7* (9), 2881-2885.
46. Huxley, H. E.; Zubay, G., PREFERENTIAL STAINING OF NUCLEIC ACID-CONTAINING STRUCTURES FOR ELECTRON MICROSCOPY. *The Journal of Biophysical and Biochemical Cytology* **1961,** *11* (2), 273-296.
47. Woods, K. E.; Perera, Y. R.; Davidson, M. B.; Wilks, C. A.; Yadav, D. K.; Fitzkee, N. C., Understanding Protein Structure Deformation on the Surface of Gold Nanoparticles of Varying Size. *The Journal of Physical Chemistry C* **2016,** *120* (49), 27944-27953.
48. Elia, P.; Zach, R.; Hazan, S.; Kolusheva, S.; Porat, Z. e.; Zeiri, Y., Green synthesis of gold nanoparticles using plant extracts as reducing agents. *International Journal of Nanomedicine* **2014,** *9*, 4007-4021.
49. Wang, G.; Wang, W.; Shangguan, E.; Gao, S.; Liu, Y., Effects of gold nanoparticle morphologies on interactions with proteins. *Materials Science and Engineering: C* **2020,** *111*, 110830.
50. Hamdy, M. E.; Del Carlo, M.; Hussein, H. A.; Salah, T. A.; El-Deeb, A. H.; Emara, M. M.; Pezzoni, G.; Compagnone, D., Development of gold nanoparticles biosensor for ultrasensitive diagnosis of foot and mouth disease virus. *Journal of Nanobiotechnology* **2018,** *16* (1), 48.
51. Narayan, S. P.; Choi, C. H. J.; Hao, L.; Calabrese, C. M.; Auyeung, E.; Zhang, C.; Goor, O. J. G. M.; Mirkin, C. A., The Sequence-Specific Cellular Uptake of Spherical Nucleic Acid Nanoparticle Conjugates. *Small* **2015,** *11* (33), 4173-4182.
52. Shankar, S.; Bhargava, S.; Sastry, M., Synthesis of gold nanospheres and nanotriangles by the Turkevich approach. *Journal of Nanoscience and Nanotechnology* **2005,** *5*, 1721-1727.
53. Ortiz-Castillo, J. E.; Gallo-Villanueva, R. C.; Madou, M. J.; Perez-Gonzalez, V. H., Anisotropic gold nanoparticles: A survey of recent synthetic methodologies. *Coordination Chemistry Reviews* **2020,** *425*, 213489.
54. Xiao, M.; Lai, W.; Wang, F.; Li, L.; Fan, C.; Pei, H., Programming Drug Delivery Kinetics for Active Burst Release with DNA Toehold Switches. *Journal of the American Chemical Society* **2019,** *141* (51), 20354-20364.

# Chapter 5 – Conclusions and future work

## 5.1 Conclusions

The DNA binding ability of a known palladium complex was investigated. The platinum analogue of this complex (PtCyl) was synthesised for the first time and also studied for its DNA binding ability. It was quickly realised that the PtCyl was much more stable in buffered solution than the Pd complex, which directed this study to focus on the PtCyl complex. Both the palladium helicate and PtCyl were shown to interact with B-DNA through CD and LD studies. Both complexes were shown, through PAGE gel experiments, to be capable of forming a 3WJ but only the PtCyl showed significant interactions with DNA 4WJ. The PtCyl appeared to interact more strongly with the DNA junctions, but it is likely that this was due to the palladium complex breaking down in buffered solutions. Molecular dynamics (MD) were used to elucidate the binding mode of these metal complexes with the DNA junction structures. MD simulations (carried out by Samuel Dettmer) suggest that the PtCyl has a specific binding mode to 3WJ where one base pair is broken and the complex forms pi-pi interactions in the junction cavity. There also appears to be a preference for the P enantiomer over the M enantiomer of the complex when binding to DNA 3WJ. Simulations with the 4WJ suggest that the PtCyl complex is simply too small to pi stack with all four faces of the junction cavity at the same time. The palladium helicate and PtCyl both display interesting interactions with B-DNA and DNA junctions. Study of the interactions of these complexes with cells should be the next steps, particularly for the PtCyl complex due to its increased stability.

Comparing the interaction of the nickel parent cylinder (NiP), gold pillarplex (AuPill), and PtCyl with B-DNA, through fluorescence displacement experiments, indicates that the NiP and AuPill have significantly higher affinities for B-DNA than the PtCyl. This could be due to the encapsulation of an anion by the PtCyl, reducing the overall charge of the complex, or due to the more flexible nature of the PtCyl. PAGE competition studies have shown that the PtCyl has a stronger preference for the 3WJ than either the AuPill or NiP. The AuPill and NiP both show strong interactions with the DNA 3WJ but also with the DNA 4WJ. In FRET melting studies, each complex induces a strong stabilisation of the 3WJ, indicated by a large increase in the melting temperature of the 3WJT6 structure. The marginal increase

in the melting temperature of the 3WJT6 with excess PtCyl confirms that the PtCyl has a strong interaction with the 3WJ cavity but only weakly interacts with the rest of the structure. Isothermal calorimetry was carried out with the metal complexes and a 3WJT6 structure. This work confirmed that the PtCyl and NiP had very comparable binding affinities for the 3WJ, and only one binding event was observed indicating no interaction with the hairpin loops of the structure. It was not possible to measure the affinity of the AuPill for the 3WJT6 by ITC due to the poor solubility of the AuPill at the required concentrations in buffered solution. Overall, this suggests that a metal cylinder with a lower charge may have more success targeting a DNA junction due to the reduced interactions with competing DNA structures.

Analysis of PAGE gels of RNA 3WJ and 4WJ structures with each metal complex was carried out. There are clear differences in the structures formed with the RNA junctions compared to the DNA junctions. The most surprising result was the formation of a unique structure with the PtCyl complex which appears to be larger than the RNA 4WJ alone. This hints that the PtCyl may have a higher affinity for RNA 4WJ than expected. Other experiments in Chapter 3 found that the PtCyl displayed a higher affinity for DNA 3WJ vs DNA 4WJ, but did not compete RNA structures.

Mass spectrometry was investigated as a technique to study the interactions of DNA junction binding metal complexes with a DNA 3WJ structure (3WJT6). The 3WJT6 structure was successfully detected by MS with metal complexes bound. Control experiments revealed that non-junction binding metal complexes could also be bound to the 3WJT6 structure but, in competition experiments, were out competed by junction binding metal complexes. This is a promising technique for studying the non-covalent interaction of metal complexes with DNA junctions but further optimisation is required.

Spherical nucleic acids (SNAs) were investigated as potential drug delivery vehicles for supramolecular cylinders. These AuNP SNAs were successfully synthesised, and attempts were made to load them with metal complexes. ICP-MS confirmed that the particles were successfully functionalised with PtCyl and NiP. This technique was not applicable to AuPill complex as the metal centres are gold: ICP-MS cannot distinguish between the gold from the complex and gold from the particles. PAGE gel experiments

showed that the metal complexes (PtCyl and NiP) were able to be released from the SNAs in the presence of a DNA 3WJ. Attempts were made to increase the loading of cylinders onto the particles by increasing the oligomer lengths; this was not successful due to partial hybridization of the larger oligomers leading to contamination of particle solutions with excess oligomers. The successfully functionalised gold-SNA particles loaded with metal complexes were shown to be non-toxic by a preliminary MTT assay. This was thought to be due to the relatively low loading of the metal complexes achieved. This work demonstrated the proof of concept for delivery of DNA junction binding metal complexes by gold-SNA particles.

Overall, a new junction binding agent, PtCyl, has been synthesised which displays a strong affinity for DNA 3WJ and is also able to bind DNA 4WJ. Competition experiments have demonstrated the high selectivity of the PtCyl for DNA 3WJ compared to other junction binding agents. This work highlights the potential to discover new junction binding agents by reassessing metal complexes which have already been published in literature for alternative applications. It was established that SNAs could be loaded with junction binding agents which could be released to their preferred binding target – DNA junctions. This has laid the groundwork for SNAs to be used as vectors for delivery of junction binding agents into cells.

## 5.2 Future work

Future work with the PtCyl should first focus on obtaining a crystal structure to confirm the helical nature of the complex. It is highly likely that the complex is helical in the same way as the palladium analogue, but this has not been confirmed in this work. Simulations have shown that the structure in solution is very flexible, so a crystal structure should not affect the conclusions from the studies presented here. The use of fluorescently labelled DNA structures to study the interactions of DNA with metal complexes has become more widespread in recent years. Recent examples of this work can be found from Nitschke,[1] Monchaud,[2] and Vazquez-Lopez.[3] Full advantage should be taken of the already published fluorescently labelled DNA structures, and experimental designs, to gain further insight into molecular interactions between PtCyl and DNA structures.

The work presented in Chapter 2 focused on one example of a palladium $M_2L_4$ helicate from the literature and its platinum analogue. The studies here have revealed a wealth of DNA interactions between these complexes and different DNA structures. There are a huge number of other platinum and palladium $M_2L_4$ complexes in the literature which have not had their DNA binding properties investigated. The most promising candidate for further research which I have come across is the palladium complex produced by Qing-Fu Sun and Li-Peng Zhou.[4] This complex has dimensions which are appropriate for DNA junction binding, it is chiral, and it has externally facing pi-surfaces which may be able to pi stack with bases in junction cavities.

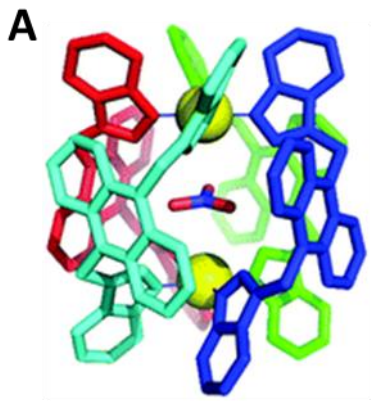


*Figure 1. Structure of a $Pd_2L_4$ metal complex from literature which is a potential DNA junction binding agent. Adapted from referenced publication with permission.[4]*

Another interesting avenue of research would be to modify the PtCyl ligands. Introducing some steric hindrance to the structure to try to lock it into one enantiomer would allow us to investigate the binding of a single enantiomer at a time with the DNA structures. If the lower charge of the platinum structure is the reason for its higher selectivity, then a less flexible cage structure may make it easier to encapsulate and hold onto the anion in its central cavity further improving its selectivity. Other modifications could include modifying the ends of the ligands to make the complex more hydrophobic/hydrophilic. Finally, naphthalene/anthracene moieties could be used instead of the central benzene of the ligands, which would make the complex substantially larger. It is unclear if this would be successful as the geometry of the complex would be drastically altered, and the distance between the central anion and the metals would be increased to such an extent that any stabilising force from this interaction would be negated.

MD simulations with RNA are inherently more difficult due to the larger number of conformations possible.[5] However, the unusual structures that appear to form with the PtCyl may warrant investigation through computational studies to gain insight into the structure which could be forming. Competition studies of DNA vs RNA structures would also be interesting, as the formation of unique structures with the RNA may be more, or less, stable than those formed with DNA.

Further work utilising isothermal calorimetry to assess the binding affinity of supramolecular cylinders synthesised in the past and present by the Hannon group with DNA and RNA junctions should be carried out. Quantification of the affinity of many different "cylinders" for various nucleic acid junctions could be used to direct the design of future junction binding agents. Other DNA structures could also be studied; for example, G-quadruplexes.

Ion mobility is an MS technique which separates ions with different cross-sectional areas, allowing for the identification of different sized species from complex solutions. This would be an invaluable technique for studying junction binding, as it may be possible to observe folding of the DNA oligomer to form a junction. This would be good evidence of the metal complexes binding in the junction cavity. Baker *et al.* were able to differentiate between two different conformations of DNA cruciform structures using ion mobility.[6]

Future work with the SNA particles should first focus on further characterisation of the particles and understanding the release of the metal supramolecular complexes in solution. This could be achieved by carrying out ICP-MS of the supernatant of the particle solutions after different periods of time to establish if the supramolecular complexes are being passively released. Melting studies of the SNAs with and without the metal complexes would also be useful for confirming their presence and understanding their impact on the structure. SNAs are known to produce sharp melting temperatures which may allow for accurate determination of drug loadings.[7] In particular, melting studies with the SNAs loaded with AuPill would be invaluable for confirming whether the AuPill is present on the SNA or not, as PAGE gels showed little to no release of the AuPill. This could either be due to the strong interaction of AuPill with dsDNA or it could be that the AuPill was not successfully loaded onto the

particles. An unexplored avenue to increase the loading of the metal complexes on the SNAs would be increasing the size of the particles. The oligomer used to load the complexes on could also be modified. Replacing the adenine spacer of the thiolated oligomers with either thymine or PEG has shown to substantially increase the loading of oligomers on gold particles.[8]

Moving forward with gold-SNA particles loaded with metal complexes would involve cell work to establish if the particles are able to improve the uptake of the metal complexes. Cytotoxicity studies should also be performed to observe any toxicity caused by the particle system alone, and when loaded with the metal complexes. If this work proves fruitful, then further work could aim to improve the targeting of the particles through the use of aptamers,[9] or to stimulate the release of the complexes in the presence of specific nucleic acid sequences.[10]

## 5.3 References


1. Zhu, J.; Haynes, C. J. E.; Kieffer, M.; Greenfield, J. L.; Greenhalgh, R. D.; Nitschke, J. R.; Keyser, U. F., FeII4L4 Tetrahedron Binds to Nonpaired DNA Bases. *Journal of the American Chemical Society* **2019,** *141* (29), 11358-11362.
2. Zell, J.; Duskova, K.; Chouh, L.; Bossaert, M.; Chéron, N.; Granzhan, A.; Britton, S.; Monchaud, D., Dual targeting of higher-order DNA structures by azacryptands induces DNA junction-mediated DNA damage in cancer cells. *Nucleic Acids Research* **2021,** *49* (18), 10275-10288.
3. Alcalde-Ordóñez, A.; Barreiro-Piñeiro, N.; McGorman, B.; Gómez-González, J.; Bouzada, D.; Rivadulla, F.; Vázquez, M. E.; Kellett, A.; Martínez-Costas, J.; López, M. V., A copper(ii) peptide helicate selectively cleaves DNA replication foci in mammalian cells. *Chemical Science* **2023,** *14* (48), 14082-14091.
4. Zhou, L.-P.; Sun, Q.-F., A self-assembled Pd2L4 cage that selectively encapsulates nitrate. *Chemical Communications* **2015,** *51* (94), 16767-16770.
5. Šponer, J.; Bussi, G.; Krepl, M.; Banáš, P.; Bottaro, S.; Cunha, R. A.; Gil-Ley, A.; Pinamonti, G.; Poblete, S.; Jurečka, P.; Walter, N. G.; Otyepka, M., RNA Structural Dynamics As Captured by Molecular Simulations: A Comprehensive Overview. *Chemical Reviews* **2018,** *118* (8), 4177-4338.
6. Baker, E. S.; Dupuis, N. F.; Bowers, M. T., DNA Hairpin, Pseudoknot, and Cruciform Stability in a Solvent-Free Environment. *The Journal of Physical Chemistry B* **2009,** *113* (6), 1722-1727.
7. Cutler, J. I.; Auyeung, E.; Mirkin, C. A., Spherical Nucleic Acids. *Journal of the American Chemical Society* **2012,** *134* (3), 1376-1391.
8. Hurst, S. J.; Lytton-Jean, A. K. R.; Mirkin, C. A., Maximizing DNA Loading on a Range of Gold Nanoparticle Sizes. *Analytical Chemistry* **2006,** *78* (24), 8313-8318.
9. Zheng, J.; Zhu, G.; Li, Y.; Li, C.; You, M.; Chen, T.; Song, E.; Yang, R.; Tan, W., A Spherical Nucleic Acid Platform Based on Self-Assembled DNA Biopolymer for High-Performance Cancer Therapy. *ACS Nano* **2013,** *7* (8), 6545-6554.
10. Kyriazi, M.-E.; Giust, D.; El-Sagheer, A. H.; Lackie, P. M.; Muskens, O. L.; Brown, T.; Kanaras, A. G., Multiplexed mRNA Sensing and Combinatorial-Targeted Drug Delivery Using DNA-Gold Nanoparticle Dimers. *ACS Nano* **2018,** *12* (4), 3333-3340.

# Chapter 6 – Experimental

## 6.1 Oligomers used throughout thesis

All DNA oligomers were purchased from Sigma Aldrich purified by HPLC and dried. RNA oligomers were purchased from Integrated DNA Technologies (IDT) purified by HPLC and dried. All oligomers were then used without further purification.

3WJ S1 = CGGAACGGCACTCG

3WJ S2 = CGAGTGCAGCGTGG

3WJ S3 = CCACGCTCGTTCCG

FAM-3WJ S1 = [6FAM]- CGGAACGGCACTCG

4WJ S1 = GCCTAGCATGATACTGCTACCG

4WJ S2 = CGGTAGCAGTACCGTTGGTGGC

4WJ S3 = GCCACCAACGGCGTCAACTGCC

4WJ S4 = GGCAGTTGACGTCATGCTAGGC

3WJ18 S1 = GTGGCGAGAGCGACGATC

3WJ18 S2 = GATCGTCGCAGAGTTGAC

3WJ18 S3 = GTCAACTCTTCTCGCCAC

Bulge S1 = CGTAGCCGATGC

Bulge S2 (0) = GCATCGGCTACG

Bulge S2 (1) = GCATCGTGCTACG

Bulge S2 (2) = GCATCGTTGCTACG

Bulge S2 (3) = GCATCGTTTGCTACG

Bulge S2 (4) = GCATCGTTTTGCTACG

Bulge S2 (5) = GCATCGTTTTTGCTACG

Bulge S2 (6) = GCATCGTTTTTTGCTACG

Bulge S2 (7) = GCATCGTTTTTTTGCTACG

ds26 S1 = CCTTCACGCGAACGTAATCCTAGGATTACGTTCGCGTGAAGG

ds26 S2 = GGAAGTGCGCTTGCATTAGGATCCTAATGCAAGCGCACTTCC

ds21 S1 = CCTTCACGCGAACGTAATCCT

ds21 S2 = AGGATTACGTTCGCGTGAAGG

polyA 42mer = AAAAAAAAAAAAAAAAAAAAAAAAAAAAAAAAAAAAAA

polyT 22mer = TTTTTTTTTTTTTTTTTTTT

3WJT6 = ACTCTTCTCGTTTTTTCGAGAGCGACTTTTTTGTCGCAGAGT

3WJT6 FRET = [6FAM]-ACTCTTCTCGTTTTTTCGAGAGCGACTTTTTTGTCGCAGAGT-[TAM]

3WJT6 loop (Loop) = GCTCTCGTTTTTTCGAGAGC

RNA 3WJ S1 = CGGAACGGCACUCG

RNA 3WJ S2 = CGAGUGCAGCGUGG

RNA 3WJ S3 = CCACGCUCGUUCCG

RNA 4WJ S1 = GCCUAGCAUGAUACUGCUACCG

RNA 4WJ S2 = CGGUAGCAGUACCGUUGGUGGC

RNA 4WJ S3 = GCCACCAACGGCGUCAACUGCC

RNA 4WJ S4 = GGCAGUUGACGUCAUGCUAGGC

htelo = AGGGTTAGGGTTAGGGTTAGGG

DNA1 S1 = [ThiC6]-AAAAAAAAACCCAGGTTCTCT

DNA1 S2 = AGAGAACCTGGG

DNA2 S1 = [ThiC6]-AAAAAAAAACCACGCCGTTCAATGTCGCAGAGGGGAAGGAGGTG

DNA2 S2 = CACCTCCTTCCCCTCTGCGACATTGAACGGCGTGG

DNA3 S1 = [ThiC6]-AAAAAAAAACCTTCACGCGAACGTAATCCT

DNA3 S2 = AGGATTACGTTCGCGTGAAGG

## 6.2 Chapter 2

### 6.1.1 Materials

All solvents used were purchased form Sigma-Aldrich, Fisher Scientific, Acros Organics, and VWR with no further purification. Water used was purified to Nanopure™ standard. All glassware utilised for synthesis was oven dried before use. NMR was carried out on a Bruker 400 mHz NMR spectrometer with Bruker 9.39 T Ultrashield magnet, and 5 mm BBFO “smart” probe. Elemental analysis was obtained using a CE Instruments EA1110 elemental analyzer by the University of Birmingham analytical facilities. Mass spectra were recorded using a Waters SYNAPT G2 with an Advion TriVersa Nanomate® source nanomate delivery.

### 6.1.2 Synthesis

**Synthesis of $L_1$**

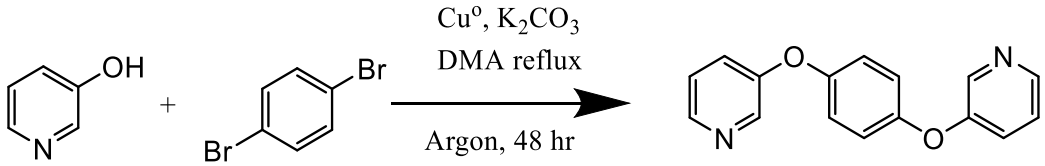


Used the same synthesis method described by Nikita Frolov *et al*.[1] 1,4-Dibromobenzene (236 mg, 1 mmol), 3-hydroxypyridine (209 mg, 2.2 mmol), potassium carbonate (607 mg, 4.4 mmol), and copper powder (279 mg, 4.4 mmol) were dissolved in dimethyl acetamide. The reaction mixture was refluxed for 48 hr under argon. After the reflux, the solvent was removed under reduced pressure and ethyl acetate (5 mL) was added. The resulting solution was refluxed for a further 1 hr before the mixture was filtered and washed through with more hot ethyl acetate. The filtrate was concentrated under reduced pressure and purified by silica column chromatography (hexane : ethyl acetate, 50:50 to 100:0). (Yield = 65 %)

$^{1}$H NMR (400 MHz, $CD_3CN$): δ 8.40-8.435 (m, 2H), 8.33 (dd, *J* = 4.0, 2.0 Hz, 2H), 7.37-7.32 (m, 4H), 7.10 (s, 4H) ppm

$^{1}$H NMR (400 MHz, $d_6$-DMSO): δ 8.42-8.38 (m, 2H), 8.36 (dd, *J* = 4.1, 1.9 Hz, 2H), 7.47-7.38 (m, 4H), 7.15 (s, 4H) ppm

$^{13}$C NMR (400 MHz, $CD_3CN$): δ 155.24, 141.71, 153.54, 145.32 ppm

**Synthesis of $Pd_2(L_1)_4(BF_4)_4$**

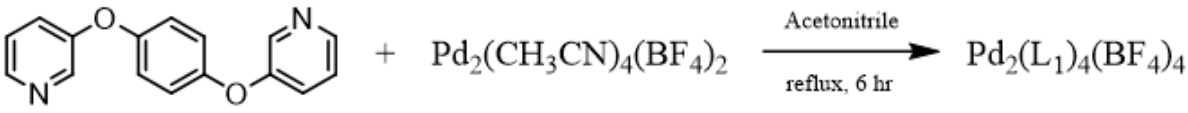


Adapted from referenced publication.[2] $L_1$ (20.1 mg, 0.076 mmol) was dissolved in acetonitrile (4 mL). $Pd(ACN)_4(BF_4)_2$ (16.8 mg, 0.038 mmol) was dissolved separately in acetonitrile (1mL) and added to the ligand solution and washed in with a further 1 mL acetonitrile. The solution was refluxed for 3 hours before removing the solvent under reduced pressure. The crude product was triturated with diethyl ether (5 mL) before being filtered and washed with more diethyl ether (20 mL). (Yield = 24 mg, 78 %)

$^{1}$H NMR (400 MHz, $CD_3CN$): δ 8.63 (dd, *J* = 5.6, 1.1 Hz, 8H), 8.57 – 8.53 (m, 8H), 7.86 – 7.79 (m, 8H), 7.65 (dd, *J* = 8.6 Hz, 5.6 Hz, 8H), 6.74 (s, 16H)

HRMS (ESI-MS) for $[Pd_2(L_1)_4(BF_4)]^{3+}$ $C_{64}H_{48}BF_4N_8O_8Pd_2$ = 452.3905 m/z, Found = 452.3930 m/z

**Synthesis of $Pt_2(L_1)_4(NO_3)_4$**

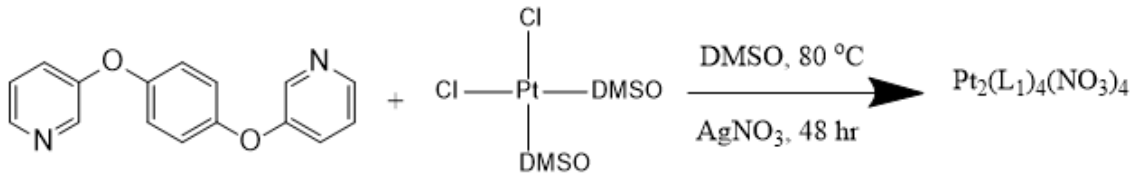


$Pt_2(DMSO)_2Cl_2$ was first prepared by dissolving $K_2Pt_2Cl_4$ (250 mg, 0.6 mmol) was dissolved in the minimum volume of water (~1.5 mL). DMSO (107 µL, 1.5 mmol) was added dropwise to the solution with stirring. The solution was stirred for a further 1 hr at room temperature in the dark. Once a off white/yellow precipitate had begun to form the flask was then placed in the fridge or 4 hours. The yellow precipitate was collected by filtration, washed with cold water, methanol, then ether and dried under vacuum.

$Pt_2(DMSO)_2Cl_2$ (40 mg, 0.095 mmol) was dissolved in DMSO (3 mL) under argon. $L_1$ (50.3 mg, 0.19 mmol) was dissolved separately in DMSO (3 mL) before being added to the Pt solution. The flask was washed with a further 3 mL DMSO to ensure maximum recovery. The reaction solution was heated to 80 °C, this temperature was maintained for 18 hr. After 18 h the solution is filtered through a syringe filter (0.2 uM, PTFE) to remove the AgCl precipitate. The DMSO was then removed by sequential washes and centrifugations with large excesses of diethyl ether (approximately 3 x 30 mL) until the product precipitated. The product was washed with a final wash of diethyl ether before being collected by filtration and dried under high vacuum. (Yield = 65 mg, 80 %)

$^{1}$H NMR (400 MHz, $d_6$-DMSO): δ 6.77 (s, 16H), 7.85 (dd, *J* = 8.6, 5.6 Hz, 4H), 8.03 (ddd, *J* = 8.6, 2.7, 1.1 Hz, 4H), 8.84 (d, *J* = 2.7 Hz, 4H), 8.89 (dd, *J* = 5.6, 1.1 Hz, 4H) ppm

$^{13}$C NMR (400 MHz, $d_6$-DMSO): δ 155.07, 151.69, 146.64 119.24, 141.31, 131.58, 128.25 ppm

HRMS (ESI-MS) for $[Pt_2(L_1)_4(NO_3)]^{3+}$ $C_{64}H_{48}N_9O_{11}Pt_2$ calculated = 502.7583 m/z, Found = 502.7674 m/z

Elemental analysis: Expected: C 45.34, H 2.85, N9.91 Measured: C 45.41, H 2.85, N9.68

### 6.2.7 Biophysical studies

Nanopure™ water was used for all work with DNA. Calf thymus sodium salt (Sigma Aldrich) was used as representative B-DNA in this work. Stock solutions were prepared by dissolving calf thymus DNA in Nanopure™ water and measuring the concentration by measuring the absorbance at 258 nm on Vary 5000 NIR spectrophotometer and using the absorption coefficient of 13,200 $mol^{-1}dm^3cm^{-1}$ to give the concentration of the solution in DNA base pairs.

**CD and LD titrations**

LD experiments were carred out on a Applied Photophysics Chirascan Plus using the LD accessory and a quartz flow cell with a pathlength of 0.5 mm. The initial sample volume started at 150 µL of a 100 µM (measured in base pairs) ct-DNA solution in Tris-HCl buffer (Tris 1mM, NaCl 20 mM, pH 7.4). A spectrum was recorded of the initial sample and each subsequent addition of relevant complex/solution with the DNA concentration being kept constant throughout the experiment. The flow cell was rotated at 40 revolutions per second. After each addition of sample, the solution was allowed to equilibrate for 3 mins before beginning measurements. Each scan was run three times to acquire an average and ensure the sample was not changing over time. CD experiments were carried out in the same way but with an initial sample volume of 1000 µL in a quartz cuvette with a 1cm path length.

**UV titrations**

The UV titration of PtCyl was carried out in the exact same way as the CD titration described above on a Varian Cary 5000 UV-Vis-NIR spectrophotometer.

**Agarose gels**

A 0.8 % agarose gel was prepared using TB buffer (Tris base 89 mM, boric acid 89 mM, pH 8.3). Agarose (3.2 g) was added to 1xTB solution (400 mL) and heated in a microwave to dissolve the agarose powder. The gel solution was poured into a gel cast, with the combs carefully inserted, and left to cool for 1

hour to ensure the gel had fully set. PBR322 plasmid concentration was determined through the use of a Shimadzu Biospec-nano. Samples were prepared to a concentration of 30 µM PBR322 (in base pairs) with varying equivalents of PtCyl in 1xTBN buffer (89 mM Tris, 89 mM boric acid, 10 mM NaCl, pH 8.4). The samples were allowed to equilibrate at room temperature for 1 hour before glycerol was added to each sample. Each well in the gel was loaded with 20 µL sample and run for 2.5 hours at 140 V. Lane 1 contained Thermo Scientific GeneRuler 1 kb DNA Ladder.

**PAGE gels**

PAGE gels were prepared using electrophoresis grade reagents. The water used was Nanopure™.

TB buffer was used for all PAGE experiments (10xTB = 890 mM Tris base, 890 mM boric acid, pH 8.3).

Oligomers used were purchased from Merck (shown 5'-3'):

The 15% polyacrylamide gel was prepared by first mixing a solution of 10xTB buffer (5 mL), water (20 mL), and 30% acrylamide/bis-arylamide 37.5:1 solution (25 mL). To this solution ammonium persulfate (10% w/v solution, 400 µL) and TEMED (40 µL) were added simultaneously. The solution was immediately mixed and pipetted into the gel cassette. The gel was left to set for 30 minutes.

Before running the gel the wells were washed out with buffer solution and the gel was pre-run for 10 minutes at 120 V.

Samples were prepared to volume of 30 µL in 1xTBN buffer (Tris base 89 mM, boric acid 89 mM, NaCl 10 mM). Each well contained 1 µM of each oligomer designated for the lane with the appropriate volume of metal complex added from stock solutions. Each sample was incubated at room temperature for 1 hour before a glycerol solution was added to increase the density of the solution (7.5 µL, 75% glycerol). The wells of the gel were then loaded with 12 µL of each sample. The gel was run at 120 V for 2.5 hours.

After the gel was run it was stained with SYBR Gold solution for 30 mintutes before imaging on an Alpha Innotech AlphaImager HP at 302 nm.

**UV stability experiments**

Stability of the palladium and platinum tetrastranded cylinder complexes were determined by monitoring their UV absorbance profiles over time. Stock solutions of the PtCyl and PdCyl were prepared (2.5 mM) in DMSO. The complexes were then diluted to a concentration of 25 µM in 1xTBN buffer (final DMSO concentration 1 %) and a UV-vis spectrum was immediately recorded on a Varien Cary 5000 UV-vis-NIR spectrometer. The absorbance was then recorded every hour for 24 hours.

## 6.3 Chapter 3

### 6.3.1 Synthesis

**Gold pillarplex (AuPill)**

Synthesis of the gold pillarplex was carried out by Alexandra A. Heidecker at Technische Universität München under the supervision of Dr Alexander Pöthig and generously supplied to the Hannon group.[3]

**Nickel parent cylinder (NiP)**

Synthesis of the Nickel parent cylinder (NiP) was carried out by James Craig (a former member of the Hannon group) following published protocols.[4]

**Nickel pyridine rotaxane (PyRot)**

Synthesis of the nickel pyridine rotaxane cylinder was carried out by Catherine Hooper (a Hannon group member) as published in literature.[4]

**Platinum tetrastranded complex (PtCyl)**

Synthesis is described in Section  of this thesis.

### 6.3.2 Biophysical studies

Nanopure™ water was used for all work with DNA. Calf thymus sodium salt (Sigma Aldrich) was used as representative B-DNA in this work. Stock solutions were prepared by dissolving calf thymus DNA in Nanopure™ water and measuring the concentration by measuring the absorbance at 258 nm on Vary 5000 NIR spectrophotometer and using the absorption coefficient of 13,200 $mol^{-1}dm^3cm^{-1}$ to give the concentration of the solution in DNA base pairs.

**Fluorescence displacement**

Fluorescence displacement experiments were adapted from the procedure reported by Chaoyang Li *et al*.[5] Fluorescence measurements were taken on a Jasco FP-8500 in a 1 cm quartz cuvette. Ethidium Bromide and DNA stock solution: 100 µM ctDNA (in base pairs), 2 mM Tris-HCl pH 7.4, 40 mM NaCl, and 50 µM Ethidium bromide. Hoechst 33258 and DNA stock solution: 100 µM ctDNA (in base pairs), 2 mM Tris-HCl pH 7.4, 40 mM NaCl, and 10 µM Hoechst 33258.

The stock solutions were diluted to a DNA concentration of 50 µM and a volume of 1 mL. The fluoresce of this sample was then recorded before aliquots of the relevant metal complex and an equal volume of the stock solution were added to the working solution. The solution was allowed to equilibrate with gentle stirring for 5 minutes before acquiring the fluorescence measurement. Each measurement was taken three times to ensure the fluorescence intensity of the sample was not changing over time.

Parameters for Ethidium bromide fluorescence displacement: $\lambda_{exc}$ = 500 nm, $\lambda_{em}$ = 520 – 750 nm, Data interval = 1 nm, Sensitivity = High, Excitation bandwidth = 2.5 nm.

Parameters for Hoechst 33258 fluorescence displacement: $\lambda_{exc}$ = 350 nm, $\lambda_{em}$ = 400 – 650 nm, Data interval = 1 nm, Sensitivity = Medium, Excitation bandwidth = 2.5 nm.

**UV melting**

UV melting studies were carried out on a Varien Cary 5000 UV-vis-NIR spectrometer with a sample changer and temperature controller. The stability of the DNA structures with or without metal complexes was determined by monitoring the absorbance at 260 nm (bandwidth, 1 nm, average time 15 s, heating rate 1.0 $^{o}Cmin^{-1}$, measurement interval 0.5 $^{o}C$) with increasing temperature. Quartz cuvettes with a 1 cm path length were used for all measurements. For all samples, the DNA was annealed by heating to 95 $^{o}C$ for 5 minutes and allowing to cool slowly before being kept in the fridge until required. Samples were then prepared to a total volume of 1 mL with cacodylate buffer (10 mM cacodylate, NaCl 100 mM, pH 7.4) with a DNA concentration of 1 µM or 2 µM depending on the number of bases in the structure. The samples were heated from 15 – 95 $^{o}C$ and the melting temperature ($T_m$) was calculated using the thermal heating programs in-built smoothing function and first derivative

calculation (the change in UV absorbance was plotted against the temperature in order to determine when the greatest change in absorbance occurred, this was said to be the $T_m$). Each condition was run in triplicate with the reported $T_m$ an average of the three individual runs.

**FRET melting**

FRET melting studies were carried out using a FRET tagged DNA 3WJT6 structure on a BioRad MyIQ instrument.

All samples were prepared and run in triplicate to obtain an average. 3WJT6 oligomer stock solution was prepared in buffer and annealed at 95 $^oC$ before addition of the metal complexes. Each sample was prepared in a 100 µL clear PCR tubes to a final volume of 20 µL. Each sample contained 3WJT6 (1 µM) in sodium cacodylate buffer (10 mM sodium cacodylate, 100 mM NaCl, pH 7.4) with the stated concentration of metal complex added. Samples were left at room temperature for 1 hour in the dark to equilibrate before carrying out the melting. The temperature was ramped from 15 – 95 $^oC$ at a rate of 1.0 $^oC\ min^{-1}$ with fluorescence measured at 0.5 $^oC$ temperature increments. Samples were excited at 480 nm with a bandwidth of 40 nm, and the emission was measured at 540 nm with a bandwidth of 50 nm. Melting temperature were determined by plotting the differential to determine when the maximum change in fluorescence intensity was occurring. The change in fluorescence intensity was plotted against the temperature in order to determine when the greatest change in fluorescence occurred, this was said to be the $T_m$.

**PAGE gels**

The 15% polyacrylamide gel was prepared by first mixing a solution of 10xTB buffer (5 mL), water (20 mL), and 30% acrylamide/bis-arylamide 37.5:1 solution (25 mL). To this solution ammonium persulfate (10% w/v solution, 400 µL) and TEMED (40 µL) were added simultaneously. The solution is immediately mixed and pippeted into the cast for the gel. The gel was left to set for 30 minutes.

Before running the gel the wells were washed out with buffer solution and the gel was pre-run for 10 minutes at 120 V.

Samples were prepared to volume of 30 µL in 1xTBN buffer (Tris base 89 mM, boric acid 89 mM, NaCl 10 mM). Each well contained 1 µM of each oligomer designated for the lane with the appropriate volume of metal complex added from stock solutions. Each sample was incubated at room temperature for 1 hour before a glycerol solution was added to increase the density of the solution (7.5 µL, 75% glycerol). The wells of the gel were then loaded with 12 µL of each sample. The gel was run at 120 V for 2.5 hours.

After the gel was run it was stained with SYBR Gold solution for 30 mintutes before imaging on an Alpha Innotech AlphaImager HP at 302 nm.

**Fluorescent competition PAGE**

The PAGE gels were prepared in the same way as the PAGE gels described above.

Samples were prepared up to 30 uL with 1µM of S1-FAM, S2, and S3, and either 0, 0.5, 1, 2, or 4 equivalents of the competition strands followed by 1 equivalent of metal complex all in 1xTBN (89 mM Tris, 89 mM Boric acid, 10 mM NaCl, pH 8.3). The samples were incubated at room temperature for 1 hr before 7.5 uL of 50% glycerol solution was added to each solution. Sample aliquots of 12 µL were then loaded into the appropriate wells in the gel which was run for 1 hr at 120V in 1xTB buffer. The gel was imaged on a Innotech AlphaImager (the gel was subsequently stained SYBRTM Gold Nucleic Acid Gel Stain (Thermofisher scientific) in 1xTB buffer for 30 minutes and imaged again to confirm the presence of the expected structures).

ImageJ was used to quantify the intensity of the 3WJ-FAM bands formed. The band intensities of 3WJ-FAM formed with a metal complex and competitors were compared to the intensity of the 3WJ-FAM band formed with the same metal complex and **No** competitors to give a relative intensity. All experiments were undertaken as at least triplicate repeats.

**G-quadruplex PAGE gels**

PAGE gels of the G-quadruplex were carried out in the same way as the regular PAGE gels in 1xTB but with the addition of 100 mM KCl. The htelo sequence was annealed in prior to preparation of the

samples. A 22mer oligo was used as a control to ensure the htelo sequence had folded to form the g-quadruplex. Due to the higher ionic strength of the buffer the gel was also cooled with ice water throughout the 2.5 hour run time.

**Mass spectrometry**

DNA samples (10 µL total volume) were prepared at a concentration of 50 µM DNA (2.5 µL, 200 µM) structure in ammonium acetate buffer 10 mM, pH 7.0 (2 µL, 50 mM) with water (5.5 µL ). Samples were then allowed to equilibrate for 1 hour at room temperature (20 °C). Samples with the addition of metal complexes were prepared in the same way using 1 mM stock solutions of the metal complexes and reducing the volume of water added. The solutions were then diluted to 10% MeOH immediately before running on the mass spectrometer in order to achieve a stable spray for the MS measurement. All mass spectrometry was carried out on a Waters SYNAPT G2 with an Advion TriVersa Nanomate® source. Injection method used gas pressure 0.7 psi, Voltage 2.2 kV, source temperature 70 °C, and a cone voltage 80 V. The mass was scanned from 100 – 2400 m/z. Data was processed using UniDec software.[6]

**Isothermal Calorimetry (ITC)**

ITC was carried out on a Malvern Microcal PEAQ-ITC instrument. Before using the instrument, a blank was always run of a water titration into water. All ITC measreuments were carried out in sodium cacodylate buffer (sodium cacodylate 10 mM, NaCl 100 mM, pH 7.4). Stock solutions of the metal complexes in buffer were prepared at a concentration of 150 µM.

A DNA stock solution of 3WJT6 was annealed at 95 °C for 5 minutes then allowed to cool slowly. The DNA solution was then diluted to 10 µM an placed into the cell. The metal complex solution was loaded into the syringe and titrated into the cell. Each titration was repeated 3 times to ensure reproducible results. Controls were also carried out where the metal complex was titrated into buffer and where buffer was titrated into the 3WJT6 solution.

It should be noted that the platinum complex required 0.5 % acetonitrile to fully dissolve.

## 6.4 Chapter 4

### 7.4.1 Materials

Dynamic light scattering measurements were carried out on a Malvern Zetasizer Nano ZSP. Measurements of nanoparticle sizes were carried out in water/buffer/media as stated in experiment at an approximate concentration of 1 nM calculated from the UV-vis spectra and the known approximate diameter of the particles synthesised. Each measurement is the average of 5 separate runs.

HPLC purified DNA oligomers were purchased from Merck as dry solids. The oligomers were dissolved in Nanopure™ water to a stock concentration of 200 µM which was kept frozen at -20 $^{o}$C when not in use.

The thiol-modified oligomers are produced as a disulfide to avoid spontaneous oxidation of the thiols and dimer formation of the oligomers which would render them useless. The disulfide was reduced using tris(2-Carboxyethyl)phosphine HCl (TCEP) immediately prior to use.

### 6.4.2 Synthesis

**Gold nanoparticles (AuNP13)**

Method adapted from literature.[7] An aqueous solution of sodium citrate dihydrate (63.7 mg, 0.217 mmol), citric acid (17.3 mg, 0.090 mmol), and EDTA (0.88 mg, 0.003 mmol) with a volume of 150 mL was brought to a vigorous reflux and left for 15 minutes. A solution of $HauCl_4.3H_2O$ (9.8 mg, 0.024 mmol) in water (1 mL) was rapidly injected into the centre of the vortex. The solution was refluxed for a further 15 minutes before removing the heat source and allowing the solution to cool to room temperature. The final solution was a bright red wine colour.

SPR UV absorption = 518.5 nm

DLS diameter by Intensity = 18.77 nm (PDI = 0.113)

TEM diameter = 13.5 $\pm$ 0.9 nm

**First attempt at functionalisation of AuNP13 with DNA**

This functionalisation of gold nanoparticles was adapted from the publication by Xu Zhang *et al*.[8]

TCEP (1 µL, 10 mM) and water (2.75 µL) were added to DNA1 S1 (75 µL, 105 µM) and left at room temperature in the dark for 2 hours.

The activated DNA1 S1 (52.8 µL, 54 µM) was added to AuNP13 (10 nM, 2.4 mL) with stirring. Citrate buffer (48 µL, 500 mM, pH 3) is immediately added after the DNA solution and the solution is stirred for 30 min in the dark at room temperature. Sodium chloride solution (1080 µL, 1M) was then added dropwise to the solution with stirring over a 30 min period. The whole solution was stirred at room temperature in the dark for a further 30 min. The excess salt solution and DNA was removed by centrifugation. The particle concentration was adjusted to 6.7 nM with a final buffer concentration of HEPES 5mM, NaCl 300 mM. DNA S2 (30 µL, 100 µM) was added and the solution was incubated for 1 hour before centrifugation to remove excess DNA S2.

It was estimated that the coating of dsDNA on the particles based on literature should be roughly 120 dsDNA oligomers per particle. Nickel parent cylinder (1 µL, 1000 µM) was added to AuNP13dsDNA (400 µL, 6.7 nM) giving a ratio of 3 metal complexes per particle. A second solution was prepared with a ratio of 15 metal complexes per particle.

**Coating of AuNP13 with ssDNA and dsDNA**

Synthesis of DNA coated gold nanoparticles by salt aging was adapted from Hurst *et al*.[9]

*Preparation of dsDNA1/2/3:*

TCEP (20 µL, 100 mM) was added to a solution of S1 (100 µL, 200 µM) and left at room temperature for 2 hours. This activated oligomer was then utilised without further purification. S2 (100 µL, 200 µM) was added to the S1 solution along with buffer (5xTBN 27.5 µL, pH 8.3) and incubated at 37 $^{o}$C for 1 hour.

*Preparation of dsDNA1/3 + metal complex:*

Metal complex solution (15 µL, 1000 µM) was added to dsDNA1/3 (68.75 µL, 72.7 µM) with water (35 µL) and incubated at 37 $^{o}$C for 1 hour.

*Preparation of dsDNA2 + metal complex:*

Metal complex solution (50 µL, 1000 µM) was added to dsDNA2 (68.75 µL, 72.7 µM) and incubated at 37 °C for 1 hour.

*Preparation of ssDNA1/2/3:*

ssDNA solutions were prepared in the same way as the dsDNA but with water added instead of S2 and metal complex where appropriate to keep concentrations the same for all of the solutions.

The final concentration of each solution described above = 42.1 µM

Each of the DNA solutions described above (56.4 µL, 42.1 µM) was added to AuNP13 (1 mL, 10nM) with water (43.6 µL) in 2 mL eppendorfs. The solutions were left to incubate at room temperature for 18 hours. PBS buffer was added to the solution to give a final concentration of 10 mM pH 7.2. The salt concentration of the solutions was then gradually increased to 0.3 M, by the addition of aliquots of a 1M stock solution of NaCl every hour, over a period of 8 hours. The particles were purified by centrifugation (2 x 20min x 10G) where the supernatant is removed after each centrifugation and replaced with water. The particles are then transferred into Vivaspin 500 centrifugal concentrators and washed with three volumes of water before being concentrated to 25 nM (0.4 mL). Prepared particles were stored at 4 °C until needed.

### 6.4.3 PAGE gels

PAGE gels were prepared using electrophoresis grade reagents. The water used was Nanopure™ (18.2 MΩ).

TB buffer was used for all PAGE experiments (10xTB = 890 mM Tris base, 890 mM boric acid, pH 8.3).

Oligomers used were purchased from Merck (shown 5'-3'):

**Preparation of PAGE gels**

The 15% polyacrylamide gel was prepared by first mixing a solution of 10xTB buffer (5 mL), water (20 mL), and 30% acrylamide/bis-arylamide 37.5:1 solution (25 mL). To this solution ammonium persulfate (10% w/v solution, 400 µL) and TEMED (40 µL) were added simultaneously. The solution is immediately mixed and pippeted into the cast for the gel. The gel was left to set for 30 minutes.

Before running the gel the wells were washed out with buffer solution and the gel was pre-run for 10 minutes at 120 V.

Samples were prepared to volume of 30 µL in 1xTBN buffer (Tris base 89 mM, boric acid 89 mM, NaCl 10 mM). Each well contained 1 µM of each oligomer designated for the lane with the appropriate volume of metal complex added from stock solutions. Each sample was incubated at room temperature for 1 hour before a glycerol solution was added to increase the density of the solution (7.5 µL, 75% glycerol). The wells of the gel were then loaded with 12 µL of each sample. The gel was run at 120 V for 2.5 hours.

After the gel was run it was stained with SYBR Gold solution for 30 mintutes before imaging on an Alpha Innotech AlphaImager HP at 302 nm.

**PAGE gel for measuring the release of metal complexes from AuNP13dsDNA**

Samples were prepared to volume of 30 µL in 1xTBN buffer (Tris base 89 mM, boric acid 89 mM, NaCl 10 mM). Each well contained 1 µM of each oligomer designated for the lane with the appropriate volume of metal complex or particle solution added from stocks. Each sample was incubated at room temperature for 1 hour before a glycerol solution was added to increase the density of the solution (7.5 µL, 75% glycerol). The wells of the gel were then loaded with 12 µL of each sample. The gel was run at 120 V for 2.5 hours.

Lane 18 was prepared by mixing the appropriate volume of buffer and 3WJ oligomer stocks with the water replaced by the final wash solution of the particles in question.

After the gel was run it was stained with SYBR Gold solution for 30 mintutes before imaging on an Alpha Innotech AlphaImager HP.

### 6.4.4 Agarose gels

**Agarose gel of particles coated with DNA and metal complexes**

A 0.8% agarose gel was prepared using TB buffer (Tris base 89 mM, boric acid 89 mM, pH 8.3). Agarose (3.2 g) was added to 1xTB solution (400 mL) and heated in a microwave to dissolve the agarose powder.

The gel solution was poured into a gel cast, with the combs carefully inserted, and left to cool for 1 hour to ensure the gel had fully set.

Particle solutions were prepared by diluting 25 nM stock solutions to 10 nM with a volume of 50 µL. (10xTB 5 µL, water 20 µL, and particle stock solution 20 µL). To each sample 7.5 µL of 75% glycerol solution was added to increase the density. The gel was submerged in 1xTB buffer solution and each well was loaded with 30 µL of sample solution. The gel was run at 140 V for 2 hours. The gel was then removed and imaged on a Alpha Innotech AlphaImager HP imager where negative contrast indicates the presence of the gold nanoparticles due to their high UV absorbance.

**Agarose gel of functionalised particles with 3WJ18**

The gel used for this experiment was prepared in the same way described above but using 6 g Agarose powder to create a 1.5% agarose gel.

Particle solutions were prepared by diluting 25 nM stock solutions. Each solution was prepared by addition of 40 µL of particle stock solution with 5 µL of 10xTB and either water (5 µL) or 3WJ18 stock (5 µL, 50 µM). The solutions were then incubated at room temperature for 1 hour before addition of glycerol solution (7.5 µL, 75% solution). The samples were then loaded into the wells of the gel (30 µL per well). The gel was run for 6 hours at 50 V.

The gel was stained with SYBR Gold staining solution and imaged using a Alpha Innotech AlphaImager HP imager at 365 nm.

### 6.4.4 ICP-MS

All samples were run on a Perkin Elmer Nexion 300X. TraceSELECT™ water was used for all ICP-MS solutions. Ultra pure nitric and hydrochloric acids, and polypropylene tubes were used for sample preparation.

Stock solutions containing platinum, gold, and nickel were prepared by diluting standard solutions of 1 g/L to a range of 0.1 – 2500 ppb in 4% nitric acid. The gold particle concentrations were approximated using the particle size by DLS and UV absorbance at 450 nm to make 25 nM stock solutions. The

solutions were diluted to 1.6 nM, 8 nM, and 16 nM to a volume of 150 uL with 4% nitric acid. The minimum volume of aqua regia possible was added in aliquots until the solutions went clear (indicating all particles had been dissolved). The concentrated solutions were then diluted 1 in 100 with 4% nitric acid to make the final 4 mL solutions. Each sample was run in triplicate.

### 6.4.5 TEM

TEM samples were prepared by diluting the particle samples to 1 nM and then pipetting 2 µL of that sample onto a copper on carbon 400 mesh copper on carbon TEM grid. The grids were left to air dry at room temperature for at least 24 hours prior to imaging. The imaging was carried out on a Jeol 1400 Bio TEM.

Uranyl acetate staining was carried out by Theresa Morris, Electron Microscope Applications Technician, School of Metallurgy and Materials, University of Birmingham.

### 6.4.6 Cell studies

Cell studies were carried out with Dr Nik Hodges, School of Biosciences, University of Birmingham.

MDA-MB-231 cell line was used for all cell studies which was purchased from European Collection of Authenticated Cell Cultures. Cells were grown in $T_{75}$ cell culture flasks in DMEM supplemented with foetal bovine serum (10 % w/v), penicillin (100 U/mL), streptomycin (100 mg/mL), and L-glutamine (2mM). The cells were maintained int a 5% $CO_2$ humidifier at 37 $^{o}$C. Cell cultures were discarded after 20 passages.

**MTT assay**

Cells were seeded to a density of 6,500 cells per well in a 96 well plate where varying concentration of nanoparticles were added. The cells were incubated for a further 24 hours before removing the media, washing with PBS solution and adding MTT in media at a concentration of 0.5 mg/mL. The cells were incubated for a further 3 hours. The media was removed before addition of DMSO (200 µL) to solubalise the formazan crystals. The absorbance of each well was recorded at 490 nm on a Tecan Infinite F200 Pro.

**Cell fractionation**

Adapted from Green *et al*.[10] MDA-MB-231 cells were to a density of $6x10^5$ cells/flask in $T_{75}$ cell culture flasks. The cells were grown to confluence in 15 mL media which was changed as required. Once confluent the cells were treated with nanoparticles to a concentration of 5 nM. After 24 hours the cell media was removed, the cells were washed with PBS, and the cell pellet was collected by trypsinisation. The cells were resuspended in a homogenization buffer (500 µL, 250 mM sucrose, 1mM $Na_2EDTA$, 10 mM triethanolamine, pH 7.8) and incubated on ice for 30 minutes. After incubation the cell membranes were disrupted by vigorous pipetting with a 1 mL pipette. The solution was then centrifuged 400 rpm for 10 min at 4 $^oC$ to collect the nuclear fraction. The supernatant was carefully pipetted off and collected as the cytosolic fraction. The fractions were kept frozen at -80 $^oC$ until preparing for ICPMS (see section 7.4.4).

## 6.5 References


1. Frolov, N. A.; Fedoseeva, K. A.; Hansford, K. A.; Vereshchagin, A. N., Novel Phenyl-Based Bis-quaternary Ammonium Compounds as Broad-Spectrum Biocides. *ChemMedChem* **2021,** *16* (19), 2954-2959.
2. McMorran, D. A.; Steel, P. J., The First Coordinatively Saturated, Quadruply Stranded Helicate and Its Encapsulation of a Hexafluorophosphate Anion. *Angewandte Chemie International Edition* **1998,** *37* (23), 3295-3297.
3. Altmann, P. J.; Pöthig, A., Pillarplexes: A Metal–Organic Class of Supramolecular Hosts. *Journal of the American Chemical Society* **2016,** *138* (40), 13171-13174.
4. Hooper, C. A. J.; Cardo, L.; Craig, J. S.; Melidis, L.; Garai, A.; Egan, R. T.; Sadovnikova, V.; Burkert, F.; Male, L.; Hodges, N. J.; Browning, D. F.; Rosas, R.; Liu, F.; Rocha, F. V.; Lima, M. A.; Liu, S.; Bardelang, D.; Hannon, M. J., Rotaxanating Metallo-supramolecular Nano-cylinder Helicates to Switch DNA Junction Binding. *Journal of the American Chemical Society* **2020,** *142* (49), 20651-20660.
5. Li, C.; Xu, F.; Zhao, Y.; Zheng, W.; Zeng, W.; Luo, Q.; Wang, Z.; Wu, K.; Du, J.; Wang, F., Platinum(II) Terpyridine Anticancer Complexes Possessing Multiple Mode of DNA Interaction and EGFR Inhibiting Activity. *Frontiers in Chemistry* **2020,** *8*.
6. Marty, M. T.; Baldwin, A. J.; Marklund, E. G.; Hochberg, G. K. A.; Benesch, J. L. P.; Robinson, C. V., Bayesian Deconvolution of Mass and Ion Mobility Spectra: From Binary Interactions to Polydisperse Ensembles. *Analytical Chemistry* **2015,** *87* (8), 4370-4376.
7. Schulz, F.; Homolka, T.; Bastús, N. G.; Puntes, V.; Weller, H.; Vossmeyer, T., Little Adjustments Significantly Improve the Turkevich Synthesis of Gold Nanoparticles. *Langmuir* **2014,** *30* (35), 10779-10784.
8. Zhang, X.; Servos, M. R.; Liu, J., Instantaneous and Quantitative Functionalization of Gold Nanoparticles with Thiolated DNA Using a pH-Assisted and Surfactant-Free Route. *Journal of the American Chemical Society* **2012,** *134* (17), 7266-7269.
9. Hurst, S. J.; Lytton-Jean, A. K. R.; Mirkin, C. A., Maximizing DNA Loading on a Range of Gold Nanoparticle Sizes. *Analytical Chemistry* **2006,** *78* (24), 8313-8318.
10. M.Green, R.; Graham, M.; R.O'Donovan, M.; Chipman, J. K.; J.Hodges, N., Subcellular compartmentalization of glutathione: Correlations with parameters of oxidative stress related to genotoxicity. *Mutagenesis* **2006,** *21* (6), 383-390.

# Appendix

## Appendix - Chapter 2

### A2.1 NMR of $L_1$

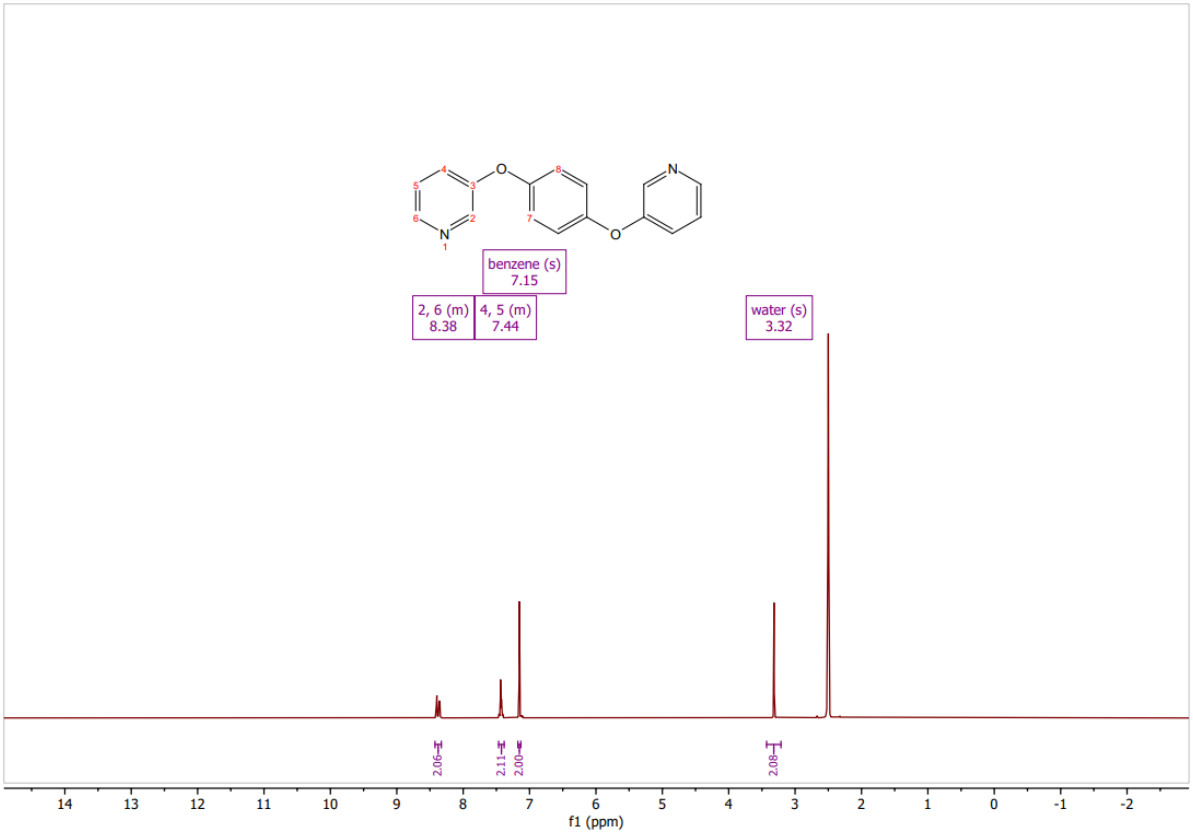


$^1$H NMR (400 MHz, $d_6$-DMSO, 298 K) of $L_1$.


$^1$H NMR (400 MHz, $d_6$-DMSO, 298 K) of $L_1$ (zoom).

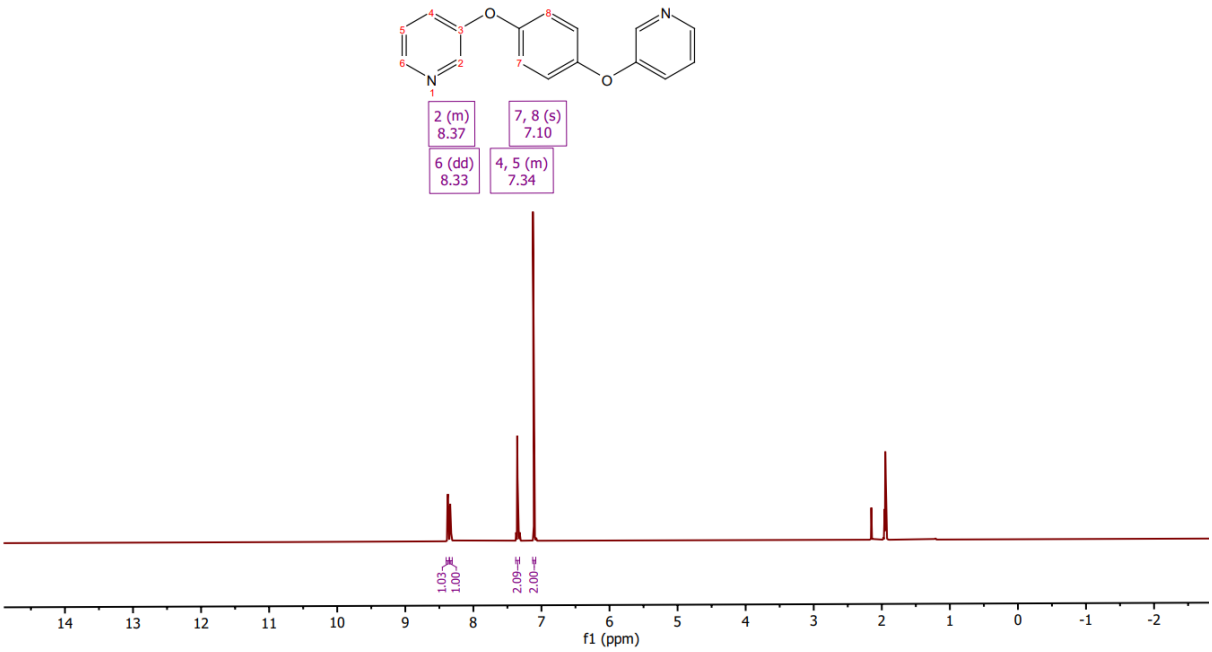


$^1$H NMR (400 MHz, $CD_3CN$, 298 K) of $L_1$.

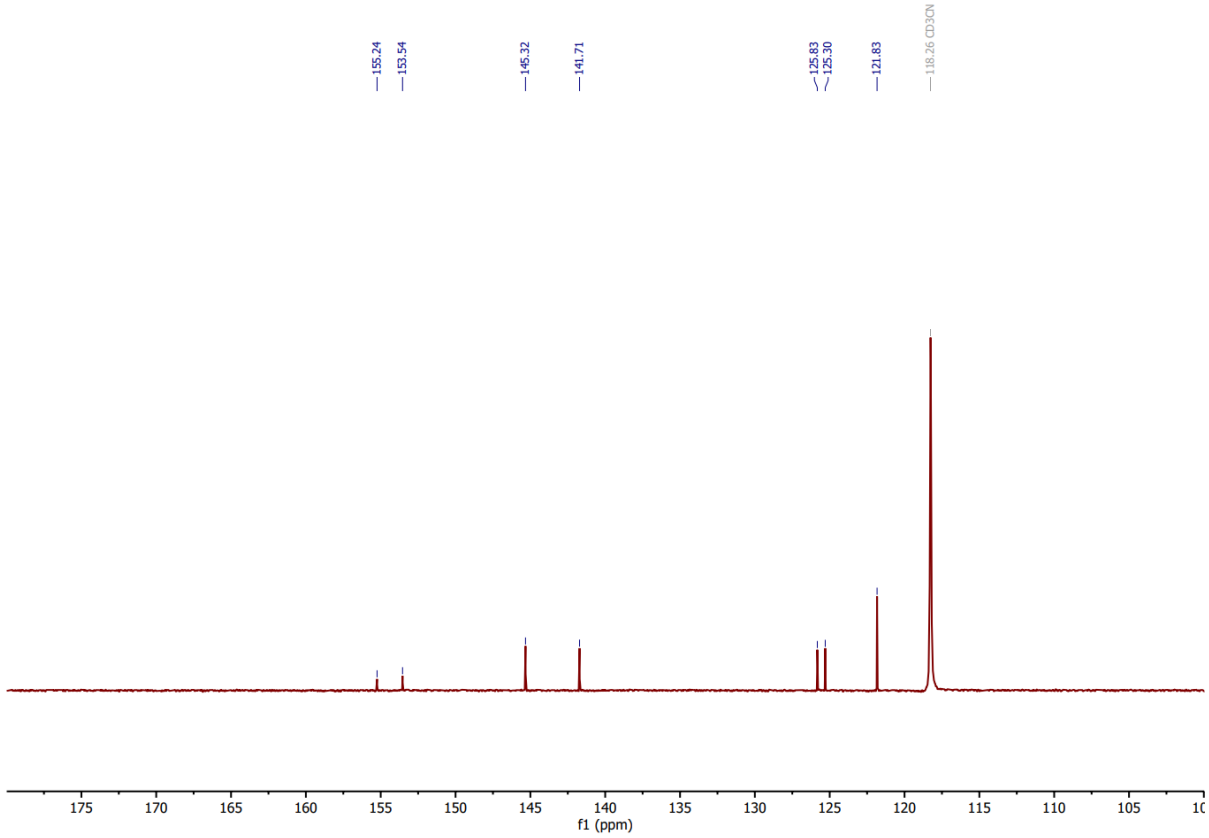


$^{13}$CNMR (400 MHz, $CD_3CN$, 298 K) of $L_1$.

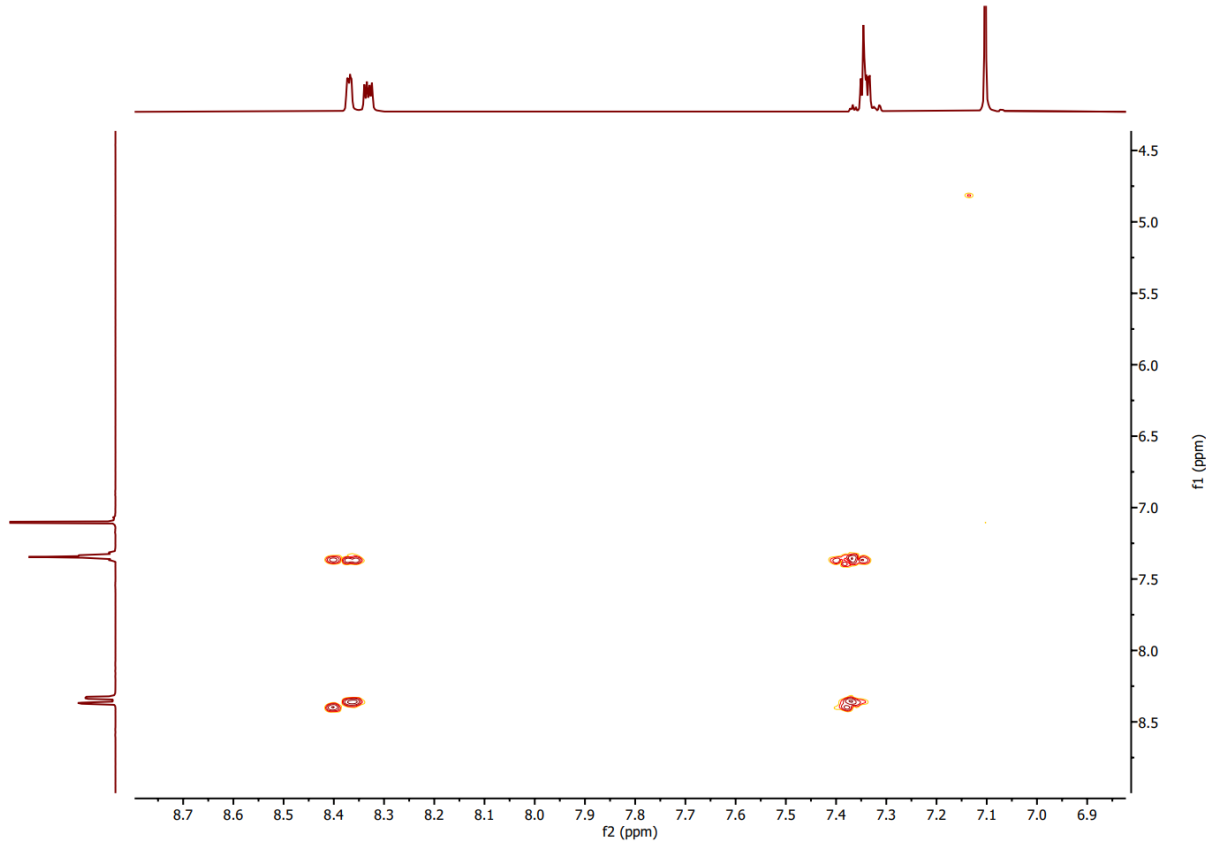


COSY NMR (400 MHz, $CD_3CN$, 298 K) of $L_1$.

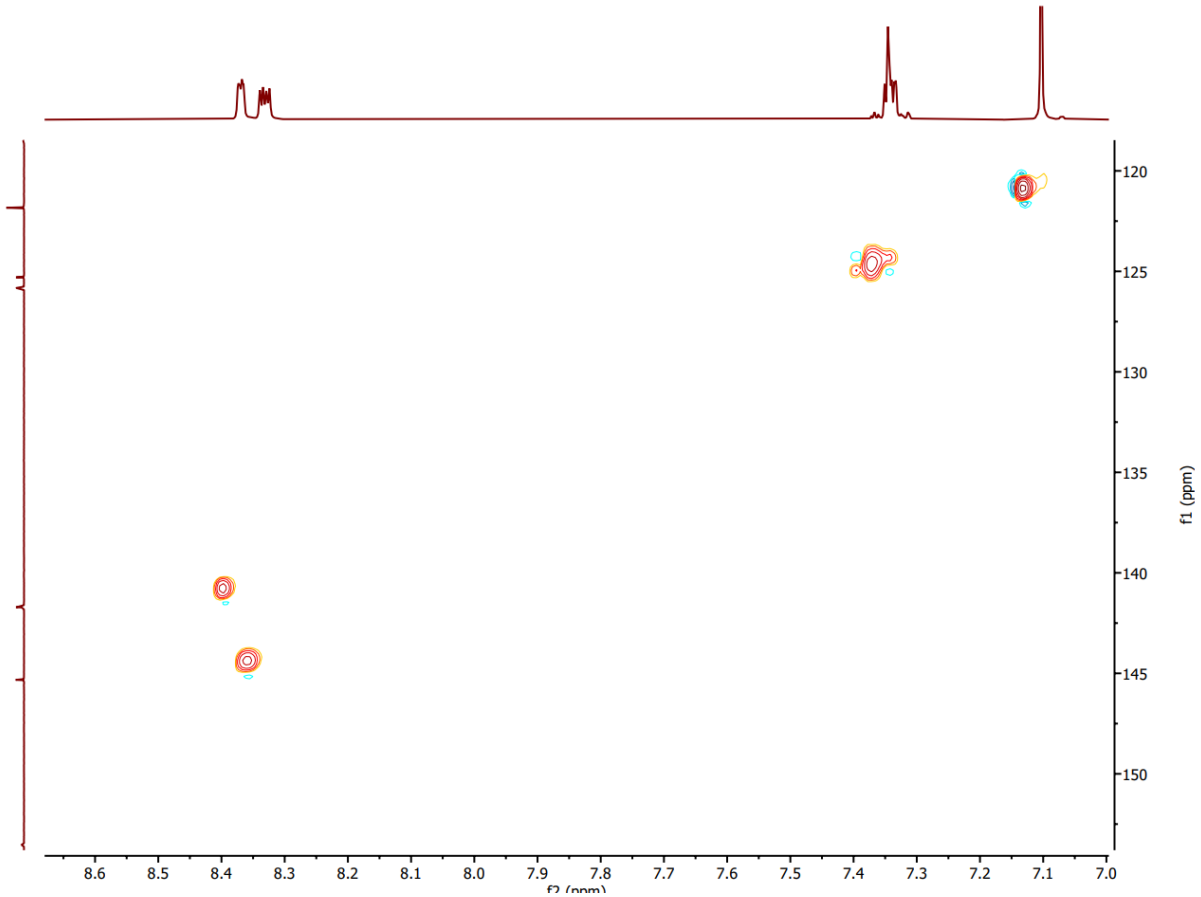


HSQC NMR (400 MHz, $CD_3CN$, 298 K) of $L_1$.

## A2.2 NMR of $Pd_2(L_1)_4(BF_4)_4$

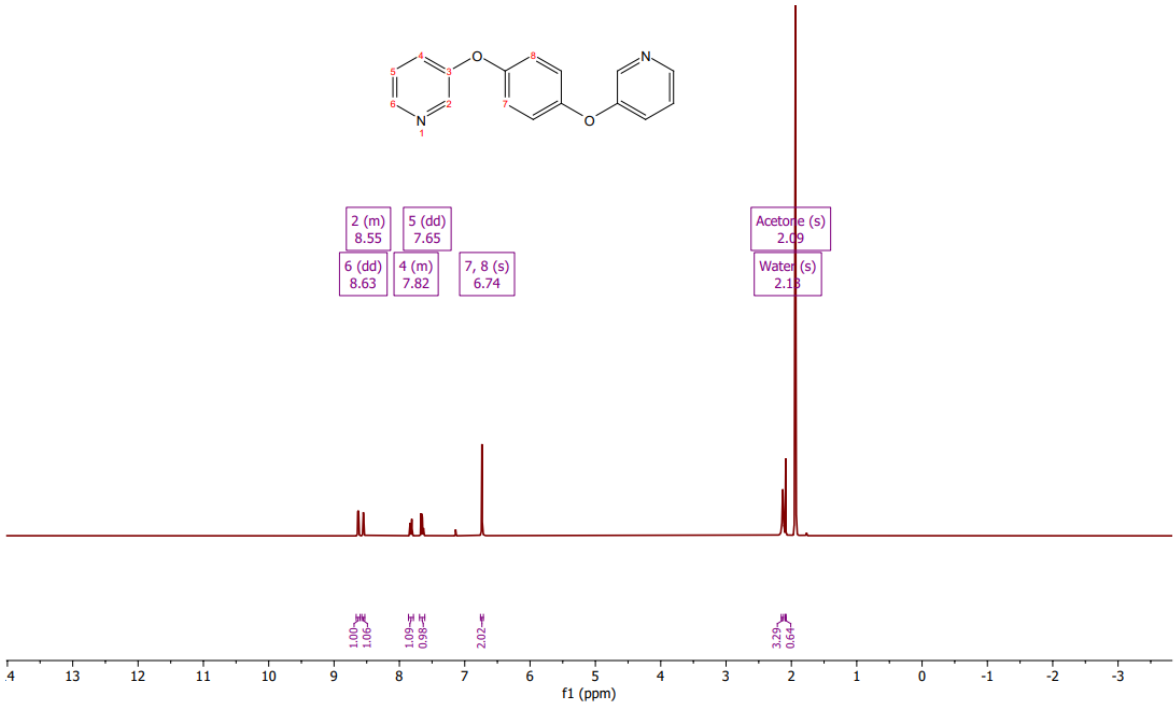


$^1H$ NMR (400 MHz, $CD_3CN$, 298 K) of $Pd_2(L_1)_4(BF_4)_4$.

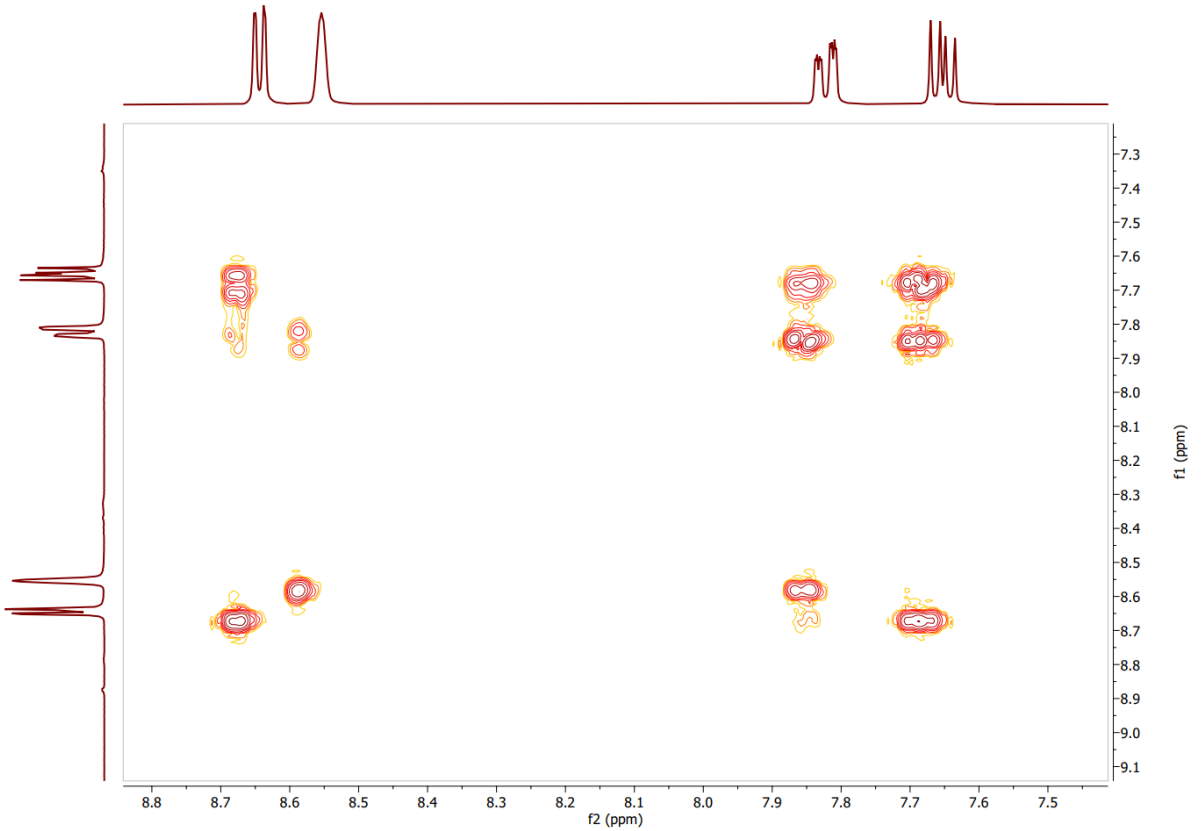


COSY NMR (400 MHz, $CD_3CN$, 298 K) of $Pd_2(L_1)_4(BF_4)_4$.

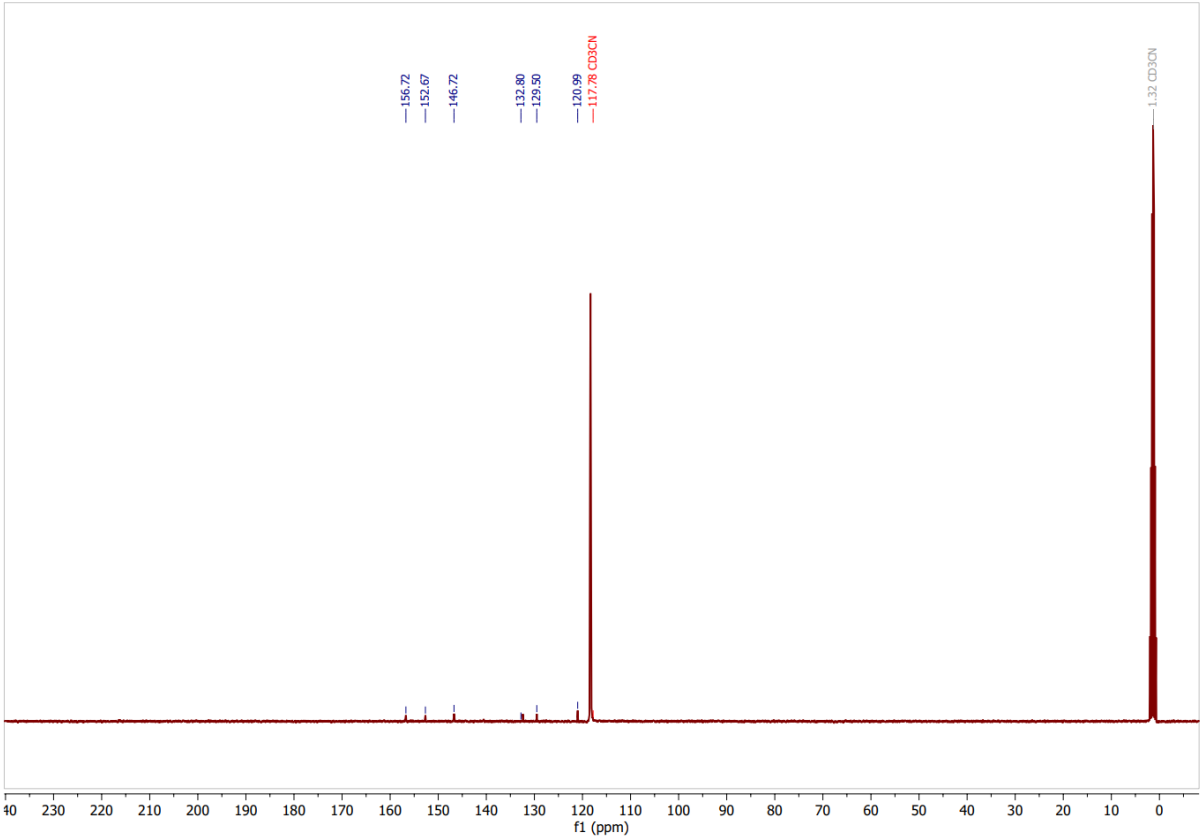


$^{13}C$ NMR (400 MHz, $CD_3CN$, 298 K) of $Pd_2(L_1)_4(BF_4)_4$.

## A2.3 NMR of $Pt_2(L_1)_4(NO_3)_4$


$^{1}$H NMR (400 MHz, $d_6$-DMSO, 298 K) of $Pt_2(L_1)_4(NO_3)_4$.

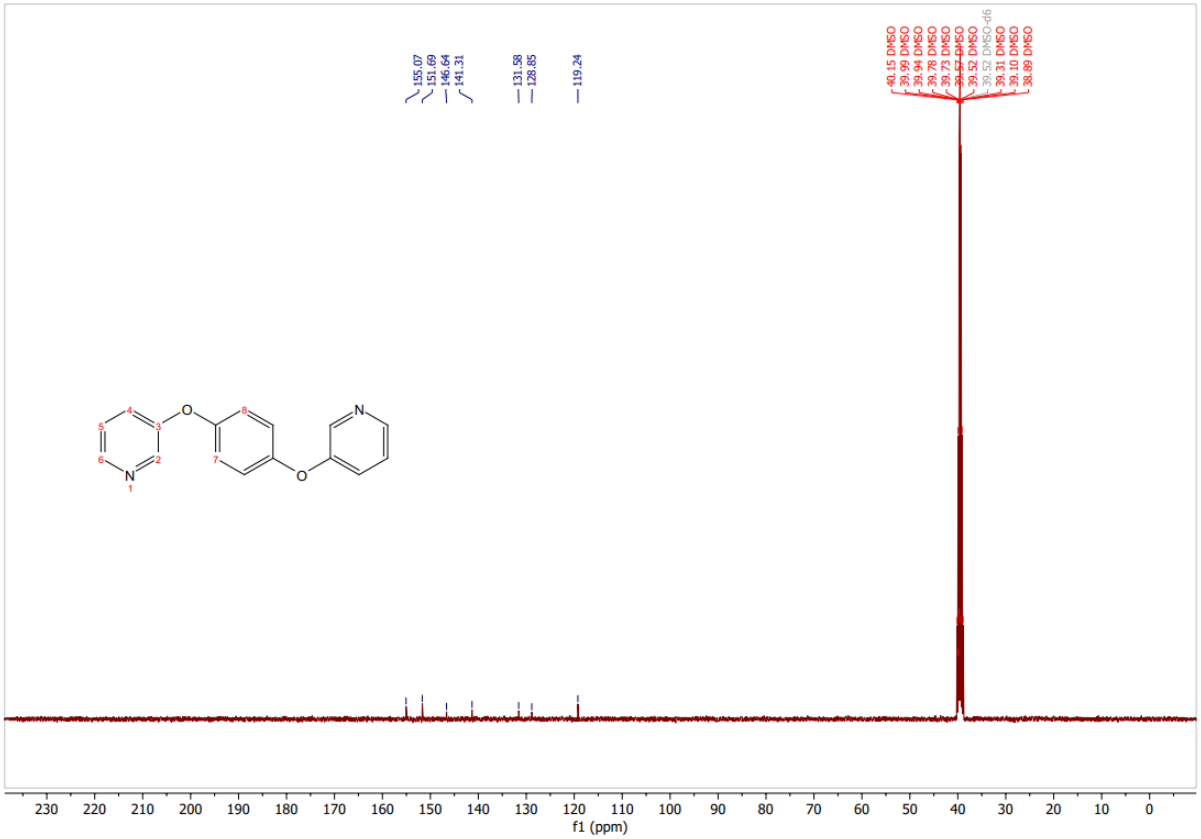


$^{13}$CNMR (400 MHz, $d_6$-DMSO, 298 K) of $Pt_2(L_1)_4(NO_3)_4$.

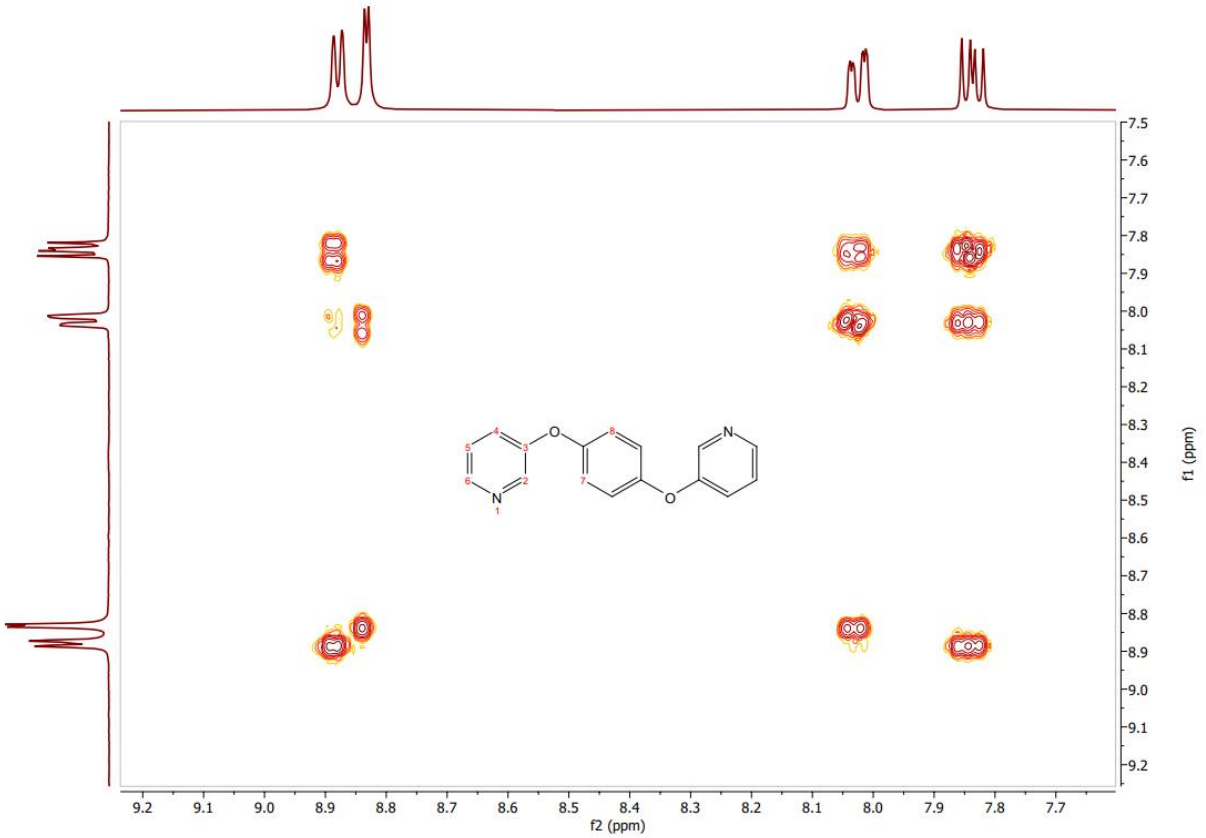


COSY (400 MHz, $d_6$-DMSO, 298 K) NMR of $Pt_2(L_1)_4(NO_3)_4$.

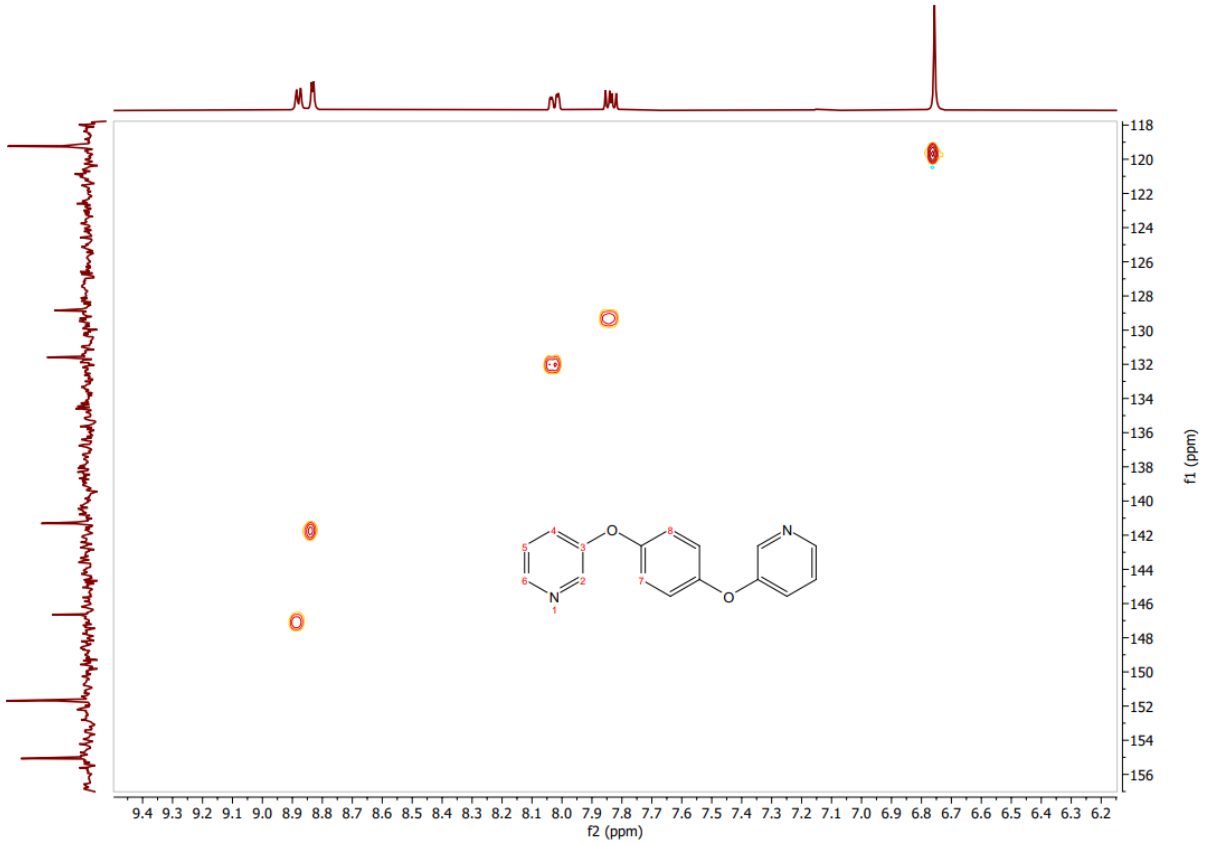


HSQC (400 MHz, $d_6$-DMSO, 298 K) NMR of $Pt_2(L_1)_4(NO_3)_4$ in DMSO.

## A2.4 Full CD titrations of $Pt_2(L_1)_4(NO_3)_4$ and $Pd_2(L_1)_4(BF_4)_4$ with ctDNA

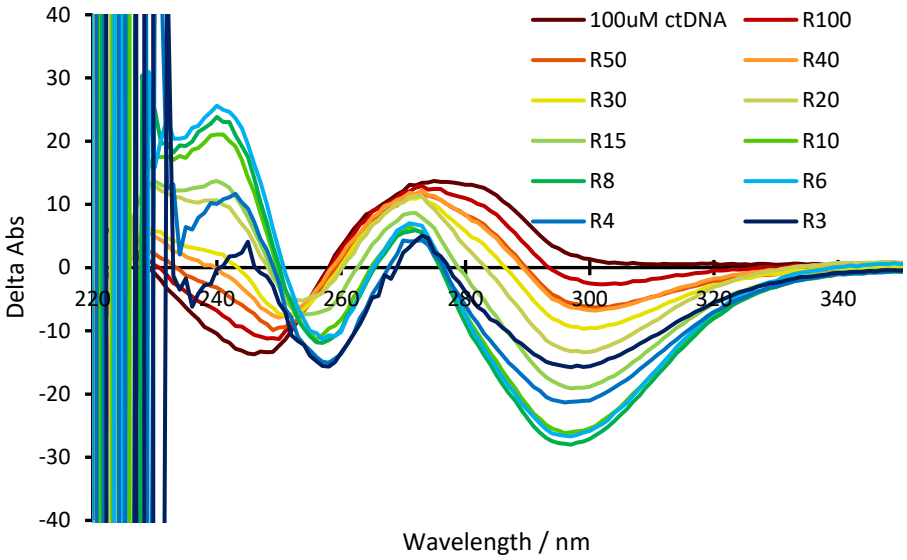


Circular dichroism of 100 µM ct-DNA in 1 mM Tris-HCl buffer pH 7.4, 20 mM NaCl with increasing concentration of $Pd_2(L_1)_4(BF_4)_4$ where RX = [DNA base pairs]:[Pd helicate].

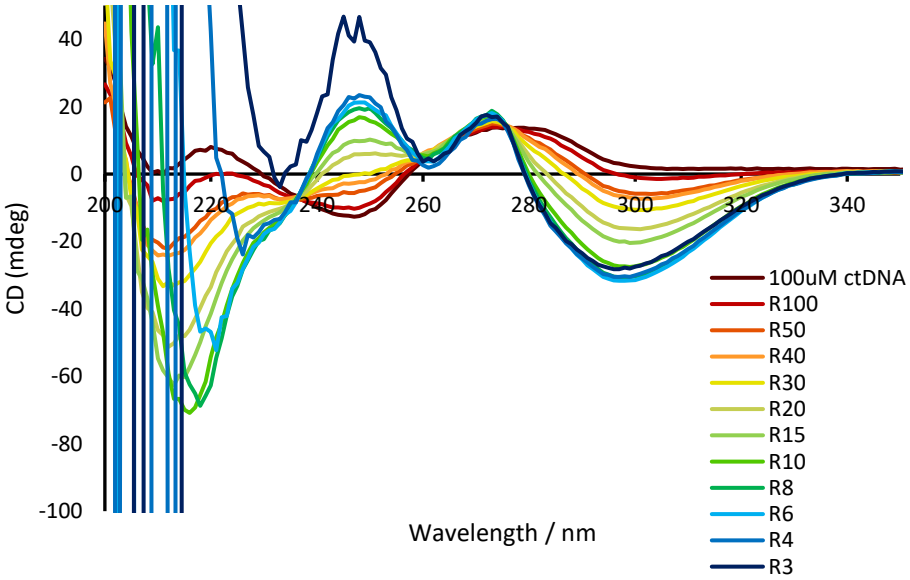


Circular dichroism of 100 µM ct-DNA in 1 mM Tris-HCl buffer pH 7.4, 20 mM NaCl with increasing concentration of $Pt2(L_1)_4(NO_3)_4$ where RX = [DNA base pairs]:[Pt helicate].

# Appendix - Chapter 3

## A3.1 Testing metal complex fluorescence

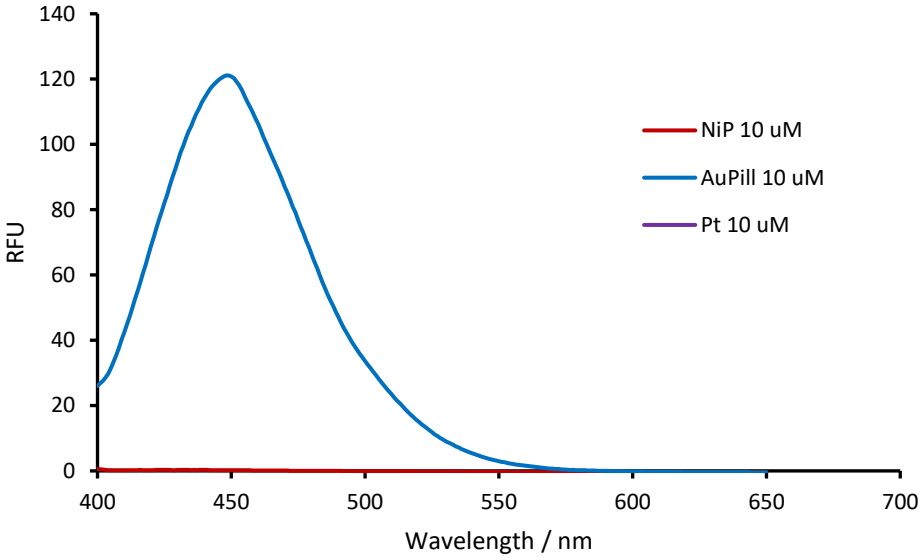


Control to test fluorescence of the nickel parent, AuPill, and platinum tetrastranded complex excited at same wavelength as the Hoechst 33258 fluorophore. (Excitation wavelength 350 nm, Emission wavelength 400-650 nm).

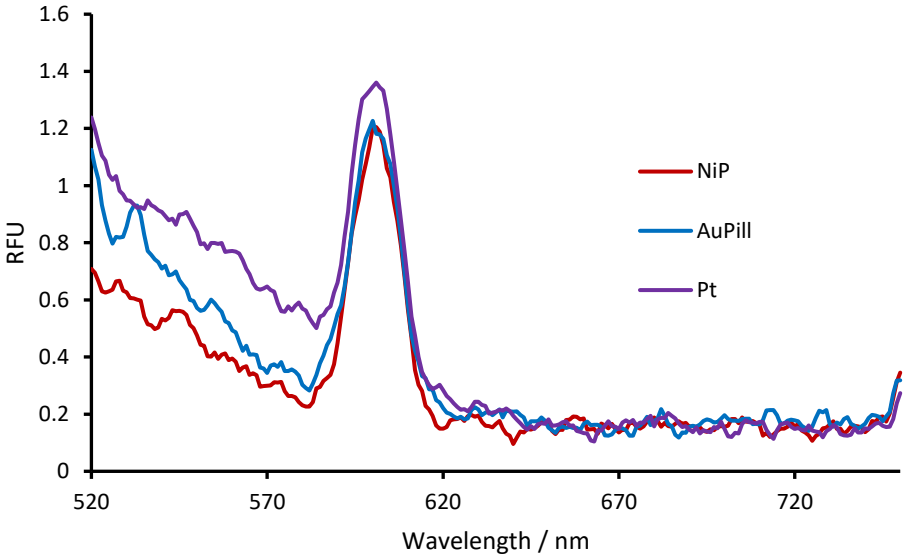


Control to test fluorescence of the NiP, AuPill and PtCyl complex excited at the same wavelength as ethidium bromide. (Excitation wavelength 500 nm, Emission wavelength 520-750 nm)

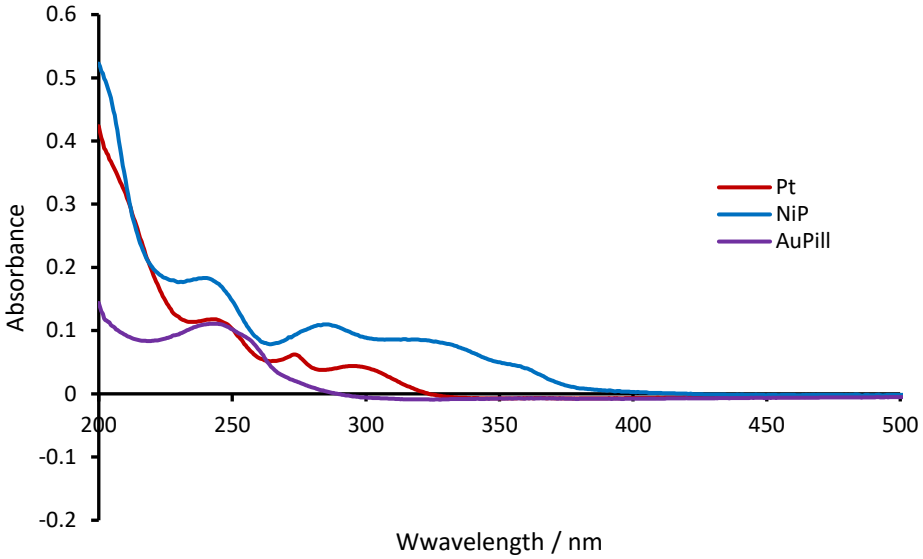


UV-vis absorbance of PtCyl, NiP and AuPill (water, 1mm cuvette, 2.5 µM).

## A3.2 EtBr displacement control

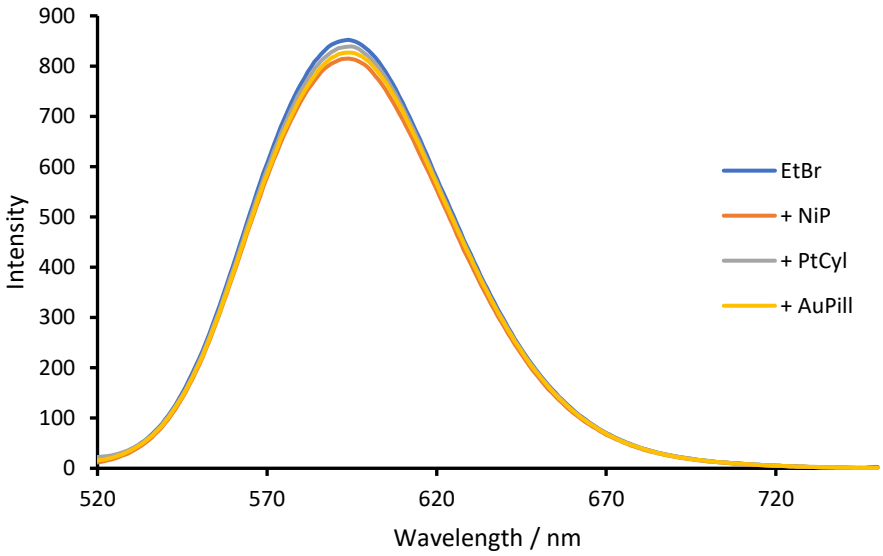


Control for fluorescence displacement of EtBr from ctDNA. EtBr 25 µM (Tris-HCl 1mM, NaCl 20 mM, pH 7.4) with the addition of NiP/PtCyl/AuPill 50 µM. EtBr and buffer concentration kept constant after addition of metal complex. (Excitation wavelength 500 nm, Emission wavelength 520-750 nm).

## A3.3 Hoechst 33258 displacement control

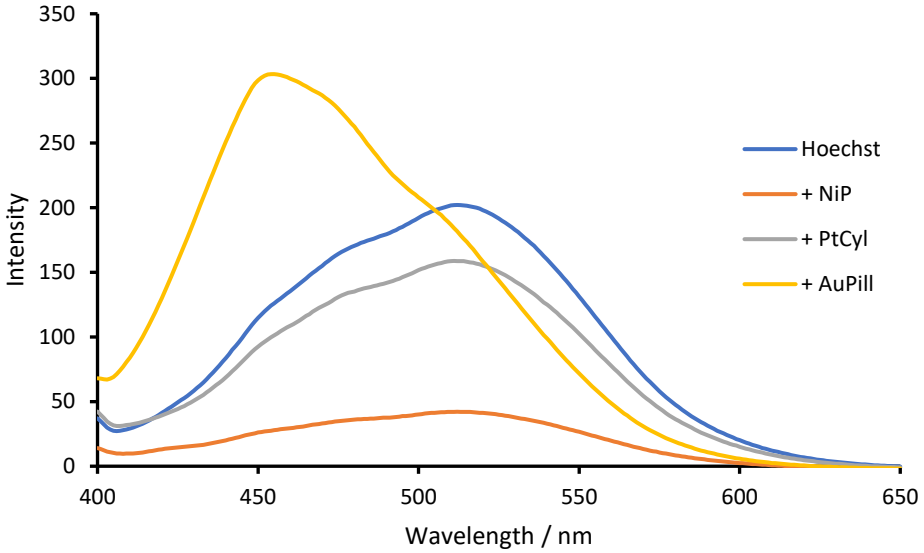


Control for fluorescence displacement of Hoechst 33258 from ctDNA. Hoechst 33258 5 µM (Tris-HCl 1mM, NaCl 20 mM, pH 7.4) with the addition of NiP/PtCyl/AuPill 50 µM. Hoechst 33258 and buffer concentration kept constant after addition of metal complex. (Excitation wavelength 350 nm, Emission wavelength 400-650 nm).

## A3.4 Calculating $C_{50}$ from fluorescence displacement data

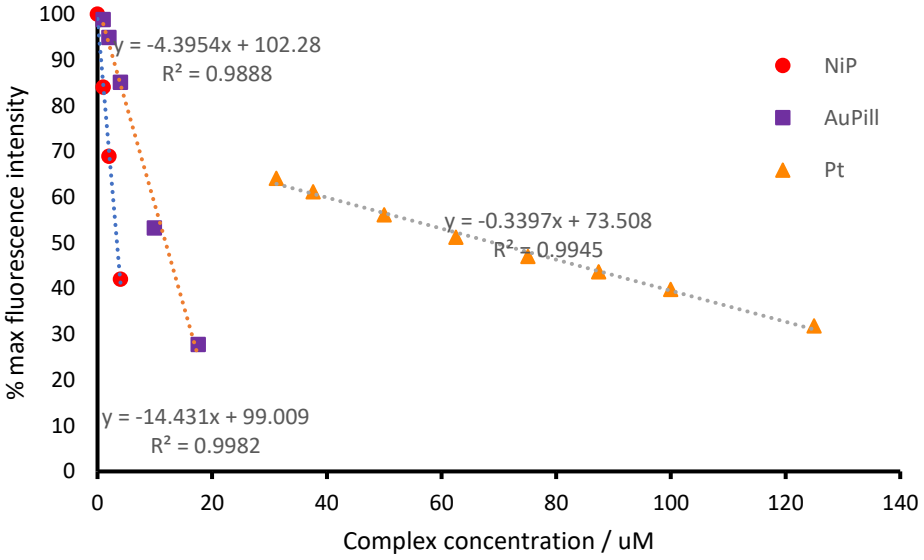


Trendlines plotted on EtBr fluorescence displacement data to calculate the concentration of complex required to reduce max fluorescence intensity to 50%.

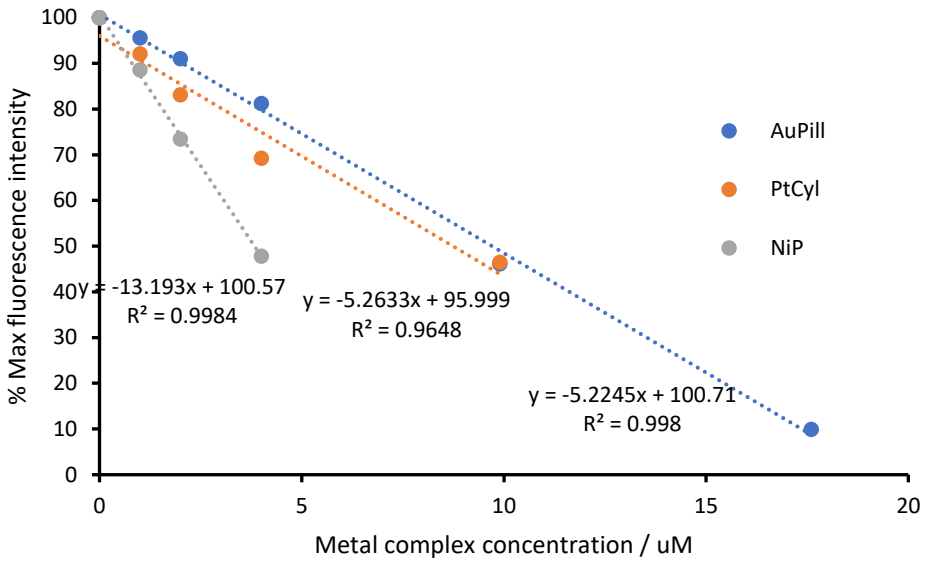


Trendlines plotted on Hoechst 33258 fluorescence displacement data to calculate the concentration of complex required to reduce max fluorescence intensity to 50%.

## A3.5 UV melting derivatives

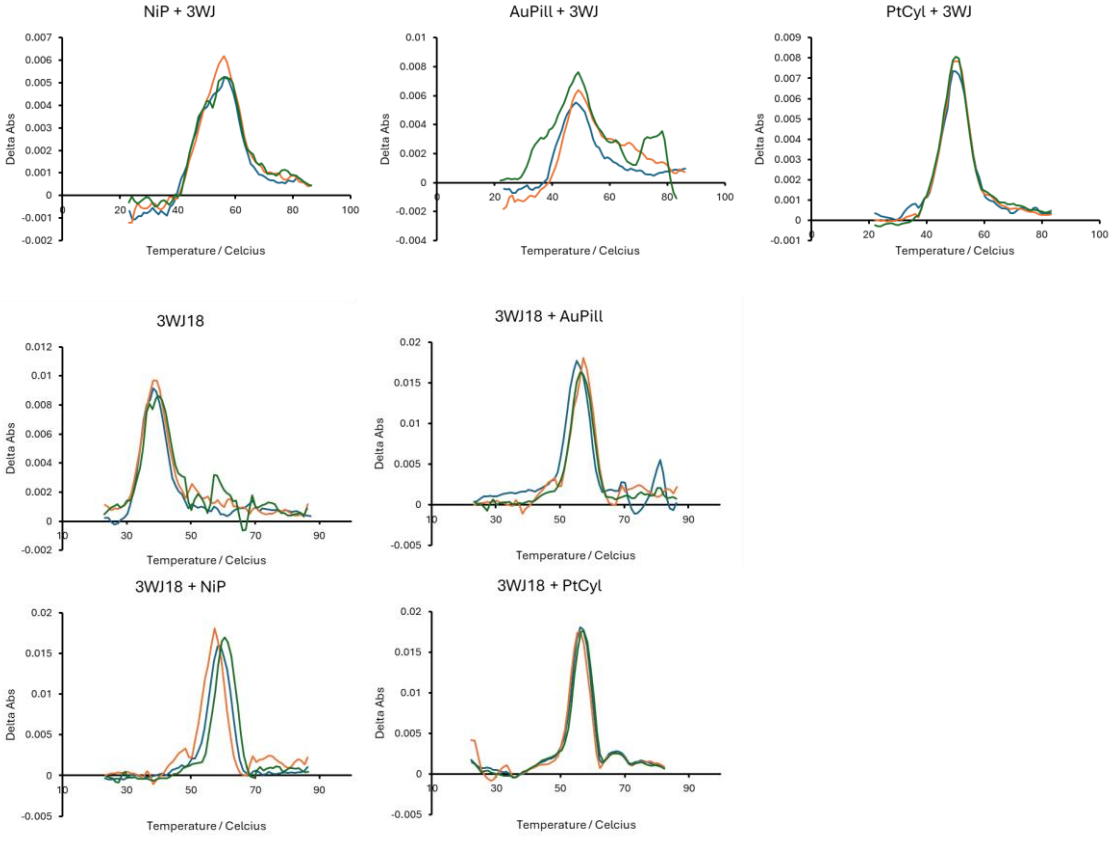

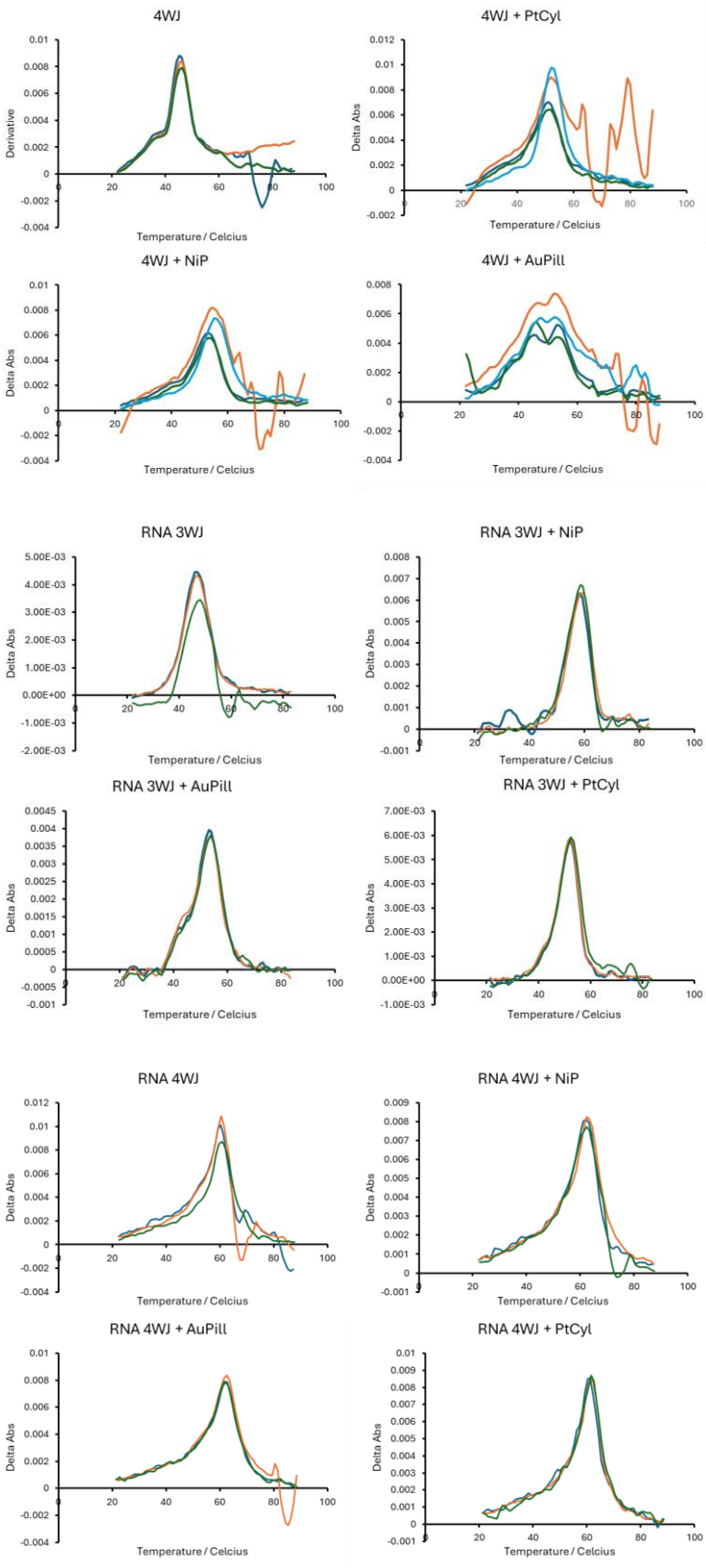
4WJ
Derivative
Temperature / Celcius
4WJ + PtCyl
Delta Abs
Temperature / Celcius
4WJ + NiP
Delta Abs
Temperature / Celcius
4WJ + AuPill
Temperature / Celcius
RNA 3WJ
Delta Abs
Temperature / Celcius
RNA 3WJ + NiP
Delta Abs
Temperature / Celcius
RNA 3WJ + AuPill
Delta Abs
Temperature / Celcius
RNA 3WJ + PtCyl
Delta Abs
Temperature / Celcius
RNA 4WJ
Delta Abs
Temperature / Celcius
RNA 4WJ + NiP
Delta Abs
Temperature / Celcius
RNA 4WJ + AuPill
Delta Abs
Temperature / Celcius
RNA 4WJ + PtCyl
Delta Abs
Temperature / Celcius

## A3.6 PAGE gel 3WJ18 alone and with metal complexes

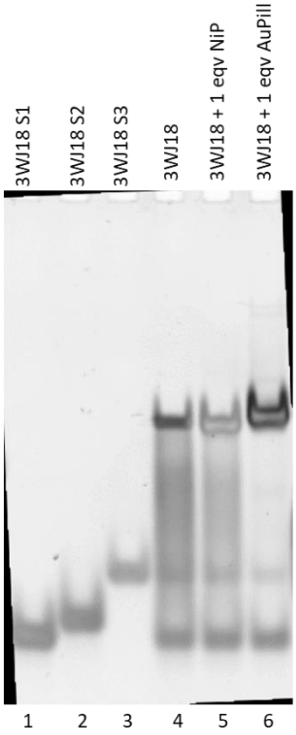


PAGE gel of 3WJ18 single strands and with NiP/AuPill (Tris base 89 mM, Boric acid 89 mM, pH 8.3, 2.5 hrs)

## A3.7 FRET melting derivatives

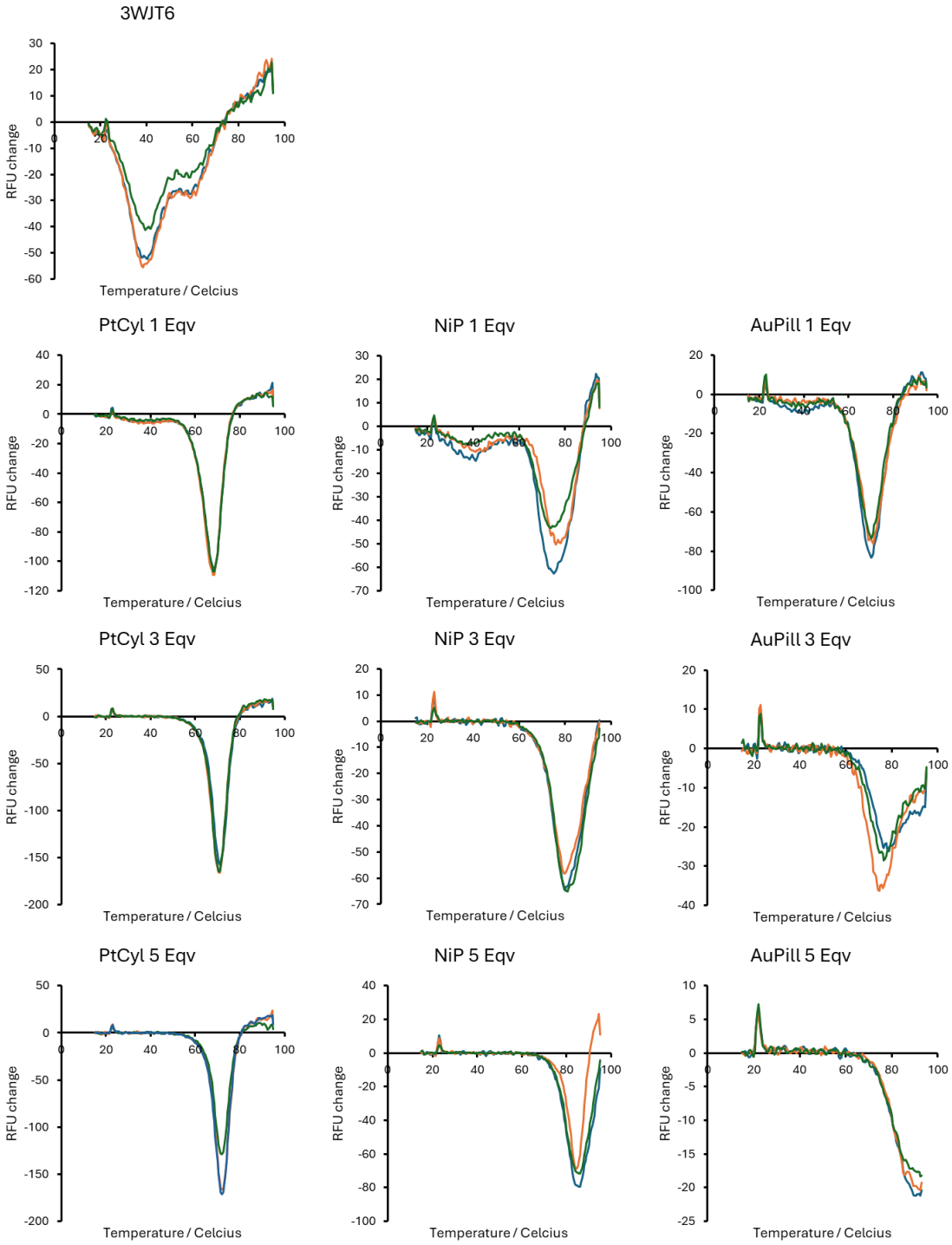


Each condition had three separate repeats shown on each graph.

## A3.8 FRET melting of 3WJT6 DNA structure

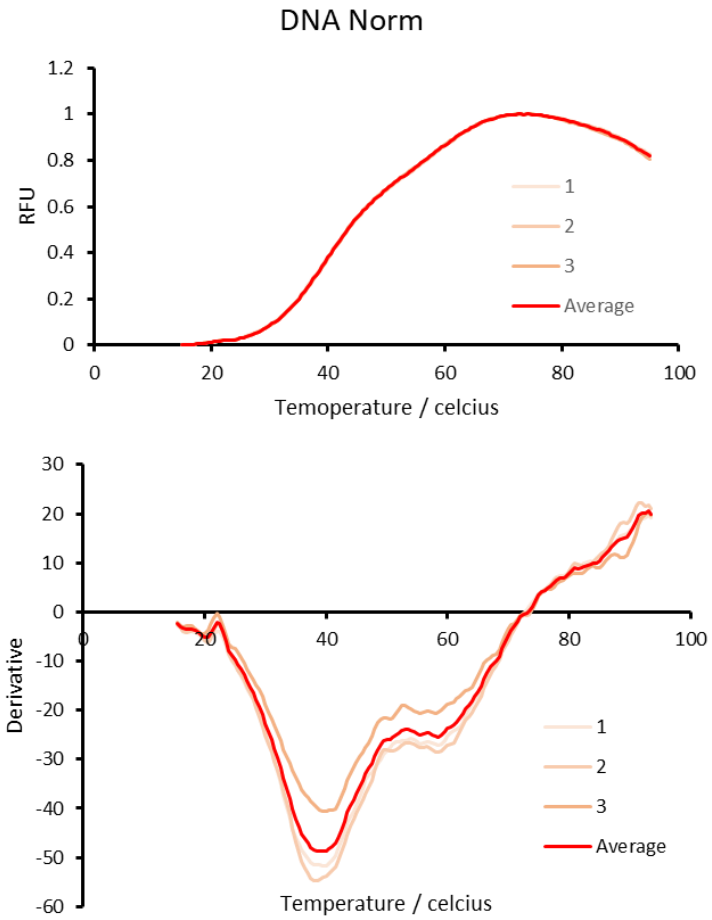


Fluorescent melting data for TAMRA-3WJT6-FAM oligo (0.2 µM, 20 µL) in sodium cacodylate buffer (10 mM Sodium Cacodylate, 100 mM NaCl pH 7.4). The derivate data was smoothed before plotting.

## A3.9 Example of PAGE competition gel processing

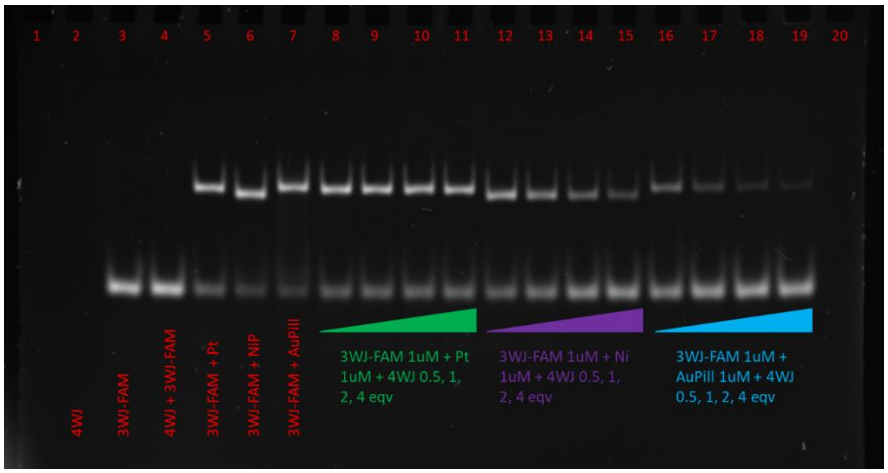


PAGE gel of FAM-3WJ competition with 4WJ (1xTris Borate buffer pH 8.3, 120 V, 2.5 hours).

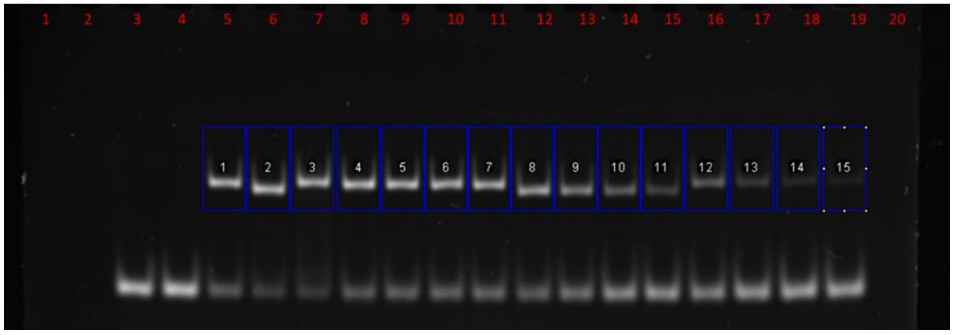


Quantification using ImageJ

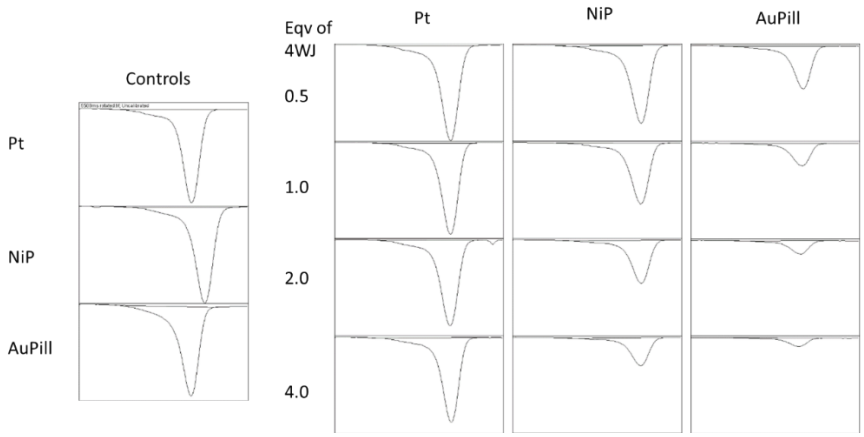


Intensity plots produced from the areas selected in imageJ

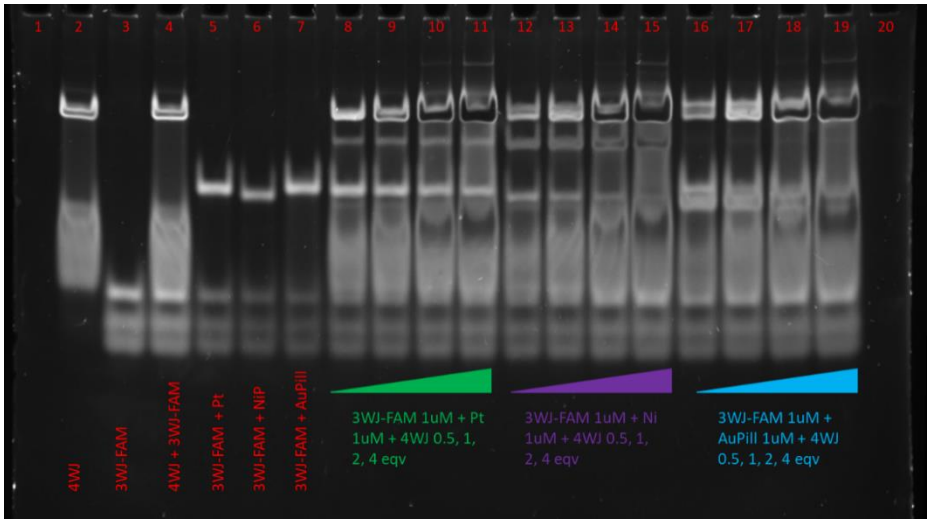


(Same PAGE gel as above but after staining) PAGE gel of FAM-3WJ competition with 4WJ (1xTris Borate buffer pH 8.3, 120 V, 2.5 hours) stained with SYBR Gold.

## A3.10 PAGE competition gels considering 4WJ as two Y-forks

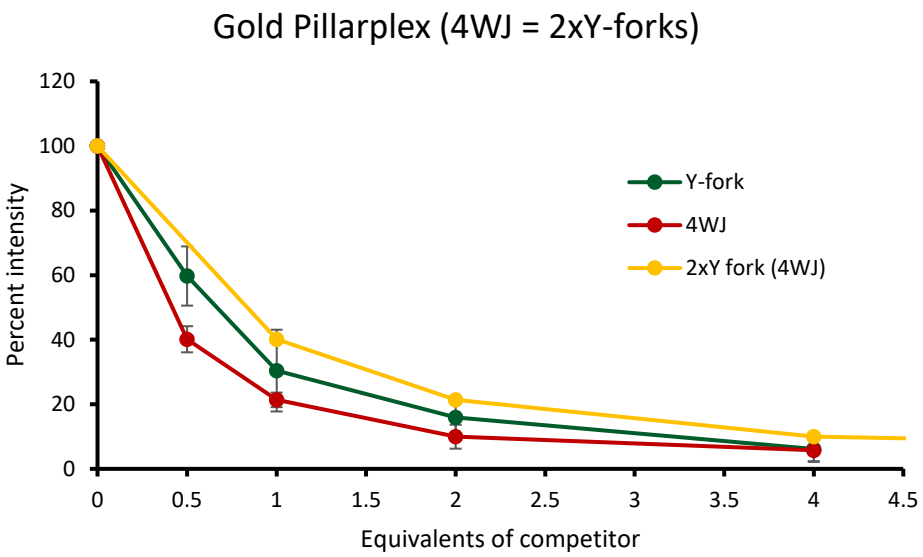


PAGE competition of 3WJ-FAM vs dsDNA, Y-fork, and 4WJ with AuPill (1xTris Borate buffer pH 8.4, 120 V, 2.5 hours, average of 3 gels). Quantification of 3WJ-FAM band intensity carried out using ImageJ. The 4WJ structure has been adjusted to consider it as two Y-forks instead of a single cruciform structure.

## A3.11 DNA base pairing predicted by RNAStructure software

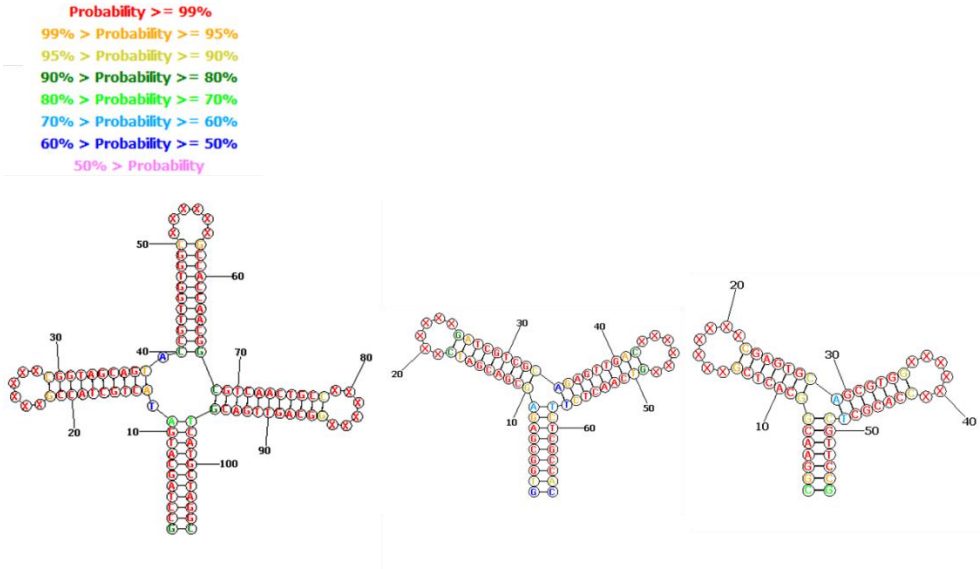


DNA 4WJ (left), 3WJ18 (middle), and 3WJ (right) structures. X represents an unknown base which is forced single stranded in this model. The X loops were added due to software limitations (maximum two strands can be folded together at a time).

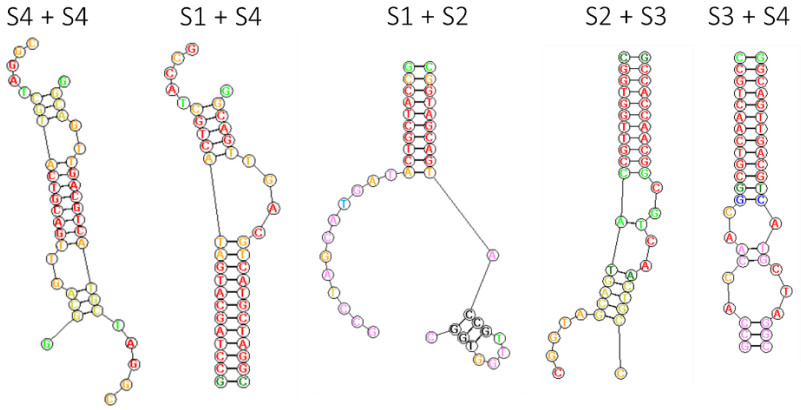


Combinations of two DNA 4WJ oligomers. Partial complementarity of S4 with S4 is shown (left).

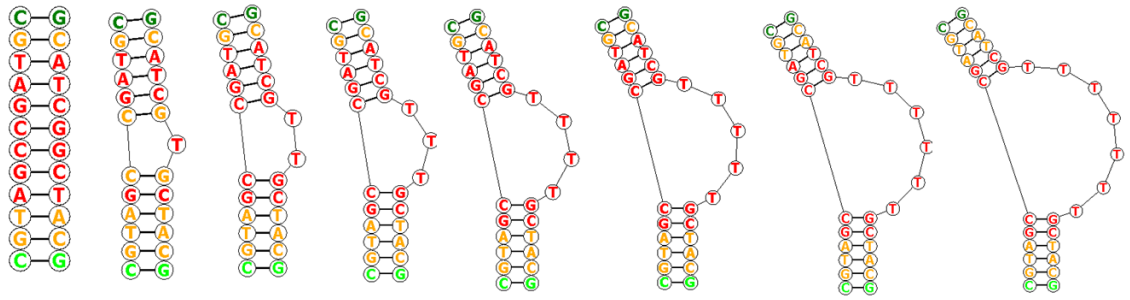

Structures of DNA bulges studied S1 + S2(0-7).

## A3.12 RNA base pairing predicted by RNAStructure software

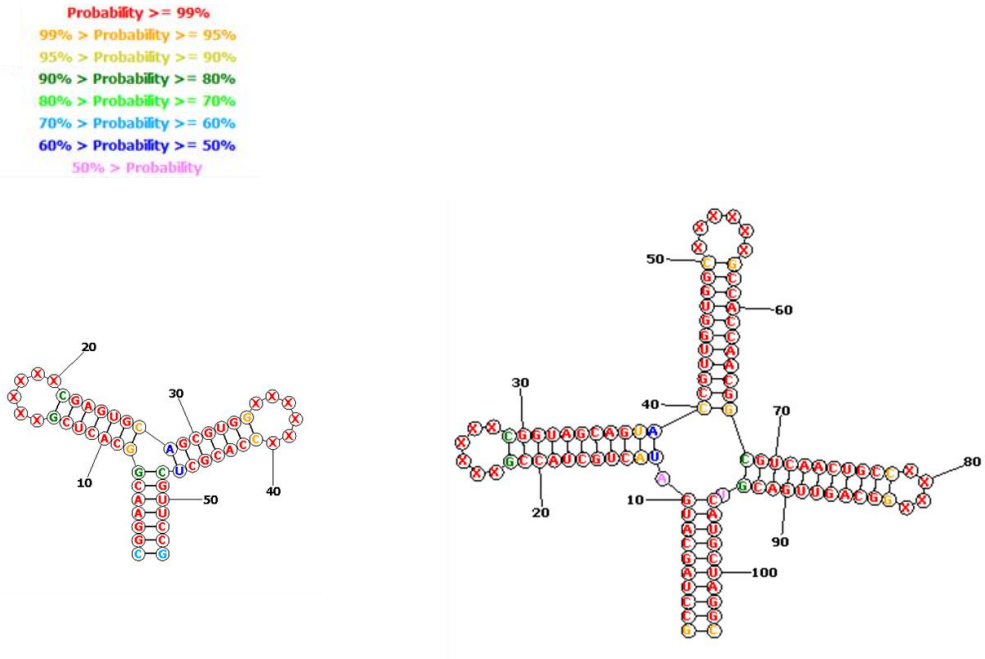


RNA 3WJ (left) and RNA 4WJ (right). X represents an unknown base which is forced single stranded in this model. The X loops were added due to software limitations (maximum two strands can be folded together at a time).

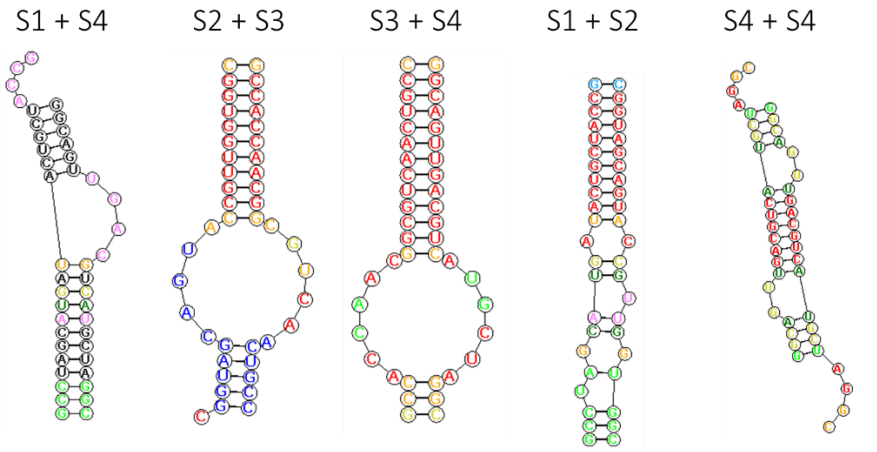


Combinations of two RNA 4WJ oligomers. Partial complementarity of S4 with S4 is shown (right).

## A3.13 Determining appropriate ammonium acetate concentration for MS

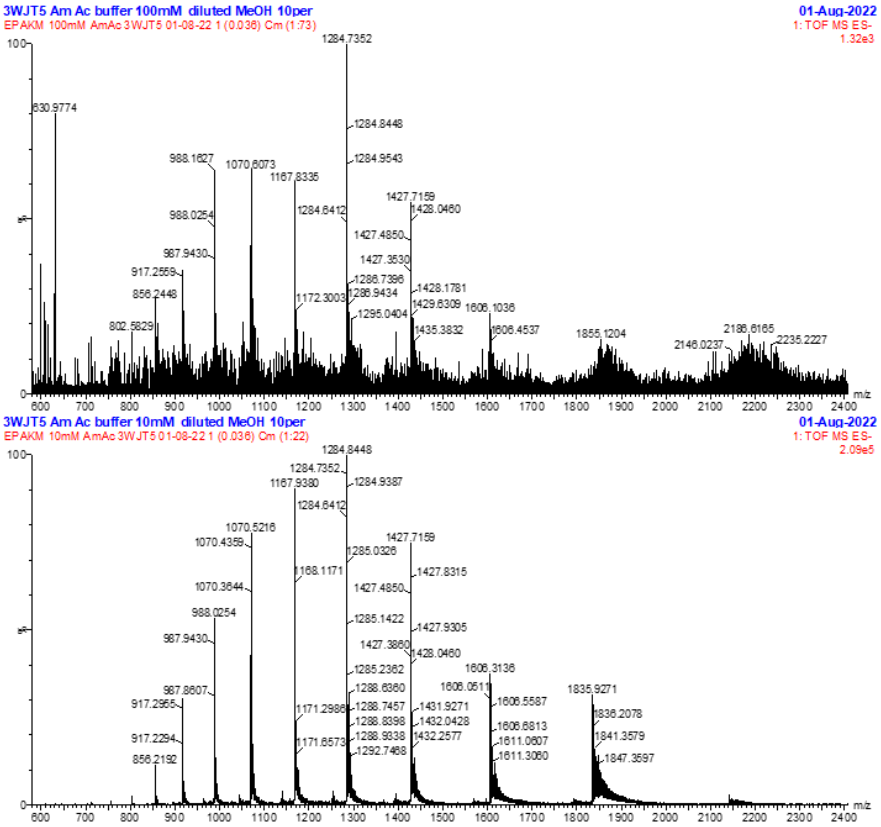


ESI-MS negative mode of 3WJT6 DNA with either 10 mM (bottom) or 100 mM (top) ammonium acetate and 10% MeOH.

## A3.14 PAGE gel of $Pd_2(L_1)_4(BF_4)_4$ with DNA bulges

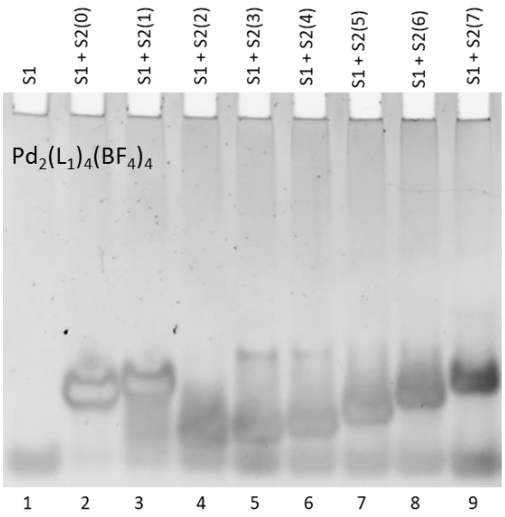


PAGE gel of $Pd_2(L_1)_4(BF_4)_4$ complex with DNA bulges (1xTris Borate buffer pH 8.3, 120 V, 2.5 hours, average of 3 gels).

## A3.15 ITC data for NiP with 3WJT6 with 0.5% ACN

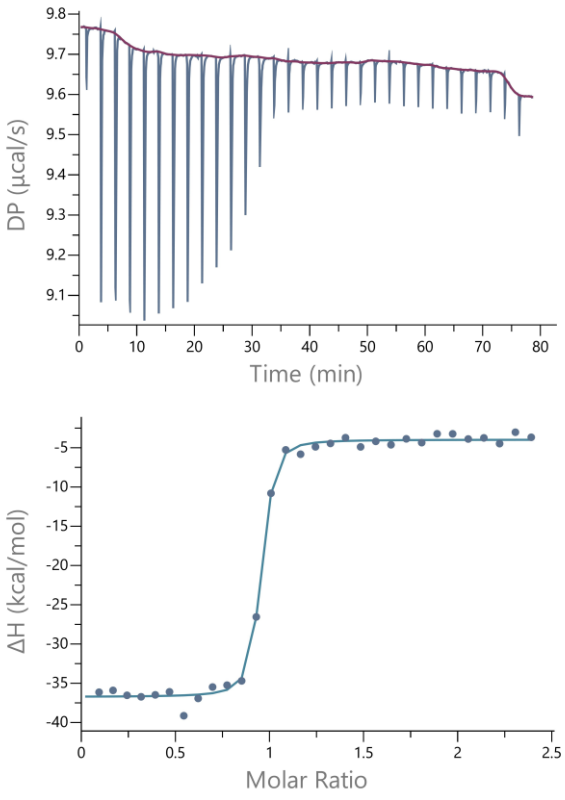


ITC titration of $Ni_2L_4Cl_4$ in sodium cacodylate buffer solution 10 mM, pH 7.4 100 mM NaCl with 0.5% acetonitrile into a solution of 3WJT6 10mM in the same buffer acetonitrile mixture. $K_D = 9.54x10^{-9}$ M, N = 0.915, ΔH = -32.7 kcalmol$^{-1}$, ΔG = -10.9 kcalmol$^{-1}$, TΔS = -21.8 kcalmol$^{-1}$

# Appendix - Chapter 4

## A4.1 Base pairing of DNA1, DNA2 and DNA3 predicted using RNAStructure software

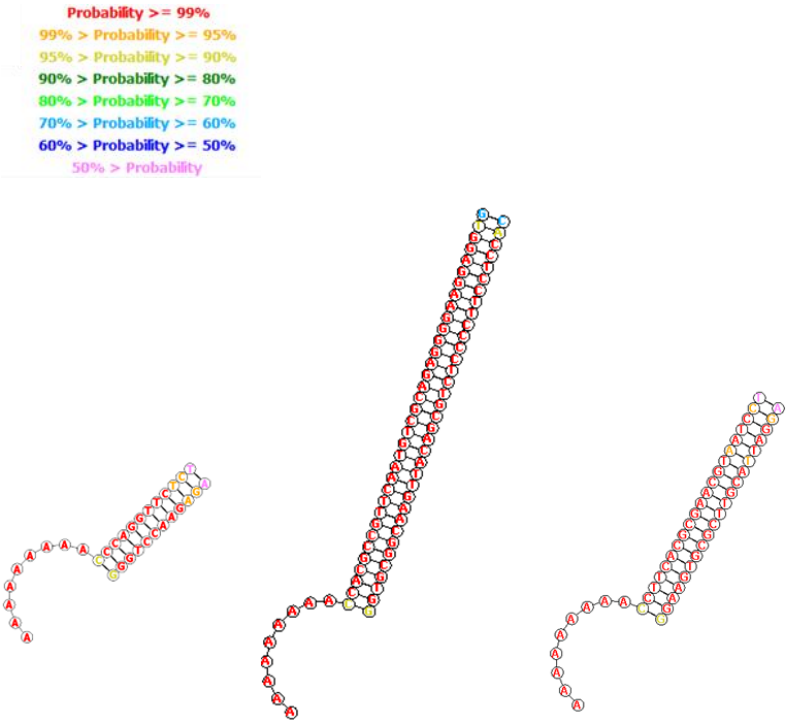


DNA1 S1 + S2 (left), DNA2 S1 + S2 (middle), and DNA3 S1 + S2 (right).

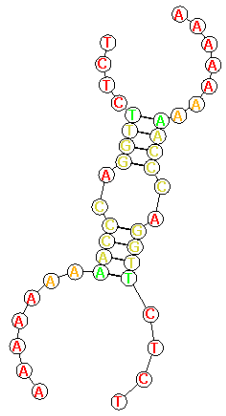

DNA1 S1 + DNA1 S1

## A4.2 Zeta potential of particles

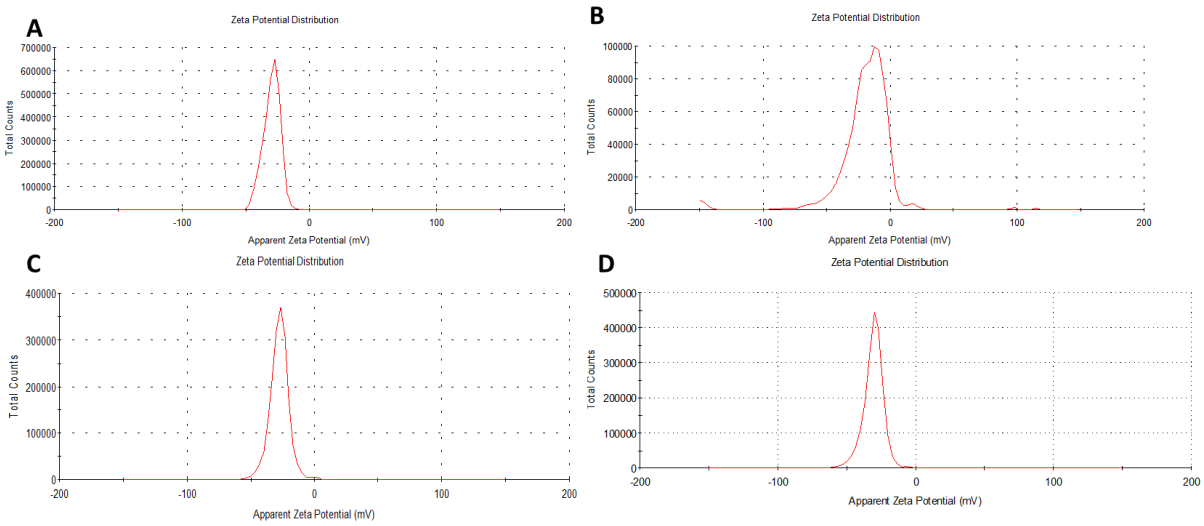


Zeta potential measurements acquired on a Malvern Zetasizer Nano ZSP. Each measurement is the average of three runs. A) AuNP13dsDNA, B) AuNP13dsDNANiP, C) AuNP13dsDNAPtCyl, and D) AuNP13dsDNAAuPill.

| Sample | Zeta / mV |
|---|---|
| AuNP13dsDNA | -29.5±6.48 |
| AuNP13dsDNANiP | -18.2±13.24 |
| AuNP13dsDNAAuPill | -30.7±6.95 |
| AuNP13dsDNAPtCyl | -27.4±7.46 |

## A4.3 Limit of detection PAGE gel

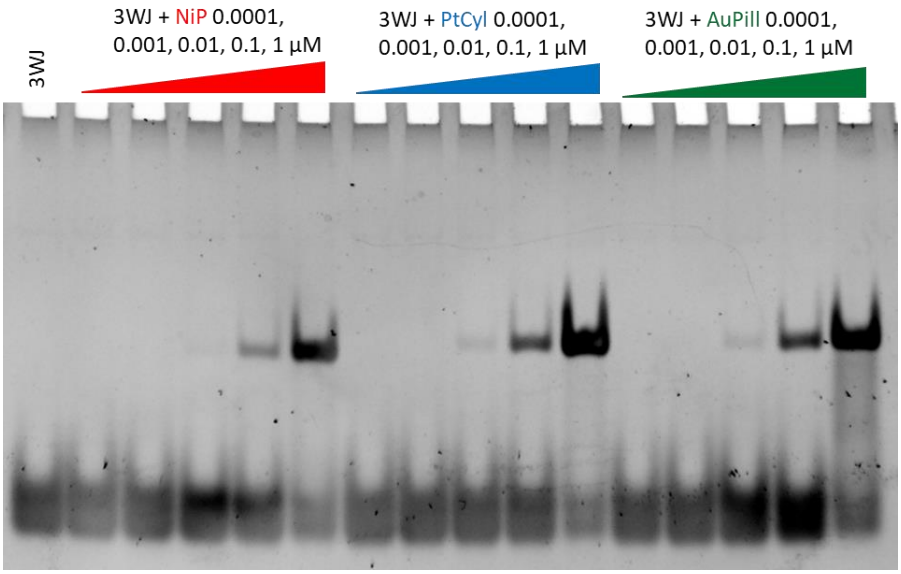


Limit of detection of each metal complex. Verified by ImageJ below.

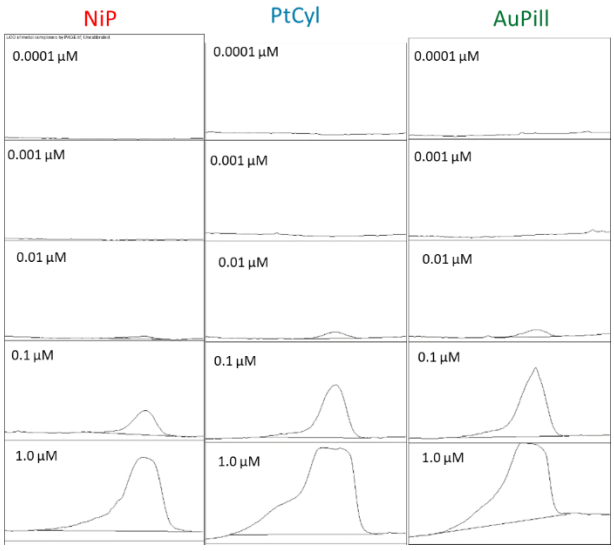


## A4.4 LD of ctDNA with higher concentration AuNp13dsDNANiP

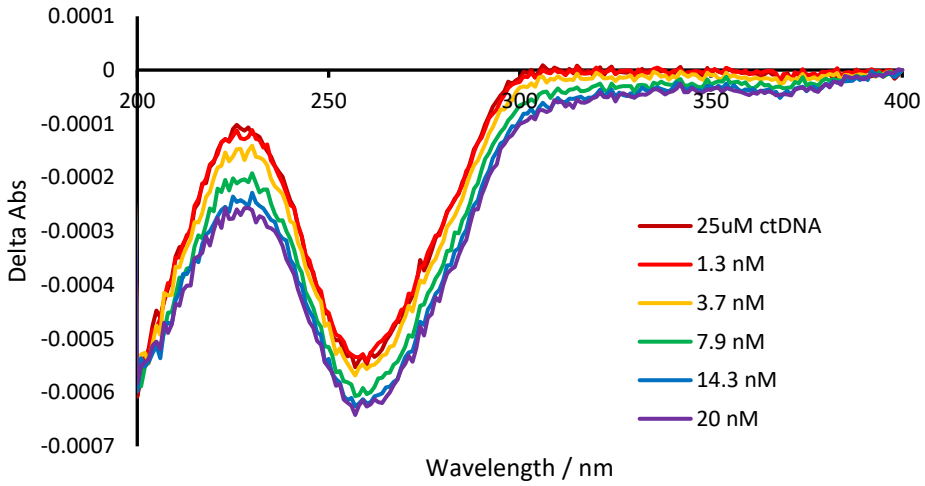


LD of ctDNA 25 µM with AuNP13dsDNA in Tris-HCl buffer (Tris 10 mM, NaCl 20 mM pH 7.2). Assuming 320 NiP per particle as calculated by ICP-MS, 20 nM AuNP13 corresponds to 6.4 µM NiP, a ratio of 4 base pairs per complex (R4)

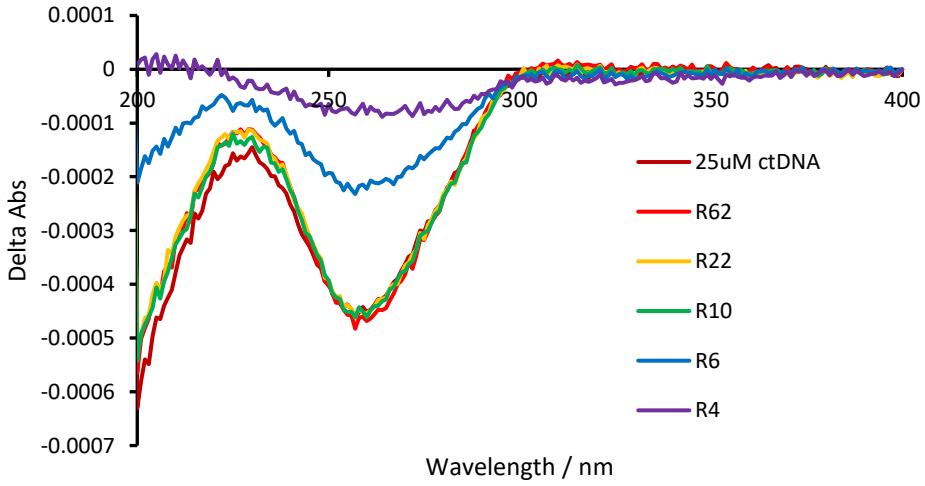


LD of ctDNA 25 µM with NiP (Tris 10 mM, NaCl 20 mM pH 7.2).

## A4.5 Full agarose gel of AuNP13dsDNA particles with 3WJ18

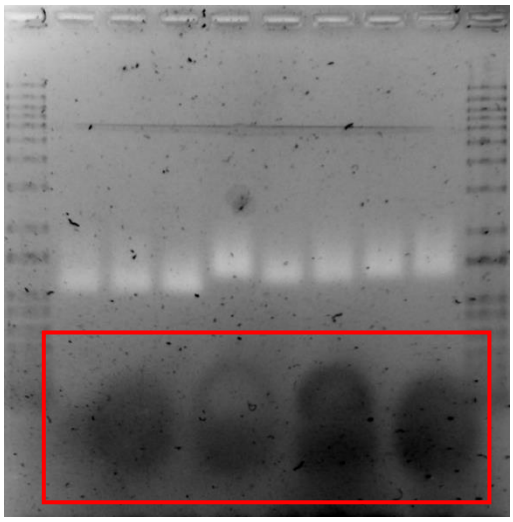

Agarose gel of AuNP13 with thiolated DNA1 oligomers and loaded with no metal complex, NiP, PtCyl, or AuPill, with and without the presence of 3WJ18 (89 mM Tris base, 89 mM Boric acid, pH 8.3, 1.6 % agarose, 50 V, 6 hours, SYBR Gold stained). 3WJ18 oligomers are highlighted in red box.

## A4.6 Method for determining particle concentration from TEM and ICPMS

Calculating number of gold atoms per particle:

$$N = \frac{N_A \rho \pi D^3}{6Mr}$$

Where $N_A$ = Avagadro's number, ρ = Density of gold (19.32 $gcm^{-3}$)[1], D = diameter of particles, and Mr is the molecular mass of gold. Since ρ, $N_A$, and Mr are known, this equation simplifies to:

$$N = 30.89685812D^3$$

This can be used to calculate the mass of a gold nanoparticle with diameter D by multiplying by the mass of a gold atom.

Dividing the concentration of gold measured by the mass of a gold particle, and dividing by avagadro's number gives the molar concentration of gold in the solution. Dilution factors for the ICP-MS experiment must then be taken into account to give the concentration of gold in the starting solution.

Calculating the concentration of a metal complex in solution was carried out in much the same way with the mass of the given metal in a single metal complex used instead of the mass of a particle. This can then be divided by the concentration of gold particles to calculate the number of metal complexes per particle.

It was not practical to carry out ICP-MS on all gold nanoparticles solutions. The concentration of gold nanoparticles was estimated from the UV absorbance SPR band if the size of the particles are known.[2] (Final concentrations of reported particle solutions were determined by ICP-MS)

## A4.7 TEM image used to quantify AuNP size

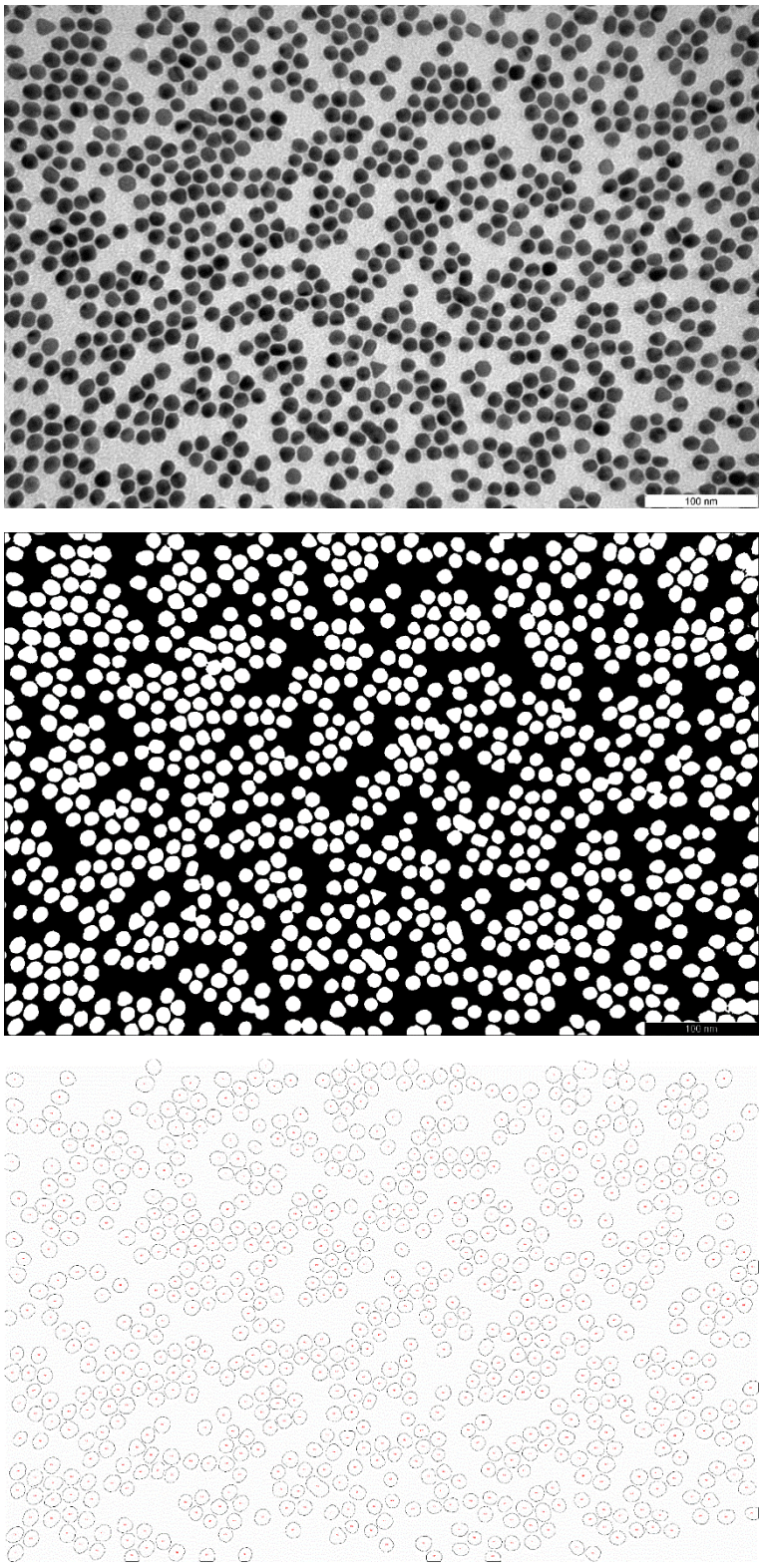


ImageJ used for segmenting image, resulting histogram is plotted in Chapter 4.

## A4.8 DLS data monitoring stability of particles tabulated

DLS data for the UV measurements of the particle stability in water over a period of 32 days

| Sample | SPR / nm | Abs @ SPR | FWQM / nm |
|---|---|---|---|
| AuNP13dsDNA | 523.5 | 0.372 | 65.0 |
| + 3 days | 523.5 | 0.356 | 63.0 |
| + 7 days | 523.5 | 0.362 | 64.0 |
| + 32 days | 523.0 | 0.356 | 64.5 |
| AuNP13dsDNA Pt | 524.0 | 0.262 | 60.5 |
| + 3 days | 524.5 | 0.257 | 61.0 |
| + 7 days | 524.0 | 0.244 | 59.0 |
| + 32 days | 535.5 | 0.364 | 97.5 |
| AuNP13dsDNA AuPill | 524.0 | 0.308 | 64.5 |
| + 3 days | 524.5 | 0.312 | 64.5 |
| + 7 days | 523.5 | 0.315 | 66.0 |
| + 32 days | - | - | - |
| AuNP13dsDNA NiP | 526.0 | 0.272 | 60.5 |
| + 3 days | 527.0 | 0.274 | 61.5 |
| + 7 days | 530.0 | 0.262 | 60.0 |
| + 32 days | 527.0 | 0.273 | 63.5 |

DLS data for the stability of particles in water over time a period of 32 days

| **Sample** | **Hydrodynamic diameter / nm** | **PDI** |
|---|---|---|
| AuNP13 | 18.08 | 0.125 |
| AuNP13dsDNA 0 days | 28.52 | 0.173 |
| AuNP13dsDNA 3 days | 26.62 | 0.173 |
| AuNP13dsDNA 7 days | 25.56 | 0.166 |
| AuNP13dsDNA 32 days | 25.99 (98.8%)<br>4853 (1.2%) | 0.219 |
| AuNP13dsDNA NiP 0 days | 42.42 (97.5%)<br>4497 (2.5%) | 0.232 |
| AuNP13dsDNA NiP 3 days | 41.82 (97.7%)<br>4698 (2.3%) | 0.229 |
| AuNP13dsDNA NiP 7 days | 40.91 (97.5%)<br>4590 (2.5%) | 0.227 |
| AuNP13dsDNA NiP 32 days | 41.95 (70.3%)<br>748.5 (23.8%)<br>482 (5.9%) | 0.526 |
| AuNP13dsDNA Pt 0 days | 26.18 | 0.111 |
| AuNP13dsDNA Pt 3 days | 25.98 | 0.12 |
| AuNP13dsDNA Pt 7 days | 25.32 | 0.124 |
| AuNP13dsDNA Pt 32 days | 91.77 (88%)<br>860.1 (9.7%)<br>4269 (2.4%) | 0.357 |
| AuNP13dsDNA AuPill 0 days | 26.85 | 0.192 |
| AuNP13dsDNA AuPill 3 days | 27.09 | 0.198 |
| AuNP13dsDNA AuPill 7 days | 26.00 | 0.184 |
| AuNP13dsDNA AuPill 32 days | 27.63 (99.8%)<br>4716 (0.2%) | 0.219 |

## A4.9 Stability of functionalised particles in DMEM

Monitoring the stability of AuNP13dsDNA, AuNP13dsDNANiP, AuNP13dsDNAPt, and AuNP13dsDNAAuPill in DMEM media over a period of 18 hours by UV-vis absorbance. (The baseline measurement for AuNP13dsDNA did not work due to experimental error, but the trend observed is still visible)

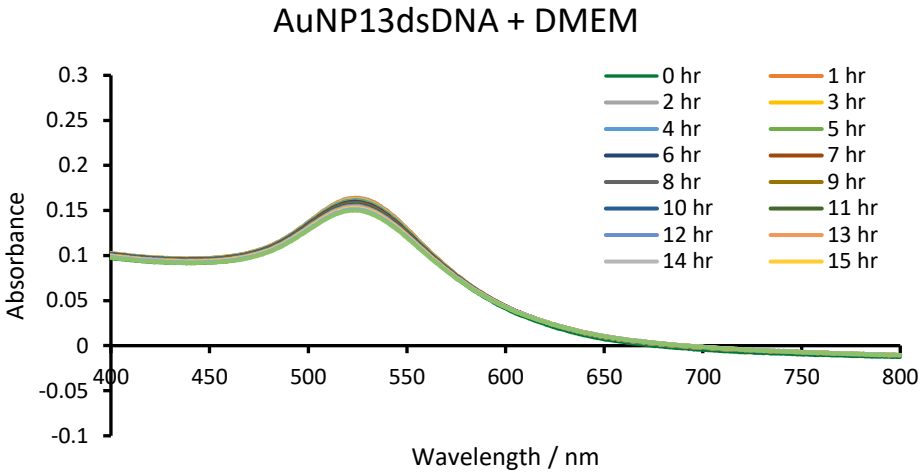


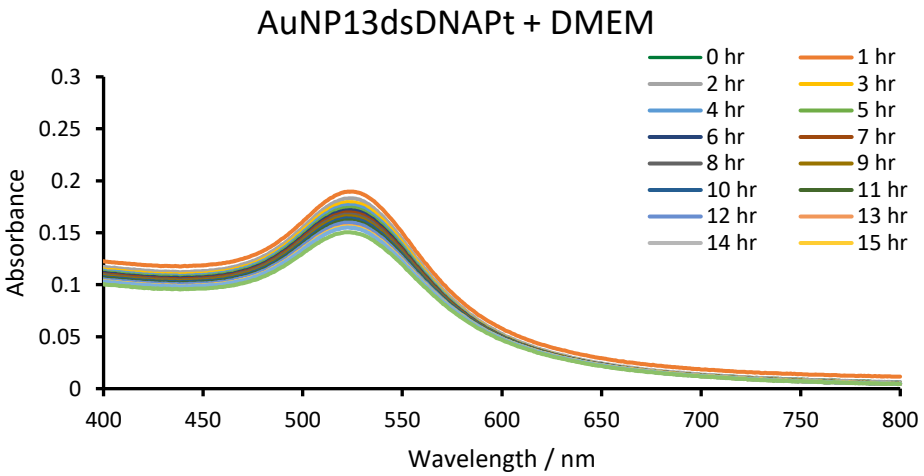


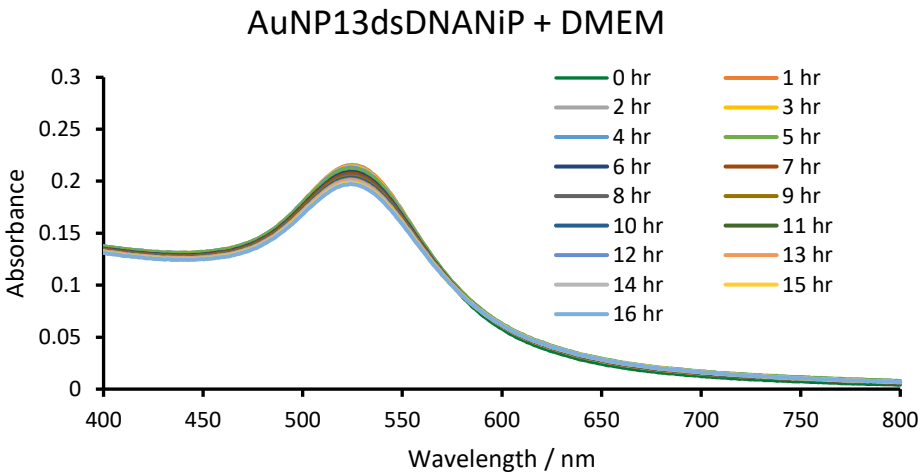

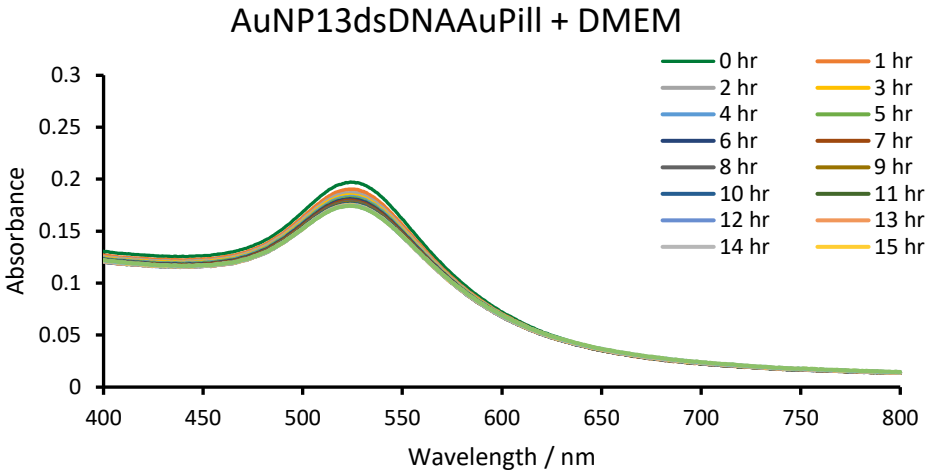


## References

1. Carney, R. P.; Kim, J. Y.; Qian, H.; Jin, R.; Mehenni, H.; Stellacci, F.; Bakr, O. M., Determination of nanoparticle size distribution together with density or molecular weight by 2D analytical ultracentrifugation. *Nature Communications* **2011,** *2* (1), 335.

2. Haiss, W.; Thanh, N. T. K.; Aveyard, J.; Fernig, D. G., Determination of Size and Concentration of Gold Nanoparticles from UV−Vis Spectra. *Analytical Chemistry* **2007,** *79* (11), 4215-4221.